water

Rainfall-Induced Landslides

Influencing, Modelling and Hazard Assessment

Edited by
Qingzhao Zhang and Danyi Shen

mdpi.com/journal/water

MDPI

Rainfall-Induced Landslides: Influencing, Modelling and Hazard Assessment

Rainfall-Induced Landslides: Influencing, Modelling and Hazard Assessment

Guest Editors

Qingzhao Zhang
Danyi Shen

Guest Editors

Qingzhao Zhang
Department of Geotechnical Engineering
College of Civil Engineering
Tongji University
Shanghai
China

Danyi Shen
Institute of Geotechnical Engineering
College of Civil Engineering
and Architecture
Zhejiang University
Hangzhou
China

For citation purposes, cite each article independently as indicated on the article page online and as indicated below:

Lastname, A.A.; Lastname, B.B. Article Title. *Journal Name* **Year**, *Volume Number*, Page Range.

Contents

Editorial

Rainfall-Induced Landslides: Influencing, Modelling and Hazard Assessment

Qingzhao Zhang [1,*] and Danyi Shen [2]

[1] Department of Geotechnical Engineering, College of Civil Engineering, Tongji University, Shanghai 200092, China

[2] Institute of Geotechnical Engineering, College of Civil Engineering and Architecture, Zhejiang University, Hangzhou 310058, China; shendanyi@zju.edu.cn

* Correspondence: zhangqingzhao@tongji.edu.cn

1. Introduction to the Special Issue

Landslide hazards pose a great threat to people's lives and the safety of their property all over the world, especially in mountainous areas. Rainfall is one of the main trigger factors of landslides, and the induced mechanism is complicated and affected by multiple environmental factors such as rainfall intensity, rainfall duration, landform and soil layer structure, and has a high degree of regional specificity and sudden occurrence [1,2]. Rainfall has a significant impact on the mechanical properties of slope soil and underground rock mass, which usually leads to soil softening and pore water pressure increase, and then leads to landslide instability, forming a large number of destructive debris flow or collapse [3,4]. The occurrence process of landslides induced by rainfall includes soil and water loss and erosion on the surface, and also involves water infiltration into the underground, causing deep soil saturation, thus triggering a landslide. The migration and convergence patterns of water flow under different rainfall characteristics have a key influence on the triggering mechanism of a landslide [5]. Extreme rainfall events caused by climate change have become more frequent in recent years, exacerbating the risk of landslides. Therefore, landslide prediction and risk management have received more and more attention from the scientific community [6–8]. This Special Issue is devoted to cutting-edge research on the causes, mechanisms, modeling and disaster management methods of rain-induced landslides, with a view to providing new insights and effective mitigation strategies.

In the Special Issue, the research covers the analysis and monitoring of landslide formation, the development and verification of landslide prediction models, the influencing factors and failure prediction of slope stability, the cause and prediction of debris flow and so on. The 14 articles in the Special Issue are roughly divided into three categories. (1) Rainfall-induced landslides: Based on a variety of methods, such as model tests, numerical simulation, artificial intelligence algorithms and theoretical deduction, these papers (nine in total) deeply analyzed how rainfall causes a landslide and its prediction methods, including the development and application of rainfall-induced landslide monitoring systems, the establishment of risk prediction models and the analysis of rainfall-induced landslide mechanisms. (2) Slope stability analysis: Based on field investigations, laboratory tests, numerical simulation and other methods, these papers (three in total) put forward the control factors affecting slope stability and the method of instability prediction. (3) Mutual control factors and prediction methods of debris flow stability: Based on actual debris flow disaster cases, these papers (two in total) used indoor experiments and numerical algorithms to study the factors affecting the stability of debris flow areas and their prediction schemes, revealed the spatial distribution characteristics and causes of the mutual control factors of debris flow, and established a risk prediction method for debris flow disasters based on automatic calculation algorithms.

In some papers, the correlative mechanism and prediction method of rainfall-induced landslides are studied by using physical models. Paswan et al. [Contribution 1] developed a rain-induced landslide monitoring system to solve the problem of limited landslide prediction in northern India during the rainy season which can record the real-time displacement and volumetric water content of the slope. Meanwhile, to further test the applicability of the monitoring system, a physical slope model was made based on actual scenarios, and a physical test of the rain-induced slope was carried out. The results show that the developed system can effectively monitor the gradient and abrupt change process of rainfall-induced landslides. Taking the Woda landslide in the upper reaches of the Jinsha River as the engineering background, Li et al. [Contribution 2] designed a model test to study the development of paleo-landslides with cracks under the action of rainfall infiltration and revealed the activation mechanism of rainfall and cracks on paleo-landslides. The depth of slope infiltration directly affects the depth of landslide failure. Therefore, Xiao et al. [Contribution 3], taking the Xiashu loess slope as the engineering background, conducted field rainfall model tests and obtained the main discrimination index of slope rainfall infiltration depth, which laid the foundation for the establishment of a slope rainfall infiltration prediction model.

In addition, some other papers have used numerical simulation to analyze the failure mode and mechanical response characteristics of a slope under the action of rainfall. Huang et al. [Contribution 4] took an overturning bank slope of Lancang River in China as the engineering background and adopted a numerical simulation method to analyze the seepage field characteristics and mechanical response characteristics (displacement, stress-strain, plastic deformation, etc.) of the bank slope under the action of rainfall from two and three dimensions, respectively, for the hydrodynamic failure modes of the bank slope under different rainfall conditions. The evolution model of overturning slope deformation under the action of rainfall was revealed. Based on the DuMux, which is a simulator of fluid flow in porous media, and the concept of the local factor of safety (LFS), Moradi et al. [Contribution 5] conducted a comparative study on the application effects of three simplified models (without considering the dynamic interaction between groundwater flow and soil mechanics) and the complete two-phase flow fully coupled fluid mechanics model for the evaluation of the stability of variable saturated landslide-prone slopes under two rainfall intensity conditions. The results show that the LFS results obtained by the three simplified models and the fully coupled model are consistent. KC et al. [Contribution 6] took the landslide and debris flows in Kalli village, which is in the Acham District of Nepal, located in the Lesser Himalayas Mountains, as the engineering research background; they carried out numerical simulation based on a multiphase flow model and adopted GRASS GIS 8.3 to analyze the evolution characteristics of debris flow during landslide movement. Yu et al. [Contribution 7] took the fanling landslide in Shandong, China, as the engineering background; they conducted a numerical study on the response characteristics of the seepage field of the landslide under different rainfall conditions and found that short-term fluctuating rainstorms were more likely to cause landslides than long-term stable rainfall.

At the same time, some papers systematically analyze the landslide disasters induced by rainfall through theoretical research, establishing a disaster analysis model and putting forward a landslide failure time prediction method. Tseng et al. [Contribution 8] took the landslide in Pingtung County, Taiwan Province, as the research object. By establishing the evaluation indexes, namely, the rainfall trigger index (I_{RT}) and an index of slope environmental strength potential (I_{SESP}), of landslide damage to land use after four heavy rainfall events, they could effectively estimate the damage of rainfall-induced landslides to land use. Tao et al. [Contribution 9] used four kinds of filters to test the velocity time series, compared and analyzed the prediction effect of landslide failure time, and finally proposed a hierarchical prediction method combining a short-term smoothing filter (SSF) and a long-term smoothing filter (LSF). They then verified its practicability. Both debris flow disasters and landslides have the characteristics of sudden occurrence and are closely

related to topography, precipitation and geological conditions. However, the main cause of debris flow is the increase in surface runoff caused by sudden rainfall or snowmelt, and the hydraulic action makes the soil and rock mixed materials flow rapidly in the gully, which is very likely to pose a threat to people's lives and the safety of their property along the entire foot of the slope [9]. Wang et al. [Contribution 10] collected soil samples in the Beichuan mud flow gully region, chosen as the engineering background, and analyzed the spatial distribution pattern and causes of the mutual control factors of stability in the dangerous area of debris flow, which mainly include soil particle size, permeability coefficient, shear strength, porosity, etc., so as to provide a scientific basis for the prediction of debris flow disasters in this area.

Furthermore, some papers have studied the induced behavior prediction of landslides and debris flow under the action of rainfall by using artificial intelligence algorithms. Choo et al. [Contribution 11] adopted the CTRL-T automatic calculation algorithm to obtain the optimal allowable distance between the weather station and the debris flow disaster area suitable for the topography of Korea in order to solve the problem of researchers' subjectivity in the selection of weather stations in previous studies of debris flow in South Korea, which affected the reliability of the results. A nomogram for sediment disaster risk prediction and early warning was further established and applied to past projects. The results showed that the risk of sediment flow could be predicted 4–5 h in advance. Based on a field test, Xiao et al. [Contribution 3] further optimized a BP neural network by using the particle swarm optimization algorithm; they established a PSO-BP neural network prediction model and compared it with the other two models. The results show that the new model has a higher prediction accuracy in predicting the infiltration depth of the Xiashu loess slope under different rainfall conditions. Yang et al. [Contribution 12] used the decision tree model (GBDT) after gradient elevation of the Google Earth Engine (GEE) cloud platform to conduct a dynamic assessment of landslide risk and a landslide sensitivity analysis of the Three Gorges Reservoir area of China. The research results show that the model maintained a high accuracy in the dynamic assessment of landslide hazards. Subsequently, it can provide theoretical and technical support for real-time landslide hazard assessments and disaster reduction strategies in similar areas around the world.

Finally, in addition to rainfall-induced landslides, some scholars have focused their research on the causes of slope instability and the resolution of uncertainty in slope stability evaluation. Gui et al. [Contribution 13] took a large landslide-prone area in the Central Mountain Range of Taiwan as the research object and adopted multi-temporal satellite and aerial images, field investigations, geophysical tests and other technical means to propose the main trigger factors that induced sudden and local slope instability failure, namely, rainwater intrusion, the rising of river bed elevation and the erosion of large slope foot banks. Li et al. [Contribution 14] regarded the spatial distribution of slope soil shear strength parameters as random and utilized their mean value, variance and correlation scale as characteristics to establish the correlation between relevant parameters and the factor of safety (FS), providing an economical and effective tool for dealing with uncertainty in slope stability analysis.

2. A Summary of the Special Issue

This Special Issue focuses on the multidimensional effects of rainfall-induced landslides, numerical simulation methods and disaster assessment systems. A rainfall-induced landslide is an important type of geological disaster; its triggering mechanism is complicated, and it is affected by many factors such as rainfall intensity, geological structure, terrain slope and so on. The research in this Special Issue covers the physical mechanism of landslide occurrence, the relationship between rainfall intensity and landslide incidence, the construction and optimization of landslide models, and risk assessment models of landslide hazards. Through the combination of physical model tests, artificial intelligence algorithms, numerical simulation, theoretical analysis and other methods, this collection of

studies provides a scientific basis for establishing a comprehensive and effective landslide disaster management and emergency response system.

The research results in this Special Issue provide a new perspective and method for understanding and coping with rainfall-induced landslides. Future research can further integrate multidisciplinary monitoring and modeling techniques to achieve accurate landslide prediction and risk control through dynamic acquisition and analysis of real-time data. At the same time, strengthening regional and international cooperation will be a key step in dealing with landslide disasters under climate change.

Author Contributions: The two authors contributed equally to the preparation of the article. Conceptualization, Q.Z. and D.S.; writing—original draft preparation, Q.Z. and D.S.; writing—review and editing, Q.Z. and D.S. All authors have read and agreed to the published version of the manuscript.

Conflicts of Interest: The authors declare no conflicts of interest.

List of Contributions

1. Paswan, A.P.; Shrivastava, A.K. Evaluation of a Tilt-Based Monitoring System for Rainfall-Induced Landslides: Development and Physical Modelling. *Water* **2023**, *15*, 1862.
2. Li, X.; Wu, R.; Han, B.; Song, D.; Wu, Z.; Zhao, W.; Zou, Q. Evolution Process of Ancient Landslide Reactivation under the Action of Rainfall: Insights from Model Tests. *Water* **2024**, *16*, 583.
3. Xiao, P.; Guo, B.; Wang, Y.; Xian, Y.; Zhang, F. Research on the Prediction of Infiltration Depth of Xiashu Loess Slopes Based on Particle Swarm Optimized Back Propagation (PSO-BP) Neural Network. *Water* **2024**, *16*, 1184.
4. Huang, J.; Tang, S.; Liu, Z.; Zhang, F.; Dong, M.; Liu, C.; Li, Z. A Case Study for Stability Analysis of Toppling Slope under the Combined Action of Large Suspension Bridge Loads and Hydrodynamic Forces in a Large Reservoir Area. *Water* **2023**, *15*, 4037.
5. Moradi, S.; Huisman, J.A.; Vereecken, H.; Class, H. Comparing Different Coupling and Modeling Strategies in Hydromechanical Models for Slope Stability Assessment. *Water* **2024**, *16*, 312.
6. KC, D.; Naqvi, M.W.; Dangi, H.; Hu, L. Rainfall-Triggered Landslides and Numerical Modeling of Subsequent Debris Flows at Kalli Village of Suntar Formation in the Lesser Himalayas in Nepal. *Water* **2024**, *16*, 1594.
7. Yu, P.; Shi, W.; Cao, Z.; Cao, X.; Wang, R.; Wu, W.; Luan, P.; Wang, Q. Numerical Analysis of Seepage Field Response Characteristics of Weathered Granite Landslides under Fluctuating Rainfall Conditions. *Water* **2024**, *16*, 1996.
8. Tseng, C.-M.; Chen, Y.-R.; Tsai, C.-Y.; Hsieh, S.-C. An Integration of Logistic Regression and Geographic Information System for Development of a Landslide Hazard Index to Land Use: A Case Study in Pingtung County in Southern Taiwan. *Water* **2024**, *16*, 1038.
9. Tao, Y.; Zhang, R.; Du, H. Failure Prediction of Open-Pit Mine Landslides Containing Complex Geological Structures Using the Inverse Velocity Method. *Water* **2024**, *16*, 430.
10. Wang, Q.; Xie, J.; Yang, J.; Liu, P.; Xu, W.; Yuan, B. Research on Spatial Distribution Pattern of Stability Inter-Controlled Factors of Fine-Grained Sediments in Debris Flow Gullies—A Case Study. *Water* **2024**, *16*, 634.
11. Choo, K.-S.; Choi, J.-R.; Lee, B.-H.; Kim, B.-S. Parameter Sensitivity Analysis of a Korean Debris Flow-Induced Rainfall Threshold Estimation Algorithm. *Water* **2024**, *16*, 828.
12. Yang, K.; Niu, R.; Song, Y.; Dong, J.; Zhang, H.; Chen, J. Dynamic Hazard Assessment of Rainfall Induced Landslides Using Gradient Boosting Decision Tree with Google Earth Engine in Three Gorges Reservoir Area, China. *Water* **2024**, *16*, 1638.
13. Gui, M.-W.; Chu, H.-A.; Ding, C.; Lee, C.-C.; Ho, S.-K. Hazard Mitigation of a Landslide-Prone Area through Monitoring, Modeling, and Susceptibility Mapping. *Water* **2023**, *15*, 1043.
14. Li, Y.; Zhang, F.; Yeh, T.-C.J.; Hou, X.; Dong, M. Cross-Correlation Analysis of the Stability of Heterogeneous Slopes. *Water* **2023**, *15*, 1050.

References

1. Sun, Y.; Zhang, J.; Wang, H.; Lu, D. Probabilistic thresholds for regional rainfall induced landslides. *Comput. Geotech.* **2024**, *166*, 106040. [CrossRef]
2. Lu, M.; Wang, H.; Sharma, A.; Zhang, J. A stochastic rainfall model for reliability analysis of rainfall-induced landslides. In *Georisk: Assessment and Management of Risk for Engineered Systems and Geohazards*; Taylor & Francis: Abingdon, UK, 2024; pp. 1749–9518.
3. Luo, C.; Chen, T.; Fu, Q.; Chen, G.; Li, S. Analysis of Characteristics and Cause of Debris Flow in Yangjia Gully in Beichuan County. *J. Southwest Univ. Sci. Technol.* **2019**, *34*, 25–31.
4. Liu, S.; Kou, G.; Feng, J. Discussion on the geological environment of the causes on the debris flow in Beichuan County. *Technol. Innov. Appl.* **2018**, *1*, 177–179.
5. Mahima, D.; Jayasree, P.K.; Balan, K. Mechanism of Root Reinforcement Involved in Rainfall-Induced Shallow Landslide Mitigation: A Review. *Indian Geotech. J.* **2024**, *54*, 244–257. [CrossRef]
6. Pakash, S. Historical Records of Socio-Economically Significant Landslides in India. *South Asia Disaster Stud.* **2011**, *4*, 177–204.
7. Guerriero, L.; Prinzi, E.P.; Calcaterra, D.; Ciarcia, S.; Di Martire, D.; Guadagno, F.M.; Ruzza, G.; Revellino, P. Kinematics and Geologic Control of the Deep-Seated Landslide Affecting the Historic Center of Buon Albergo, Southern Italy. *Geomorphology* **2021**, *394*, 107961. [CrossRef]
8. Smith, D.M.; Oommen, T.; Bowman, L.J.; Gierke, J.S.; Vitton, S.J. Hazard Assessment of Rainfall-induced Landslides: A Case Study of San Vicente Volcano in Central El Salvador. *Nat. Hazards* **2015**, *75*, 2291–2310. [CrossRef]
9. Choi, J.R. An Analysis of Debris-Flow Propagation Characteristics and Assessment of Building Hazard Mapping Using FLO-2D-The Case of Chuncheon Landslide Area. *Crisis Emerg. Manag.* **2018**, *14*, 91–99. [CrossRef]

Numerical Analysis of Seepage Field Response Characteristics of Weathered Granite Landslides under Fluctuating Rainfall Conditions

Peng Yu [1,2,3], Wenqing Shi [1], Zhonghua Cao [1], Xichong Cao [1], Ran Wang [2], Wenyu Wu [4], Pengyu Luan [1,*] and Qigang Wang [5,*]

[1] Key Laboratory of Geological Safety of Coastal Urban Underground Space, Ministry of Natural Resources, Qingdao Geo-Engineering Surveying Institute, Qingdao 266101, China; 13210276328@163.com (P.Y.)
[2] Key Laboratory of Coupling Process and Effect of Natural Resources Elements, Beijing 100055, China
[3] Key Laboratory of Geological Disaster Risk Prevention and Control of Shandong Provincial Emergency Management Department (Under Preparation), Jinan 250014, China
[4] Department of Environmental Science and Engineering, Ocean University of China, Qingdao 266100, China
[5] Qingdao Geotechnical Investigation and Surveying Research Institue, Qingdao 266035, China
* Correspondence: luanpy@qddzgckc.com (P.L.); baomidanwei@126.com (Q.W.)

Abstract: The threat and destructiveness of landslide disasters caused by extreme rainfall are increasing. Rainfall intensity is a key factor in the mechanism of rainfall-induced landslides. However, under natural conditions, rainfall intensity is highly variable. This study focuses on the Fanling landslide and investigates the effects of varying rainfall intensity amplitudes, rainfall durations, and total rainfall amounts on landslide behavior. Three experimental groups were established, and ten rainfall conditions were simulated numerically to analyze the seepage field response of the landslide under fluctuating rainfall conditions. The results indicate that (1) there are positive correlations between the final pore pressure and both the amplitude and duration of rainfall intensity; (2) the pore water pressure response in the upper slope changes significantly, initiating deformation; and (3) the total rainfall amount is the most direct factor affecting the pore pressure response and landslide deformation. Compared to long-term stable rainfall, short-term fluctuating rainstorms are more likely to trigger landslides. These findings enhance our understanding of landslide mechanisms under fluctuating rainfall, providing valuable insights for disaster prevention and mitigation.

Keywords: fluctuating rainfall; rainfall-induced landslides; seepage field response; numerical simulation

1. Introduction

With the frequent human activities and the increasing scale of construction projects, urbanization has accelerated globally, especially in China [1]. This rapid urbanization has led to an increase in extreme weather events and has posed greater challenges and costs in managing these events due to the higher population density in cities [2–4]. Among these extreme weather events, irregular heavy rainfall has become increasingly threatening and destructive [5,6]. In 2023, China experienced a total of 37 heavy rainfall processes, with a cumulative surface rainfall of 240 mm. According to the statistical yearbook of the Ministry of Emergency Management [7], there were 3666 geological disasters in China in 2023, with landslides being the most prevalent (Figure 1). For instance, in July 2023, a rainstorm in Chongqing led to a series of geological disasters resulting in 25 deaths and disappearances. In August, a sudden landslide in Liangshan Prefecture, Sichuan Province, caused by short-term heavy rainfall resulted in 52 casualties.
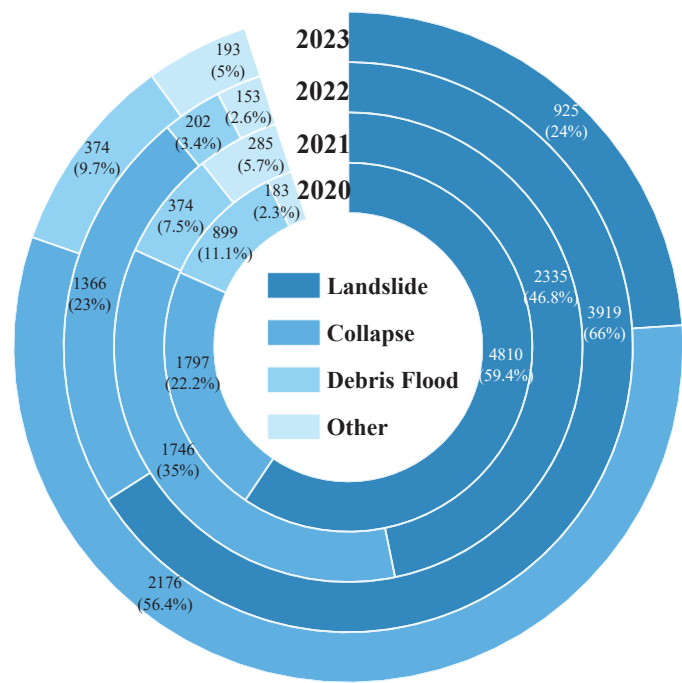
Figure 1. Number of geological hazards in China (2020–2023) [7].

Many engineering studies have shown that slope soil under rainfall infiltration is prone to instability and failure due to water seepage [8]. Rainwater infiltration during rainfall increases the saturation of slope soil and pore water pressure, reducing the shear resistance of the soil due to increased pore pressure and decreased matric suction in unsaturated soil areas. Key indicators for measuring rainfall include rainfall intensity [9], rainfall duration [10], and rainfall type [11]. Researchers have studied how these rainfall factors affect landslide occurrences. Concepts such as the cumulative rainfall duration [12] and intensity [13], critical cumulative rainfall [14], continuous probability rainfall threshold [15], and rainfall attenuation coefficient [16] have been proposed to explore the relationship between rainfall and landslides and to develop warning curves. Liu et al. [17] proposed a regional LEW slope units model combining rainfall threshold modeling and a susceptibility evaluation to predict the probability of landslides caused by rainfall in Chongqing. Soumik and Biswajit [18] determined the relationship between rainfall and landslide occurrence based on previous methods and the intensity duration (I-D). They determined the optimal fitting distribution of rainfall data in the Gawar Himalayas. Sun et al. [19] proposed a probability threshold statistical method based on support vector machines using machine learning, which can consider whether to trigger complex boundaries of mountain landslides. Rashad et al. [20] proposed a suitable hydraulic model for uncertainty propagation analysis to address the nonlinear and high-dimensional rainfall-induced landslide RILS problem. Hugh et al. [21] studied the impact of spatial rainfall patterns on shallow landslides. Ma et al. [22] set different rainfall patterns and improved the accuracy of predicting the landslide failure probability from the perspective of the spatial variability of soil.

Although rainfall intensity is a crucial factor in landslide research, it is highly volatile under natural conditions. There is no systematic consensus on how changes in rainfall intensity, amplitude, and rate affect the evolution and stability of landslides. Previous studies by the author's team on fully weathered granite landslides have examined the impact of rainfall intensity on slope stability and proposed a landslide warning curve [23]. This article extends that research by focusing on the impact of rainfall intensity fluctuations

on the seepage field, an area not comprehensively covered in prior research. The findings will deepen our understanding of the mechanisms behind landslides induced by fluctuating rainfall and guide disaster prevention and mitigation efforts.

2. Summary of the Research Area

2.1. Landslide Characteristics

The Fanling landslide is in Laoshan District, Qingdao, Shandong Province, China (Figure 2). As of 2023, the permanent population is 513,700 and the gross domestic product is 115.089 billion yuan. The Fanling landslide is an ancient landslide, formed from loose accumulated layers during the Quaternary and modern periods. The front edge of the landslide is about 3–4 m away from the sea surface of the Yellow Sea. The sliding surface is located in fully weathered granite and is in a pushover-type broken line sliding failure mode. There have been two recorded landslide events in this area, occurring on 11 August 2007, and 23 July 2020, both of which were triggered by extreme rainfall.
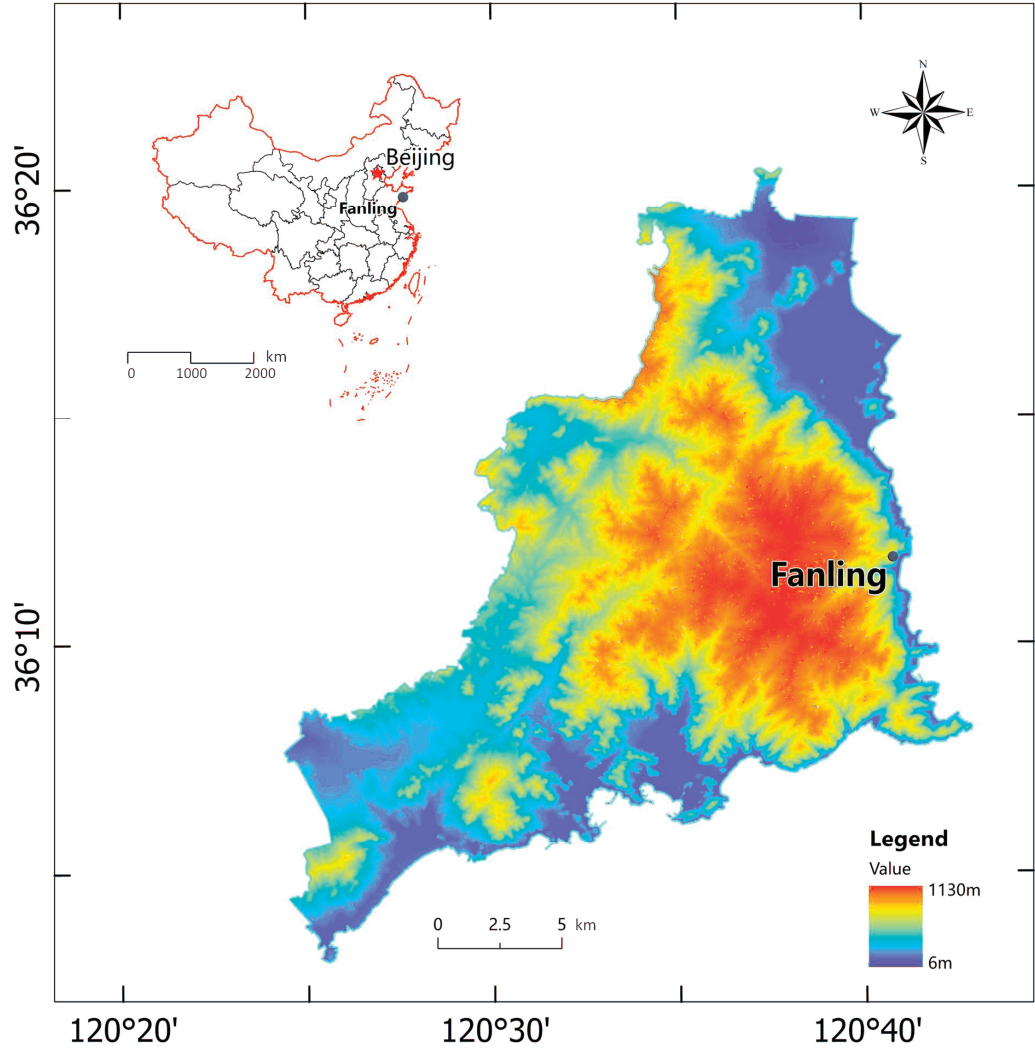
Figure 2. Overview of the Fanling landslide.

2.2. Analysis of Fluctuating Rainfall Characteristics

The research area has a temperate continental monsoon climate with marine influences. The interaction between subtropical airflow moving westward and northward and cold air moving eastward and southward frequently results in rainfall. When these airflows intersect strongly, they often induce extreme rainfall. According to years of monitoring data, heavy rainfall in the study area mainly occurs from early July to late August (Figure 3). The area experiences three primary heavy precipitation patterns, shear lines, cold eddies, and typhoon precipitation, which are relatively evenly distributed [24].
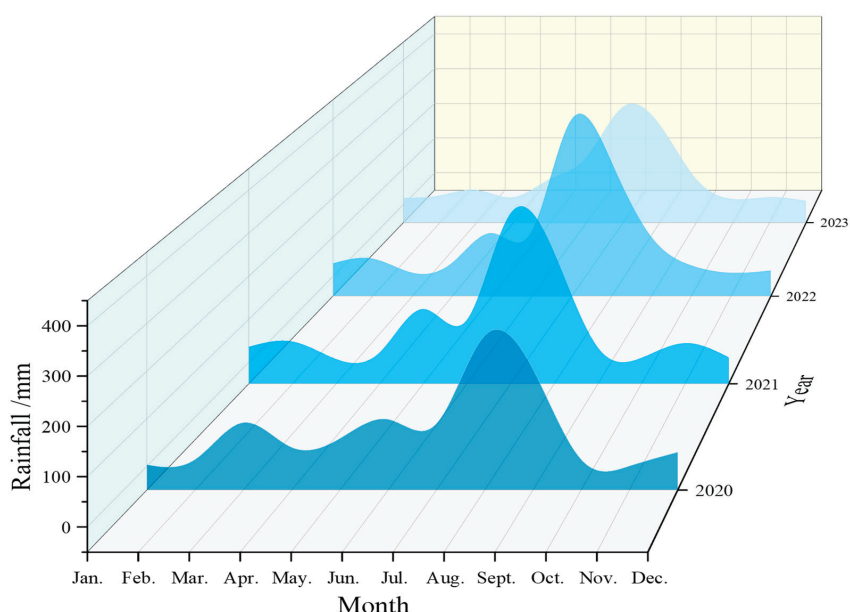
Figure 3. Monthly average rainfall in the research area (2020~2023).

On 11 August 2007, Laoshan District experienced a heavy rainstorm once in 50 years, leading to the Fanling landslide (Figure 4a,c), and according to rainfall data, 6 consecutive days of rainfall in the week led up to the landslide disaster in 2007. Starting from August 8th, the precipitation gradually increased daily until the landslide occurred on the evening of the 11th. The average rainfall intensity from 6th to 11th was 0.69 mm/h, 2.25 mm/h, 0.39 mm/h, 0.81 mm/h, 2.14 mm/h, and 2.53 mm/h, respectively. The accumulated precipitation during these 6 days reached 209 mm. Heavy rainfall began at noon on 10 August 2007, when the landslide occurred. The rainfall intensity was not constant but had strong fluctuations, and the hourly rainfall intensity also varied. There were four high peaks in rainfall intensity, with peak rainfall intensities of 4.15 mm/h, 4.48 mm/h, 4.75 mm/h, and 4.53 mm/h, respectively, indicating a multi-peak fluctuating heavy rainfall. The maximum amplitude ratio of rainfall intensity per hour was 983%, and the cumulative precipitation induced by disasters reached 107.5 mm, a typical extreme rainfall-induced landslide (Figure 4b).

On 23 July 2020, also affected by heavy rainfall, the Fanling landslide experienced another slide (Figure 4d,f). Before the landslide disaster on 22 July, the daily rain reached 175.96 mm, with a cumulative precipitation of nearly 350 mm and an average rainfall intensity of 7.33 mm/h. At 0:00 on the 23rd, the peak rainfall intensity of the landslide reached 25.21 mm/h, which was an unimodal heavy rainfall with one rainfall peak. The maximum amplitude of rainfall intensity per hour was 186%, and the cumulative pre-

cipitation induced by the disaster reached 170.3 mm, ultimately leading to the landslide (Figure 4e).
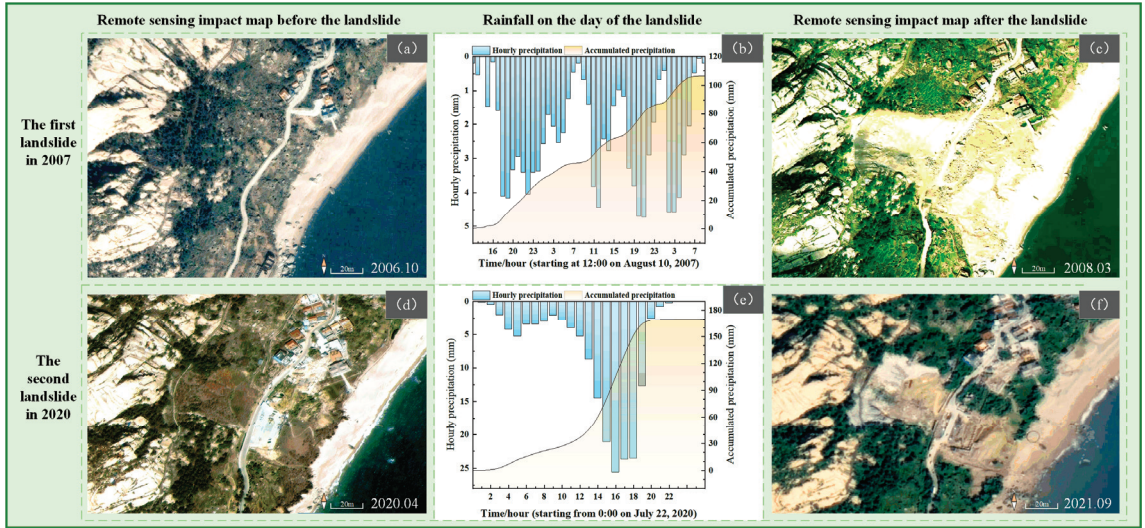
Figure 4. Comparison of two landslides in 2007 and 2020. (**a,c,d,f**) Remote sensing images of Fanling in October 2006, March 2008, April 2020, and September 2021. (**b**) Average rainfall during the first landslide. (**e**) Average rainfall during the second landslide.

3. Numerical Modeling

3.1. Theoretical Model

3.1.1. Soil Constitutive Model

The traditional Mohr–Coulomb criterion often exhibits sharp corners on its yield surface, leading to challenges such as slow convergence in numerical calculations. To address this, the classical Mohr–Coulomb model is extended in this study using a continuous smooth flow potential function to describe the failure and deformation of slope soil (Figure 5) [25].

The equation for the hyperbolic flow potential function is as follows:

$$G = \sqrt{(\varepsilon c_0 \tan\varphi)^2 + (R_{mc}q)^2} - p\tan\varphi \tag{1}$$

In the formula, φ indicates the shear dilation angle on the meridian plane under high confining pressure; c_0 represents the initial cohesive force; ε represents the shape parameter on the meridian plane, used to define the flow potential function, with a default value of 0.1; e represents the rate of deviation on the π plane; q represents generalized shear stress; and p represents the ball stress.

The calculation process of R_{mc} is as follows:

$$R_{mc}(\theta, e) = \frac{4(1-e^2)\cos^2\theta + (2e-1)^2}{2(1-e^2)\cos\theta + (2e-1)\sqrt{4(1-e^2)\cos^2\theta + 5e^2 - 4e}} \times R_{mc}\left(\frac{\pi}{3}, \varphi\right) \tag{2}$$

$$R_{mc}\left(\frac{\pi}{3}, \varphi\right) = \frac{3 - \sin\varphi}{6\cos\varphi} \tag{3}$$

In the formula, $e = (3 - \sin\varphi)/6\cos\varphi$, and the required range of e is (0.5, 1.0).
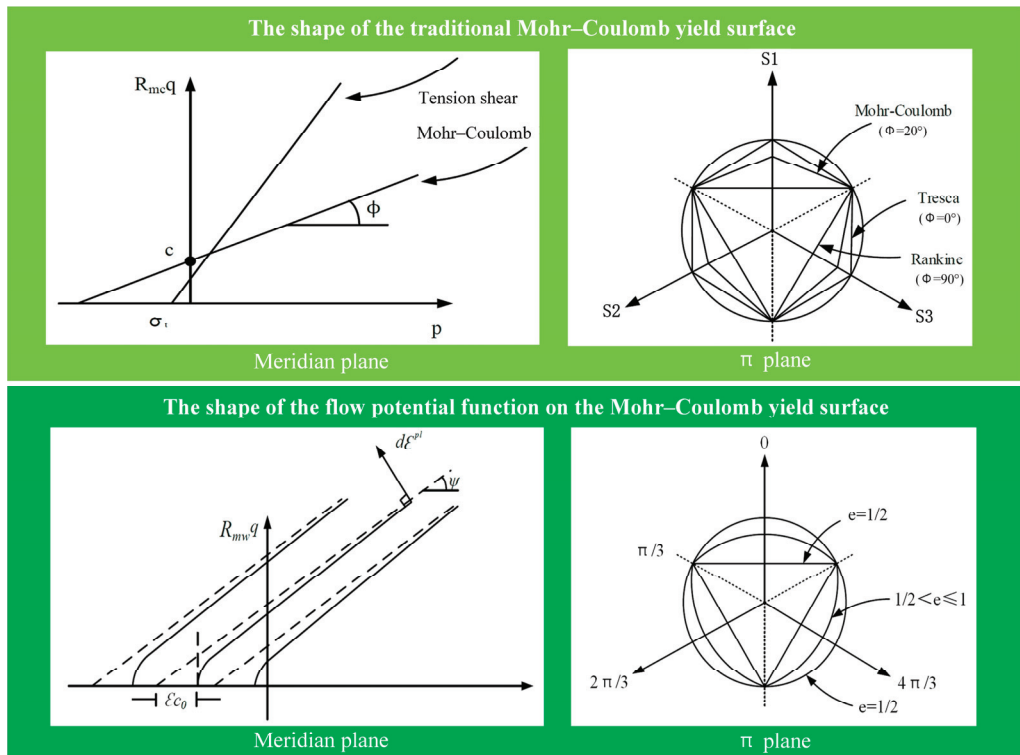
Figure 5. The shape of the Mohr–Coulomb yield surface on the meridian and π planes.

3.1.2. Rainfall Seepage Theory of Unsaturated Soil

During rainfall-induced landslides, the sliding interface typically transitions from saturated to unsaturated conditions as groundwater flow accompanies the saturation process. Water flows through soil pores under the influence of gravity and hydraulic head. The sliding body in the study area consists of weathered rock with high permeability; thus, the study focuses on unsaturated soil rainfall seepage.

The fluid–structure coupling equation needs to follow the following basic assumptions: ① Only the influences of soil and water are considered, neglecting gas impacts. ② Soil particles and water are treated as incompressible and do not undergo compression deformation. ③ Temperature changes are disregarded during the analysis. ④ Solids undergo linear, nonlinear, elastic, and small plastic deformations. The governing equation for its seepage field is as follows:

$$\begin{cases} \int \delta u_w \frac{1}{J} \frac{d}{dt} (J \rho_w n_w) dV + \int \delta u_w \frac{\partial}{\partial x} [\rho_w n_w n \cdot v_w] dV = 0 \\ I^N - P^N = 0 \end{cases} \quad (4)$$

In the formula, *V* represents the volume of the model; *J* is the hydraulic gradient; u_w is the pore water pressure; v_w is the fluid velocity; n is the porosity of the soil; n_w is the soil water storage rate; ρ_w is the fluid density; and I^N and P^N are, respectively, represented as internal and external force matrices, which form a simplified discrete stress equilibrium equation.

3.2. Model Settings

Based on field data and previous research by Yu [23], the landslide model is simplified into two parts: a sliding body and sliding bed. The numerical model includes 12,494 grid units and 5 monitoring points, as depicted in Figure 6, with the modeling process outlined in Figure 7.

	Soil weight (KN/m³)	Elastic modulus (kPa)	Poisson's ratio	Internal friction angle (°)	Cohesive force (kPa)	Permeability coefficient (mm/h)
Sliding mass	19	5,0000	0.25	20	25	0.08
Sliding bed	26	100,0000	0.2	37	1000	0.00001
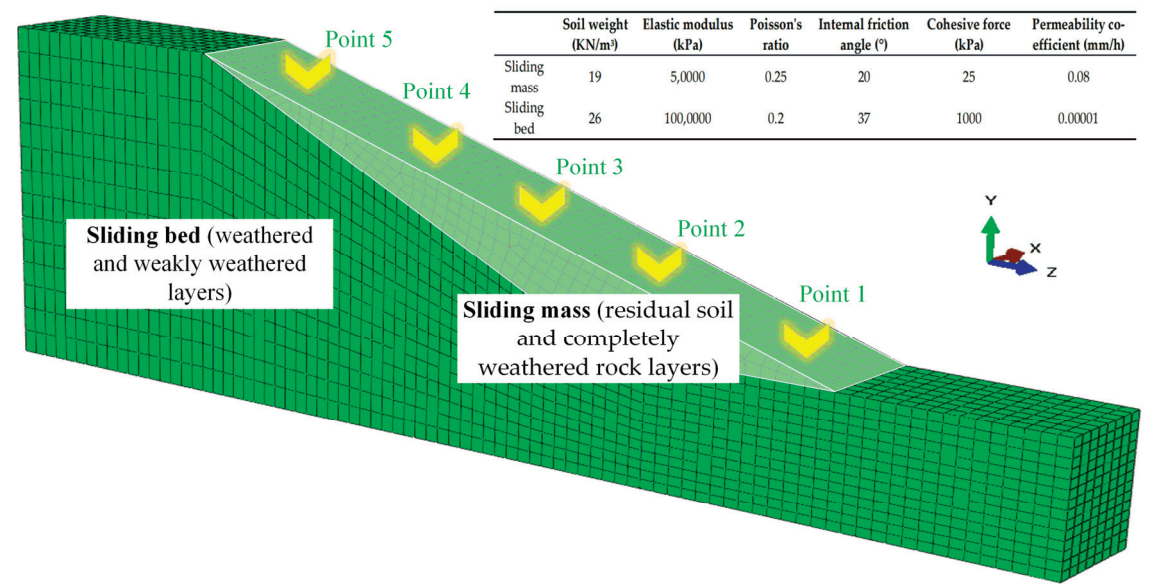
Figure 6. Numerical model diagram and parameters.
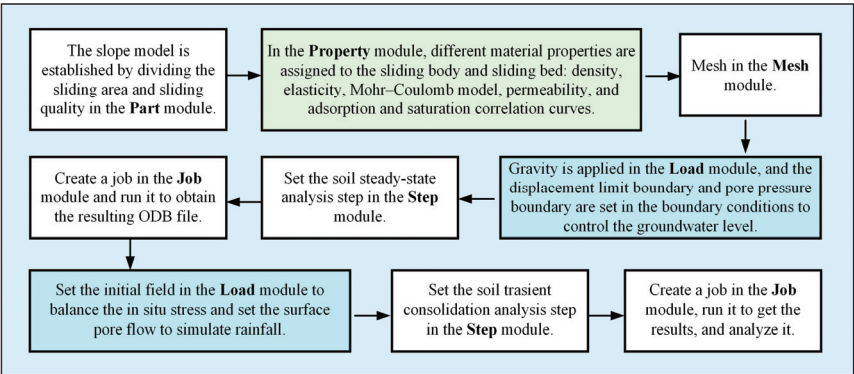
Figure 7. Process of numerical model establishment.

Based on local rainfall data, three experimental groups were set up, E1 (rainfall duration unchanged, changing rainfall intensity amplitude), E2 (rainfall intensity amplitude unchanged, changing rainfall duration), and E3 (total rainfall unchanged, changing rainfall intensity amplitude), to simulate 10 different rainfall fluctuation conditions, as detailed in Table 1. The parameter settings refer to the data of landslides in 2007 and 2020, with the rainfall time controlled within 24 h and rainfall intensity controlled between 10 mm/h and 60 mm/h. It should be noted that N2, N6, and N12 are operating conditions under the same conditions. To facilitate comparison between the experimental groups, they are

represented separately. To balance the model and make it more realistic, a lead time of 1 h was set to achieve the expected initial rainfall intensity.

Table 1. Rainfall fluctuation conditions.

Group	Condition	Rainfall Intensity (mm/h)			Rainfall Duration (h) (+1)
		Initial	End	Amplitude	
E1	N1	10	30	200%	24
	N2	10	40	300%	24
	N3	10	50	400%	24
	N4	10	60	500%	24
E2	N5	10	40	300%	32
	N6	10	40	300%	24
	N7	10	40	300%	16
	N8	10	40	300%	8
E3	N9	25	25	0%	24
	N10	20	30	50%	24
	N11	15	35	133%	24
	N12	10	40	300%	24

4. Results

4.1. Analysis of the Seepage Field

Numerical simulations were conducted to analyze changes in saturation (SAT) and pore water pressure (POR). Figure 8 depicts the initial state without rainfall, showing the aeration zone (black area) and the infiltration surface at the bottom boundary where the pore water pressure equals zero.
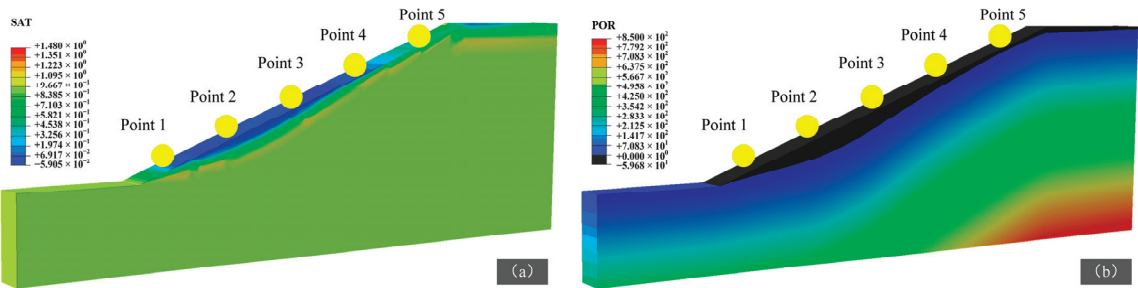
Figure 8. Cloud map of the initial slope state without rainfall. (**a**) Saturation; (**b**) pore water pressure.

4.1.1. Different Rainfall Intensity Amplitudes

Figures 9 and 10 present the results of numerical simulations varying the rainfall intensity amplitude while keeping the rainfall duration constant. Increasing the amplitude of rainfall intensity causes significant shifts in the slope's saturated area and alters the position of the infiltration surface. The pore water pressure gradually decreases towards the surface and peaks at the bottom foundation section as rainfall infiltrates the soil. In the N1 scenario with a 200% amplitude, groundwater infiltration nears the surface in the upper section, leaving substantial unsaturated areas in the middle and lower parts. In N2 (300% amplitude), the infiltration surface rises higher, reducing the unsaturated zone. This trend continues in N3 (400% amplitude) and N4 (500% amplitude), where the infiltration surface elevation increases and the unsaturated area diminishes further. Upon conversion, increasing the amplitude from 200% to 500% raises the extreme pore water pressure to 18.72 kPa, 22.07 kPa, 25.51 kPa, and 29.48 kPa, respectively.
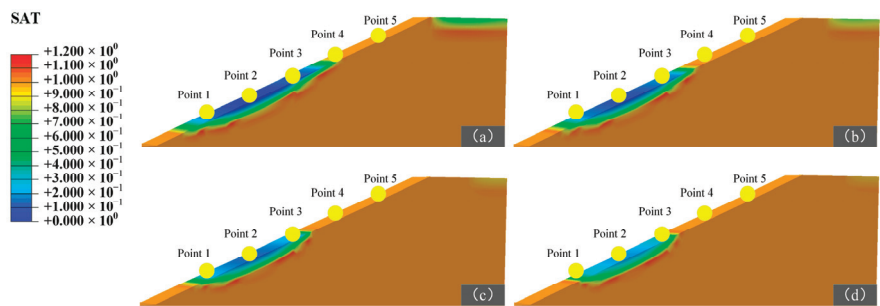
Figure 9. SAT cloud maps of the E1 group. (**a**) Amplitude = 200%; (**b**) amplitude = 300%; (**c**) amplitude = 400%; (**d**) amplitude = 500%.
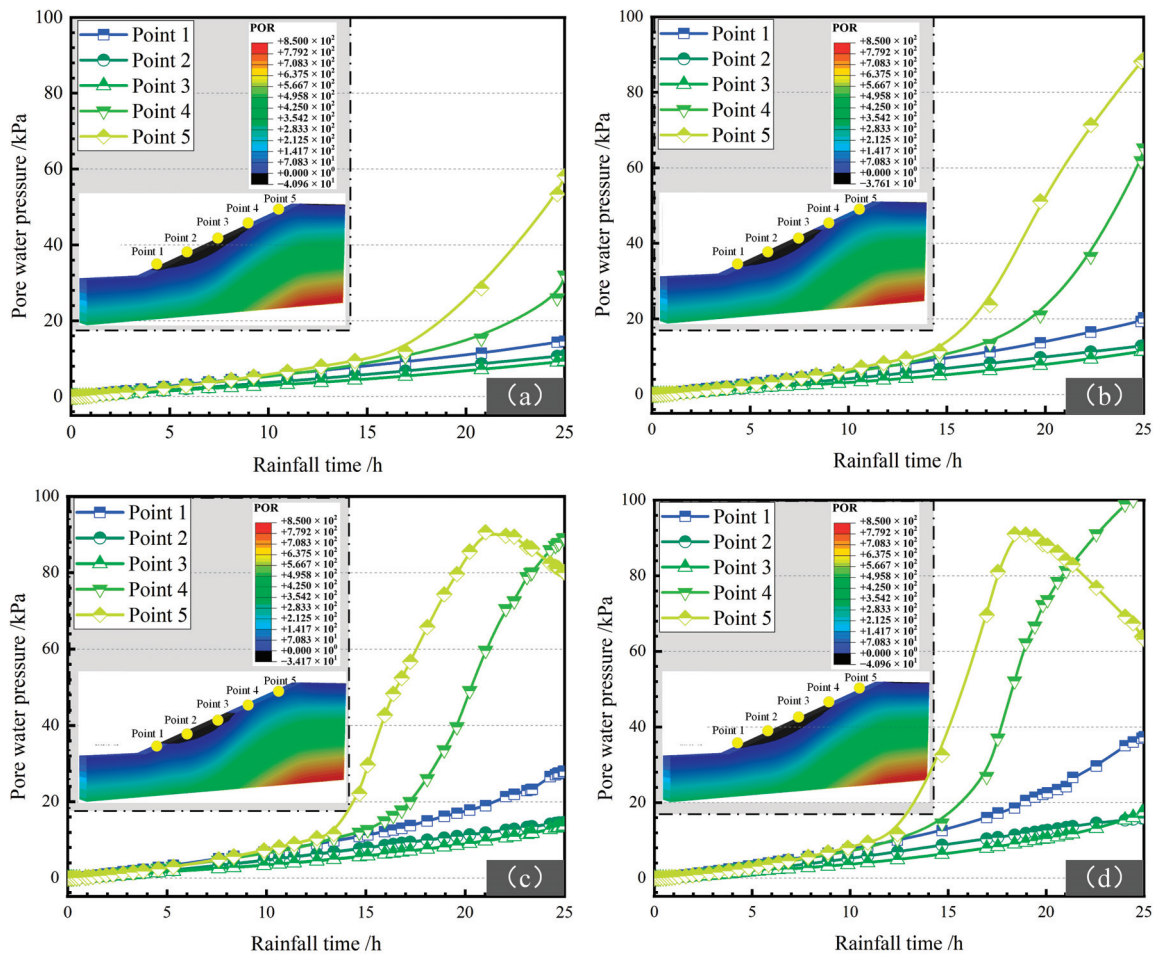
Figure 10. POR cloud maps and response maps of the E1 group. (**a**) Amplitude = 200%; (**b**) amplitude = 300%; (**c**) amplitude = 400%; (**d**) amplitude = 500%.

As the amplitude of rainfall intensity increases, total rainfall and soil infiltration rise continuously, leading to higher pore water pressures and increased soil saturation across

various locations, even at the same amplitude. The changes in the values at points 4 and 5 have significant responses, while monitoring point 3 has a significant response when the rainfall intensity amplitude is strong. The rate of increase in pore water pressure at the exact point location varies significantly under varying rainfall conditions and is positively correlated with changes in the rainfall intensity amplitude. After 18 h of rainfall under N1 working conditions, the values at points 4 and 5 began to show a slight increase. It means that the infiltration surface has already risen above this point. Under N2 conditions, a similar phenomenon occurs around 16 h of rainfall. Under N3 working conditions, this phenomenon occurs at points 3, 4, and 5 after about 14 h of rainfall. This phenomenon happens at points 3, 4, and 5 at around 12 h of rainfall under the N4 working condition, indicating that as the amplitude increases, the rate of infiltration surface elevation also increases. Its saturation time is linearly related to the degree of the rainfall intensity amplitude. These findings underscore the critical influence of rainfall intensity variations on pore water pressure dynamics and slope stability, emphasizing the need for precise meteorological data in landslide risk assessment and early warning systems.

4.1.2. Different Rainfall Durations

Numerical simulations were conducted with a fixed rainfall intensity amplitude and varying rainfall durations, as depicted in Figures 11 and 12. Under a consistent amplitude of rainfall intensity, an increasing rainfall duration leads to notable shifts in the slope's saturated area and the position of the infiltration surface. In the N5 scenario with a duration of 32 h, the groundwater infiltration surface reaches near the slope's surface, resulting in a minimal unsaturated area in the middle and bottom sections. Conversely, N6 (24 h duration) shows a lower infiltration surface compared to N5, accompanied by an increase in unsaturated areas. In N7 (16 h duration), the infiltration surface further recedes compared to N5 and N6, reducing the unsaturated area. By N8 (8 h duration), the infiltration surface significantly diminishes compared to previous conditions, expanding the unsaturated zone towards the upper slope and forming a complete aeration zone. Upon conversion, reducing the duration from 32 h to 8 h decreases the extreme pore water pressure to 24.82 kPa, 22.07 kPa, 19.77 kPa, and 16.72 kPa, respectively.
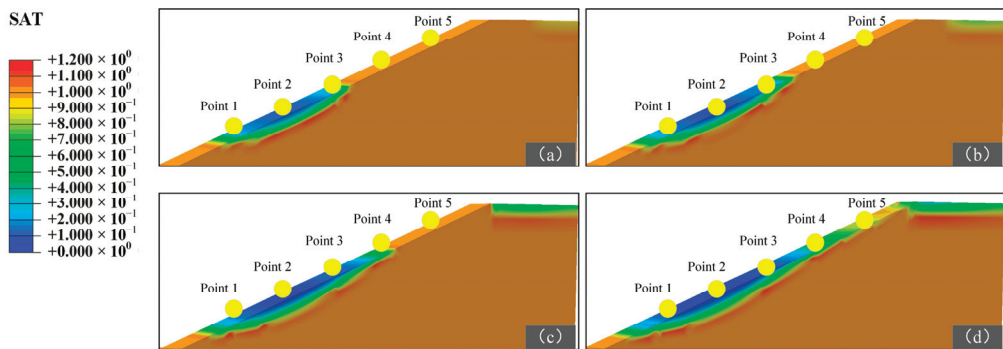
Figure 11. SAT cloud maps of the E2 group. (**a**) Duration = 32 h; (**b**) duration = 24 h; (**c**) duration = 16 h; (**d**) duration = 8 h.

As the rainfall duration increases, the infiltration line within the slope rises, indicating increasing soil saturation over time. Pore water pressure values vary across different points, showing rapid increases in the upper part where the weathered layer is thin, causing the infiltration surface to rise swiftly. Significant variations in the pore water pressure amplitude and velocity at specific points correlate positively with the rainfall duration. Under N5 conditions, significant increases at points 4 and 5 occur after 16 h of rainfall, while N6 shows this phenomenon around 14 h. In N7, point 5 experiences significant

changes after approximately 13 h of rainfall, while N8 shows no significant changes. Points 1, 2, and 3 exhibit a steady increase in pore pressure, indicating that the infiltration surface surpasses these points. These observations suggest that shorter rainfall durations accelerate changes in the rainfall intensity amplitude, resulting in earlier significant pore pressure changes at the monitoring points. However, the final pore pressure response correlates positively with the rainfall duration, despite the unchanged rainfall intensity amplitude.
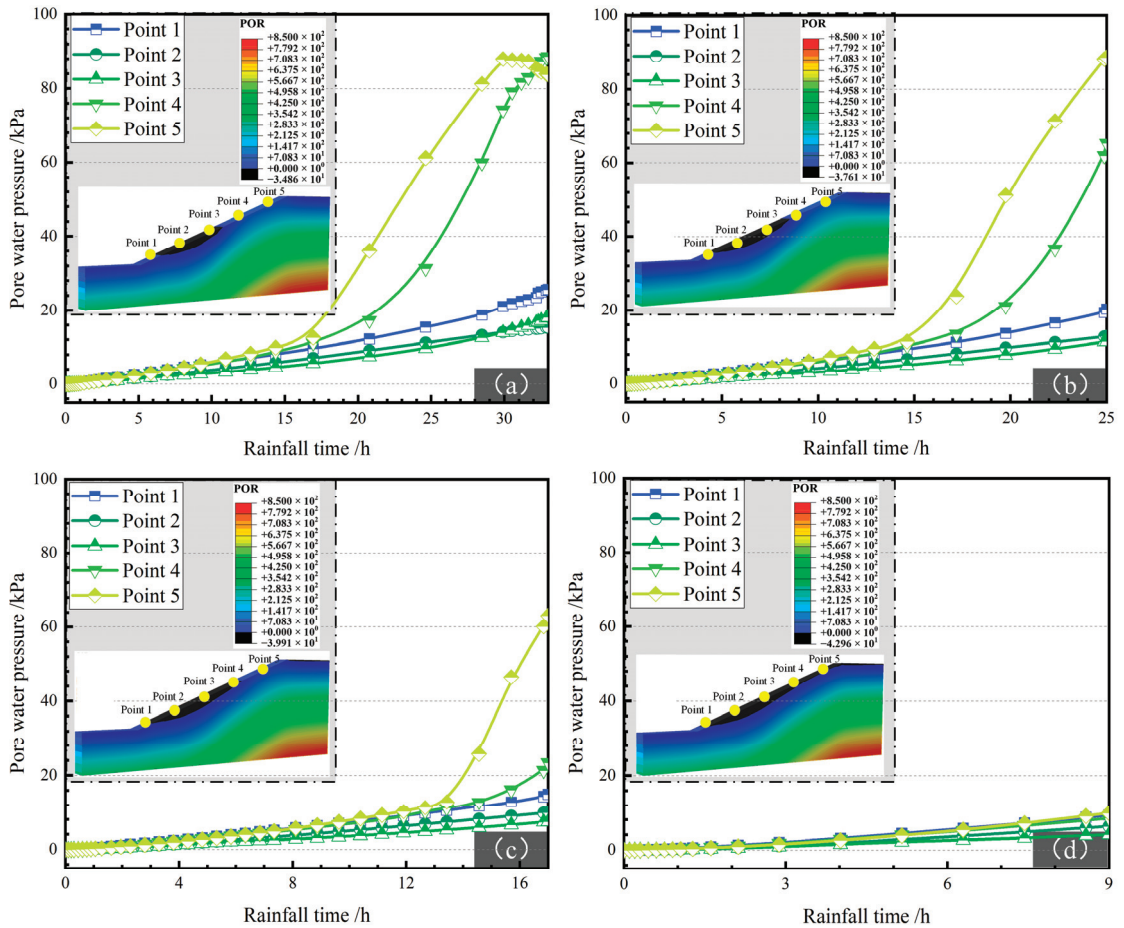
Figure 12. POR cloud and response maps of the E2 group. (**a**) Duration = 32 h; (**b**) duration = 24 h; (**c**) duration = 16 h; (**d**) duration = 8 h.

4.1.3. Different Rainfall Intensity Amplitudes (Constant Rainfall)

Numerical simulations were conducted under conditions of fixed total rainfall to analyze the effects of varying rainfall intensity amplitudes, as illustrated in Figures 13 and 14. With total rainfall held constant, changes in the rainfall intensity amplitude did not significantly alter the position of the groundwater infiltration surface or the saturation area. However, higher amplitudes did result in slight increases in soil pore pressure. In the N9 scenario, where the rainfall intensity amplitude was 0%, the infiltration surface approached the surface near the thinner upper sliding mass, with noticeable unsaturated areas in the middle and bottom sections. Similarly, in N10 (50% amplitude), there was minimal change in the infiltration surface position compared to N9, but the maximum pore

pressure increased. Under N11 (133% amplitude), the infiltration surface rose compared to N9 and N10, further reducing the unsaturated area. N12 (300% amplitude) showed the highest infiltration surface elevation with the smallest unsaturated area. Upon conversion, increasing the amplitude from 0% to 300% raised the extreme pore water pressure increases to 18.93 kPa, 20.14 kPa, 21.04 kPa, and 22.07 kPa, respectively.
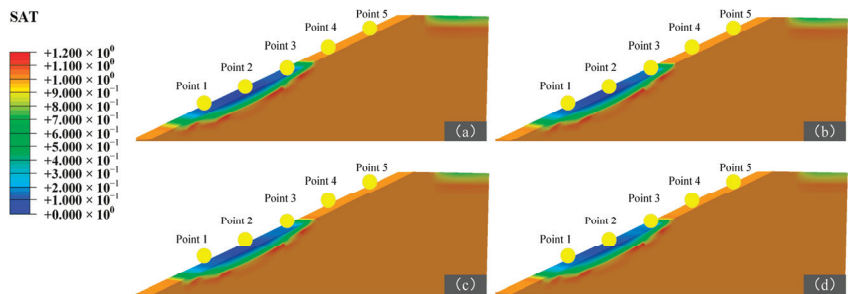
Figure 13. SAT cloud maps of the E3 group. (**a**) Amplitude = 0%; (**b**) amplitude = 50%; (**c**) amplitude = 133%; (**d**) amplitude = 300%.
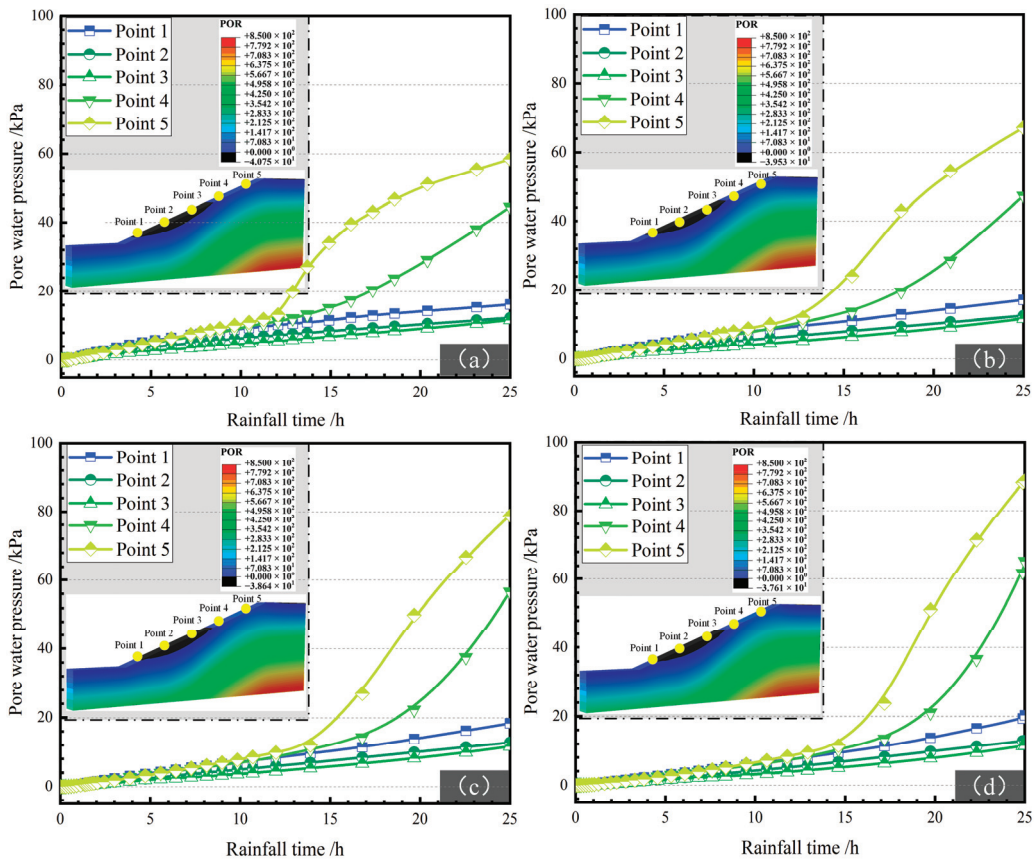
Figure 14. POR cloud and response maps of the E3 group. (**a**) Amplitude = 0%; (**b**) amplitude = 50%; (**c**) amplitude = 133%; (**d**) amplitude = 300%.

The pore water pressure amplitude and velocity varied slightly across different rainfall conditions at specific monitoring points, correlating positively with changes in the rainfall intensity amplitude. Under N9 conditions, significant pore pressure increases occurred at points 5 and 4 after 12 h of rainfall. Similar trends were observed in N10 after approximately 13 h, N11 around 14 h, and N12 at about 15 h, indicating that a higher rainfall intensity amplitude delayed the pore pressure response but ultimately increased the final pore pressure amount. These findings underscore how variations in the rainfall intensity amplitude, under constant total rainfall, affect pore water pressure dynamics and highlight implications for slope stability assessments under varying meteorological conditions.

4.2. Comprehensive Analysis and Comparison of Working Conditions

To elucidate the relationship between the seepage field response and landslide development, final pore water pressure values (Figure 15) and displacement response values (Figure 16) were extracted for a comprehensive analysis across each monitoring point.
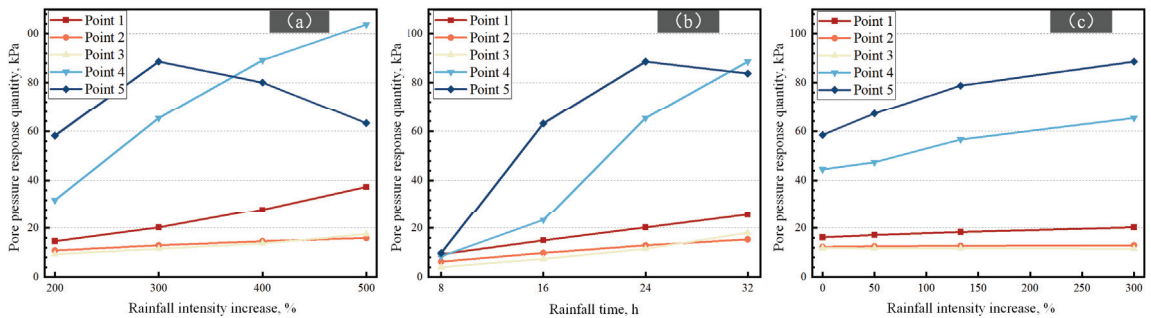
Figure 15. The final response of pore pressure under different working conditions: (**a**) E1; (**b**) E2; and (**c**) E3.
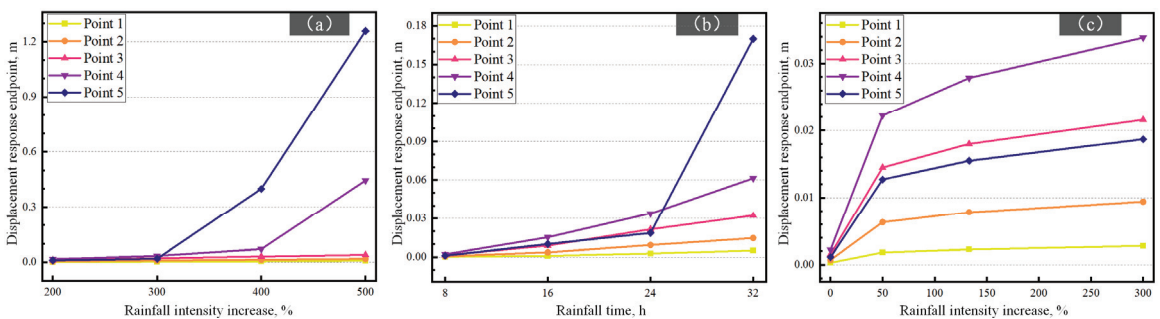
Figure 16. The final response of displacement under different working conditions: (**a**) E1; (**b**) E2; and (**c**) E3.

In the experimental groups of E1 and E2, where the total rainfall amount varied, the pore water pressure response rate remained consistent with increasing rainfall intensity amplitude and duration. The final pore water pressure positively correlated with both factors. However, point 5 in the upper part showed a reversed pore pressure trend, potentially due to surface runoff formation from the excessive rainfall intensity and accumulated precipitation. This excessive rainfall also induced substantial displacement at the slope's top, leading to slope instability and increased displacement rates. Larger amplitudes and durations of rainfall intensified these effects. In the E3 experimental group with constant total rainfall, increasing the rainfall intensity amplitude slightly reduced the rate of pore pressure change while slightly increasing the final amount. Similarly, the rate

of displacement change decreased with increasing amplitude, but the final displacement quantities rose.

For weathered granite landslides triggered by natural rainfall, rainwater infiltrates the rock–soil body, saturating it and accelerating shear creep. As the plastic zone develops, a failure surface forms, transitioning the slope from creep to slide stages. The initial pore water pressure increases in the upper part due to infiltration, leaving significant unsaturated areas in the middle and bottom sections. Thinner completely weathered rock layers in the upper part expedite the groundwater level rise, explaining why upper sections deform first.

The total rainfall amount is the primary factor influencing the pore pressure response and landslide deformation. In E1 and E2, the increased rainfall amplitude and duration amplified the total rainfall, thereby escalating the pore pressure response and deformation. Rainfall intensity also significantly impacted the pore pressure and slope deformation, intensifying infiltration and slope scour. These changes reduced the rock–soil body shear strength, rendering the slope more susceptible to unstable deformation. Short-term fluctuating rainstorms posed higher landslide risks compared to long-term stable rainfall.

4.3. Model Reliability Verification

Physical model testing serves as a critical validation method for numerical simulations, particularly with large-scale models that closely mirror natural landslide conditions. In this study, the reliability of the numerical model was verified using pore water pressure and deformation data from the Fanling landslide physical model established by Liu [26] (Figure 17). To ensure consistency with physical model conditions, parameters for the N9 condition in the E3 experimental group were adjusted accordingly (see Table 2 for comparison).
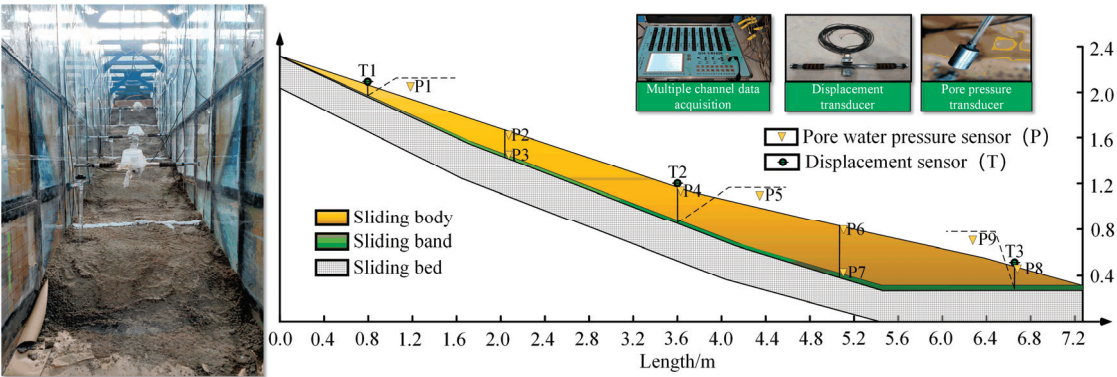
Figure 17. Physical model testing.

Table 2. Model parameters.

Method	Rainfall Intensity (mm/h)		Rainfall Duration (h)		Rainfall (mm)	
	R	S	R	S	R	S
Physical model test	20	3.6	24	2.2	480	7.92
Numerical simulation	20	20	24	24	480	480

Pore water pressure and displacement data from the physical model and numerical simulation were extracted and compared (Figure 18). Although differences were observed, the overall response trends were consistent between the physical and numerical models, confirming the numerical model's accuracy and reliability.
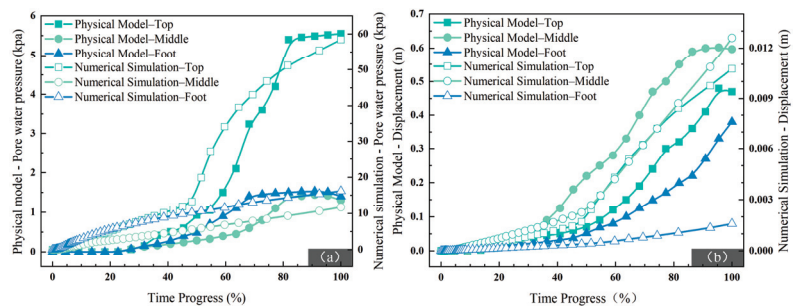
Figure 18. Physical model experiment–numerical simulation comparison. (**a**) Pore water pressure; (**b**) displacement.

5. Conclusions

This article presents a numerical model of a weathered granite landslide under fluctuating rainfall conditions, conducting 10 sets of simulations across varying rainfall intensities and durations to investigate the response characteristics of landslide seepage fields. The findings are summarized below.

(1) Pore Water Pressure Distribution: During rainfall, the pore water pressure decreases gradually towards the slope's surface, peaking at the bottom foundation section. Variations in rainfall intensity and duration notably influence the infiltration surface position, with the upper part responding first.

(2) Impact of Rainfall Characteristics: Increased rainfall intensity and duration amplify final pore pressures. Higher intensity accelerates pore pressure changes and groundwater infiltration rates, shortening the time to reach peak values. Variations in rainfall intensity, under constant total rainfall, do not significantly alter the position of the groundwater infiltration surface or saturation area of the slope. However, a higher intensity delays the pore pressure response while increasing the final amount.

(3) Rainfall Effects on Landslide Dynamics: The total rainfall amount directly affects pore pressure responses and landslide deformation. Rainfall intensity also significantly influences pore pressure and slope deformation. Short-term, intense rainstorms pose a higher landslide risk compared to long-term stable rainfall. A comprehensive analysis of meteorological data is crucial for landslide early warning systems, enabling proactive emergency measures ahead of extreme rainstorms, rather than relying solely on monitoring anomalies.

Author Contributions: Conceptualization, P.L. and Q.W.; formal analysis, W.S. and Z.C.; data curation, X.C. and R.W.; writing—original draft preparation, P.Y. and P.L.; writing—review and editing, P.Y. and Q.W.; visualization, W.W.; project administration, P.L. and Q.W.; funding acquisition, P.Y. and R.W. All the authors have approved the final manuscript. All authors have read and agreed to the published version of the manuscript.

Data Availability Statement: The data presented in this study are available on request from the corresponding author.

References

1. Balsa-Barreiro, J.; Li, Y.; Morales, A.; Pentland, A.S. Globalization and the shifting centers of gravity of world's human dynamics: Implications for sustainability. *J. Clean. Prod.* **2019**, *239*, 117923.1–117923.17. [CrossRef]
2. Cai, W.; Lan, F.; Huang, X.; Hao, J.; Xia, W.; Tang, R.; Feng, P.; Li, H. Generative probabilistic prediction of precipitation induced landslide deformation with variational autoencoder and gated recurrent unit. *Front. Earth Sci.* **2024**, *12*, 1394129. [CrossRef]

3. Feng, Y.; Yang, W.; Wan, J.; Li, H. Granular risk assessment of earthquake induced landslide via latent representations of stacked autoencoder. *Front. Environ. Sci.* **2023**, *11*, 1308808. [CrossRef]
4. Xiang, G.; Jiang, T.; Yang, Q.; Cui, S.; Zhu, L.; He, Y.; Li, H. The Influence of Vertical Seismic Acceleration on the Triggering of Landslides Constrained by Bedding Faults under an Inertial Frame Reference: The Case of the Daguangbao (DGB) Landslide. *Appl. Sci.* **2023**, *13*, 12911. [CrossRef]
5. Marín-Rodríguez, N.J.; Vega, J.; Zanabria, O.B.; González-Ruiz, J.D.; Botero, S. Towards an understanding of landslide risk assessment and its economic losses: A scientometric analysis. *Landslides* **2024**. [CrossRef]
6. Niyokwiringirwa, P.; Lombardo, L.; Dewitte, O.; Deijns, A.A.J.; Wang, N.; Van Westen, C.J.; Tanyas, H. Event-based rainfall-induced landslide inventories and rainfall thresholds for Malawi. *Landslides* **2024**, *21*, 1403–1424. [CrossRef]
7. Ministry of Emergency Management of the People's Republic of China. Available online: https://www.gov.cn/lianbo/bumen/202401/content_6927328.htm (accessed on 21 January 2024).
8. Fedato, E.; Fubelli, G.; Kurilla, L.; Tiranti, D. Predisposing Factors for Shallow Landslides in Alpine and Hilly/Apennines Environments: A Case Study from Piemonte, Italy. *Geosciences* **2023**, *13*, 252. [CrossRef]
9. Borga, M.; Dalla Fontana, G.; Cazorzi, F. Analysis of topographic and climatic control on rainfall-triggered shallow landsliding using a quasi-dynamic wetness index. *J. Hydrol.* **2002**, *268*, 56–71. [CrossRef]
10. Urmi, Z.A.; Saeidi, A.; Chavali, R.V.P.; Yerro, A. Failure mechanism, existing constitutive models and numerical modeling of landslides in sensitive clay: A review. *Geoenvironmental Disasters* **2023**, *10*, 14. [CrossRef]
11. Dikshit, A.; Satyam, D.N. Estimation of rainfall thresholds for landslide occurrences in Kalimpong, India. *Innov. Infrastruct. Solut.* **2018**, *3*, 1–10. [CrossRef]
12. Jéssica, C.M.; Guilherme JC, G.; Raquel, Q.V.; Eurípedes AV, J.; Rafael, S.N.; Nelson, F.F. Exploring extreme rainfall-triggered landslides using 3D unsaturated flow, antecedent moisture and spatially distributed soil depth. *CATENA* **2023**, *229*, 107241. [CrossRef]
13. Kim, S.W.; Chun, K.W.; Kim, M.; Catani, F.; Choi, B.; Seo, J.I. Effect of antecedent rainfall conditions and their variations on shallow landslide-triggering rainfall thresholds in South Korea. *Landslides* **2020**, *182*, 569–582. [CrossRef]
14. Lee, J.J.; Song, M.S.; Yun, H.S.; Yum, S.G. Dynamic landslide susceptibility analysis that combines rainfall period, accumulated rainfall, and geospatial information. *Sci. Rep.* **2022**, *12*, 18429. [CrossRef]
15. La Porta, G.; Leonardi, A.; Pirulli, M.; Cafaro, F.; Castelli, F. Time-resolved triggering and runout analysis of rainfall-induced shallow landslides. *Acta Geotech.* **2024**, *19*, 1873–1889. [CrossRef]
16. Islam, M.A.; Chattoraj, S.L. Modelling landslides in the Lesser Himalaya region using geospatial and numerical simulation techniques. *Arab. J. Geosci.* **2023**, *16*, 480. [CrossRef]
17. Liu, S.H.; Du, J.; Yin, K.L.; Zhou, C.; Huang, C.C.; Jiang, J.; Yu, J. Regional early warning model for rainfall induced landslide based on slope unit in Chongqing, China. *Eng. Geol.* **2024**, *333*, 107464. [CrossRef]
18. Soumik, S.; Biswajit, B. Rainfall threshold for prediction of shallow landslides in the Garhwal Himalaya, India. *Geosystems Geoenvironment* **2024**, *11*, 100285. [CrossRef]
19. Sun, Y.; Zhang, J.; Wang, H.; Lu, D.G. Probabilistic thresholds for regional rainfall induced landslides. *Comput. Geotech.* **2024**, *166*, 106040. [CrossRef]
20. Rashad, A.; Marwan, F.; Anis, Y.; Hossein, N.; Knut, J.M.; Renaud, T. Modeling rainfall-induced landslide using the concept of local factor of safety: Uncertainty propagation and sensitivity analysis. *Comput. Geotech.* **2024**, *167*, 106102. [CrossRef]
21. Hugh, G.S.; Andrew, J.N.; Harley, B.; Raphael, S. The influence of spatial patterns in rainfall on shallow landslides. *Geomorphology* **2023**, *437*, 108795. [CrossRef]
22. Ma, J.H.; Yao, Y.Q.; Wei, Z.R.; Meng, X.M.; Zhang, Z.L.; Yin, H.L.; Zeng, R.Q. Stability analysis of a loess landslide considering rainfall patterns and spatial variability of soil. *Comput. Geotech.* **2024**, *167*, 106059. [CrossRef]
23. Yu, P.; Liu, H.H.; Yu, H.B.; Xie, Y.J.; Yu, Y.; Zhu, C.H.; Dong, J.; Guan, Y. Study on Fluid–Solid Coupling Numerical Simulation and Early Warning of Weathered Granite Landslides Induced by Extreme Rainfall. *Sustainability* **2023**, *15*, 11738. [CrossRef]
24. Yu, P.; Dong, J.; Hao, H.; Xie, Y.; Zhang, H.; Wang, J.; Zhu, C.; Guan, Y.; Yu, H. Risk Assessment and Prevention Planning for Collapse Geological Hazards Considering Extreme Rainfall—A Case Study of Laoshan District in Eastern China. *Land* **2023**, *12*, 1558. [CrossRef]
25. Yu, P.; Zhang, J.K.; Jia, S.X.; Cao, L.; Zhao, L. Numerical simulation study on the embedding depth of anti slip piles in fully weathered granite landslides. *J. Phys. Conf. Ser.* **2024**, *2732*, 012008. [CrossRef]
26. Liu, H.H.; Yu, P.; Lu Xie, Y.J.; Wang, Z.S.; Hao, S.Y.; Liu, H.J.; Fu, Y.X. Experimental study on disaster mechanism of completely weathered granite landslide induced by extreme rainfall. *Geoenvironmental Disasters* **2023**, *10*, 5. [CrossRef]

Dynamic Hazard Assessment of Rainfall-Induced Landslides Using Gradient Boosting Decision Tree with Google Earth Engine in Three Gorges Reservoir Area, China

Ke Yang [1], Ruiqing Niu [2,*], Yingxu Song [3,*], Jiahui Dong [2], Huaidan Zhang [2] and Jie Chen [2]

[1]   Institute of Geography and Information Engineering, China University of Geosciences, Wuhan 430074, China; yangke@cug.edu.cn
[2]   Institute of Geophysics and Geomatics, China University of Geosciences, Wuhan 430074, China; ivy.dong@cug.edu.cn (J.D.); seashell@cug.edu.cn (H.Z.); chenjie@cug.edu.cn (J.C.)
[3]   School of Information Engineering, East China University of Technology, Nanchang 330013, China
*   Correspondence: niuruiqing@cug.edu.cn (R.N.); yxsong@ecut.edu.cn (Y.S.)

Abstract: Rainfall-induced landslides are a major hazard in the Three Gorges Reservoir area (TGRA) of China, encompassing 19 districts and counties with extensive coverage and significant spatial variation in terrain. This study introduces the Gradient Boosting Decision Tree (GBDT) model, implemented on the Google Earth Engine (GEE) cloud platform, to dynamically assess landslide risks within the TGRA. Utilizing the GBDT model for landslide susceptibility analysis, the results show high accuracy with a prediction precision of 86.2% and a recall rate of 95.7%. Furthermore, leveraging GEE's powerful computational capabilities and real-time updated rainfall data, we dynamically mapped landslide hazards across the TGRA. The integration of the GBDT with GEE enabled near-real-time processing of remote sensing and meteorological radar data from the significant "8–31" 2014 rainstorm event, achieving dynamic and accurate hazard assessments. This study provides a scalable solution applicable globally to similar regions, making a significant contribution to the field of geohazard analysis by improving real-time landslide hazard assessment and mitigation strategies.

Keywords: Three Gorges Reservoir area; rainfall-induced landslide; Google Earth Engine; GBDT; dynamic hazard assessment

1. Introduction

Landslides are common and dangerous in the Three Gorges Reservoir area (TGRA) due to its complex geographic, geologic, and hydrologic conditions. Rainfall is one of the main inducing factors of landslides in the TGRA [1,2]. The effects of rainfall are mainly manifested in the massive infiltration of rainwater, which leads to the saturation of the slope's soil and rock layer and even the accumulation of water at the slope's lower water barrier, increasing the weight of the slide body and reducing the shear strength of the soil and rock layer, resulting in landslides [3,4]. Rain-induced landslides are characterized by regional and clustered occurrences and can cause significant catastrophic damage in a short period of time [5–7]. Therefore, it is of great practical importance to use a reliable method to dynamically evaluate the regional risk of rainfall-induced landslides, improving the level of landslide hazard early warning and providing decision support for regional disaster prevention and mitigation.

Landslide hazard assessment is based on the results of landslide susceptibility mapping to forecast the likelihood of landslide deformation in a given area under the dynamic influence of inducing factors (such as rainfall, earthquakes, and human construction activities) [8–10]. Therefore, landslide hazard assessment can provide regional landslide early warning. The degree of difficulty of landslide occurrence at different spatial locations in the

region is referred to as landslide susceptibility [11]. Since the first attempt to assess landslide susceptibility in the mid-1970s, various mathematical–physical models have been introduced in related research [12–15]. The purpose of landslide susceptibility mapping is to use geology, engineering, statistics, remote sensing, GIS, data mining, and other technologies to establish the relationship between the spatial location of landslides and the factors that influence them in order to achieve spatial identification of landslide-prone areas. With the rise of machine learning, data-driven methods have been introduced for studying landslide susceptibility mapping, including informativeness, the weight of evidence, logistic regression, support vector machines, and convolutional neural networks [12,16–19]. Ensemble learning, which constructs and combines multiple weak machine learners to achieve strong learning capabilities, has become a hot topic in machine learning in recent years because it provides stable models and high prediction accuracy. The bagging method, represented by Random Forest, and the boosting method, represented by AdaBoost, are the two main types of ensemble learning methods. The Gradient Boosting Decision Tree (GBDT) has achieved good predictive performance in landslide susceptibility mapping as an improved method of AdaBoost [20]. In geohazard analysis and other structured data applications, the GBDT demonstrates superior performance compared to other machine learning models, such as artificial neural networks (ANNs) or deep learning techniques. The GBDT leverages its strong interpretability, reduced overfitting through ensemble learning, and efficient feature utilization, making it particularly effective for predicting landslide susceptibility. As a result, incorporating the GBDT algorithm into the entire TGRA's landslide susceptibility mapping has promising application potential. In the study of rainfall-induced landslide hazards, critical precipitation grading is an effective tool for performing quantitative analysis of landslides. Current methods for establishing critical precipitation gradings are mainly physical, empirical, mathematical, and statistical models. Physical models have limited applicability in a large study area [21]. When calculating the critical precipitation threshold, empirical, mathematical, and statistical models mainly use the combination of single or multiple precipitation parameters to determine the correlation between precipitation and landslides, such as the accumulated rainfall (E) and rainfall duration (D), accumulated rainfall and rainfall intensity (I), rainfall duration and rainfall intensity, the total rainfall amount and rainfall intensity, etc. [22–26]. The choice of empirical, mathematical, and statistical models must be made in conjunction with the study area's actual geological environment and precipitation events.

Remote sensing and GIS applications are changing due to the explosion of geographic big data and recent advances in cloud computing and big data processing services. The Google Earth Engine (GEE) cloud platform is widely used for regional and even global remote sensing applications and geospatial data analysis [27]. Landslide susceptibility mapping and dynamic hazard assessment on a regional scale require large amounts of data and high computational power. GEE provides a new approach to geospatial data processing that addresses the challenges of data acquisition and processing faced by remote sensing researchers [28]. It provides a large number of remote sensing datasets as well as hundreds of pre-built functions that are simple to understand and use for users from various background. GEE allows researchers, scientists, and developers to quickly extract valuable information from large remote sensing datasets [29,30]. NASA researchers initiated regional landslide hazard studies previously, but they still encountered challenges such as data preprocessing difficulties and the simplicity of susceptibility evaluation models [31,32]. To date, GEE has been applied to both landslide susceptibility mapping research and landslide hazard assessment on a region scale [33,34].

Given the considerations detailed previously, this study aims to develop a dynamic, near-real-time method for assessing the risk of rainfall-induced landslides across a broad area using the Google Earth Engine (GEE) cloud platform. Our objectives are as follows: (1) Employ remote sensing big data from the GEE cloud platform to map landslide susceptibility throughout the Three Gorges Reservoir area (TGRA). (2) Utilize accumulated rainfall data and susceptibility maps from GEE's meteorological datasets to facilitate dynamic

hazard assessments of rainfall-induced landslides in the TGRA. (3) Examine the efficacy of this dynamic hazard assessment approach by analyzing remote sensing interpretation data of landslides in the TGRA before and after the significant rainfall event on 31 August 2014.

To innovate and extend the current knowledge base, this study introduces a novel application of GEE's comprehensive big data capabilities for real-time monitoring and analysis. This approach allows for a more timely and precise identification of potential landslide risks, contributing significantly to disaster risk management and mitigation in large, vulnerable regions.

2. Study Area and Dataset

2.1. Study Area

The Three Gorges Reservoir area (TGRA) ($28°56'$~$31°44'$ N, $106°16'$~$111°28'$ E) is located in the junction of the Sichuan Basin and the middle and lower reaches of the Yangtze River Plain in China (see Figure 1), spanning the canyons in the medium mountains of Hubei Province and the eastern valleys of Sichuan Province [35]. The TGRA covers the areas inundated or affected by the Three Gorges Project, encompassing 26 counties and districts in Hubei and Chongqing, with a total area of 58,377 km^2 and a shoreline length of about 650 km along the Yangtze River's main channel. With Fengjie as the boundary, the Three Gorges Reservoir area can be roughly divided into two major geomorphological units, the low and medium mountains of the Three Gorges, and the low hills of the Sichuan Basin. The TGRA is characterized by its highly complex geological and structural features. The stratigraphic composition primarily comprises sedimentary rocks from the Paleozoic, Mesozoic, and Cenozoic eras, with sandstone, shale, and limestone being predominant. Extensive tilting and folding are common, resulting in complex geological structures. Additionally, the area is interspersed with several active fault zones, such as the Badong and Zigui faults, which elevate the risk of geological hazards. The region's rugged terrain is dominated by high mountains and deep valleys, with steep slopes and significant topographical relief, alongside swiftly flowing rivers in the valleys. These geomorphological conditions play a crucial role in influencing the occurrence of geological disasters. Furthermore, the increasing number of human engineering activities have disrupted the natural balance of the original ecological environment, promoting the emergence and formation of geological hazards. The Three Gorges Reservoir area is a subtropical monsoon zone with a mild and humid climate, high air humidity, abundant rainfall, and high average temperature. About 70% of the annual precipitation in the region occurs from May to September, most of which is heavy rain and rainstorms that frequently raise groundwater levels, causing abnormal pore water pressure or hydrodynamic pressure and prompting the resurgence of landslides [36,37]. Over the past few decades, heavy rain events have repeatedly triggered major geological disasters in the TGRA. The TGRA is the main ecologically fragile area on the upper reaches of the Yangtze River and one of the most special ecological functional areas in China and even the world [38–41].
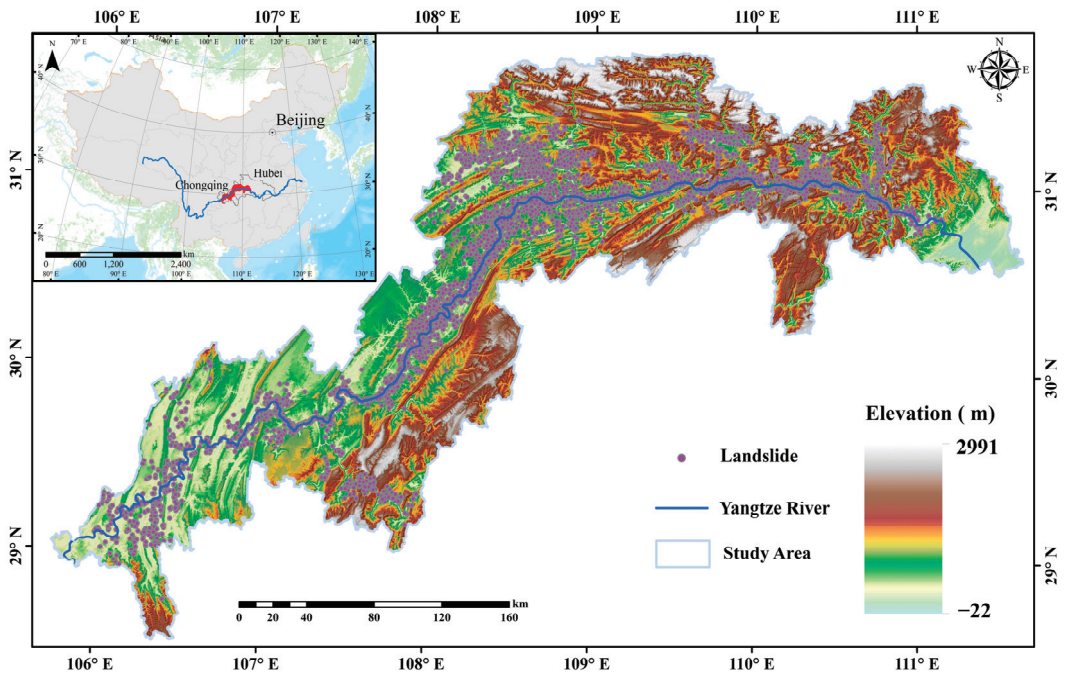
Figure 1. Location of Three Gorges Reservoir area and distribution of documented rainfall-induced landslides.

2.2. Datasets

Traditional data collection via the archives and online data collection via the Google Earth Engine (GEE) cloud platform are the primary data sources for this study. The documented rainfall-induced landslide data were obtained from the China Institute of Geo-Environment Monitoring and included a total of 5008 landslide points, whose spatial location and size are shown in Figure 1. Landslides predominantly consist of soil and rock, with a minor proportion of mixed rock–soil slides. The size distribution of these landslides is categorized as follows: mega-landslides, with volumes exceeding 10 million cubic meters, totaling 148; large landslides, with volumes ranging from 1 million to 10 million cubic meters, totaling 1292; medium landslides, encompassing volumes from 100,000 to 1 million cubic meters, accounting for 2443; and small landslides, less than 100,000 cubic meters, comprising 1125 instances. The current stability assessment reveals that 2037 landslides are relatively stable, 2048 exhibit moderate stability, and 503 are classified as unstable. The overall trend in landslide stability is deteriorating. These landslides primarily pose threats to human populations, residential structures, infrastructure such as roads, agricultural lands, and navigational routes. Landslides have threatened a total of 789,078 people, resulting in a direct economic loss of CNY 429,585,800 up to 2013 in the TGRA. The 1:200,000-scale base geological map and engineering geological map were obtained from the archives of China University of Geosciences (Wuhan). They were used to extract the engineering rock groups and geological formations. The following are the data obtained through the GEE cloud platform: high-precision digital elevation models for calculating elevation, slope, and aspect; multispectral remote sensing images from Landsat 8 OLI for calculating the type of land cover, the intensity of water influence, and the normalized difference vegetation index; precipitation radar satellite data from 23 August to 3 September 2014; the soil moisture index obtained from the inversion of a microwave remote sensing satellite; the dataset of annual average precipitation in the TGRA. The high-resolution

remote sensing imagery used in this study includes unmanned aerial vehicle (UAV) flights conducted by the Geological Disaster Management Department of Chongqing Municipal Government and Google Earth time-series images captured before and after the disaster events. These images were primarily employed for the visual interpretation of landslides following intense rainfall events. The interpretation adhered to the Chinese national standard for landslide hazard investigation to ensure scientific rigor and accuracy in landslide identification [42]. Detailed statistical characteristics and the criteria are presented in Table 1.

Table 1. Description and statistical characteristics of the datasets.

Dataset	Description	Source	Period Covered	Resolution
Landslides	Quantity, scale, location, and occurrence time of recorded landslides	China Institute of Geo-Environment Monitoring	8 July 1980–4 September 2012	Event-based
Rainfall	Spatial distribution of rainfall in millimeters	Global Precipitation Measurement (GPM) obtained from GEE	2000–2020	1 km
DEM	Digital elevation model for calculating topographic factors	Shuttle Radar Topography Mission (SRTM) obtained from GEE	2010	30 m
Multispectral imagery	Used for calculating the type of land cover, the intensity of water influence, and the normalized difference vegetation index	Landsat 8 Operational Land Imager (OLI) obtained from GEE	2014	30 m (9 bands)
High-spatial-resolution imagery	Used for interpreting landslides caused by heavy rainfall events	UAV aerial images obtained from the Geological Disaster Management Department and Google Earth time-series images obtained from GEE	2014	1~2 m (3 bands)

2.3. Influencing Factors of Landslides

The selected influencing factors in this study for rainfall-induced landslides refer to the influencing factors used in the consultation meeting on the development of geological disasters in the TGRA in 2020. This combination was determined by experts in the relevant fields who are familiar with the evolution of geological disasters in the TGRA and is a reasonable scheme. This combination of factors includes topographic factors, geological factors, land cover type, water system influence, the normalized difference vegetation index, the average annual precipitation, and soil moisture.

2.3.1. Topographic Factors

Topographic factors include elevation, slope, and aspect.

Elevation: The elevation of the terrain has a significant influence on the development of landslides. It mainly affects the surface type of the landslide, human activities, and the vegetation cover of the surface. Elevation changes result in changes in temperature, rainfall, vegetation types, and human activities, which indirectly affect the landslide development environment. Elevation can be obtained directly from the DEM (see Figure 1).

Slope: Slope is used to describe the degree of change in surface elevation. The angle of inclination directly affects the stability of the slope. Slope has a great influence on the stress distribution of the rock and soil mass, the runoff of surface water on the slope, the recharge and discharge of groundwater on the slope, the thickness of the weathered layer on the slope, vegetation cover, land use, and so on. It affects the stress distribution of the slope mass. In general, the larger the slope, the less stable the slope; the smaller the slope, the

lower the potential energy of the slope and the less susceptible it is to landslides. In this paper, the slope factor is extracted by using the DEM (see Figure 2).
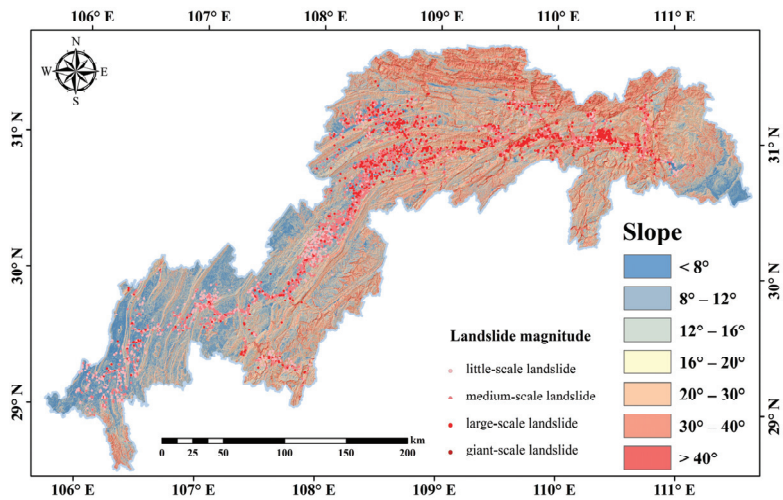
Figure 2. Slope distribution in the TGRA. The slope from small to large was divided into <8°, 8°–12°, 12°–16°, 16°–20°, 20°–30°, 30°–40°, and >40°, a total of 7 levels.

Aspect: There is a close relationship between solar radiation and the aspect. Different aspects result in varying intensities of solar radiation and weathering, which affect factors such as vegetation cover, water evaporation, and soil moisture. These lead to changes in pore pressure distribution as well as the physical and mechanical properties of groundwater in rocks and soil mass, thus indirectly affecting the stability of the slope. The aspect factors are extracted from the DEM data in this paper (see Figure 3).
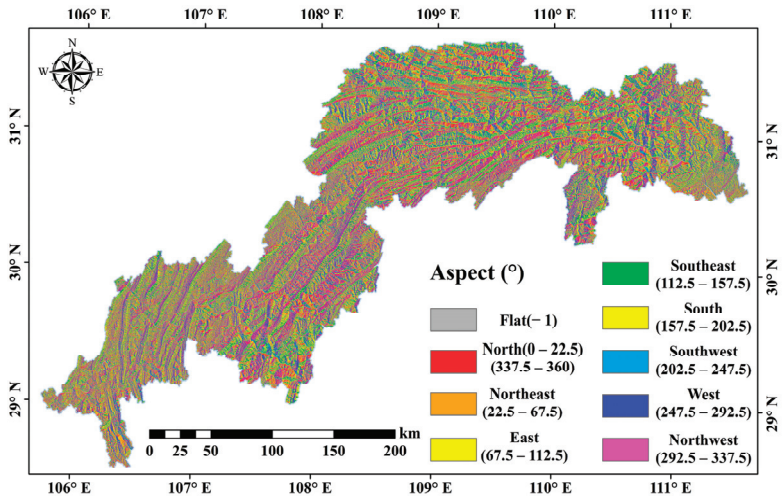
Figure 3. Aspect distribution in the TGRA. The slope was divided into nine directions: flat, north, northeast, east, southeast, south, southwest, west, and northwest, with each of the other eight directions taking 45°, except the flat one.

2.3.2. Geological Factors

Engineering rock groups: Statistics show that mineral hardness has a strong relationship with the spatial distribution of landslides in the study area. In areas with relatively strong rocks, it is hard for the slope to be deformed and destructed, so landslides are difficult to form. In areas with soft rocks, the slope is more easily deformed and destructed, making landslides more likely. Based on the 1:200,000 geological base map, the strata exposed in the TGRA were classified into different lithology groups according to their geotechnical properties. Strata with identical or similar petrophysical and mechanical properties were classified into the same engineering rock group. Landslides are greatly affected by unstable strata, which occur in stratified layers with soft surfaces or weak layers (belts). They are mainly clastic rocks (sandstone with a soft and hard interlayer, mudstone, and weak mudstone) belonging to Jurassic Penglaizhen Formation, Suining Formation, Shaximiao Formation, Xintiangou Formation, and Triassic Badong Formation. The factor of engineering rock groups after informatization is shown in Figure 4.
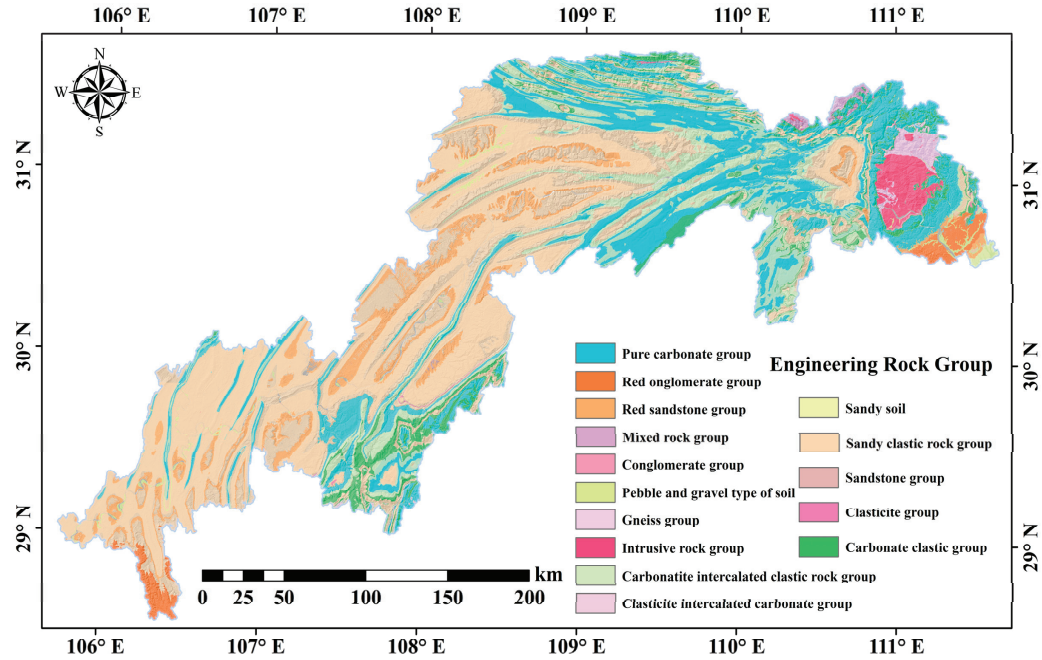
Figure 4. Engineering rock groups' distribution in TGRA.

Influence intensity of geological structures. The formation and development of landslides are closely related to tectonic movements, and geological structures are the fundamentals that control the formation and development of landslides. The magnitude, main slide direction, and spatial distribution of landslides are all controlled by the geological structure. It also regulates the formation and combination of soft and weak structural surfaces, the degree of rock weathering, topographic and geomorphological features, and the recharge of groundwater in landslide areas. Therefore, the geological structure is one of the crucial factors influencing landslide stability. In this study, a multilevel buffer zone was established to determine the intensity of tectonic influence depending on the distance from the geological structure to the landslides (see Figure 5).
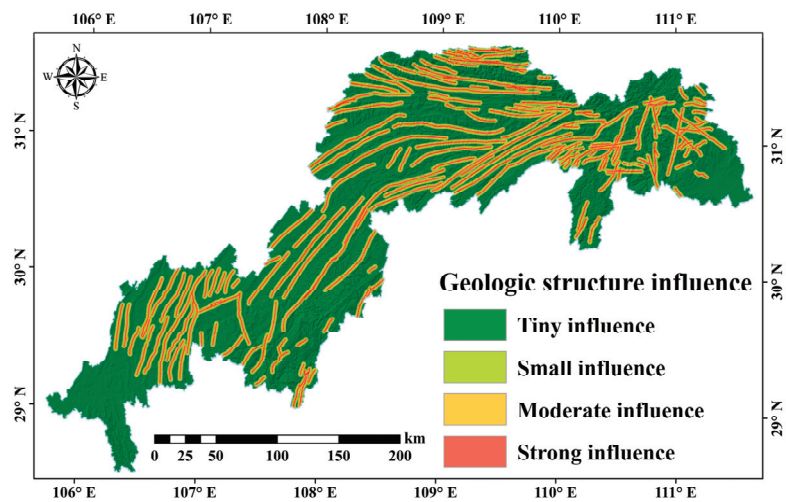
Figure 5. Influence intensity distribution of geological structures in the TGRA. Based on the distance from the geological structure to the landslides, there are four categories: strong influence, moderate influence, small influence, and tiny influence.

2.3.3. Land Cover Type

Human demand for land has increased tremendously due to the need for production and construction. And land has been changed significantly. Slopes must be cleared and land developed for infrastructure construction, which reduces slope stability and makes landslides more likely. Slope stability in terms of surface runoff and slope structure are affected by factors such as vegetation type and degree of cover, which vary from land to land. The land cover types in this paper were formed through supervised classification using multispectral data from the Landsat 8 resource satellite OLI and were divided into four categories: construction land, agricultural land, vegetation cover, and water body (see Figure 6).
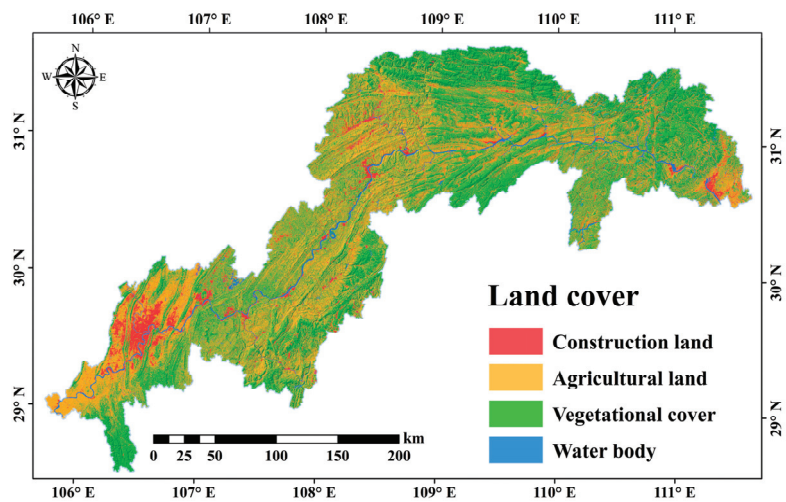
Figure 6. Land cover map of TGRA.

2.3.4. Influence Intensity of River Systems

Rock and soil mass near the river are prone to softening due to the inundation of the river. At the same time, the underlying rock layer in the river is eroded by the water flow, resulting in the suspension of the landslide mass. As a result, water flow has a negative impact on the stability of the geotechnical slope mass. Landslides are more likely to occur in areas near water. The intensity of the water influence involves both the distance from the landslides to water and the river grade. This article used remote sensing images taken from GEE to identify and extract information about the surface of the water system (see Figure 7).
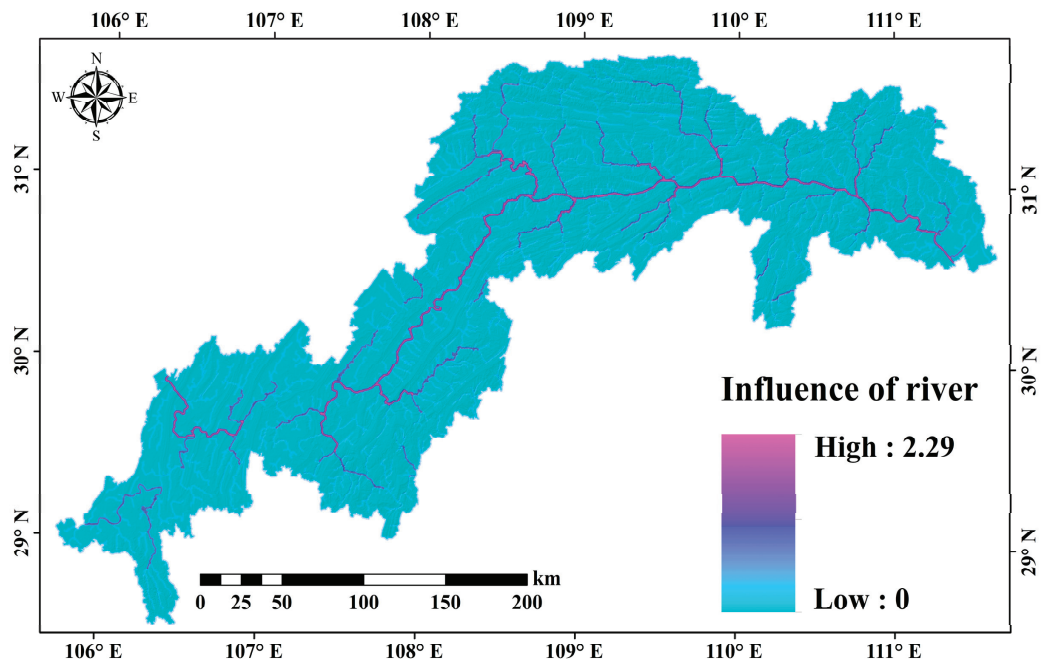
Figure 7. Influence intensity distribution of river system in TGRA.

2.3.5. Normalized Difference Vegetation Index (NDVI)

Vegetation plays a vital role in geological disasters because its root system increases the shear strength of the slope, reduces the impact of rain on the slope, and makes it more stable. At the same time, the leaves can help resist the erosion of rainwater, reduce the impact of rainwater on the slope, reduce surface runoff, and increase soil infiltration. The NDVI is defined as $(R_{NIR} - R_{RED})/(R_{NIR} + R_{RED})$. It is obtained through the inversion of remote sensing images from GEE, and it indicates the vegetation coverage and growth status (see Figure 8).
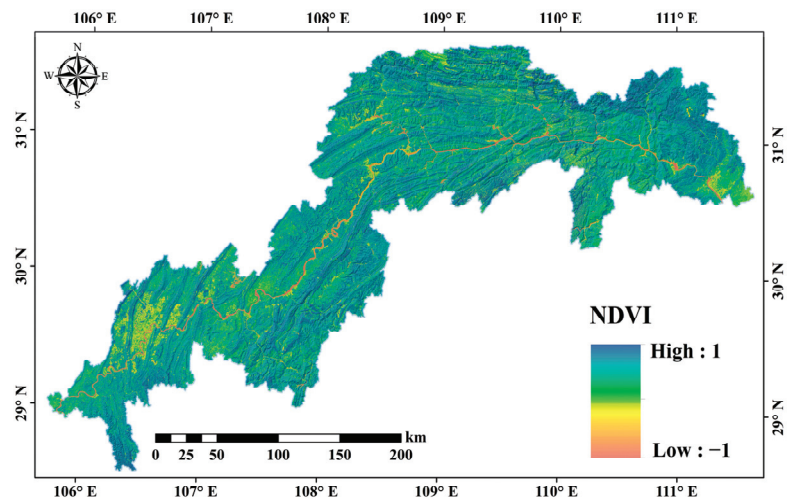
Figure 8. Normalized difference vegetation index distribution in the TGRA. The NDVI value ranges from −1 to 1. Higher values indicate higher vegetation cover for agricultural land, grassland, and forests, while lower values indicate lower vegetation cover for construction land, water bodies, or bare land.

2.3.6. Average Annual Precipitation

Rainfall is one of the factors that causes slope instability and landslides. The risk of landslides is higher during the rainy season. Rainfall infiltration increases the dead weight of the slope, weakens the shear strength, and unbalances the previously stable slope. Moreover, rainwater cannot percolate quickly enough during heavy rain events, so it converges in the valleys to form floods, which severely erode the slopes and lead to landslides. The average annual precipitation data came from NASA's Global Precipitation Measurement (GPM) through GEE (see Figure 9).
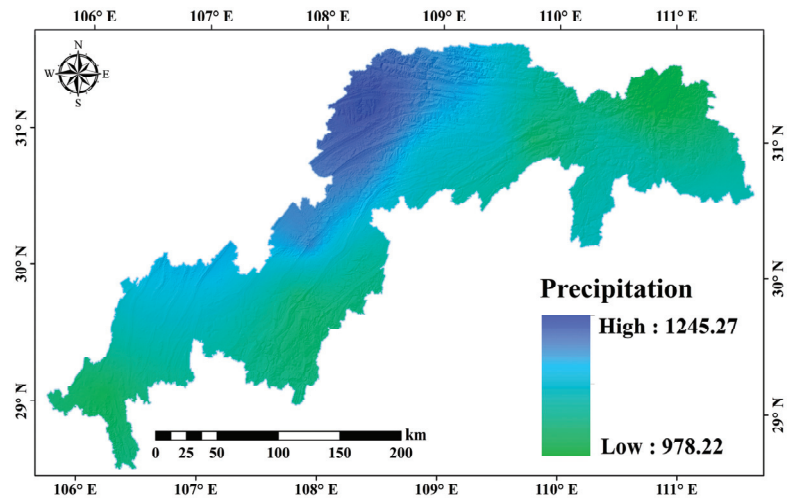
Figure 9. The average annual precipitation of the TGRA. The average annual precipitation ranges from 978.22 to 1245.27, with more rain in the middle and less at the two ends.

2.3.7. Soil Moisture Index

The soil's water content affects the shear strength of soil. The percentage of sand and the porosity affects the formation of landslides, especially as the clay at the interface acts as a lubricant during the interaction of rainwater. As a result, landslides link intimately with soil moisture. Landslides are most common in areas with high soil moisture. The soil moisture index was determined on the GEE cloud platform. The spatial resolution of the soil moisture data is 0.25°, allowing for the determination of soil moisture distribution on the surface and in the subsurface, as well as data of abnormal soil moisture (see Figure 10).
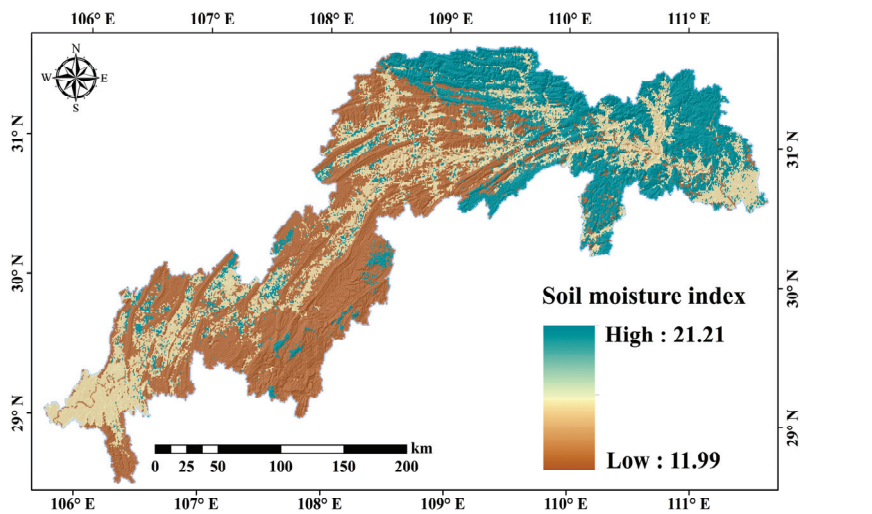
Figure 10. Soil moisture index distribution of the TGRA.

3. Methodology

Figure 11 illustrates the comprehensive process of landslide risk assessment using the Google Earth Engine cloud computing platform. The process begins with the collection of landslide and remote sensing data, including data from Landsat OLI and Google Earth for geographic and land cover information, as well as precipitation data from sources such as GPM, TRMM, and CHIRPS. These data inputs feed into an analysis of various landslide factors, categorized into geology, hydrology, geomorphology, and meteorology, which are essential in understanding the conditions contributing to landslide susceptibility.

The collected data are then processed and compiled into a set of features that are used to train the Gradient Boosting Decision Tree (GBDT) model. This model predicts the susceptibility of different areas to landslides, classifying them into categories ranging from very low to very high susceptibility. The output from the GBDT model is integrated with current or historical rainfall data to predict and classify the landslide risk levels. This integration aids in producing a dynamic and spatially aware map of landslide risk, crucial for effective disaster management and mitigation planning. The diagram effectively conveys a systematic approach to leveraging advanced data collection and modeling techniques to assess and predict landslide risks using the capabilities of cloud computing for real-time analysis and decision support.
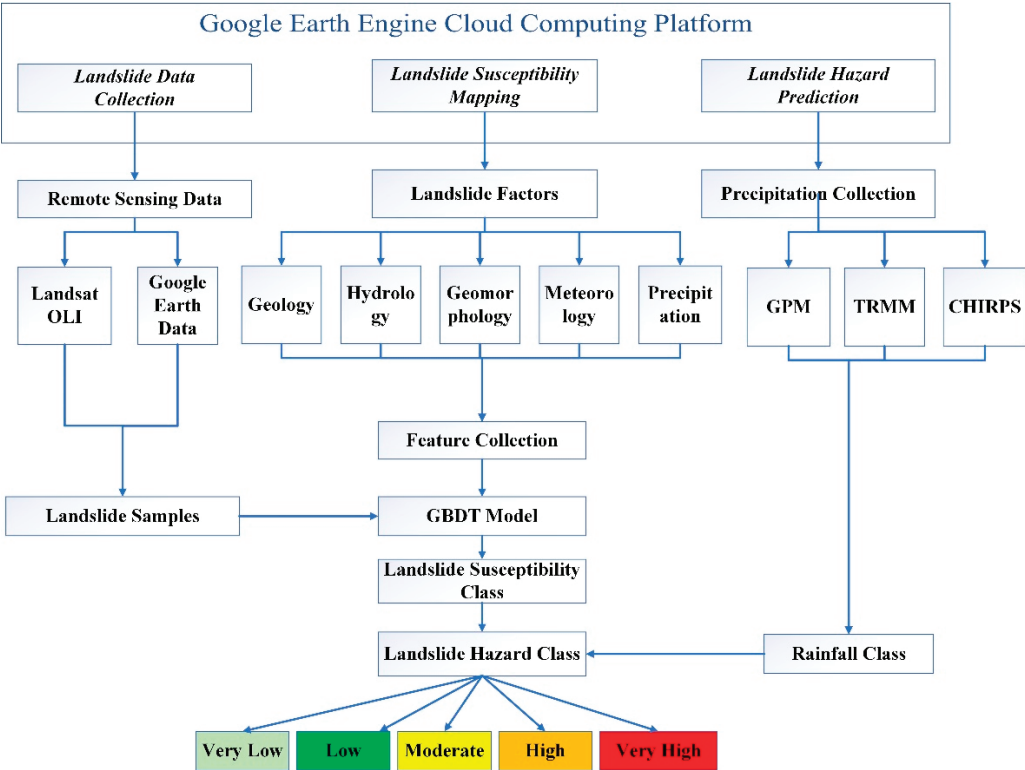
Figure 11. Flowchart of study.

3.1. Basic Landslide Interpretation Method

It is necessary to learn the formation law of landslides before interpreting rainfall-induced landslides to avoid blindness in interpretation and to facilitate interpretation. From a morphological standpoint, when a landslide occurs, micro-geomorphic features of a circle chair shape with a steep surrounding and gentle middle tend to appear on the slope. A fully developed landslide usually has elements such as landslide mass, landslide perimeter, landslide cliff, landslide terrace, landslide tongue, landslide spindle, landslide drumlins, landslide cracks, sliding surface, sliding zone, and sliding bed. In reality, landslides have different shapes and often do not have all of the above elements, but landslide cliff, landslide mass, landslide perimeter, sliding zone, and landslide bed are present in all landslides [43–45]. As for remote sensing observations, the only basic elements that can be interpreted are the surface landslide cliff and landslide perimeter. Starting from the basic image characteristics of landslides, this paper establishes the remote sensing interpretation markers of rainfall-induced landslides in the TGRA: (1) Landslides are mainly flat or have irregular shapes such as a dustpan, tongue, and pear. Larger-scale landslides can have micro-topographic shapes such as landslide cliffs, landslide terraces, landslide drumlins, closed depressions, landslide tongues, and landslide cracks. (2) Landslides often manifest as sudden destruction of the continuous landforms. They are composed of two types of geomorphic units: steep slopes and gentle slopes. Due to the compression of the soil, uneven landforms can sometimes be seen below the slope. The gentle slopes often have relatively deep gullies developed, and the terrain is relatively fragmented. (3) Landslides are more often formed in the gentle slopes of the canyons and the shady slopes of the watershed. They can also form at the intersection of the main and branch ditches, where the erosion base level changes sharply, and at the head of the ditch.

3.2. Gradient Boosting Decision Tree Model

The Gradient Boosting Decision Tree (GBDT) model is one of the more successful algorithms in the boosting family and can be used for classification and regression [17]. It creates a decision tree from an initial value. The leaves of the tree show the predicted value and the residual, and the next decision tree is learned based on this residual. Each iteration improves on the previous result, reduces the residual of the previous model, and builds a new combinatorial model in the direction of the gradient of residual reduction. In the iteration of the GBDT, we assume that the strong classifier that we obtained in the previous step is $F_t - 1(x)$, and the loss function at this point is $L(y, F_t - 1(x))$. Then, the next step is to find a weak classifier $h_t(x)$. On the one hand, this classifier is part of the CART regression tree model; on the other hand, it can minimize the loss function:

$$L(y, F_t(x)) = L(y, F_t - 1(x)) + h_t(x) \tag{1}$$

where $F_t(x)$ is the model prediction at iteration t for input x. $h_t(x)$ is the weak learner (e.g., a decision tree) added at iteration t. $L(y, F_t(x))$ is the loss function.

For the *t*-th iteration of sample *i*, the negative gradient of the loss function can be expressed as follows:

$$r_{ti} = -\left[\frac{\partial L(y_i, F(x_i)))}{\partial F(x_i)} \right]_{F(x)=F_{t-1}(x)} \tag{2}$$

A regression tree can be fitted using (x_i, r_{ti}) $(i = 1, 2, \ldots m)$, where the leaf nodes of the regression tree are $R_{tj}, j = 1, 2, \ldots, J$. J is the number of leaf nodes.

For each sample of a leaf node, the best-fitting leaf node c_{tj} can be expressed as follows:

$$c_{tj} = \underset{c}{\arg min} \sum_{x_i \in R_{ij}} L(y_i, F_{t-1}(x_i) + c) \tag{3}$$

Therefore, the decision tree function for this iteration can be obtained as follows:

$$h_t(x) = \sum_{j=1}^{J} c_{tj} I(x \in R_{tj}) \tag{4}$$

For a binary classification problem, the binary loss function of the GBDT can be described as follows:

$$L(y, F(x)) = \log(1 + \exp(-yF(x))), y \in \{-1, 1\} \tag{5}$$

The negative gradient error can be described as follows:

$$r_{ti} = -\left[\frac{\partial L(y, F(x_i)))}{\partial F(x_i)} \right]_{F(x)=F_{t-1}(x)} = y_i / (1 + \exp(y_i F(x_i))) \tag{6}$$

where r_{ti} is the negative gradient of the loss function for sample *i* at iteration *t*, which serves as the pseudo-response for the next learner to fit.

The optimal residual fit of each leaf node (Leaf Node) of the final decision tree can be expressed as follows:

$$c_{tj} = \underset{c}{\arg min} \sum_{x_i \in R_{ij}} \log(1 + \exp(-y_i(F_{t-1}(x_i) + c))) \tag{7}$$

where c_{tj} is the value for leaf *j* of the new tree, which minimizes the loss when added to the existing model.

Using the Newton–Raphson formula, the above formula can be further approximated in the following form:

$$c_{tj} = \sum_{x_i \in R_{tj}} r_{ti} / \sum_{x_i \in R_{tj}} |r_{ti}|(1 - |r_{ti}|) \tag{8}$$

The final obtained $F(x)$ is related to log-odds and can be used to perform probability calculations:

$$P(x) = \frac{e^{2F(x)}}{1 + e^{2F(x)}} = \frac{1}{1 + e^{-2F(x)}} \tag{9}$$

where $P(x)$ is the probability of landslide occurrence of sample x.

3.3. Rainfall Intensity–Duration Indicator

Rainfall is an important factor in the formation of landslides. When landslide accumulation is unsaturated, the infiltration of rainfall increases the weight of the landslide body. The influence of rainfall on the landslide body is determined by both the slope body's infiltration capacity and rainfall intensity [46]. The infiltration capacity of a landslide body is related to the material composition and structure of the slope. When the rainfall intensity is low, all of the rainfall will infiltrate into the slope body; when the rainfall intensity is high, part of the rainfall infiltrates into the slope body, and the other part becomes surface runoff [47]. Rainfall intensity is mainly indicated by two factors: the amount of rainfall and rainfall duration. The Rainfall Intensity–Duration Index (I-D) takes the effects of these two factors into account. If the cumulative amount of rainfall at a given time exceeds a certain threshold, it is assumed that the rainfall at this specific time and location may cause a landslide. If the susceptibility to landslides at that location is high, then a landslide is very likely to occur at that time [48]. We use the cumulative 7-day rainfall as the measurement index and combine the rainfall threshold with the landslide susceptibility to obtain the hazard assessment results.

3.4. Dynamic Hazard Assessment System of Landslide Based on GEE (DHAS)

We created a DHAS system to make better use of the relevant data from the GEE cloud platform. The system uses JavaScript as the development language to conduct a dynamic hazard assessment of rainfall-induced landslides based on the GEE cloud platform. We extracted various factors related to landslide hazards in the TGRA on the GEE cloud platform, primarily the factor layers of elevation, slope, slope direction, rainfall, and NDVI [49,50]. We uploaded the stratigraphic lithology, geological structure, land cover type, and documented landslide data from our local system to the GEE cloud platform. The mighty computing power of the GEE cloud platform facilitates the dynamic landslide hazard assessment calculation. The results are displayed in real-time on the DASH system using big data visualization technology. This system enables dynamic monitoring and predictions in near-real time of rainfall-induced landslide hazards in the TGRA [28,51].

4. Results

4.1. Susceptibility Mapping of Rainfall-Induced Landslides

Landslide susceptibility mapping (LSM) is the prerequisite for hazard assessment. The basic idea behind landslide susceptibility mapping is to use the relationship between landslide occurrence and the factors influencing it to build a mathematical model and then to use it to calculate the probability of landslide occurrence in areas with the same geological environment, allowing for landslide spatial prediction. Quantitative landslide susceptibility mapping methods include physical-based methods and data-driven methods. This study uses the popular ensemble learning method, the GBDT, for landslide susceptibility mapping, which is a data-driven method. It is robust and can handle data of various types (continuous data or discrete data) flexibly. It has high prediction accuracy with only a few fitting parameters. The following are the main steps in implementing LSM:

(1). Selection of mapping unit. The mapping unit determines the amount of input data that we use in the model and the spatial resolution of the resulting graph. According to the needs of mapping at different scales, there are four commonly used LSM units: grid units, geographic units, slope units, and sub-watershed units. In this study, we chose the grid unit for mapping due to the large extent of the study area and discrete landslide locations. The spatial resolution of the grid was set to 30 m × 30 m, consistent with the

spatial resolution of GEE online remote sensing data. Survey data such as engineering rock groups and average annual precipitation were resampled to 30 m. There was a total of 7,480,817 mapping units for the study area.

(2). Creation of sample dataset. In this study, we initiated our research by constructing an imbalanced dataset where positive samples (labeled 1) comprised all 5008 rainfall-induced landslides in the TGRA, along with the values of 10 influencing factors at their respective spatial locations. To provide a contrast, 15,024 random points were generated in areas devoid of landslides, with the values of the same 10 influencing factors constituting the negative samples (labeled 0). This led to the creation of a 20,032 × 11 (one label, ten features) two-dimensional sample dataset by merging these positive and negative samples. To maximize the utilization of information from non-landslide areas and to ensure a robust analysis, the dataset was deliberately imbalanced with fewer landslide than non-landslide samples. Further data processing involved extracting values from various landslide factor layers to the landslide samples using the 'Extract Multi Values to Points' function in ArcGIS. The data compiled into a two-dimensional decision table were then subjected to several preprocessing steps: handling missing values, normalizing the data to ensure a uniform scale, analyzing multicollinearity to identify and correct highly correlated variables, and reducing data dimensionality. These preprocessing measures were essential to enhance the data's representativeness and the robustness of the predictive model, ensuring accurate landslide risk assessment.

(3). Building the prediction model. The sample data were randomly divided into a training set (80%) and a test set (20%). The training set was used to create the optimal model, and the test set was used to test how well the model could be generalized. We chose the log-likelihood function "deviance" as the loss function. The initial learning rate was 0.1, and the optimal hyperparameters of the model were determined step by step using the grid search method.

To provide a more comprehensive understanding of the performance metrics used to evaluate the GBDT model in our study, here are the formulas for accuracy, precision, recall, and F1 score:

$$\text{Accuracy} = \frac{TP + TN}{TP + FP + TN + FN} \tag{10}$$

Accuracy measures the proportion of true results (both true positives and true negatives) among the total number of cases examined. Here, TP (true positives) is the number of correct predictions when an instance is positive, TN (true negatives) is the number of correct predictions when an instance is negative, FP (false positives) is the number of incorrect predictions when an instance is positive, and FN (false negatives) is the number of incorrect predictions when an instance is negative.

$$\text{Recall} = \frac{TP}{TP + FN} \tag{11}$$

Recall is the ratio of correctly predicted positive observations to all observations in the actual class. It is a measure of the model's ability to find all of the relevant cases within a dataset.

$$\text{Precision} = \frac{TP}{TP + FP} \tag{12}$$

Precision is the ratio of correctly predicted positive observations to the total predicted positives. It is a measure of the accuracy of the positive predictions.

$$\text{F1} = \frac{2 \times \text{Precision} \times \text{Recall}}{\text{Precision} + \text{Recall}} \tag{13}$$

The F1 score is the weighted average of precision and recall. This score takes both false positives and false negatives into account. It is particularly useful when the classes are very imbalanced. The F1 score is a way of combining the precision and recall of the model, and it is defined as the harmonic mean of the model's precision and recall.

According to the prediction results on the test set, the accuracy, recall, precision, and F1 scores of the GBDT model were 0.951, 0.862, 0.957, and 0.907, respectively. This model had good accuracy and could be used to perform LSM.

(4). Application of the model. The influencing factor values of all grid units in the study area were derived based on their spatial position to produce the dataset to be predicted. The best model that passed the test was used on the dataset and generated the landslide probability on each grid unit. The landslide prediction index (LPI) map was then created based on the latitude and longitude of each grid unit. Using the natural breakpoint method, the LPI was classified into five categories: very low, low, moderate, high, and very high, representing the degree of landslide susceptibility. The corresponding LPI ranges were 0–0.148, 0.148–0.327, 0.327–0.576, 0.576–0.797, and 0.797–1 (see Figure 12).
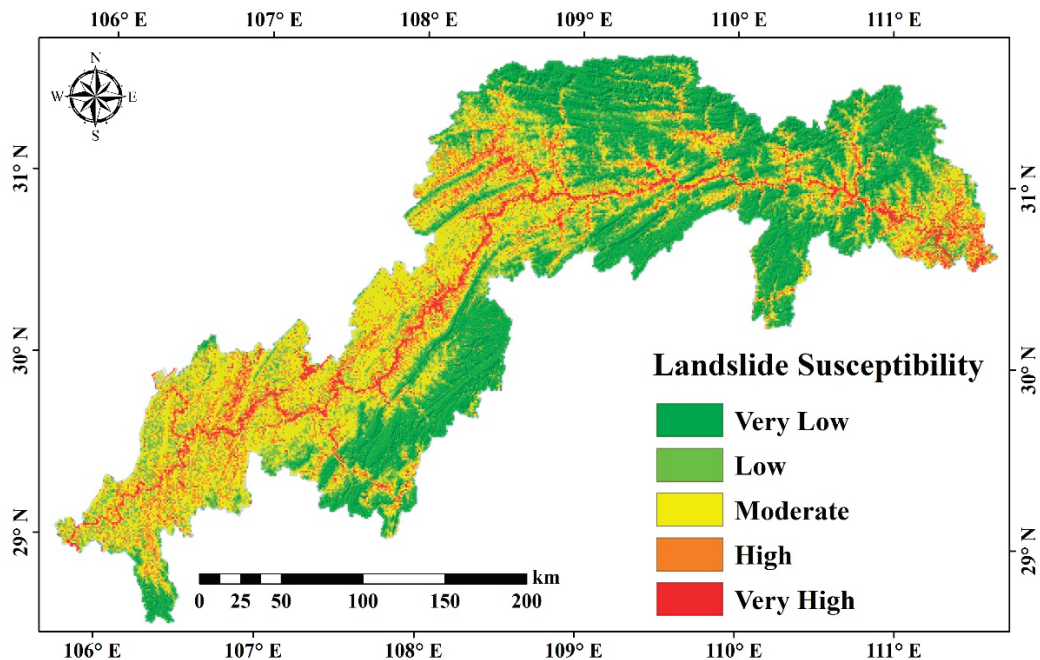
Figure 12. Susceptibility mapping of rainfall-induced landslides in the TGRA.

From the landslide susceptibility map (see Figure 12) and the distribution characteristics of the water system, we can conclude that the highly susceptible areas in terms of geological disasters in the TGRA are concentrated along the mainstream of the Yangtze River and its major tributaries, namely Xiangxi, Qinggan, Daning, Meixi, and Tangxi. Geological disasters are concentrated in the Zigui Basin and northeastern Chongqing. Based on the engineering rock group layers and landslide susceptibility mapping, we found that clastic rock areas, including the Jurassic strata and the Triassic Badong strata, are all located in the moderate or high landslide susceptible areas. For the overall distribution, susceptibility to landslides in the TGRA was primarily determined based on engineering rock groups, topography, and rivers. At the local level, landslides were influenced by geomorphic type and land cover.

4.2. Dynamic Hazard Assessment of Rainfall-Induced Landslides

In this paper, regional landslide susceptibility levels and cumulative rainfall levels are used to assess the risk of landslide disasters. Landslide susceptibility mapping provided the spatial probability of landslides, and the temporal probability of landslides was obtained

from the temporal rainfall accumulation. Combining the spatial and temporal probabilities, we could simulate the dynamic distribution on the time series of landslide hazards in the region using near-real-time spatial rainfall data provided by the GEE cloud platform.

4.2.1. Temporal Rainfall Accumulation Grading

In this paper, the method for determining the gradings of temporal rainfall accumulation used the Rainfall–Duration (I-D) Indicator. This method is an empirical mathematical–statistical model that builds on the relationship between rainfall accumulation and landslides in the real world, using the rainfall accumulation data from seven days before the occurrence of landslides as the measurement standard. There were a total of 5008 rainfall-induced landslides cataloged, with 2639 landslides with exact occurrence dates after 1980 occurring between 8 July 1980 and 4 September 2012 (see Figure 13). NOAA's National Centers for Environmental Information (NCEI) Global Summary of the Day provided the daily rainfall data from precipitation monitoring stations in the TGRA. Daily rainfall data from central monitoring stations were available from 1 January 1951 to the present. Each landslide was associated with the nearest precipitation monitoring station based on its spatial position, and precipitation accumulation data for the seven days before each landslide were obtained using the ArcGIS Python script. From the statistical relationship between historical landslides and rainfall accumulation (Figure 14), we can see that the accumulated 7-day rainfall that induced landslides could be divided into five levels, namely no occurrence of landslides, random occurrence, local occurrence, group occurrence, and massive occurrence. The accumulated precipitation levels were <100 mm, 100–140 mm, 140–170 mm, 170–200 mm, and >200 mm, respectively.
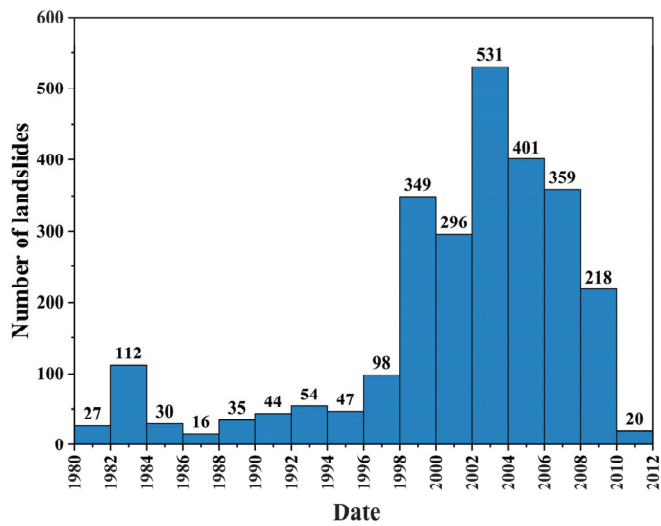
Figure 13. Temporal distribution of rainfall-induced landslides in TGRA.
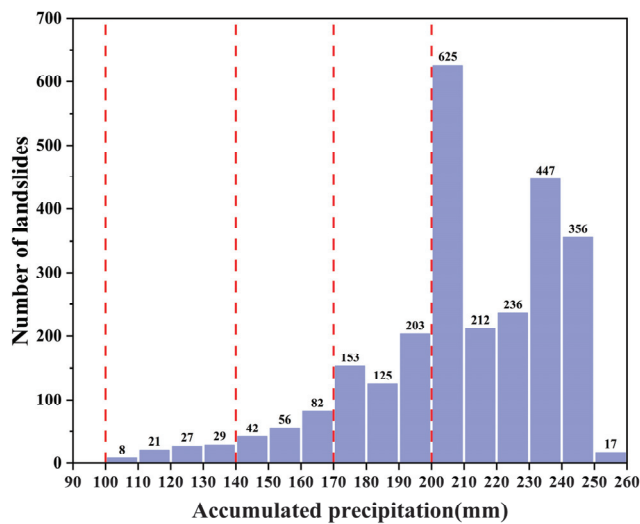
Figure 14. Statistical relationship between historical landslides and 7-day accumulative precipitation in TGRA.

4.2.2. Dynamic Hazard Assessment of Rainfall-Induced Landslides

Combining the grading of temporal rainfall accumulation with the landslide susceptibility classification yielded a semiquantitative classification table for landslide hazard assessment. The hazard of landslides can be classified into five categories, namely very high, high, moderate, low, and very low, corresponding to different susceptibilities of landslides and the threshold of temporal rainfall accumulation. These five levels are red, orange, light green, blue, and purple, as shown in Table 2. Based on this table, we can intuitively assess the hazard level of rainfall-induced landslides in any time series at any spatial position in the study area using the precipitation radar satellite data, which are updated in near-real time, to prevent and mitigate disasters in real time.

Table 2. Classification sheet of landslide risk based on gradings of temporal rainfall accumulation. Red, orange, light green, light blue, and dark blue respectively denote the five levels of landslide hazard: very high, high, moderate, low, and very low.

Temporal Rainfall Accumulation Gradings	Susceptibility Classes				
	Very High	High	Moderate	Low	Very Low
Large occurrence (>200 mm)					
Group occurrence (170~200 mm)					
Local occurrence (140~170 mm)					
Accidental occurrence (100~140 mm)					
No occurrence (<100 mm)					

After completing the modeling of the hazard assessment of rainfall-induced landslides, this paper selected a typical rainfall event in the TGRA. Based on the temporal and spatial distribution of rainfall in the study area, we successfully conducted a dynamic assessment of the risk of rainfall-induced landslides in this case and analyzed the temporal and spatial variation law of the rainfall-induced landslide hazards in the TGRA.

The majority of the TGRA experienced intense continuous rainfall from 29 August to 3 September 2014. The Global Precipitation Measurement (GPM) obtained from the GEE cloud platform recorded the daily meteorological distribution in the study area (see Figure 15a,c,e,g,i,k), providing data for the dynamic hazard assessment of landslides. Based

on the above landslide hazard assessment model, the DHAS system developed in this paper was used to produce daily updated landslide hazard assessment maps from 29 August to 3 September 2014 (see Figure 15b,d,f,h,j,l).

The landslide hazard assessment map shows that accumulated precipitation was up to 23 mm in the seven days preceding 29 August. The landslide risk in the entire TGRA was mostly low or very low. The local area had a moderate risk because the landslides had a relatively high susceptibility in this area and were thus easily influenced by rainfall. On 30 August, the accumulated precipitation exceeded 100 mm in Kaixian, Fengjie, Wushan, Badong, Zigui, and other places. The maximum local precipitation in some areas reached 138 mm. The low-risk areas gradually faded away, and the moderate-risk areas occupied the central and east of the reservoir area. Very-high-risk areas appeared sporadically in some areas. Fengjie County, Kaizhou County, northern Yunyang County, and southern Wuxi County in northeastern Chongqing received the most rainfall on 31 August. The daily maximum rainfall was 104 mm, with accumulated precipitation exceeding 200 mm. The low- and very-low-risk areas vanished. The risk of landslides was high in most areas, and some areas reached a very high risk level. Rainfall in northeast Chongqing, Zigui, and Badong decreased significantly from 1 to 3 September, with daily rainfall less than 20 mm. Some areas in southwest China gradually returned to being low-risk areas again, and the overall risk decreased. However, from the time-series map of hazard zones, the risk in Wushan, Fengjie, Yunyang, Wuxi, and other areas in northeast Chongqing had increased day by day since 30 August 2014, and remained at the very high landslide hazard level from 1 to 3 September, although rainfall decreased significantly during those days. This was mainly because the delay in the influence of rainfall on landslides was considered when calculating the landslide risk. The previous rainfall greatly influenced landslide risk, and the landslide risk was still high after the rainstorm, which was also the reason for the accumulated precipitation in the first seven days before the draft. Detailed hazard classes' sub-area statistics are shown in Table 3.

Table 3. Landslide hazard assessment result zoning statistics from 29 August 2014 to 3 September 2014.

Date	Classes of Landslide Hazard				
	Very Low	Low	Moderate	High	Very High
29 August 2014	6.31%	65.09%	28.71%	1.38%	0.00%
30 August 2014	1.25%	41.28%	55.65%	3.31%	0.00%
31 August 2014	0.08%	3.41%	57.79%	39.52%	0.69%
1 September 2014	0.00%	1.76%	34.06%	57.57%	8.10%
2 September 2014	0.00%	7.66%	38.00%	47.17%	8.66%
3 September 2014	0.00%	7.54%	37.45%	47.77%	8.73%
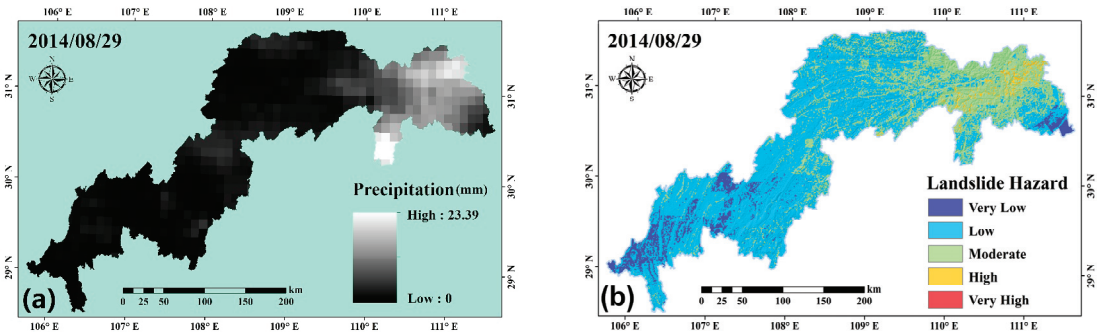
Figure 15. *Cont.*
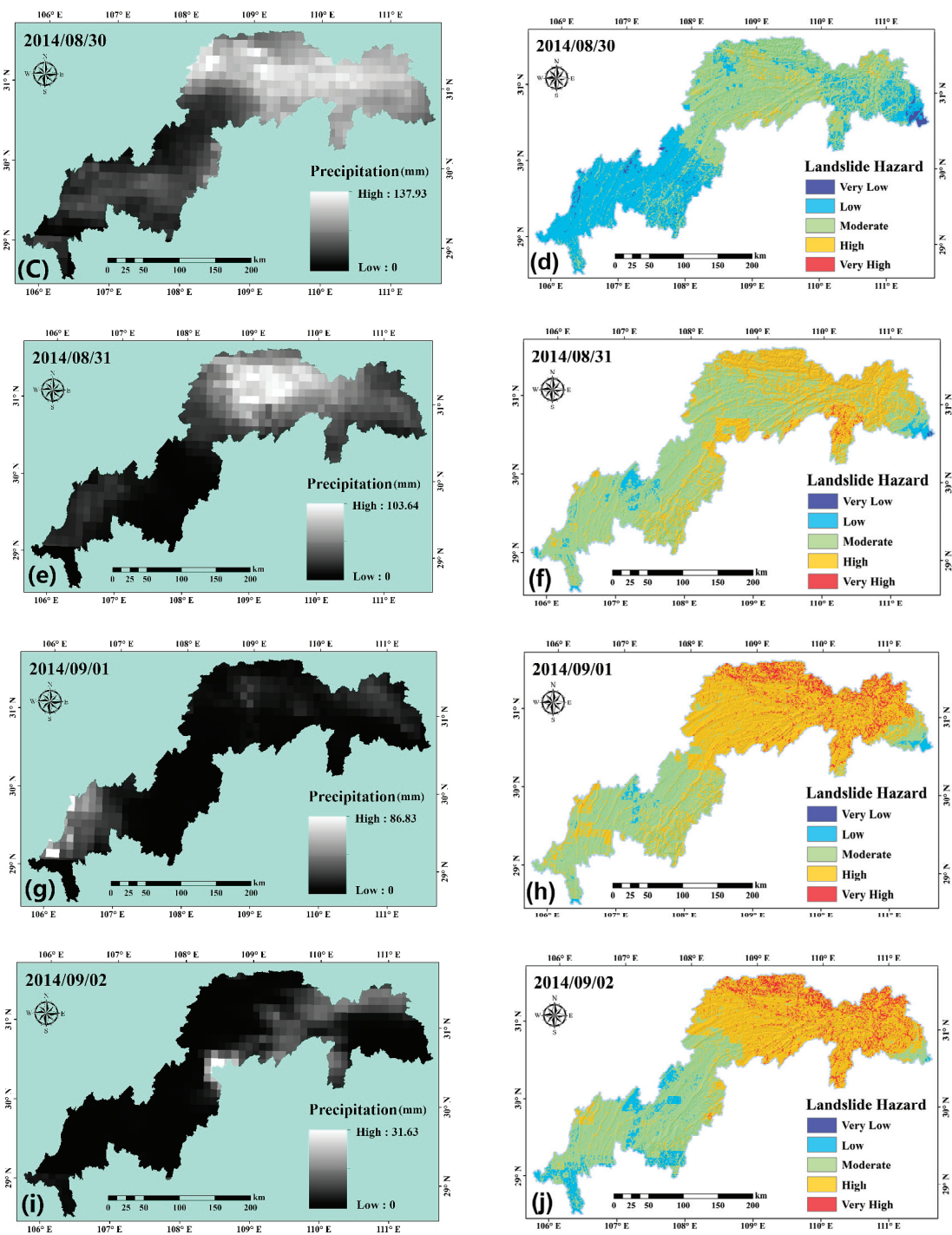
Figure 15. *Cont.*
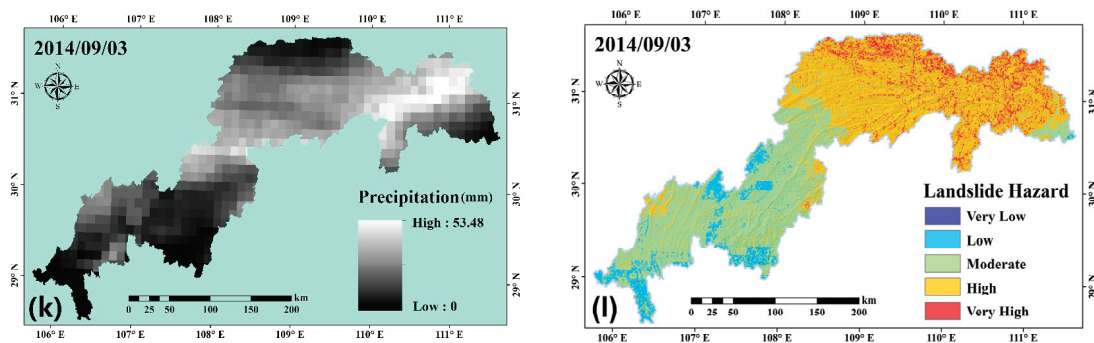
Figure 15. The distribution of daily precipitation and its corresponding landslide hazard distribution in the TGRA. (**a,c,e,g,i,k**) denote the spatial distribution of precipitation for each day of the rainfall duration; (**b,d,f,h,j,l**) denote the spatial distribution of landslide hazards for each day of the rainfall duration.

5. Discussion

The dynamic hazard assessment of rainfall-induced landslides is essential for the government to formulate disaster prevention and mitigation policies. The accuracy of the assessment results is directly related to the safety of the life and property of people in the hazard area, which should withstand the factual arguments. To verify the generalizability of the above assessment method and the validity of the assessment results, this paper used the remote sensing interpretation method of rainfall-induced landslides to identify the TGRA landslides induced by the rainstorm of 31 August 2014. The data came from the aerial images of UAVs and high-resolution satellite images before and after the rainstorm. By comparing the temporal remote sensing images of before and after, we found that the vegetation, houses, roads, and farmlands in the slope area with large-scale landslides after the heavy rainfall were destroyed. The land texture was remarkably different from the area where no landslides occurred. The deformation features of the landslide mass were prominent, and the geotechnical structure was disrupted. Cracks of different types, such as tensile cracks at the trailing edge, landslide depression, and chair-like cracks, steep ridges, or noticeable landslide cliffs were observed. In general, satellite images of the landslide areas were light in color, with exposed rocks and soil that were easy to identify (see Table 4).

This study identified a total of 622 landslides after the rainfall, with 353 in Yunyang County and 279 in Fengjie County, after excluding human intervention and analyzing remote sensing images. Analysis of the spatial location of landslides and the accumulated precipitation (Figure 16a) showed that landslides mainly occurred in areas with accumulated precipitation of more than 200 mm, indicating that the distribution of landslides correlated well with accumulated precipitation and rainfall intensity. From the distribution of landslides in the hazard assessment map, the interpreted landslides were all in high- or very-high-risk areas. Among them, 70.3% and 29.7% of the landslides were in the high- and very-high-risk areas, respectively, in Yunyang County. A total of 53% and 47% of the landslides were in the high- and very-high-risk areas in Fengjie County. This result confirmed the timeliness and accuracy of the hazard assessment.

Table 4. Remote sensing interpretation of landslides induced by extreme rainfall in "8–31" rainstorm in 2014.

No.	Position	Description	Slope	Remote Sensing Images
1	Xinli Village, Jiangkou Town, Yunyang County	Location: E 108°47′37.74″ N 31°14′37.28″ Development stratigraphy: J2x Xintiangou Formation Type: nascent landslide	24~36°	
2	Xiaoyakou Yuzhuan Town, Yunyang County	Location: E 108°50′35.62″ N 31°20′9.81″ Development stratigraphy: T3x Sujiahe Formation Type: nascent landslide	36~41°	
3	Shashi Town, Yunyang County	Location: E 108°55′46.74″ N 31°18′27.40″ Development stratigraphy: T2b Badong Formation Type: old landslide revival	31~40°	
4	Luojiapo, Shangdou Town, Wuxi County	Location: E 109°28′27.17″ N 31°16′32.79″ Development stratigraphy: J1z Pearl Rush Formation Type: nascent soil landslide	29~43°	
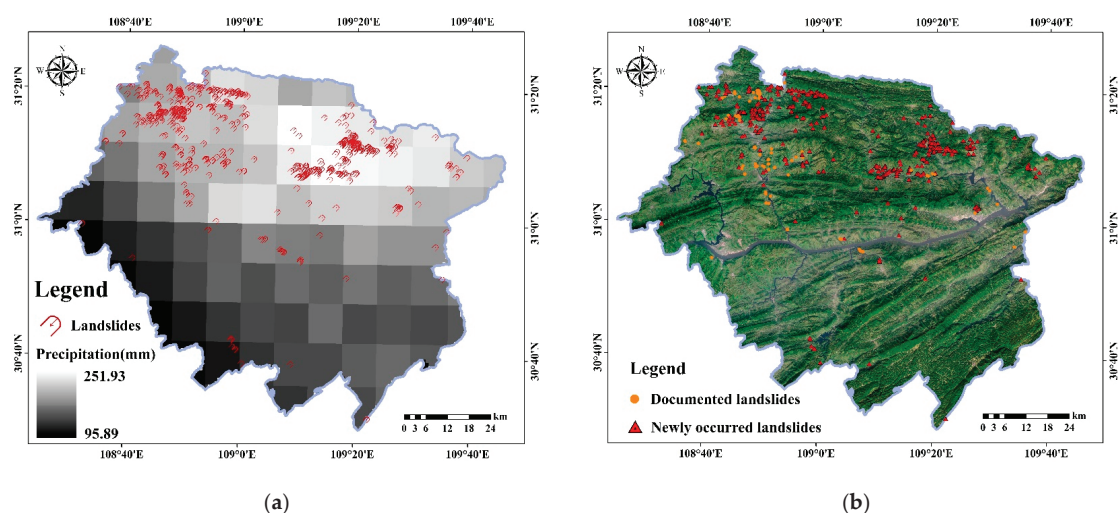
Figure 16. (**a**) Spatial distribution of landslides and accumulated rainfall interpreted by remote sensing in Yunyang and Fengjie. (**b**) Spatial distribution of nascent landslides and documented landslides in Yunyang and Fengjie.

We further analyzed the influencing factors of the interpreted rainfall-induced landslides and found that landslides were more common on slopes with summit elevations between 1000 m and 1500 m, topographic slopes of about 25°, and sunny slopes. Landslides occurred in an elevation range from 200 m to 1350 m. The number of landslides first increased and then decreased with increasing elevation. Landslides were concentrated in the elevation range of 400–700 m. Landslide development strata are mainly Jurassic and Triassic Middle Badong Formation. The primary lithology consists of sandstone, siltstone, marl, mudstones, and shales of different layer thicknesses. The strata belong to soft and hard rock groups. As for the scale of landslides, small and medium landslides dominated, accounting for 90.7% of all landslides.

Another important finding is that 83% of the landslides interpreted in this experiment were not documented (see Figure 16b) and were nascent landslides induced by this rainstorm. Some of the old landslides were found to be severely deformed or even massively slid under the influence of heavy rainfall. These findings indicate that the hazard assessment could help reveal the development direction of historical landslides as well as identify new landslides.

The severe rainstorm resulted in numerous fatalities and missing persons, as well as significant damage to critical infrastructure including roads and bridges. Furthermore, the event forced thousands of families to evacuate their homes devastated by landslides. Agricultural fields and crops suffered extensive damage, which in turn caused substantial disruptions in transportation and halted production activities, leading to considerable socioeconomic losses. The implementation of the dynamic landslide hazard assessment method proposed in this study during a heavy rainstorm could be crucial. By accurately predicting high-risk landslide zones and swiftly identifying emerging landslides, this method can significantly mitigate both human and economic losses in vulnerable areas, thereby greatly enhancing the safety of the affected populations.

Prompt dynamic hazard assessment of rainfall-induced landslides is an urgent and practical research topic because landslide evolution is a complex nonlinear process that still requires new theoretical support, and the assessment results have obvious realistic significance. The landslide hazard assessment process requires a large amount of foundational environmental data and remote sensing images. Researchers have encountered a lot of difficulties in previous landslide hazard studies in the TGRA due to the large study area. A

lot of time and effort was wasted on data acquisition and preprocessing. Therefore, based on the powerful computing power and massive image data of the GEE cloud platform, the prediction system developed in this study that integrates the GBDT machine learning model and basic data processing functions provides reliable data and technical support for landslide hazard assessment on a large regional scale. The dynamic assessment of landslide hazard requires real-time rainfall data, and GEE provides a variety of global meteorological satellite databases to offer precipitation data with a temporal resolution of 0.5 h, providing near-real-time data support for this dynamic landslide hazard assessment system. It should be noted that the dynamic hazard assessment method used in this study is semiquantitative and necessitates prior knowledge of empirical mathematical statistics on the occurrence of historical landslides and temporal rainfall accumulation in the study area, which is difficult to obtain in areas lacking historical landslide data. In a follow-up study, our goal is to create a quantitative study on dynamic hazard assessment using non-graded temporal accumulated precipitation and susceptibility mapping.

6. Conclusions

The powerful ability of machine learning to handle nonlinear relationships has led to its widespread application in areas such as groundwater prediction [52–54], landslide prediction [17,19], and land use mapping. This study introduces a novel near-real-time approach using the Google Earth Engine (GEE) platform combined with the Gradient Boosting Decision Tree (GBDT) model for dynamic hazard assessment of large-area rainfall-induced landslides. By applying the GBDT model based on various geological environmental factors, potential landslide locations were effectively predicted. Leveraging the powerful computing capabilities of GEE along with its up-to-date remote sensing and rainfall data, a dynamic evaluation of landslide risks was achieved.

Our results emphasize the effectiveness of combining cloud computing with machine learning to enhance landslide risk assessment. Specifically, the method successfully predicted landslide susceptibility with high precision, achieving a prediction accuracy of 86.2% and a recall rate of 95.7%, significantly improving the capability to predict and mitigate landslide disasters almost in real time during heavy rainfall events. For instance, the spatial and temporal analysis of the "8–31" 2014 rainstorm event in the Three Gorges Reservoir area highlighted the practical application of the model, providing closely related assessments for subsequent landslide events.

However, this study has its limitations. The accuracy of disaster prediction largely depends on the quality and resolution of the input data, and the model's performance may be compromised if applied outside the Three Gorges Reservoir area without appropriate adjustments and calibration. Moreover, although the model effectively handles the nonlinear relationships between multiple factors and landslide events, its predictive power is still limited by the inherent uncertainties of meteorological data and the dynamic nature of land cover and geological conditions.

Looking forward, the scalability and efficiency of the proposed method are expected to find broader applications in geological disaster prediction and management. Future research will focus on enhancing the model's universality across different geographic settings and exploring the integration of more diverse data types, such as real-time satellite imagery and IoT sensor data, to improve prediction accuracy. Future studies will also aim to refine the temporal resolution of hazard assessments to enable quicker responses to imminent landslide risks.

In conclusion, the integration of GEE and the GBDT for dynamic landslide hazard assessment represents a significant advancement in the field of geohazard analysis. By harnessing advanced computing and machine learning, this approach provides a powerful tool for disaster risk management and mitigation planning, making a significant contribution to the safety and resilience of vulnerable areas.

References

1. Keqiang, H.; Shangqing, W.; Wen, D.; Sijing, W. Dynamic Features and Effects of Rainfall on Landslides in the Three Gorges Reservoir Region, China: Using the Xintan Landslide and the Large Huangya Landslide as the Examples. *Environ. Earth Sci.* **2010**, *59*, 1267–1274. [CrossRef]
2. XIA, M.; REN, G.M.; MA, X.L. Deformation and Mechanism of Landslide Influenced by the Effects of Reservoir Water and Rainfall, Three Gorges, China. *Nat. Hazards* **2013**, *68*, 467–482. [CrossRef]
3. Dahal, R.K.; Hasegawa, S. Representative Rainfall Thresholds for Landslides in the Nepal Himalaya. *Geomorphology* **2008**, *100*, 429–443. [CrossRef]
4. Rosi, A.; Peternel, T.; Jemec-Auflič, M.; Komac, M.; Segoni, S.; Casagli, N. Rainfall Thresholds for Rainfall-Induced Landslides in Slovenia. *Landslides* **2016**, *13*, 1571–1577. [CrossRef]
5. Zhou, C.; Ai, D.; Huang, W.; Xu, H.; Ma, L.; Chen, L.; Wang, L. Emergency Survey and Stability Analysis of a Rainfall-Induced Soil-Rock Mixture Landslide at Chongqing City, China. *Front. Earth Sci.* **2021**, *9*, 774200. [CrossRef]
6. Hu, M.; Wang, R.; Shen, J. Rainfall, Landslide and Debris Flow Intergrowth Relationship in Jiangjia Ravine. *J. Mt. Sci.* **2011**, *8*, 603–610. [CrossRef]
7. Guzzetti, F.; Cardinali, M.; Reichenbach, P.; Cipolla, F.; Sebastiani, C.; Galli, M.; Salvati, P. Landslides Triggered by the 23 November 2000 Rainfall Event in the Imperia Province, Western Liguria, Italy. *Eng. Geol.* **2004**, *73*, 229–245. [CrossRef]
8. Lee, C.-T. Statistical Seismic Landslide Hazard Analysis: An Example from Taiwan. *Eng. Geol.* **2014**, *182*, 201–212. [CrossRef]
9. Wang, Z.; Wang, D.; Guo, Q.; Wang, D. Regional Landslide Hazard Assessment through Integrating Susceptibility Index and Rainfall Process. *Nat. Hazards* **2020**, *104*, 2153–2173. [CrossRef]
10. Golovko, D.; Roessner, S.; Behling, R.; Wetzel, H.-U.; Kleinschmit, B. Evaluation of Remote-Sensing-Based Landslide Inventories for Hazard Assessment in Southern Kyrgyzstan. *Remote Sens.* **2017**, *9*, 943. [CrossRef]
11. Samia, J.; Temme, A.; Bregt, A.; Wallinga, J.; Guzzetti, F.; Ardizzone, F.; Rossi, M. Do Landslides Follow Landslides? Insights in Path Dependency from a Multi-Temporal Landslide Inventory. *Landslides* **2017**, *14*, 547–558. [CrossRef]
12. Qiu, D.D.; Niu, R.Q.; Zhao, Y.N. Landslide Susceptibility Zonation Based on the Analytic Hierarchy Process and Information Method. *Appl. Mech. Mater.* **2014**, *580–583*, 2658–2662. [CrossRef]
13. Maharaj, R.J. Landslide Processes and Landslide Susceptibility Analysis from an Upland Watershed: A Case Study from St. Andrew, Jamaica, West Indies. *Eng. Geol.* **1993**, *34*, 53–79. [CrossRef]
14. Lee, S.; Min, K. Statistical Analysis of Landslide Susceptibility at Yongin, Korea. *Environ. Geol.* **2001**, *40*, 1095–1113. [CrossRef]
15. Ayalew, L.; Yamagishi, H. The Application of GIS-Based Logistic Regression for Landslide Susceptibility Mapping in the Kakuda-Yahiko Mountains, Central Japan. *Geomorphology* **2005**, *65*, 15–31. [CrossRef]
16. Zhao, L.; Wu, X.; Niu, R.; Wang, Y.; Zhang, K. Using the Rotation and Random Forest Models of Ensemble Learning to Predict Landslide Susceptibility. *Geomat. Nat. Hazards Risk* **2020**, *11*, 1542–1564. [CrossRef]
17. Song, Y.; Niu, R.; Xu, S.; Ye, R.; Peng, L.; Guo, T.; Li, S.; Chen, T. Landslide Susceptibility Mapping Based on Weighted Gradient Boosting Decision Tree in Wanzhou Section of the Three Gorges Reservoir Area (China). *ISPRS Int. J. Geo-Inf.* **2018**, *8*, 4. [CrossRef]
18. Zhou, C.; Yin, K.; Cao, Y.; Ahmed, B.; Li, Y.; Catani, F.; Pourghasemi, H.R. Landslide Susceptibility Modeling Applying Machine Learning Methods: A Case Study from Longju in the Three Gorges Reservoir Area, China. *Comput. Geosci.* **2018**, *112*, 23–37. [CrossRef]
19. Xu, S.; Niu, R. Displacement Prediction of Baijiabao Landslide Based on Empirical Mode Decomposition and Long Short-Term Memory Neural Network in Three Gorges Area, China. *Comput. Geosci.* **2018**, *111*, 87–96. [CrossRef]

20. Rong, G.; Alu, S.; Li, K.; Su, Y.; Zhang, J.; Zhang, Y.; Li, T. Rainfall Induced Landslide Susceptibility Mapping Based on Bayesian Optimized Random Forest and Gradient Boosting Decision Tree Models—A Case Study of Shuicheng County, China. *Water* **2020**, *12*, 3066. [CrossRef]

21. Bogaard, T.; Greco, R. Invited Perspectives: Hydrological Perspectives on Precipitation Intensity-Duration Thresholds for Landslide Initiation: Proposing Hydro-Meteorological Thresholds. *Nat. Hazards Earth Syst. Sci.* **2018**, *18*, 31–39. [CrossRef]

22. Saito, H.; Korup, O.; Uchida, T.; Hayashi, S.; Oguchi, T. Rainfall Conditions, Typhoon Frequency, and Contemporary Landslide Erosion in Japan. *Geology* **2014**, *42*, 999–1002. [CrossRef]

23. Abraham, M.T.; Satyam, N.; Rosi, A.; Pradhan, B.; Segoni, S. The Selection of Rain Gauges and Rainfall Parameters in Estimating Intensity-Duration Thresholds for Landslide Occurrence: Case Study from Wayanad (India). *Water* **2020**, *12*, 1000. [CrossRef]

24. Cannon, S.H.; Boldt, E.M.; Laber, J.L.; Kean, J.W.; Staley, D.M. Rainfall Intensity–Duration Thresholds for Postfire Debris-Flow Emergency-Response Planning. *Nat. Hazards* **2011**, *59*, 209–236. [CrossRef]

25. Peruccacci, S.; Brunetti, M.T.; Luciani, S.; Vennari, C.; Guzzetti, F. Lithological and Seasonal Control on Rainfall Thresholds for the Possible Initiation of Landslides in Central Italy. *Geomorphology* **2012**, *139–140*, 79–90. [CrossRef]

26. Ke, Q.; Tian, X.; Bricker, J.; Tian, Z.; Guan, G.; Cai, H.; Huang, X.; Yang, H.; Liu, J. Urban Pluvial Flooding Prediction by Machine Learning Approaches—A Case Study of Shenzhen City, China. *Adv. Water Resour.* **2020**, *145*, 103719. [CrossRef]

27. Deng, Y.; Jiang, W.; Tang, Z.; Ling, Z.; Wu, Z. Long-Term Changes of Open-Surface Water Bodies in the Yangtze River Basin Based on the Google Earth Engine Cloud Platform. *Remote Sens.* **2019**, *11*, 2213. [CrossRef]

28. Salcedo-Sanz, S.; Ghamisi, P.; Piles, M.; Werner, M.; Cuadra, L.; Moreno-Martínez, A.; Izquierdo-Verdiguier, E.; Muñoz-Marí, J.; Mosavi, A.; Camps-Valls, G. Machine Learning Information Fusion in Earth Observation: A Comprehensive Review of Methods, Applications and Data Sources. *Inf. Fusion* **2020**, *63*, 256–272. [CrossRef]

29. Sun, Z.; Sandoval, L.; Crystal-Ornelas, R.; Mousavi, S.M.; Wang, J.; Lin, C.; Cristea, N.; Tong, D.; Carande, W.H.; Ma, X.; et al. A Review of Earth Artificial Intelligence. *Comput. Geosci.* **2022**, *159*, 105034. [CrossRef]

30. Hu, Q.; Zhou, Y.; Wang, S.; Wang, F. Machine Learning and Fractal Theory Models for Landslide Susceptibility Mapping: Case Study from the Jinsha River Basin. *Geomorphology* **2020**, *351*, 106975. [CrossRef]

31. Farahmand, A.; AghaKouchak, A. A Satellite-Based Global Landslide Model. *Nat. Hazards Earth Syst. Sci.* **2013**, *13*, 1259–1267. [CrossRef]

32. Hong, Y.; Adler, R.; Huffman, G. Evaluation of the Potential of NASA Multi-Satellite Precipitation Analysis in Global Landslide Hazard Assessment. *Geophys. Res. Lett.* **2006**, *33*, L22402. [CrossRef]

33. Wu, W.; Zhang, Q.; Singh, V.P.; Wang, G.; Zhao, J.; Shen, Z.; Sun, S. A Data-Driven Model on Google Earth Engine for Landslide Susceptibility Assessment in the Hengduan Mountains, the Qinghai–Tibetan Plateau. *Remote Sens.* **2022**, *14*, 4662. [CrossRef]

34. Singh, P.; Maurya, V.; Dwivedi, R. Pixel based landslide identification using Landsat 8 and GEE. *Int. Arch. Photogramm. Remote Sens. Spat. Inf. Sci.* **2021**, *XLIII-B3-2021*, 721–726. [CrossRef]

35. Tang, H.; Wasowski, J.; Juang, C.H. Geohazards in the Three Gorges Reservoir Area, China—Lessons Learned from Decades of Research. *Eng. Geol.* **2019**, *261*, 105267. [CrossRef]

36. Tang, H.; Li, C.; Hu, X.; Wang, L.; Criss, R.; Su, A.; Wu, Y.; Xiong, C. Deformation Response of the Huangtupo Landslide to Rainfall and the Changing Levels of the Three Gorges Reservoir. *Bull. Eng. Geol. Environ.* **2015**, *74*, 933–942. [CrossRef]

37. Fang, Z.; Hang, D.; Xinyi, Z. Rainfall Regime in Three Gorges Area in China and the Control Factors. *Int. J. Climatol.* **2010**, *30*, 1396–1406. [CrossRef]

38. Wang, J.; Sheng, Y.; Tong, T.S.D. Monitoring Decadal Lake Dynamics across the Yangtze Basin Downstream of Three Gorges Dam. *Remote Sens. Environ.* **2014**, *152*, 251–269. [CrossRef]

39. Xiao, Y.; Xiao, Q.; Xiong, Q.; Yang, Z. Effects of Ecological Restoration Measures on Soil Erosion Risk in the Three Gorges Reservoir Area Since the 1980s. *GeoHealth* **2020**, *4*, e2020GH000274. [CrossRef]

40. Huang, C.; Huang, X.; Peng, C.; Zhou, Z.; Teng, M.; Wang, P. Land Use/Cover Change in the Three Gorges Reservoir Area, China: Reconciling the Land Use Conflicts between Development and Protection. *CATENA* **2019**, *175*, 388–399. [CrossRef]

41. Huang, D.; Gu, D.M.; Song, Y.X.; Cen, D.F.; Zeng, B. Towards a Complete Understanding of the Triggering Mechanism of a Large Reactivated Landslide in the Three Gorges Reservoir. *Eng. Geol.* **2018**, *238*, 36–51. [CrossRef]

42. *DZ/T 0261-2014*; Landslide, Collapse, and Debris Flow Hazard Investigation Standard (1:50,000). China Geological Environment Monitoring Institute, Ministry of Land and Resources of the People's Republic of China: Beijing, China, 2014.

43. Fiorucci, F.; Cardinali, M.; Carlà, R.; Rossi, M.; Mondini, A.C.; Santurri, L.; Ardizzone, F.; Guzzetti, F. Seasonal Landslide Mapping and Estimation of Landslide Mobilization Rates Using Aerial and Satellite Images. *Geomorphology* **2011**, *129*, 59–70. [CrossRef]

44. Nichol, J.E.; Shaker, A.; Wong, M.-S. Application of High-Resolution Stereo Satellite Images to Detailed Landslide Hazard Assessment. *Geomorphology* **2006**, *76*, 68–75. [CrossRef]

45. Sato, H.P.; Hasegawa, H.; Fujiwara, S.; Tobita, M.; Koarai, M.; Une, H.; Iwahashi, J. Interpretation of Landslide Distribution Triggered by the 2005 Northern Pakistan Earthquake Using SPOT 5 Imagery. *Landslides* **2007**, *4*, 113–122. [CrossRef]

46. Montrasio, L.; Valentino, R.; Losi, G.L. Towards a Real-Time Susceptibility Assessment of Rainfall-Induced Shallow Landslides on a Regional Scale. *Nat. Hazards Earth Syst. Sci.* **2011**, *11*, 1927–1947. [CrossRef]

47. Gomi, T.; Sidle, R.C.; Miyata, S.; Kosugi, K.; Onda, Y. Dynamic Runoff Connectivity of Overland Flow on Steep Forested Hillslopes: Scale Effects and Runoff Transfer. *Water Resour. Res.* **2008**, *44*, 2007WR005894. [CrossRef]

48. Kirschbaum, D.; Stanley, T. Satellite-Based Assessment of Rainfall-Triggered Landslide Hazard for Situational Awareness. *Earth's Future* **2018**, *6*, 505–523. [CrossRef] [PubMed]
49. Hu, Y.; Dong, Y.; Batunacun. An Automatic Approach for Land-Change Detection and Land Updates Based on Integrated NDVI Timing Analysis and the CVAPS Method with GEE Support. *ISPRS J. Photogramm. Remote Sens.* **2018**, *146*, 347–359. [CrossRef]
50. Peng, Y.; He, G.; Wang, G.; Cao, H. Surface Water Changes in Dongting Lake from 1975 to 2019 Based on Multisource Remote-Sensing Images. *Remote Sens.* **2021**, *13*, 1827. [CrossRef]
51. Padarian, J.; Minasny, B.; McBratney, A.B. Using Google's Cloud-Based Platform for Digital Soil Mapping. *Comput. Geosci.* **2015**, *83*, 80–88. [CrossRef]
52. Mohaghegh, A.; Farzin, S.; Anaraki, M.V. A New Framework for Missing Data Estimation and Reconstruction Based on the Geographical Input Information, Data Mining, and Multi-Criteria Decision-Making; Theory and Application in Missing Groundwater Data of Damghan Plain, Iran. *Groundw. Sustain. Dev.* **2022**, *17*, 100767. [CrossRef]
53. Farrokhi, A.; Farzin, S.; Mousavi, S.-F. Meteorological Drought Analysis in Response to Climate Change Conditions, Based on Combined Four-Dimensional Vine Copulas and Data Mining (VC-DM). *J. Hydrol.* **2021**, *603*, 127135. [CrossRef]
54. Achite, M.; Farzin, S.; Elshaboury, N.; Valikhan Anaraki, M.; Amamra, M.; Toubal, A.K. Modeling the Optimal Dosage of Coagulants in Water Treatment Plants Using Various Machine Learning Models. *Environ. Dev. Sustain.* **2022**, *26*, 3395–3421. [CrossRef]

Article

Rainfall-Triggered Landslides and Numerical Modeling of Subsequent Debris Flows at Kalli Village of Suntar Formation in the Lesser Himalayas in Nepal

Diwakar KC [1,†], Mohammad Wasif Naqvi [1,‡], Harish Dangi [2,§] and Liangbo Hu [1,*]

[1] Department of Civil and Environmental Engineering, University of Toledo, Toledo, OH 43607, USA; dibakarkc@outlook.com (D.K.); mohammadwasif.naqvi@rockets.utoledo.edu (M.W.N.)

[2] NEA Engineering Company Limited, Thapathali, Kathmandu 44600, Nepal; harish.dangi@postgrad.curtin.edu.au

[*] Correspondence: liangbo.hu@utoledo.edu

[†] Current address: Geotechnology LLC, Cincinnati, OH 45240, USA.

[‡] Current address: Department of Civil and Environmental Engineering, Michigan State University, East Lansing, MI 48824, USA.

[§] Current address: Western Australian School of Mines, Curtin University, Kalgoorlie, WA 6430, Australia.

Abstract: Hazardous debris flows are common in the tectonically active young Himalayas. The present study is focused on the recurrent, almost seasonal, landslides and debris flows initiated from Kalli village in Achham District of Nepal, located in the Lesser Himalayas. Such geological hazards pose a significant threat to the neighboring communities. The field survey reveals vulnerable engineering geological conditions and adverse environmental factors in the study area. It is found that a typical complete debris transport process may consist of two stages depending on the rainfall intensity. In the first stage, debris flows mobilized from a landslide have low mobility and their runout distance is quite modest; in the second stage, with an increase in water content they are able to travel a longer distance. Numerical simulations based on a multi-phase flow model are conducted to analyze the characteristics of the debris flows in motion, including the debris deposition profiles and runout distances in both stages. Overall, the numerical results are reasonably consistent with relevant field observations. Future debris flows may likely occur again in this area due to the presence of large soil blocks separated by tension cracks, rampant in the field; numerical simulations predict that these potential debris flows may exhibit similar characteristics to past events.

Keywords: debris flow; internal angle of friction; basal friction; deposition pattern; runout distance; numerical modeling

1. Introduction

The collision of the Eurasian plate and Indian plate beneath the Himalayas along the fault line and the continuous movement of the Indian plate at almost 17 mm/year [1] have rendered the youngest mountains of the Himalayas tectonically very active. Because of the rugged mountain topography, complex and fragile nature geological structure, soft soil cover, high-intensity rainfall in monsoon season, and frequent earthquakes, the countries along the Himalaya including Nepal, India, and Pakistan are especially vulnerable to landslides, debris flows, erosion, and other mass wasting phenomena [2]. Many destructive landslides and debris flows take place every year in Nepal [3–6]. Case studies of landslides or debris flows in different parts of Nepal have been reported in recent years [7–10] and there is a growing interest in better understanding the characteristics of landslides or debris flows in this region.

A large number of debris flows are commonly observed in the Suntar Formation of the Far-Western Development Region of Nepal. Kalli debris flows in Achham District are among the major recurring landslide-mobilized debris flows in this region. However,

these landslides and debris flows in the Suntar Formation have not yet been extensively investigated. Interestingly, similar trends of repetitive occurrences of landslides and debris flows have been reported in some case studies conducted in other parts of Nepal as well as neighboring countries, which possess similar lithofacies to the Suntar Formation; these reported debris events include several incidents at Siddhababa along the Siddhartha Highway and at Jugedi Khola along the Narayanghat Muglin Road, as well as some events in the Dagshai Formation and in the Murre Formation of India and Pakistan, respectively [11–16]. However, these studies are mainly focused on the field conditions, influencing factors and potential triggering agents; there has been very little attempt at quantitative analysis or numerical modeling of debris flows in the region. In the present study, we aim to explore both field surveys and numerical simulations to study a typical landslide-mobilized debris flow, which recurs frequently during the rainfall seasons near Kalli village in this region.

There has been a plethora of numerical models developed to examine the mechanisms of debris flows and quantify their physical processes. The main challenge in various model development lies in adopting proper rheology to represent the distinctive behavior of various mass flows. Most of the early models developed were single-phase models, which generally adopted Newtonian, Bingham, or dilatant fluid rheology for what is considered predominantly fluid flow behavior [17–19]. Granular frictional flow models were proposed for coarse-grained dry mass flows [20–23], and visco-plastic models for dense granular flows have also been developed [24]. A mixture approach has also become popular to describe the overall behavior of debris material as a whole, with various relevant models being developed [25–28]. Pudasaini [29] proposed a two-phase modeling framework to consider the solid phase and fluid phase simultaneously in the motion of the debris material and incorporate many essential physical aspects of mass flows; it was recently expanded into a multi-phase model with the introduction of an additional fine solid phase and this allows more complex material behavior to be considered in the modeling of the flow process. Since the debris flow mechanism is very intricate, determining the values of input parameters for such complex flows and phases is typically very challenging. There are very scarce resources devoted to the ranges of input parameters for such multi-phase models. The present study attempts to determine the input parameters through back analysis of past debris flow events.

The overall scope of the present study revolves around the recurring, almost seasonal, geological hazards that constantly plague the communities in this region; it is aimed to identify the key factors and explore quantitative numerical models to simulate the flow processes. A multi-phase mass flow model is employed for back analysis of past debris flows that occurred in the study area. Various flow characteristics including deposition pattern, runout distance, and impacted area are examined numerically. Numerical simulations based on the calibrated modeling parameters are also explored to assess their possible triggers and impact for potential future debris flows. These relevant parameters obtained from the back analysis of the present study can also serve as important references for further investigations as well as in the assessment of present events of debris flow hazards in this region.

2. Study Area

The study area is located in the middle mountains of the young Himalayas in the border area of the Surkhet and Achham districts of Nepal (Figure 1); it is in the proximity of the Karnali river. The coordinates of the initiation point of the major landslide that later mobilized the debris flows are 28.93° N, 81.34° E, in Kalli village of Achham District.
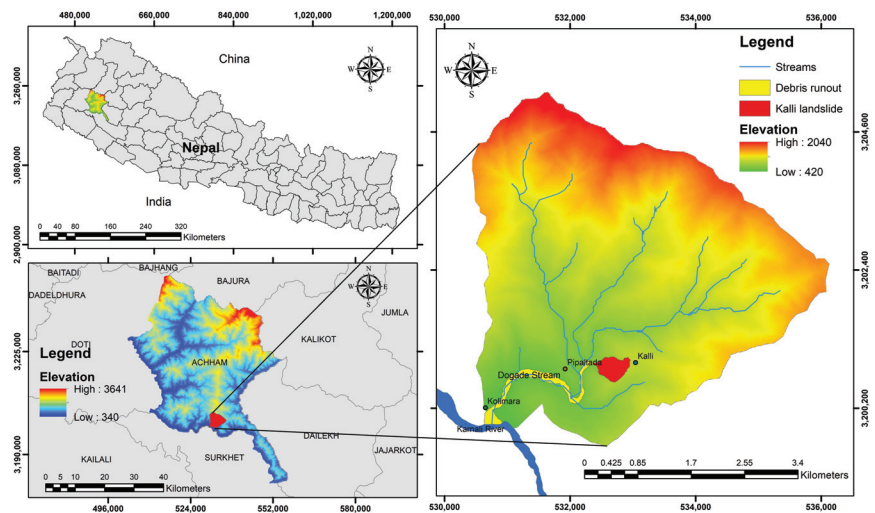
Figure 1. Study area around Kalli village of Achham District on the map of Nepal.

The study area usually receives scanty rainfall during the winter. From November to April there is very little rainfall, and then, from the middle of April to the middle of October the area typically receives intense summer rainfall. The maximum rainfall generally occurs in July. The summer rainfall storms are very intense, often flooding the ephemeral channels. There is no rainfall gauge station in the study area, therefore the rainfall in the area was estimated from several nearby rainfall gauge stations (Asara Ghat, Bangga Camp, Mangalshen, and Pusma Camp) located within 25 km of the landslide area. Figure 2a shows the Thiessen polygon of this region around the four stations. The rainfall in the study area was then estimated based on its distance away from each station and the area of each polygon [30]. These rainfall data from the years 1982 to 2018 were obtained from the Nepal Department of Hydrology and Meteorology. The cumulative rainfall during a year is presented in Figure 2b. It is worth noting that to examine one of the largest debris flow events that occurred in Kalli village in 1983, the rainfall was also similarly estimated for the location of this village; evidently it was very high and could be the major triggering factor for the debris flows in that year.
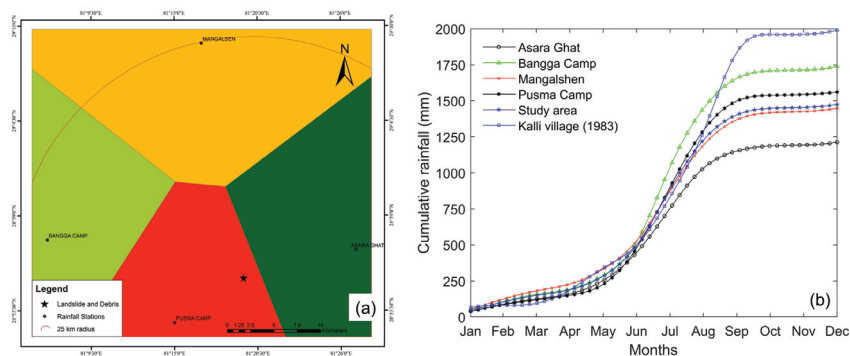
Figure 2. (**a**) Thiessen polygon for the rainfall analysis. The arc indicates the distance of 25 km away from the Kalli landslide area (marked with star) and shows that all the rainfall gauge stations are within this 25 km range. (**b**) Average cumulative rainfall recorded at nearby weather stations and estimated for the study area.

The Kalli landslide/debris flow watershed area exhibits several distinct geomorphic features. Among these, steep elevated mountains and deep river valleys with diverse landforms are particularly prominent. The highest elevation in the watershed is 2040 m and the lowest elevation, approximately 420 m is at the Karnali river. The perennial Karnali river together with its tributaries and adjoining ephemeral streams flow through the study area. Mass wasting events like landslides and debris flows are common in such topography.

Geologically, the study area is dominated by the Lesser Himalayan rocks in the Far-Western Development Region of Nepal [31]. The most prominent rock formations in the study area are the Suntar Formation and the Swat Formation [32], belonging to the Surkhet Group. The Swat Formation is mainly comprised of gray to dark gray, soft, carbonaceous shales with beds and lenses of fine-grained limestone, and the Suntar Formation consists of medium-grained, green-gray sandstones with purple shales [31,33]. The purple shale slope of the Suntar Formation is commonly exposed and visually evident in the study area (Figure 3).

Figure 3. The interbedded purple shale and gray sandstone slope common in the study area.

3. Mass Movements in the Area

3.1. Landslide and Debris Flows Events

Landslides and debris flows in the area are encountered almost every year during the heavy rainfall season. The landslides are predominantly made of solid material traveling at a moderately low velocity. A debris flow typically contains a significant fraction of water, whose presence facilitates the liquefaction of fine grains and renders the flow highly mobile [34,35]. The largest landslide and debris flows on record took place on the 12 September 1983. This event was so extreme that some of the debris material flowed over 3 km to reach Karnali river along the Dogade stream. It was initiated from fresh landslides, and then, grew significantly with the debris deposited nearby from earlier landslide events. The landslide and debris flow occurred during heavy rains. The rainfall recorded on that day at the Pusma Camp rainfall gauge station, located 9.67 km from the study area, was 230 mm; this strongly suggests that the landslide and debris flow were triggered by the heavy rainfall.

Recently, in July 2021 another landslide occurred at the same location. Figure 4 shows the mass depletion near the landslide crown area between 2020 and 2021. The crown area of the landslide has agricultural land with a thick soil deposit. The general characteristics and occurrence pattern of these recurring landslides and debris flows appeared very similar to the past events. Figure 5 shows the path of the Kalli landslide and debris runout along the

Dogade stream. It is possible to consider the primary process of debris flow development in two stages. In the first stage, the main debris flow generally initiates from a landslide whose crown is in Kalli village; subsequently the debris materials from the landslide travel further and are deposited in the Dogade stream. In smaller landslides, when there is not sufficient debris material or water to flow over a long distance, most of the debris is deposited in the Dogade stream, close to the landslide toe. Figure 6 shows the view at a distance of 600 m from the landslide crown; the trace of the Kalli landslide is evident and deposition marks of debris were left near the Dogade upstream.
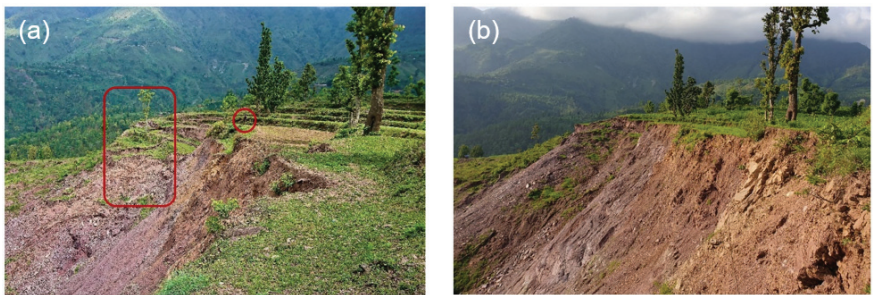
Figure 4. Photos of the landslide crown area taken (**a**) on 15 June 2020 and (**b**) on 22 June 2021. The area enclosed by the rectangle shows the displaced mass consumed by the landslide in 2021; the circle indicates a visitor (used as a scale).

Figure 5. Kalli landslide, occurring at Kalli village, and the debris runout along the Dogade stream to the Karnali river. The blue arrow indicates the landslide mobilized from the crown area at Kalli village. The red line indicates potential debris flow path along the Dogade stream. The upstream portion of the Dogade stream from the Kalli landslide area cannot be noticed clearly as the channel is constricted; but the portion between the Kalli landslide and the Karnali river is evident due to the widened channel resulting from the debris flow. A very wide debris fan along with the Karnali river constriction at the confluence point of the Dogade stream and the Karnali river due to debris deposit can be clearly observed.

Figure 6. The deposition marks remained at the sides after the debris from the first stage. The location is 600 m from the landslide crown.

Of more concern is the case of very heavy rainfall when there are large landslides along with sufficient water in the Dogade stream, the fresh debris from the landslides together with the debris deposited in the Dogade stream from earlier landslides can continue to flow to the Karnali river, which is almost 3 km away from the landslide toe (Figure 5). This stage of long runout distance along the Dogade stream is regarded as the second stage of the debris flow evolution. Figure 7 shows typical deposition patterns at the two locations, one closer to the landslide toe (Figure 7a) and the other far away and almost near the end of the Dogade stream (Figure 7b). The debris deposition pattern shows that finer particles are deposited very close to the landslide toe and the coarser particles are deposited far away from the landslide area. It is common that large boulders are found to deposit at the bank of the Karnali river, which is around 3 km from the landslide crown area [36].
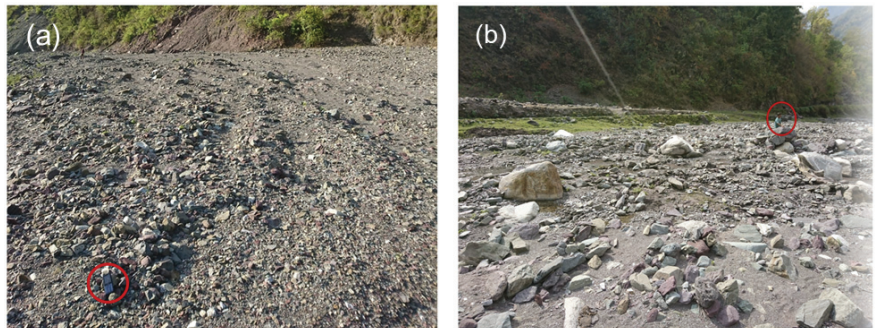
Figure 7. (**a**) Deposition of finer particles at 500 m from the landslide toe; the red circle on the left encloses a cell phone. (**b**) Deposition of coarser particles at 2500 m from the landslide toe; the circle on the right shows a visitor.

The total volume of the main debris flow that has already traveled to the Karnali river is more than hundreds of thousands of cubic meters. A few households have been displaced in Kalli village along with the loss of some agricultural land due to landslides; a large piece of agricultural land about 32,000 m^2 has been converted into a debris fan in Kolimara village. It is possible that future losses may occur as a result of such recurring flow events, hence the study of landslide/debris flow in this area is crucial from a future development perspective. There have been widely reported cases where landslides and debris flows have damaged infrastructure around the rivers in Nepal [37].

3.2. Rock and Soil Properties

To investigate the properties of the underlying rock in the landslide area, the freshly exposed part of the sandstone was drilled for sample collection. The deeper The intact shale samples could not be retrieved for strength test. Uniaxial compressive strength testing was carried out on three samples of sandstone according to the Bureau of Indian Standards [38]. The average compressive strength was 52.1 MPa, the modulus of elasticity 38.5 GPa, the modulus of rigidity 16.2 GPa and Poisson's ratio 0.19. These results indicate that the sandstone in the Kalli landslide is fairly strong.

Petrographic analysis was carried out on the collected sandstone samples to determine the mineralogical and chemical composition. The results suggest that the sandstone can be characterized as subarkose, as the fractions of quartz, feldspar, and matrix are 60%, 15%, and 5%, respectively. The remaining fraction is occupied by various cementing materials that can be qualified as calcareous, argillaceous, and ferruginous, which were found to be around 15%, 3%, and 2%, respectively.

Sieve analysis and consistency tests were carried out on the soil samples collected at the landslide crown area. Based on the results of the sieve analysis [39], the coefficient of uniformity C_u was determined to be 28.57, while the coefficient of curvature C_c was found to be 0.45. In the consistency tests [40], the liquid limit (LL) was obtained as 32% and plastic limit (PL) 26%. The soil is a poorly graded sand with silt and gravel (SP-SM) according to the Unified Soil Classification System. Based on the empirical relationship proposed by Alyamani and Sen [41], the hydraulic conductivity of the soil can be estimated as approximately 6.0×10^{-6} m/s. Table 1 summarizes the key material properties measured during the laboratory testing.

Table 1. Rock and soil properties measured in the laboratory testing.

Property	Value
	Rock
Uniaxial compressive strength	52.1 MPa
Modulus of elasticity	38.5 GPa
Modulus of rigidity	16.2 GPa
Poisson's ratio	0.19
	Soil
Coefficient of uniformity	28.57
Coefficient of curvature	0.45
Liquid limit	32
Plastic limit	26
Plasticity index	6
Hydraulic conductivity	6.0×10^{-6} m/s

The estimated hydraulic conductivity of the soil is significantly higher than generally observed hydraulic conductivities of sandstone and shale. Therefore, enough water may infiltrate from the crown area of the landslide to the underlying sandstone and shale, and thus, saturate the slope. It is worth noting that the presence of surface cracks will also facilitate the infiltration of water into the soil, aggravating the water saturation in the ground. The hydraulic conductivity of shale is in general significantly lower than sandstone. The difference in relevant physical and mechanical properties of sandstone and shale such as strength and weather resistance is very high. Hence, one major cause for repetitive landslide occurrence in Kalli village may be attributed to the interbedding of shale and sandstone, as these two rocks have likely undergone different weathering due to the difference in their physical and mechanical properties and the interbedding of these two has considerably weakened the overall in situ strength.

3.3. Present and Potential Future Landslides and Debris Flows

Recurring, almost seasonal, landslides and debris flows occur frequently in this area. Most of the landslides were detected in the northern part of the Karnali river, i.e., on the right side of the river where the slopes are comprised of sandstone and shale, or interbedding of sandstone and shale. On the southern side of the river there are steep dolomite slopes, but landslides are not common in these slopes.

The present field study strongly suggests that this site is potentially very vulnerable to future landslides or debris flows. The entire region is characterized by steep slopes, on top of which often lie paddy cultivated fields. These fields accumulate significant amounts of water, leading to saturation of the slopes. Other causes such as intense rainfall in the rainy season and heavily weathered shale are still persistent. It is worth noting that there are rampant tension cracks on the landslide crown area; many separated blocks are formed which may soon slide down initiating a landslide and debris flow. Figure 8 shows the purple shale slope and the tension cracks at the landslide crown area. The combined length of the cracks is approximately 300 m. If all these separated blocks fail, it is estimated that approximately 200,000 m^3 of debris material could be generated. This potentially poses a considerable threat to the residents and agricultural land in this area.
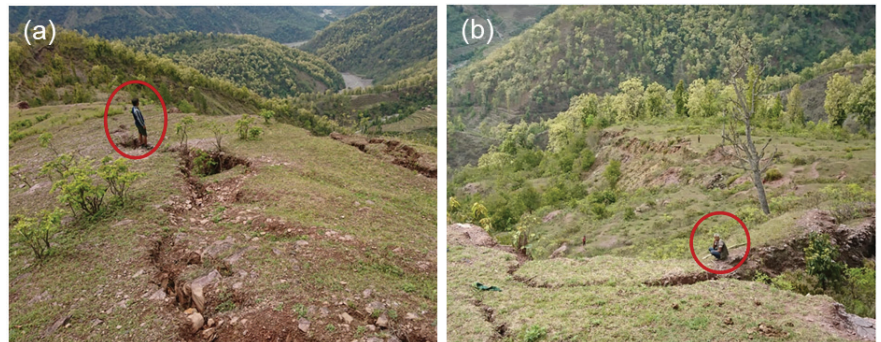
Figure 8. (**a**) The rampant tension cracks at the landslide. (**b**) Another view of the tension cracks that form separate mass blocks. The red circle in both images indicates the size of a visitor.

4. Numerical Simulations

4.1. Modeling Background Parameters of the Two-Stage Debris Flow Development

It is of great interest to assess the processes of landslide and debris flow development in a quantitative manner via theoretical or numerical simulations based on the evidence or data collected from the field survey examined so far. In particular, the debris deposition pattern as well as the debris volume have great implications in the impact on the surrounding environment or society, and consequently are the primary focus of numerical simulations in the present study. Numerical simulations are conducted with an open-source computational package, r.avaflow 2.1 [42]. It is supported by GIS software for simulations of complex multi-phase mass flows over any arbitrary topographies. It is freely available as a raster module of the GRASS GIS 8.3 software, employing the programming languages Python and C along with the statistical software R.

The computational framework is based on the multi-phase mass flow model proposed by Pudasaini and Mergili [43], which considers multiple phases in motion and incorporates many essential physical aspects of mass flows. It expands the theoretical formulations of a two-phase model [29] with the introduction of an additional phase of fine solid. This model considers the moving mass flow as composed of three phases, i.e., solid, fine solid, and fluid. The first phase, the fluid phase represents a mixture of water and very fine particles such as silt, clay, and even colloids. It is modeled with shear-rate-dependent Herschel–Bulkley rheology. The second phase, termed as fine solid, contains fine gravel and sand. The rheology of this mixture is characterized by the rate-dependent visco-plastic

behavior, as Jop et al. [24] show that dense granular flows share similarities with classical visco-plastic fluids. For this phase, shear and pressure-dependent Coulomb visco-plasticity is adopted, where both viscous stress and yield stress play a significant role. The third phase, the solid phase, is composed of coarser particles such as boulders, cobbles, and gravels. These coarse particles are considered as frictional materials with no viscous contribution. Hence, Mohr–Coulomb plasticity is used to model the constitutive behavior of this phase. It is noted that this three-phase model has been shown to be capable of unifying several widely used models [20,26,29,44] by setting specific phase fractions. Further details of the theoretical formulations can be found in Pudasaini [29] and Pudasaini and Mergili [43]. The relevant Digital Elevation Model (DEM) data are necessary for simulating a flow event on real topography. The DEM data of the study area are available online from the Alaska Satellite Facility [45]. They have a 12.5 m resolution based on the original data detected by the ALOS PALSAR satellite. The background images are obtained from Google Maps and Google Earth and subsequently geo-referenced with GIS before they are ready for the simulations.

It is necessary to calibrate the input parameters for the numerical simulations based on the collected field evidence and relevant ranges of typical material properties. They can be further modified through back analysis to match the observed trends in the debris flows reported so far; subsequently, they can be used for prediction of future debris flows. It is of particular interest to focus on the main process of sediment transport in the form of landslides or debris flows before the debris eventually reaches the stream, and the stream water flow carries the material to travel further.

Table 2 summarizes the fractions of each phase in each stage and relevant parameters for each phase. It is worth noting that the complex interactions among these phases are considered through generalized interfacial forces, including the drag forces on the particulate phases and the virtual mass force due to the relative acceleration between different phases. The internal friction angle represents the internal frictional resistance, while the basal friction angle characterizes the frictional resistance of the bed material on which the mass flow moves.

Table 2. Key parameters used in the numerical modeling.

Parameter	Value
Solid	
Density	2650 kg/m^3
Internal friction angle	30°
Basal friction angle	25° (stage 1)
	6° (stage 2)
Drag coefficient	0.02
Fine solid	
Density	2000 kg/m^3
Internal friction angle	15° (stage 1)
Basal friction angle	5° (stage 1)
	3° (stage 2)
Kinematic viscosity	100 m^2/s
Fluid	
Density	1000 kg/m^3
Kinematic viscosity	0.001 m^2/s
Fluid friction coefficient	0.01

As discussed in the preceding section, in the first stage of the landslide/debris flow development around Kalli village, a landslide typically occurs. The debris mass in this stage can only flow on very steep slopes and its runout distance is short. There is relatively a very low water content in the debris mass, the solid particles behave like purely frictional

solids. Hence, the motion of the debris in this stage is modeled by adopting a very low water content for the debris material, which travels over a short distance; the fraction of the fluid phase is set to be 15%. This is hereafter referred to as the stage 1 simulation in the present study.

In the second stage, the debris mass deposited from the first stage is mixed with more water (around 50%) in the rainy season and more fresh landslides may occur under heavy rainfall. In this stage, water mixed with fine solids (clay, silt, and fine sand) produces a high-density viscous intermediate fluid that surrounds and lubricates the other coarse materials such as coarse sand, gravels, cobbles, and boulders. The viscous intermediate fluid has the capacity to hold the large particles of coarse sand, and those large particles in turn support cobbles and boulders [46], such that the entire blended mixture flows even on relatively flat slopes. In such conditions, the resistance to the flowing mass from the surroundings is very low, i.e., the basal friction can decrease drastically due to the presence of the lubricating fluid made of water, clay, silt, and fine sand [43]. The development in this stage is modeled by employing a moderate water content, which renders a partially viscous type debris flow whose runout distance is long. It is hereafter referred to as the stage 2 simulation.

4.2. Stage 1 Numerical Simulations

4.2.1. Modeling Debris Flow Development during the First Stage

Recurring landslides and debris flows take place almost every year in the study area, as discussed in the preceding section. In the present study, we are especially interested in one of the major landslide/debris flows recorded in this area, i.e., the event that occurred in September 1983; we intend to calibrate the involved parameters to match the estimated debris volume. In this stage, the debris flow was directly initiated from slope failure, such as toppling or landslide. Hence, the debris mass did not have a high water content in this stage. The debris materials were released from the upper scarp of the landslide and later deposited along a distance of 600 m at the end of the stage. Figure 9 shows approximately the deposition area where the debris material settled, as estimated based on the debris deposition marks or traces observed in the field, as well as the information provided by the local residents.

Figure 9. Deposition area (marked in red) of debris material near Pipaltada village (Figure 5), accumulated during the first stage, as observed in the field. Deposition along the longitudinal direction, AB, and the transversal direction, CD, is examined in the subsequent simulation.

The information collected from the field is also used to estimate the volume of debris material considered in the numerical simulations. In this model, the volume of solids is

considered to be 48,600 m^3, the volume of fine solids 20,250 m^3, and the volume of water 12,150 m^3. The internal angle of friction and basal friction for the solid phase are assumed to be 30° and 25°, respectively; for the fine solid phase they are assumed to be 15° and 5°, respectively, and for the fluid, both parameters are assigned 0. The kinematic viscosity of the fine solids and fluids are considered to be 10^{-2} m^2/s and 10^{-3} m^2/s, respectively.

4.2.2. Simulation Results

Figure 10 shows the detailed deposition results generated by the numerical simulation; they match very well with the field observation of the area of the deposited mass (Figure 9). The symbols P1, P2, and P3 in Figure 10 represent the solid, fine solid, and fluid phase, respectively; H and Q represent the flow height (depth) and the discharge, respectively. The area enclosed by the red dotted line is the release area (Figure 10). The deposition height is demonstrated by contours. The outermost contour represents the lowest deposition height and the innermost contour represents the highest deposition height. Each phase is represented by a different color, as indicated in Figure 10.
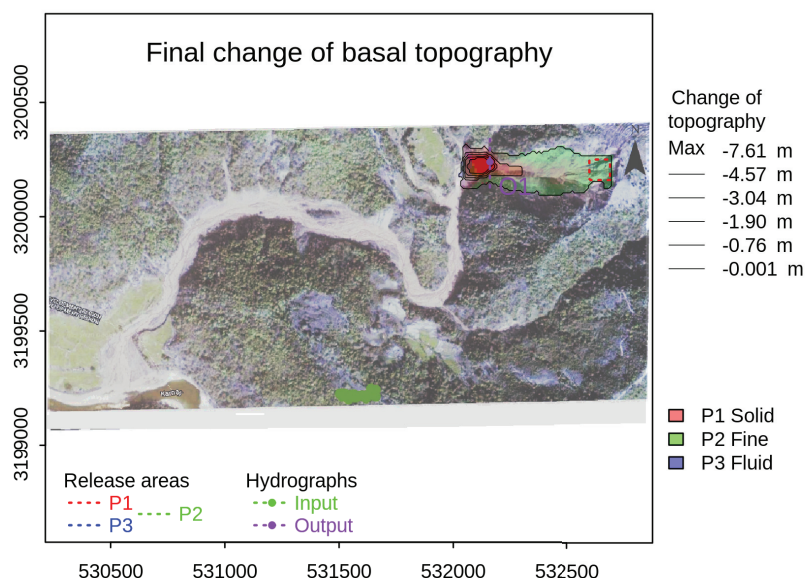
Figure 10. Deposition profile obtained from numerical simulation.

As shown in Figure 10, the fine solids mixed with water are deposited at the front, the solids at the middle, and a much lower amount of fine solids at the tail of the travel path. To analyze the deposition profile obtained from the numerical simulation in detail, two deposition profiles are selected along the longitudinal direction, AB, and the transversal direction, CD, of the deposition area, as shown in Figure 9; AB is located at the middle of the flow in the debris flow direction and CD at 50 m away from the left-most point, i.e., point A. The deposition depth (thickness) along these two distances is plotted in Figure 11. Evidently, the massive soil debris material deposits near the toe, i.e., point A of the steep slope AB. The maximum depth of deposition is about 7.6 m, roughly the half way towards CD. The depositional depth gradually declines further away from the center of CD. This depositional depth after the landslide can be observed by the depositional marks in the field.
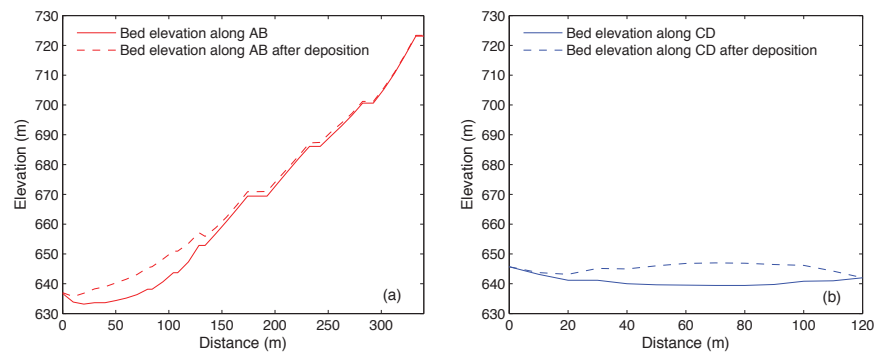
Figure 11. Deposition profile obtained from numerical simulation (**a**) along AB (the origin is established at point A); and (**b**) along CD (the origin is established at point C).

It is also of interest to examine the details of the debris flow around the area and at specific locations along its path. Figure 12 shows the overall the maximum flow height around the area. The debris is highly concentrated at the center and dominated by the solids fraction at the initiation. A point is selected and marked as O1 near the end of the deposition in Figure 12; it is located at the section 450 m from the landslide crown. Figure 13 shows the flow height of each phase and the discharge rate at this section. The debris material reaches this section at 26 s from the initial release time, and then, the maximum flow height and discharge occurs at 31 s. During this 5 s interval, the discharge rate has increased sharply, and then, decreased gradually after the peak discharge. The time from zero discharge to peak discharge is almost one-fifth of the time between peak discharge and zero again when the flow passes this section entirely. This shows that during debris flows most of the flowing mass is at the front.
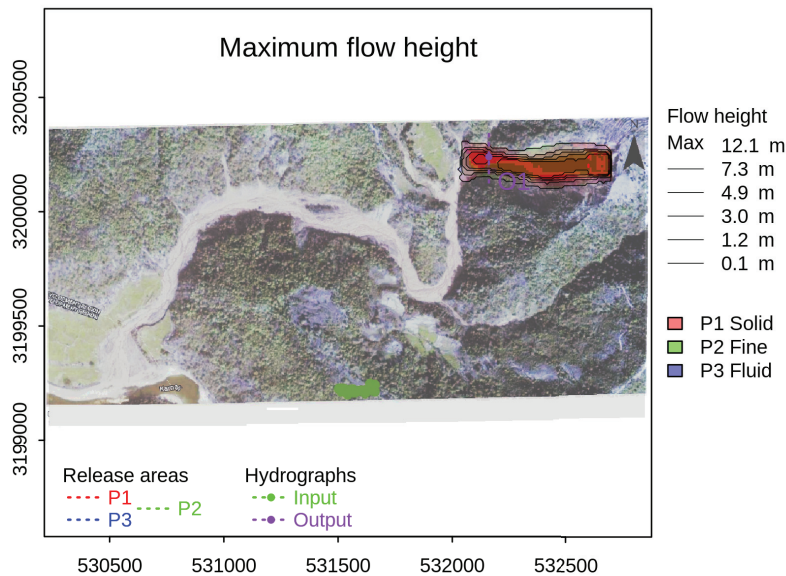
Figure 12. Distribution of maximum flow height during the first stage.
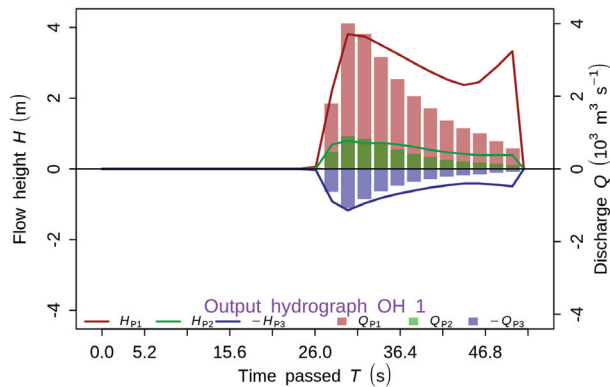
Figure 13. Debris flow height and discharge passing the specific location (O1) during the first stage.

4.3. Stage 2 Numerical Simulations

4.3.1. Modeling Debris Flow Development during the Second Stage

The initiation of the second-stage debris flow is caused by the combination of fresh landslides and the debris deposited from the first-stage debris flows, as addressed in the preceding section. With the surge in water volume in the debris mass during the intense rainfall, the motion of the debris mass typically exhibits the well-known fire-hose effect [47,48], along with the fresh debris mobilized from the fresh landslide. In September 1983, a large amount of material was transported to the Karnali river as part of a debris flow; however, it was not the only event in that year and many debris flows followed. Debris flows are generally initiated during intense rainfall. A large amount of fine soil from agricultural land was depleted by the landslides. The presence of fine solids with water made the flowing mass more viscous. The viscous mass produced by mixing fine solids and fluid lubricates the base and significantly reduces the basal friction. The internal angle of friction also decreases with the increase in water and clay content [49]. Hence, in the second-stage simulation, the relevant material constants are adjusted to incorporate the effect of water and fine solids and address the potentially different phase behavior. As summarized in Table 1, the basal angles for solids and fine solids are taken to be $6°$ and $3°$, respectively. The internal angles of friction for solids and fine solids are taken to be $25°$ and $13°$, respectively.

Although the precise volume of debris in the field is impossible to determine accurately since much of it flows along the Karnali river, based on the field analysis and information provided by the local residents, the total volume of debris is estimated to be roughly around 300,000 m^3. In the numerical simulations, the volumes of solid, fine solid, and fluid considered are 107,651 m^3, 46,126 m^3, and 153,765 m^3, respectively. Considering the fact that some portion of debris was freshly produced from the landslide and the rest was the deposited debris from the first stage, in the simulations the initial debris mass is set up to be released from the scarp of the landslide to the deposition area of the first stage.

4.3.2. Simulation Results

Figure 14 presents the final deposition of the debris material; the debris runout distance is considerably longer than in the first stage. Some portion of debris is deposited along the bank of the Karnali river, while a major portion flows into the Karnali river. The deposition pattern shows that some fine solids are deposited at the back and coarser solids are deposited at the front. The deposition height along the Karnali riverbank is around 4 m. It can be seen that the fine solids are deposited closer to the debris initiation area and the coarser solids are deposited far away from the debris flow initiation area. Such a distribution trend was observed in the field, as shown in Figure 7.
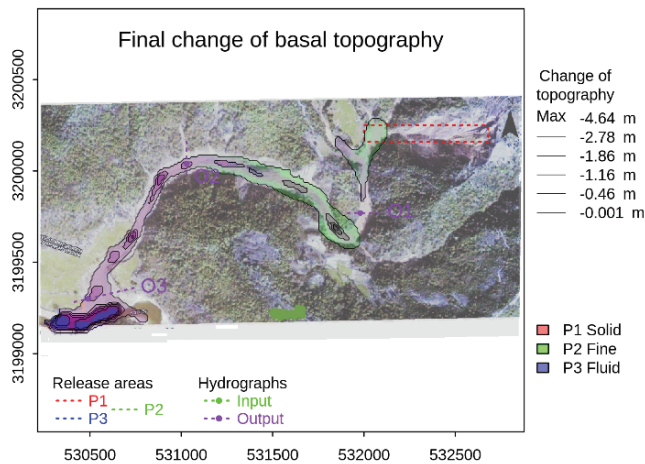
Figure 14. Final deposition of debris material at the end of the second stage.

It is worth exploring in detail the evolution of the debris flow along its path; three locations, O1 which is close to the starting point, O2 at the intermediate distance, and O3 that is close to the final deposition fan, are selected in Figure 14. They are located at 1100 m, 2200 m, and 3300 m, respectively, from the crown of the landslides. The hydrograph that shows the flow height and the discharge rate at each location is presented in Figure 15. Figure 15a shows a significant amount of solids and fine solids passing through location O1; however, at O2 (Figure 15b) and O3 (Figure 15c) there is no significant amount of fine solid. A high volume of solids passes through O3, which eventually either flows into the Karnali river or deposits along the Karnali riverbank. Combined with the results of the base change, shown in Figure 14, it can be concluded that water travels to the deepest part, i.e., the middle of the river; however, a large amount of solids (coarse debris) settle down before they reach the middle of the Karnali river. This can be clearly confirmed in the field that the continuous deposition on the right bank has shifted the river towards the left, constricting the flow path of the Karnali river.

The deposition profile along the debris flow in the Dogade stream and along the Karnali riverbank is presented in Figure 16. In this stage, with a sufficient amount of water that mixes with fine particles such as clay, silt and fine sand, the debris behaves like a moderately high density solid–fluid mixture which can hold together large particles such as boulders and cobbles during the flow. It also lubricates the coarser particles and decreases the basal friction; therefore, the whole debris mass can flow relatively easily at a high velocity and travel over a long runout distance of over 3000 m, as shown in Figure 14. In such a case, the runout distance of solids (coarser particles) is longer than fine solid. Indeed, the deposition along the Dogade stream is not very significant as the debris tends to flow along the stream. As shown in Figure 16a, the elevation change in the Dogade stream is hardly appreciable when plotted, with the elevation height ranging from 400~900 m; hence, the deposition depth, i.e, the change between the elevations, is also plotted separately on the axis on the right side in Figure 16a. It shows that the deposition is less than 2 m along the Dogade stream, except at the end of the stream where the deposition depth grows considerably to about 4 m at the fan near Kolimara village; the results are supported by the field observation of the accumulation of a large amount of debris material in this area. The simulation also shows large deposition along the Karnali riverbank (Figure 16b) after a considerable amount of debris material continues its runout and reaches the Karnali river. This is also consistent with the field observation.
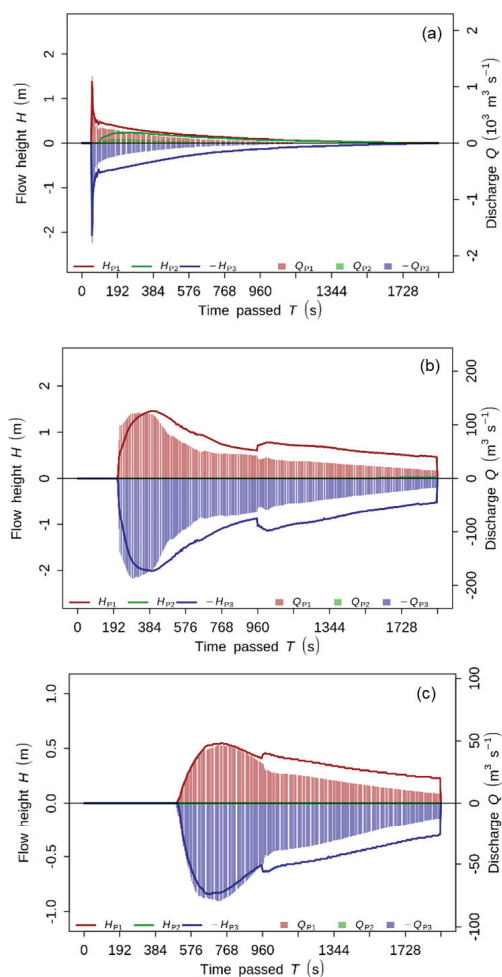
Figure 15. Hydrographs at (**a**) O1, (**b**) O2, and (**c**) O3 along the flow path.
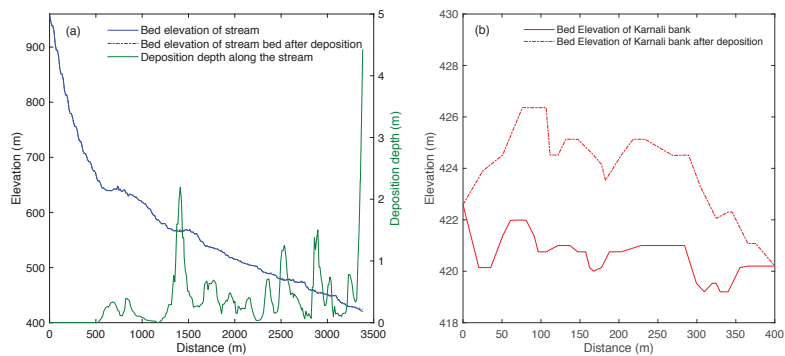
Figure 16. Deposition profile (**a**) in the Dogade stream, and (**b**) along the Karnali riverbank obtained from numerical simulation.

5. Discussion

The Himalayas in Nepal are extremely vulnerable to gravity-driven mass movement due to the presence of weak rocks in the high slopes that often receive intense summer rain. Mass wasting events such as landslides and debris flows are very common in these mountains. There are some other locations in Nepal similar to Kalli village, examined in the present study, where recurring landslides and debris flows are experienced almost every year. Rainfall is often a main triggering factor for these events; the poor underlying geology, which consists of interbedded shale and sandstone, could be the major cause of landslides. It is worth noting that extremely hazardous repetitive landslides also occur frequently in other parts of the region, including Nepal and neighboring countries. For example, at Siddhababa along the Siddhartha Highway and at Jugedi Khola along the Narayanghat Mugling Road, the geological formations have similar interbedded litho-units of sandstone and shale as those found in the Suntar Formation around Kalli village in the present study [13–15]. The Dagshai Formation and Murre Formation of India and Pakistan feature similar litho-units as the Suntar Formation and also experience extensive recurrent landslides [11,12,16]. However, effective mitigation of such geological hazards would demand more than mere identification of causes and triggers; theoretical and numerical investigations [50] may considerably benefit the understanding of the physical and mechanical processes involved in the landslides and debris flows in the studied mountainous range. In the present study, a less mobile debris flow is considered in the first stage with a greater internal angle of friction and basal friction used in the numerical simulations. The numerical results are found to match reasonably well with the actual field observation of the deposition. With the increase in water content, the internal angle of friction is assumed to decrease slightly and basal friction decreases significantly, this assumption yields results that are consistent with the observation of a long runout distance in the field.

It is of great interest to use the numerical approach examined in the present study to explore the possibilities of future debris hazards. As discussed in Section 3, at present the study area is highly susceptible to future debris flows; many large blocks are formed by the tension cracks on the crown of past landslides (Figure 8) and it is highly likely these massive blocks will slide down to form debris flows sooner or later. Additional numerical simulations are carried out by considering the estimated 200,000 m^3 of solid debris material ready to move downward to initiate the debris flow; since it is impossible to predict whether all this mass would fail at once or progressively, this choice represents a worst-case scenario, and thus, is assessed in the present study to predict the potential deposition area and runout distance.

Two stages of debris development are considered in the prediction. The first considers low-water-content debris that initiates at the current crown area (Figure 8); the volumes of solid, fine solid, and fluid are considered to be 146,023 m^3, 60,984 m^3, and 36,492 m^3, respectively. Figure 17 shows the deposition profile at the end of the debris flow. The area of deposition is mainly confined to a rather limited area, indicating little or modest threat to the nearby residents, as the debris is deposited in the stream without entering the farmland and village. However, still reasonable care should be taken around the landslide-prone areas in Kalli village and it is suggested that those areas should be avoided for animal grazing in the rainy season, as catastrophic landslides can occur at any time in the rainy season.

The second simulation examines a high-water-content debris flow that initiates in a wide area close to the Dogade upstream; the volumes of solid, fine solid, and fluid are considered to be 143,514 m^3, 61,506 m^3, and 205,020 m^3, respectively. Figure 18 shows the final deposition of the debris. A small portion of the debris can travel over almost the entire Dogade stream and reach the fields of Kolimara village. Much of the debris can also flow to the Karnali river, with considerable deposition along the banks of Karnali river. Overall, the results show the tremendous destructive potential of current geological hazards in this area. Of course, in reality, it can be debated whether all the blocks separated by tension cracks may fail at the same time in a worst-case scenario; it is more likely to flow progressively

part by part each year. The influence or destruction of future events may be not as drastic as the scenario examined in the present study.
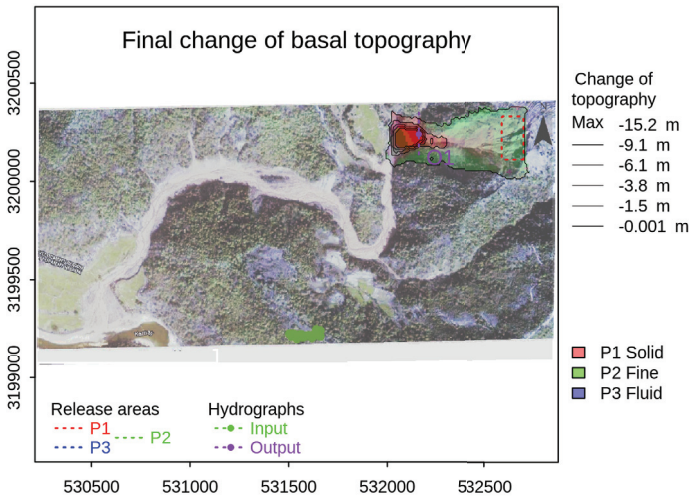
Figure 17. The deposition based on the simulation of a low-water-content debris flow.
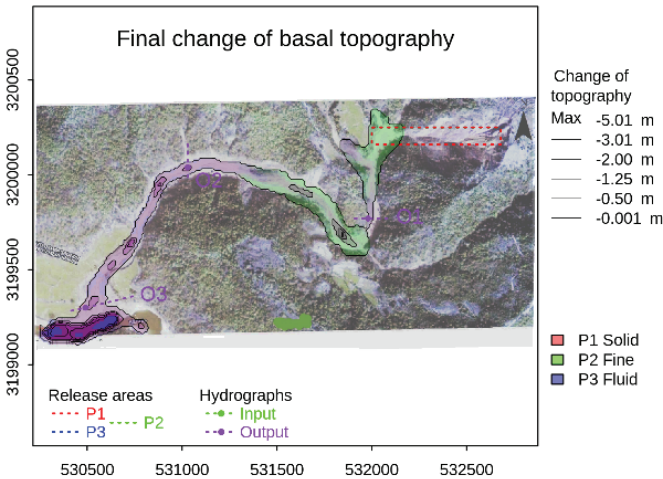
Figure 18. The final deposition of probable future debris flow based on a moderate-water-content model.

6. Conclusions

The present study focuses on a field study of recurring landslides and debris flows in the Kalli village in Achham District in Nepal. It shows that rainfall is the primary triggering factor for such gravity-driven mass wasting events. The poor underlying geological conditions that feature interbedding of shale and sandstone are a major cause. It is observed that debris flows may occur in two different stages. In the first stage, when the rainfall is not extremely high, smaller landslides occur and the runout distance of the debris generated is quite modest, approximately only a few hundred meters away from the landslide crown due to insufficient fluid in the debris mass. The second stage may occur during extreme rainfall when the debris mass contains a very high water content. A combination of the debris from the fresh landslides and the debris from the earlier landslides may flow to the

Karnali river that is located around over three kilometers from the original landslide crown area. The field study shows that debris deposition follows a unique pattern, where the larger particles tend to travel farther from the initiation area while the finer particles are deposited closer to the initiation area.

Numerical simulations based on a multi-phase computational framework are conducted to quantitatively analyze the characteristics of the debris flows in motion. The deposition profile and runout distance in both stages are simulated. In the first stage, the debris is largely accumulated at the toe of the hill and spread laterally along the slope. In the second stage, the debris flow travels over a very long distance to reach the Karnali river; large deposition is concentrated at the fan area and along the Karnali riverbank. Overall, the major trends from the numerical simulations are reasonably consistent with the field observations. At present in the field there are still large blocks separated by tension cracks that are rampant in the landslide crown area; which pose a considerable hazard for future landslides and debris flows. Additional numerical simulations are performed to predict the fate of an estimated volume of 200,000 m^3 of potential debris material present in the field. The numerical results show that the characteristics of such future events would be very similar to past incidents. Depending on the availability of water content, affected by the rainfall conditions, a potentially very destructive debris flow scenario is likely, as it may travel over the entire Dogade stream and reach Kolimara village and the Karnali river.

References

1. Bilham, R.; Larson, K.; Freymueller, J. GPS measurements of present-day convergence across the Nepal Himalaya. *Nature* **1997**, *386*, 61–64. [CrossRef]
2. Upreti, B.N.; Dhital, M.R. *Landslide Studies and Management in Nepal*; International Center for Integrated Mountain Development: Kathmandu, Nepal, 1996 .
3. Watanabe, T.; Dali, L.; Shiraiwa, T. Slope denudation and the supply of debris to cones in Langtang Himal, Central Nepal Himalaya. *Geomorphology* **1998**, *26*, 185–197. [CrossRef]
4. Adhikari, D.P.; Koshimizu, S. Debris flow disaster at Larcha, upper Bhotekoshi Valley, central Nepal. *Isl. Arc* **2005**, *14*, 410–423. [CrossRef]
5. Kayastha, P.; Dhital, M.R.; De-Smedt, F. Landslide susceptibility mapping using the weight of evidence method in the Tinau watershed, Nepal. *Nat. Hazard* **2012**, *63*, 479–498. [CrossRef]
6. Pyakurel, A.; KC, D.; Dahal, B.K. Enhancing co-seismic landslide susceptibility, building exposure, and risk analysis through machine learning. *Sci. Rep.* **2024**, *14*, 5902. [CrossRef]
7. Dahal, R.K.; Hasegawa, S. Representative rainfall thresholds for landslides in the Nepal Himalaya. *Geomorphology* **2008**, *100*, 429–443. [CrossRef]
8. Bhandari, B.P.; Dhakal, S. Evolutional characteristics of debris flow in the Siwalik Hills of Nepal. *Int. J. Geosci.* **2019**, *10*, 1049–1067. [CrossRef]
9. Dangi, H.; Bhattarai, T.N.; Thapa, P.B. An approach of preparing earthquake induced landslide hazard map: A case study of Nuwakot District, central Nepal. *J. Nepal Geol. Soc.* **2019**, *58*, 153–162. [CrossRef]
10. KC, D.; Dangi, H.; Hu, L. Assessing landslide susceptibility in the northern stretch of Arun Tectonic Window, Nepal. *CivilEng* **2022**, *3*, 525–540. [CrossRef]

11. Abbasi, A.; Khan, M.A.; Ishfaq, M.; Moon, P.K. Slope failure and landslide mechanism in Murree area, North Pakistan. *Geol. Bull. Univ. Peshawar* **2002**, *35*, 125–137.
12. Khan, A.N.; Collins, A.E.; Qazi, F. Causes and extent of environmental impacts of landslide hazard in the Himalayan region: A case study of Murree, Pakistan. *Nat. Hazard.* **2011**, *57*, 413–434.
13. Regmi, A.D.; Devkota, K.C.; Yoshida, K.; Pradhan, B.; Pourghasemi, H.R.; Kumamoto, T.; Akgun, A. Application of frequency ratio, statistical index, and weights-of-evidence models and their comparison in landslide susceptibility mapping in Central Nepal Himalaya. *Arab. J. Geosci.* **2014**, 7, 725–742. [CrossRef]
14. Gnyawali, K.R.; Shrestha, R.; Bhattarai, A.; Magar, P.R.; Dhungana, A.R.; Sukupayo, I.; Dumaru, R. Rockfall characterization and structural protection in the Siddhababa section of Siddhartha highway H10, Nepal. *J. Inst. Eng.* **2015**, *11*, 1–11. [CrossRef]
15. Dahal, R.K. Initiatives for rockfall hazard mitigation in Nepal. *Bull. Nepal Geol. Soc.* **2016**, *33*, 51–56.
16. Alsabhan, A.H.; Singh, K.; Sharma, A.; Alam, S.; Pandey, D.D.; Rahman, S.A.S.; Khursheed, A.; Munshi, F.M. Landslide susceptibility assessment in the Himalayan range based along Kasauli-Parwanoo road corridor using weight of evidence, information value, and frequency ratio. *J. King Saud Univ.-Sci.* **2022**, *34*, 101759. [CrossRef]
17. DeLeon, A.A.; Jeppson, R.W. *Hydraulic and Numerical Solutions of Steady-State but Spatially Varied Debris Flow*; Utah Water Research Laboratory, Utah State University: Logan, UT, USA, 1982; pp. 4–24.
18. Takahashi, T.; Tsujimoto, H. Delineation of the debris flow hazardous zone by a numerical simulation method. In Proceedings of the International Symposium on Erosion, Debris Flow and Disaster Prevention, Tsukuba, Japan, 3–5 September 1985; pp. 457–462.
19. O'Brien, J.S. Physical Processes, Rheology and Modeling of Mudflows. Ph.D. Thesis, Colorado State University, Fort Collins, CO, USA, 1986.
20. Savage, S.B.; Hutter, K. The motion of a finite mass of granular material down a rough incline. *J. Fluid Mech.* **1989**, *199*, 177–215. [CrossRef]
21. Ancey, C. Dry granular flows down an inclined channel: Experimental investigations on the frictional-collisional regime. *Phys. Rev.* **2001**, *65*, 011304. [CrossRef] [PubMed]
22. Midi, G.D.R. On dense granular flows. *Eur. Phys. J.* **2001**, *14*, 341–365.
23. Parez, S.; Aharonov, E.; Toussaint, R. Unsteady granular flows down an inclined plane. *Phys. Rev.* **2016**, *93*, 042902. [CrossRef]
24. Jop, P.; Forterre, Y.; Pouliquen, O. A constitutive law for dense granular flows. *Nature* **2006**, *441*, 727–730. [CrossRef]
25. Denlinger, R.P.; Iverson, R.M. Flow of variably fluidized granular masses across three dimensional terrain: 2. Numerical predictions and experimental tests. *J. Geophys. Res. Solid Earth* **2001**, *106*, 553–566. [CrossRef]
26. Pitman, E.B.; Le, L. A two-fluid model for avalanche and debris flows. *Philos. Trans. R. Soc. Lond. Ser.* **2005**, *363*, 1573–1601. [CrossRef]
27. Hutter, K.; Schneider, L. Important aspects in the formulation of solid-fluid debris-flow models. Part I: Thermodynamic implications. *Contin. Mech. Thermodyn.* **2010**, *22*, 363–390. [CrossRef]
28. Luca, I.; Tai, Y.C.; Kuo, C.Y. *Shallow Geophysical Mass Flows down Arbitrary Topography*; Springer: Berlin/Heidelberg, Germany, 2016; pp. 203–250.
29. Pudasaini, S.P. A general two-phase debris flow model. *J. Geophys. Res. Earth Surf.* **2012**, *117*, F03010. [CrossRef]
30. Thiessen, A.H. Precipitation averages for large areas. *Mon. Weather Rev.* **1911**, *39*, 1082–1084. [CrossRef]
31. Department of of Mines and Geology (DMG). *Geological Map of Far-Western Nepal*; Department of of Mines and Geology (DMG): Kathmadu, Nepal, 1987.
32. Neupane, B.; Zhao, J.; Ju, Y.; Baral, U. Occurrence of unconventional hydrocarbon deposits and its structural relation in Nepal Himalaya: Implication for future exploration. *Arab. J. Geosci.* **2020**, *13*, 81. [CrossRef]
33. Kayastha, N.B. Stratigraphy of the lower Tertiary rocks of Nepal Himalaya. *J. Nepal Geol. Soc.* **1992**, *8*, 21–30. [CrossRef]
34. Jakob, M.; Hungr, O. *Debris-Flow Hazards and Related Phenomena*; Springer: Berlin/Heidelberg, Germany, 2005.
35. KC, D. Post Wildfire Debris Flows: Mechanisms of Enhanced Overland Flow and Erosion and Numerical Simulations. Ph.D. Thesis, University of Toledo, Toledo, OH, USA, 2023.
36. Diwakar, K.C.; Dangi, H.; Naqvi, M.W.; Kadel, S.; Hu, L.B. Recurring landslides and debris flows near Kalli Village in the Lesser Himalayas of Western Nepal. *Geotech. Geol. Eng.* **2023**, *41*, 3151–3168. [CrossRef]
37. Ojha, S. Rehabilitation of Sunkoshi Small Hydropower Plant (2.6 MK), Nepal after Sequences of Natural Disaster. *Int. J. Eng. Technol. Sci.* **2018**, *5*, 75–90. [CrossRef]
38. *IS 1943-1979*; Method for Determination of Unconfined Compressive Strength of Rock Materials. Department of Consumer Affairs: New Delhi, India, 2016.
39. *IS 2720*; Method of Test for Soils Part 4, Grain Size Analysis. Department of Consumer Affairs: New Delhi, India, 2006.
40. *IS 2720*; Method of Test for Soils Part 5, Determination of Liquid Limit and Plastic Limit. Department of Consumer Affairs: New Delhi, India, 2006.
41. Alyamani, M.S.; Sen, Z. Determination of hydraulic conductivity from complete grain-size distribution curves. *Ground Water* **1993**, *31*, 551–555. [CrossRef]
42. Mergili, M.; Jaboyedoff, M.; Pullarello, J.; Pudasaini, S.P. Back calculation of the 2017 piz cengalo-bondo landslide cascade with r.avaflow: What we can do and what we can learn. *Nat. Hazards Earth Syst. Sci.* **2020**, *20*, 505–520. [CrossRef]
43. Pudasaini, S.P.; Mergili, M. A multi-phase mass flow model. *J. Geophys. Res. Earth Surf.* **2019**, *124*, 2920–2942. [CrossRef]

44. Iverson, R.M.; Denlinger, R.P. Flow of variably fluidized granular masses across three-dimensional terrain: 1. Coulomb mixture theory. *J. Geophys. Res.* **2001**, *106*, 537–552. [CrossRef]
45. Alaska Satellite Facility (ASF). Available online: https://search.asf.alaska.edu/ (accessed on 10 January 2022).
46. Davies, T.R.H. Large debris flows: A macro-viscous phenomenon. *Acta Mech.* **1986**, *63*, 161–178. [CrossRef]
47. Chen, H.X.; Zhang, L.M.; Chang, D.S.; Zhang, S.D. Mechanisms and runout characteristics of the rainfall-triggered debris flow in Xiaojiagou in Sichuan Province, China. *Nat. Hazards* **2019**, *62*, 1037–1057. [CrossRef]
48. Morino, C.; Conway, S.J.; Balme, M.R.; Hillier, J.; Jordan, C.; Sæmundsson, Þ.; Argles, T. Debris-flow release processes investigated through the analysis of multi-temporal LiDAR datasets in north-western Iceland. *Earth Surf. Process. Landforms* **2019**, *44*, 144–159. [CrossRef]
49. Al-Shayea, N. The combined effect of clay and moisture content on the behavior of remolded unsaturated soils. *Eng. Geol.* **2001**, *62*, 319–342. [CrossRef]
50. Komu, M.P.; Nefeslioglu, H.A.; Gokceoglu, C. Modeling shallow landslide runout distance in Eocene Flysch Facies using empirical-statistical models (Western Black Sea Region of Türkiye). *ISPRS Int. J. Geo-Inf.* **2024**, *13*, 84. [CrossRef]

Article

Research on the Prediction of Infiltration Depth of Xiashu Loess Slopes Based on Particle Swarm Optimized Back Propagation (PSO-BP) Neural Network

Pan Xiao [1], Bingyue Guo [2,*], Yi Wang [2], Yujian Xian [2] and Faming Zhang [1]

[1] Earth Sciences and Engineering College, Hohai University, Nanjing 210098, China; 211309080026@hhu.edu.cn (P.X.); zhangfm@hhu.edu.cn (F.Z.)

[2] Geological Exploration Technology Institute of Jiangsu Province, Nanjing 211100, China; wangyi_cumt@126.com (Y.W.); xianyjian@126.com (Y.X.)

* Correspondence: guoby1121@tom.com; Tel.: +86-139-1384-3271

Abstract: The Xiashu loess exhibits expansion when in contact with water and contraction when water is lost, making it highly susceptible to the influence of rainfall. Therefore, it is essential to investigate the infiltration behavior of rainwater in Xiashu loess slopes under various conditions. The depth of infiltration in slopes directly affects the depth of landslide failure and serves as an important indicator for studying slope infiltration characteristics; only a handful of academics have delved into its study. This article is based on on-site rainfall experiments on Xiashu loess slopes, using three main factors, rainfall intensity, rainfall duration, and slope angle, as discrimination indicators for the infiltration depth of Xiashu loess slopes. The particle swarm optimization algorithm is employed to optimize the BP neural network and establish a PSO-BP neural network prediction model. The experimental data are accurately predicted and compared with the multivariate nonlinear regression model and traditional BP neural network models. The results demonstrate that the PSO-BP neural network model exhibits a better fit and higher prediction accuracy than the other two models. This model provides a novel approach for rapidly determining the infiltration depth of Xiashu loess slopes under different rainfall conditions. The results of this study lay the foundation for the prediction of the landslide damage depth and infiltration of Xiashu loess slopes.

Keywords: Xiashu loess; infiltration depth; particle swarm optimization; BP neural network; multivariate nonlinear regression

1. Introduction

Studies indicate that since the 21st century, landslides have emerged as a major geological challenge for China [1]. Rainwater infiltration leads to erosion of the slope's surface and the softening of its internal rock and soil, diminishing its stability and triggering landslides, with the Xiashu loess landslide being a common example. The Xiashu loess is mainly distributed in the area of Nanjing and Zhenjiang, Jiangsu Province [2], which poses a great threat to the safety issues of people's lives and properties in the region. The Xiashu loess has characteristics such as swelling when encountering water and shrinking when losing water [3], which is significantly affected by rainfall and is prone to landslides in the rainy season. Therefore, it is crucial to study the infiltration characteristics of the Xiashu loess slopes under rainfall conditions.

Lately, an increasing number of academics have delved into the issues associated with the Xiashu loess. Hu et al. [4,5] studied the failure modes of the Xiashu loess under different moisture contents through experiments and investigated the infiltration pattern and damage mechanism of Xiashu loess slopes under different rainfall conditions; Liu et al. [6] researched the changes in mechanical properties of the Xiashu loess after undergoing different wet and dry cycles through unsaturated direct shear tests; Chen et al. [7] revealed

the seismic response mechanism of Xiashu loess slopes through large-scale shaking table tests on the Xiashu loess; Sun et al. [8] experimentally analyzed a large number of Xiashu loess samples and found that the slope stability of the Xiashu loess is mainly affected by the soil water content. It can be seen that research on landslides in the Xiashu loess has focused on analyzing the causes of landslides as well as on early warning, and less research has been conducted on the depth of infiltration of Xiashu loess slopes under rainfall conditions.

For other soil slopes, some scholars have explored the infiltration depth of slopes under different rainfall conditions through simulated rainfall experiments [9,10] but have not conducted predictive research. At present, in the prediction of slopes, most scholars focus on the prediction of slope deformation and stability [11–15], and there are few studies on the prediction of landslide damage depth [16]. Landslide damage depth is affected by a variety of factors [17], its uncertainty is higher, and it is more difficult to predict directly. Some scholars believe that shallow landslides parallel to the surface of soil slopes often occur (failure at wet fronts) [18,19]; thus, the range of landslide damage depths can be indirectly determined from rainfall infiltration depths and the prediction of slope infiltration depths is better implementable.

Various methods are employed for prediction, including support vector machine, neural networks, extreme learning machine, multiple regression, etc. Each method has its own set of advantages and disadvantages, and they have collectively yielded improved prediction results [20–23]. The above method can realize the rapid estimation of landslide characteristics by building a prediction model, which is different from the traditional numerical simulation analysis method because of its high efficiency and excellent prediction accuracy [24]. Among these, neural networks are utilized to establish relationships between variables by simulating biological neural networks. They possess a strong capability to accommodate nonlinearity and exhibit autonomous learning, making them widely employed in slope prediction research. However, it also has limitations, such as the issue of too rapid a convergence and the susceptibility to becoming trapped in local minima [25]. In order to make up for the deficiencies in neural networks, many scholars have used different algorithms to optimize neural networks, and these algorithms include the Genetic Algorithm [26,27], Bird Swarm Algorithm [28], particle swarm algorithm [29–31], Sparrow Algorithm, etc., which are all able to overcome the limitations of local optimums and assign optimized weights and thresholds to the neural network to improve the prediction accuracy of the neural network. In this paper, based on the experimental situation, we consider optimizing the BP neural network with the particle swarm algorithm (PSO) to make up for the shortcomings of the neural network, so that the optimized neural network has a better prediction effect [32,33]. This study forecasts the infiltration depth of Xiashu loess slopes using a BP neural network enhanced by the particle swarm algorithm (PSO), aiming to clarify the relationship between rainfall duration, rainfall intensity, slope angle, and the depth of slope infiltration. Concurrently, a comparison is made between the PSO-BP neural network model, the multivariate nonlinear regression prediction model, and the unoptimized BP neural network to evaluate the pros and cons of these models and to formulate the prediction model effectively. A rapid method for determining the infiltration depth of Xiashu loess slopes is proposed to provide the basis for the subsequent prediction of landslide damage depth and infiltration studies of Xiashu loess slopes.

2. Methodology

2.1. Principles of Multivariate Nonlinear Regression Model

Regression analysis is a quantitative depiction of uncertain relationships between things that exist in the objective world with the help of mathematical models. In the analysis of a nonlinear link between a dependent variable Y and one or several independent variables ($X_1 \sim X_n$), employing a nonlinear regression model is feasible, along with the use of statistical analysis techniques and functions for the analytical interpretation and formal depiction of the relationship. The multiple regression equation allows the relationship between input and output values to be established in order to quickly and efficiently estimate

the output values from the input values. Based on the output values, this information is useful for risk assessment. In nonlinear regression models, least-squares stands as the predominant technique for estimating parameters, and the models developed through this approach are considered a posteriori models in the realm of statistical mathematical modeling. This technique is applicable for forecasting the depth of rainfall infiltration on slopes, employing a linear function to mimic a nonlinear function, and repeating this method to achieve the best parameter solution.

Presently, two primary varieties of nonlinear mathematical models exist, linking several independent variables with a single dependent variable. In Type I nonlinear mathematical models, the initial step is to examine the functional link between an independent variable and its dependent counterpart independently, followed by overlaying this connection between the dependent and independent variables. Should the overlaid functional link fail to meet specific criteria, it becomes essential to delve deeper into the interplay among the independent variables. Nonlinear mathematical models of Type I are straightforward, highly suitable, and broadly applicable. In contrast, Type II nonlinear mathematical models have been less applied by scholars due to their excessive complexity. Thus, the considered nonlinear mathematical models are currently dominated by Type I. The mathematical expression for the nonlinear mathematical model of Type I is given in the following equation:

$$y = k_0 + \sum_{i=1}^{n} k_i f_i(x_i) + \sum_{i=1}^{n} k_j x_i x_j, \tag{1}$$

where y is the dependent variable; k_i is the regression coefficient; x_i and x_j are independent variables, $i = 0, \cdots, n$; $j = 0, \cdots, n$; and $f_i(x_i)$ is the functional relationship between a particular independent variable and the dependent variable.

2.2. Principles of BP Neural Network

Developed in the 1980s, BP neural networks have found extensive application among researchers in control, optimization, and nonlinear prediction, owing to their straightforward design and user-friendliness. Neural networks reflect the structure and function of the human brain's nerves, abstracting the properties of the real brain and simplifying it into an information processing system. Typically, a BP neural network is composed of three distinct layers: input, hidden, and output layers. The learning principle is as follows: During forward propagation, a set of weights and thresholds is randomly generated. This set of randomly generated numbers, along with the excitation function, jointly act on the input parameters. The input parameters are passed from the input layer to the output layer through the implicit layer. The output value is compared to the expected value. If the error between the two exceeds the accepted range, the error is back-propagated from the output layer. The initial randomly generated weights and thresholds are then adjusted and corrected to continue the learning process through continuous iterative learning. This process continues until the final output value and the expected value have an error within an acceptable range. At this point, the training ends. Research has demonstrated that a tri-layered BP neural network meets the criteria for general function mapping, and various multivariate functions can be estimated with any desired precision using a limited set of hidden-layer BP neural networks. The structure of the BP neural network is shown in Figure 1.

2.3. Particle Swarm Optimization

Eberhart and Kennedy jointly introduced the particle swarm optimization (PSO) algorithm in 1995, drawing inspiration from the collective food-seeking patterns of animal birds. This algorithm mimics bird foraging for group iteration and seeks the most suitable area within the particle group to identify the optimal particles for the desired solution space. Each particle in the algorithm represents a solution. The initial state of all particles in the population is continuously iterated. At each iteration, the particles update themselves to keep track of the optimal value, in order to find the optimal solution.
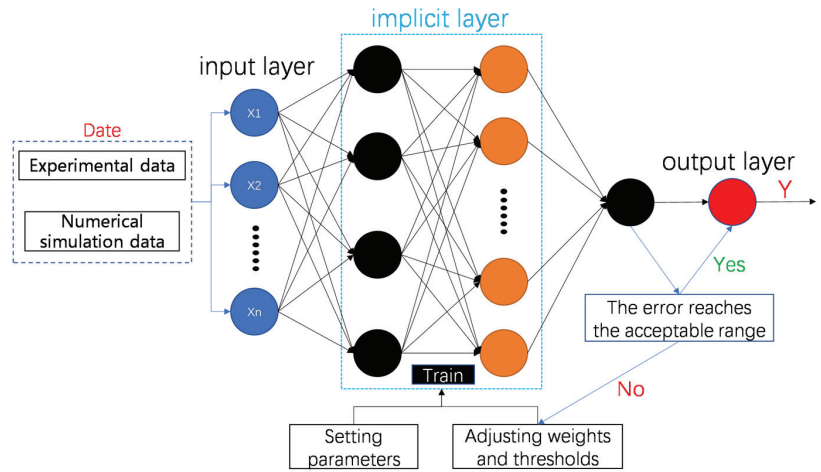
Figure 1. BP neural network structure.

The particle swarm algorithm begins by initializing a group of random particles. Assuming there are m particles in the swarm, each particle has an n-dimensional vector that represents a solution in the n-dimensional optimization space. X_j represents the positional vector for particle j, and V_j denotes the velocity vector for particle j.

$$X_j = X_{j1}, X_{j2}, \cdots X_{jn}, \tag{2}$$

$$V_j = V_{j1}, V_{j2}, \cdots V_{jn}, \tag{3}$$

In the iterative phase, vectors representing particle positions are integrated into the fitness function E_k to obtain their fitness values. The optimal fitness values of the particles are compared to search for the particle swarm's successive single best position P_j and global best position G_j.

$$P_j = P_{j1}, P_{j2}, \cdots, P_{jn}, \tag{4}$$

$$G_j = G_{j1}, G_{j2}, \cdots, G_{jn}, \tag{5}$$

The individual optimal solution achieved by each particle during the search process is represented by P_j, while the global optimal solution achieved by the particles during the search process, the optimal solution of the particle swarm algorithm, is represented by G_j. The particle swarm algorithm updates and optimizes based on four values: X_j, V_j, P_j, and G_j. These values are used to determine the position and velocity vectors after each iteration, with the algorithm's evolution equation being

$$V_j(k+1) = w \cdot V_j(k) + c_1 \cdot r_1 \cdot \left[P_j(k) - X_j(k)\right] + c_2 \cdot r_2 \cdot \left[G_j(k) - X_j(k)\right], \tag{6}$$

$$X_j(k+1) = X_j(k) + V_j(k+1), \tag{7}$$

where w is the inertia weight; c_1 and c_2 are learning factors, usually taking a value between 0 and 2; and r_1 and r_2 represent a pair of random numbers in the range of [0, 1], typically distributed evenly. To prevent a blind search process, it is important to limit the speed of the particle swarm during the search process. Typically, the speed V_j should be limited to a range of $[v_{min}, v_{max}]$.

The effectiveness of particle swarm algorithms is significantly influenced by inertia weights w. Higher inertia weights are conducive to the overall optimization of searches, whereas lower inertia weights support the optimization of local searches. In this paper, by adaptively adjusting the inertia weights in the algorithm, w decreases as the number of iterations continues to increase, with the following equation:

$$w = w_{max} - (w_{max} - w_{min})\frac{k}{k_{max}}, \tag{8}$$

where k is the current number of iteration steps; k_{max} is the maximum number of iteration steps; and w_{max} and w_{min} represent the maximum and minimum values of the inertia weight w.

The particle swarm algorithm optimizes the neural network by continuously updating its weights and thresholds and assigning the optimized values to the neural network.

2.4. PSO-BP Neural Network Model Prediction Process

As previously noted, the BP neural network's predictive capabilities suffer from sluggish convergence rates, susceptibility to local extremes, and heightened sensitivity to weight and threshold values, yet the PSO algorithm compensates for these shortcomings in the BP neural network. Therefore, the PSO algorithm can be combined with a BP neural network to achieve higher accuracy and convergence speeds. The PSO-BP neural network model prediction process is as follows:

(1) Import the forecasted data; introduce random disturbances to the dataset; segregate the training, validation, and test datasets; and normalize the data:

$$X = \frac{(X - X_{min})}{(X_{max} - X_{min})}, \tag{9}$$

where X_{max} and X_{min} represent the maximum and minimum values of each group of samples, respectively.

(2) Establish a BP neural network, and set the number of nodes and training parameters. The number of hidden layers is generally determined by empirical formulae to give an approximate range:

$$h_j \leq \sqrt{h_i \times (h_k + 3)}, \tag{10}$$

where h_j is the number of nodes in the hidden layer; h_i is the number of nodes in the input layer; and h_k is the number of nodes in the output layer.

(3) Set the PSO parameters (learning factors, population size, number of population renewals, etc.) and randomly initialize the particle position and velocity.

(4) If the particle's current adaptation value X_j is better than the historical optimal adaptation value P_j, then $P_j = X_j$; if the particle's historical optimal adaptation value is better than the global optimal adaptation value G_j, then $G_j = P_j$. Based on Equations (6) and (7), the particles are updated to determine if the end condition is reached, and if not, iteration continues until the optimal weights and thresholds are obtained.

(5) Assign the optimal connection weights and thresholds to the BP neural network and continue training the BP neural network to complete the prediction and output the prediction results.

Based on the above process, Figure 2 depicts the flowchart of the PSO-BP neural network experiment.
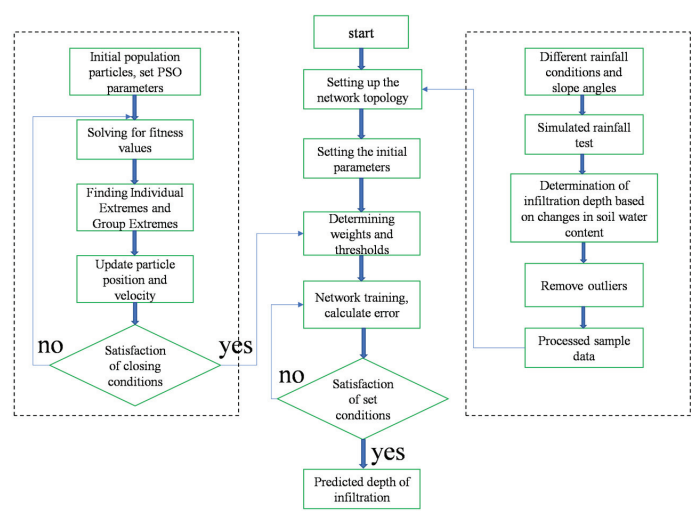
Figure 2. Experimental diagram of neural network structure.

3. Case Study

3.1. Sample Plot Overview

The study area is situated in Jurong City, Jiangsu Province, China, specifically in Xiashu Town Zhu Li Village, West Xu group, southwest of the slope, in the northwestern part of Zhenjiang City. The topography of the study area is dominated by plains and hills, with the east being low and the west being high. The area falls under the subtropical monsoon climate, with rainfall mainly concentrated in the spring and summer. The groundwater conditions are complex, with relatively shallow depths. During the rainy season, the Nanjing–Zhenjiang area experiences a high frequency of landslides, posing a serious threat to the safety of residents, factory workers, and tourists in the affected areas. This issue is closely linked to the widespread distribution of the Xiashu loess in the Zhenjiang area of Jiangsu Province.

Tea trees have been planted on the slopes of the test site, with the northeast side of the slope being close to a natural water pond located 5–6 m away. The main threats in the area are crops in farmland. The surface lithology of the slope body consists mainly of a 1.5 m thick layer of powdery clay from the Xiashu Formation, which is the focus of the experiment. The slope body has an overall height difference of about 8~10 m, with a gentle front edge and a steeper back edge. The first step involves a 5–6 m slope with an angle of 35–40°, while the rear may be the back wall of a previous localized landslide, with an angle of approximately 50°; a height difference of 3–4 m; and an exposed, dry, and loose back edge wall. Gullies and soil fissures have developed on the slope, with initial fissures distributed in an F-shape and measuring 1–2 cm wide. The preliminary investigation indicated that the slope morphology and angle of the test section were representative of most slopes in the area, leading to the selection of this slope as the test site.

Damage to the Xiashu loess slope occurs when the slope angle, rainfall intensity, and rainfall duration reach certain values during testing (Figure 3e).

3.2. Field Rainfall Test Program Setup

The slope test site measures 4 × 5 m and is constructed using steel frames. The equipment required for the test includes steel frames to build the test platform, artificial rainfall devices, and a monitoring system. The purpose of this integrated test device is to monitor the change in water content of the slope soil over time under continuous rainfall, in order to elucidate the effect of rainfall on the depth of infiltration of slopes. Water content monitoring points are distributed at various depths on the top, middle, and foot of the

Xiashu loess slope to compare and analyze infiltration at different locations. Additionally, a probe slot is located on the right side of the slope in the test section for convenient sampling and observation of the wetting front. Figure 4 shows the layout of the test setup.
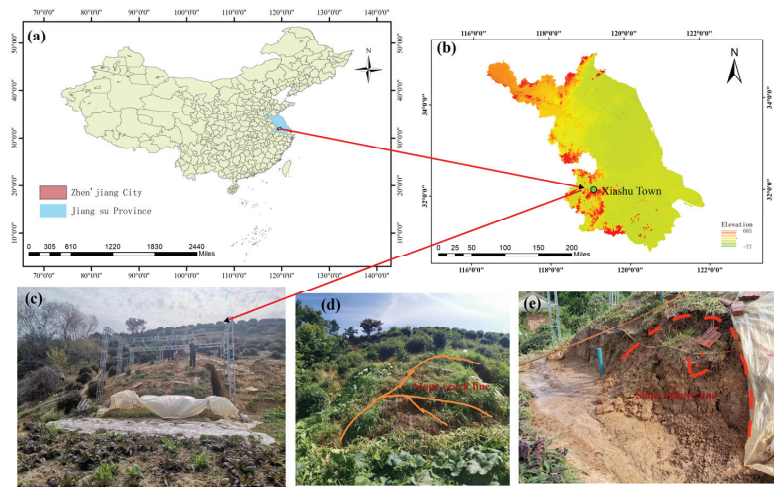
Figure 3. Study area: (**a**) map of China; (**b**) elevation map of Jiangsu Province; (**c**) field test site; (**d**) slope cracks; (**e**) landslides occurring during the test.
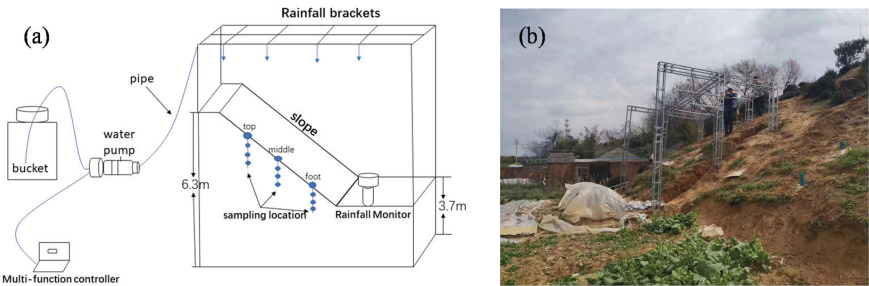
Figure 4. The layout of the test setup: (**a**) sketch of the test setup; (**b**) ield test setup diagram.

The experimental rainfall setting takes into account the rainfall and evaporation in the region. Through the collection of meteorological data in recent years in the Ningzhen area, it can be seen that the area is dominated by short-term heavy rainfall, the duration of rainfall in most cases is not more than 12 h, and the maximum intensity of rainfall that occurs is 63.2 mm/h. Therefore, the field rainfall test program setup in this paper consists of three types of rainfall intensities, 30 mm/h, 60 mm/h, and 90 mm/h, and four types of rainfall duration, 1 h, 2 h, 4.5 h, and 8 h. Additionally, there are three types of experimental slope angles: 35°, 40°, and 45°. Due to the limited test conditions, it was not possible to analyze the depth of infiltration for slopes with slower slope angles. To obtain more extensive and reliable prediction results, numerical simulation was considered to compensate for slopes with 20°, 25°, and 30° slope angles. This allowed the established prediction model to predict the depth of infiltration for most of the slopes in the Nanjing–Zhenjiang area. The numerical simulation results and the test results were compared and verified under the same conditions. It was found that the two infiltration results were basically the same, despite possible differences between them.

3.3. Partial Analysis of Results

During the test, it was observed that the depth of infiltration varied at different locations on the slope. The infiltration depth was found to be largest at the foot of the slope, followed by the middle of the slope, and smallest at the top of the slope. To simplify the analysis of the slope as a whole, the average depth of infiltration at the top, middle, and foot of the slope was used as the predicted data. The distribution of slope wetting fronts under a rainfall intensity of 60 mm/h and rainfall duration of 1 h, 2 h, 4.5 h, and 8 h is presented in Figure 5.
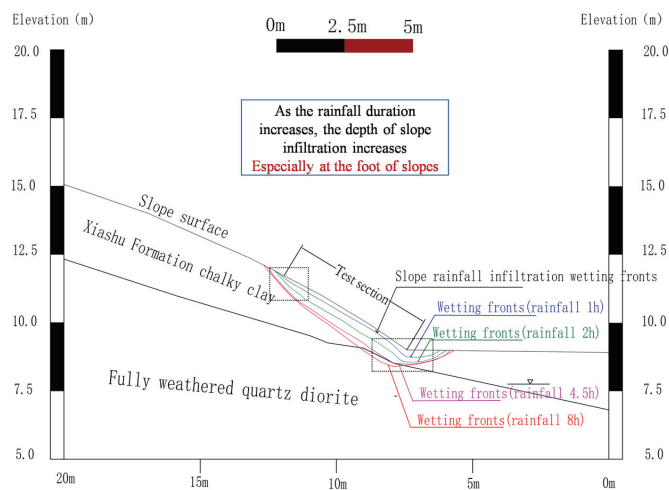
Figure 5. Distribution of wetting fronts with different rainfall durations.

To examine the impact of rainfall intensity and duration on the infiltration of Xiashu loess slopes, an artificial rainfall simulation device was used to apply varying levels of rainfall. Figure 6 displays a 3D surface plot of the infiltration depth ranging from 32 mm to 77 mm. The plot is based on a 35° slope angle, a rainfall intensity ranging from 30 mm/h to 90 mm/h, and a rainfall duration ranging from 1 h to 8 h. It is evident that the depth of infiltration generally increases with the increase in both rainfall intensity and duration. The impact of rainfall with varying intensity and duration on the depth of infiltration is significant. However, as can be seen from the figure, the increase in rainfall duration is more significant for the increase in slope infiltration depth than the increase in rainfall intensity.

3.4. Impact Factors and Data Sources

Researchers have continuously analyzed the factors affecting the depth of slope infiltration, including soil particle structure, infiltration rate, rainfall, and slope morphology. However, analyzing intrinsic factors such as soil structure and infiltration rate is complicated, and obtaining real-time parameters inside the soil is difficult. On the other hand, analyzing slope morphology and rainfall is relatively straightforward and manageable. This paper analyzes the effect of rainfall intensity, rainfall duration, and slope angle on the depth of slope infiltration based on field tests. This study found that rainfall duration and intensity have a positive correlation with slope infiltration depth, while slope angle has a negative correlation. These factors have a significant impact on slope infiltration depth.

The data presented were obtained through artificial simulated rainfall tests and numerical simulations on a typical Xiashu loess slope in Jurong City. The analysis focused on the depth of slope infiltration under different rainfall conditions by applying rainfall of varying intensities and durations to the Xiashu loess slope in the test section. After the slope-cutting treatment, we analyzed infiltration on slopes with varying angles. The

soil's water content at various depths within the slope was used to determine the depth of infiltration.
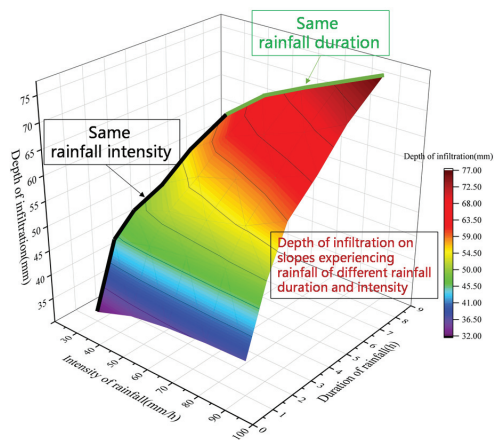
Figure 6. Infiltration depth diagrams for different rainfall intensities and durations.

This article obtained 72 sets of sample data, which were divided into training, validation, and prediction sets in a certain proportion. Table 1 displays some of the test data.

Table 1. Partial test data.

Serial Number	Slope Angle/°	Rainfall Intensity/mm·h^{-1}	Rainfall Duration/h	Infiltration Depth/cm
1	35	30	2	44
2	30	60	4.5	62
3	40	30	4.5	47
4	40	90	1	33
5	25	30	8	70
6	30	60	1	38
7	35	90	2	50
8	20	60	4.5	69
9	25	30	2	54
10	30	60	2	52

4. Modeling and Validation

4.1. Multiple Nonlinear Regression Modeling and Solution Validation

Based on the previous section, it is evident that changes in rainfall intensity, duration, and slope angle significantly affect the infiltration results. These results can serve as an indicator for predicting the depth of slope infiltration using the multiple nonlinear regression model.

To analyze the nonlinear effect of each factor on the depth of slope infiltration, we used experimental data to establish a regression model in SPSS 22 software. The model included the three aforementioned factors as independent variables and the depth of infiltration as the dependent variable. This paper adopts the type I nonlinear mathematical model due to the complexity of the type II model, making it difficult to accurately determine its form. The model considers the interaction between the independent variables and linearizes the nonlinear term through substitution, converting the nonlinear problem into a linear problem for analysis and solution. Because the multivariate nonlinear regression model does not have a unique solution, this paper first analyzes a single factor and then considers the impact of all factors. After several trial calculations, the ENTER analysis method of

regression analysis is used for linear regression to exclude terms with collinearity and obtain the mathematical expression of the regression model. The fitting results are as follows:

$$y = 49.99 - 0.96 * X_1 + 0.088 * X_2 + 9.19 * X_3 + 0.005 * X_1^2$$
$$-0.539 * X_3^2 - 0.028 * X_1 * X_3 + 0.021 * X_2 * X_3, \tag{11}$$

where X_1 is the slope angle; X_2 is the rainfall intensity; X_3 is the rainfall duration; and y is the depth of infiltration.

The regression equation shows that rainfall duration has the greatest impact on infiltration depth, followed by slope angle and then rainfall intensity. Based on the regression equation, the slope infiltration depth can be estimated by rainfall duration, rainfall intensity, and slope angle, and the results of this study can also be applied to the assessment of landslide damage depth.

The equation analysis results of the regression model are shown in Table 2. ANOVA and significance tests give $D - W = 2.669$, indicating that the data satisfy the independence requirement. The significance test for the nonlinear mathematical model F resulted in $F = 250.308$, which is much larger than $F_{0.05}(8,63) = 2.79$, with a p-value of 0.000, indicating that the model is statistically significant at the 0.05 test level. Therefore, it can be determined that the multivariate nonlinear regression equations are valid. At the same time, $R^2 = 0.936$, which is closer to 1. It indicates that the strong linear relationship between y and x in the equation accurately reflects the actual change pattern, and the fitting effectiveness of the nonlinear regression equation is superior.

Table 2. Equation analysis of regression models.

Project	Sum of Squares	Free Degree	Mean Square	F Value	p
Model	15,760.152	8	1970.019	250.308	0.000
Error	1008.650	63	16.010	-	-
Total	16,768.802	71	-	-	-

The depth of slope infiltration was analyzed using the established multivariate nonlinear regression equation, which was validated through testing 10 additional sets of field data selected at random. The regression equation was used to calculate the slope infiltration depth by substituting the input parameters into Equation (11). The relative error was analyzed by comparing the calculated values with the test data, as presented in Table 3. Table 3 shows that the nonlinear regression model has a minimum relative error of 1.68%, a maximum relative error of 9.82%, and an average relative error of 6.13%. Therefore, this model is suitable for prediction.

Table 3. Nonlinear regression model test results.

Serial Number	Infiltration Depth Obtained from the Experiment/cm	Model Calculation of Infiltration Depth/cm	Error
1	50	54.11	8.22%
2	58	61.45	5.95%
3	34	36.35	6.92%
4	49	44.19	−9.82%
5	56	59.07	5.48%
6	71	68.58	−3.41%
7	36	39.14	8.73%
8	51	47.60	−6.67%
9	67	64.02	−4.44%
10	77	75.71	−1.68%

4.2. PSO-BP Neural Network Modeling and Solution Validation

The information from 72 data sets was used to create a predictive model. Totals of 50 sets were used for training, 11 for validation, and 11 for testing. This means that 70% of the total data were used for training and 30% for testing and validation.

The PSO-BP neural network modeling process begins by importing the predicted data into Matlab R2018b. The data are then randomly disrupted and divided into training and test sets, followed by normalization. The neural network structure consists of three layers: three input nodes, one output node, and a hidden layer with three nodes. The number of hidden-layer nodes was determined through Matlab program training experiments using Equation (10). This structure was found to be optimal. The parameters of the particle swarm were set as follows: the population size was 10, the number of population iterations was set to 50, the learning factor was $C_1 = C_2 = 4.494$, and the particle flight speed range was $[-1, 1]$. The population iterates until optimal weights and thresholds are achieved, which are then assigned to the BP neural network for training. Training continues until preset conditions are met.

The neural network is trained using the Sigmoid function as the transfer function, and the lattice training function uses the BP algorithm training function Trainlm of L-M. The maximum number of lattice training times is 1000, the learning rate is 0.01, and the target error is 1×10^{-6}. The number of nodes in the hidden layer and the target error is constantly varied and trained in different combinations. To demonstrate the impact of the particle swarm optimization algorithm, we compared the training results of the PSO-BP neural network with those of the BP neural network. Figures 7 and 8 display the training results of the BP neural network and PSO-BP neural network, respectively. The figures show that the R^2 of the prediction model trained by the BP neural network is 0.943, while the R^2 of the prediction model trained by the PSO-BP neural network is 0.997. Compared to the multiple nonlinear regression model, both models are closer to 1 and have a better fitting effect.
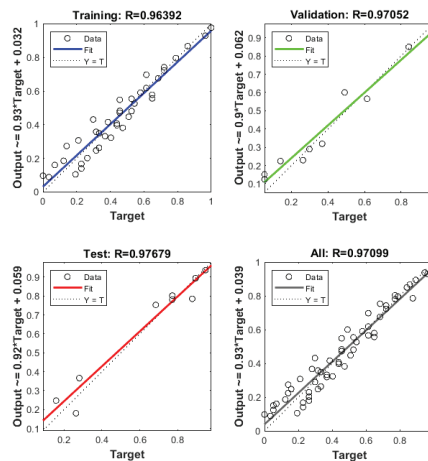
Figure 7. Graphs of BP neural network training, validation, and testing results.

The depth of infiltration of the Xiashu loess slope was calculated through iterative optimization and compared with the BP neural network using the PSO-BP neural network algorithm. Figures 9 and 10 display the time and value of the optimal variance occurrence calculated by the BP neural network algorithm and the PSO-BP neural network algorithm for iterative optimization search. The BP neural network achieved its optimal mean square error of 0.0044243 after the 37th iteration, while the PSO-BP neural network achieved its optimal mean square error of 0.0003304 after the 19th iteration.
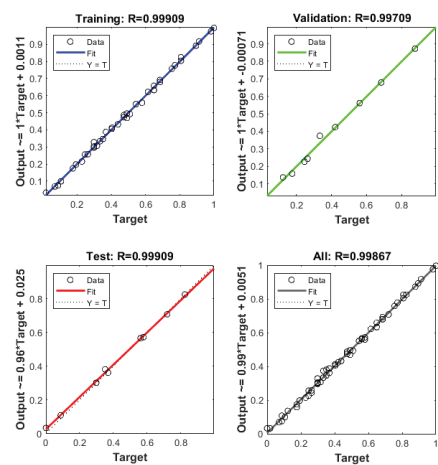
Figure 8. Graphs of PSO-BP neural network training, validation, and testing results.
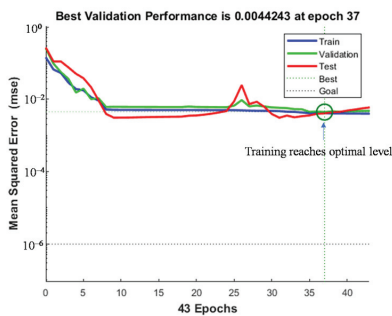
Figure 9. BP neural network iterative optimization training process diagram.
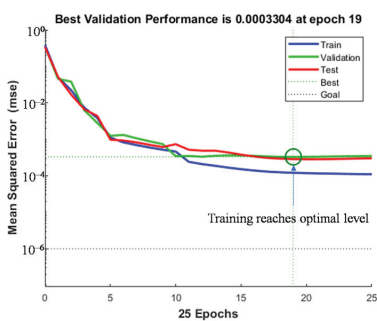
Figure 10. PSO-BP neural network iterative optimization training process diagram.

The accuracy of the model is measured using relative error and average relative error. To compare the predicted depth of infiltration with the actual depth of infiltration, other experimental data are randomly substituted into the PSO-BP neural network prediction model. The results of the relative error comparison are shown in Table 4. The figure illustrates that the PSO-BP neural network model has a minimum relative error of 0.10%, a maximum relative error of 1.68%, and an average relative error of 0.78%. The results indicate that the BP neural network model optimized by the particle swarm algorithm has achieved the expected goal with good prediction accuracy.

Table 4. PSO-BP neural network model test results.

Serial Number	Infiltration Depth Obtained from the Experiment/cm	Model Calculation of Infiltration Depth/cm	Error
1	72	73.12	1.56%
2	30	30.50	1.68%
3	54	54.32	0.59%
4	71	71.29	0.41%
5	56	55.69	−0.55%
6	83	83.09	0.10%
7	51	51.19	0.38%
8	38	37.77	−0.60%
9	49	49.17	0.36%
10	42	42.64	1.52%

After obtaining prediction results from the multivariate nonlinear regression model and the PSO-BP neural network model, the experimental data were trained for prediction using the unoptimized BP neural network model. The prediction accuracies of the three models were then comprehensively compared. Table 5 displays the coefficients of determination (R^2) and mean absolute percentage error (*MAPE*) for the three models. The formula for calculating the two is as follows:

$$R^2 = 1 - \frac{\sum_{i=1}^{n}(y_i - \hat{y}_i)^2}{\sum_{i=1}^{n}(y_i - \overline{y})^2}, \tag{12}$$

$$MAPE = \frac{1}{n}\sum_{i=1}^{n}\left[\frac{|\hat{y}_i - y_i|}{\hat{y}_i}\right] \times 100\%, \tag{13}$$

where n is the predicted sample size, y_i is the i-th measured value, $\hat{y}_i$ is the i-th predicted value, and $\overline{y}$ is the sample mean.

Table 5. Comparison of three models.

Model	Multiple Nonlinear Regression	BP Neural Network	PSO-BP Neural Network
R^2	0.936	0.943	0.997
MAPE	6.13%	5.29%	0.78%

Table 5 shows that all three models predicted the infiltration depth of the Xiashu loess slope well. However, the PSO-BP neural network model had the highest prediction accuracy compared to the other two models. The prediction accuracies of the three models were ranked as follows: PSO-BP neural network model > BP neural network model > multivariate nonlinear regression model.

To verify the applicability of the developed PSO-BP neural network model, it was applied to other slopes for infiltration prediction. The infiltration of other slopes in the area after experiencing natural rainfall was monitored during the test. The angle of the monitored slopes was about 33°, and the rainfall intensity and duration of natural rainfall were obtained by monitoring with a test instrument. The predicted values were compared with the real monitoring values using the established model, and the comparison results are shown in Figure 11. This confirms the validity of the model.

The PSO-BP neural network model predicts these three sets of data with an average relative error of 1.04%, which is higher than the other two models. This suggests that the model is applicable to other slopes in the region with good applicability.
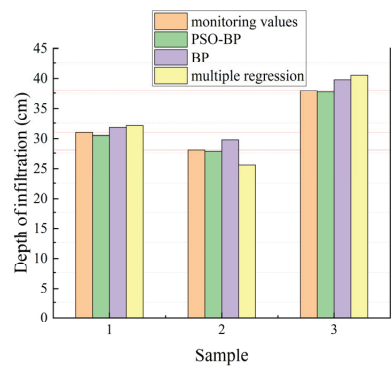
Figure 11. Comparison of predictive effects of different models.

5. Discussion

To mitigate the risks of landslides in the Xiashu loess during rainfall, it is essential to promptly evaluate the depth of infiltration of the Xiashu loess slopes. This assessment can roughly determine the extent of landslide damage and provide a new approach for the early warning and hazard assessment of landslides.

During the test, it was observed that the Xiashu loess slope suffered damage after 8 h of rainfall with a slope angle of 40° and a rainfall intensity of 90 mm/h. The diagram in Figure 12 shows the Xiashu loess landslide. The depth of the landslide is approximately 0.55 m, while the depth of infiltration is around 0.7 m. The depth of the landslide damage is about 0.8 times the depth of infiltration. Slopes undergo localized damage at the foot of the slope in the form of a circular arc, which is related to the fact that the depth of infiltration at the foot of the slope is greater than the depth of infiltration at the top of the slope and in the middle of the slope.
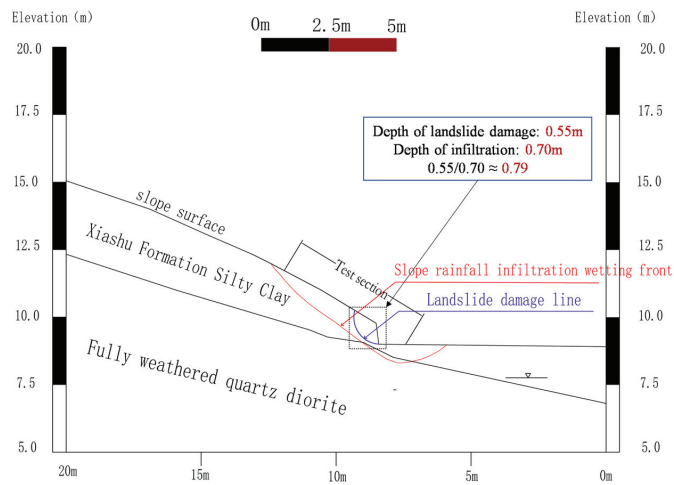
Figure 12. Analysis of landslide results.

The Xiashu loess exhibits high water sensitivity, with its shear strength significantly impacted by water content. The angle of internal friction and cohesion decreases rapidly as the water content of the soil increases. During the rainfall process, the wetting front in the slope constantly moves forward, causing the thickness of the softened soil inside the slope to increase. This, in turn, leads to a dramatic decrease in the shear strength of the

soil within the depth range of the wetting front, significantly increasing the probability of landslides occurring in the infiltration depth range of the soil. When the shear strength decreases to a certain threshold, it is not enough to support the force that causes the slope to slide. This leads to damage under the Xiashu loess slope, which is why most landslides occur at a certain depth of infiltration.

In a numerical simulation study of slope stability, it was found that the depth of infiltration has a significant effect on the slope stability coefficient. Particularly at the start of rainfall, an increase in infiltration depth results in a sharp decrease in the slope stability coefficient. The relationship between the depth of infiltration and the slope stability coefficient can be established, and the slope stability coefficient can be predicted based on the depth of infiltration.

As only one landslide occurred during the field test, it was not possible to establish a clear relationship between the depth of landslide damage and the depth of slope infiltration. Further tests can be conducted in future studies to explore this connection. The PSO-BP neural network-based slope infiltration depth prediction model presented in this paper offers a novel approach for determining the infiltration depth of Xiashu loess slopes. This lays the foundation for predicting the depth of Xiashu loess landslides and provides a new index for evaluating the stability of Xiashu loess slopes.

6. Conclusions

(1) This paper presents a prediction model for the infiltration depth of the Xiashu loess slope. The prediction data were obtained through field tests, using rainfall intensity, rainfall duration, and slope angle as input parameters, and infiltration depth as the output parameter. The particle swarm algorithm (PSO) was used to optimize the BP neural network, resulting in a model with improved convergence speed and generalization ability.

(2) The infiltration depth regression model for the Xiashu loess slope was expressed mathematically using the Class I nonlinear mathematical model. The model considered the interaction between independent variables, and the test results were predicted using the regression expression. The predicted results had an error range controlled within 10%, indicating that the nonlinear regression model was reasonable. This model provides a fast calculation method for determining the infiltration depth of the Xiashu loess slope.

(3) After comparing the slope infiltration depth prediction model established by the PSO-BP neural network with the multivariate nonlinear regression model and the traditional BP neural network model, it was found that all three methods have a good fitting effect and prediction ability. However, the PSO-BP neural network prediction model has a higher prediction accuracy than the other two models. The three models' prediction accuracy is ranked as follows: PSO-BP neural network model > BP neural network model > multivariate nonlinear regression model. This ranking fully demonstrates the effectiveness of the PSO-BP neural network model in predicting the depth of infiltration of the Xiashu loess slope.

Due to the limitations of the test, the established prediction model only considered three factors: rainfall duration, rainfall intensity, and slope angle. To improve the model's completeness, the effects of other factors should be further considered in subsequent tests.

Author Contributions: Conceptualization, P.X.; methodology, P.X.; software, F.Z.; validation, Y.W., B.G. and Y.X.; investigation, Y.W., B.G. and Y.X.; writing—review and editing, P.X. All authors have read and agreed to the published version of the manuscript.

Data Availability Statement: The data presented in this study are available on request from the corresponding author.

Conflicts of Interest: Authors Yi Wang, Bingyue Guo, and Yujian Xian were employed by the Geological Exploration Technology Institute of Jiangsu Province. The remaining authors declare that the research was conducted in the absence of any commercial or financial relationship that could be constructed as a potential conflict of interest.

References

1. Huang, R.Q. Large-Scale Landslides and Their Sliding Mechanisms in China Since the 20th Century. *Chin. J. Rock Mech. Eng.* **2007**, *26*, 433–454. [CrossRef]
2. Liu, B.S.; Song, J.L.; Hao, S.F.; Jiang, B.; Zhang, J.X. Analysis and emergent control measures of the typical Xiashu loess landslides in Nanjing-Zhenjiang area, Jiangsu Province. *Chin. J. Geol. Hazard Control* **2019**, *30*, 31–36. [CrossRef]
3. Xia, J.; Huang, G.L.; Liu, Z.T.; Chen, X.M. Cyclic Variability in Chemical Composition and Swelling-Shrinkage Properties of the Xiashu Loess Stratum near Nanjing, China. *Pedosphere* **2007**, *17*, 7. [CrossRef]
4. Hu, Y.R.; Sun, S.R.; Li, K. Study on influence of moisture content on strength and brittle-plastic failure characteristics of Xiashu loess. *Adv. Civ. Eng.* **2023**, *2023*, 5919325. [CrossRef]
5. Hu, Y.R.; Sun, S.R.; Sun, Y. Model Test Study of Rainfall Factors on Failure Process of Xiashu Loess Slope with Gravel Layer. *Adv. Civ. Eng.* **2024**, *2024*, 5564418. [CrossRef]
6. Liu, S.Q.; Wang, Y.L.; Cai, G.J.; Jiang, P.M.; Wang, J.; Zhang, M. Experimental study on the effects of wet-dry cycles and suction on the mechanical properties of unsaturated Xiashu loess. *J. Southeast Univ. (Nat. Sci. Ed.)* **2021**, *51*, 473–479. [CrossRef]
7. Chen, X.M.; Shen, J.; Wei, P.; Yang, J. Large-scale Shaking Table Test of Seismic Stability of Xiashu Loess Slopes: Analysis of Test Results(II). *J. Disaster Prev. Mitig. Eng.* **2010**, *30*, 587–594. [CrossRef]
8. Sun, S.; Wang, W.; Wei, J.; Song, J.; Yu, Y.; He, W.; Zhang, J. The physical–mechanical properties degradation mechanism and microstructure response of acid–alkali-contaminated Xiashu loess. *Nat. Hazards* **2021**, *106*, 2845–2861. [CrossRef]
9. Luo, Y.; Zhang, J.M.; Zhou, Z.; Shen, Z.J.; Chong, L.; Victor, C. Investigation and prediction of water infiltration process in cracked soils based on a full-scale model test. *Geoderma* **2021**, *400*, 115111. [CrossRef]
10. Tu, X.B.; Kwong, A.K.L.; Dai, F.C.; Tham, L.G.; Min, H. Field monitoring of rainfall infiltration in a loess slope and analysis of failure mechanism of rainfall-induced landslides. *Eng. Geol.* **2009**, *105*, 134–150. [CrossRef]
11. Malekian, M.; Momayez, M.; Bellett, P.; Carrea, F.; Tennakoon, E. Machine Learning for Slope Failure Prediction Based on Inverse Velocity and Dimensionless Inverse Velocity. *Min. Metall. Explor.* **2023**, *40*, 1557–1566. [CrossRef]
12. Pei, T.; Qiu, T.; Shen, C. Applying knowledge-guided machine learning to slope stability prediction. *J. Geotech. Geoenvironmental Eng.* **2023**, *149*, 04023089. [CrossRef]
13. Liu, C.; Jiang, Z.; Han, X.; Zhou, W. Slope displacement prediction using sequential intelligent computing algorithms. *Measurement* **2019**, *134*, 634–648. [CrossRef]
14. Zhang, Z.; Qin, L.; Ye, G.; Wang, W.; Zhang, J. Physical Modeling and Intelligent Prediction for Instability of High Backfill Slope Moisturized under the Influence of Rainfall Disasters. *Appl. Sci.* **2023**, *13*, 4218. [CrossRef]
15. Li, B.; Qiu, J. Displacement prediction of open-pit mine slope based on SSA-ELM. *Front. Earth Sci.* **2023**, *11*, 1126394. [CrossRef]
16. Yang, C.; Yang, Y.H.; Wang, J.Y.; Xu, Q.; Chen, Q.; Tao, X.X.; Hu, Z.Q. Inferring landslide depth based on ascending and descending InSAR deformations-example of TAOPING village ancient landslide. *J. Eng. Geol.* **2023**, *31*, 868–879. [CrossRef]
17. Culler, E.S.; Badger, A.M.; Minear, J.T.; Tiampo, K.F.; Zeigler, S.D.; Livneh, B. A Multi-sensor Evaluation of Precipitation Uncertainty for Landslide-triggering Storm Events. *Hydrol. Process.* **2021**, *35*, e14260. [CrossRef] [PubMed]
18. Chang, J.Y.; Bao, H.; Wu, F.Q.; Chen, Z.H.; Hao, L. Discussion on stability of shallow landslide under rainfall. *J. Rock Soil Mech.* **2015**, *36*, 995–1001. [CrossRef]
19. Cui, Y.F.; Zhou, X.J.; Guo, C.X. Experimental study on the moving characteristics of fine grains in wide grading unconsolidated soil under heavy rainfall. *J. Mt. Sci.* **2017**, *14*, 417–431. [CrossRef]
20. Nur, A.S.; Kim, Y.J.; Lee, J.H.; Lee, C.W. Spatial prediction of wildfire susceptibility using hybrid machine learning models based on support vector regression in sydney, australia. *Remote Sens.* **2023**, *15*, 760. [CrossRef]
21. Ling, Q.; Zhang, Q.; Wei, Y.; Kong, L.; Zhu, L. Slope reliability evaluation based on multi-objective grey wolf optimization-multi-kernel-based extreme learning machine agent model. *Bull. Eng. Geol. Environ.* **2021**, *80*, 2011–2024. [CrossRef]
22. Kang, M.T.; Zhu, Y.Q.; Chen, C.; Shao, B.R.; Wang, T. Research on landslide sliding distance prediction model based on multiple nonlinear regression and BP neural network. *Geol. Bull. China* **2022**, *41*, 2281–2289. [CrossRef]
23. Bharati, A.K.; Ray, A.; Khandelwal, M.; Rai, R.; Jaiswal, A. Stability evaluation of dump slope using artificial neural network and multiple regression. *Eng. Comput.* **2022**, *38* (Suppl. S3), 1835–1843. [CrossRef]
24. Chen, X.J.; Li, D.Q.; Tang, X.S.; Liu, Y. A three-dimensional large-deformation random finite-element study of landslide runout considering spatially varying soil. *Landslides* **2021**, *18*, 3149–3162. [CrossRef]
25. Zhang, Y.G.; Tang, J.; Liao, R.P.; Zhang, M.F.; Zhang, Y.; Wang, X.M.; Su, Z.Y. Application of an enhanced BP neural network model with water cycle algorithm on landslide prediction. *Stoch. Environ. Res. Risk Assess.* **2021**, *35*, 1273–1291. [CrossRef]
26. Xu, J.; Zhao, Y. Stability Analysis of Geotechnical Landslide Based on GA-BP Neural Network Model. *Comput. Math. Methods Med.* **2022**, *2022*, 3958985. [CrossRef] [PubMed]
27. Dai, M.L.; Qu, J.L.; Liu, X.Q.; Li, Q.W.; Ma, L.Z. Study on GA-BP hybrid algorithm-based prediction model and its application to rock slope stability and reinforcement effect. *Water Resour. Hydropower Eng.* **2018**, *49*, 165–171. [CrossRef]
28. Cao, X.Y.; Man, X.Y.; Wang, J.P.; Mai, R.Z.; Guo, Y.K. Deformation prediction of treated landslides based on BP neural network optimized by bird swarm algorithm. *Bull. Surv. Mapp.* **2023**, *5*, 27. [CrossRef]
29. Hu, S.W.; Li, Y.H.; Shan, C.X.; Xue, X.; Yang, H.Q. Research on Slope Stability Based on Improved PSO-BP Neural Network. *J. Disaster Prev. Mitig. Eng.* **2023**, *43*, 854–861. [CrossRef]

30. Dai, X.; Li, X.; Zhang, Y.; Li, W.; Meng, X.; Li, L.; Han, Y. A Prediction Model of Coal Seam Roof Water Abundance Based on PSO-GA-BP Neural Network. *Water* **2023**, *15*, 4117. [CrossRef]
31. Zheng, Y.; Zhang, L.; Hu, X.; Zhao, J.; Dong, W.; Zhu, F.; Wang, H. Multi-Algorithm Hybrid Optimization of Back Propagation (BP) Neural Networks for Reference Crop Evapotranspiration Prediction Models. *Water* **2023**, *15*, 3718. [CrossRef]
32. Al-Andoli, M.N.; Tan, S.C.; Sim, K.S.; Lim, C.P.; Goh, P.Y. Parallel Deep Learning with a hybrid BP-PSO framework for feature extraction and malware classification. *Appl. Soft Comput.* **2022**, *131*, 109756. [CrossRef]
33. Zhang, X.C.; Chen, X.J.; Song, Y.; Ma, P.X. Application of BP Neural Network Optimized by Particle Swarm Optimization Algorithm in Slope Stability. *Min. Res. Dev.* **2022**, *42*, 71–76. [CrossRef]

An Integration of Logistic Regression and Geographic Information System for Development of a Landslide Hazard Index to Land Use: A Case Study in Pingtung County in Southern Taiwan

Chih-Ming Tseng [1,*], Yie-Ruey Chen [2], Ching-Ya Tsai [3] and Shun-Chieh Hsieh [2]

[1] Department of Hydraulic and Ocean Engineering, National Cheng Kung University, Tainan 701401, Taiwan
[2] Department of Land Management and Development, Chang Jung Christian University, Tainan 711301, Taiwan; yrchen@mail.cjcu.edu.tw (Y.-R.C.); sch@mail.cjcu.edu.tw (S.-C.H.)
[3] Disaster Prevention Research Center, National Cheng Kung University, Tainan 701401, Taiwan; h64371281@gmail.com
* Correspondence: cmtseng@gs.ncku.edu.tw

Abstract: In Taiwan, mountainous areas account for approximately two-thirds of the total area. The steep terrain and concentrated rainfall during typhoons cause landslides, which pose a considerable threat to mountain settlements. Therefore, models for analyzing rainfall-induced landslide hazards are urgently required to ensure adequate land use in mountainous areas. In this study, focusing on Pingtung County in southern Taiwan, we developed a landslide hazard index (I_{RL}) to land use. Using FORMOSA-2 and SPOT-5 satellite images, data were collected before and after four typhoons (one in 2009 and three in 2013). The ArcGIS random tree classifier was used for interpreting satellite images to explore surface changes and disasters, which were used to analyze slope disturbances. The product of the maximum 3-h rolling rainfall intensity and effective accumulated rainfall was used as a rainfall trigger index (I_{RT}). Considering environmental and slope disturbance factors, an index of slope environmental strength potential (I_{SESP}) was developed through logistic regression (LR). Landslide hazard to land use was estimated using I_{RT} and I_{SESP}. The average coefficient of agreement (Kappa) was approximately 0.71 (medium to high accuracy); the overall accuracy of slope environmental strength potential analysis was approximately 80.4%. At a constant I_{SESP}, I_{RT} increased with the increasing hazard potential of rainfall-induced landslides. Furthermore, I_{RT} and I_{SESP} were positively correlated with landslide occurrence. When large I_{SESP} values occur (e.g., fragile environment and high land development intensity), small I_{RT} values may induce landslides.

Keywords: land use; mountainous area; rainfall; landslide hazard; random tree classifier; logistic regression; geographic information system; Taiwan

1. Introduction

Taiwan is an island located in the North Pacific subtropical monsoon region, which is vulnerable to typhoons. More than two-thirds of Taiwan's total area is mountainous with steep slopes. Recently, climate anomalies have resulted in frequent extreme rainfall events. The number of typhoons that hit Taiwan has increased every year, and large-scale landslides and debris flows have become likely. As stated in the 2012 White Paper on Disaster Management [1], remote mountainous settlements in Chiayi County, Kaohsiung City, Tainan City, Pingtung County in southern Taiwan account for approximately 24% of the total area in Taiwan. Recent large-scale sediment disasters due to typhoon-induced concentrated rainfall occurred mostly in the remote mountainous areas of southern Taiwan. Such disasters pose a major threat to the environmental security of the settlements in remote mountainous areas. For example, Typhoon Morakot on August of 2009, with a maximum precipitation of over 2884 mm in 5 days, induced over 22,705 landslides, covering

a total area of 274 km^2 in mountainous area throughout southern Taiwan [2]. Typhoon Morakot resulted in 619 deaths, 76 missing persons, and the temporary evacuation of 24,950 residents, flooding, and approximate USD five billion in economic losses [3]. Since Typhoon Morakot struck, the slopes of the remote mountainous areas of southern Taiwan have become highly unstable. Therefore, studies on the land use risk of the aforementioned settlements during rainfall disasters are essential.

Jan and Lee [4] used the product of effective accumulated rainfall (*EAR*) and rainfall intensity as a rainfall trigger index (I_{RT}) for determining debris flow; they discovered relevant geological factors (average stream bed slope, catchment area, landslide rate, and lithology) for establishing comprehensive geological indicators. A rainfall prediction model for debris flow was constructed using the rainfall warning and comprehensive physiographic indices. For rainfall warning, the following occurrence possibilities were set: 10%, 50%, and 90%. Chen et al. [5] demonstrated that extreme rainfall events cause frequent landslide erosion; they reported that a maximum 24-h rainfall amount of >600 mm resulted in the average landslide erosion rate of 64–79%. Jan et al. [6] mentioned that the effects of typhoon rainfall depend not only on the rainfall amount but also on its intensity. Tseng et al. [7] reported that the number and area of rainfall-induced landslides were positively correlated with the degree of land disturbance. Chen et al. [8] investigated areas with high and low susceptibility to landslides; they identified cumulative rainfall to be the primary factor for landslide occurrence in areas with high susceptibility; in contrast, in areas with low susceptibility, the rainfall intensity was found to be the key factor. Due to climate extremes, areas with high susceptibility exhibited a higher magnitude and frequency of landslides than those with low susceptibility.

Lee et al. [9] explored the mechanisms underlying landslide disasters due to the intensity of Typhoon Soudelor-induced rainfall on the mountainous areas of northern Taiwan; they revealed that most sediment disasters occurred 1 or 2 h after peak rainfall. Moreover, the maximum rainfall occurring 3, 6, and 12 h after this event was higher than that in the 200-year return period. To estimate a rainfall alert value for landslide occurrence, Caracciolo et al. [10] analyzed historical data on the rainfall that led to a landslide as well as data on rainfall occurring 5, 15, and 30 days before a landslide in southern Sicily, Italy. Chen and Wu [11] focused on a state-owned forest land in Taiwan and analyzed various internal (e.g., elevation, slope, terrain roughness, distance from the fault, and distance from the river) and external (total accumulated rainfall after event) factors through logistic regression (LR) to build an internal potential level without external factors; subsequently, they evaluated the changes in the potential value and rainfall to estimate a reference value for the prediction of landslides induced by rainfall. Shahabi et al. [12] combined remote sensing and a geographic information system (GIS) to statistically delineate areas susceptible to landslides; for this, they considered the following factors: slope, aspect, elevation, lithology, normalized difference vegetation index, vegetation, rainfall, distance from the fault, distance from the river, and distance from the road. Tseng et al. [7] focused on the periods before and after a typhoon that recently caused a road slope landslide in the study area; through image interpretation, they identified surface changes before and after the landslide disaster and developed a model for assessing landslide susceptibility. Then, the GIS platform was used to construct landslide susceptibility maps. Among the statistical methods used for evaluating landslide susceptibility, LR analysis has been proven to be one of the most reliable approaches [13–20].

In the past, studies seldom focused on the landslide hazard to land use, therefore models for analyzing rainfall-induced landslide hazards to ensure adequate land use in mountainous areas are necessary. The data processing and flowchart of research work of the present study is shown in Figure 1. Coupled with the use of the ArcGIS platform, random tree classifier (RTC) was employed to classify and interpret satellite images to obtain land use information and disasters. Furthermore, considering the regional environmental characteristics and land disturbance, we analyzed the potential of slope environmental intensity, factors associated with slope disasters, and the rainfall characteristics of the study

area and investigated the correlation between rainfall trigger and slope environmental strength potential to develop I_{RL}. Our research findings can provide considerable references for the strategies of land use in mountainous settlements. However, only the influence from the natural environment was considered; the socio-economic, governmental policy aspects that should be overall considered in decision making for land use were excluded in this study. This could lead to the potential research direction in the next step.
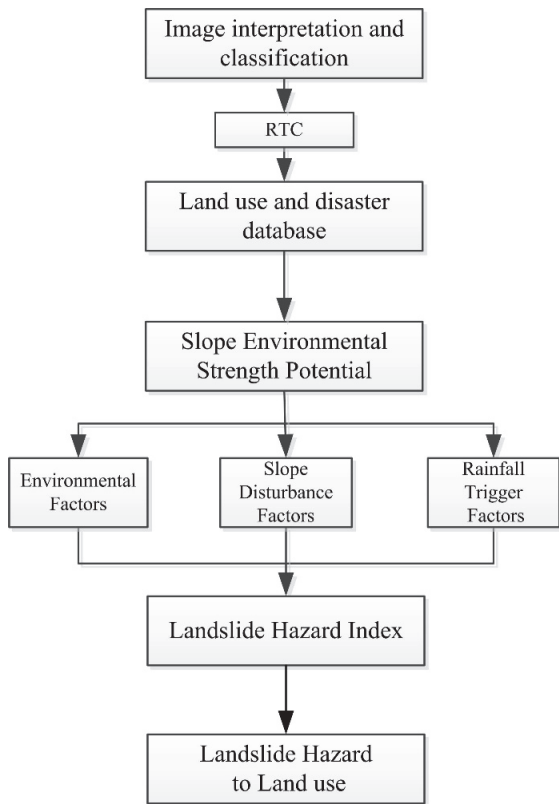
Figure 1. Flowchart of the research work.

2. Methods and Materials

2.1. Study Area

This study was conducted in Sandimen Township and certain mountainous areas of Wutai Township in Pingtung County in southern Taiwan (Figure 2). Pingtung County is located in the south of the Tropic of Cancer. Except for elevated mountainous areas, the county has a tropical monsoon climate and the temperature does not vary substantially throughout the year. The annual average temperature and rainfall is approximately 25.5 °C and 2325 mm, respectively. It is humid and rainy in summer. However, because of the barrier between the Dawu Mountain Range and the Central Mountain Range, the cold northeast monsoon is blocked from entering the county; this blockage, combined with a low latitude and sufficient sunshine, reduces the intensity of winter in Pingtung, where the average high and low temperatures are 24–27 °C and 16–19 °C, respectively [21,22]. In Sandimen and Wutai Townships, most of the strata are Chaozhou and Bilushan Formations; low contents of alluvial and grounding deposits are observed. Lithologically, the study area is mainly interbedded with hard shale, slate, and sandy shale. In addition, low contents of gravel, sand, clay, and slate interbedded with metamorphic sandstone and metamorphic igneous rock lens, mud, sand, and gravel, lenticular sandstone bodies are noted [23].

Sandimen Township is located at an altitude of 100–2159 m and at the intersection of mountains and plains and features, mostly hilly terrain. Wutai Township is located in the northeast area of Pingtung County (in the Central Mountain Range). This township has steep terrain and is located at an average altitude of >1000 m. The largest tributary flowing through the study area is the Ailiao River, which is the largest tributary of the Gaoping River. Its farthest source stream is Eluowu River, which flows south to Babanaban River and then turns southwest to Laibuan River (where it is called the Ailiao North Stream); subsequently, it turns south to join Hayou Creek and Qiaoguo Laci Creek (among others) and finally turns south to converge into Ailiao South Stream in Dalai Village; this is called Ailiao Creek in Sandimen Township. The main rivers in Wutai Township are Erchong and Ailiao Beixi, whereas the main rivers in Wutai Township are Ailiao Beixi and Qiaoguolaci [21].

Figure 2. Study area.

In Sandimen Township, the Sandi and Dalai villages have the highest (n = 1683) and lowest (n = 402) populations, respectively. In Wutai Township, Wutai and Jilu Villages have the highest (n = 1325) and lowest (n = 210) populations, respectively [24]. The residents of Sandimen Township are mainly Paiwan individuals (Taiwan Aborigines); some Rukai individuals also reside in this township such as in Qingye Village, which has recently been included in the Maolin National Scenic Area. The main economy in Sandimen Township is agriculture, and the main agricultural products are sweet potato, millet, taro, mango, pineapple, red quinoa, and coffee [25]. The residents of Wutai Township are mainly Rukai individuals [26]. The main agricultural products of the township are love jade, red quinoa, millet, coffee, taro, and sweet potato [27].

2.2. Image Interpretation and Classification

2.2.1. Preprocessing of Satellite Images

FORMOSA 2 (FS-2) or SPOT-5 satellite images of the areas affected by typhoons or rainstorms were acquired. Data on the 2009 Typhoon Morakot, 0517 rainfall in 2013, 2013 Typhoon Soulik, and 2013 Typhoon Kongrey were obtained to explore the land development types and landslide areas in the study area. We used six satellite images with image resolutions of 8 m × 8 m and 10 m × 10 m (Table 1).

Table 1. Basic satellite imagery data.

Image Shooting Date	Before/after Event	Image Resolution	Type	Location	X TWD97	Y TWD97
22 July 2009	Before Typhoon Morakot	8 m × 8 m				
9 May 2009				Upper left	211584	2530416
15 August 2009	After Typhoon Morakot	8 m × 8 m		Bottom right	230432	2511176
11 January 2010						
15 January 2013	Before 0517 Rainfall	8 m × 8 m	FS-2			
19 January 2013						
3 June 2013	After 0517 Rainfall Before Typhoon Soulik	8 m × 8 m		Upper left	211584	2530408
29 June 2013				Bottom right	230424	2511184
27 August 2013	After Typhoon Soulik Before Typhoon Kongrey	8 m × 8 m				
11 September 2013						
9 September 2013	After Typhoon Kongrey	10 m × 10 m	SPOT-5	Upper left Bottom right	211570 230440	2530430 2511160

The FS-2 and SPOT-5 satellite images are multispectral and contain four spectral bands [28]. FS-2 spectral bands are red, green, blue, and near-infrared (NIR), whereas SPOT-5 spectral bands are red, green, NIR, and short-wave infrared. The telemetry image processing software ERDAS IMAGINE (2013) [29] was used to fuse and locate the images.

2.2.2. Selection of Satellite Imagery Classifications

In this study, FS-2 or SPOT-5 satellite images of four typhoons or rainstorms were selected as the base map. Using GIS ArcGIS, each classification factor was manually digitized and circled. We compared the Tiff files of the satellite images (resolution, 2 m × 2 m) of the study area to increase the accuracy of the sampling area delineation; furthermore, we selected the following eight classifications suitable for the scope of this study: river, road, building, farmland, forest, meadow, streamway, and bare land (Figure 3).

Figure 3. Current land use in the study area.

2.3. Rainfall Projection

2.3.1. Effective Accumulative Rainfall (EAR)

We referred to the rainfall analysis methods described by Seo and Funasaki [30] and Tseng et al. [7]. Concentrated rainfall is considered to be continuous if no rainfall occurs 24 h before and after the rainfall event. The rainfall field with continuous rainfall inducing a landslide is regarded as the main rainfall field. The beginning of rainfall was defined as the time point when the first rainfall reached $\geq$4 mm in the main rainfall field. Cumulative rainfall inducing a landslide was calculated. Cumulative rainfall was divided into previous indirect rainfall (P_b) and previous direct rainfall (P_r). Previous indirect rainfall refers to the amount of rainfall in the main rainfall field within 7 days [30] and can be calculated using Equation (1).

$$\sum_{n=1}^{7} k^n P_n = P_b \tag{1}$$

where P_n is the amount of rainfall (mm) in n days before the main rainfall field; k is the decreasing coefficient. In the present study, k was 0.9 [31]. EAR can be calculated as follows:

$$EAR = P_r + P_b \tag{2}$$

where P_r is the amount of cumulative rainfall from the first rainfall in the main rainfall field from the time of the landslide disaster (a time point when the first rainfall reaches $\geq$4 mm) to the occurrence of the landslide.

2.3.2. Rolling Rainfall Intensity

Rain-induced landslides may be triggered by continuous rainfall for several hours. Therefore, rolling rainfall intensity can be expressed using Equation (3):

$$I_{mR} = \sum_{i=t-m+1}^{m} I_i = I_{t-m+1} + I_{t-m+2} + \cdots + I_m \tag{3}$$

where I is the rainfall intensity, m is the unit time of rain rolling, and $m = 3$ h [7]. I_{mR} is the I_R in m h, and I_t is the rainfall intensity in t h.

2.4. Random Tree Classifier (RTC)

We used the RTC in the ArcGIS supervised image classification module to classify images. The RTC does not lead to overfitting and can process segmented images and auxiliary grid datasets [32]. The classifier can be used to construct several decision trees, and selects a random subset of variables for each tree and uses the most frequent tree output for the overall classification. Therefore, random trees correct for the tendency of decision trees to overfit the training data. Random trees are a collection of individual decision trees; each tree is generated from different subsets of sample and training data. Decisions are made in the order of the importance of each pixel being classified. An image is drawn for a certain pixel that appears as a tree branch. After the entire dataset is processed, each branch forms a whole tree; this is the concept of random trees. In the operation of random trees, each tree has decision-making power; this process reduces overfitting. In the random tree method, analogically, many trees continue to grow; the changes in the trees of a forest are projected into randomly selected subspaces through training data, and each node's decision is optimized through a random process [32].

2.5. Logistic Regression (LR)

In regression analysis, dependent variables serve as categorical variables, whereas independent variables serve as continuous or dummy variables. Dummy variables represent categorical data; the corresponding numerical values are the basis for classification and have no comparative significance. The primary feature of LR is that dependent variables are categorical variables, whereas independent variables can be continuous or categorical variables [33].

LR is used for analyzing dichotomous dependent variables. One or more independent variables may be included in the model. Response variables can be categorical or continuous variables. Previously, landslide susceptibility was analyzed by mostly considering the distribution patterns of binary variables [34]. Through a statistical induction method, a set of regression patterns may be identified to differentiate between landslide and non-landslide. The value range of the logistic distribution function is 0–1, and the distribution of the value range follows an S-shaped curve [35].

As shown in Equation (4), linear regression assumes a linear function and includes dependent and independent variables (and random residual values) [33].

$$Y = \beta_0 + \beta_1 \times x_1 + \beta_2 \times x_2 + \beta_3 \times x_3 + e \tag{4}$$

where Y is a dependent variable; x_1, x_2, and x_3 are independent variables; and e represents a residual value. $\beta_0 + \beta_1 x_1 + \beta_2 x_2 + \beta_3 x_3$ is a linear function between expectation $E(Y)$ and the three independent variables.

LR is used to construct practical and reasonable allocation models for predicting the correlations between a dependent variable (y) and a set of independent variables (x). The relationship usually refers to the relationship between a set of independent variables (x_s), which is used to predict the probability of the dependent variable being equal to 1 such as the probability of landslide occurrence. The ratio of the probability of event occurrence to that of event non-occurrence is called the event odds. A linear function can be obtained using its natural logarithm, which is the logit model, as shown in Equation (5) [33].

$$\ln\left(\frac{P}{1-P}\right) = \alpha + \sum_{i=1}^{k} \beta_i x_i \tag{5}$$

where P is an independent variable; x_1, x_2, ..., x_k are the probabilities of event occurrence. In this study, y indicates the probability of landslides, and the aforementioned x parameters represent various independent variables. A logistic curve can be constructed using the logit function; its mathematical formula is shown in Equation (6).

$$P = \frac{1}{1 + e^{-\left(\alpha + \sum_{i=1}^{k} \beta_i x_i\right)}} \tag{6}$$

In general, the probability threshold is set at 0.5. A predicted probability (p) of ≥ 0.5 indicates the likelihood of a landslide event; in contrast, if $p < 0.5$, a landslide event is not expected to occur.

3. Results

3.1. Interpretation of Images and Assessment of Accuracy

Considering the aforementioned eight classifications, the RTC module was used with the results of texture analysis to interpret the images. The research scope was interpreted using a total of six satellite images obtained before and after the 2009 Typhoon Morakot, 0517 rainfall in 2013, 2013 Typhoon Soulik, and 2013 Typhoon Kongrey. Figure 4 depicts the results of image interpretation. To confirm the accuracy of the interpretation results, we randomly selected a total of 25 points (interpretation grids; checkpoints) for each classification and compared them with high-resolution aerial photos and on-site survey data. The most common accuracy evaluation method is the error matrix [36], which is used to calculate the coefficient of agreement (Kappa index) and overall accuracy. The value of the Kappa index proposed by Cohen [37] ranges from 0 to 1. Kappa values of <0.4, 0.4–0.8, and >0.8 indicate low, medium, and high accuracies, respectively. Table 2 summarizes the OAs before and after the rainfall events in the study area. In this study, the average Kappa value of each satellite image was approximately 0.71, and the average overall accuracy was approximately 74% (medium to high accuracy).

Before Typhoon Morakot

After Typhoon Morakot

Before 0517 rainfall

After 0517 rainfall and before Typhoon Soulik

After Typhoon Soulik and before Typhoon Kongrey (resolution, 8 m)

After Typhoon Soulik and before Typhoon Kongrey (resolution, 10 m)

After Typhoon Kongrey
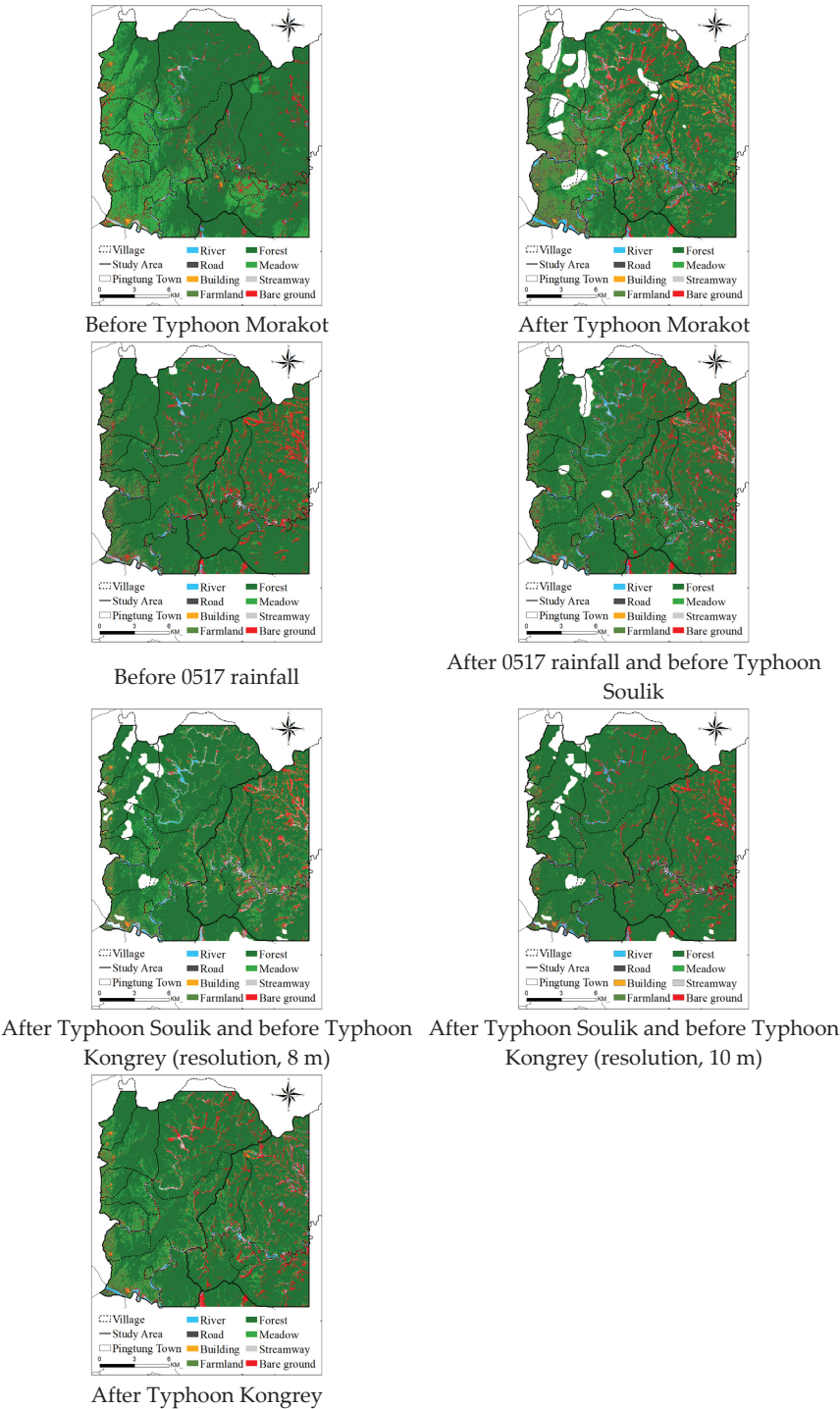
Figure 4. Images obtained before and after various rainfall events.

Table 2. Coefficients of agreement and overall accuracies of the satellite image interpretation results.

Year	Rainfall Event	Resolution	Kappa	OA (%)
2009	Before Typhoon Morakot	8 m	0.66	70.0
	After Typhoon Morakot	8 m	0.70	73.0
2013	Before 0517 rainfall	8 m	0.69	72.5
	After 0517 rainfall and before Typhoon Soulik	8 m	0.70	73.3
	After Typhoon Soulik and Before Typhoon Kongrey	8 m	0.78	79.5
	After Typhoon Soulik and Before Typhoon Kongrey	10 m	0.77	79.5
	After Typhoon Kongrey	10 m	0.74	76.5

3.2. Identification of Landslides through Image Interpretation

After image classification, to identify rainfall-induced landslides in the study area, we subtracted bare land grids before and after rainfall events by using the image subtraction method. The river, streamway, and bare land classifications with a slope percentage of <5% were deducted. High-resolution aerial photos of the study area were compared, and manual inspection was performed to identify landslides; then, the locations of the rainfall-induced landslides in the study area were obtained (Figure 5). Among the types of slope failure, debris slides were the easiest and most reliable type to be identified in the satellite images since vegetation was effectively stripped off from the slopes. Therefore, debris slides are the major landslides mapped in our study. The 2009 Typhoon Morakot resulted in the highest rainfall and the largest landslide area (1313.12 ha). The areas of landslides induced by the other events were as follows: 0517 rainfall in 2013, 813.92 ha; Typhoon Kongrey, 789.44 ha; and Typhoon Soulik, 635.04 ha.

| After Typhoon Morakot | After 0517 rainfall | After Typhoon Soulik | After Typhoon Kongrey |
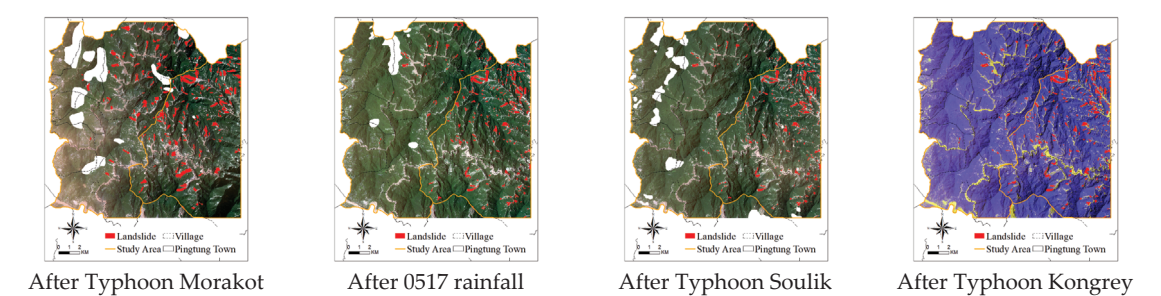
Figure 5. Distribution map of landslides occurring after various rainfall events.

3.3. Development of a Model for Assessing Rainfall-Induced Landslide Susceptibility

3.3.1. Selection of Factors Associated with Landslide

Landslides can be attributed to factors such as artificial slope land use, environment, and rainfall triggers. Human activities may negatively affect water and soil conservation on slope lands, which compromises the safety of slope land. Therefore, referring to studies of Chen et al. [38] and Tseng et al. [7], we divided the aforementioned factors into the following three categories: environmental, slope disturbance, and rainfall trigger factors. The environmental factors assessed in this study included elevation, slope, aspect, slope roughness, terrain roughness, distance from the river, and geology. The slope disturbance factors included road density, building density, farmland planting rate, forest density, grassland density, and bare density. The rainfall trigger factor was the product of EAR and the maximum 3-h rolling rainfall intensity ($I_{3R,max}$).

The digital elevation model (DEM) was used to analyze the environmental factors using ArcGIS Spatial Analyst. A basic grid of 40 m × 40 m was constructed for the factors

related to landslide occurrence, followed by the development of a GIS database of the study area. The hazard factors are described below.

Environmental Factors

- Elevation (*El*)

The elevation of a place refers to its height from the sea level. In Taiwan, the elevation datum comprises the mean sea level of Keelung Port, and the elevation of the terrain is called the elevation difference. When other factors are constant, higher degrees of elevation are associated with a higher sliding force. We used a 20 m × 20 m DEM for analysis. The elevation of the study area is 78–2437 m, which was divided into a total of seven grades and coded. Table 3 presents the elevation classification codes, ranging from an elevation of <350 m coded as 1 to an elevation of >2100 m coded as 7.

Table 3. Elevation codes.

Grade Range of Elevation (m)	Code
Above 2101	7
1751–2100	6
1401–1750	5
1051–1400	4
701–1050	3
351–700	2
Below 350	1

- Slope (*Sl*)

Here, slope indicates the inclination of a slope. Higher degrees of inclination indicate steeper slopes and vice versa. High inclination as well as poor soil and water conservation may facilitate the development of landslides. In this study, the slope value of each grid was obtained through DEM and ArcGIS slope analysis. According to the Classification Standards for Land Utilization Limits of Hillside Lands outlined in the Regulations of Soil and Water Conservation [39], we graded and coded slopes (Table 4). A first-grade slope was coded as 1, whereas a seventh-grade slope was coded as 7.

Table 4. Slope codes.

Slope Grade	Grade Range of Slope (%)	Code
7	Above 100	7
6	50–100	6
5	40–55	5
4	30–40	4
3	15–30	3
2	5–15	2
1	Below 5	1

- Slope Roughness (*Slr*)

Slope roughness reflects the changes in a slope (standard deviation). Higher degrees of slope roughness indicate higher extents of changes, which may facilitate the occurrence of landslides. Cluster analysis was performed to classify the slope roughness of the study area. A slope roughness of <18.15 was coded as 1, whereas that of >63.34 was coded as 7 (Table 5).

Table 5. Slope roughness codes.

Grade Range of Slope Roughness (°)	Code
Above 63.34	7
56.80–63.33	6
49.47–56.79	5
41.02–49.46	4
31.21–41.01	3
18.16–31.20	2
Below 18.15	1

- Aspect (*As*)

Each slope has a different aspect. Aspect refers to the inclination direction of a slope and affects wind flow and rainfall distribution. In this study, using DEM and ArcGIS aspect analysis, the aspect data of each grid were obtained. The inclination angle may be as follows: north, northeast, east, southeast, south, southwest, west, northwest, and flat ground (clockwise). In this study, a flat ground was coded as 1, whereas the southwestern part of a windward side was coded as 6 (Table 6).

Table 6. Aspect codes.

Aspect	Inclination Angle (°)	Code
Flat ground	—	1
Northeast	22.5–67.5°	2
East	67.5–112.5°	3
Southeast	112.5–157.5°	4
South	157.5–202.5°	5
Southwest	202.5–247.5°	6
West	247.5–292.5°	5
Northwest	292.5–337.5°	4
North	337.5–0° 0–22.5°	3

- Surface Roughness (*Tr*)

Surface roughness reflects the changes in a surface (standard deviation). Higher degrees of surface roughness indicate higher extents of changes, which may facilitate landslide occurrence. In the present study, cluster analysis was performed to classify the surface roughness of the study area. A surface roughness of <417.62 was coded as 1, whereas that of >2298.55 was coded as 7 (Table 7).

Table 7. Surface roughness codes.

Grade Range of Surface Roughness (m)	Code
Above 2298.55	7
2114.26–2298.54	6
1849.33–2114.25	5
1457.87–1849.32	4
957.51–1457.86	3
417.63–957.50	2
Below 417.62	1

- Distance from the River (*Dr*)

The distance of an area from a water body may affect the occurrence of landslides. A shorter distance is associated with higher levels of groundwater, which softens soil, thereby facilitating landslide occurrence. We used a river map to calculate the distance of each grid from a river; for this, the ArcGIS buffer analysis function was used. The analysis results were coded as shown in Table 8.

Table 8. Codes corresponding to the distance of an area from a water body.

Grade Range of Distance from the River (m)	Code
Below 350	7
351–700	6
701–1050	5
1051–1400	4
1401–1750	3
1751–2100	2
Above 2101	1

- Geology (*Gs*)

We used the geological map of the Central Geological Survey of the Ministry of Economic Affairs (2021) to obtain information on the geological conditions corresponding to each grid in the study area. On the basis of geological age and lithological data, it was divided into four strengths: very weak, medium, medium strong, and strong [40]. The highest strength was coded as 1, whereas the lowest strength was coded as 4 [38].

Slope Disturbance Factors

Using RTC with texture analysis for image interpretation and classification, we assessed the slope disturbance of the research area. The following six factors were included in further analysis: road density, building density, farmland planting rate, forest density, grassland density, and bare density. To quantify the slope disturbance in each basic grid, slope disturbance was defined as the area percentage ratio of each disturbance factor in each basic grid. The degree of land development of hillsides and its index were evaluated in reference to earlier studies [7,38]. Because we regarded environmental and slope disturbance factors as independent factors influencing landslides, a slope disturbance index was developed and is shown in Equation (7).

$$I_{DC} = \sum G_{DC} \times R \tag{7}$$

DC refers to the disturbance condition. G_{DC} is a *DC* grade, which is the score corresponding to slope land use disturbance in each grid. *R* is the ratio of the area occupied by each slope and the utilization factor corresponding to the grid. Table 9 presents the grades corresponding to the *DC*s of the aforementioned six slope disturbance factors. For grading, we referred to a study conducted by Chen et al. [38].

Table 9. Scores of various slope disturbance factors.

Slope Disturbance Factor	Forest Density	Grassland Density	Farmland Planting Rate	Road Density	Building Density	Bare Density
Score	1	2	3	4	5	6

Rainfall Trigger Factors

We obtained relevant data from the following 12 rainfall measurement stations within and near the study area: Weiliaoshan, Majia, Hongyeshan, Shangdewun, Dajin, Jinfeng, Ligang, Meinong, and Gusia [22] as well as Zhiben-5, Ali, and Sandimen [41]. Through inverse distance weighting (ArcGIS), the EAR and $I_{3R,max}$ values were calculated for each station (Tables 10 and 11) for four rainfall events occurring in 2009 and 2013.

Table 10. EAR of each station after various rainfall events.

Management Unit	Station Code	Station Name	EAR (*mm*)			
			Morakot	0517 Rainfall	Soulik	Kongrey
CWB	C0R100	Weiliaoshan	1437.03	85.46	248.38	417.93
	C0R140	Majia	882.32	–	–	–
	C0S680	Hongyeshan	337.62	46.40	154.62	38.69
	C1R120	Shangdewun	1745.22	121.64	–	378.98
	C1V340	Dajin	–	168.74	129.19	–
	C1S820	Jinfeng	298.88	19.97	201.45	93.82
	C0R590	Ligang	466.82	–	–	233.36
	C0V310	Meinong	312.16	138.47	–	648.74
	C1R110	Gusia	492.67	269.31	87.05	263.33
WRA	01S210	Zhiben-5	91.57	16.49	130.31	54.73
	01Q910	Ali	1205	698.56	141.25	585.02
	01Q930	Sandimen	552.93	146.85	42.03	245.55

Table 11. $I_{3R,max}$ of each station after various rainfall events.

Management Unit	Station Code	Station Name	$I_{3R,max}$ (mm/3 h)			
			Morakot	0517 Rainfall	Soulik	Kongrey
CWB	C0R100	Weiliaoshan	274	68.5	78	183.5
	C0R140	Majia	194	–	–	–
	C0S680	Hongyeshan	75	27.5	52.5	21
	C1R120	Shangdewun	206	83	–	153.5
	C1V340	Dajin	–	84	81	–
	C1S820	Jinfeng	199.5	12	108	25
	C0R590	Ligang	154.5	–	–	97
	C0V310	Meinong	114.5	61	–	176.5
	C1R110	Gusia	192	54	46.5	82
WRA	01S210	Zhiben-5	78	15	81	14
	01Q910	Ali	286	117	65	131
	01Q930	Sandimen	171	60	33	107

3.3.2. Analysis of Slope Environmental Strength Potential

We performed correlation analyses of environmental and slope disturbance factors. After highly correlated factors were eliminated, LR was performed to analyze the slope environmental strength; thus, a slope environmental strength regression model was constructed. Then, we established the index of slope environmental strength potential (I_{SESP}). A basic

grid of 40 m × 40 m was constructed using ArcGIS; subsequently, the slope environmental strength potential value in each grid of the study area was calculated.

Correlation Analyses of Slope Environmental Strength Potential Factors

The slope environmental strength potential factors initially selected in this study included environmental factors such as elevation, slope, aspect, slope roughness, surface roughness, distance from the river, and geology and slope disturbance factors. To ensure that the factors were independent and exerted no mutual effects, we performed correlation analyses of the selected factors before LR analysis to identify the degree of correlations between the factors. Elevation, slope, slope roughness, surface roughness, and slope disturbance index served as continuous variables, whereas aspect, distance from the river, and geology served as categorical variables. In LR, categorical variables only represent the data distribution of factor codes and not the effects of the code size on dependent variables. Hence, we focused only on continuous variables. Statistical analysis was performed using SPSS [42]. For the four rainfall events, the correlations between the factors were investigated through Pearson correlation analysis. If the absolute value of the correlation coefficient is closer to 0, the degree of correlation is weaker; in contrast, if it is closer to 1, the degree of correlation is stronger. Table 12 presents the correlations between the slope environmental strength potential factors. Elevation exhibited high-level correlations with surface roughness. Slope exhibited medium-to-high-level correlation with slope roughness. The remaining factors exhibited low-level correlations. Hence, surface roughness was not included in the LR model.

Table 12. Correlations between the slope environmental strength potential factors.

		Elevation (*El*)	Slope (*Sl*)	Slope Roughness (*Slr*)	Surface Roughness (*Tr*)	IDC
Elevation (*El*)	Correlation	1				
	Significance (Two-tailed)					
	N	170,651				
Slope (*Sl*)	Correlation	0.299 **	1			
	Significance (Two-tailed)	0.000				
	N	170,651	170,651			
Slope Roughness (*Slr*)	Correlation	0.473 **	0.731 **	1		
	Significance (Two-tailed)	0.000	0.000			
	N	170,651	170,651	170,651		
Surface Roughness (*Tr*)	Correlation	1.000 **	0.299 **	0.473 **	1	
	Significance (Two-tailed)	0.000	0.000	0.000		
	N	170,651	170,651	170,651	170,651	
IDC	Correlation	−0.369 **	−0.282 **	−0.363 **	−0.369 **	1
	Significance (Two-tailed)	0.000	0.000	0.000	0.000	
	N	170,651	170,651	170,651	170,651	170,651

Note: ** Correlation is significant at 0.01 level (two-tailed).

Results of the Analysis of Slope Environmental Strength Potential

To reduce errors due to the evaluation model and subjective errors due to selection bias (human errors), we randomly sampled the same number of landslide and non-landslide

samples. After sampling, the data were randomly divided into training (70%) and test (30%) datasets. An environmental strength assessment model was constructed through LR [42].

The dependent variable was landslide or non-landslide, and the independent variables were environmental factors such as slope, aspect, elevation, distance from the river, slope roughness, geology, and slope disturbance factors. Through LR, a regression formula was developed for analyzing the slope environmental strength potential. The formula is shown in Equation (8).

$$L = \alpha + \beta_1 \times El + \beta_2 \times Sl + \beta_3 \times Slr + \beta_4 \times I_{DC} + \sum_{i=1}^{4} \beta_{As,i} D_{As,i} + \sum_{i=1}^{6} \beta_{Dr,i} D_{Dr,i} + \sum_{i=1}^{3} \beta_{Gs,i} D_{Gs,i} \tag{8}$$

where El denotes the elevation, Sl is the slope, Slr is the slope roughness, I_{DC} is the slope disturbance index, As is the aspect grade, Dr is the distance from the river, Gs is the geological grade, β is the regression coefficient of continuous variables, and α is a constant. D represents a dummy variable, which is a value coded for the category corresponding to a factor. Substituting each regression coefficient and constant value into Equation (8) and substituting it into Equation (9), we can calculate the probability value of each grid, which represents the value of I_{SESP}.

$$P = \frac{1}{1 + e^{-L}} \tag{9}$$

LR was performed to evaluate the training classification results of various rainfall events. The accuracies of classifications performed using the training and test data after 2009 Typhoon Morakot were 68.3% and 68.1%, respectively. Training data were used to deduce the accuracies of classifications for the entire study area. The estimated accuracy was 65.2% (Table 13). Table 14 presents the errors in the evaluation of various rainfall events. The accuracies of classifications performed using training data after the 0517 rainfall, Typhoon Soulik, and Typhoon Kongrey were 83.8%, 86.2%, and 86.4%, respectively; the corresponding values for the test datasets were 84.3%, 86.4%, and 87.5%. The average accuracy of the overall classification was approximately 80.4%.

Table 13. Errors in the evaluation of Typhoon Morakot.

		Training			Testing			Overall		
		Predicted		Accuracy (%)	Predicted		Accuracy (%)	Predicted		Accuracy (%)
		Non-landslide	Landslide		Non-landslide	Landslide		Non-landslide	Landslide	
Actual	Non-landslide	4021	1692	70.4	1787	712	71.5	105,419	57,025	64.9
	Landslide	1946	3831	66.3	858	1572	64.7	2391	5816	70.9
Overall accuracy				68.3			68.1			65.2

Table 14. Accuracies of the classifications performed using training and test data after the four rainfall events.

Accuracy Rainfall Event	Training (%)	Testing (%)	Overall (%)
Typhoon Morakot	68.3	68.1	65.2
0517 Rainfall	83.8	84.3	83.5
Typhoon Soulik	86.2	86.4	87.3
Typhoon Kongrey	86.4	87.5	85.7
Average accuracy	81.2	81.6	80.4

3.3.3. Establishment of a Landslide Hazard Index

Higher values of slope environmental strength potential are associated with larger amounts of rainfall and thus higher probabilities of landslides. By referring to the study of Jan and Lee [4], we adjusted this, and I_{RT} can be calculated as shown in Equation (10).

$$I_{RT} = EAR \times I_{3R,\max} \tag{10}$$

We established a landslide hazard index (I_{RL}) using I_{RT} and I_{SESP}. The formula is shown in Equation (11).

$$I_{RL} = I_{RT} \times I_{SESP} \tag{11}$$

Higher values of I_{RL} indicate a higher probability of landslides. At a constant I_{RL}, I_{RT} is inversely proportional to I_{SESP}. Thus, if I_{SESP} is relatively stable, a large amount of rainfall would induce landslides. In contrast, if I_{SESP} is low, only a small amount of rainfall would induce landslides. We used the following comprehensive indicators of rainfall-induced landslides [4]: I_{RL1}, I_{RL10}, I_{RL25}, I_{RL50}, and I_{RL90}. The index development method is described below.

1. I_{RL1}: From the I_{RL} values corresponding to the grid data of all rainfall-induced landslides in the study area, the value with a cumulative probability of 1% is selected (Weber's method) and is indicated as I_{RL1}. Grids with I_{RL} values less than that of I_{RL1} have landslide probabilities of <1%.
2. I_{RL10}: From the I_{RL} values corresponding to the grid data of all rainfall-induced landslides in the study area, the value with a cumulative probability of 10% is selected (Weber's method) and is indicated as I_{RL10}. Grids with I_{RL} values between the values of I_{RL1} and I_{RL10} have landslide probabilities of 1%–10%.
3. I_{RL90}: Landslide and non-landslide grids with values less than that of I_{RL10} are excluded. From the I_{RL} values corresponding to the remaining grids, the value with a cumulative probability of 90% (Weber's method) is selected and indicated as I_{RL90}. Grids with I_{RL} values exceeding that of I_{RL90} have landslide probabilities of >90%.
4. I_{RL10}–I_{RL90}: To determine a landslide probability corresponding to a comprehensive index between I_{RL10} and I_{RL90}, the relationship between the aforementioned index and landslide probability can be expressed as shown in Equation (12).

$$\frac{I_{RLi} - I_{RL10}}{I_{RL90} - I_{RL10}} = \frac{P - 0.1}{0.9 - 0.1} \tag{12}$$

Equation (12) can be rewritten as Equation (13).

$$I_{RLi} = I_{RL10} + \Delta I_{RL} \left(\frac{P - 0.1}{0.8} \right) \tag{13}$$

where $\Delta I_{RL} = I_{RL90} - I_{RL10}$. Thus, the landslide probability corresponding to the landslide comprehensive index I_{RLi} can be obtained.

4. Discussion

4.1. Correlation between Slope Environmental Strength Potential and Rainfall-Induced Landslide

We first explored the distribution of landslide and non-landslide grids with the same I_{RL} value for each event and performed stratified random sampling according to the ratio of the numbers of landslide and non-landslide grids with the same I_{RL} value. To calculate the I_{RL} values corresponding to I_{RL1}, I_{RL10}, I_{RL25}, I_{RL50}, and I_{RL90}, after merging the data points of each rainfall event, we sorted the landslide grids; then, using Equation (12), the I_{RL} values corresponding to different cumulative probabilities were calculated. Table 15 presents the I_{RL} indices and the corresponding values.

Table 15. Various I_{RL} values.

Various I_{RL}	I_{RL} Value
I_{RL1}	1417.30
I_{RL10}	6563.47
I_{RL25}	28,307.89
I_{RL50}	64,548.59
I_{RL90}	122,533.70

Using the I_{RL} indices presented in Table 15, the correlation between I_{RT} and slope environmental strength potential was calculated after merging the data points of each rainfall event (Figure 6). The product of I_{RT} and I_{SESP} was the closest to the grids with different cumulative probabilities. The trend line corresponding to each I_{RL} value was drawn using the power method. As shown in Figure 5, the I_{RT} of 2009 Typhoon Morakot was the highest among the four rainfall events; thus, most of its landslide grids were distributed above I_{RL50}. For the 0517 rainfall in 2013, the grids were mostly below I_{RL90}. The I_{RT} of 2013 Typhoon Soulik was the lowest among the four rainfall events; most of its landslide grids were distributed below I_{RL25}, while the I_{RT} of 2013 Typhoon Kongrey was higher than those of the Typhoon Soulik and 0517 rainfall events; for Typhoon Kongrey, the grids were distributed between I_{RL1} and I_{RL90}.
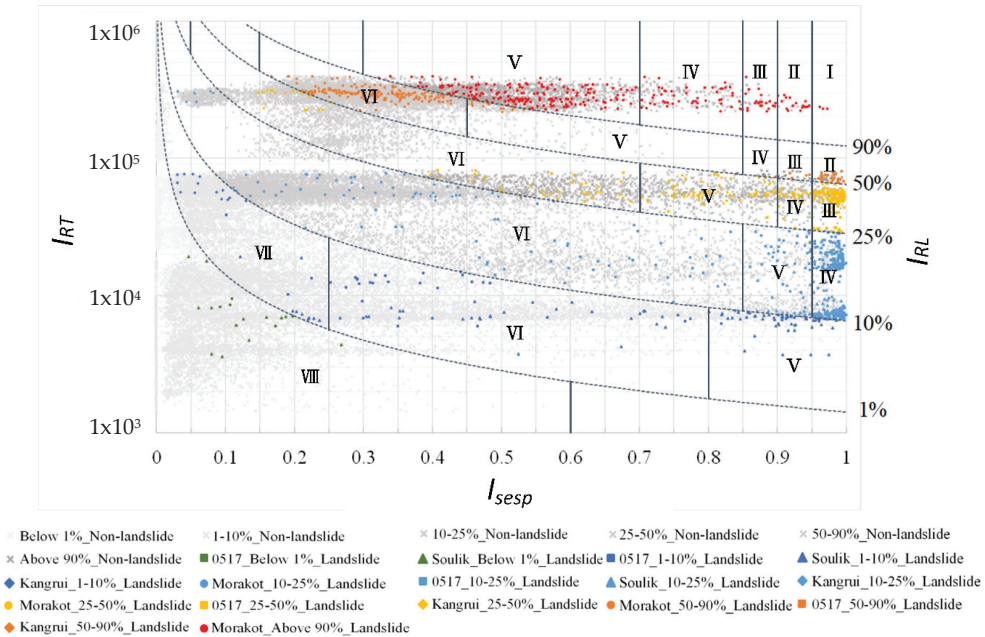
Figure 6. Slope environmental strength potential index versus rainfall trigger index.

4.2. Evaluation of Landslide Hazards to Land Use

After the classification of I_{RL} indices with different cumulative probabilities, the number of landslide and non-landslide grids with different I_{SESP} grades and the landslide ratio (landslide/non-landslide) were estimated. Considering that higher values of I_{RT} are associated with higher values of I_{SESP} (and higher degrees of hazard), we investigated the most reasonable average distribution of the landslide ratio in an inductive manner. Then, the degree of hazard was calculated for each distribution situation and substituted into the

grids of each event. Thus, the hazard degree of rainfall-induced landslide in each grid of each event was obtained. Table 16 presents the landslide ratios (before and after induction) of various I_{SESP} grades of different I_{RL} indices. The same color in the table represents the same category of landslide ratio intervals ($n = 8$). Figure 6 illustrates the results presented in Table 16. The landslide ratio intervals were normalized using the average landslide ratio of the same interval, as shown in Equation (14).

$$Z_{norm} = \left(\frac{X - X_{\min}}{X_{\max} - X_{\min}} \right) \tag{14}$$

where Z_{norm} represents the value after normalization, X represents the value to be normalized, X_{min} represents the minimum value in the data, and X_{max} represents the maximum value in the data. In this study, the normalized value was regarded as the degree of rainfall-induced landslide hazard. The estimated degree of hazard was substituted into the grid of each rainfall event to obtain the degree of hazard corresponding to each rainfall event grid in the study area. The normalized value is a value between 0 and 1. Landslide probabilities of (I_{RL}) of <1% still represent the possibility of landslide. Therefore, the minimum value of I_{RL1} indicates its risk probability. Table 17 presents the hazard value of each landslide ratio interval. The color reference in Table 17 is the same as that in Table 16. The hazard value of each grid of each rainfall event was substituted into each grid, and hazard maps were constructed. Higher degrees of hazard indicate higher probabilities of landslide and vice versa.

The hazard value of each interval was substituted into each grid of each rainfall event, and the hazard maps of the study area after each rainfall event were constructed (Figure 7). Hazard degree was classified into eight grades, and the classification was based on the method in Table 17. The I_{RT} of 2009 Typhoon Morakot was the highest among all rainfall events, and the number of landslide grids was 8207; thus, the degree of landslide hazard in the study area after this typhoon was the highest. The I_{RT} of 2013 Typhoon Kongrey was higher than that of 0517 rainfall in 2013; thus, the degree of landslide hazard after Typhoon Kongrey was higher than that after 0517 rainfall in 2013. The I_{RT} of 2013 Typhoon Soulik was the lowest, and the number of landslide grids was also the lowest ($n = 3969$); thus, the degree of landslide hazard after this typhoon was the lowest.
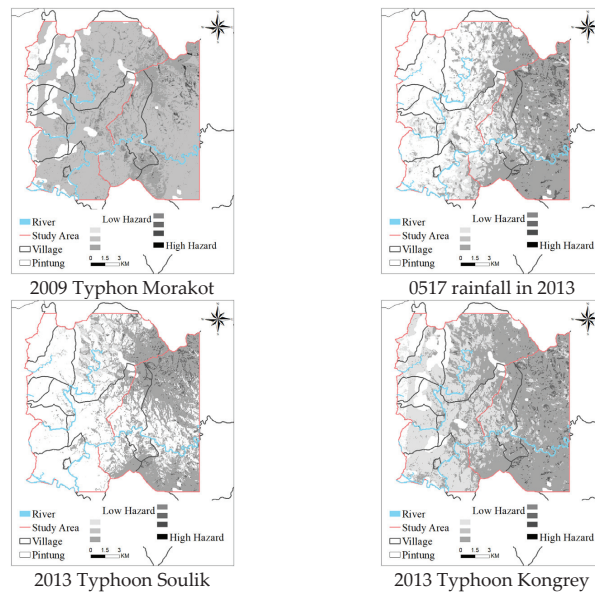
Figure 7. Potential maps of landslide hazards to land use after various rainfall events.

Table 16. Landslide ratios of various I_{SESP} grades of different I_{RL} classifications.

I_{SESP}	Below I_{RL1}			I_{RL1}–I_{RL10}			I_{RL10}–I_{RL25}			I_{RL25}–I_{RL50}			I_{RL50}–I_{RL90}			Above I_{RL90}		
	Landslide	Non-landslide	Landslide Ratio	Landslide	Non-landslide	Landslide Ratio	Landslide	Non-landslide	Landslide Ratio	Landslide	Non-landslide	Landslide Ratio	Landslide	Non-landslide	Landslide Ratio	Landslide	Non-landslide	Landslide Ratio
0<0.05																		
0.05<0.10																		
0.10<0.15				26	6317	0.00412												
0.15<0.20																		
0.20<0.25																		
0.25<0.30	18	11,097	0.00162										196	4564	0.04294			
0.30<0.35							101	8528	0.01184	53	2889	0.01835						
0.35<0.40																		
0.40<0.45																		
0.45<0.50				56	3987	0.01405										184	1629	0.11295
0.50<0.55																		
0.55<0.60																		
0.60<0.65													20	317	0.06309			
0.65<0.70																		
0.70<0.75																		
0.75<0.80				57	318	0.17925				63	507	0.12426				51	148	0.34459
0.80<0.85																		
0.85<0.90							55	368	0.14946				1	7	0.14286	22	19	1.15789
0.90<0.95										27	131	0.20611	5	12	0.41667	17	6	2.83333
0.95<1.00							255	294	0.86735	157	129	1.21705	29	17	1.70588	3	0	3

Table 17. Hazard value of each interval.

Hazard Interval	Average Landslide Ratio	Hazard Value
Interval VIII	0.001	0.00001
Interval VII	0.004	0.00083
Interval VI	0.022	0.00673
Interval V	0.125	0.04142
Interval IV	0.39	0.1296
Interval III	0.93	0.30981
Interval II	2.27	0.7564
Interval I	3	1

5. Conclusions

In the present study, we developed an index to evaluate landslide hazards to land use after four prominent rainfall events in Sandimen and Wutai Townships in Pingtung County. Using RTC and texture analysis, we interpreted and classified the satellite images of the study area captured before and after four rainfall events. The average Kappa value was approximately 0.71, which indicated medium to high accuracy. A comparison of the satellite images captured before and after the rainfall events in terms of exposure revealed that the area of landslide due to 2009 Typhoon Morakot was the largest (1313.12 ha); the areas of landslides due to the other rainfall events were as follows: 0517 rainfall in 2013, 813.92 ha; Typhoon Kongrey, 789.44 ha; and Typhoon Soulik, 635.04 ha. Environmental factors (e.g., elevation, slope, aspect, slope roughness, distance from the river, and geology) and slope disturbance factors (e.g., road density, building density, farmland planting rate, forest density, grassland density, and bare density) were assessed in this study to analyze the slope environmental strength potential I_{SESP}. The average overall classification accuracy was approximately 80.4%. I_{RT} was calculated by multiplying EAR with $I_{3R,max}$. A new comprehensive index of rainfall-induced landslide I_{RL} ($I_{RL} = I_{RT} \times I_{SESP}$) was established to determine the hazard of rainfall-induced landslides to land use. Using the correlation between I_{SESP} and I_{RT}, we determined the degrees of rainfall-induced landslide hazards to land use. At a constant I_{SESP}, higher values of I_{RT} indicate higher degrees of landslide hazard to land use; similarly, at a constant I_{RT}, higher values of I_{SESP} indicate higher degrees of landslide hazard to land use. Landslide occurrence is positively correlated with I_{RT} and I_{SESP}. In cases of large I_{SESP} values (e.g., fragile environment and high land development intensity), small I_{RT} values may cause landslides.

References

1. *Disaster Management White Paper*; Central Disaster Prevention and Response Council, Executive Yuan: Taipei, Taiwan, 2012.
2. Lin, C.W.; Chang, W.S.; Liu, S.H.; Tsai, T.T.; Lee, S.P.; Tsang, Y.C.; Shieh, C.L.; Tseng, C.M. Landslides triggered by the 7 August 2009 Typhoon Morakot in Southern Taiwan. *Eng. Geol.* **2011**, *123*, 3–12. [CrossRef]

3. National Disasters Prevention and Protection Commission. *Typhoon Morakot Disaster Responses Reports from Typhoon Morakot Central Emergency Operating Center 74th Report*, National Disasters Prevention and Protection Commission: New Taipei City, Taiwan, 2009.

4. Jan, C.D.; Lee, M.H. A debris-flow rainfall-based warning model. *J. Chin. Soil Water Conserv.* **2004**, *35*, 275–285.

5. Chen, Y.R.; Tsai, K.J.; Hsieh, S.C.; Ho, Y.L. Evaluation of Landslide Potential due to Land Use in the Slope. *Electron. J. Geotech. Eng.* **2015**, *20*, 4277–4292.

6. Jan, C.D.; Yang, S.Y.; Su, Y.W.; Haung, W.S. Investigation about rainfall-induced shallow landslides in CYL and TWR watersheds, Taiwan. *Environ. Earth Sci.* **2016**, *75*, 898. [CrossRef]

7. Tseng, C.M.; Chen, Y.R.; Wu, S.M. Scale and spatial distribution assessment of rainfall-induced landslides in a catchment with mountain roads. *Nat. Hazards Earth Syst. Sci.* **2018**, *18*, 687–708. [CrossRef]

8. Chen, C.W.; Tung, Y.S.; Liou, J.J.; Li, H.C.; Cheng, C.T.; Chen, Y.M.; Oguchi, T. Assessing landslide characteristics in a changing climate in northern Taiwan. *Catena* **2019**, *175*, 263–277. [CrossRef]

9. Lee, C.F.; Chou, H.T.; Wei, L.W.; Huang, W.K.; Chi, S.Y.; Chen, S.C.; Huang, W.C. Geomorphic Evolution of The Dong-Ao Peak Landslide, North Eastern Taiwan. *J. Chin. Soil Water Conserv.* **2014**, *45*, 174–183.

10. Caracciolo, D.; Arnone, E.; Conti, F.L.; Noto, L.V. Exploiting historical rainfall and landslide data in a spatial database for the derivation of critical rainfall thresholds. *Environ. Earth Sci.* **2017**, *76*, 222. [CrossRef]

11. Chen, S.C.; Wu, C.Y. Establishment of Landslide Susceptibility Early Warning Model in National Forest Areas Based on Geo-intrinsic and Hydro-extrinsic Factors. *J. Chin. Soil Water Conserv.* **2018**, *49*, 89–97.

12. Shahabi, H.; Khezri, S.; Ahmad, B.B.; Hashim, M. Landslide susceptibility mapping at central Zab basin, Iran: A comparison between analytical hierarchy process frequency ratio and logistic regression models. *Catena* **2014**, *115*, 55–70. [CrossRef]

13. Dai, F.C.; Lee, C.F.; Ngai, Y.Y. Landslide risk assessment and management: An overview. *Eng. Geol.* **2002**, *64*, 65–87. [CrossRef]

14. Ayalew, L.; Yamagishi, H. The application of GIS-based logistic regression for landslide susceptibility mapping in the Kakuda-Yahiko Mountains, Central Japan. *Geomorphology* **2005**, *65*, 15–31. [CrossRef]

15. Chau, K.T.; Chan, J.E. Regional bias of landslide data in generating susceptibility maps using logistic regression: Case of Hong Kong Island. *Landslides* **2005**, *2*, 280–290. [CrossRef]

16. Chen, Z.; Wang, J. Landslide hazard mapping using logistic regression model in Mackenzie Valley, Canada. *Nat. Hazards* **2007**, *42*, 75–89. [CrossRef]

17. Lee, S.; Pradhan, B. Landslide hazard mapping at Selangor, Malaysia using frequency ratio and logistic regression models. *Landslides* **2007**, *4*, 33–41. [CrossRef]

18. Sun, X.; Chen, J.; Bao, Y.; Han, X.; Zhan, J.; Peng, W. Landslide Susceptibility Mapping Using Logistic Regression Analysis along the Jinsha River and Its Tributaries Close to Derong and Deqin County, Southwestern China. *ISPRS Int. J. Geo-Inf.* **2018**, *7*, 438. [CrossRef]

19. Wubalem, A.; Meten, M. Landslide susceptibility mapping using information value and logistic regression models in Goncha Siso Eneses area, northwestern Ethiopia. *SN Appl. Sci.* **2020**, *2*, 807. [CrossRef]

20. Sujatha, E.R.; Sridhar, V. Landslide Susceptibility Analysis: A Logistic Regression Model Case Study in Coonoor, India. *Hydrology* **2021**, *8*, 41. [CrossRef]

21. Pingtung County Government, Taiwan. 2022. Available online: https://www.pthg.gov.tw/en/Default.aspx (accessed on 1 October 2022).

22. Central Weather Bureau. 2021. Available online: https://www.cwb.gov.tw/eng/ (accessed on 1 January 2021).

23. Central Geological Survey, Ministry of Economic Affairs. 2022. Available online: https://www.moeacgs.gov.tw/ (accessed on 1 January 2022).

24. Neipu Household Registration Office, Pingtung County Government, Taiwan. 2022. Available online: https://www.neipu.gov.tw/Default.aspx (accessed on 11 November 2022).

25. Sandimen Township Office, Pingtung County Government, Taiwan. 2022. Available online: https://www.pthg.gov.tw/sandimen/Default.aspx (accessed on 11 November 2022).

26. Wutai Township Office, Pingtung County Government, Taiwan. 2022. Available online: https://www.wutai.gov.tw/index.php (accessed on 11 November 2022).

27. Maolin National Scenic Area Administration, Tourism Bureau, MOTC. 2022. Available online: https://www.maolin-nsa.gov.tw/EN/ (accessed on 11 November 2022).

28. Lin, C.W.; Shieh, C.J.; Yuan, B.D.; Shieh, Y.C.; Huang, M.L.; Lee, S.Y. Impact of Chi-Chi earthquake on the occurrenceof landslides and debris flows: Example from the Chenyulan River watershed, Nantou, Taiwan. *Eng. Geol.* **2004**, *71*, 49–61. [CrossRef]

29. ERDAS. *ERDAS IMAGINE®Tour Guide*; ERDAS World Headquarter: Atlanta, GA, USA, 2011.

30. Seo, K.; Funasaki, M. Relationship between sediment disaster (mainly debris flow damage) and rainfall. *Int. J. Erosion Control Eng.* **1973**, *26*, 22–28.

31. Chen, C.Y.; Chen, T.C.; Yu, F.C.; Yu, W.H.; Tseng, C.C. Rainfall duration and debris-flow initiated studies for real-time monitoring. *Environ. Geol.* **2005**, *47*, 715–724. [CrossRef]

32. ESRI. ArcGIS. 2019. Available online: https://www.esri.com/en-us/home (accessed on 1 September 2019).

33. Hosmer, D.W.; Lemeshow, S. *Applied Logistic Regression*, 2nd ed.; Wiley: Hoboken, NJ, USA, 2000; ISBN 978-0-471-35632-5.

34. Cox, D.R. *The Analysis of Binary Data*; Methuen: London, UK, 1970.

35. Ohlmacher, G.C.; Davis, J.C. Using multiple logistic regression and GIS technology to predict landslide hazard in northeast Kansas, USA. *Eng. Geol.* **2003**, *69*, 331–343. [CrossRef]
36. Verbyla, D.L. *Satellite Remote Sensing of Natural Resources*; CRC Press: New York, NY, USA, 1995.
37. Cohen, J. A coefficient of agreement for nominal scales. *Educ. Psychol. Meas.* **1960**, *20*, 37–46. [CrossRef]
38. Chen, Y.R.; Chen, J.W.; Hsieh, S.C.; Ni, P.N. The Application of Remote Sensing Technology to the Interpretation of Land Use for Rainfall-Induced Landslides Based on Genetic Algorithms and Artificial Neural Networks. *IEEE J. Sel. Top. Appl. Earth Obs. Remote Sens.* **2009**, *2*, 87–95. [CrossRef]
39. Regulations of soil and water conservation, Soil and Water Conservation Bureau. 2022. Available online: https://www.ardswc.gov.tw/Home/eng/Info/item_list?mid=392 (accessed on 26 March 2024).
40. ISRM. *Rock Characterization, Testing and Monitoring*; Pergamon Press: Oxford, UK, 1981.
41. Water Resources Agency, Ministry of Economic Affairs. 2021. Available online: https://www.wra.gov.tw/ (accessed on 1 January 2021).
42. SPSS. *SPSS 14.0 Brief Guide*; SPSS Inc.: Chicago, IL, USA, 2005.

Parameter Sensitivity Analysis of a Korean Debris Flow-Induced Rainfall Threshold Estimation Algorithm

Kyung-Su Choo [1], Jung-Ryel Choi [2], Byung-Hyun Lee [3] and Byung-Sik Kim [4,*]

[1] Department of Urban and Environmental and Disaster Management, Graduate School of Disaster Prevention, Kangwon National University, Samcheok 25913, Republic of Korea; chu_93@kangwon.ac.kr

[2] Technology Research Division, Korea Slope Safety Association, Sejong-si 30128, Republic of Korea; lovekurt82@gmail.com

[3] Laboratory of Climate and Smart Disaster Management, Kangwon National University, Samcheok 25913, Republic of Korea; hydrobh2@kangwon.ac.kr

[4] Department of Artificial Intelligence and Software, Graduate School of Disaster Prevention, Kangwon National University, Samcheok 25913, Republic of Korea

* Correspondence: hydrokbs@kangwon.ac.kr; Tel.: +82-33-570-6819

Abstract: With the increase in both rainfall and intensity due to climate change, the risk of debris flows is also increasing. In Korea, the increasing damage caused by debris flows has become a social issue, and research on debris-flow response is becoming increasingly important. Understanding the rainfall that induces debris flows is crucial for debris-flow response, and methods such as the I-D method have been used to evaluate and predict the risk of debris flows. However, previous studies on debris flow-induced rainfall analysis have been limited by the subjective decision of the researcher to select the impact meteorological stations, which greatly affects reliability. In this paper, in order to establish an objective standard, various maximum allowable distances between debris-flow disaster areas and meteorological stations were adjusted to 1, 3, 5, 7, 9, 11, 13, and 15 km using the CTRL-T automatic calculation algorithm, and the optimal maximum allowable distance suitable for Korean terrain was derived through parameter sensitivity analysis. Based on this, we developed a nomogram for sediment disaster risk prediction and warning in Gangwon-do, and applied it to past disaster cases, and found that, although the prediction time for each stage varies depending on the maximum allowable distance, on average, it is possible to predict the risk of sediment flows 4 to 5 h in advance. It is believed that the results of this study can be used to reduce sediment flow damage in advance.

Keywords: debris flow; rainfall threshold; automatic calculation algorithm; rainfall intensity–duration relationship

1. Introduction

Increasing rainfall intensity due to climate change has raised the hazard of a debris-flow disaster in the vicinity of mountainous areas in Korea, resulting in higher risks to human lives and properties [1]. In particular, 43 people died from torrential rains caused by debris-flow disaster damage in Woomyeonsan in Seoul and Majeoksan in Chuncheon City in July 2011. In 2020, five deaths occurred in Gokseong-gun, Jeollanam-do. The damage caused loss of life and property, further emphasizing the social issue at hand. To address debris-flow disasters, establishing standards for early forecasting and alert issuance is essential. Preceding rainfall conditions, which influence soil stress and pore water pressure, are crucial factors that should be considered the direct cause of a debris-flow disaster [2–5].

Many studies have been conducted on debris-flow disaster research recently. Ref. [6] developed a low-cost tilt-based rainfall-induced landslide monitoring system using the economical and precise MEMS sensor to record displacement and volumetric water content. Ref. [7] introduced a methodology for establishing rainfall thresholds critical for debris flow early warnings in regions lacking extensive data, utilizing a hydraulic initiation

model. This research confirmed the approach's reliability through analysis in the Guojuan Gorge, further suggesting an early warning model based on precise rainfall thresholds. Such advancements are pivotal for improving disaster response and mitigation efforts in mountainous territories with similar geographical characteristics. Ref. [8] studied the specific rainfall intensity and cumulative precipitation levels required for the initiation of soil flow in the region through an in-depth analysis of three major storms in Beijing and proposed integrating real-time rainfall intensity for accurate soil flow prediction and early warning systems. Ref. [9] employed rainfall data spanning 2012 to 2015 to elucidate rainfall patterns and identify critical thresholds that instigate periglacial debris flows in the Parlung Zangbo Basin, located in the southeastern Tibetan Plateau. The study underscored the significant influence of varied sediment conditions and rainfall dynamics on the initiation of debris flows, advocating for the necessity of conducting site-specific assessments to enhance the precision and reliability of debris flow monitoring and early warning mechanisms. Ref. [10] details a data-driven methodology combining artificial neural networks (ANNs) and particle swarm optimization (PSO) for establishing rainfall thresholds crucial for debris flow initiation. This approach, when applied to the Beijing and Wenchuan earthquake regions, refines early warning models by accurately identifying intricate, non-linear thresholds for rainfall intensity and duration. This strategy surpasses traditional linear regression techniques in enhancing debris flow hazard prediction and management efficacy. Ref. [11] developed and tested an algorithm for the objective and reproducible reconstruction of rainfall events that have resulted in landslides. Ref. [12] used a new release of the algorithm that allows calculating reproducible rainfall thresholds from multiple ED rainfall conditions that have resulted in landslides. and tested the algorithm in Sicily, southern Italy.

In a previous study on the threshold rainfall that triggers debris flows, ref. [13] identified 683 rainfall-induced landslides in Lombardy over the period 1927–2008 and calculated thresholds using mean annual precipitation (MAP)-normalized intensity–duration thresholds. The results showed that debris flows frequently occurred within 1 to 3 h of the maximum recorded rainfall intensity in summer and within 5 h in spring or fall. Ref. [14] proposed an equation to determine the rainfall duration–intensity threshold for predicting debris flows using data from the Sichuan region of China, and indicated that $I = 2.09D^{-0.12}$. Ref. [15] indicated that although debris flows and warning thresholds have been derived from existing 30-year studies, they vary across the United States and thresholds should be derived for each region, using soil wetting functions, precipitation characteristics, etc. Ref. [16] defined four groups of rainfall thresholds for landslide occurrence using regression values at each quantile level of quantile regression based on landslides that occurred in China from 1998 to 2017, including the original rainfall event–duration (E-D) threshold and the normalized (normalizing cumulative rainfall to annual mean rainfall) and merged (EMAP-D) rainfall and Climate Prediction Center Morphing Technique (CMORPH) rainfall products, respectively. The E-D thresholds defined in the paper were generally lower than other thresholds in previous studies on a global scale and on a regional or national scale in China, suggesting that this was due not only to the larger number of landslide cases used, but also to the combined effects of China's special geological environment, climatic conditions, and human activities. Ref. [17] analyzed 85 debris flows from 1910 to 2019 in the protofino promotor and used 69 clusters of rainfall events that triggered 94 slope failures for which landslide and rainfall information were known with sufficient geographic and temporal accuracy to set empirical ID thresholds adopting a frequentist approach, and used the Mann–Kendall test and Hurst exponent to detect potential trends. The analysis of the long-term rainfall time series showed a statistically significant increasing trend in short-term precipitation events and rainfall amounts, suggesting the possibility of future scenarios where thresholds are exceeded more frequently and landslide risk increases. Ref. [18] analyzed the occurrence of debris flows in Taiwan and presented short-term (less than 12 h) high-intensity rainfall, high-intensity and cumulative rainfall, and long-term (more than 36 h) high-accumulative rainfall as rainfall characteristics that trigger landslides.

The study proposed a combination of warning models for landslides from cumulative rainfall–duration plots with rainfall intensity classification and average rainfall–duration plots with cumulative rainfall classification, and suggested that the thresholds are being lowered due to climate change.

The concept of marginal rainfall using prior rainfall and rainfall intensity was proposed [19]. Subsequently, an equation for the rainfall intensity-duration curve has been derived from empirical debris-flow data, leading to the development of various methodologies aimed at the probabilistic forecasting of debris flows [20–22]. Recently, ref. [23] introduced a methodology for automatically selecting rainfall observatories that affect debris-flow disasters using rainfall and topographic data and calculating the preceding rainfall for debris-flow disasters. Meanwhile, ref. [24] applied the relevant algorithm to Slovenia to establish an early warning system for debris-flow disasters. Then, ref. [25] suggested improving the algorithm's results using neural networks. Ref. [26] used GLDAS (Global Land Data Assimilation System) to analyze the effects of air temperature and precipitation on the characteristics of soil moisture in the eastern region of China from 1961 to 2011, and found that the temperature and precipitation in different seasons have different degrees of influence on the characteristics of soil moisture in each layer. Ref. [27] introduced and applied the innovative RSI-Net, which aims to improve the distinguishability of correlations among adjacent land covers and address the issue of boundary blurring in high-resolution remote sensing imagery. Ref. [28] proposed an improved bat algorithm for dam deformation prediction based on a hybrid-kernel extreme learning machine.

Ref. [29] develops slope-specific thresholds for dimensionless discharge and Shields stress to forecast debris flow initiation following wildfires. This work further presents a process-oriented approach for deriving rainfall intensity-duration thresholds, showcasing their consistency with empirical data. This synergy between process-based hydrologic models and empirical observations significantly advances the accuracy of debris flow warning systems. Ref. [30] presented the capability of a deep learning algorithm to determine the distribution of landslide rainfall thresholds in a potential large-scale landslide area and to assess the distribution of recurrence intervals using probability density functions, as well as to assist decision makers in early responses to landslides and reduce the risk of large-scale landslides. Ref. [31] analyzed Kalimpong town in the Darjeeling Himalayas, which is among the regions most affected by landslides, using the SIGMA model, and calculated threshold rainfall. Among domestic research cases, refs. [3,32] applied the Rainfall Triggering Index (RTI), which is the product of the preceding rainfall duration and intensity, to Korea, and proposed a debris-flow risk criteria using a probability density function. Ref. [33] proposed the risk criterion using quantile regression analysis based on the duration and the intensity of rainfall before the occurrence of a debris-flow disaster. To establish a Korean early warning system for a debris-flow disaster, a program-based automation algorithm is required, and an evaluation of the applicability of such an automation algorithm is deemed necessary.

Based on the above studies, it was found that existing empirical equations are mainly used in studies to analyze the damage of debris flows or to calculate the critical rainfall amount that causes debris flows. In this paper, we selected Gangwon-do province, where many landslides have occurred, as the target area, and collected debris flow occurrence information, as well as rainfall and topography information. Using this information, we conducted an analysis using statistical techniques, and finally defined various maximum allowable distances from debris-flow damage points and meteorological zones to establish objective criteria. Through the parameter sensitivity analysis of the algorithm proposed by [12], we derived the optimal maximum allowable distance suitable for Korean terrain.

2. Theoretical Background

2.1. Automated Rainfall Estimation Program for Debris Flow Disasters

Rainfall standards that cause debris-flow disasters are mainly presented using the intensity–duration (I-D) method, which analyzes the relationship between rainfall intensity

and duration, and various domestic and overseas studies have been conducted in this regard. In using the I-D method, selecting meteorological stations and the maximum allowed delay time between the end of the rainfall season and the occurrence of the debris-flow disaster are important input parameters that researchers may define differently. Ref. [22] proposed an automatic rainfall threshold calculation tool to predict debris flows applicable in southern Sicily, Italy, to address this issue objectively. In this study, the tool proposed by [12] was adapted and developed with the R language to suit the Korean terrain. Figure 1 shows the flowchart of this study, while Figure 2 shows the algorithm components of the rainfall threshold. In the input section, information on the occurrence of debris-flow disasters (debris-flow.csv), rain gauge stations (table_of_raingauge.csv), and rainfall time series (TimeSeries_Sensor.csv) are provided. The computation section comprises utils, a useful utility for programming and developing R packages; caTools for encoders, decoders, and classifiers; ggmap for spatial data visualization; and MASS for statistical functions. Finally, the output section provides reconstructed rainfall events affecting debris-flow disasters and the analysis results of reconstructed rainfall conditions and thresholds.
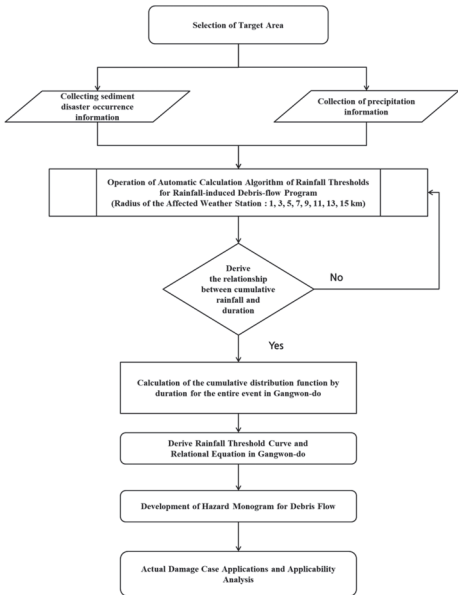

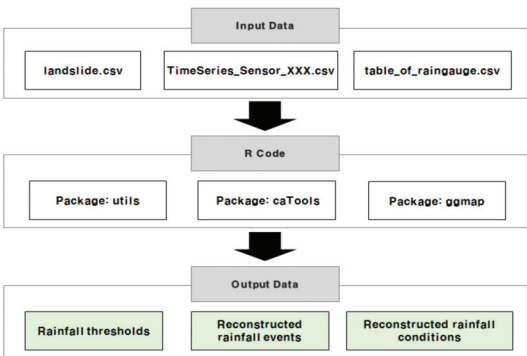**Figure 1.** Flow chart of study.

Figure 2. Components of algorithm for the rainfall threshold.

2.2. Algorithm for Calculating Debris Flow-Induced Rainfall Thresholds

The computation of the debris flow-induced rainfall threshold is based on the continuous time rainfall data, geographical coordinates of debris-flow disaster locations, and the occurrence time of the debris-flow disaster. The algorithm reconstructs rainfall events and determines the events influencing debris-flow disasters. In this process, the maximum allowed distance between the representative rain gauge and the debris-flow disaster location and the maximum allowed delay time between the end of the rainfall event and the occurrence of the debris-flow disaster are defined. In this study, the maximum allowed distance was defined as 15 km, and the maximum allowed delay time was defined as 48 h.

Separate blocks perform threshold calculation in the automatic threshold calculation program, and each block performs a specific operation (Figure 3). In the first block, the individual rainfall ideology is reconstructed based on a continuous rainfall time series, and the duration (*D*, h) and cumulated rainfall (*E*, mm) for each rainfall event are calculated. The separation of continuous rainfall time series is based on climate and seasonal environments. This study defined the suitable period for Korea, the warm season (March–August). In the second block, the rain gauge closest to the area where the debris flow occurred is selected. At this time, the maximum allowed distance between the debris-flow disaster occurrence point and the rain gauge is selected within a circular area with the defined allowed distance radius, and the inverse distance weighting (IDW) method is used to determine the multiple rainfall conditions (MRCs). The stations near the debris flow occurrence site are weighted by the distance of the rainfall station from the rainfall duration (D_L) and cumulative rainfall (E_L) to select the stations most associated with debris flows [15].

$$w = f(d, E_L, D_L) = d^{-2} E_L^2 D_L^{-1} \tag{1}$$

where w is a weighting factor for the impact on debris flow occurrence, E_L is the cumulative rainfall, and D_L is the duration. When reconstructing the rainfall event, missing data along with no rainfall (0.2 mm) are removed to construct the rainfall event.

Lastly, in the third block, the different exceedance probabilities (EPs) are used to calculate the relationship between the cumulated rainfall (*E*) and duration (*D*). At this time, the threshold is defined using a frequency approach (Equation (2)) and calculated as a power function.

$$E = (\alpha \pm \Delta\alpha) \bullet D^{(\gamma \pm \Delta\gamma)} \tag{2}$$

where α is the scaling parameter (the intercept) and γ is the shape parameter (that defines the slope of the power law curve). $\Delta\alpha$ and $\Delta\gamma$ represent the relative uncertainty of the two parameters. See Ref. [34] for a detailed description of the above equation.
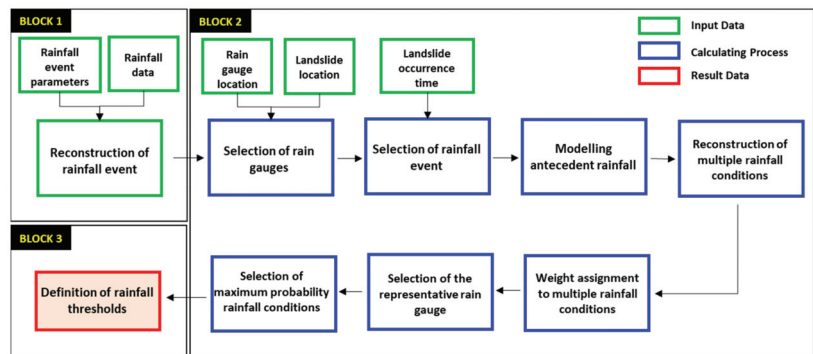

Figure 3. Data analysis process by block intervals [35].

3. Calculation and Verification of Rainfall Thresholds

3.1. Collection of Information on the Occurrence of Debris-Flow Disasters

The area of Gangwon Province, characterized by its mountainous terrain which accounts for more than 80% of Korea's frequent debris flow incidents, was selected as the focal region for this investigation. The geographical distribution of these debris flows is illustrated in the subsequent figure (Figure 4). Furthermore, an exhaustive literature review was conducted to amass a historical dataset of debris flow occurrences, with entries lacking precise locational and temporal data being systematically eliminated. As a result, the specific locations and times of occurrence for 18 debris flow events between 27 July 2011 and 5 August 2020 were compiled (Table 1). Additionally, rainfall data were sourced from the Korea Meteorological Administration (https://www.weather.go.kr). While the conventional methodology relied on the nearest rain gauge to establish a link between debris flows and rainfall, this study introduces an advanced methodology that automatically incorporates all viable gauges within a defined radius. This method applies weighting factors that account for both the spatial distance between the debris flow site and the gauge and hydrological attributes such as the volume of rainfall and the event's duration, recognizing that a debris flow may be precipitated by multiple rainfall events. Moreover, the applicability of the proposed methodology was validated through its application to the 2019 debris-flow disaster in Gangwon-do, which tragically resulted in human casualties.
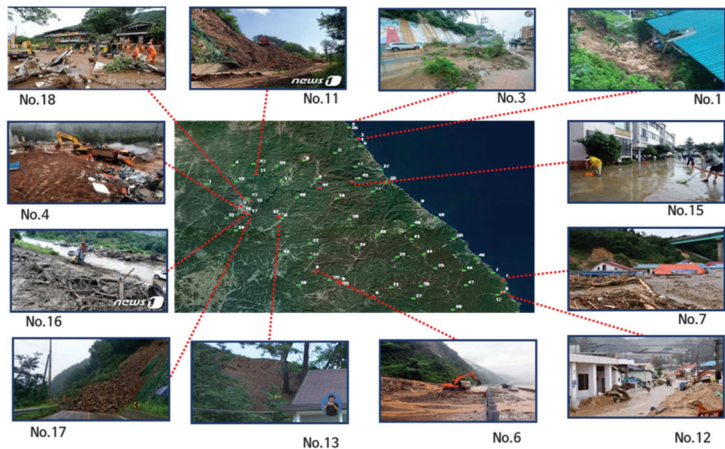

Figure 4. Analysis area and historical damage [35].

Table 1. Status of debris flow occurrence time and location.

No.	Date (Year Month Day Hour Minute)	Longitude	Latitude	Administrative Division	Start Date and End Date of the Rainfall	Cumulated Rainfall (mm)
1	5 August 2020, 06:00	128.4609	38.4484	Geojin-eup, Goseong-gun	3 August 2020–5 August 2020	348
2	5 August 2020, 06:00	128.4627	38.4510	Geojin-eup, Goseong-gun	3 August 2020–5 August 2020	348
3	5 August 2020, 06:00	128.4042	38.5438	Hyeonnae-myeon, Goseong-gu	3 August 2020–5 August 2020	348
4	3 August 2020, 09:00	127.7334	37.8923	Chuncheon-si	3 August 2020–3 August 2020	179
5	2 August 2020, 02:00	128.1731	37.3508	Gangnim-myeon, Hoengseong-gun	3 August 2020–3 August 2020	136
6	2 August 2020, 06:00	128.5316	37.1413	Yeongwol-gun	2 August 2020–2 August 2020	204
7	3 October 2019, 00:56	129.3241	37.2703	Wondeok-eup, Samcheok-si	2 October 2019–3 October 2019	390
8	2 October 2019, 20:00	129.3209	37.1614	Wondeok-eup, Samcheok-si	2 October 2019–3 October 2019	390
9	2 October 2019, 23:00	128.3314	37.2569	Wondeok-eup, Samcheok-si	2 October 2019–3 October 2019	390
10	2 October 2019, 23:00	128.3264	37.2525	Wondeok-eup, Samcheok-si	2 October 2019–3 October 2019	390
11	12 August 2019, 21:20	127.8270	38.1604	Hwacheon-eup, Hwacheon-gun	11 August 2019–12 August 2019	48
12	20 August 2017, 02:30	127.9584	37.8150	Hwachon-myeon, Hongcheon-gun	19 August 2017–20 August 2017	33
13	20 August 2017, 02:30	127.9650	37.7980	Hwachon-myeon, Hongcheon-gun	19 August 2017–20 August 2017	33
14	14 July 2013, 07:30	128.2136	38.0402	Inje-eup, Inje-gun	14 July 2013–14 July 2013	142
15	14 July 2013, 08:20	128.4138	38.0919	Seo-myeon, Chuncheon-si	14 July 2013–14 July 2013	125

Table 1. *Cont.*

No.	Date (Year Month Day Hour Minute)	Longitude	Latitude	Administrative Division	Start Date and End Date of the Rainfall	Cumulated Rainfall (mm)
16	14 July 2013, 08:50	127.7564	37.8454	Dongsan-myeon, Chuncheon-si	14 July 2013–14 July 2013	125
17	14 July 2013, 09:30	127.7822	37.8247	Dongnae-myeon, Chuncheon-si	14 July 2013–14 July 2013	125
18	27 July 2011, 00:08	127.7920	37.9356	Sinbuk-eup, Chuncheon-si	27 July 2011–27 July 2011	262

3.2. Meteorological Stations and Collection of Rainfall Information

As shown in Figure 4, we collected weather and rainfall data from 46 Automatic Weather System (AWS) locations in Gangwon Province provided by the Korea Meteorological Administration. The data included hourly rainfall data from 00:00 on 1 January 2010 to 23:00 on 31 December 2020. Only 22 of the 46 rain gauges corresponded to the rainfall that caused the debris-flow disaster and were used to build the data. The final data, including the ID, name, and location of the 46 weather stations, are shown in Table 2.

Table 2. Location of meteorological stations and points.

No.	ID	Name	Lon.	Lat.
1	310	GungChon	129.2647	37.32471
2	320	Hyangnobong	128.3138	38.33104
3	321	Wontong	128.1963	38.1147
4	322	Sangseo	127.6857	38.23158
5	517	Ganseong	128.4745	38.38536
6	518	Haean	128.1211	38.26958
7	519	Sanae	127.5194	38.07545
8	522	Hwachon	127.9838	37.78712
9	523	Jumunjin	128.8214	37.89848
10	524	Gangmun	128.9248	37.78579
11	527	Sindong	128.6413	37.21108
12	529	Wondeok	129.2859	37.14156
13	536	Hoengseong	127.9724	37.4876
14	537	Imgye	128.8459	37.48323
15	554	Misiryeong	128.4371	38.21439
16	555	Hwacheon	127.7029	38.09638
17	556	Yanggu	127.9853	38.09799
18	557	Girin	128.3186	37.95263
19	558	Palbong	127.7007	37.68614
20	559	Nae-myeon	128.3973	37.77805
21	560	Jinbu	128.5645	37.64793
22	561	Cheongil	128.1528	37.58219
23	562	Yeongwol-Jucheon	128.2694	37.27534
24	563	Bukpyeong	128.6828	37.46356
25	579	Hajang	128.9133	37.36684
26	580	Okgye	129.0289	37.61345

Table 2. *Cont.*

No.	ID	Name	Lon.	Lat.
27	581	Sangdong	128.7744	37.11663
28	582	Sillim	128.0799	37.23146
29	583	Anheung	128.1551	37.46463
30	585	Sinnam	128.0742	37.95996
31	587	Bangsan	127.9533	38.22642
32	588	Namsan	127.6429	37.79066
33	593	Yangyang-Yeongdeok	128.5407	38.00731
34	597	Daehwa	128.4411	37.54548
35	661	Hyeonnae	128.4025	38.54385
36	670	Yangyang	128.6297	38.08725
37	671	Cheongho	128.5936	38.19091
38	674	Sabuk	128.8214	37.21963
39	678	Gangneung-Seongsan	128.778	37.7244
40	679	Gangneung-Wangsan	128.7726	37.61058
41	681	Wondong	127.8117	38.24379
42	684	Chunchon-Sinbuk	127.7763	37.9546
43	696	Singi	129.0861	37.34661
44	875	Seorak	128.4606	38.12107
45	876	Samcheok	129.1621	37.45003
46	878	Dogye	129.0961	37.22379

3.3. Setting the Influence Distance of Meteorological Stations

The radius was adjusted to 1, 3, 5, 7, 9, 11, 13, and 15 km from the individual debris-flow disaster point to analyze the parameter sensitivity of the automatic rainfall threshold calculation algorithm. Here, the reason why the maximum threshold is assumed to be 15 km is that Korea has a small land area and a close distance between weather stations. Stations within the affected radius from the location of the individual debris-flow disaster were selected, and the cumulative rainfall for each duration of the disaster was calculated for 24 h before the occurrence of the debris-flow disaster (Figure 5).
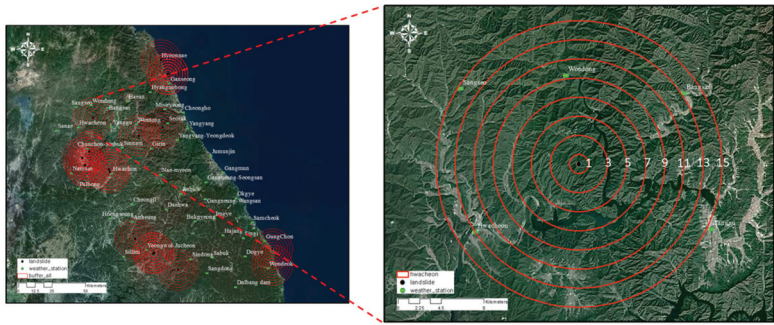

Figure 5. Status map of the influence distance setting for meteorological stations.

4. Analysis Results

Using the debris flow-induced rainfall threshold calculation program, 16,423 rainfall events were reconstructed during the study's target period (2010–2020). In addition, it

was derived that 14 of the 18 debris-flow disaster events entered, considering the location of the debris-flow disaster and the distance from the rain gauge, were caused by rainfall. thirty-six rainfall events were identified as being closely associated with the occurrence of fourteen debris-flow disaster events. For these, the logarithmic distribution of cumulative event rainfall (EL) and rainfall event duration (DL) is shown in Figure 6a. Meanwhile, the empirical cumulative distribution function (ECDF) and duration relationship curve (Figure 6b) and ECDF and cumulative rainfall (E) relationship curve (Figure 6c) were derived. As a result of the derivation, it was found that about 40% of debris-flow disasters occurred within 24 h and 80% occurred in the cumulative rainfall section of less than 200 mm. It can be seen that debris-flow disasters take place due to torrential rains that occur in a short period of time. In the final nomogram, a logarithmic scale was not utilized to examine the sensitivity of station distance to debris flow occurrences. Instead, the focus was on determining the amount of lead time that can be secured prior to a debris flow event, based on the time of day.
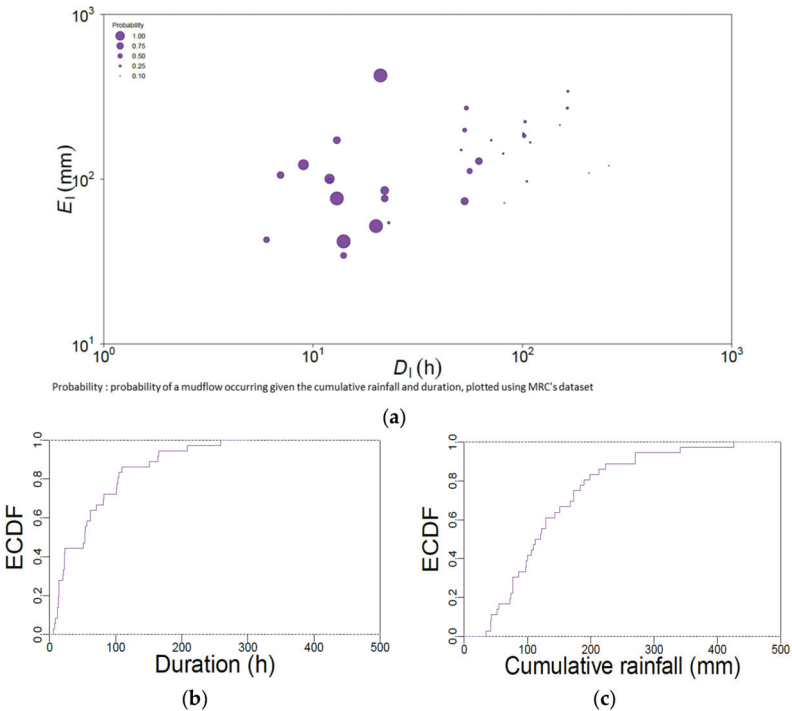

Figure 6. (**a**) Distribution of the DL (rainfall event duration) and EL (cumulated event rainfall) pairs, in log-log coordinates (purple dots); (**b**) ECDF (the empirical cumulative distribution function) of D (duration); (**c**) ECDF of E (cumulated rainfall) [35].

Utilizing the compiled datasets of rainfall and debris-flow incidents, thresholds for cumulative rainfall (E) and event duration (D) across the designated study area were established. Subsequently, correlation analyses yielded graphs and equations linking cumulative precipitation to duration for exceedance probabilities (EPs) of 70% (represented in blue), 50% (in gray), and 10% (in yellow), as illustrated in Figure 7. Nevertheless, the absence of meteorological stations precluded the generation of graphs for maximum permissible distances of 1, 3, 5, and 7 km. Conversely, at extended distances of 9, 11, 13, and 15 km, significant correlations were identified. The analysis indicated an increase in the optimal maximum allowable distance for cumulative rainfall duration at 11 km compared to 9 km, with a subsequent decrease in correlation strength at distances of 13 and 15 km.
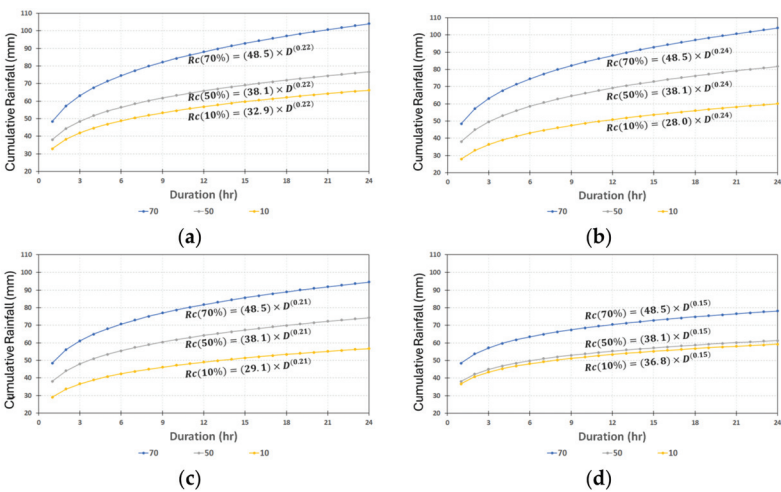
Figure 7. Plot with the ED (cumulative event rainfall–duration) conditions that triggered debris-flow corresponding to 70%, 50%, and 10% thresholds (maximum allowed distance: 9 km (**a**), 11 km (**b**), 13 km (**c**), and 15 km (**d**)).

Table 3 details the parameters α and γ, along with the outcomes of the analysis on the relationship between cumulative rainfall and duration, contingent upon the maximum permissible distance from the influencing meteorological station. Table 4 summarizes the results of calculating cumulative rainfall and rainfall intensity according to the duration of each maximum allowed distance.

Table 3. Parameters α and γ, at various exceedance probabilities.

No.	Maximum Allowed Distance (km)	Exceedance Probability (%)	α	$\Delta\alpha$	γ	$\Delta\gamma$
1		70	48.5	23.8	0.22	0.13
2	9	50	38.1	19.6	0.22	0.13
3		10	32.9	16.6	0.22	0.13
4		70	48.5	23.8	0.24	0.15
5	11	50	38.1	19.6	0.24	0.15
6		10	28.0	15.5	0.24	0.15
7		70	48.5	23.8	0.21	0.13
8	13	50	38.1	19.6	0.21	0.13
9		10	29.1	15.9	0.21	0.13
10		70	48.5	23.8	0.15	0.12
11	15	50	38.1	19.6	0.15	0.12
12		10	36.8	17.5	0.15	0.12

Table 4. Rainfall analysis results Based on exceedance probability by maximum allowed distance.

Maximum Allowed Distance (km)	Exceedance Probability (%)	Rainfall Duration (h)	Cumulative Rainfall (mm)	Rainfall Intensity (mm/h)
		6	74.6	12.4
	70	12	88.1	7.3
		24	104.0	4.3
		6	56.5	9.4
9	50	12	65.8	5.5
		24	76.7	3.2
		6	48.8	8.1
	10	12	56.8	4.7
		24	66.2	2.8

Table 4. *Cont.*

Maximum Allowed Distance (km)	Exceedance Probability (%)	Rainfall Duration (h)	Cumulative Rainfall (mm)	Rainfall Intensity (mm/h)
11	70	6	74.6	12.4
		12	88.1	7.3
		24	104.0	4.3
	50	6	58.6	9.8
		12	69.2	5.8
		24	81.7	3.4
	10	6	43.0	7.2
		12	80.5	4.2
		24	60.0	2.5
13	70	6	70.7	11.8
		12	81.7	6.8
		24	94.5	3.9
	50	6	55.5	9.3
		12	64.2	5.4
		24	74.3	3.1
	10	6	42.4	7.1
		12	49.0	4.1
		24	56.7	2.4
15	70	6	63.5	10.6
		12	70.4	5.9
		24	78.1	3.3
	50	6	49.8	8.3
		12	55.3	4.6
		24	61.4	2.6
	10	6	48.1	8.0
		12	53.4	4.5
		24	59.3	2.5

Using the results of Table 4 and debris-flow disaster occurrence information and rainfall information in Gangwon-do, a soil disaster risk nomogram according to the maximum allowable distance (9, 11, 13, and 15 km) by excess probability (70%, 50%, and 10% range) was developed. In this paper, the warning stage was classified according to the excess probability, and the 10–50% section was classified as alert, the 50–70% section as warning, and emergency when it was 70% or more. Based on the case of Samcheok Sinnam Village, an area affected by the debris-flow disaster in October 2019, the applicability of the time-specific risk matrix was reviewed. Figure 8a illustrates the hyetograph for a case where a debris flow occurred. In Figure 8b, the formula based on exceedance probability is presented, with the vertical dashed line indicating the moment when the debris flow occurred. Figure 8c shows the warning levels according to cumulative rainfall. When applying the nomogram with a maximum allowed distance of 9 km, it was observed that it reached the most dangerous "severe" level about 4 h before the debris-flow disaster occurred (3 October 2019, 01:00), as shown in Figure 8.
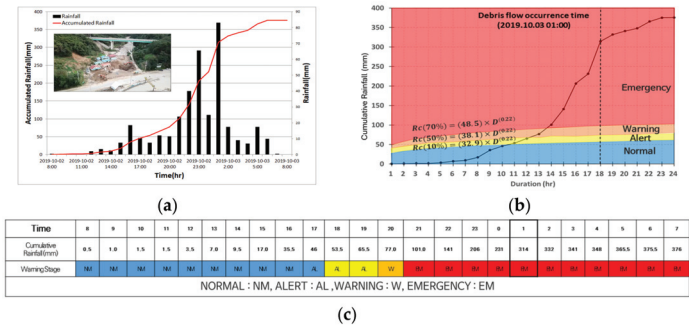

(a) (b)

(c)

Figure 8. Application to Samcheok Sinnam Village damage case and risk rating status [35].

Upon applying the nomogram to each maximum allowable distance, the analysis revealed that Figure 9a entered the severe level approximately 4 h prior to the debris flow disaster, based on a maximum allowable distance of 9 km. Figure 9b entered the severe level about 4 h before, with a maximum allowed distance of 11 km. Figure 9c, with a maximum allowed distance of 13 km, entered the severe level about 5 h before, and Figure 9d, with a maximum allowed distance of 15 km, was found to enter the severe level about 5 h before. In this context, the arrow indicates the transition from a warning to an emergency phase, while the black circle denotes the moment when the debris flow occurred.
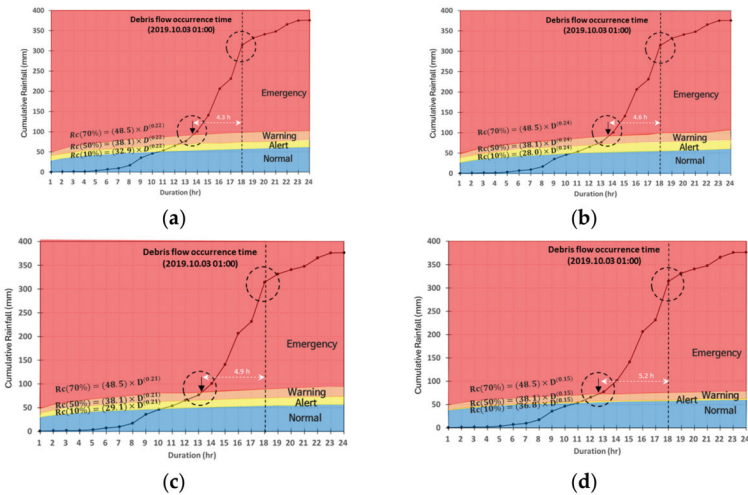

(a)

(b)

(c)

(d)

Figure 9. Results by maximum allowable distance ((**a**) maximum allowable distance 9 km: entered emergency stage about 4.3 h before the debris-flow disaster event occurred; (**b**) maximum allowable distance 11 km: entered emergency stage about 4.6 h before; (**c**) maximum allowable distance 13 km: entered emergency stage about 4.9 h before; and (**d**) maximum allowable distance 15 km: entered emergency stage about 5.2 h before).

In [32], radar rainfall was used to estimate the rainfall of localized debris flows in mountainous areas, and a radar rainfall calibration model was developed using machine learning techniques. The basin average rainfall of the calibrated radar rainfall was calculated and applied to the same area as the subject of this study. The result of [32] showed a forecasting time of 3 h, as shown in Figure 10, but in this study, an average forecasting time of 4 to 5 h can be obtained.
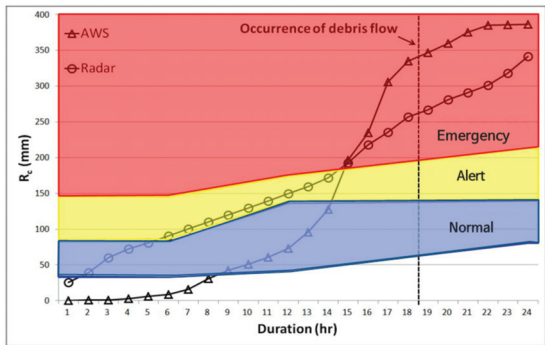

Figure 10. Evaluation and verification of applicability to debris-flow forecasting using mean areal rainfall [32] (R_c: Critical Accumulated Rainfall).

When comparing the results of this study with other studies, it was found that appropriate values were obtained, and although there are limitations in the terrain characteristics of Gangwon-do, it was concluded that the influence range of each rain gauge could be applied up to 15 km.

5. Summary and Conclusions

Due to climate change, there has been an increase in rainfall intensity over time, leading to an escalation in debris-flow occurrence and damages, making it a significant social issue. Rainfall is a direct factor that causes debris-flow disasters. Therefore, analyzing the relationship between rainfall and debris-flow disasters is essential as a proactive measure in developing debris-flow disaster forecasting and response systems. In this study, the tool proposed by [21] was adapted to calculate the amount of debris flow-induced rainfall suitable for the Korean terrain through a parameter sensitivity analysis of the automatic threshold estimation algorithm of rainfall for debris-flow disasters. The main research content and conclusions are as follows:

(1) Rainfall criteria that cause sediment disasters are mainly presented using the I-D method for analyzing the relationship between rainfall intensity and duration. However, the methodologies for selecting the representative rain gauge and the definition of rainfall that causes debris-flow disasters may vary. Thus, it is necessary to use an automatic program that can derive objective results for them. Overseas, the development and applicability evaluation of automatic rainfall calculation programs for debris-flow disasters has been conducted in Italy and India. This study conducted basic research to develop programs suitable for Korea and evaluate their applicability.

(2) In previous studies, there were limitations in using subjective methodologies for selecting impact meteorological stations and preceding rainfall, which had a high impact on the reliability of the criteria for debris flow-induced rainfall. This study adjusted the maximum allowed distance to 1, 3, 5, 7, 9, 11, 13, and 15 km using an automatic calculation algorithm for debris flow-induced rainfall thresholds, and a sensitivity analysis was performed automatically. As a result of applying the automatic calculation algorithm and the maximum allowed distance scenario to the Gangwon-do region, quantitatively checking the change in the cumulative rainfall by duration according to EPs was possible. Based on this information, a nomogram was developed for the prediction and warning of the risk of sediment disasters in the Gangwon-do region.

(3) The results of applying this study to Sinnam Village, Samcheok City, which was affected by a debris-flow disaster in 2019, showed that the risk of debris-flow disasters increases with the occurrence of rainfall, and that the risk forecast for the severe stage can be predicted as early as 4.3, 4.6, 4.9, and 5.2 h in advance of the very severe stage, depending on the maximum allowable distance from the rain gauge (9, 11, 13, and 15 km, respectively).

In this study, an algorithm-based approach was utilized to determine rainfall thresholds for the major debris flow occurrence areas in Korea. By deriving quantitative rainfall thresholds based on the relationship with the maximum allowable distance of rain gauges from debris-flow disaster site information, we presented a practical methodology that complements the theoretical limitations of existing studies. The results proposed in this study were analyzed assuming a maximum allowable distance of 15 km, but the applicability of the results by expanding the range requires further analysis and further research in conjunction with predicted rainfall information. In addition, since this study utilized only debris-flow disaster information limited to the Gangwon region, it is necessary to verify and improve the algorithm by expanding the region, and further verification through comparison with physics-based debris flow models is required. If the algorithm and its accuracy are improved through further research, it is believed that the algorithm used in this study can be applied to the system to reduce damage before a debris-flow disaster occurs.

References

1. Choi, J.R. An Analysis of Debris-Flow Propagation Characteristics and Assessment of Building Hazard Mapping Using FLO-2D–The Case of Chuncheon Landslide Area. *Crisis Emerg. Manag.* **2018**, *14*, 91–99. [CrossRef]
2. Gariano, S.L.; Melillo, M.; Peruccacci, S.; Brunetti, M.T. How much does the rainfall temporal resolution affect rainfall thresholds for landslide triggering? *Nat. Hazards* **2019**, *100*, 655–670. [CrossRef]
3. Chae, B.-G.; Choi, J.; Jeong, H.K. A Feasibility Study of a Rainfall Triggeirng Index Model to Warn Landslides in Korea. *J. Eng. Geol.* **2016**, *26*, 235–250. [CrossRef]
4. Aleotti, P. A warning system of rainfall-induced shallow failure. *Eng. Geol.* **2004**, *73*, 247–265. [CrossRef]
5. Keefer, D.K.; Wilson, R.C.; Mark, R.K.; Brabb, E.E.; Brown, W.M., III; Ellen, S.D.; Harp, E.L.; Wieczorek, G.F.; Alger, C.S.; Zatkin, R.S. Realtime landslide warning during heavy rainfall. *Science* **1987**, *238*, 921–925. [CrossRef] [PubMed]
6. Paswan, A.P.; Shrivastava, A.K. Evaluation of a Tilt-Based Monitoring System for Rainfall-Induced Landslides: Development and Physical Modelling. *Water* **2023**, *15*, 1862. [CrossRef]
7. Pan, H.-L.; Jiang, Y.-J.; Wang, J.; Ou, G.-Q. Rainfall threshold calculation for debris flow early warning in areas with scarcity of data. *Nat. Hazards Earth Syst.* **2018**, *18*, 1395–1409. [CrossRef]
8. Wang, H.; Xu, B.; Zhang, J.; Guo, X.; Zeng, Q.; Zhang, L. Rainfall thresholds of debris flows based on varying rainfall intensity types in the mountain areas of Beijing. *Geomat. Nat. Hazards Risk* **2022**, *13*, 2166–2181. [CrossRef]
9. Deng, M.; Chen, N.; Ding, H. Rainfall characteristics and thresholds for periglacial debris flows in the Parlung Zangbo Basin, southeast Tibetan Plateau. *J. Earth Syst. Sci.* **2018**, *127*, 11. [CrossRef]
10. Yan, Y.; Zhang, Y.; Hu, W.; Guo, X.; Ma, C.; Wang, Z.; Zhang, Q. A multiobjective evolutionary optimization method based critical rainfall thresholds for debris flows initiation. *J. Mt. Sci.* **2020**, *17*, 1860–1873. [CrossRef]
11. Melillo, M.; Brunetti, M.T.; Peruccacci, S.; Gariano, S.L.; Guzzetti, F. An algorithm for the objective reconstruction of rainfall events responsible for landslides. *Landslides* **2015**, *12*, 311–320. [CrossRef]
12. Melillo, M.; Brunetti, M.T.; Peruccacci, S.; Gariano, S.L.; Guzzetti, F. Rainfall thresholds for the possible landslide occurrence in Sicily (Southern Italy) based on the automatic reconstruction of rainfall events. *Landslides* **2015**, *13*, 165–172. [CrossRef]
13. Luino, F.; De Graff, J.; Roccati, A.; Biddoccu, M.; Cirio, C.G.; Faccini, F.; Turconi, L. Eighty Years of Data Collected for the Determination of Rainfall Threshold Triggering Shallow Landslides and Mud-Debris Flows in the Alps. *Water* **2020**, *12*, 133. [CrossRef]
14. Wu, M.-H.; Wang, J.P.; Chen, I.-C. Optimization approach for determining rainfall duration-intensity thresholds for debris flow forecasting. *Bull. Eng. Geol. Environ.* **2018**, *78*, 2495–2501. [CrossRef]
15. Baum, R.L.; Godt, J.W. Early warning of rainfall-induced shallow landslides and debris flows in the USA. *Landslides* **2010**, *7*, 259–272. [CrossRef]
16. He, S.; Wang, J.; Liu, S. Rainfall Event–Duration Thresholds for Landslide Occurrences in China. *Water* **2020**, *12*, 494. [CrossRef]
17. Roccati, A.; Paliaga, G.; Luino, F.; Faccini, F.; Turconi, L. Rainfall Threshold for Shallow Landslides Initiation and Analysis of Long-Term Rainfall Trends in a Mediterranean Area. *Atmosphere* **2020**, *11*, 1367. [CrossRef]
18. Chen, H.-W.; Chen, C.-Y. Warning Models for Landslide and Channelized Debris Flow under Climate Change Conditions in Taiwan. *Water* **2022**, *14*, 695. [CrossRef]
19. Campbell, R.H. *Soil Slips, Debris Flows, and Rainstorms in the Santa Monica Mountains and Vicinity, Southern California*; US Government Printing Office: Washington, DC, USA, 1975.
20. Caine, N. The rainfall intensity-duration control of shallow landslides and debris flows. *Geogr. Ann.* **1980**, *62*, 23–27.
21. Brunetti, M.T.; Peruccacci, S.; Rossi, M.; Luciani, S.; Valigi, D.; Guzzetti, F. Rainfall thresholds for the possible oc-currence of landslides in Italy. *Nat. Hazards Earth Syst. Sci.* **2010**, *10*, 447–458. [CrossRef]
22. Piciullo, L.; Gariano, S.L.; Melillo, M.; Brunetti, M.T.; Preruccacci, S.; Guzzetti, F. Definition and performance of a threshold-based refional early warning model for rainfall-induced landslides. *Landslides* **2017**, *14*, 995–1008. [CrossRef]
23. Melillo, M.; Brunetti, M.T.; Peruccacci, S.; Gariano, S.L.; Roccati, A.; Guzzetti, F. A tool for the automatic calculation of rainfall thresholds for landslide occurrence. *Environ. Model. Softw.* **2018**, *105*, 230–243. [CrossRef]

24. Jordanova, G.; Gariano, S.L.; Melillo, M.; Peruccacci, S.; Brunetti, M.T.; Auflič, M.J. Determination of Empirical Rainfall Thresholds for Shallow Landslides in Slovenia Using an Automatic Tool. *Water* **2020**, *12*, 1449. [CrossRef]
25. Distefano, P.; Peres, D.; Scandura, P.; Cancelliere, A. Brief communication: Rainfall thresholds based on Artificial neural networks can improve landslide early warning. *Nat. Hazards Earth Syst. Sci.* **2021**, *22*, 1–9.
26. Cai, J.; Zhang, Y.; Li, Y.; Liang, X.S.; Jiang, T. Analyzing the Characteristics of Soil Moisture Using GLDAS Data: A Case Study in Eastern China. *Appl. Sci.* **2017**, *7*, 566. [CrossRef]
27. Shuang, H.; Xia, L.; Jason, G.; Haitong, T.; Qin, Y.; Kaiyue, L.; Haozhou, D.; Chungqi, C.; Nizhuan, W. RSI-Net: Two-Stream Deep Neural Network for Remote Sensing Images-Based Semantic Segmentation. *IEEE Access.* **2022**, *10*, 34858–34871. [CrossRef]
28. Youliang, C.; Xiangjun, Z.; Hamed, K.; Gang, X.; Jinsong, H. A novel framework for prediction of dam deformation based on extreme learning machine and Lévy flight bat algorithm. *J. Hydroinform.* **2021**, *23*, 935–949. [CrossRef]
29. Tang, H.; McGuire, L.A.; Rengers, F.K.; Kean, J.W.; Staley, D.M.; Smith, J.B. Developing and testing physicallybased triggering thresholds forrunoff-generated debris flows. *Geophys. Res. Lett.* **2019**, *46*, 8830–8839. [CrossRef]
30. Chiang, J.-L.; Kuo, C.-M.; Fazeldehkordi, L. Using Deep Learning to Formulate the Landslide Rainfall Threshold of the Potential Large-Scale Landslide. *Water* **2022**, *14*, 3320. [CrossRef]
31. Abraham, M.T.; Satyam, N.; Kushal, S.; Rosi, A.; Pradhan, B.; Segoni, S. Rainfall Threshold Estimation and Landslide Forecasting for Kalimpong, India Using SIGMA Model. *Water* **2020**, *12*, 1195. [CrossRef]
32. Nam, D.H.; Lee, S.H.; Kim, M.I.; Kim, B.S. Calculation of Rainfall Triggering Index (RTI) to Predict the Occurrence of Debris Flow. *J. Eng. Geol.* **2018**, *28*, 47–59.
33. Lee, J.S.; Kang, H.S.; Suk, J.W.; Kim, Y.T. Development of Hazard Level-based Rainfall Threshold for Prediction of Rainfall-induced Landslide Occurrence in Korea. *J. Korean Soc. Hazard Mitig.* **2019**, *19*, 225–236. [CrossRef]
34. Pruccacci, S.; Brunetti, M.T.; Luciani, S.; Vennari, C.; Guzzetti, F. Lithological and seasonal control on rainfall thresholds for the possible initiation of landslides in central Italy. *Geomorphology* **2012**, *139–140*, 79–90. [CrossRef]
35. Choi, J.R.; An, S.W.; Choo, K.S.; Kim, D.H.; Lim, H.K.; Kim, B.S. Development of An Automatic Calculation Algorithm for Rainfall Thresholds of Debris Flow in Korea. *J. Korean Soc. Hazard Mitig.* **2022**, *22*, 113–123. [CrossRef]

water

MDPI

Research on Spatial Distribution Pattern of Stability Inter-Controlled Factors of Fine-Grained Sediments in Debris Flow Gullies—A Case Study

Qinjun Wang [1,2,3,4,5,*], **Jingjing Xie** [1,2,3], **Jingyi Yang** [1,2,3], **Peng Liu** [1,2,3], **Wentao Xu** [1,2,3] **and Boqi Yuan** [1,2,3]

[1] International Research Center of Big Data for Sustainable Development Goals, Beijing 100094, China; xiejingjing19@mails.ucas.ac.cn (J.X.); yangjingyi211@mails.ucas.ac.cn (J.Y.); liup@aircas.ac.cn (P.L.); 07182642@cumt.edu.cn (W.X.); yuanboqi23@mails.ucas.ac.cn (B.Y.)

[2] Key Laboratory of Digital Earth Science, Aerospace Information Research Institute, Chinese Academy of Sciences, Beijing 100094, China

[3] University of Chinese Academy of Sciences, Yanqi Lake Campus of Chinese Academy of Sciences University, Beijing 101408, China

[4] Key Laboratory of the Earth Observation of Hainan Province, Hainan Aerospace Information Research Institute, Sanya 572029, China

[5] Kashgar Zhongke Aerospace Information Research Institute, Kashgar 844199, China

[*] Correspondence: wangqj@radi.ac.cn

Abstract: Studies on the stability inter-controlled factors of fine-grained sediments in debris flow gullies play an important role in predicting the scale and danger of debris flows. However, up to the present, few studies have been carried out on the spatial distribution pattern and causes of stability inter-controlled factors of fine-grained sediments in debris flow gullies, leading to difficulty in finding the dangerous section of debris flow gullies to be monitored and controlled to reduce disaster losses. Therefore, the objective of this paper is to analyze the spatial distribution pattern and causes of stability inter-controlled factors (grain size, permeability coefficient, shear strength, and porosity), taking the Beichuan Debris Flow Gully, China, as a case. After collecting soil samples in the field, we carried out experiments to measure the stability inter-controlled factors and, from these, the results show that (1) fine-grained sediments in this case are mainly silty loams, which are stable under non-heavy rains; (2) the grain size of silty loams is mainly concentrated between 10 and 20 μm, with a spatial distribution pattern of fine in the middle and coarse at both ends; (3) the permeability coefficient of silty loams is concentrated between 1.15 and 2.17 m/d, with a spatial distribution pattern of high in the middle and low at both ends; (4) the average cohesion of silty loams is mainly concentrated between 20 and 30 kPa, with a spatial distribution pattern of low in the middle and high at both ends; and (5) the internal friction angle of silty loams is concentrated between 18.98 and 21.8°, with a spatial distribution pattern of high in the middle and low at both ends. The main reasons for these spatial distribution patterns are analyzed from three aspects of shear strength, water flow velocity, and terrain, which can provide a scientific basis for the prediction of debris flow disasters in such areas.

Keywords: debris flow gully; fine-grained sediments; soil stability; inter-controlled factors; Beichuan; particle size

1. Introduction

In recent years, due to the comprehensive impacts of tectonic activities and climate change, the frequency and scale of debris flow disasters have increased, causing serious impacts on people's lives and property, and have attracted a lot of attention from countries and scholars to carry out research.

The effects of slope on water flow, the influence of material composition and grain size distribution on the initiation conditions of debris flows [1–5], and the disaster mechanisms were studied from the aspects of material source characteristics [6–8], rainfall conditions [9–12], terrain and geomorphic conditions [13], tectonic activities [14], etc. Based on these, debris flow initiation models were established, such as mathematical modeling [15] and hydrodynamic models [16–18].

Debris-flow-influencing factors and their relationships with the outflow, disaster chains, and principles of lateral erosion were studied, such as relationships between maximum runout amount and risk-assessment-influencing factors [19–22]. Based on these, models for danger sensing and prediction for debris flows were established, such as critical rainfall patterns [23], gully formation types [24], and hazard assessment and prevention models [25–29].

Based on three disaster modes (channel blocked, channel undercut, and landslide recharged), plans for disaster prevention and control were proposed, such as sediment mitigation measures [30], and hazard source analysis and prevention were based on hazard assessment and formation mechanism analysis [31–36].

As we know, during the initiation, transportation, and aggregation of debris flow, fine-grained sediments (quaternary sediments with a grain size of less than 2 mm) in debris flow gullies play a starring role, increasing the density, amplifying the danger of debris flows, and thus increasing the difficulty of debris flow prevention and control. Therefore, strengthening the research on stability inter-controlled factors of fine-grained sediments in debris flow gullies plays an important role in predicting the scale and danger of debris flows.

The stability inter-controlled factors of fine-grained sediments mainly include grain size, permeability coefficient, shear strength, and porosity. Grain size refers to the particle diameter of sediments; the permeability coefficient is the unit flow rate under a unit hydraulic gradient; shear strength refers to the ultimate strength of soil to resist shear failure, which includes cohesion and effective internal friction angle; and porosity is the percentage of soil pores per unit volume.

There are some studies on fine-grained sediments in debris flow gullies: (1) erosion characteristics [37], hydrodynamic conditions [38], and grain size distribution characteristics of sediments were studied [39], and (2) the relationship between permeability coefficient and its influencing factors [40], as well as that between cohesion and its influencing factors, was analyzed [41]. Based on these, hyperspectral detection models for cohesion [42] and permeability coefficient were also established [43], and (3) the permeability characteristics and transport principles of channel sediments were summarized, and a start-up model for loose sediments was established [44].

However, up to the present, there is no research on the spatial distribution pattern and causes of the stability inter-controlled factors of fine-grained sediments in debris flow gullies, resulting in difficulty in locating dangerous river sections for prevention. Therefore, the objective of this paper is to analyze the spatial distribution pattern and causes of the stability inter-controlled factors. According to this, we can find unstable river sections for debris flow disaster prevention.

2. Study Area

As shown in Figure 1, the study area is located in Laobeichuan County, Sichuan Province, China, with geographic coordinates of 104°14′–104°33.5′ E, 31°47.9′–31°53.5′ N, covering an area of 341 km^2. It belongs to a subtropical humid monsoon climate zone, with an annual average temperature of 15.6 °C and an annual average rainfall of 1399.1 mm. Of this, 70% of the annual rainfall is concentrated from June to September [11,34]. The strata of the study area mainly include the Dengying strata from the Upper Sinian, the Qingping strata from the Lower Cambrian, the Maoxian Group from the Upper and Middle Silurian, and the Quaternary sediments. In these, the main rock types include dark gray

siltstone, siliceous rock, phosphorous mudstone, phosphorous limestone, phyllite, slate, schist, limestone, sand shale, and sandy soils [13].
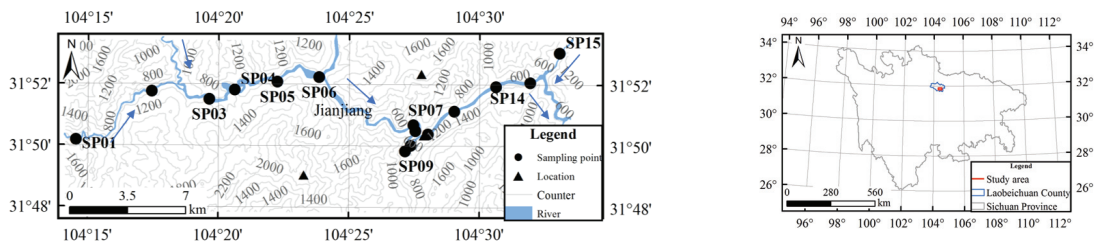

Figure 1. Map of the study area (**left**), the blue arrow indicates the direction of water flow) with location in Sichuan Province (**right**).

The main lithology in the study area indicates that most of the metamorphic rocks, marls, and Quaternary sediments have poor stability and could easily form debris flows. Especially, the Wenchuan earthquake with MS8.0 magnitude on 12 May 2008 caused severe strata fragmentation, resulting in a large number of loose sediment events like landslides, landslips, etc. Under the triggering of heavy rainfall, multiple serious debris flow disasters occurred on 20 August 2019, 11 July 2018, 28 July 2016, etc. They not only destroyed farmlands, roads, and bridges but also broke power and communication facilities, causing significant economic losses and posing a serious threat to the residential settlements [28].

3. Data and Equipment

As shown in Table 1, the Gaofen-2 (GF-2) remote sensing image covering the study area is first acquired with the highest spatial resolution of 0.8 m. Using this, the locations of fine-grained sediments in the debris flow gully are extracted (SP01–SP15 sampling points in Figure 1). Then, the DEM data are acquired to analyze elevation of the study area. Finally, after the debris flow disaster on 20 August 2019, 200 soil samples were obtained from 15 sampling points using a ring cutter between 19 and 25 March 2021 and the number of samples at each sampling points is shown in Table 2. Each sample has a volume of 600 mL and a weight of about 1 kg. With a diameter of 7 cm and a depth of 5.2 cm, the volume of the ring knife is 200 mL. Using this, the sampling procedure for a soil sample is as follows: ① clean the ring knife using a soft cloth; ② put it into the sediment vertically. When it is full of soil, pull it out and cut off the over-flowing soil with a knife. Thus, a soil sample with a volume of 200 mL is collected; ③ put the soil sample into a plastic bag and seal it immediately. After collecting three soil samples in the same plastic bag according to the above steps, seal the plastic bag and consider it as a sample with a volume of 600 mL and put it into a cotton bag; ④ record the sample number and its geographical location using a global positioning system (GPS) and write the sample number on the cloth sample bag with a marker [43].

Table 1. Data and equipment table.

Materials	Equipment	Manufacturer/Provider
Remote sensing images	Gaofen-2 (GF-2)	Land satellite remote sensing application center, Beijing, China
Digital elevation model (DEM)	Advanced Spaceborne Thermal Emission and Reflection Radiometer (ASTER)	Ministry of International Trade and Industry, Tokyo, Japan
Soil	Ring knife (200 mL)	Longnian Hardware Tools Store, Suqian, China
Particle size	Mhcrotra-S3500	Microtrac MR B, Montgomeryville, PA, USA

Table 1. *Cont.*

Materials	Equipment	Manufacturer/Provider
Permeability coefficient	TST-55 permeameter	Zhejiang Dadi Instrument Co., Ltd., Shaoxing, Zhejiang, China
Density	MDJ-300A solid densitometer	Shanghai Lichen Instrument Technology Co., Ltd., Shanghai, China
Porosity	TST-55 permeameter	Zhejiang Dadi Instrument Co., Ltd., Shaoxing, Zhejiang, China
Shear strength	ZJ strain-controlled direct shear instrument	Nanjing soil instrument factory Company Limited (Co., Ltd.), Nanjing, Jiangsu, China

Table 2. Number of samples at each sampling points.

Sampling Points	Number	Sampling Points	Number
SP01	20	SP09	20
SP02	15	SP10	10
SP03	15	SP11	10
SP04	15	SP12	10
SP05	20	SP13	10
SP06	15	SP14	10
SP07	10	SP15	10
SP08	10		
Total			200

Based on these steps, experiments are carried out to measure density, grain size, permeability coefficient, and shear strength of samples.

4. Methodology

The flow chart for studying stability inter-controlled factors of fine-grained sediments is shown in Figure 2. On the basis of obtaining remote sensing, DEM, and geological background data of the study area, experiments are carried out to measure the stability inter-controlled factors, such as grain size, permeability coefficient, shear strength, and porosity. Based on these, the spatial distribution patterns of stability inter-controlled factors of fine-grained sediments are summarized, and the risk of debris flow disasters is analyzed to provide a scientific basis for the prevention and control of geological disasters in the study area.

4.1. Grain Size Measurement

Grain size refers to the particle diameter, which has some impacts on the porosity and permeability coefficient of fine-grained sediments, thereby controlling the sediment stability. We use the Microtrac S3500 laser analyzer to measure the grain size of the sediments whose main steps and results can be found in [43]. The results indicate that the grain size of fine-grained sediments in the study area is mainly concentrated between 10 and 20 μm, belonging to the silty loams [45]. The average grain size of each sampling point is shown in Figure 3, showing a spatial distribution pattern of fine in the middle and coarse at both ends.

4.2. Permeability Coefficient Measurement

The permeability coefficient, also known as the hydraulic conductivity coefficient, is the unit flow rate under a unit hydraulic gradient. It mainly reflects the size, number, and connectivity of soil pores [46], and is the main parameter controlling the stability of fine-grained sediments. The permeability coefficient of fine-grained sediments in the study area is measured using a TST-55 permeability meter, whose process and results are shown in [40]. The permeability coefficients of most fine-grained sediments in the study area are concentrated between 1.15 and 2.17 m/d, which can be classified as medium permeability

and stable in the case of non-heavy rains. The average permeability coefficient of each sampling point is shown in Figure 4, showing a spatial distribution pattern of high in the middle and low at both ends.
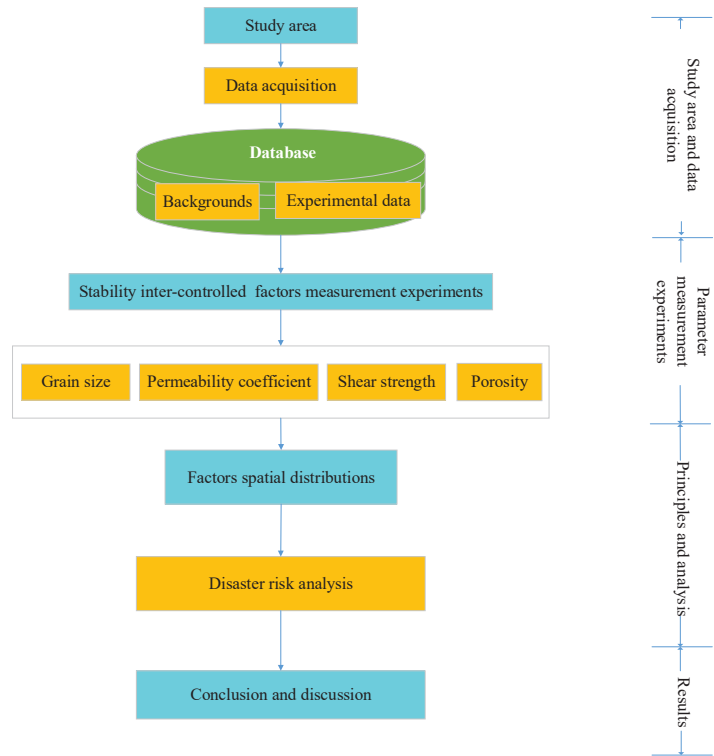

Figure 2. Flow chart for studying the spatial distribution pattern of stability inter-controlled factors of fine-grained sediments in debris flow gullies.
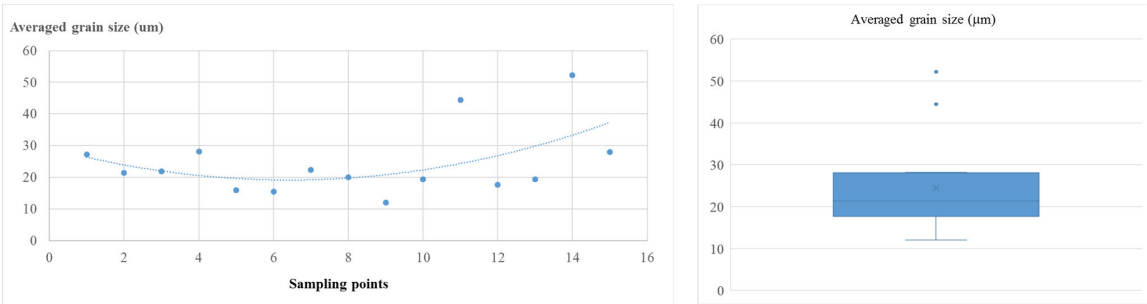

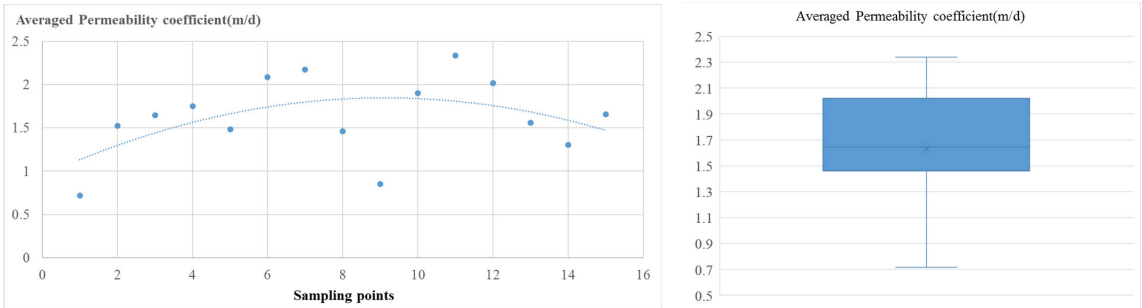**Figure 3.** Average grain size distribution pattern of fine-grained sediments (**left**) and its box–whisker plot (**right**).

Figure 4. Distribution pattern of the average permeability coefficient of fine-grained sediments (**left**) and its box–whisker plot (**right**).

4.3. Shear Strength Measurement

Including cohesion and effective internal friction angle, shear strength refers to the ultimate strength of soil to resist shear failure, which is an important parameter to measure stability of fine-grained sediments. Cohesion is the mutual attraction between adjacent parts within the same substance; the effective internal friction angle indicates the magnitude of internal friction between soil particles, including the surface friction forces and the biting forces generated by the embedding and interlocking between soil particles. To measure the cohesion and effective internal friction angle of fine-grained sediments in the study area, a ZJ strain-controlled direct shear instrument is used, whose steps and results are shown in [43]. As shown in Figure 5, the average cohesion is mainly concentrated between 20 and 30 kPa with a spatial distribution pattern of low in the middle and high at both ends. On the other hand, as shown in Figure 6, the internal friction angle is concentrated between 18.98 and 21.8° with a spatial distribution pattern of high in the middle and low at both ends.
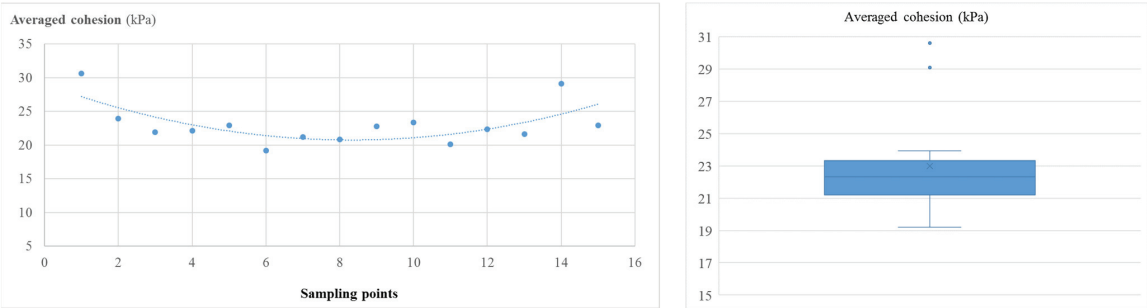

Figure 5. Spatial distribution pattern of averaged cohesion of fine-grained sediments (**left**) and its box–whisker plot (**right**).

4.4. Porosity Measurement

Porosity is the percentage of soil pores per unit volume, which is the space for water movement and storage, and the key factor influencing soil permeability and thus determining surface runoff rate. The steps and results of measuring porosity using a TST-55 permeameter can be found in [43]. The porosity of fine-grained sediments in the study area is mainly concentrated between 52 and 68%, belonging to the medium to high porosity. The average porosity of each sampling point is shown in Figure 7. The average porosity is relatively high at SP09.
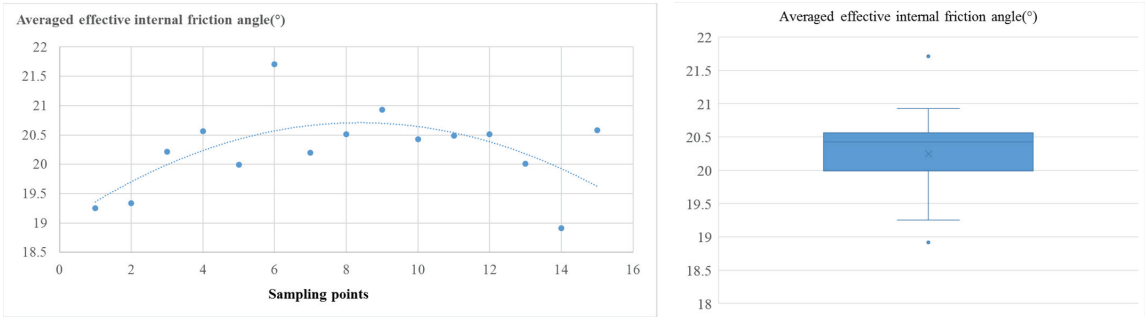
Figure 6. Spatial distribution pattern of averaged internal friction angle of fine-grained sediments (**left**) and its box–whisker plot (**right**).
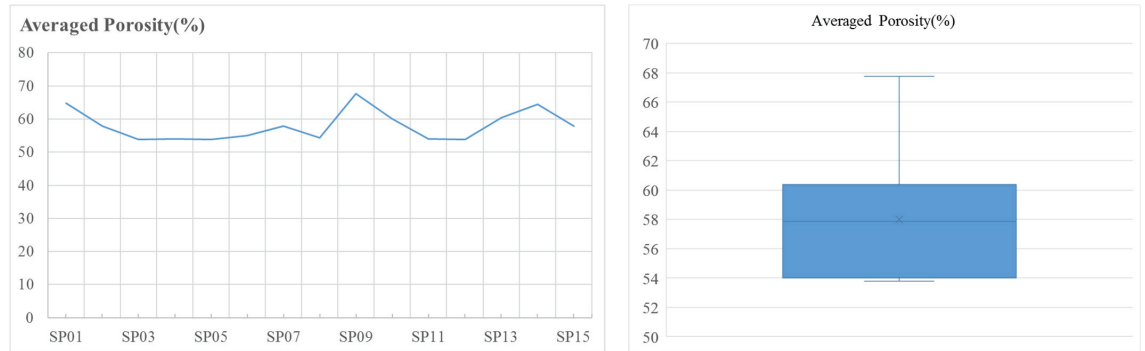

Figure 7. Spatial distribution pattern of averaged porosity of fine-grained sediments (**left**) and its box–whisker plot (**right**).

5. Results

Based on the variation characteristics of grain size, permeability coefficient, cohesion, and internal friction angle of fine-grained sediments along the Jianjiang River (Figures 3–7), the sampling points are divided into three sections: upstream (SP01–SP05), midstream (SP06–SP12), and downstream (SP13–SP15). Their characteristics are summarized as follows.

In the upstream (SP01–SP05), (1) the fine-grained sediments are mainly composed of silty loams, with an average grain size of 22.94 μm, and a downward trend from SP01 to SP05; (2) the average permeability coefficient is 1.42 m/d, belonging to medium permeability and showing an upward trend from SP01 to SP05; (3) the average cohesion is 24.3 kPa, showing a decreasing trend from SP01 to SP05 (Figure 5), and the average internal friction angle is 19.87°, showing an upward trend from SP01 to SP05 (Figure 6); (4) the cumulative distribution pattern of grain size (Figure 8) shows inflection points at 10, 20, and 30 μm, indicating poor sorting characteristics. On-site photos (SP01–SP05, Figure 8) also confirm the above conclusion: soils at SP01 are in a plate condensed state with the characteristics of high cohesion and strong erosion resistance. However, the following photos of SP02–SP05 show that the sediments are loosely accumulated, indicating low cohesion and high permeability. Therefore, for SP01 to SP05, we draw a conclusion that the soil's ability to resist water flow erosion becomes strong to weak, resulting in the risk of debris flow disasters becoming weak to strong.
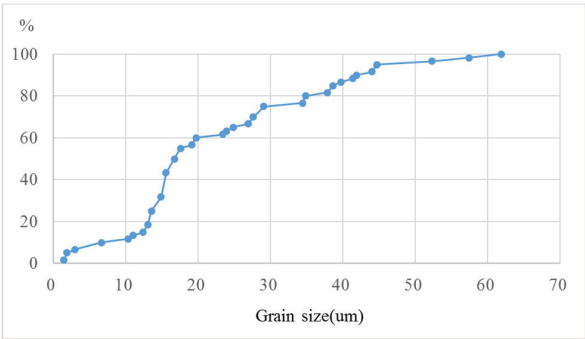
Grain size cumulative distribution curve of SP01–SP05

Photo of SP01 (No. 567)

Photo of SP02 (No. 563)
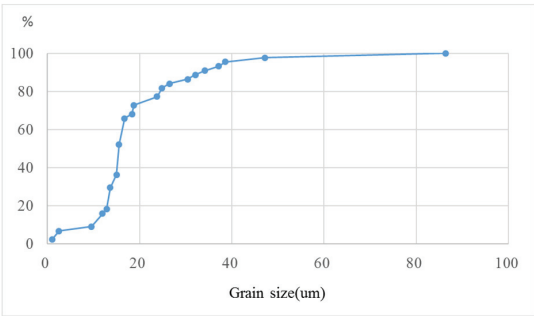

Photo of SP03 (No. 560)

Photo of SP04 (No. 557)

Photo of SP05 (No. 553)

Zoomed-in image of SP01 (No. 567)

Figure 8. Cumulative grain size distribution curve and field photos of fine-grained sediments in upstream river (SP01–SP05).

In the midstream (SP06–SP12), the fine-grained sediments are mainly composed of silty loams. (1) The average grain size of the sediments in this section is 17.83 μm. Except for the coarse grain size at SP11, grain sizes at other points are almost the same and distributed horizontally (Figure 3). The cumulative distribution curve indicates the distribution of grain size in this section concentrates between 10 and 40 μm with good sorting; (2) the average permeability coefficient of the sediments in this section is 1.83 m/d, belonging to medium permeability (Figure 4); (3) the average cohesion of the sediments in this section is 21.4 kPa with an averaged internal friction angle of 20.68°. Except for the high internal friction angle at SP06, internal friction angles at other points are horizontally distributed (Figure 6). On-site photos (SP06–SP12, Figure 9) also confirm the above conclusion: the silty loams in this section are in a loose accumulation state with fine grain size, high moisture content, good sorting, and relatively poor erosion resistance, leading to increased instability of the sediments and the high risk of debris flow disasters.
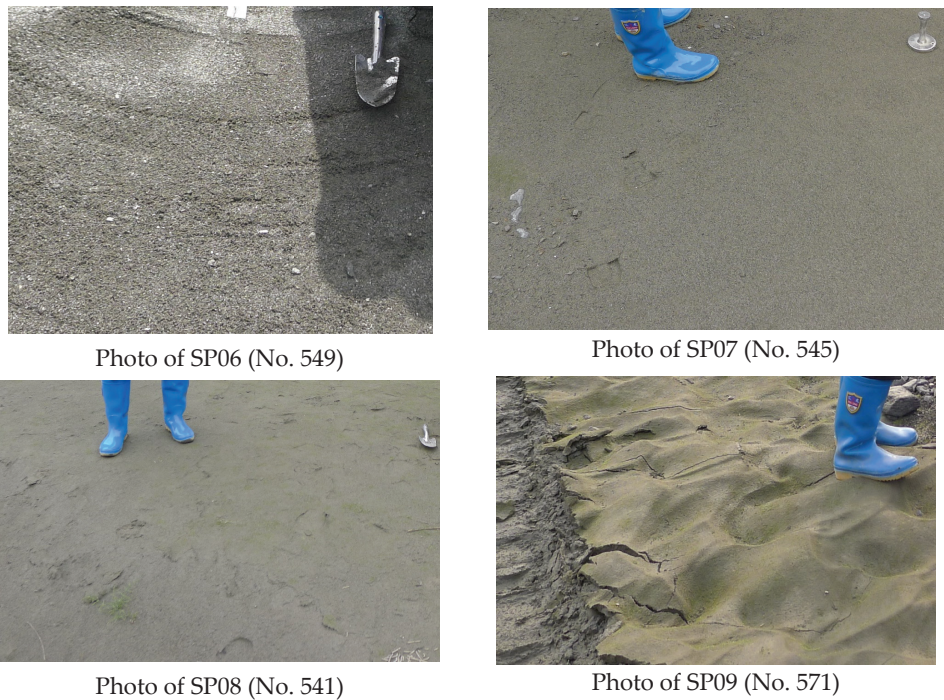

Grain size cumulative distribution curve of SP06–SP12

Photo of SP06 (No. 549)

Photo of SP07 (No. 545)

Photo of SP08 (No. 541)

Photo of SP09 (No. 571)

Figure 9. *Cont.*

Photo of SP10 (No. 536)

Photo of SP11 (No. 516)

Photo of SP12 (No. 518)

Zoomed-in image of SP08 (No. 541)

Figure 9. Cumulative grain size distribution curve and field photos of fine-grained sediments in midstream river (SP06-SP12).

In the downstream (SP13–SP15), the fine-grained sediments are mainly composed of silty loams, with an average grain size of 33.23 μm. (1) Compared to the sediments in the upstream and midstream, their grain size is coarser and gradually increases from SP13 to SP15 (Figure 3). The cumulative distribution curve of grain size in the downstream shows that, except for a sharp increase at 22 μm, the grain size of the sediments is concentrated from 10 to 52 μm, indicating the general sorting characteristics (Figure 10); (2) the average permeability coefficient of the sediments is 1.51 m/d, belonging to medium permeability, showing a gradually decreasing trend from SP13 to SP15 (Figure 4); (3) the average cohesion of the sediments is 24.53 kPa, showing an upward trend from SP13 to SP15 (Figure 5), and the average internal friction angle is 19.83° and, except for the high internal friction angle at SP15, it shows a decreasing trend (Figure 6). The on-site photos (SP13–SP15, Figure 10) also confirm the above conclusion: the silty loams in this section are in a loose accumulation state with low water content, coarse sand particles filled with clays, average sorting, and relatively strong erosion resistance, which increases the sediment stability and thus reduces the risk of debris flow disasters.
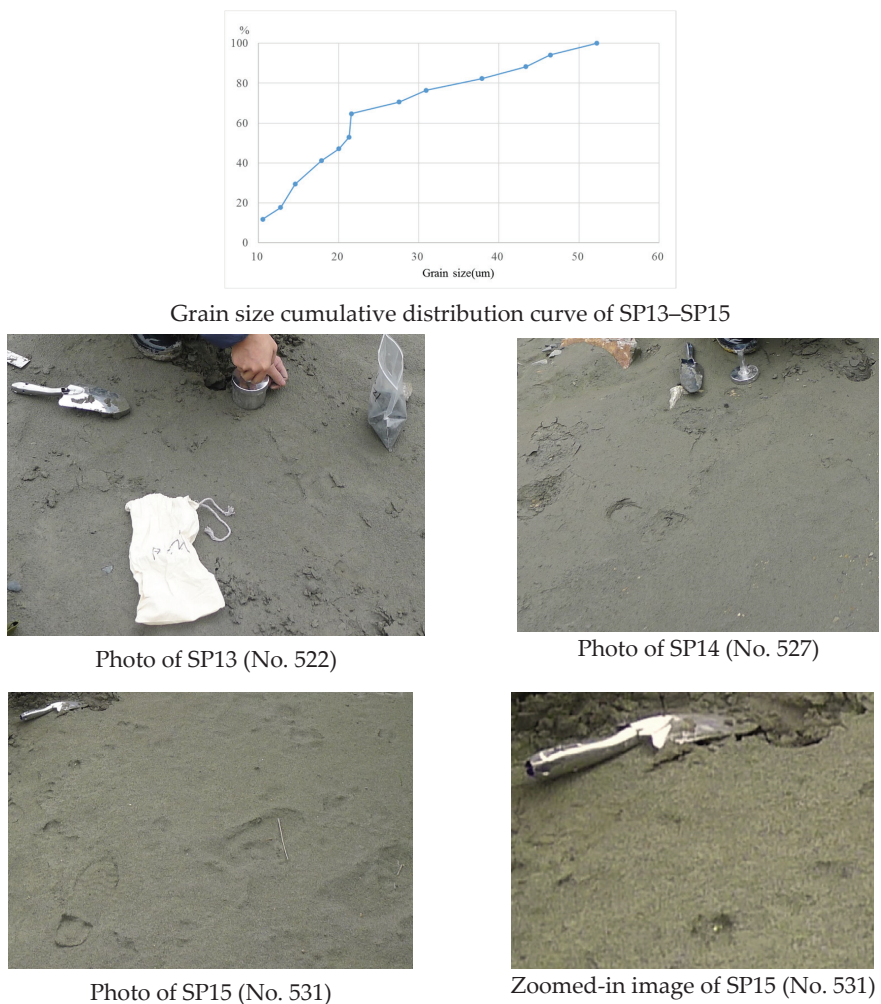
Grain size cumulative distribution curve of SP13–SP15

Photo of SP13 (No. 522)

Photo of SP14 (No. 527)

Photo of SP15 (No. 531)

Zoomed-in image of SP15 (No. 531)

Figure 10. Cumulative grain size distribution curve and field photos of fine-grained sediments in downstream river (SP13–SP15).

6. Discussion

Reasons for the results are discussed as follows.

In the upstream (SP01–SP05), compared to midstream (SP06–SP12), this section has the characteristics of low permeability coefficient, low effective internal friction angle, and high cohesion. Reasons for this phenomenon are mainly because it is located in the upstream river and easily eroded due to the water flow, tributary effect, elevation difference between this section and its surroundings, etc. The relatively fine-grained sediments are carried to the middle and downstream of the river, thus depositing relatively coarse-grained sediments. Clay minerals can easily fill in the large pores between coarse particles, resulting in relatively poor sorting of the sediments in this section with low permeability coefficient, low effective internal friction angle, and high cohesion. From these, we can see that the risk of debris flow disasters becomes weak to strong from SP01 to SP05 and the outbreak of debris flow is the result of the comprehensive effects of sediment seepage field and stress field: ① the permeability coefficient is the main parameter of the sediment seepage field. The seepage field is not only a storage environment but also a component of sediments.

Sediments with high permeability coefficients are prone to let water infiltrate to the bottom, increasing their own gravity and forming pore water pressure to break the sediment stability, thereby increasing the probability of debris flow disasters. The permeability coefficient shows an upward trend from SP01 to SP05 and the risk of debris flow disasters becomes weak to strong from SP01 to SP05. ② Shear strength is the main parameter of sediment stress field. When the shear stress meets the maximum shear strength of the sediments, they collapse and then slide with the water flow, resulting in debris flow disasters. Sediments with high shear strength have strong cohesion, high stability, and are less prone to erosion, thus providing fewer material sources for debris flow disasters. On the contrary, sediments with low shear strength can provide more material sources, resulting in a larger scale and more dangerous debris flow disaster. Cohesion shows a decreasing trend from SP01 to SP05, and the risk of debris flow disasters becomes weak to strong.

In the midstream (SP06–SP12), compared to upstream and downstream, sediments in this section have the characteristics of high permeability coefficient, high effective internal friction angle, and low cohesion. The main reason for this phenomenon is that the terrain of this section is relatively low and the river channels are winding with high curvature: the low river terrain in the high surrounding mountain terrain results in the accumulation of water during the rainy season, leading to a large water supply and causing severe soil erosion. Based on this, the high-density debris flow forms from west to east. At the same time, this section is also blocked by its high curvature, especially the highest curvature from SP07 to SP09, resulting in a severe decrease in water flow velocity, which weakens the river's sand-carrying capacity and makes it easily form good sorting sediments. Therefore, compared to the sediments in the upstream and downstream, the silty loams in this section have the characteristics of finer grain size and better sorting with high permeability coefficient, high effective internal friction angle, and low cohesion, and thus leading to high instability of sediments. So, the risk of debris flow disasters in this section is relatively high and thus needs more attention to monitor and control it, especially from SP07 to SP09 with the highest curvature.

In the downstream (SP13–SP15), compared to the sediments in the midstream, the sediments in this section show the characteristics of coarse grain size, low permeability coefficient, low effective internal friction angle, and high cohesion. The main reason for this phenomenon is mainly that there is a significant elevation difference between this section and its surroundings, resulting in high water flow speed with strong sediment-transporting capacity. Fine-grained sediments are transported far, while the coarse-grained sediments are left here, which are prone to adsorb clay particles, and thus resulting in low permeability coefficient, low effective internal friction angle, and high cohesion. According to poor conditions of low permeability coefficient and high cohesion, the risk of debris flow disasters happening in this section is relatively low.

As to the spatial distribution pattern of the stability inter-controlled factors of fine-grained sediments in the whole debris flow gully, we can discuss it as follows.

The average grain size of fine-grained sediments in the study area is relatively coarse with poor sorting in the upstream and downstream river, while it is relatively fine with good sorting in the midstream. The reason for this phenomenon is that the finer the grain size of sediments is, the farther they can be transported. Therefore, in general, rivers always show a characteristic of coarse to fine grain size from upstream to downstream. However, in this study area, due to the impact of high curvature in the middle stream, the water flow velocity slows down, which decreases the sand-carrying capacity, thus forming a sedimentary environment to make the sediments deposit with the characteristics of fine grain, good sorting, and high permeability coefficient.

The average permeability coefficient is relatively low in the upstream and downstream river and high in the middle. This is mainly related to the sediment properties: the grain size of the upstream and downstream sediments is heterogeneous and fine-grained particles are easily adsorbed among coarse-grained ones, resulting in pore blockage and thereby reducing their permeability coefficients. Meanwhile, the grain size of the sediments in the

midstream river is relatively uniform, with good sorting and independent space between particles, thus leading to relatively large porosity and good permeability coefficient.

At 22.99 kPa, the average cohesion of the whole gully has a medium to low level with poor stability [47], which is relatively high in the upstream and downstream and low in the midstream. Therefore, it is prone to erosion and transportation, resulting in the formation of debris flows and thus needing to be monitored and controlled with more attention in the midstream river.

Based on sedimentology, the main reasons for the spatial distribution of the stability inter-controlled factors of fine-grained sediments in debris flow gullies are discussed as follows.

The first reason is shear strength. Sediments with high shear strength have strong cohesion, are not easily eroded, and thus have a high stability and a short transporting distance in rivers, making them form coarse-grained sediments with poor sorting. On the contrary, sediments with low shear strength have lower stability and longer transporting distances in rivers, making them easily form fine-grained sediments with good sorting.

The second reason is water flow velocity. The water flow velocity determines the erosion and transporting capacity of a river. Under the same conditions, the faster the velocity of the water flow is, the higher the erosion ability and the stronger the carrying capacity of the rivers. The grain size of sediments is relatively coarse, with poor sorting and low permeability coefficient. On the contrary, the slower the water flow velocity is, the weaker the transporting capacity of the river becomes, and the easier it is to form a sedimentary environment. The grain size of sediments becomes finer and the permeability coefficient becomes higher. This also explains why the sediments from SP07–SP09 show finer grain size with higher permeability coefficient: due to the high curvature of the river in this section, the water flow velocity slows down. Sediments transported from upstream are prone to deposit, leading to the formation of fine-grained sediments with good sorting and high permeability coefficient.

The third reason is terrain. As we know, terrain controls potential energy and water flow velocity, thereby controlling the degree and scope of sediment erosion and thus controlling the danger of debris flow disasters. Under the same rainfall, the steeper the terrain is, the faster the water flow on the surrounding slopes becomes, thus resulting in stronger erosion ability, which generates more sources of sediments with longer transporting distances. On the contrary, the gentler the terrain is, the fewer material sources are generated and the shorter the sediments' transport. Therefore, terrain also controls the spatial distribution pattern of the sediments.

7. Conclusions

In this study, the spatial distribution patterns of stability inter-controlled factors of fine-grained sediments in debris flow gullies are first summarized. Then, a relationship between stability inter-controlled factors of fine-grained sediments and outbreak probability of debris flow disasters is discussed.

(1) The spatial distribution pattern of stability inter-controlled factors of fine-grained sediments in debris flow gullies is summarized.

We have summarized the spatial distribution characteristics of stability inter-controlled factors (grain size, permeability coefficient, and shear strength) of fine-grained sediment in the upstream, midstream, and downstream river: ① the average grain size of fine-grained sediments in the study area is 24.39 μm, belonging to silty loams. In space, it is characterized by relatively coarse grain size and poor sorting in the upstream and downstream river, and the grain size of sediments in the midstream river is relatively fine with good sorting; ② the average permeability coefficient of silty loams in the study area is 1.63 m/d, which can be classified as medium permeability. In space, it is relatively low in the upstream and downstream river and relatively high in the midstream river; ③ the average effective internal friction angle of silty loams in the study area is 20.24°, being a medium to low effective internal friction angle. In space, it is relatively low in the

upstream and downstream river and high in the midstream river. On the other hand, the average cohesion of silty loams in the study area is 22.99 kPa, belonging to the low cohesion level. In space, it is relatively high in the upstream and downstream river and low in the midstream river.

(2)   A relationship between stability inter-controlled factors of fine-grained sediments and outbreak probability of debris flow disasters has been discussed.

The outbreak of debris flow is the result of the comprehensive effects of sediment seepage field and stress field. Sediments with high stability (low permeability coefficient and high shear strength) are less prone to erosion, thus providing fewer material sources and forming a less dangerous debris flow disaster. On the contrary, sediments with low stability (high permeability coefficient and low shear strength) can provide more material sources to form a larger-scale and more dangerous debris flow disaster.

Author Contributions: Conceptualization, Q.W. and J.X.; methodology, Q.W., J.X., J.Y. and P.L.; validation, Q.W., J.X. and P.L.; formal analysis, Q.W. and J.X.; investigation, Q.W., J.X., P.L., W.X. and B.Y.; data curation, J.X., J.Y. and P.L.; writing—original draft preparation, Q.W., J.X. and J.Y.; writing—review and editing, Q.W.; visualization, W.X.; supervision, B.Y.; project administration, Q.W.; funding acquisition, Q.W. All authors have read and agreed to the published version of the manuscript.

Data Availability Statement: Data are contained within the article.

Conflicts of Interest: The authors declare no conflicts of interest.

References

1.   Qu, Y. The research on the Dynamic Characteristics of Urgent Steep-channel Debris Flows in Meizoseismal Area. Ph.D. Thesis, Chengdu University of Technology, Chengdu, China, 2016. Available online: https://kns.cnki.net/KCMS/detail/detail.aspx?dbname=CDFDLAST2020&filename=1019216954.nh (accessed on 1 October 2023).
2.   Li, Z. Study on the characteristics and outthrust of debris flow in steep gully in earthquake region. Master's Thesis, Chengdu University of Technology, Chengdu, China, 2019. Available online: https://kns.cnki.net/KCMS/detail/detail.aspx?dbname=CMFD202001&filename=1019216296.nh (accessed on 1 October 2023).
3.   Qi, X.; Yu, B.; Zhu, Y. Experimental Study on the clastic deposition forming Debris Flow. *J. Jilin Univ.* **2014**, *44*, 1950–1959. [CrossRef]
4.   Suo, W. Study on the Grain-size Distribution for Initiation and Catastrophe Mechanism of Slag-type Debris Flow. Master's Thesis, Chang'an University, Xi'an, China, 2019. Available online: https://kns.cnki.net/KCMS/detail/detail.aspx?dbname=CMFD202001&filename=1019674844.nh (accessed on 1 October 2023).
5.   Fan, S. Solid Source Characteristics and Early Warning of Debris Flow in Zhouqu. Ph.D. Thesis, Lanzhou University, Lanzhou, China, 2018. Available online: https://kns.cnki.net/KCMS/detail/detail.aspx?dbname=CDFDLAST2018&filename=1018829194.nh (accessed on 1 October 2023).
6.   Xiong, K. Study on Material Erosion Characteristics of Loose Accumulation on Slope after Jiuzhaigou Earthquake. Master's Thesis, Chengdu University of Technology, Chengdu, China, 2021. Available online: https://kns.cnki.net/KCMS/detail/detail.aspx?dbname=CMFD202301&filename=1022671932.nh (accessed on 1 October 2023).
7.   Zhang, Z. Study On Erosion and Initiation Characteristics of Debris Flow Deposition Under the Influence of Rainfall and Over-dam Flow: A Case Study of Chutou Gully, Wenchuan, Sichuan. Master's Thesis, JiLin University, Changchun, China, 2022. Available online: https://kns.cnki.net/KCMS/detail/detail.aspx?dbname=CMFD202202&filename=1022529781.nh (accessed on 1 October 2023).
8.   Gu, W. Study on Provenance Characteristics and Initiation Mechanism of Debris Flows in Meizoseismal Areas of Wenchuan Earthquake—Taking Study Areas, Gaochuan Village, Qingping Village and Yinxiu Town as Example. Master's Thesis, Chengdu University of Technology, Chengdu, China, 2015. Available online: https://kns.cnki.net/KCMS/detail/detail.aspx?dbname=CMFD201601&filename=1015312750.nh (accessed on 1 October 2023).
9.   Yang, F.; Zhou, H.; Huo, M.; Cao, H.; Liang, Y.; Lin, K. Rainfall Induced Debris Flow Characteristics and Mechanisms of Plagues after the Outbreak of the Earthquake in Wenchuan. *China Rural. Water Hydropower* **2016**, *12*, 38–42+48.

10. Yu, Z.; Yuan, L.; Liu, J.; Liu, P.; Wu, H. Study on Distribution and Activity Characteristics of Giant Debris Flow in Wenchuan Earthquake Zone. *Subgrade Eng.* **2018**, *1*, 209–215. [CrossRef]
11. Tang, C.; Tie, Y. Reconnaissance and Analysis on the Rainstorm induced Debris Flow in Weijiagou Valley of Beichuan City after Wenchuan Earthquake. *J. Mt. Sci.* **2009**, *27*, 625–630.
12. Tie, Y.; Tang, C. Response Characteristics between Wenchuan Earthquake and the Rainfall Induced Debris Flow in Beichuan Country, Sichuan. *J. Catastrophology* **2011**, *26*, 73–75+81.
13. Luo, C.; Chen, T.; Fu, Q.; Chen, G.; Li, S. Analysis of Characteristics and Cause of Debris Flow in Yangjia Gully in Beichuan County. *J. Southwest Univ. Sci. Technol.* **2019**, *34*, 25–31.
14. Liu, S.; Kou, G.; Feng, J. Discussion on the geological environment of the causes on the debris flow in Beichuan County. *Technol. Innov. Appl.* **2018**, *01*, 177–179.
15. Legiman, M.K.A.; Mohamad, E.T.; Hasbollah, D.Z.A.; Suparmanto, E.K.; Rathinasamy, V. An overview of debris-flow mathematical modelling. *Phys. Chem. Earth* **2023**, *129*, 103301. [CrossRef]
16. Xia, X.; Jarsve, K.; Dijkstra, T.; Liang, Q.; Meng, X.; Chen, G. An integrated hydrodynamic model for runoff-generated debris flows with novel formulation of bed erosion and deposition. *Eng. Geol.* **2023**, *326*, 107310. [CrossRef]
17. Jiang, X.; Wörman, A.; Chen, X.; Zhu, Z.; Zou, Z.; Xiao, W.; Lia, P.; Liu, G.; Kang, D. Internal erosion of debris-flow deposits triggered by seepage. *Eng. Geol.* **2023**, *314*, 107015. [CrossRef]
18. Domènech, G.; Fan, X.; Scaringi, G.; van Asch, T.W.J.; Xu, Q.; Huang, R.; Hales, T.C. Modelling the role of material depletion, grain coarsening and revegetation in debris flow occurrences after the 2008 Wenchuan earthquake. *Eng. Geol.* **2019**, *250*, 34–44. [CrossRef]
19. Ma, C.; Hu, K.; Tian, M. Post-earthquake relationships of maximum runout amount and loose matter mass in debris flow gully. *J. Nat. Disasters* **2013**, *22*, 76–84. [CrossRef]
20. Wang, J. The Development Characteristics and Risk Assessment of High Debris Flow in Wenchuan Earthquake Area. Master's Thesis, Chengdu University of Technology, Chengdu, China, 2014. Available online: https://kns.cnki.net/KCMS/detail/detail.aspx?dbname=CMFD201801&filename=1016227078.nh (accessed on 1 October 2023).
21. Zhang, X. Study on Source Erosion, Movement Characteristics and Risk Assessment of Debris Flows—A Case Study of Debris Flows Along Du-Wen Highway. Master's Thesis, Chengdu University of Technology, Chengdu, China, 2015. Available online: https://kns.cnki.net/KCMS/detail/detail.aspx?dbname=CMFD201601&filename=1015312745.nh (accessed on 1 October 2023).
22. Wei, B.; Zhao, Q.; Han, G.; Zhang, H. Grey Correlation Method Based Hazard Assessment of Debris Flow in Quake-Hit Area—Taking Debris Flows in Beichuan as An Example. *J. Eng. Geol.* **2013**, *21*, 525–533.
23. Chang, M.; Dou, X.; Fan, X.; Yao, C. Critical Rainfall Patterns for Rainfall-induced Debris Flows in the Wenchuan Earthquake Area. *Geoscience* **2018**, *32*, 623–630. [CrossRef]
24. Chu, S. The Weathering Factor Study on the Formation of Gully—Type Debris Flow—Take Wenchuan Earthquake as an Example. Master's Thesis, Chengdu University of Technology, Chengdu, China, 2012. Available online: https://kns.cnki.net/KCMS/detail/detail.aspx?dbname=CMFD201301&filename=1012500162.nh (accessed on 1 October 2023).
25. Shi, S.; Tu, L.; Shen, W. Geological Characteristics and Dynamics Features of the Debris Flow in Yingtao Gully of Beichuan County, Sichuan Province. *Geol. Surv. Res.* **2014**, *37*, 34–38.
26. Wang, X. Hazard Assessment and Prevention of Wuxinggou Debris Flow in Beichuan County. Master's Thesis, Southwest University of Science and Technology, Mianyang, China, 2014. Available online: https://kns.cnki.net/KCMS/detail/detail.aspx?dbname=CMFD201801&filename=1017720833.nh (accessed on 1 October 2023).
27. Hu, S. The Prediction Explores of Secondary Geological Disaster Caused by 5.12 Earthquake in Beichuan County. Master's Thesis, Sichuan Normal University, Chengdu, China, 2015. Available online: https://kns.cnki.net/KCMS/detail/detail.aspx?dbname=CMFD201601&filename=1015372910.nh (accessed on 1 October 2023).
28. Mei, Y. 5.12 Earthquake in Beichuan County, Sichuan Province Area Debris Flow Hazard Assessment. Master's Thesis, Chengdu University of Technology, Chengdu, China, 2011. Available online: https://kns.cnki.net/KCMS/detail/detail.aspx?dbname=CMFD2012&filename=1011235513.nh (accessed on 1 October 2023).
29. Zhang, Q.; Pan, Q.; Chen, Y.; Luo, Z.; Shi, Z.; Zhou, Y. Characteristics of landslide-debris flow accumulation in mountainous areas. *Heliyon* **2019**, *5*, e02463. Available online: http://creativecommons.org/licenses/by-nc-nd/4.0/ (accessed on 1 October 2023).
30. Hu, T. The Research on Formation Mechanism and Mitigation Measures of Large-Scale Debris Flow in the Wenchuan Earthquake Area. Ph.D. Thesis, Chengdu University of Technology, Chengdu, China, 2017. Available online: https://kns.cnki.net/KCMS/detail/detail.aspx?dbname=CDFDLAST2020&filename=1019216142.nh (accessed on 15 October 2023).
31. Zhang, S.; He, Y.; He, M. Source analysis and prevention plan determination of debris flow in Yangjiagou, Beichuan earthquake stricken area. *Sichuan J. Geol.* **2014**, *34*, 80–84.
32. Li, C.; Dong, T. Types and characteristics of geological disasters in Beichuan County. *J. Mianyang Teach. Coll.* **2017**, *36*, 93–97. [CrossRef]
33. Wang, Y. Hazard Assessment on Rainstorm Induced Debris Flows in Beichuan County of Wenchuan Earthquake Affected Area. Master's Thesis, Chengdu University of Technology, Chengdu, China, 2009. Available online: https://kns.cnki.net/KCMS/detail/detail.aspx?dbname=CMFD2010&filename=2009221507.nh (accessed on 15 October 2023).
34. Yuan, L.; Chen, X.; Wu, H.; Qiu, E. Study on Formation Mechanism of Debris Flow in Xijia Valley and the Engineering Measures for Control. *Subgrade Eng.* **2020**, *4*, 212–221. [CrossRef]

35. Hu, K.; You, Y.; Zhuang, J.; Chen, X. Characteristics and Countermeasures of Debris Flows in Beichuan's Meizoseismal Area. *Sci. Geogr. Sin.* **2010**, *30*, 566–570. [CrossRef]
36. Yu, Y.; Wei, L.; Chen, T. Characteristics of Debris flows and Control in Jiangjia Gully of Beichuan, Sichuan. *J. Geol. Hazards Environ. Preserv.* **2012**, *23*, 5–9.
37. Wu, Q.; Xu, L.; Zhou, K.; Liu, Z. Starting analysis of loose accumulation of gully-startup debris flow. *J. Nat. Disasters* **2015**, *24*, 89–96. [CrossRef]
38. Xie, M.; Wang, Y.; Zhang, H.; Zhao, Y.; Zhao, R. The Deposite Analysis of Water Dynamic Conditions to Form Debris Flow and to Set up Mathematical Model in Debris Flow Valley. *J. Beijing For. Univ.* **1993**, *15*, 1–11.
39. Xu, X.; Chen, J.; Shan, B. Study of Grain Distribution Characteristics of Solid Accumulation in Debris Flow. *Yangtze River* **2015**, *46*, 51–54. [CrossRef]
40. Wang, Q.; Xie, J.; Yang, J.; Liu, P.; Chang, D. A hyperspectral detection model for permeability coefficient of debris flow fine-grained sediments, Southwestern China. *Int. J. Digit. Earth* **2023**, *16*, 1589–1606. [CrossRef]
41. Wang, Q.; Xie, J.; Yang, J.; Liu, P.; Chang, D.; Xu, W. A Model between Cohesion and Its Inter-Controlled Factors of Fine-Grained Sediments in Beichuan Debris Flow, Sichuan Province, China. *Sustainability* **2022**, *14*, 12832. [CrossRef]
42. Wang, Q.; Xie, J.; Yang, J.; Liu, P.; Chang, D.; Xu, W. A Research on Cohesion Hyperspectral Detection Model of Fine-Grained Sediments in Beichuan Debris Flow, Sichuan Province, China. *Land* **2022**, *11*, 1609. [CrossRef]
43. Wang, Q.; Xie, J.; Yang, J.; Liu, P.; Chang, D.; Xu, W. Research on Permeability Coefficient of Fine Sediments in Debris-Flow Gullies, Southwestern China. *Soil Syst.* **2022**, *6*, 29. [CrossRef]
44. Yu, J. Study on Permeability Characteristic and Fine Particle Migration Law of Deposited Soil in Debris Flow Channel. Master's Thesis, Sichuan Normal University, Chengdu, China, 2020. Available online: https://kns.cnki.net/KCMS/detail/detail.aspx?dbname=CMFD202101&filename=1020746689.nh (accessed on 20 October 2023).
45. *GB/T 50145-2007*; Engineering Classification Standard for Soil. China Planning Press: Beijing, China, 2008.
46. Liu, Y. Research on Test Method for Permeability Coefficient of Cohesionless Coarse grained Soil in Hydraulic Engineering. *Shaanxi Water Resour.* **2020**, *12*, 211–213.
47. Sun, X.; Wang, D. Analysis of Soil Cohesion Values. *Liaoning Build. Mater.* **2010**, *3*, 39–42.

Article

Evolution Process of Ancient Landslide Reactivation under the Action of Rainfall: Insights from Model Tests

Xiang Li [1,2], Ruian Wu [1,3,*], Bing Han [4,*], Deguang Song [1,5], Zhongkang Wu [1,2], Wenbo Zhao [1,2] and Qijun Zou [1,2]

1   Institute of Geomechanics, Chinese Academy of Geological Sciences, Beijing 100081, China; lix1228@cug.edu.cn (X.L.)
2   School of Engineering, China University of Geosciences (Wuhan), Wuhan 430074, China
3   Key Laboratory of Active Tectonics and Geological Safety, Ministry of Natural Resources, Beijing 100081, China
4   China Institute for Geo-Environment Monitoring, Beijing 100081, China
5   Yunnan Geological Engineering Second Survey Institute Co., Ltd., Kunming 650218, China
*   Correspondence: wuruian1991@126.com (R.W.); hanbing@mail.cgs.gov.cn (B.H.)

Abstract: Under rapid global climate change, the risk of ancient landslide reactivation induced by rainfall infiltration is increasing significantly. The contribution of cracks to the reactivation of ancient landslides, as an evolutionary product, is a topic that deserves attention; however, current research on this issue remains insufficient. In this study, taking the Woda landslide in the upper Jinsha River as a case study, we investigated the reactivation mechanisms of ancient landslides with and without cracks under rainfall based on model tests. The study showed that cracks influence the reactivation range and depth of ancient landslide. In cases where no cracks develop on ancient landslides, rainfall can only cause shallow sliding with failure concentrated at its front edge. Conversely, when cracks develop on ancient landslides, rainwater can quickly infiltrate into the sliding zone along the cracks and induce overall reactivation of the ancient landslide. Furthermore, the reactivation mechanism of ancient landslides without cracks is that the failure of ancient landslide foot results in progressive failure at the front of the ancient landslide. When cracks have developed at ancient landslides, the reactivation mechanism of which involves mid-rear ancient landslide creeping, tensile cracks develop on the mid-rear ancient landslide, with localized sliding at the front edge, tensile cracks extending, local sliding range extending, accelerated creeping, and progressive failure of the mid-rear ancient landslide. These findings shed light on how cracks influence rainfall-induced mechanisms of ancient landslide reactivation and hold great significance for advancing our understanding regarding these mechanisms.

Keywords: ancient landslide; reactivation mechanism; rainfall; crack; model test

1. Introduction

The technical term "paleo-landslide" typically refers to landslides that have been formed for a relatively long time, the classification of which has been subject to varying perspectives [1–5]. In engineering geological practice, considerable attention is given to the present stability status of ancient landslides. With the increasing intensity of human activities and the frequent occurrence of extreme conditions such as strong earthquakes and heavy rainfall, the risk of ancient landslide reactivation has sharply risen, severely constraining human engineering programming and construction and causing significant losses to the lives and properties of local people [6–9]. For example, in 2014, under the combined actions of excavation at the foot of the landslide, Thompson River erosion, and heavy rainfall near the ancient landslide group in the Thompson River valley, Canada's national railway (CN and CP) reactivated, severely affecting the operational safety of the railway [10]. In 2016, extreme rainfall caused multiple ancient landslides to reactivate in the

upstream area of the Tanarello River, Italy, resulting in the destruction of buildings and highways [9]. In July 2018, continuous heavy rainfall induced the reactivation of the Jiangdingya ancient landslide in Zhouqu County, Gansu Province, China, blocking the Bailong River, submerging upstream hydropower stations, and damaging the S313 highway [8].

The problem of ancient landslide reactivation has been extensively studied by many scholars, both domestically and internationally. The main influencing factors include active faults and earthquakes, mechanical properties of weak interlayers within the accumulation body, changes in reservoir water levels, heavy rainfall, river erosion, and human engineering activity, etc. [11–16]. Among them, the relationship between ancient landslide reactivation and rainfall has attracted widespread attention. Most scholars have a significant opinion that there is a rainfall threshold for ancient landslide deformation instability, and usually infer the possibility of ancient landslide instability according to rainfall intensity [17–19]. Furthermore, they also point out that the rainfall thresholds in different regions and different types of landslides show significant differences [17–19]. For example, Gil and Długosz (2006) collected and analyzed meteorological data and ancient landslide data in the Flysch Carpathians area. The results indicated that there are significant differences in the rainfall thresholds for different types of ancient landslide reactivation, with lower rainfall thresholds for muddy ancient landslides compared to sandy ancient landslides [17]. In addition, some scholars have pointed out that various changes in the ancient landslide accumulation body caused by rainfall infiltration are also important factors in ancient landslide reactivation, such as increases in bulk density of ancient landslide rock–soil mass, the softening of the landslides' mechanical properties, and the increase in pore water pressure and groundwater levels [20–28]. For example, Borja and White (2010), based on theoretical and numerical analyses, revealed the trend of landslide accumulation deformation and failure under hydrological driving. They pointed out that rainfall leads to an increase in the saturation degree of the slope rock–soil mass, reducing its cohesive strength and weakening the frictional resistance of the sliding zone [22].

Although the connection between ancient landslide reactivation and rainfall has been extensively explained, little attention has been paid to the influence of the interaction between rainfall and cracks on ancient landslide reactivation. The cracks play a significant indicative role in the reactivation deformation trend and instability range of the next stage of ancient landslides. Existing studies have shown that, under rainfall conditions, the deformation and instability of ancient landslides have typical stress–permeability–damage coupling characteristics [29–31]. When no cracks have developed on an ancient landslide, the influence of rainfall on the ancient landslide is limited in depth and range [32–34]. However, when cracks have developed on the ancient landslide, rainfall has a significant controlling effect on the ancient landslide's reactivation [33,35,36]. Macroscopic deformations such as cracks are products of the evolutionary process of ancient landslide reactivation, and serve as important preferential pathways for rainwater infiltration. The coupling effect of rainfall and cracks makes significant contributions to the further deformation and instability of ancient landslides.

Currently, effective methods for evaluating landslide stability and studying the mechanisms of landslide instability include engineering geological analysis, physical modeling, and numerical simulation. The model tests of landslide are based on the similarity theory and consider the influence of internal and external factors on landslide stability, which can allow us to monitor the parameter variation of the model [37–39]. The model test has the characteristics of high efficiency, accuracy, and cost-effectiveness, and is widely used in the study of landslides' instability mechanisms, deformation, and movement processes [40–45].

In this study, the Woda landslide, located in the upper Jinsha River in the eastern edge of the Qinghai–Tibet Plateau, is taken as a case study. Through landslide model tests, the deformation and failure patterns of the model slope, with and without cracks, under rainfall are studied, and the influence of cracks on the reactivation mechanism of an ancient landslide is revealed. The research results contribute to our understanding of the contribution of cracks to the reactivation mechanism of ancient landslides induced by

rainfall, as well as to predicting the deformation and failure patterns of ancient landslides. The results also provide theoretical references for local geological disaster prevention and mitigation efforts.

2. Landslide Prototype

The Woda landslide is located at Woda Village, Yanbi Township, Jiangda County, Qamdo City, Tibet, China. It is situated on the right bank of the upper Jinsha River on the southeastern edge of the Qinghai–Tibet Plateau (Figure 1). The overall landform of the Woda landslide resembles a chair shape, with mountain ridges forming the boundaries on both sides (Figures 1 and 2). The main sliding direction is 30°, with a longitudinal length of about 2100 m and a transverse width of about 1660 m. The total area of the Woda landslide is estimated to be around 2.64×10^6 m^2, and the maximum height difference between the sliding outlet and the front edge of the Jinsha River is up to 247 m (Figure 3). The accumulation area of the Woda landslide has an area of about 1.32×10^6 m^2. The Woda landslide has two sliding zones, with burial depths of 15 m and 25.5 m, respectively [46]. Based on this information, it is estimated that the volume of the Woda landslide deposit is approximately 28.81×10^6 m^3, making it an extremely large, high-level landslide [46,47]. According to field investigations, the underlying bedrock of the Woda landslide is mainly composed of shale and carbonaceous shale, with strike angles ranging from 280° to 310° and dip angles of 25° to 30°. The main components of the accumulation are gravelly soil and residual slope material. The gravel content ranges from 30% to 45%, with particle sizes ranging from 20 cm to 50 cm, showing angular shapes and poor roundness. In the sliding outlet of the front edge of the Woda landslide, a sliding zone soil composed of gravelly clay was found. It had a thickness of about 50~75 cm, appeared grayish-green, and exhibited a soft-plastic to flowing-plastic state. The gravel content was approximately 13% to 25%, with particle sizes ranging from 2 mm to 20 mm, showing distinct angular shapes and relatively poor roundness.

Our field investigation found that the accumulation area of the Woda landslide is currently in a stage of overall reactivation, and its deformation can be divided into two distinct zones: Zone I, with intense deformation, and Zone II, with weak deformation. Zone I exhibits several localized sliding areas, down scarps, and tensile cracks (Figure 2). The localized sliding areas are located at the front edge of the Woda landslide and the rear part of the accumulation area. The tensile cracks and downs scarps are concentrated in the front part of the accumulation area, indicating the direction of reactivation deformation of the Woda landslide. The down scarps have a vertical displacement ranging from 30 cm to 120 cm and lengths ranging from 30 m to 230 m. The tensile cracks have lengths ranging from 20 m to 130 m, widths ranging from 10 cm to 30 cm, and depths ranging from 50 cm to 300 cm. Most of the down scarps and tension cracks are arranged in a circular arc, and the strike is roughly perpendicular to the main sliding direction of the landslide or at a large oblique angle. Zone II shows less pronounced deformation characteristics, with the development of four down scarps and one localized sliding area. Considering the deformation characteristics of the Woda landslide accumulation and the topographic features, the probability of overall sliding occurrence is much higher in Zone I than in Zone II. Because the sliding surface of the localized sliding area at the front edge of Zone I is located near the deep sliding zone, the upper accumulation area has a steep free surface. Based on this, it can be inferred that Zone I may experience destabilization and failure along the deep sliding zone, with an estimated volume of instability of approximately 17.83×10^6 m^3.
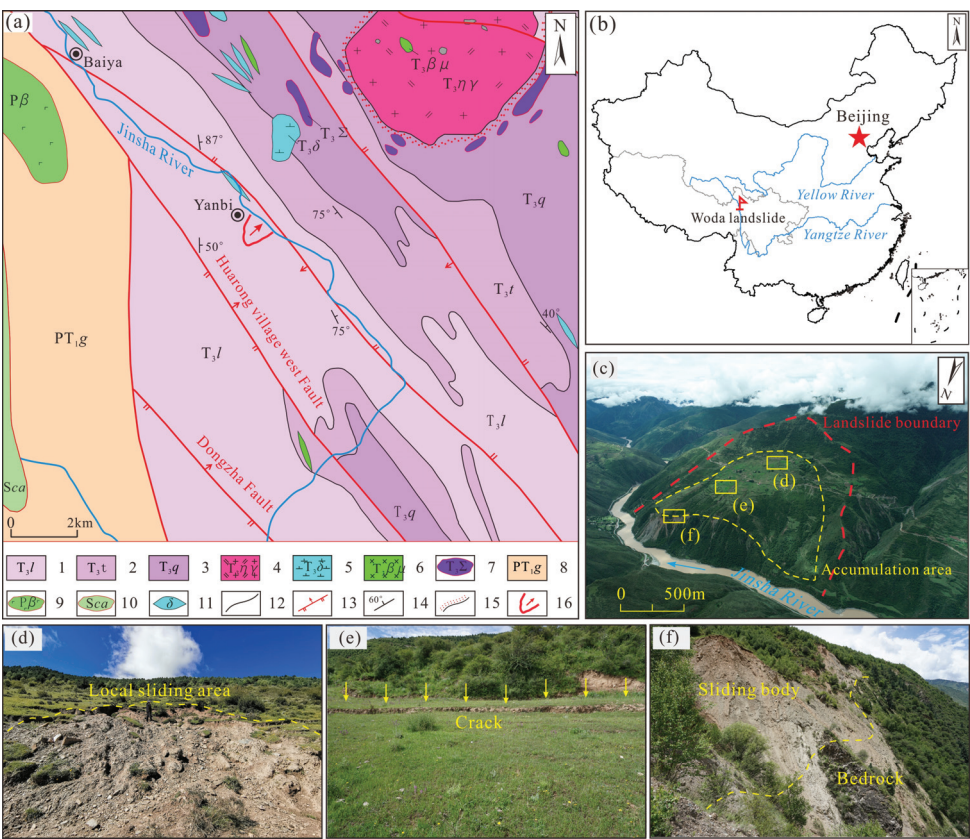
Figure 1. Geological setting of the Woda landslide (Modified according to Wu et al., 2023 [47]).
(**a**) Tectonic and lithology map, (**b**) The Woda landslide location, (**c**) The Woda landslide panorama,
(**d**) Local slide zone, (**e**) Tensile crack, (**f**) Leading edge shear outlet. 1—Schist, slate, shale in the Upper
Triassic Lanashan Formation; 2—Crystal-line limestone, sandstone in the Upper Triassic Tumugou
Formation; 3—Crystalline limestone in the Upper Triassic Qugasi Formation; 4—Monzonitic granites
in the Upper Triassic; 5—diorite in the Upper Triassic; 6—dolerites in the Upper Triassic; 7—ultrabasic
rocks in the Upper Triassic; 8—The sericite–quartz schist and the two-mica schist of the Gangtuoite
Group in the Lower Permian-Triassic; 9—Basalt Blocks in the Permian; 10—Carbonate blocks in the
Silurian; 11—Diorite dike; 12—Strata boundary; 13—Thrust fault; 14—Occurrence; 15—Hornfelsic
zone; 16—The Woda landslide.

Wu et al. (2023) conducted a study indicating that the reactivation deformation rate
of the Woda landslide is primarily controlled by the influence of seasonal rainfall [47].
Under the combined effects of rainfall infiltration and gravity, the slope deforms towards
the downslope direction, resulting in the formation of down scarps and tensile cracks.
These down scarps and tensile cracks serve as preferred infiltration pathways for rainfall,
providing favorable conditions for the subsequent stage of deformation instability of the
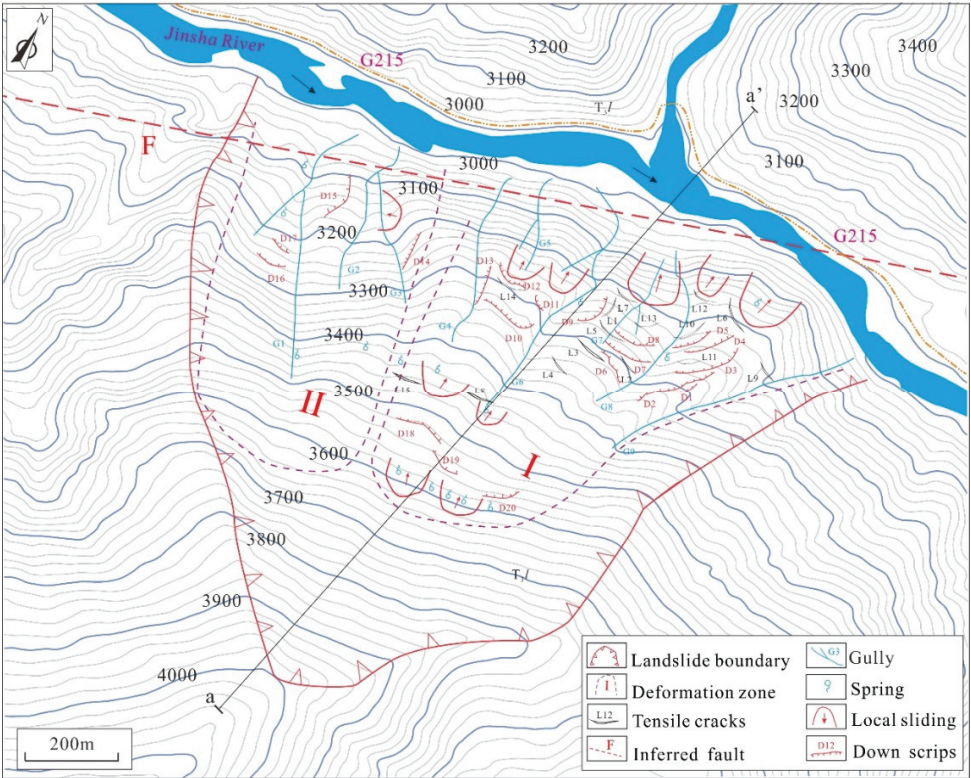Woda landslide.

Figure 2. Engineering geological planar graph of the Woda landslide. I: intense deformation area, II: weak deformation area.
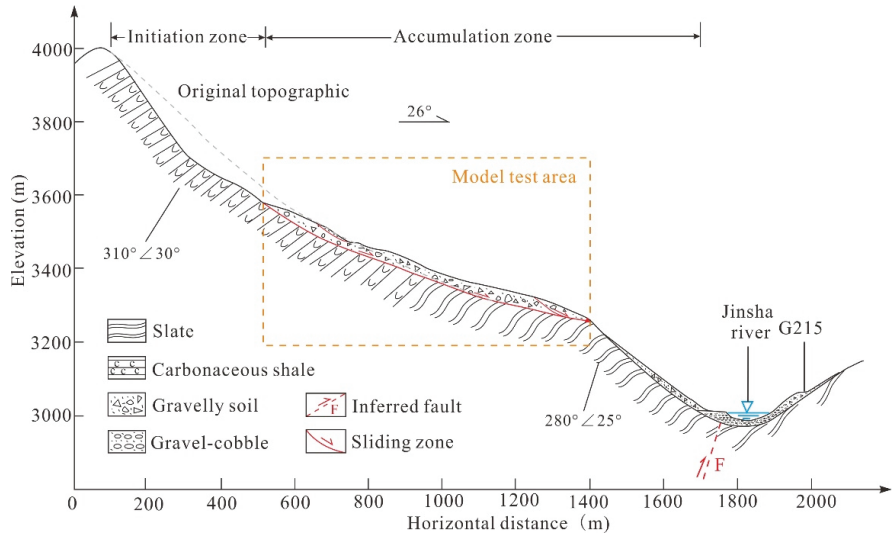

Figure 3. Engineering geological profile (a–a') of the Woda landslide.

3. Materials and Methods

3.1. Model Test Equipment

The model test was conducted in the Landslide Physical Model Laboratory of the Institute of Geomechanics, Chinese Academy of Geological Sciences. The main equipment of the landslide model test included a model box, rainfall simulation system, internal monitoring system, and slope surface monitoring system (Table 1 and Figure 4). With this comprehensive experimental setup, it was possible to monitor the real-time macro deformation and failure process of the physical model's slope surface, as well as pore water pressure and soil pressure inside the model slope under continuous rainfall conditions. The monitoring instruments and their key technical parameters used in this model test are shown in Table 1.
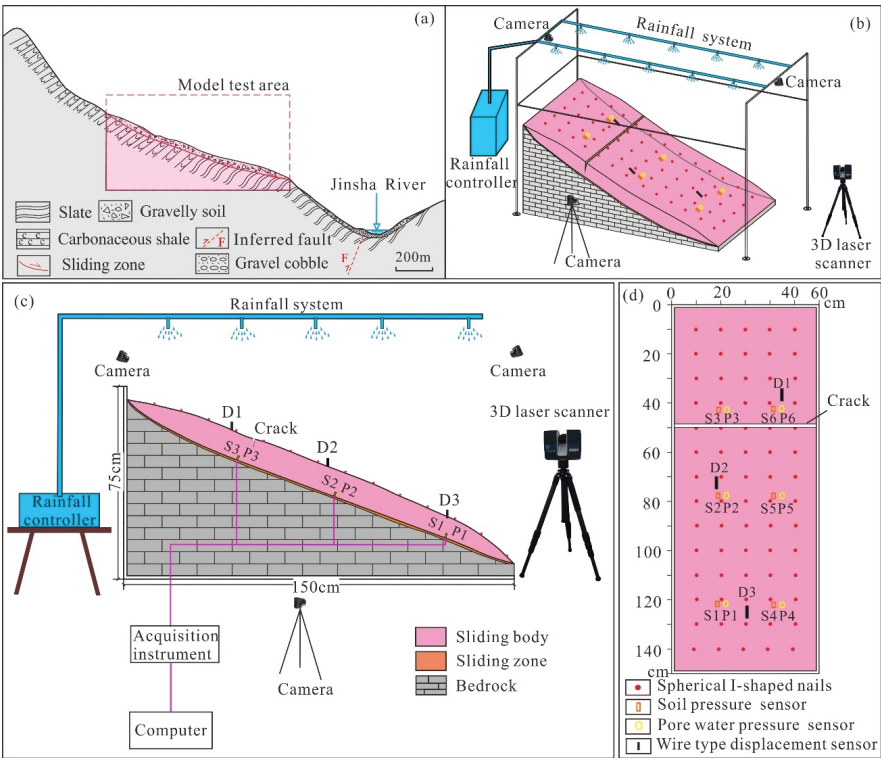

Figure 4. Equipment and instrument layout for the Woda landslide model test: (**a**) Model test area of the Woda landslide; (**b**) Three-dimensional view of the experimental model design effect; (**c**) Side view of the experimental model design effect; (**d**) Top view of the experimental model design effect.

3.2. Similar Materials

According to the similarity theory, the intense deformation Zone I of the Woda landslide was scaled down proportionally. The similarity ratio of 1:550 was determined based on the dimensions of the prototype and a physical model of the Woda landslide. A physical model was constructed based on the structural characteristics and potential unstable range of the Zone I in the Woda landslide. The model slope was divided into three parts: sliding body, sliding zone, and bedrock (Figure 4b,c). The dimensions of the model slope were approximately 165 cm in length, 60 cm in width, and 70 cm in height. The sliding zone had a thickness of about 2 cm, and the maximum thickness of the sliding body was 15 cm.

The similarity of the physical model to the Woda landslide was determined using dimensional analysis and similarity theory (Table 2). The main parameters of the similar

materials in the physical model included the geometric similarity ratio (*l*), density (*ρ*), moisture content (*w*), Poisson's ratio (*μ*), internal friction angle (*φ*), cohesion (*c*), displacement (*δ*), and permeability coefficient (*k*). Based on dimensional analysis and the homogeneity theorem, the above parameters can be expressed as follows:

$$f\,(l,\,\rho,\,w,\,\mu,\,\varphi,\,c,\,\delta,\,k) = 0$$

Table 1. Technical parameters of the model experimental instruments for the Woda landslide.

System Unit	Instruments	Model	Number	Key Technical Parameters
Model box	Model box	—	1	Size: 150 cm × 60 cm × 100 cm (length × width × height)
Rainfall simulation system	Atomizing nozzle	TW3010	5	Diameter: 0.3 mm; rainfall intensity: 0.063–0.251 mm/min.
	Atomizing nozzle	TW5010	5	Diameter: 0.5 mm; rainfall intensity: 0.163–0.433 mm/min.
	Water tank	—	1	Volume: 25 L
	Compressor	XK06-020	1	Rated voltage: 220 V; pressure: 0.5–3 MPa; volumetric flow rate of 0.032 m^3/min; output power: 0.55 kW
Internal monitoring system of the model	Soil pressure gauge	CYY2	6	Diameter: 6 mm; output voltage: 0–5 V; range: 0–4 kPa; accuracy: 0.01 kPa; dynamic frequency: 50 kHz
	Pore water pressure gauge	CYY9	6	Diameter: 6 mm; output voltage: 0–5 V; range: 0~2 kPa; accuracy: 0.01 kPa; dynamic frequency: 50 kHz
Model surface monitoring system	3D laser scanner	Faro S70	1	Scanning range: 0–360°; maximum scanning speed: 97 Hz; power consumption: 25 W; ranging error: <1 mm
	Camera	SONY-ILCE-6000	3	Sensor: Exmor APS-HD-CMOS; APS frame: 23.5 × 15.6 mm; maximum resolution: 6000 × 4000; optical zoom: 1–16 times
	Wire displacement meter	MPS-S	3	Range: 50–2000 mm; accuracy: 1 mm; tensile force: <600 g

Table 2. Similarity coefficient table for the model test of the Woda landslide.

Physical Quantity	Similarity Constant Code	Similarity Coefficient
Geometric dimensions, *l*	C$_l$	1:550
Density, *ρ*	C$_\rho$	1:1
Moisture content, *w*	C$_w$	1:1
Poisson's ratio, *μ*	C$_\mu$	1:1
Internal friction angle, *φ*	C$_\varphi$	1:1
Cohesion, *c*	C$_c$	1:1
Displacement, *δ*	C$_\delta$	1:550
Permeability coefficient, *k*	C$_k$	1:550$^{1/2}$

The bedrock of the physical model was simplified as impermeable or low-permeability bedrock, and was constructed by stacking bricks. A layer of cement mortar was applied onto the bedrock's top surface to achieve impermeability or low permeability. The selection and proportions of similar materials in the model were determined through comparative tests between multiple sets of similar material ratios and the prototype materials of the Woda landslide (sliding body and sliding zone) (Table 3). Among them, the sliding zone material consisted of gravel (2~5 mm), sand, bentonite, and water, with a ratio of 1:2:3:1.

The sliding body material consisted of gravel (5~10 mm), sand, heavy mineral powder (weighting material), silt, bentonite (binding material), and water, with a ratio of 1:2:8:9:3:3. Figure 5 shows the particle size distribution curves of the prototype and model materials of the Woda landslide, and Table 4 lists the physical and mechanical parameters of the prototype's and physical model's materials. In addition, to reduce the shear interaction between the side walls of the model box and the physical model of the landslide, Vaseline was uniformly applied to the contact area between the model box and the soil layer. The sensors were also positioned at a certain distance from the side walls of the model box (Figure 4d).

Table 3. Composition and proportion relationships between similar materials for the Woda landslide model test.

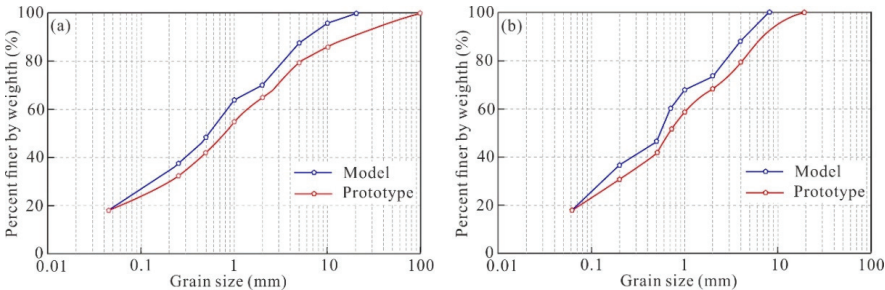| Material Type	Material Size (mm)	Material Proportion Sliding Zone	Sliding Body	Illustrate
Gravel	2~5	1/6	-	
Sand	1~0.5	2/6	-	
Bentonite	<0.002	3/6	3/26	Binding material
Water	-	1/6	3/26	
Gravel	5–10	-	1/26	
Sand	0.2–2	-	2/26	
Barite powder	0.05–0.2	-	8/26	Weighting material
Silt soil	0.05–0.2	-	9/26	

Figure 5. Particle size distribution curves of prototype and model materials: (**a**) Sliding body; (**b**) Sliding zone.

Table 4. Physical and mechanical parameters of the Woda landslide prototype materials and model materials.

Material Type		Density ρ (g/cm^3)	Moisture Content w (%)	Cohesion c (kPa)	Internal Friction Angle φ (°)	Permeability Coefficient k (m/s)	Volumetric Weight γ (kN/m^3)
Sliding body	Prototype	2.25	12	71.14	21.35	4.44×10^{-5}	22.05
	Model	2.24	12	63.34	22.62	1.92×10^{-6}	22.34
Sliding zone	Prototype	2.20	19	12.06	21.16	3.57×10^{-6}	21.56
	Model	2.21	19	10.14	20.06	1.51×10^{-7}	21.93

3.3. Test Conditions

Due to long-term geological evolution processes, the accumulation of an ancient landslide forms a gentle slope, and the internal body of the slope becomes compacted. The rock–soil mass has good cementing property and low permeability, making it more stable [30,36]. The shear outlet at the front edge of the Woda landslide is exposed, and the slope of the accumulation body is about 23°~25°, which has good deformation potential.

Under the infiltration of rainfall, tensile cracks gradually appear on the slope's surface. Under the action of gravity, rainwater infiltrates into the deep part of the slope along the cracks. This process promotes the development of cracks, which have wide upper parts and a narrow lower parts, resembling a "V" shape. Field investigations indicated that the tensile cracks in the intense-deformation Zone I of the Woda landslide did not penetrate the accumulation body.

In order to elucidate the evolution of the rainfall-induced deformation and destruction process of the Woda landslide, and to reveal the destabilization mechanism of the Woda landslide under the coupling effect of cracks and rainfall, two physical models of the landslide were created in this study (Table 5): (1) a physical model without cracks (Figure 6a), and (2) a physical model with a "V"-shaped crack at the rear edge, with 3 cm in top width, 7 cm in depth, and 60 cm in length (Figure 6b). Previous studies have indicated that rainfall intensity has a significant impact on the stability of ancient landslides [12,14,48]. To realistically reflect the influence of rainfall on the reactivation and deformation of the Woda landslide, meteorological data were collected, revealing that the monthly maximum rainfall in the study area is about 167 mm (Figure 6c), and the maximum daily rainfall is about 49.8 mm (Figure 6d). Combining with the similarity theory, the rainfall intensity in the model test was determined to be 7.02 mm/h, corresponding to a rainfall intensity of 50 mm/d in the real environment. The model test was conducted under continuous rainfall during the test period (Figure 6e). Because rainfall has a certain negative influence on data collected by 3D laser scanners and cameras, we stopped the rainfall and collected data for some important time nodes, such as local sliding and crack expansion, during the model tests.

Table 5. Experimental conditions of landslide model tests.

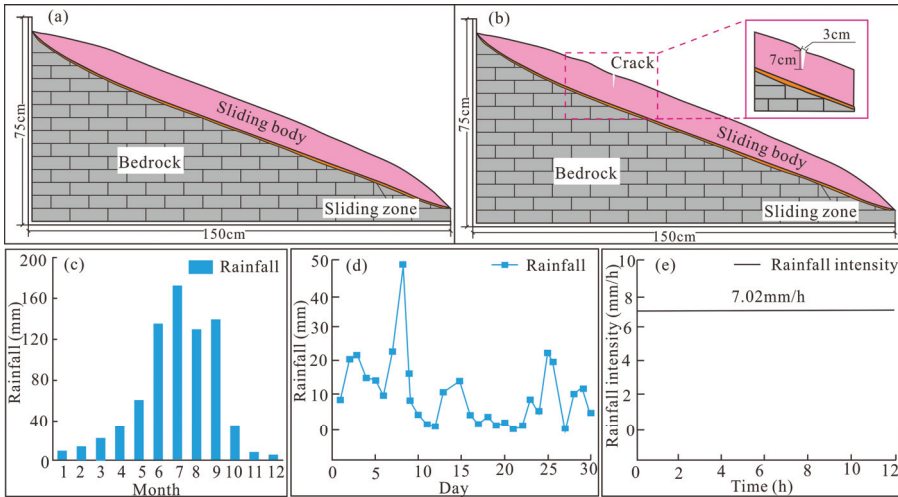| Scenario	Test Conditions	Rainfall Intensity (mm/h)	Crack Location	Crack Geometry Parameter
Scenario 1	Rainfall Coupling effect of rainfall and crack	7.02	-	-
Scenario 2			Model trailing edge	V-shaped, 3 cm in width, 7 cm in height, 60 cm in length

Figure 6. Physical model setup and rainfall schedule for the Woda landslide: (**a**) Model 1; (**b**) Model 2. (**c**) Monthly rainfall in the study area (2018); (**d**) Daily rainfall in the study area (July 2020); (**e**) Continuous rainfall process.

3.4. Instrument Layout

During the model test, three cameras and one 3D laser scanner were utilized to obtain the surface deformation characteristics of the physical model. The application of 3D laser scanning technology enables rapid acquisition of high-precision and high-resolution topographic data in the field, which is of great significance for landslide deformation monitoring. It has been widely used in the deformation monitoring of landslides and other geological disasters, as well as in landslide model tests [49–52]. Small cylindrical nails with diameters of 1 cm were strategically positioned on the model surface as monitoring points, with an interval spacing of 10 cm. Prior to rainfall, the model was scanned to obtain its undeformed shape, which served as a reference for measuring the deformation of the model during the model test.

Additionally, three monitoring sections were established at the front, middle, and rear parts of the physical model to acquire response characteristics related to surface displacement, internal soil pressure, and pore water pressure. Each section was equipped with a displacement sensor installed on the model surface. Furthermore, three soil pressure sensors and pore water pressure sensors were placed on each side of the central axis at approximately 10 cm intervals. These sensors were installed near the interface between the sliding zone and the sliding body (as depicted in Figure 4c,d).

4. Results

4.1. Deformation Processes of Landslides

In the model test process of scenario 1, several phenomena were observed. Initially, settlement deformation was predominantly exhibited during the onset of rainfall. After approximately 178 min of continuous rainfall, a shallow surface collapse occurred at the foot of the slope (Figure 7c). Between 178 and 362 min, an arc-shaped expansion of the collapsed area took place at the foot of the slope, accompanied by non-uniform settlement in the middle section, where greater settlement was observed on the right side compared to the left side (Figures 7d and 8d). From 362 to 838 min, localized instability and subsequent backward expansion were experienced on the right side of the model's front edge, with a fan-shaped failure pattern evident within this region (Figure 7e). The maximum thickness of this instability zone reached approximately 5.49 cm (Figure 8e), while non-uniform settlement continued expanding on the right side of the slope. At around 1108 minutes into rainfall, complete collapse occurred along with failure of the entire front edge in the model (Figure 7f), reaching a maximum instability thickness close to 10.95 cm (Figure 8f). By minute 1300 of rainfall, no further signs of deformation were observed in the model, and thus, the model test was concluded.

In the model test process of scenario 2, several phenomena were observed. During the initial stage of rainfall, settlement deformation with a magnitude of approximately 2 mm primarily occurred in the model (Figures 9 and 10). From 112 to 220 min, localized sliding took place in the middle part of the model's front edge, resulting in a tongue-shaped morphology measuring approximately 35 cm in length and approximately 20 cm in width. Seven tensile cracks developed in the middle-rear part of the slope (Figure 9c), while four tensile cracks appeared at the rear edge of the slope. The main tensile crack, L_1, had a length of approximately 42 cm and a width of approximately 1 cm. On both sides of the L_1 tensile crack, three tensile cracks, L_{1-1} to L_{1-3}, were distributed, measuring 4 to 20 cm in length and approximately 0.3 cm in width (Figure 9c$_1$). At 10 cm from the preset crack, three tensile cracks, L_2, L_3, and L_4, were formed in the middle part of the slope. The L_2 and L_3 tensile cracks were approximately 48 to 55 cm in length and 0.5 to 1 cm in width, while the L_4 tensile crack was approximately 23 cm in length and 0.3 cm in width (Figure 9c$_2$). During the period of 220 to 397 min, localized sliding at the front edge of the model intensified, and new two tensile cracks, L_5 and L_6, formed in the middle part of the slope. Tensile cracks L_2 to L_4, in the middle part of the slope, were basically connected laterally (Figure 9d). From 397 to 492 min, a larger-scale sliding occurred on the right side of the model, and the tensile cracks in the middle and rear parts of the slope further expanded (Figure 9e).

During the period of 492 to 556 min, the entire front edge of the model experienced sliding, and the rear part of the slope lost support. Tensile crack L_3 connected with L4; the slope located before them experienced a slide of approximately 0.5~1.5 cm, with a maximum instability thickness of approximately 10.4 cm (Figure 10e). From 556 to 653 min of rainfall, progressive failure occurred in the mid-rear area of the model. Failure of the model's middle sliding body occurred, which was located at front of the L_3 and L_4 tensile cracks (Figure 9f), leading to the sliding of the block in front of the L_2 crack at the rear of the model (Figure 9g), with a maximum instability thickness of approximately 15.2 cm (Figure 10f). By 660 min of rainfall, no new signs of deformation were observed in the model, and the model test was concluded.
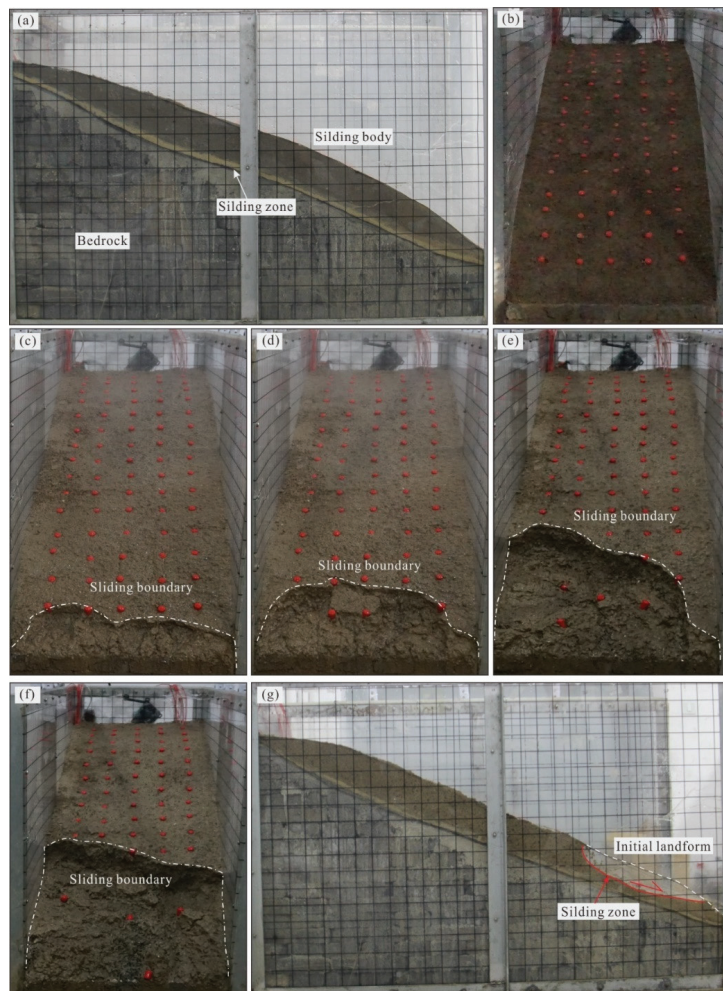

Figure 7. Deformation and failure characteristics of the model slope in different stages under working scenario 1: (**a**) Side view of the model slope, (**b**) Front view of the model slope, (**c**) Deformation and failure characteristics of the slope during the 0–178 min stage, (**d**) Deformation and failure characteristics of the slope during the 178~362 min stage, (**e**) Deformation and failure characteristics of the slope during the 362–838 min stage, (**f**) Deformation and failure characteristics of the slope during the 838~1108 min stage, (**g**) Deformation and failure characteristics of the slope during the 838~1108 min stage (side view).
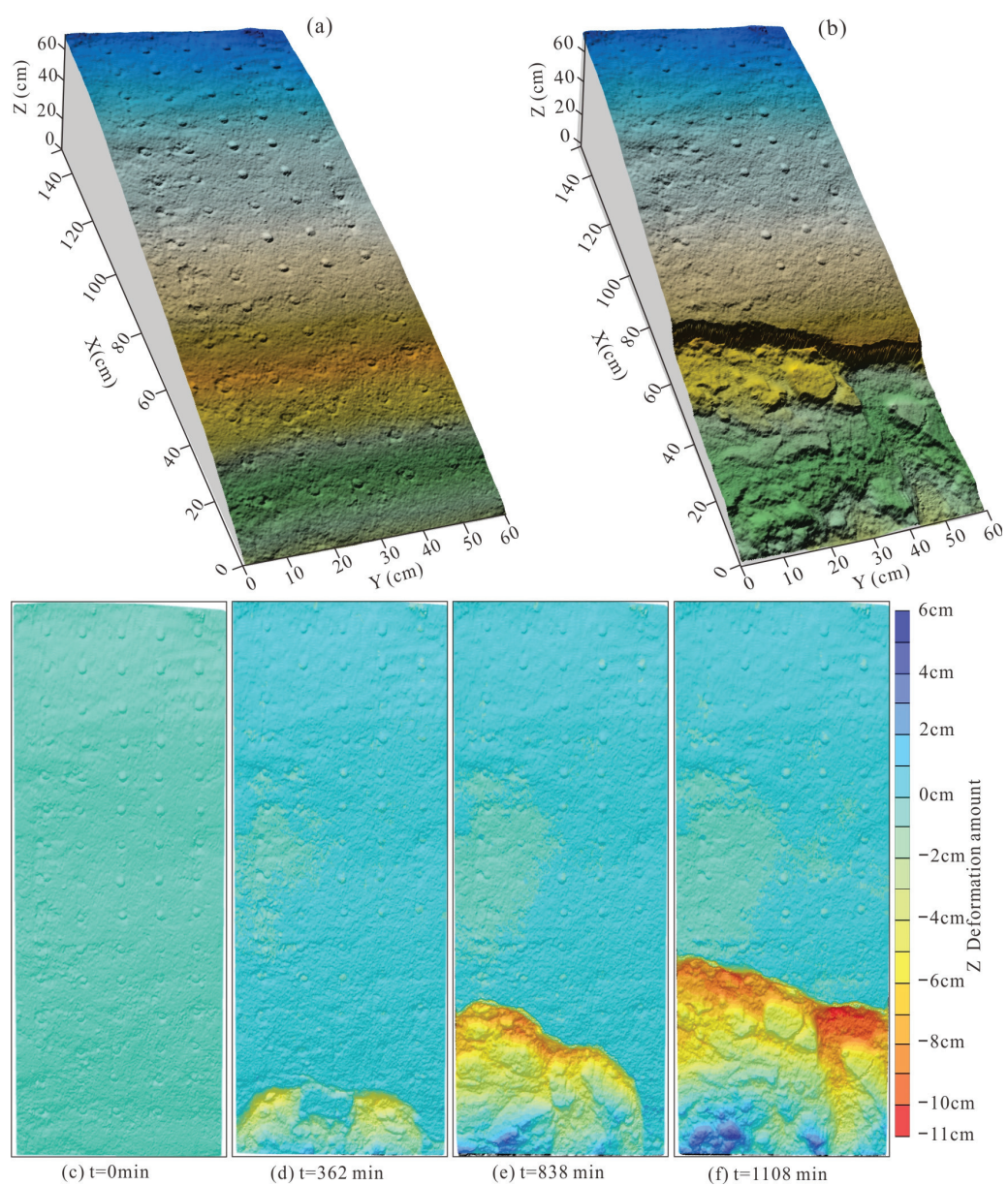
Figure 8. Orthophoto evolution of the landslide model test under working scenario 1: (**a**) Three-dimensional model slope before the model test; (**b**) Three-dimensional model slope after the model test; (**c–f**) Cloud maps in the Z-deformation amount of the slope at different times.
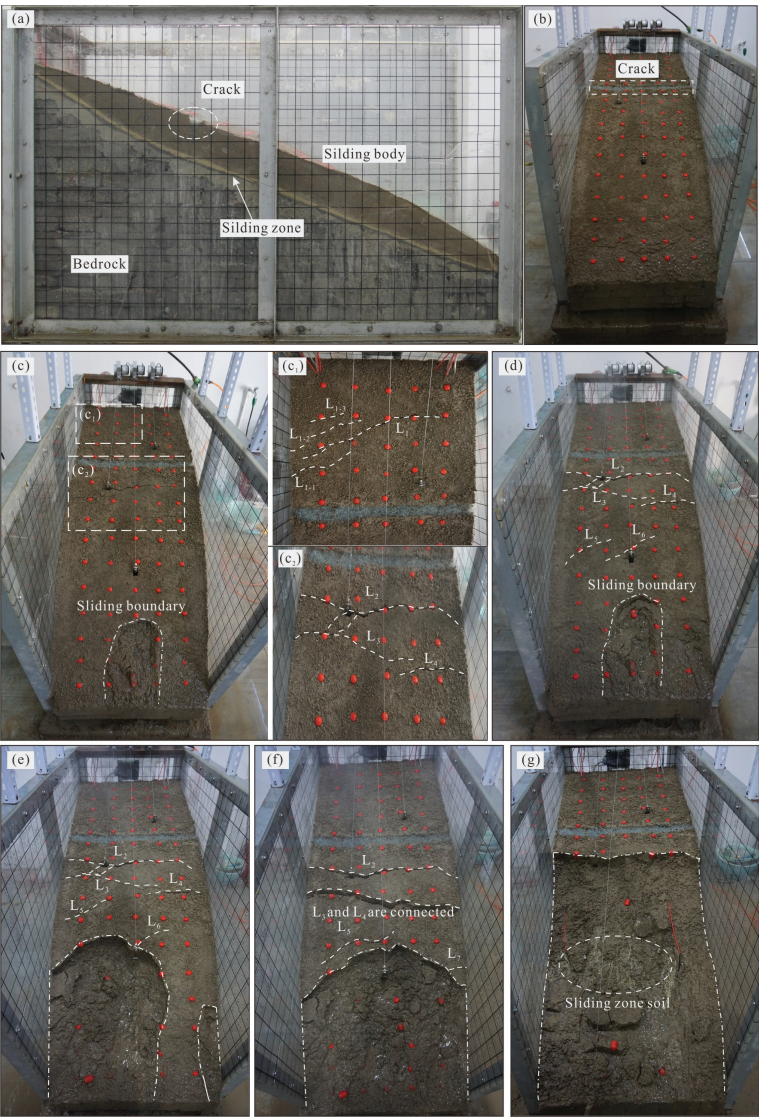
Figure 9. Deformation and failure characteristics of the model slope in different stages under working scenario 2: (**a**) Side view of the model slope; (**b**) Front view of the model slope; (**c,c$_1$,c$_2$**) Deformation characteristics of the slope body during the 112~220 min stage; (**d**) Deformation characteristics of the slope body during the 220~397 min stage; (**e**) Deformation characteristics of the slope body during the 397~492 min stage; (**f**) Deformation characteristics of the slope body during the 492~556 min stage; (**g**) Deformation characteristics of the slope body during the 556~653 min stage.
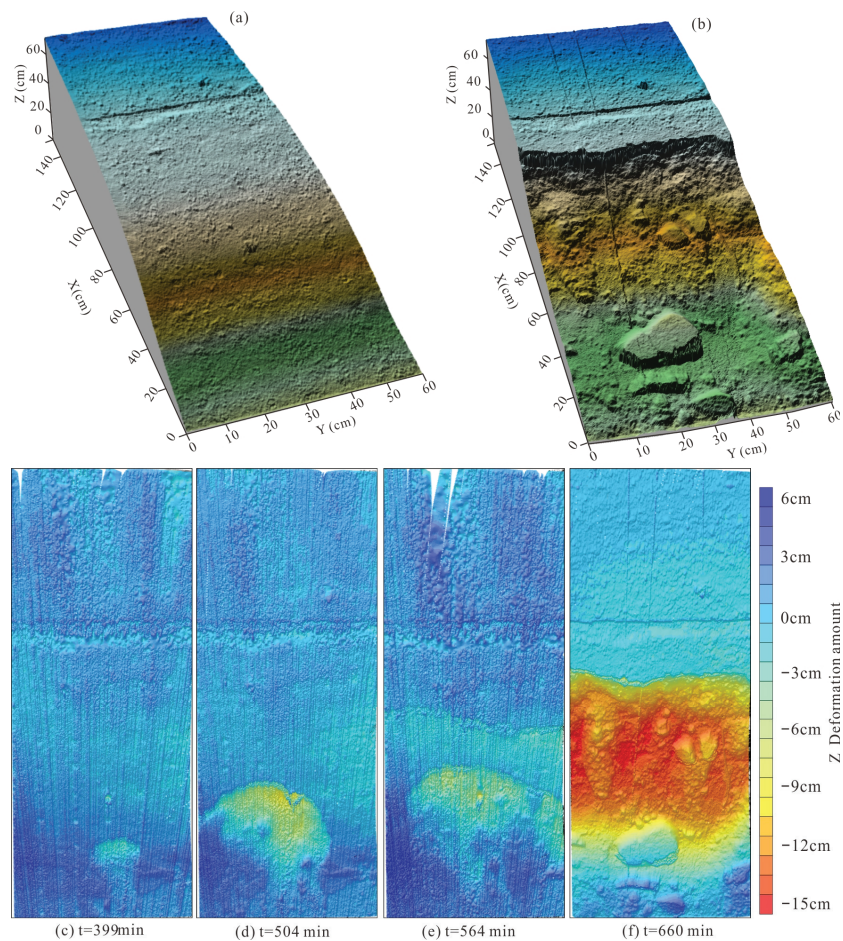
Figure 10. Evolution orthophotos of the model slope under working scenario 2. Evolution orthophotos of the model slope under working scenario 2: (**a**) Three-dimensional model slope before the model test; (**b**) Three-dimensional model slope after the model test; (**c**–**f**) Cloud maps of the Z-deformation of the model slope at different times.

4.2. Variation in Pore Water Pressure

In the model test process of scenario 1, a significant change in the pore water pressure at the mid-front of the model was observed. During the 0~100 min period of rainfall, the pore water pressure near the sliding zone in the slope was relatively low. At 105 min of rainfall, pore water pressure was first observed at monitoring point P4. The pore water pressure of P4 exhibited a transient sharp increase followed by a slow increase. At 248 min, the pore water pressure of P4 remained stable after a temporary reduction. From 130 to 435 min, there was a slow increase in pore water pressure at monitoring point P2. At 362~435 min, the pore water pressure of P4 rapidly raised after a temporary reduction. From 435 to 448 min, when the rainfall stopped, the pore water pressure of P2 and P4 continued to decrease. After 450 min, there was a sharp rise in pore water pressure at monitoring points P1 and P4. At time nodes 572 and 850 min, both P1 and P4 exhibited decreasing trends in pore water pressure, with decreases of 0.04 kPa, 0.07 kPa, 0.03 kPa, and 0.12 kPa, respectively. During the 950~975 min period, when the rainfall ceased, the pore water pressure decreased at all monitoring points at the mid-front of the model. Around 1108 min

of rainfall, there was a significant decrease in the pore water pressure at monitoring points P1, P2, P4, and P5, with reductions of 0.34 kPa, 0.02 kPa, 0.14 kPa, and 0.02 kPa, respectively. Throughout the entire model test, no pore water pressure was detected at monitoring points P3 or P6, which were located at the sliding zone on the rear edge of the slope (Figure 11).
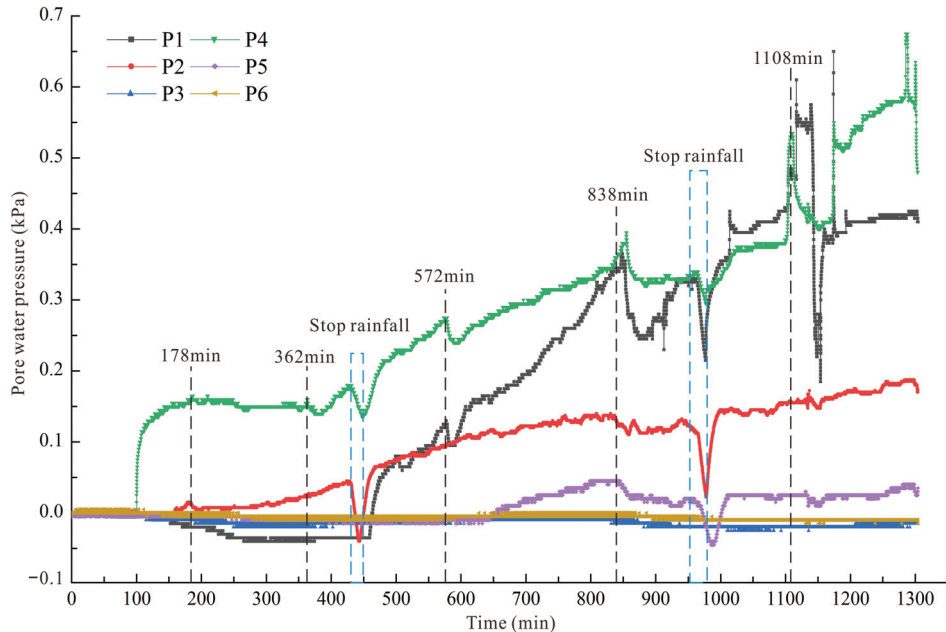

Figure 11. Process of pore water pressure changes under working scenario 1.

In the model test process of scenario 2, significant changes in the pore water pressure at all monitoring points of the model were observed. During the first 40 min of rainfall, there were no changes in pore water pressure. From 42 to 75 min, there was a sharp increase in the pore water pressure at five monitoring points, i.e., P5, P2, P4, P6, and P1, in order. From 104 to 158 min, except for monitoring point P3, the pore water pressure exhibited a transient decrease followed by another increase. At approximately 158 min, there was a sharp increase in the pore water pressure at monitoring point P3. From 175 to 187 min, when the rainfall stopped, the pore water pressure continued to decrease at all monitoring points. Around 220 min of rainfall, the pore water pressure decreased at all monitoring points, with the greatest reductions observed at monitoring points P1 and P3 on the right side of the slope. From 225 to 504 min, the pore water pressure slowly increased at all monitoring points, and at 490 min, the pore water pressure decreased again at all monitoring points. During the 504~520 min period of rainfall, there was a sudden increase followed by a sharp decrease in the pore water pressure at all monitoring points. From 510 to 525 min, when the rainfall ceased, the pore water pressure continued to decrease at all monitoring points. From 530 to 575 min, the pore water pressure at all monitoring points rose sharply and remained stable. There was a sudden drop in pore water pressure at monitoring point P4 at 560 min, while the remaining monitoring points showed a slowly decreasing trend. From 580 to 660 min, the pore water pressure initially increased slightly and then sharply decreased at all monitoring points. Pore water pressure reductions of 0.53 kPa, 1.09 kPa, 0.66 kPa, and 0.31 kPa were observed at monitoring points P1, P2, P4, and P5, respectively. The reductions in pore water pressure at monitoring points P3 and P6 were relatively small (Figure 12).
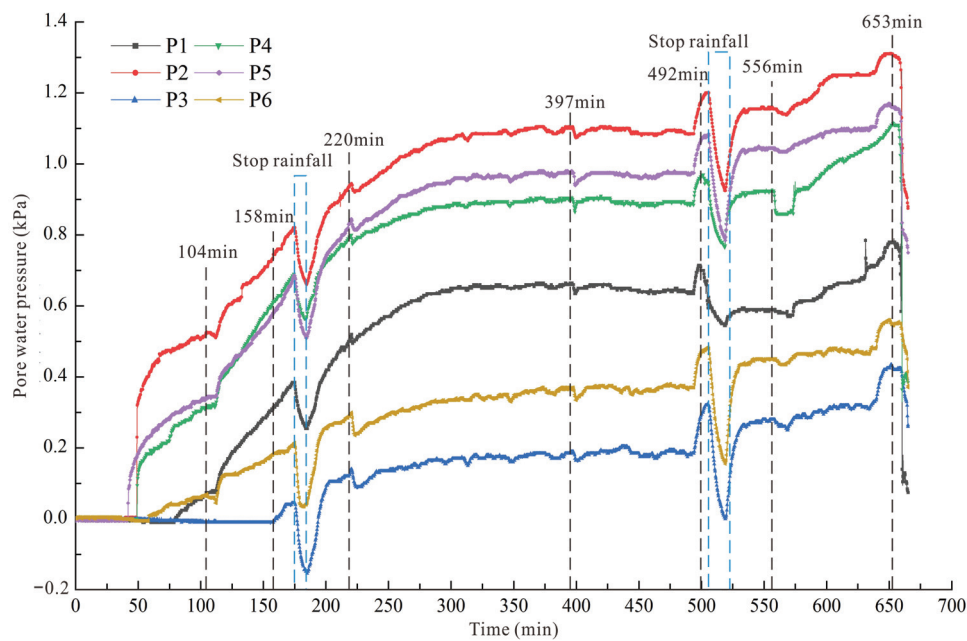
Figure 12. Process of pore water pressure changes under working scenario 2.

4.3. Variation in Soil Pressure

In the model test process of scenario 1, a significant change in soil pressure at the mid-front of the model was observed. During the 60 min before rainfall, the soil pressure at monitoring points S2 and S5 in the middle of the model gradually decreased and then sharply increased. The maximum soil pressures were 2.94 kPa and 1.98 kPa, respectively. Subsequently, during the model test, the soil pressures of S2 and S5 gradually decreased. From the 138th minute until the end of the model test, the soil pressure at monitoring point S6 slowly increased and exhibited oscillatory fluctuations, and the soil pressure at S3 remained stable throughout the process. From 38 to 150 min of rainfall, the soil pressures at S2 and S4 sharply increased and then slowly decreased. The maximum soil pressures reached were 2.46 kPa and 3.52 kPa, respectively. From 200 to 500 min, the soil pressures of S1 and S4 gradually increased, reaching peak values at the 342nd minute before slowly decreasing. From 500 to 830 min, the soil pressure at S1 remained constant, gradually increasing after the 742nd minute. The soil pressure of S4 gradually increased, experienced a sudden decrease at 595 min, increased again, reached its peak value after the 742nd minute, and remained stable thereafter. From 830 to 1108 min, the soil pressure at S1 continued to increase, reaching its peak value at the 950th minute and remaining stable. It then decreased in a stepped manner after the 1013th minute, and experienced a sharp decrease at the 1108th minute. The soil pressure at S4 briefly decreased, slowly increased, and rapidly decreased after the 1108th minute (Figure 13).
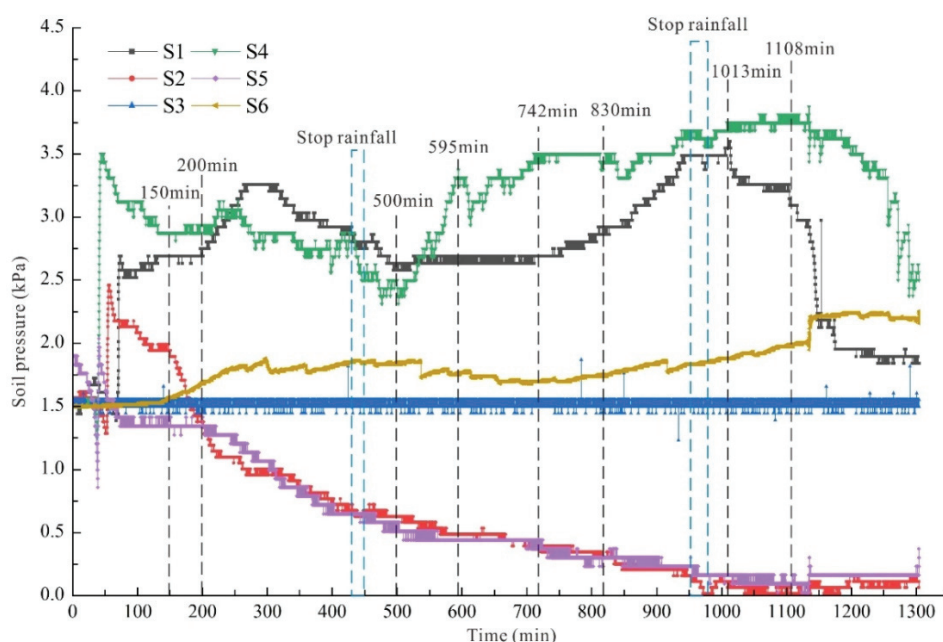
Figure 13. Monitoring curve of soil pressure under working scenario 1.

In the model test process of scenario 2, significant changes in soil pressure at all monitoring points were observed. At 0 to 104 min of rainfall, the soil pressure in the front part of the slope fluctuated intensively, while the rear crack area of the slope remained relatively stable. The soil pressure at monitoring point S3 remained unchanged, and the soil pressure at monitoring point S6 gradually increased and then stabilized until the end of the test. From 150 to 168 min, there was an increase, followed by a sudden drop in soil pressure at monitoring points S1 and S4. From 190 to 228 min, there was a brief increase followed by a decrease in soil pressure at monitoring points S1 and S4. From 228 to 400 min, the variation in soil pressure at all monitoring points was small during continuous rainfall. From 400 to 500 min, there was a slight decrease in the soil pressure at monitoring points S2 and S3 in the middle of the slope, while the soil pressure at S1 slowly increased. From 525 to 580 min, the soil pressure at monitoring points S1, S2, S4, S5, and other monitoring points slowly increased, followed by a gradual decrease in the soil pressure at monitoring point S4. From 580 to 650 min, there was a sudden increase followed by a sharp decrease in soil pressure at monitoring point S4 in the front left part of the slope, while the soil pressure at monitoring points S1, S2, S5, and others slowly increased and then gradually decreased (Figure 14).
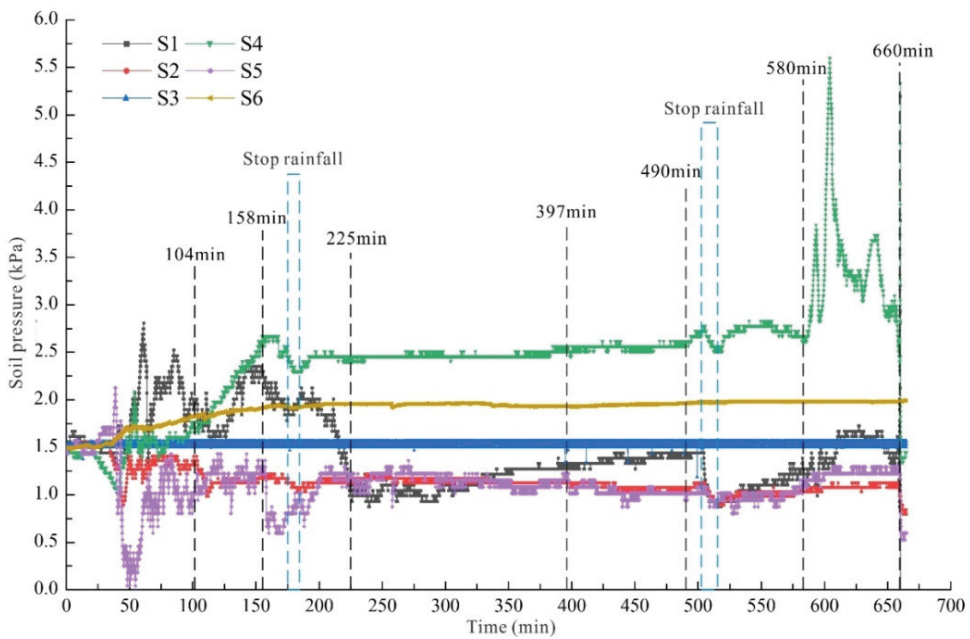
Figure 14. Monitoring curve of soil pressure under working scenario 2.

5. Discussion

5.1. The Mechanism of Ancient Landslide Reactivation

Under the action of rainfall, the reactivation mechanism of ancient landslides is closely related to cracks. When cracks develop on the slope's surface, surface water can rapidly infiltrate into the sliding zone along the preferential channels formed by the cracks [53]. This not only weakens the strength of the sliding zone soil, but also increases the groundwater and pore water pressure, thereby inducing ancient landslide reactivation [54,55]. The results of these model tests show that there are significant differences in the internal response characteristics of slopes with and without cracks. This leads to differences in the reactivation mechanisms of landslides under different conditions.

When a slope has no cracks, under the influence of gravity, rainwater rapidly accumulates at the foot of the slope. The saturation zone appears first at the foot of the slope, and it takes a relatively long time for rainfall to penetrate to the position of the sliding zone in the slope (at least 100 min). The pore water pressure at the front edge of the slope (P1 and P4) is greater than that at the middle and rear parts of the slope (P2 and P5, P3, and P6) (Figure 11). The results show that the influence of rainfall infiltration on the pore water pressure in the sliding zone of a slope occurs at the foot of the slope, the middle of the slope, and the back edge of the slope, in order. When a predetermined crack exists at the rear edge of the slope, the rainfall rapidly infiltrates into the deep part of the slope along the crack (about 50 min) and travels towards the middle and front edge under the influence of gravity, resulting in maximum pore water pressure at the middle part of the slope (P2 and P5), followed by the pore water pressure at the front edge of the slope (P1 and P4) and the minimum pore water pressure at the rear edge of the slope (P3 and P6) (Figure 12). The results show that the effect of rainfall infiltration on the pore water pressure in the sliding zones of cracked slopes is significantly different from that in slopes without cracks. In addition, the soil pressure at P3 on the right side of the rear edge of the landslide remained unchanged, and the soil pressure at P6 on the left side increased slowly, indicating that the rainfall quickly penetrated into the middle and lower parts of the slope after reaching the right side of the rear edge, while the water infiltration on the left side slowly led to

an increase in the body weight of the slope, which was consistent with the local slide first occurring on the right side of the slope.

Under rainfall conditions, the internal soil pressure response characteristics of slopes with and without cracks are significantly different. When a slope has no cracks, the maximum soil pressure is observed at the front edge (S1 and S4), followed by the rear edge (S3 and S6), and the minimum is found in the middle part (S2 and S5) (Figure 13). The soil pressure in the middle part (S2 and S5) continues to decrease, indicating that the influence from the rear edge gradually weakens in the middle part. This means that the rainfall's impact on the landslide is mainly concentrated in the middle and front parts. When the soil pressure in the middle part tends to stabilize, it indicates that there are no further signs of deformation in the rear edge of the slope. In addition, the soil pressure on the right side of the slope is less than that on the left side, which is consistent with the local sliding on the right side of the slope first. However, when predetermined cracks exist at the rear edge of the slope, the rainfall quickly affects the deep part of the slope along the crack and infiltrates into the middle and front parts of the slope. The soil pressure in the middle part fluctuates within a small range during the experimental process (Figure 14), indicating that the rear edge of the landslide continues to deform and pushes against the middle and front parts. As a result, the front part of the slope collapses and further triggers deformation and failure in the middle and rear parts, ultimately leading to overall instability of the landslide. The comparison between monitoring data and slope deformation and failure process shows that, before local sliding occurs, the soil pressure inside the slope increases abruptly for a short time and then decreases sharply after local sliding of the slope.

Based on the aforementioned analysis, solely considering rainfall conditions, significant disparities in reactivation mechanisms of slopes with and without cracks can be observed. When the slope had no cracks, the reactivation mechanism of the ancient landslide under rainfall primarily manifested as foot erosion and localized progressive failure at the front edge, with a limited impact range and depth (Figure 15a). However, when cracks existed on the slope, the mechanical behavior of the reactivation mechanism became complex. It exhibited mid-rear sliding body creeping, tensile cracks developed on the mid-rear sliding body, localized sliding at the front edge, extension of the tensile cracks in the mid-rear sliding body, extension of the local sliding range at the front edge, accelerated creeping in the mid-rear sliding body, and progressive failure of the mid-rear sliding body (Figure 15b). The presence of dominant seepage as crack channels promotes the evolution process of ancient landslide reactivation under the same rainfall conditions, causing an increased range of deformation and failure of ancient landslides.
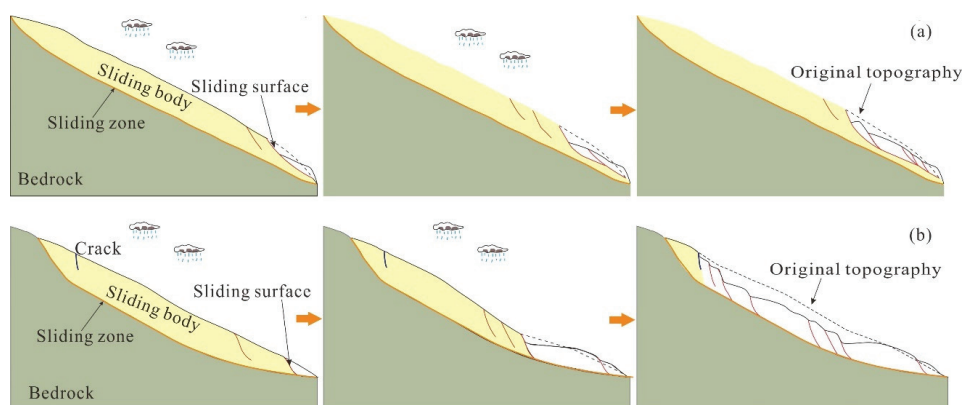

Figure 15. Reactivation mode of an ancient landslide with and without cracks: (**a**) Scenario 1, (**b**) Scenario 2.

5.2. The Evolution Process of Ancient Landslide

The model tests demonstrate that, under rainfall conditions, both slopes with and without cracks exhibit progressive retrogressive failure in terms of deformation and failure patterns. However, there are notable distinctions in the extent of failure. When there are no cracks in the slope, only the front edge of the slope body experiences local sliding before the landslide, followed by the extension of deformation and failure towards the rear. The concentrated deformation and failure range is located at the front edge of the slope, and the front edge of the slope does not slide along the predetermined sliding zone, but forms a new sliding zone at a certain depth inside the sliding body. When a crack is present at the rear part of the slope, the middle and rear parts of the slope firstly develop some tensile cracks, followed by local sliding at the front edge. Under continuous rainfall, the range of local sliding at the front edge further expands and the deformation in the middle and rear parts intensifies, resulting in overall reactivation along the predetermined sliding zone.

Based on the analysis of the experimental results, this study roughly divides the evolution process of ancient landslide reactivation into the following three stages.

Stage 1: Non-uniform settlement and crack formation stage (Figure 16a,b,e,f): After undergoing long-term geological transformation, the material composition and structural characteristics of ancient landslides exhibit high density, high cementation, low permeability, and heterogeneity [56]. During the initial stage of rainfall, water only affects the shallow surface of the slope. The heterogeneity on the plane leads to non-uniform settlement of the landslide, resulting in tensile stress near the boundary of the non-uniform settlement in the shallow layer of the slope. This provides favorable conditions for the generation of micro-cracks on the slope surface. Subsequently, rainwater infiltrates into the internal part of the slope along the micro-cracks, and the micro-cracks extend longitudinally and transversely, interconnecting with each other and eventually forming cracks.
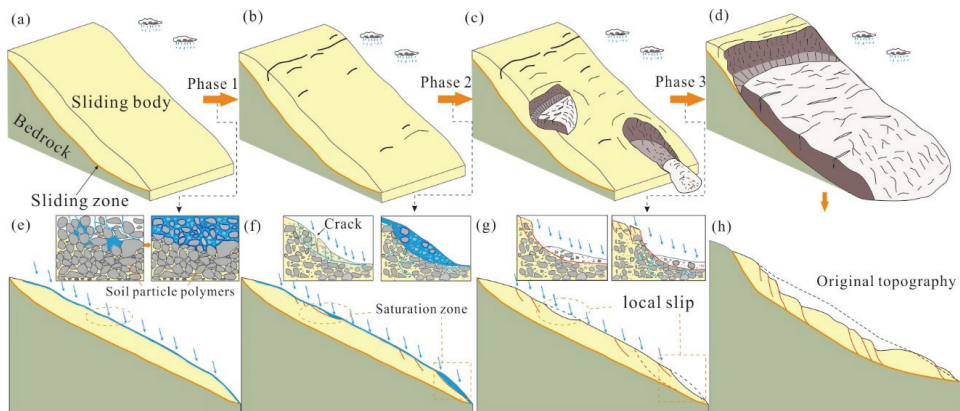

Figure 16. Evolution process of ancient landslide reactivation: (**a**) Initial model of ancient landslide; (**b**) Rainfall infiltration and crack formation on the slope surface; (**c**) Overall deformation and local sliding; (**d**) Progressive instability and failure; (**e**) Early stage of rainfall infiltration; (**f**) Process of flow channel formation; (**g**) Local sliding; (**h**) Progressive instability.

Stage 2: Crack extension and local sliding stage (Figure 16c,g): The crack in the shallow layer of the slope becomes the main preferential pathway for rainwater infiltration into the deep part of the slope in the later stage. Under the influence of gravity, rainwater gradually infiltrates into the deep part of the slope and towards the direction of the free face. This causes the cracks on the slope to gradually extend towards the deep part and the direction of the free face, gradually evolving into local weak structural planes. The sliding body undergoes creep deformation along these local weak structural planes towards the direction of the free face (Figure 16g). Influenced by the topography, relatively flat areas

such as the accumulation platform and the foot of the slope are prone to forming locally water-rich, saturated zones. As a result, the pore water pressure rises within the slope, reducing the shear resistance of the structural planes, eventually leading to localized sliding of the sliding body.

Stage 3: Progressive failure and overall instability stage (Figure 16d,h): After localized sliding occurs at the front and middle parts of the slope, a free face with a steeper slope is formed. The weak structural planes or sliding zones are exposed to the free face, developing a series of tensile cracks around the boundary of the localized sliding (Figure 16c). Rainwater quickly infiltrates along these tensile cracks to the slip bands, resulting in the degradation of the mechanical properties of the sliding zone and a significant reduction in shear resistance. The rear part of the slope undergoes accelerated creep deformation, and the cracks in the middle and rear parts extend, eventually leading to instability and failure. This evolutionary process is nearly identical to the process of excavation-induced instability of landslides, but the effects of water are slow. Rainfall-induced landslide deformation has characteristics such as multi-stage and multi-phase occurrence [37].

5.3. Limitations and Inspirations of Model Test

By analyzing the deformation and failure processes and the characteristics of model slopes with and without cracks under rainfall conditions, the reactivation mechanisms of ancient landslides under the influence of rainfall or the coupling effect between rainfall and cracks were revealed. However, this model test has certain limitations and is not sufficient for the evaluation of the hazard or stability of a landslide. The cracks in this model test were only considered in terms of depth and position, without considering factors such as the number of cracks, their extension lengths, or their directions. Therefore, they cannot truly reflect the current state of the landslide.

Currently, both our model test and numerical simulation are effective methods to evaluate landslide stability. Numerical simulation has been widely used due to its efficiency, convenience, accuracy, flexibility, and low cost [57,58]. In landslide engineering, the accuracy of stability evaluation results obtained through model tests and numerical simulations depends mainly on whether the evaluation models truly reflect the landslide prototype. Most researchers generalize the landslide prototype and ignore certain factors, such as slope body cracks, and establish generalized models based on the major factors for evaluation [57,59,60]. Although some results have been achieved through this approach, it also ignores the factors that influence the evaluation results, such as groundwater, cracks, etc. Based on the analysis of the results of this experimental study, for the evaluation of stability in ancient landslides, it is necessary to further consider the geometric characteristics of landslide cracks and their influences on stability, such as depth, width, length, and orientation.

6. Conclusions

In this study, the Woda landslide was taken as a case study, and the deformation and instability processes of different model slopes with and without cracks were investigated under rainfall conditions based on model tests. The influence of cracks on ancient landslide reactivation was analyzed, and the reactivation mechanism of ancient landslides under the coupling effect of rainfall and cracks was revealed. The following main conclusions are drawn:

1. The influence of rainfall on the deformation process, instability, and range of an ancient landslide is closely related to cracks. When there are no cracks in an ancient landslide, the deformation and failure of the ancient landslide are concentrated mainly in the front part, with the impact mainly limited to the shallow sliding body at the front part of the ancient landslide. However, when cracks develop on an ancient landslide, rainwater can rapidly infiltrate into the deep sliding zone along the cracks, resulting in overall deformation and instability of the ancient landslide.

2. Under rainfall conditions, significant differences can be observed in the response characteristics of pore water pressure and soil pressure in the deep parts of ancient landslides with and without cracks. When cracks develop on ancient landslides, the time required for rainwater to infiltrate into the deep sliding area is twice as long as in ancient landslides with cracks. Rainfall first causes changes in the pore water pressure and soil pressure at the foot of the ancient landslide, followed by the middle of the ancient landslide, with the least impact at the rear of the ancient landslide. When cracks develop on an ancient landslide, rainfall first causes changes in the pore water pressure and soil pressure at the mid-rear of the ancient landslide, followed by changes in the pore water pressure and soil pressure at the foot of the ancient landslide.

3. The reactivation mechanisms of ancient landslides under rainfall conditions and the coupling effect of rainfall and cracks show significant differences. In cases where there are no cracks present, the overall behavior involves erosion at the toe of the ancient landslide and progressive localized failure at the front edge, with the impact range and depth being limited. However, when cracks develop on ancient landslides, the mechanical behavior of the reactivation mechanism becomes more complex, including mid-rear ancient landslide creeping, tensile cracks developing at the mid-rear of the ancient landslide, localized sliding at the front edge, extension of tensile cracks, extension of the local sliding range, accelerated creeping, and progressive failure at the mid-rear of the ancient landslide.

4. Cracks play an important role in promoting the deformation and failure of ancient landslides. The characteristics of crack development in different stages of the reactivation of ancient landslides vary. It is recommended to consider the influence of crack development characteristics of ancient landslides, such as crack location, quantity, depth, length, and orientation, on their stability in the evaluation of landslide stability.

References

1. Cruden, D.M.; Varnes, D.J. Landslide types and processes. In *Landslides: Investigation and Mitigation: Special Report 247*; Turner, A.K., Schuster, R.L., Eds.; National Academy Press: Washington, DC, USA, 1996; pp. 36–75.
2. Lu, Z.Y. Theory of landslide classification and sliding historical category. In Proceedings of the Sichuan Landslide Research and Prevention Experience Exchange Meeting, Chengdu, China, 1983.
3. Cruden, D.M.; Varnes, D.J. Landslide types and processes, special report, transportation research board. *Nat. Acad. Sci.* **1996**, *247*, 36–75.
4. Zhang, Y.S.; Guo, C.B.; Lan, H.X.; Zhou, N.J.; Yao, X. Reactivation mechanism of ancient giant landslides in the tectonically active zone: A case study in Southwest China. *Environ. Earth. Sci.* **2015**, *74*, 1719–1729. [CrossRef]
5. Li, Y.F.; Ji, Q.K. Short discussion on the distinction of paleo landslides. *West-China Explor. Eng.* **2006**, *128*, 287–296.
6. Zhang, M.S.; Li, T.L. Triggering factors and forming mechanism of loess landslides. *J. Eng. Geol.* **2011**, *19*, 530–540.

7.   Iverson, R.M.; George, D.L.; Allstadt, K.; Reid, M.E.; Collins, B.D.; Vallance, J.W.; Schilling, S.P.; Godt, J.W.; Cannon, C.M.; Magirl, C.S.; et al. Landslide mobility and hazards: Implications of the 2014 Oso disaster. *Earth Planet. Sci. Lett.* **2015**, *412*, 197–208. [CrossRef]

8.   Guo, C.B.; Zhang, Y.S.; Li, X.; Ren, S.S.; Yang, Z.H.; Wu, R.A.; Jin, J.J. Reactivation of giant Jiangdingya paleo landslide in Zhouqu County, Gansu Province, China. *Landslides* **2019**, *17*, 179–190. [CrossRef]

9.   Notti, D.; Wrzesniak, A.; Dematteis, N.; Lollino, P.; Fazio, N.L.; Zucca, F.; Giordan, D. A multidisciplinary investigation of deep-seated landslide reactivation triggered by an extreme rainfall event: A case study of the Monesi di Mendatica landslide, Ligurian Alps. *Landslides* **2021**, *18*, 2341–2365. [CrossRef]

10. Macciotta, R.; Hendry, M.; Martin, C.D. Developing an early warning system for a very slow landslide based on displacement monitoring. *Nat. Hazards.* **2016**, *81*, 887–907. [CrossRef]

11. Muller, L. New Considerations on the Vaiont Slide. *Rock Mech. Eng. Geol.* **1968**, *6*, 1–91.

12. Liu, G.; Tong, F.G.; Zhao, Y.T.; Tian, B. A force transfer mechanism for triggering landslides during rainfall infiltration. *J. Mt. Sci.* **2018**, *15*, 2480–2491. [CrossRef]

13. Hu, X.W.; Huang, R.Q.; Zhu, H.Y.; Lv, X.P.; Zhang, X.; Shi, Y.B. Earthquake reactivation effects and stability study of malingyan landslide in Tangjiashan dammed lake. *Chin. J. Rock Mech. Eng.* **2009**, *28*, 1270–1278.

14. Guo, C.B.; Yan, Y.Q.; Zhang, Y.S.; Wu, R.A.; Yang, Z.H.; Li, X.; Ren, S.S.; Zhang, Y.Y.; Wu, Z.K.; Liu, J.X. Research Progress and Prospect of the Failure Mechanism of Large Deep-seated Creeping Landslides in the Tibetan Plateau, China. *Earth Sci.* **2022**, *47*, 3677–3700. Available online: https://kns.cnki.net/kcms/detail/42.1874.P.20220808.1553.020.html (accessed on 14 January 2024).

15. Yang, Y.T.; Dai, Z.W.; Lu, Y.S.; Zhang, C.Y.; Yan, H.; Hou, X.F.; Tang, J. Deformation characteristics and stability changes characteristics of reservoir landslides with double-sliding zones. *Earth Sci.* **2022**, 1–15. Available online: https://kns.cnki.net/kcms/detail/42.1874.P.20220809.1707.013.html (accessed on 14 January 2024).

16. Deng, L.X.; Xu, S.G.; Zheng, T.; Wu, J.; He, S.L. Analysis on the Reactivation Deformation Characteristics and Stability of Paleolandslide in Yongshan County. *Sci. Tech. Eng.* **2023**, *23*, 2308–2316.

17. Govi, M.; Sorzana, P.; Tropeano, D. Landslide mapping as evidence of extreme regional events. *Stud. Geomorphol Carpatho-Balc.* **1982**, *15*, 81–98.

18. Giannecchini, R. Rainfall triggering soil slips in the southern Aquan Alps. *Adv. Geosci.* **2005**, *2*, 21–24. [CrossRef]

19. Gil, E.; Długoszm, M. Threshold values of rainfalls triggering selected deep-seated landslides in the polish Flysch Carpathians. *Stud. Geomorphol Carpatho-Balc.* **2006**, *40*, 21–43.

20. De Vita, P.; Reichenbach, P.; Bathurst, J.C.; Marco, B.; Crosta, G.; Crozier, M.; Glade, T.; Guzzetti, F.; Hansen, A.; Wasowski, J. Rainfall-triggered landslides: A reference list. *Environ. Geol.* **1998**, *35*, 219–233. [CrossRef]

21. Iverson, R.M. Landslide triggering by rain infiltration. *Water Resour. Res.* **2000**, *36*, 1897–1910. [CrossRef]

22. Borja, R.I.; White, J.A. Continuum deformation and stability analyses of a steep hillside slope under rainfall infiltration. *Acta Geotech.* **2010**, *5*, 1–14. [CrossRef]

23. Borja, R.I.; White, J.A.; Liu, X.; Wu, W. Factor of safety in a partially saturated slope inferred from hydro-mechanical continuum modeling. *Int. J. Numer. Anal. Methods Geomech.* **2012**, *36*, 236–248. [CrossRef]

24. Cojean, R.; Cai, Y.J. Analysis and modeling of slope stability in the Three-Gorges Dam reservoir (China)—The case of Huangtupo landslide. *J. Mt. Sci.* **2011**, *8*, 166–175. [CrossRef]

25. Lee, Y.F.; Chi, Y.Y. Rainfall-induced landslide risk at Lushan. Taiwan. *Eng. Geol.* **2011**, *123*, 113–121. [CrossRef]

26. Qi, S.; Vanapalli, S.K. Computers and Geotechnics Influence of swelling behavior on the stability of an infinite unsaturated expansive soil slope. *Comput. Geotech.* **2016**, *76*, 154–169. [CrossRef]

27. Zhou, J.W.; Cui, P.; Hao, M.H. Comprehensive analyses of the initiation and entrainment processes of the 2000 Yigong catastrophic landslide in Tibet, China. *Landslides* **2016**, *13*, 39–54. [CrossRef]

28. Chen, M.L.; Lv, P.F.; Zhang, S.L.; Zhou, J.W.; Chen, M.L.; Chen, X.Z. Time evolution and spatial accumulation of progressive failure for Xinhua slope in the Dagangshan reservoir, Southwest China. *Landslides* **2018**, *15*, 565–580. [CrossRef]

29. Li, S.H.; Wang, Y.N. Selection study of computational parameters for DEM in geomechanics. *Chin. J. Rock Mech. Eng.* **2004**, *23*, 3642–3651.

30. Wang, Y.; Li, X.; He, J.M.; Wu, Y.F.; Wu, Y.S. Research status and prospect of rock and soil aggregate. *J. Eng. Geol.* **2014**, *22*, 112–123. [CrossRef]

31. Hu, F.; Li, Z.Q.; Hu, R.L.; Zhou, Y.X.; Yuan, R.Q. Research on the deformation characteristics of shear band of soil-rock mixture based on large scale direct shear test. *Chin. J. Rock Mech. Eng.* **2018**, *37*, 766–778. [CrossRef]

32. Li, A.G.; Yue, Z.Q.; Tham, L.G.; Li, A.G.; Law, K.T. Field-monitored variations of soil moisture and matric suction in a saprolite slope. *Can. Geotech. J.* **2005**, *42*, 13–26. [CrossRef]

33. Li, T.L.; Xi, Y.; Hou, X.K. Mechanism of surface water infiltration induced deep loess landslide. *J. Eng. Geol.* **2018**, *26*, 1113–1120. [CrossRef]

34. Hu, R.L.; Lc, X.; Wang, Y.; Gao, W.; Xia, J.G.; Li, Z.Q.; Gao, W.W.; Sun, Y.S. Research on engineering geomechanics and structural effect of soil-rock mixture. *J. Eng. Geol.* **2020**, *28*, 255–281. [CrossRef]

35. Zhou, Z.; Shen, J.h.; Li, Y.; Duan, W.F.; Yang, R.C.; Shu, J.C.; Li, H.W.; Tao, S.Y.; Zheng, S.Z. Mechanism of colluvial landslide induction by rainfall and slope construction: A case study. *J. Mt. Sci.* **2021**, *18*, 1013–1033. [CrossRef]

36. Zhang, Y.S.; Wu, R.A.; Ren, S.S. Influence of rainfall preponderance infiltration path on reactivation of ancient landslides. *Chin. J. Rock Mech. Eng.* **2021**, *40*, 777–789. [CrossRef]
37. Take, W.A.; Bolton, M.D.; Wong, P.C.P.; Yeung, F.J. Evaluation of landslide triggering mechanisms in model fill slopes. *Landslides* **2004**, *1*, 173–184. [CrossRef]
38. Rahardjo, H.; Lee, T.; Leong, E.C.; Rezaur, R. Response of a residual soil slope to rainfall. *Can. Geotech. J.* **2005**, *42*, 340–351. [CrossRef]
39. Luo, X.Q.; Liu, D.F.; Wu, J.; Cheng, S.G.; Sheng, H.; Xu, K.X.; Huang, X.B. Model test study on landslide under rainfall and reservoir water fluctuation. *Chin. J. Rock Mech. Eng.* **2005**, *24*, 2476–2483.
40. Jia, G.W.; Zhan, T.L.T.; Chen, Y.M.; Fredlund, D.G. Performance of a large-scale slope model subjected to rising and lowering water levels. *Eng. Geol.* **2009**, *106*, 92–103. [CrossRef]
41. Lin, M.L.; Wang, K.L. Seismic slope behavior in a large-scale shaking table model test. *Eng. Geol.* **2006**, *86*, 118–133. [CrossRef]
42. Moriwaki, H.; Inokuchi, T.; Hattanji, T.; Sassa, K.; Ochiai, H.; Wang, G. Failure processes in a full-scale landslide experiment using a rainfall simulator. *Landslides* **2004**, *1*, 277–288. [CrossRef]
43. Ochiai, H.; Okada, Y.; Furuya, G.; Okura, Y.; Matsui, T.; Sammori, T.; Terajima, T.; Sassa, K. A fluidized landslide on a natural slope by artificial rainfall. *Landslides* **2004**, *1*, 211–219. [CrossRef]
44. Rianna, G.; Pagano, L.; Urciuoli, G. Rainfall patterns triggering shallow flowslides in pyroclastic soils. *Eng. Geol.* **2014**, *174*, 22–35. [CrossRef]
45. Ma, J.W.; Tang, H.M.; Hu, X.L.; Bobet, A.; Yong, R.; Eldin, M.A.M.E. Model testing of the spatial–temporal evolution of a landslide failure. *Bull. Eng. Geol. Environ.* **2016**, *76*, 1–17. [CrossRef]
46. Wu, R.A.; Ma, H.S.; Zhang, J.C.; Yang, Z.H.; Li, X.; Ni, J.W.; Zhong, N. Developmental characteristics and damming river risk of the Woda landslide in the upper reaches of the Jinshajiang River. *Hydrogel. Eng. Geol.* **2021**, *48*, 120–128. [CrossRef]
47. Wu, R.A.; Yang, Z.H.; Guo, C.B.; Zhang, Y.S.; Song, D.G.; Ma, H.S.; Li, X.; Ni, J.W. Reactivation and dynamic process prediction of the Woda landslide in the upper Jinsha River Basin, China. *Environ. Earth Sci.* **2023**, *82*, 528. [CrossRef]
48. Ren, D.; Leslie, L.M.; Lynch, M.J.; Duan, Q.Y.; Dai, Y.J.; Wei, S.G. Why was the August 2010 Zhouqu landslide so powerful? *Georg. Environ.Sustain.* **2013**, *6*, 67–79. [CrossRef]
49. Abellan, A.; Vilaplana, J.M.; Martinez, J. Application of a long-range terrestrial laser scanner to a detailed rockfall study at Vall de Nuria (Eastern Pyrenees, Spain). *Eng. Geol.* **2006**, *88*, 136–148. [CrossRef]
50. Fanti, R.; Gigli, G.; Lombardi, L.; Tapete, D.; Canuti, P. Terrestrial laser scanning for rockfall stability analysis in the cultural heritage site of Pitigliano (Italy). *Landslides* **2013**, *10*, 409–420. [CrossRef]
51. Jaboyedoff, M.; Oppikofer, T.; Abellan, A.; Derron, M.H.; Loye, A.; Metzger, R.; Pedrazzini, A. Use of LIDAR in landslide investigations: A review. *Nat. Hazards.* **2012**, *61*, 5–28. [CrossRef]
52. Wang, G.Q.; Joyce, J.; Phillips, D.; Shrestha, R.; Carter, W. Delineating and defining the boundaries of an active landslide in the rainforest of Puerto Rico using a combination of airborne and terrestrial LIDAR data. *Landslides* **2013**, *10*, 503–513. [CrossRef]
53. Krzeminska, D.; Bogaard, T.; Malet, J.P.; van Beek, L.P.H. A model of hydrological and mechanical feedback of preferential fissure flow in a slow-moving landslide. *Hydrol. Earth Syst. Sci.* **2013**, *17*, 947–959. [CrossRef]
54. Lacroix, P.; Handwerger, A.L.; Bièvre, G. Life and death of slow-moving landslides. *Nat. Rev. Earth Environ.* **2020**, *1*, 404–419. [CrossRef]
55. Simoni, B.A. Observation and analysis of near-surface pore-pressure measurements in clayshales slopes. *Hydrol. Process.* **2012**, *26*, 2187–2205. [CrossRef]
56. Wang, R.B.; Wan, J.X.; Cheng, R.L.; Wang, Y.Z.; Wang, Z.Y. Physical and Numerical Simulation of the Mechanism Underpinning Accumulation Layer Deformation, Instability, and Movement Caused by Changing Reservoir Water Levels. *Water* **2023**, *15*, 1289. [CrossRef]
57. Zhang, X.; Tan, Z.Y.; Zhou, C.M. Seepage and stability analysis of landslide under the change of reservoir water levels. *Chin. J. Rock Mech. Eng.* **2016**, *35*, 713–723. [CrossRef]
58. Gu, T.F.; Wang, J.D.; Wang, N.Q. Geological features of loess landslide at Lüliang airport and its 3D stability analysis. *Rock Soil Mech.* **2013**, *34*, 2009–2016. [CrossRef]
59. Shen, T.; Wang, Y.S.; Huang, Z.Q.; Li, J.; Zhang, X.; Cao, W.Z.; Gu, J. Formation mechanism and movement processes of the Aizigou paleolandslide, Jinsha River, China. *Landslides* **2018**, *16*, 409–424. [CrossRef]
60. Shao, W.; Bogaard, T.A.; Bakker, M.; Greco, R. Quantification of the influence of preferential flow on slope stability using a numerical modelling approach. *Hydrol. Earth Syst. Sci.* **2015**, *19*, 2197–2212. [CrossRef]

Article

Failure Prediction of Open-Pit Mine Landslides Containing Complex Geological Structures Using the Inverse Velocity Method

Yabin Tao [1], Ruixin Zhang [1] and Han Du [2,*]

1   School of Energy and Mining Engineering, China University of Mining and Technology (Beijing),
     Beijing 100083, China; bqt2000101026@student.cumtb.edu.cn (Y.T.); 47170039@lntu.edu.cn (R.Z.)
2   State Key Laboratory of Hydroscience and Engineering, Department of Hydraulic Engineering,
     Tsinghua University, Beijing 100084, China
*   Correspondence: duh@tsinghua.edu.cn

Abstract: In the field of open-pit geological risk management, landslide failure time prediction is one of the important topics. Based on the analysis of displacement monitoring data, the inverse velocity method (INV) has become an effective method to solve this issue. To improve the reliability of landslide prediction, four filters were used to test the velocity time series, and the effect of landslide failure time prediction was compared and analyzed. The results show that the sliding process of landslide can be divided into three stages based on the INV: the initial attenuation stage (regressive stage), the second attenuation stage (progressive stage), and the linear reduction stage (autoregressive stage). The accuracy of the INV is closely related to the measured noise of the monitoring equipment and the natural noise of the environment, which will affect the identification of different deformation stages. Compared with the raw data and the exponential smoothing filter (ESF) models, the fitting effect of the short-term smoothing filter (SSF) and long-term smoothing filter (LSF) in the linear autoregressive stage is better. A stratified prediction method combining SSF and LSF is proposed. The prediction method is divided into two levels, and the application of this method is given.

Keywords: failure time of landslide; open-pit coal mine; inverse velocity; early warning; field monitoring

1. Introduction

Rockfalls and ground surface deformation, which are notoriously known due to their strong abruptness, intermittent occurrence, and destructive harm, are among the most critical issues both during mining and for many years after the cessation of mining [1,2]. In open-pit mining (also known as open-cut or open-cast mining), geomorphic processes possibly result in slope failures with alterations that entail potential sources of risk to personnel, apparatus, and infrastructures, in addition to dislocating mining scenarios and multiplying production expenditures [3–5]. Nevertheless, production work at a high rate could be hindered by major slope failure or the over-conservative nature of the ultimate design [6–8]. The mitigation of slope failure is a crucial topic of particular concern in open-pit mines, where production works must proceed with economic benefit yield, and simultaneously the safety of the personnel and the integrity of the mining equipment must be guaranteed [9].

Discerning ongoing processes of rock slope deformation that may lead to instability covers essential miscellaneous aspects of engineering geology and geomechanics [10–12]. The management of and substantial information on slope failure-associated risks are integral to having an adequate understanding of the lithostructural predisposition, the driving forces, and the different mechanisms and environmental conditions in the monitored area [13–15]. Irrespective of spatial and temporal terms, displacement and its derivatives (velocity and acceleration) are widely considered to be the most reliable alert indicators that can provide an early warning of potential movements [16]. Systematic efforts have gone

into implementation for early-warning precautions of a near-real-time slope monitoring network by utilizing the correlation among these kinematic parameters. The rationale for the majority failure forecast method (FFM) [17] is based on the observation that slopes undergo velocity increases asymptotically towards failure ("tertiary" or "accelerating" creep) [18]. Albeit clearly, FFM is on the temporal prediction of landslides and imminent collapse, which can be defined as time-of-failure (TOF) [19]. This leads to the necessity of integrating TOF analysis and alert indicators with a real-time assessment tool. Such a precursory tool was first suggested by Saito [20], incorporating discovering the inversely proportional relationship between time to slope failure and existing strain rate within the tertiary creep phase, and later improved by Fukuzono [21], who introduced a phenomenological method that takes into account the inverse of the velocity against time, the so-call inverse velocity (INV) method, leading to effective forecast results before the ultimate failure. Voight [22,23] went on to present successful applications of this method and extended the results to other types of natural phenomena or failure mechanisms, e.g., volcanic eruptions. Astonishingly, although the INV method was developed based on laboratory tests more than 30 years ago, it does not appear to have achieved implementation and verification for real-time slope failure prediction in the mining industry or mining-related technical literature until 2001 [24]. Since the early 21st century, in order to develop approaches to evaluate the failure time (t_f) of landslides, published examples (from the investigation of some large open-pit slope failures) of successful implementation are proposed to predict impending failure based on the results of the conventional application of INV methods [25–28].

Several studies of the INV method have been carried out to define rules and procedures to estimate the time of landslides in open-pit mines, including Rose and Hungr [24], Mufundirwa et al. [29], Dick et al. [19], Carlà et al. [30,31], Zhou et al. [32], and Chen and Jiang [33]. By presenting three large rockfall events of open-pit mines (1, 2, and 18 million m^3) in Northeastern Nevada, Rose and Hungr [24] demonstrated the accuracy and efficacy of this method. The result of the largest event was even forecasted 3 months before the impending failure. Dick et al. [19] further discussed the application of the INV method in open-pit mines by using new systematic multi-pixel and machine-learning models to complement the scarcity of conventional geodetic monitoring programs for near-real-time deformation measurements. Carlà et al. [9] took an anonymous copper open-pit mine into account and defined the appropriate strategy for the setup of alarms, which were deduced from the presented nine cases of slope instability and the relationship between the reciprocal displacement rate and duration time in the accelerating stage before the slope failure. To address the reliability of the prediction method and simultaneously provide guidelines for the proficient usage of this method, Zhou et al. [32] developed the modified INV method when analyzing the five landslides of Fushun West Pit slope failure. Similarly, Chen and Jiang [33] supposed that the selection of thresholds is usually over-conservative, considering the low-risk tolerance, and therefore introduced a dimensionless inverse velocity method (DINV) to provide a general solution framework that was used to assess the slope failure risk and avoid false alarms. The main characteristic of the inverse velocity method is its simplicity of use which has provided a useful tool for the interpretation of instrument data to anticipate eventual slope failure. These developments notwithstanding, the practical usefulness of the INV method for early warning in open-pit mines may be fairly constrained because of the following major drawbacks. In general, the INV method was formulated from fixed and human-controlled laboratory conditions, which are extremely unlikely to suffice in engineering slopes and field conditions. Furthermore, limitations connected to previous point-wise monitoring analysis of the INV method in open-pit mines are significant, often resulting in undersampled or poorly collected data. Additionally, the surface mining environment produces manifold noise patterns (e.g., mining extraction action, transportation equipment destabilization, human activities, measurement errors, etc.), which are considered to be a defect for early-warning purposes. Finally, the prediction performance of the INV method under different displacement scales does not appear to have

been analyzed to date. All these mentioned gaps can decisively hinder the interpretation of the inverse velocity plot and affect the precision and dependability of t_f prediction.

In this context, it is essential to propose the application of a conventional inverse modeling tool, based on the moving average transfer function, for eliminating as many as possible disturbing effects related to the prediction of displacements and compensating for other defects. To manifest the feasibility and punctuality of the FINV (filter inverse velocity) method for time-of-failure analyses in a mining environment, the back analysis of a large slope failure that occurred in August 2016 at Fushun, an open-pit coal mine in northeast China, is examined in detail. On this basis, we examined velocity time series using four filters and analyzed the validity of landslide damage time predictions.

2. Materials and Methods

2.1. Study Area

The Fushun West open-pit mine is located in the western part of the Fushun coalfield, at the northern foot of Qiantai Mountain on the southern bank of the Hun River. The geographical coordinates of the mine range from approximately $41°38'0''$ N to $42°14'0''$ N and $123°39'12''$ E to $124°28'0''$ E, as shown in Figure 1a. The open pit has a length of approximately 6.6 km, a width of around 2.2 km, and a total area of about 14.52 km^2. The mining depth reaches 400 m. However, the Fushun West open-pit mine faces serious landslide hazards due to factors including open-pit mining, underground excavation, faults, and weak layers. Specifically, the mine has experienced over 900 collapse events attributable to landslides. More than 50% of these incidents occurred from June to September when rainfall is relatively concentrated. These landslide events have resulted in a total damaged area of 635,000 m^2 and have given rise to a series of safety and geological environmental issues concerning open-pit mining.

On the evening of 25 July 2016, the Fushun area was struck by a rainfall event with a return period of 50 years, resulting in nearly 200 mm of precipitation. At 5:00 a.m. the following day, a partial landslide occurred on the northern slope of the Fushun West open-pit mine, as shown in Figure 1b. The elevation of the landslide's rear edge was approximately +75 m, while the shear location at the front edge was around -25 m. The landslide spanned a north–south width of approximately 300 m, with a height difference of 110 m, and with an east–west width of approximately 500 m. The total area affected by the landslide was approximately 150,000 m^2. The landslide caused the burial of the bottom sections 12 and 14 of the mainline, with the sliding tongue extending. This resulted in the complete interruption of the internal electrical railway lines in the eastern section of the mine, as well as the disruption of the western slope's transportation roads, including the Xingping Road and the car transport highway. These disruptions had a significant impact on the internal drainage of the eastern open pit and the upper soil removal in the western area of the mine, severely impeding normal production in the mining area.
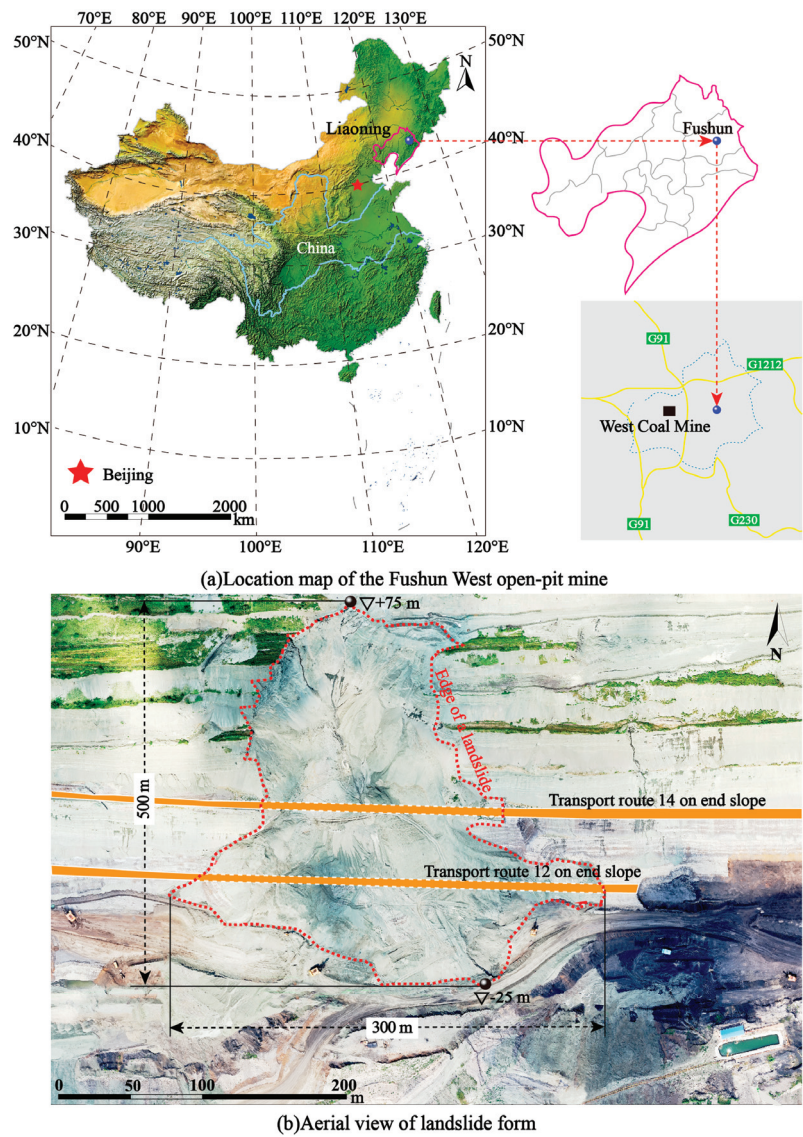
(a)Location map of the Fushun West open-pit mine

(b)Aerial view of landslide form

Figure 1. Location of the study area and geomorphology of the open-pit mine: (**a**) Location map of the Fushun West open-pit mine; (**b**) aerial view of landslide form.

2.2. Geological Setting

By studying the exploration data of the initial mining area, along with a large volume of geological exploration information and conducting geological surveys, the rock masses of the slopes in the Fushun West open-pit mine have been classified into various lithologies, including granite gneiss, basalt, coal, oil shale, tuff, green mudstone, and miscellaneous fill soil. The exposed strata, from the oldest to the youngest, mainly consist of Precambrian granite gneiss, Paleogene Paleocene Lao Hutai Formation, Lizigou Formation, Eocene Guchengzi Formation, Jijuntun Formation, and West Open-Pit Formation. Quaternary artificial deposits also exist in the area. A comprehensive stratigraphic column is shown in Figure 2, and a profile of the landslide area is presented in Figure 3.

| Lithology	Minimum thickness–Maximum thickness(m)	Average thickness(m)	Description
Loess layer	4.00–24.3	14.15	
Rammell	11.37–338.05	224.71	
Mudstone layer	358.63–484.50	421.56	
Oil base layer	28.51–362.35	194.08	
Main seam	8.57–110.50	59.58	
Tuff	8.00–51.50	29.75	
Basaltic layer	26.00–336.0	181.00	
Boulder bed	47.25–991.00	519.12	
Andesite	27.15–356.07	192.56	

Figure 2. Lithology of the typical borehole.
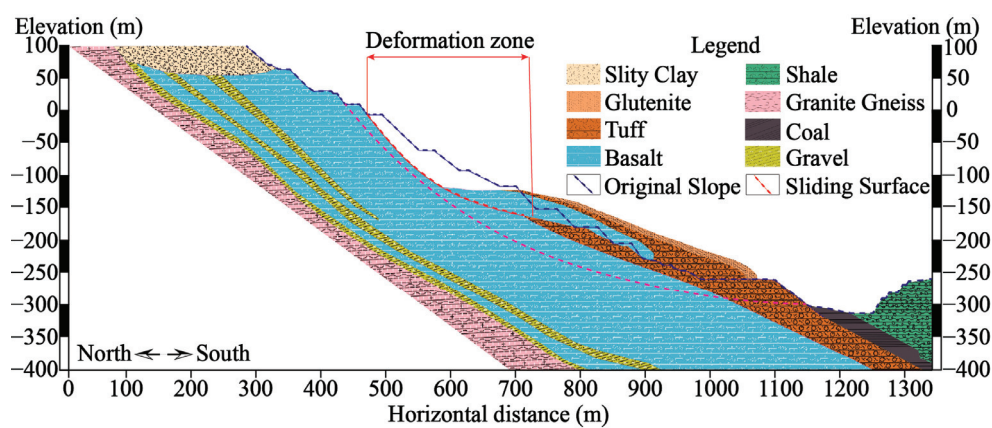
Figure 3. Section view of the landslide area.

2.3. Data Description

GPS (Global Positioning System, hereafter called "GPS") is a huge satellite-based system with global coverage for radio navigation and positioning. GPS technology has been developed rapidly in the application fields of navigation, positioning, precision

measurement, etc. In particular, the GPS real-time monitoring system has been widely used in the field of real-time monitoring of landslide deformation in open-pit mines for its real-time nature, and has achieved better results.

In order to reduce the threat of landslide disasters in open-pit mines to national property and people's lives, the Fushun West open-pit mine introduced a GPS real-time monitoring system, whose framework is shown in Figure 4. The system realizes the 24 h uninterrupted monitoring of geological disaster bodies and the remote automatic transmission of landslide displacement monitoring data, providing effective technical guarantees for the early warning of disaster bodies and the activation of emergency plans.
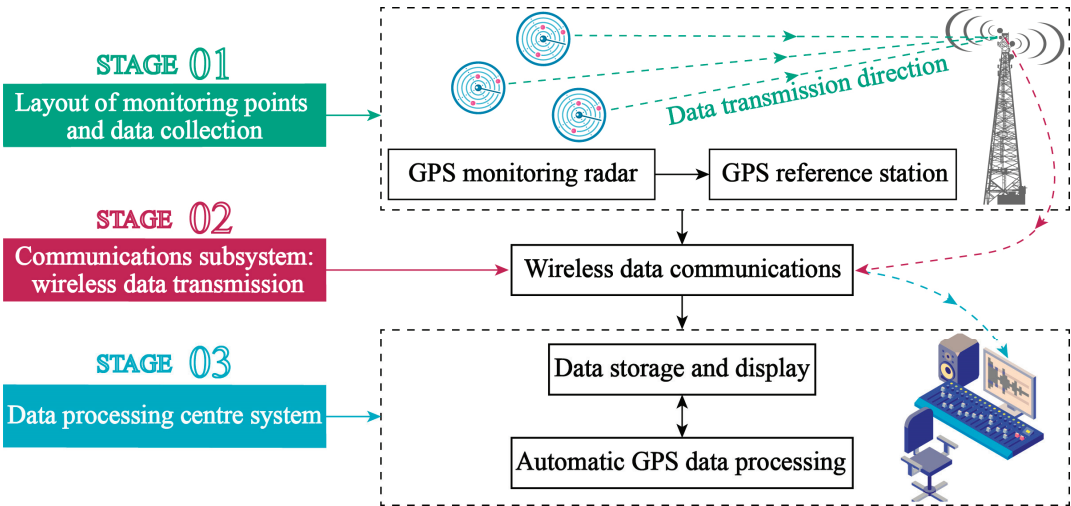

Figure 4. GPS monitoring system framework for the Fushun West open-pit mine.

The system monitoring point deployment and GPS monitoring data are presented in detail below. A total of 11 monitoring profiles were established in different directions on the northern end slope of the Fushun West open-pit mine, Namely, E200, E300, E400, E500, E600, E700, E800, E900, E1000, E1100, and E1200. The engineering geological plan of the landslide is illustrated in Figure 5. As of June 2015, a total of 12 GPS monitoring points were deployed along the monitoring profile, as shown in Figure 5b. Its monitoring technology is mainly based on the main radar sensor transmitting microwaves, using differential aperture radar remote prism monitoring technology. The radar nominal precision is 0.1 mm, the frequency signal is 1575.42 Hz, and the wavelength is about 30~50 cm. These monitoring points were named GN1, GN2, GN3, GN, GN5, GN6, GN7, GN8, GN9, GN10, GN11, and GN12. For this study, data were selected from the period of 14 March 2016 to 31 August 2016.

Let the three-dimensional coordinate information of the landslide monitoring point at a certain time point acquired by remote prism synthetic aperture radar monitoring be (x, y, z). The 3D coordinate value corresponding to the initial moment t_0 is (x_0, y_0, z_0), the 3D coordinate value corresponding to any moment t_n is (x_n, y_n, z_n), and the cumulative displacement $(\Delta x, \Delta y, \Delta z)$ component of the monitoring point within the moment from t_0 to t_t is:

$$\begin{cases} \Delta x = x_n - x_0 \\ \Delta y = y_n - y_0 \\ \Delta z = z_n - y_0 \end{cases} \tag{1}$$

The change in total displacement Δ*s* at the monitoring point is:

$$\Delta s = \sqrt{\Delta x^2 + \Delta y^2 + \Delta z^2} \qquad (2)$$

The cumulative displacement of the landslide is divided into cumulative horizontal displacement and cumulative vertical displacement, where cumulative vertical displacement is the cumulative displacement component in the z-direction and cumulative horizontal displacement Δ*h* is:

$$\Delta h = \sqrt{\Delta x^2 + \Delta y^2} \qquad (3)$$

The direction of landslide sliding is indicated by the displacement azimuth, which is *α*:

$$\alpha = \arctan(\Delta x / \Delta y) \qquad (4)$$

From the above definition, when *α* is positive, the displacement direction of the monitoring point is upward; when *α* is negative, the displacement direction of the monitoring point is downward. From the above derivation process, it can be seen that the size as well as the direction of the deformation of the landslide body is jointly determined by the magnitude of the *x*, *y*, and *z* directions. The deformation at any monitoring point on a landslide can be expressed in terms of the displacement components in the three directions of the monitoring point, or by horizontal displacement, vertical displacement, and displacement azimuth.
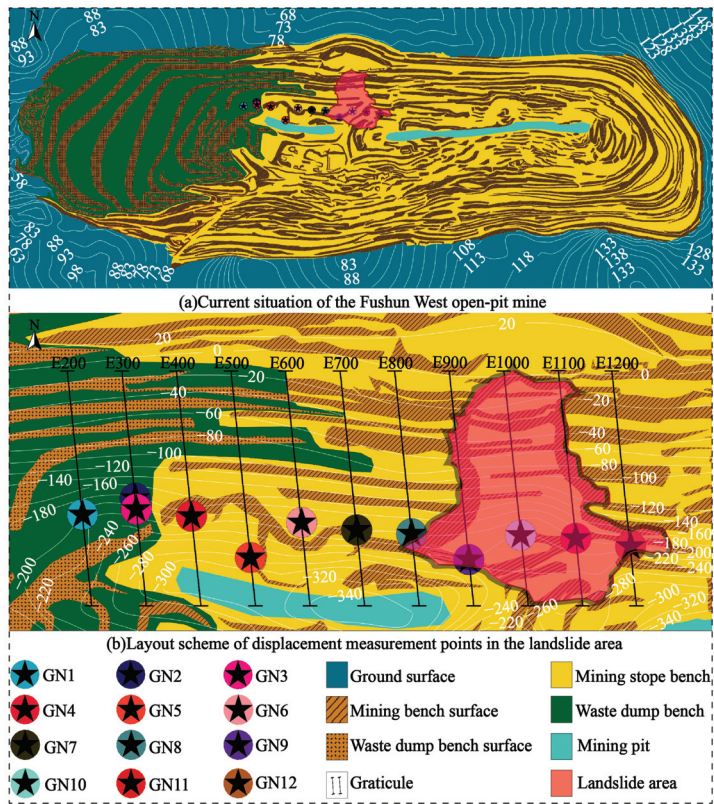

Figure 5. Landform and diagram of the open-pit mine landslide: (**a**) current situation of the open-pit mine; (**b**) layout scheme of displacement measurement points in the landslide area.

2.4. The Basal INV Method

The failure mechanism of slopes is defined as a complete paroxysmal collapse of rock and soil material. By analyzing a multitude of triaxial compression laboratory tests and in situ monitoring research, researchers have discovered that the deformation process of most landslides complies to the progressive characteristics [34–36] and three-stage law [37–40], as shown in Figure 6a. The whole process, from the initial deformation to the eventual failure, representatively comprises three stages: decelerating (green proportion), steady-state deformation (blue proportion), and acceleration deformation (pink proportion). Although the described methods have occasionally been successfully applied to a variety of cases such as man-made walls [30,41], rock and soil specimens [42–44], volcanic eruptions [45,46], or tunnels [45,47], these methods are primarily applied to unstable slopes. Hence, landslides are regarded as the principal research objects.
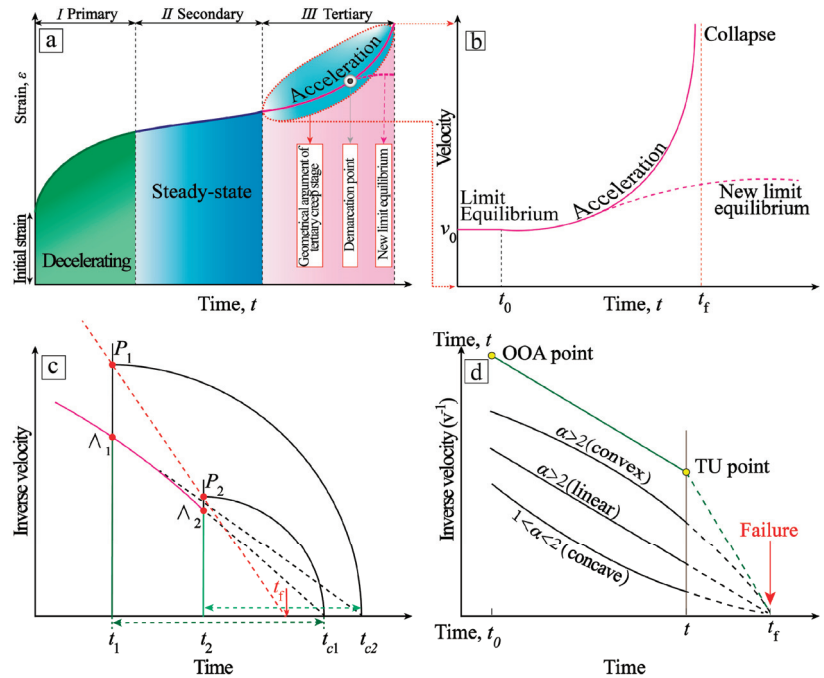

Figure 6. Conventional three-stage interpretation of creep behavior. (**a**) Three-stage deformation process of the progressive landslide (modified after Saito, [20]); (**b**) kinematic evolution of a landslide (modified after Intrieri et al. [16]); (**c**) graphical approach for determining the time of failure in the tertiary creep stage (Intrieri et al. [16]); and (**d**) schematic diagram of INV (modified after Fukuzono, [21]).

Fukuzono [21] further elaborated the classic three-stage creep theorem by propounding a simpler diagrammatic method (Figure 6b), which could be the most used and simple approach to provide a reasonable estimate of failure time. This method is valid for the tertiary stage. It is noteworthy that the method detects an OOA (onset of acceleration) point, which approximately distinguishes the secondary stage and the tertiary stage. The curve (Figure 6a) is separated into two segments by a demarcation point in the tertiary stage during the acceleration evolution process. (I) After an initial acceleration, Figure 6b displays a dotted line that is approximately parallel to the time axis with the landslide reaching equilibrium state; (II). Meanwhile, Figure 6b likewise displays a line whose value is towards ∞ (i.e., $v^{-1} \rightarrow 0$) as the velocity asymptotically increases.

Several authors successively supplied suggestions and guidelines for proficient usage based on a mathematical generalization of Fukuzono's solution. Representatively, Voight [22,23] encompassed the prediction of failure behavior and proposed the following equation (Equation (5)).

$$d^2\Omega/d^2t^2 = A(d\Omega/dt)^\alpha \tag{5}$$

where Ω is the displacement, $d\Omega/dt$ and represents the "velocity" and "acceleration" of Ω, respectively. A and α are two empirical constants that denote characteristics of slope failure; recent investigations revealed that A and α are not independent of each other, varying with several factors comprising kinematic motion patterns [48], versatile types of materia, and macro or micro scales [49]. Consequently, Fukuzono proposed the following equation (Equation (6)) for predicting the failure time by combining the aforementioned equation (Equation (5)) with time:

$$\Lambda \equiv v^{-1} = [A(\alpha-1)(t_f - t)]^{(\alpha-1)^{-1}} \tag{6}$$

where t_f is the time of failure. This method consists in depicting a tangent line to the curve at an arbitrary point Λ_1 that tallies to moment t_1. The tangent passes across the horizontal axis at moment t_{c1} (t_{c1},0). Afterward, the point P_1 is plotted vertically above Λ_1, on a line that passes through Λ_1 and parallel to the Y axis. The segments of $t_1\Lambda_1$ and t_1t_{c1} have an equal displacement from the perspective of geometric shapes. The abovementioned procedure is repeated for another random point Λ_2. Then, the time of failure t_f can be obtained as the abscissa of the intercept of a straight line that passes through P_1 and P_2 (Figure 6c).

The major drawback of Equation (5) is represented by the necessity of determining two constants A and α. According to closely controlled laboratory conditions and studies by several authors [50,51], α commonly spans over three orders of magnitude. For $\alpha = 2$, $1 < \alpha < 2$, and $\alpha > 2$, the curve of inverse-velocity has a linear, concave, or convex shape (Figure 6d), respectively. For this condition, Segalini et al. [52], who considered 26 emblematic pre-failure landslide cases, proposed that A inclines to take on extremely low or high values as α deviates from 2. While α appears as intermediate fluctuation, this attribute can be sufficient to sensibly influence prediction results.

To solve this issue, the value of α with the assumption that it is equal to 2 can be generally applied to evaluating the time of failure. In terms of guaranteeing production schedules and staff safety, the assumption of $\alpha = 2$ is often integrated with the mining industry environment because of its demanding promotion of visual feedback. Thus, Equation (6) is simplified into the following equation (Equation (7)):

$$v^{-1} = A(t_f - t) \tag{7}$$

As a result, the failure time t_f is presumably provided for the point of abscissa of the extrapolated linear inverse velocity trend with the time axis.

2.5. The Moving Average Filtering INV Method Architecture

As formerly stated, the most powerful aspect of the INV method is probably its simplicity, and it is a useful resource in different instances, bypassing the intrinsic restriction for knowing the slope size, state of activity, and types of material. In addition, the tool resource also provides great convenience under many other aspects (e.g., risk assessment and management), if users can count on agile and suitable methods of appraising the state of the monitored circumstance and establish the probability of impending disastrous accidents, a task which is not always achievable because of hardly compensating restrictions as a consequence of measurement errors and random instrumental noise. Correspondingly, we verify two of the utmost prevalent and foolproof smoothing algorithms, i.e., finite impulse response models (also called moving average filter models). Three types of filter models are described below.

1. Short-term simple box filter (*SSBF*). As each new velocity datum sampling occurs, users can extract the unweighted mean of the antecedent data points through *SSBF* algorithm processing. This ensures that the alterations of v in the mean are coordinated with the alterations in the data (v) rather than being shifted in time. An example of a v simple equally weighted running mean is the mean over the latest k entries of a data set involving t entries. Let those velocity data points be $v_1, v_2, \ldots, v_t$. The mean over the latest k velocity data points is represented as $SSBF_k$ ($\overline{v}_t$) and calculated as follows:

$$\begin{aligned} \overline{v}_t &= \tfrac{1}{m}\left(v_{t-k+1} + v_{t-k+2} \cdots v_t\right) \\ &= \tfrac{1}{m}\sum_{i=t-k+1}^{t} v_i \end{aligned} \tag{8}$$

when the new velocity datum ($SSBF_{k,\ next}$, $\overline{v}_t'$) is collected with the invariable sampling width m, the scope from $t - k + 2$ to $t + 1$ is considered. A new value v_{t+1} comes into the sum and the earliest value v_{t+1} drops out. This simplifies the computations by proceeding with the antecedent mean $SSB_{Fk,\ antecedent}$: ($\overline{v}_t$)

$$\begin{aligned} \overline{v}_t' &= 1/k\left(\sum_{i=t-k+2}^{t+1} v_i\right) \\ &= 1/k(\underbrace{v_{t-k+2} + v_{t-k+3} + \cdots v_t + v_{t+1}}_{\sum_{i=t-k+2}^{t+1} v_i} + \underbrace{v_{t-k+1} - v_{t-k+1}}_{=0}) \\ &= 1/k(\underbrace{v_{t-k+1} + v_{t-k+2} + \cdots v_t}_{=\overline{v}_t'}) - \tfrac{v_{t-k+1}}{k} + \tfrac{v_{t+1}}{k} \\ &= \overline{v}_t + \tfrac{1}{k}(p_{t+1} - p_{t-k+1}) \end{aligned} \tag{9}$$

where the moving average cycle (k) of the *SSBF* model was set to 2 days ($k = 2$).

2. Long-term simple box filter (*LSBF*), where the moving average cycle (k) was selected to be 6 days ($k = 6$).

3. Exponentially weighted moving average (*EWMA*). Whereas in the short-term simple box filter (*SSBF*) and long-term simple box filter (*LSBF*), the past signal processing is weighted equally, the *EWMA* model is used to assign exponentially decreasing weights over time. The *EWMA* for a series can be calculated as follows:

$$\overline{v}_t = \begin{cases} v_0 & t = 0 \\ \xi v_t + (1 - \xi)\overline{v}_{t-1} & t > 1 \end{cases} \tag{10}$$

where coefficient ξ represents the scale of recursion, a constant smoothing factor between 0 and 1. The smaller ξ is, the stronger the real-time performance of the moving average ($\overline{v}_t$) is. On the contrary, the larger ξ is, the stronger the ability to absorb instantaneous burst value is, and the better the stability of the prediction model is. Hence, the smoothing factor with the assumption that $\xi = 0.5$ can be generally used to express and balance the recursion and attenuation properties of the prediction model.

Because the measurement instrument can be easily controlled by the geologist, the time interval between adjoining measurements can be given over a constant time interval. The pattern of filtering as in Equation (8) is equivalent to the easy mathematical statement utilized by Osansan and Stacey [52].

$$d\Omega_i/dt_i = (\Omega_i - \Omega_{i-n})/(t_i - t_{i-n}) \tag{11}$$

In Equation (11), we set $1/\Omega$ equal to $1/\Omega_i$ ($1/\Omega_i$ is the reciprocal of displacement rate at t_i) and t equal to t_i (t_0 is the most recent instant).

The *SSBF* and *LSBF* models are customizable because they can be calculated for different numbers of time cycles (also called the order of the moving average). The biggest distinction of the *SSBF* and *LSBF* models is over setting the length of time cycles (k).

Significantly, there is no regularly precise guideline or standard definition to set up the boundary between short-term and long-term cycles. It is noted that the selection of a suitable time cycle (*k*) value is due to the following two major elements: (i) monitoring data accuracy/quality; and (ii) data sampling frequency. To observe what the trend-cycle estimate looks like under different orders of moving average, we plot it (Figure 7) along with a group of monitoring data from an anonymous open-pit mine. It should be noted that the trend cycle (in red) is smoother than the original data after processing several moving averages (n < m < p < q) and captures the main movement of the time series without any of the minor fluctuations.
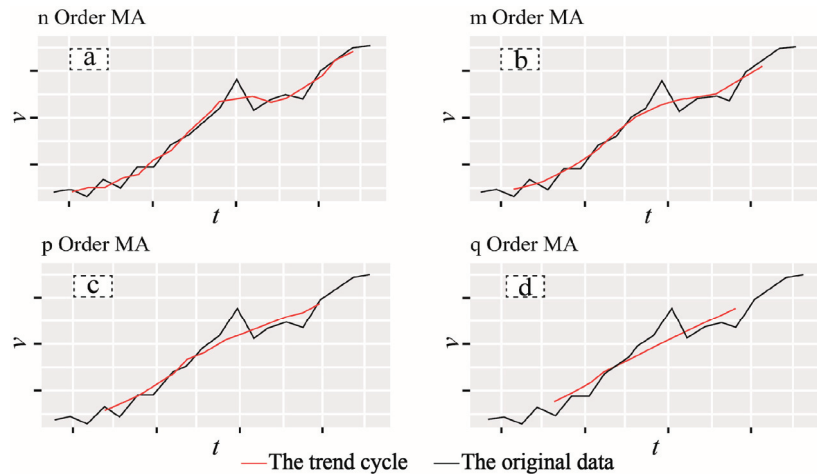

Figure 7. Different orders of moving average applied to displacement rates in an anonymous open-pit mine of the instability before the failure. n, m, p, and q represent the four order values of successive increments (i.e., n < m < p < q). (**a**) Displacement rate at successive incremental order values of n; (**b**) Displacement rate at successive incremental order values of m; (**c**) Displacement rate at successive incremental order values of p; (**d**) Displacement rate at successive incremental order values of q.

In Carlà et al. [30], the high-frequency rates of data acquisition, in the area of landslide monitoring programs, are representative of state-of-the-art radar monitoring technology (e.g., GPS [53,54], ground-based radar [31,55], total stations [56], and laser scanning [57]), and commonly require researchers to carry out smoothing over the bulk of measurements. Contrariwise, the low-frequency rates of data acquisition will produce low acquisition rates and will hide much of the background noise, resulting in the inability to trace short-term movements and delaying the identification of eventual trend changes; in such instances, smoothing should be performed over relatively lower measurements, compared to data obtained at high acquisition rates. Short-term averages respond quickly to changes in the price of the underlying security, while long-term averages are slower to react. The order of the moving average determines the smoothness of the trend-cycle estimate. In general, a large order means a smoother curve. The role played by the features of data sampling frequency and quality for the selection of suitable time cycles (k) is notable.

3. Results

3.1. Slope Displacement Velocity, Acceleration, and Cumulative Displacement Analysis

We collated the monitoring data with the period of 28 June 2016 to 31 August 2016, and plotted the velocity–acceleration–cumulative displacement curve of slope displacement, as shown in Figure 8. We divided the curve into three phases according to the trend of the velocity curve, i.e., the initial phase, the second phase, and the third phase. The phase splitting time points of the three phases of the different monitoring sites are not the same.

The splitting time point of the first phase and the second phase is in the time interval from 12 July to 24 July, and the splitting time point jumps more, within 12 days, whereas the splitting time point of the second stage and the third stage is in the time interval from 9 August to 13 August, and the splitting time point jumps less; see the summary in Table 1 for details.
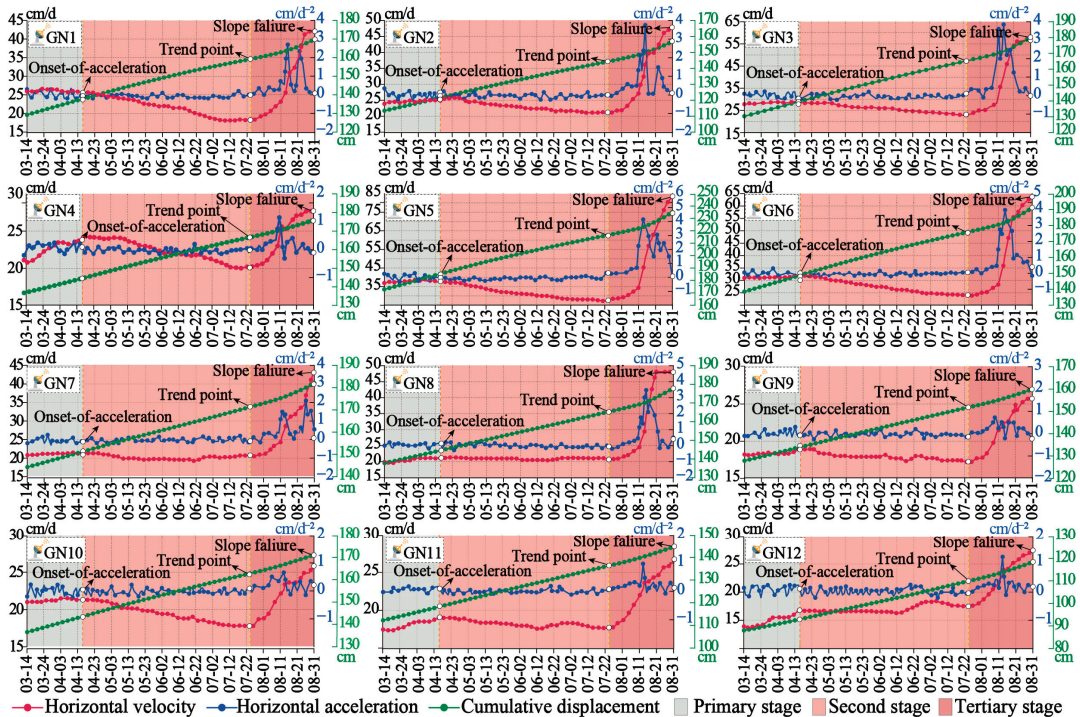

Figure 8. Slope displacement velocity, acceleration, and cumulative displacement curve.

Table 1. Results of correlation analysis between vegetation and climate indicators.

Monitoring Point	The Initial Stage		The Second Stage		The Third Stage	
	Start	End	Start	End	Start	End
GN1-E200-200		15 July	16 July	11 August	12 August	
GN2-E300-184		12 July	13 July	10 August	11 August	
GN3-E400-200		22 July	23 July	10 August	11 August	
GN4-E400-188		21 July	22 July	10 August	11 August	
GN5-E500-280		22 July	23 July	10 August	11 August	
GN6-E500-200	28 June	24 July	25 July	10 August	11 August	31 August
GN7-E600-200		22 July	23 July	10 August	11 August	
GN8-E700-200		18 July	19 July	10 August	11 August	
GN9-E800-232		22 July	23 July	9 August	10 August	
GN10-E900-220		22 July	23 July	12 August	13 August	
GN11-E1000-200		16 July	17 July	11 August	12 August	
GN12-E1200-200		14 July	15 July	11 August	12 August	

As shown by the red curve in Figure 8, in the whole period, the overall velocity curve showed a downward trend and then an upward trend. In the first stage, the overall velocity curve showed a downward trend, but the downward trend was relatively gentle; in the second stage, the overall velocity curve showed a downward concave upward trend. In

the third stage, the overall speed curve showed a trend of sharp rise and then a slow rise, and finally reached the highest point on 31 August. The time interval of the sharp rise of the curve in this stage was roughly distributed from 11 August to 15 August. In terms of numerical values, the velocity data of the monitoring points in the whole stage reached the highest point on 31 August, and the minimum velocity was measured by the monitoring point GN9 on 25 July, with a value of 17.00 cm/d. The maximum velocity, which was 83.50 cm/d, was measured by the monitoring point GN5 on 31 August. The velocity value span of GN4 was the smallest, ranging from 19.90 to 27.90 cm/d. The velocity value span of GN5 at the monitoring point was the largest, ranging from 27.00 to 83.50 cm/d.

As shown by the blue curve in Figure 8, in the first two stages, the acceleration curve fluctuates above and below 0, and the fluctuation range is the smallest in the whole stage. In the second stage, the acceleration curve is above 0 as a whole and shows an upward trend of fluctuation. The fluctuation range of the acceleration curve in the third stage is the largest in the whole stage, and the overall trend of fluctuation is decreasing. In terms of numerical value, the acceleration data of monitoring points in the whole stage reached the highest point on 14 August. The minimum absolute value of acceleration, which was -0.13 cm/d^2, was measured by the monitoring point GN11 on 13 July. The maximum acceleration, which was 4.30 cm/d^2, was measured by the monitoring point GN5 on 14 August. The acceleration value span of GN10 is the smallest, ranging from -0.2 to 0.65 cm/d^2. The acceleration value of GN5 at the monitoring point has the largest span, ranging from -0.2 to 4.30 cm/d^2.

As shown by the green curve in Figure 8, in the whole period, the cumulative displacement curve presents a linear upward trend. In the first stage, the cumulative displacement curve presents an upward convex trend. In the second stage, the cumulative displacement curve presents a linear upward trend. In the third stage, the cumulative displacement curve presents a linear downward concave upward trend. In terms of numerical value, the cumulative displacement data of monitoring points in the whole stage reached the highest point on 31 August. The minimum cumulative displacement, which was 105.19 cm, was measured by the monitoring point GN12 on 28 June. The maximum cumulative displacement was measured by the monitoring point GN5. On 31 August, the value was 234.99 cm. The cumulative displacement value span of GN9 is the smallest, ranging from 147.20 to 159.92 cm. The cumulative displacement value span of GN5 is the largest, ranging from 209.27 to 234.99 cm.

3.2. Analysis of Slope Displacement Inverse Velocity and Cumulative Displacement

According to the displacement–reverse velocity curve and the accumulated displacement curve drawn at 12 monitoring points, as shown in Figure 9 the trend of the reverse velocity curve mainly experienced three stages: slow acceleration, upward convex deceleration, and upward concave deceleration in the whole period. In the first stage, the reverse velocity curve showed an overall upward trend, but the upward trend was gentle. In the second stage, the inverse velocity curve presents an upward convex deceleration trend. The inverse velocity curve of the third stage showed an upward concave deceleration trend and finally reached its lowest point on 31 August. The time interval of the sharp downward trend of the curve at this stage was roughly distributed from 11 August to 15 August. In terms of numerical value, the inverse velocity data of monitoring points in the whole stage fell to the lowest point on 31 August. The minimum inverse velocity, which was 0.012, was measured by the monitoring point GN5 on 31 August. The maximum inverse velocity was measured by the monitoring point GN9 on 31 July, with a value of 0.059. The inverse velocity value span of GN4 is the smallest, ranging from 0.036 to 0.050. The inverse velocity value of GN8 has the largest span, ranging from 0.021 to 0.049.
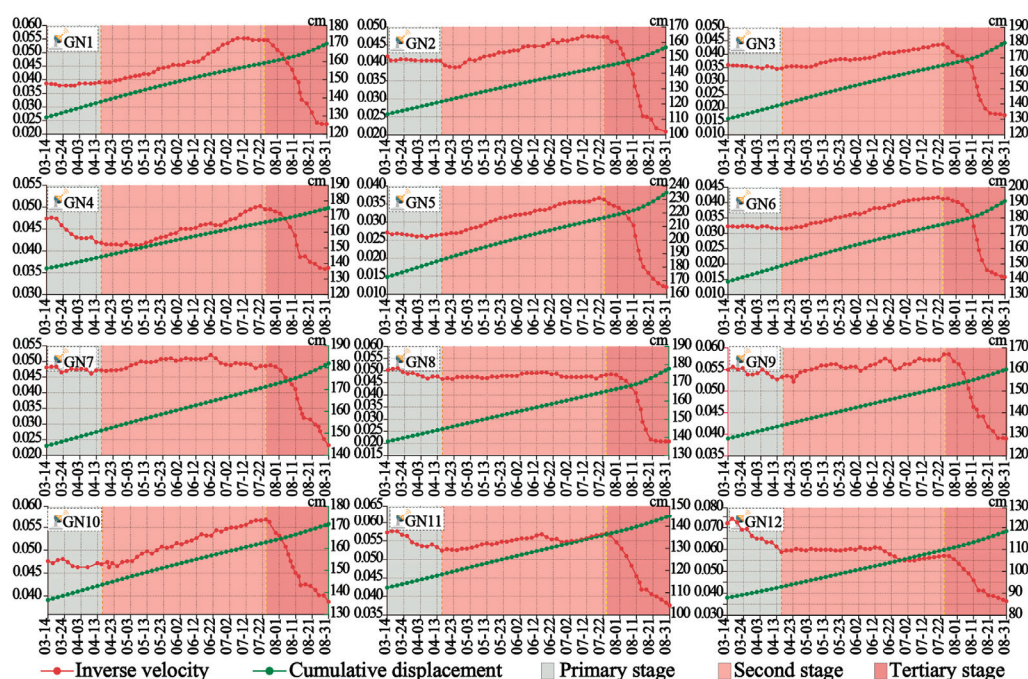
Figure 9. Slope displacement inverse velocity and cumulative displacement curve.

3.3. Source Velocity Data Model Analysis

The 12 monitoring points were transformed by the multiplicative inverse representation of velocity data under the time series model (as shown in Figure 10).

As shown in Figure 10, from 28 June 2016, the monitoring data acquisition starting point, the stage of large fluctuation ended on 31 August, and the period from 22 July to 31 August was the initial decay stage under the velocity multiplicative inverse representation. The curve trend of the 12 monitoring points is mainly presented as constant velocity attenuation–convex attenuation–concave attenuation–constant velocity attenuation. In terms of smoothness, this model is worse than other models. At the same time, since 11 August, the slope has completed the initial attenuation stage of large scale and also entered the next attenuation stage of relatively stable amplitude. At this stage, the amplitude of oscillation decreases compared with the initial attenuation stage. It is worth noting that under the representation mode of the multiplicative inverse meta-model of source velocity data, the curve shows obvious linear expression characteristics since 15 August. Linear and nonlinear fitting (as shown in Figure 10) was carried out for data under the multiplicative inverse meta-model of source velocity data. The landslide time predicted by 12 monitoring points is about 1–5 days earlier than the actual landslide time. Under the nonlinear fitting condition, the landslide time predicted by the 12 monitoring points under the model is about 1–3 days earlier than the actual landslide time, and the landslide time predicted by the GN1 and GN9 monitoring points under the model lags behind the actual landslide time by 2 days and 1 day, respectively. In terms of fitting effect and prediction effect, nonlinear fitting has better performance than linear fitting, and the overall prediction effect shows that the actual landslide time can be predicted in advance.
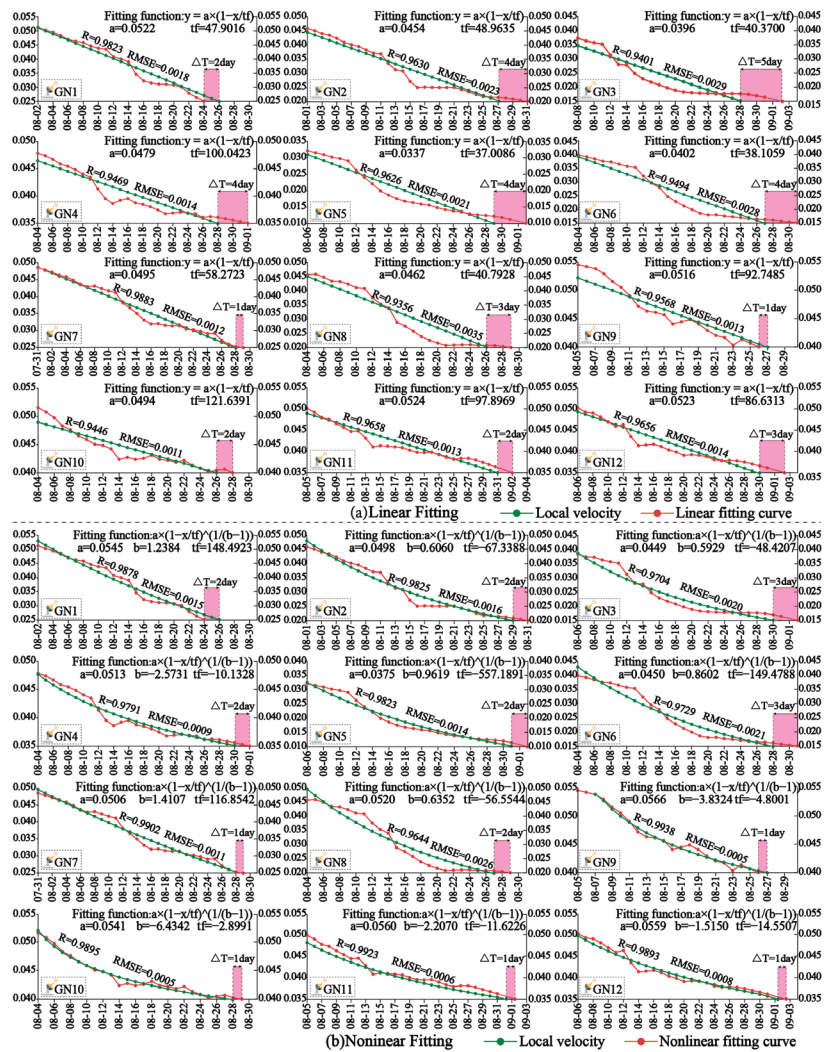
Figure 10. Source velocity data model analysis curve.

3.4. SMA Model Analysis

After the source velocity data were transformed by the multiplicative inverse representation of SMA model velocity data under the time series model (as shown in Figure 11), the stage of large oscillation amplitude ended on 31 August, and the period from 22 July to 31 August was the initial attenuation stage of SMA model. From the perspective of curve shape, the SMA model has an obvious tendency to eliminate the ladder shape of the curve based on the source velocity data model. Through the linear and nonlinear fitting of the data under the source velocity data SMA model, it can be obtained that under the linear fitting condition, the landslide time predicted by 12 monitoring points is about 1–5 days earlier than the actual landslide time. Under the nonlinear fitting condition, the landslide time predicted by the 12 monitoring points under the model is about 1–4 days earlier than the actual landslide time, and the landslide time predicted by the GN1 monitoring point is 2 days behind the actual landslide time. In terms of fitting effect and prediction effect, nonlinear fitting is better than linear fitting. The prediction effect of the SMA model is

1–2 days earlier than that of the multiplicative inverse model, but the overall prediction effect is worse than that of the multiplicative inverse model. The overall prediction effect is that the actual landslide time is predicted in advance.
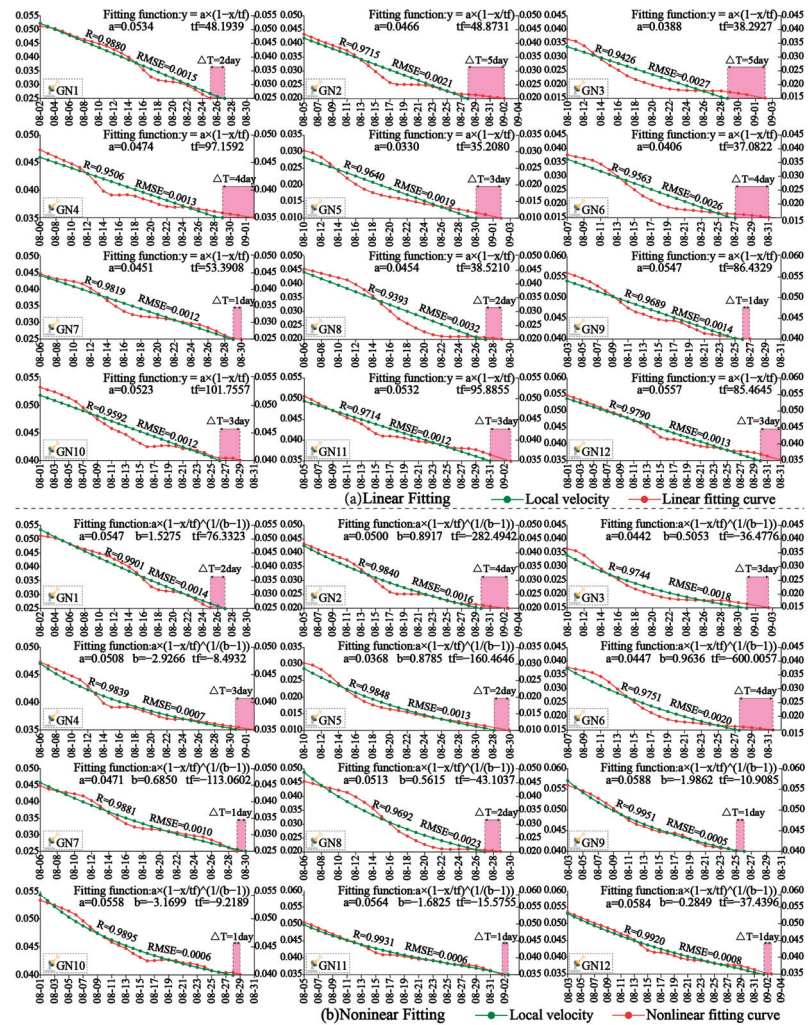

Figure 11. SMA model analysis curve.

3.5. LMA Model Analysis

After the source velocity data were transformed by the multiplicative inverse representation of the velocity data of the LMA model under the time series model (as shown in Figure 12), the stage of large oscillation amplitude ended on 31 August, and the period from 22 July to 31 August was the initial attenuation stage of the LMA model. From the perspective of curve shape, the LMA model further smoothed the curve shape based on the source velocity data model. The linear and nonlinear fitting of source velocity data under the LMA model showed that the fitting accuracy of the LMA model was the highest. Under the linear and nonlinear fitting conditions, the landslide time predicted by the model of 12 monitoring points is about 1–4 days earlier than the actual landslide time, and the landslide time predicted by the GN5 monitoring point is 1 day behind the actual landslide time.

In terms of fitting effect and prediction effect, nonlinear fitting has a better performance than linear fitting. The landslide prediction time under the LMA model is 1–2 days shorter than that of the multiplication inverse model. The overall prediction effect is better than that of the multiplication inverse model, and the actual landslide time can be predicted in advance.
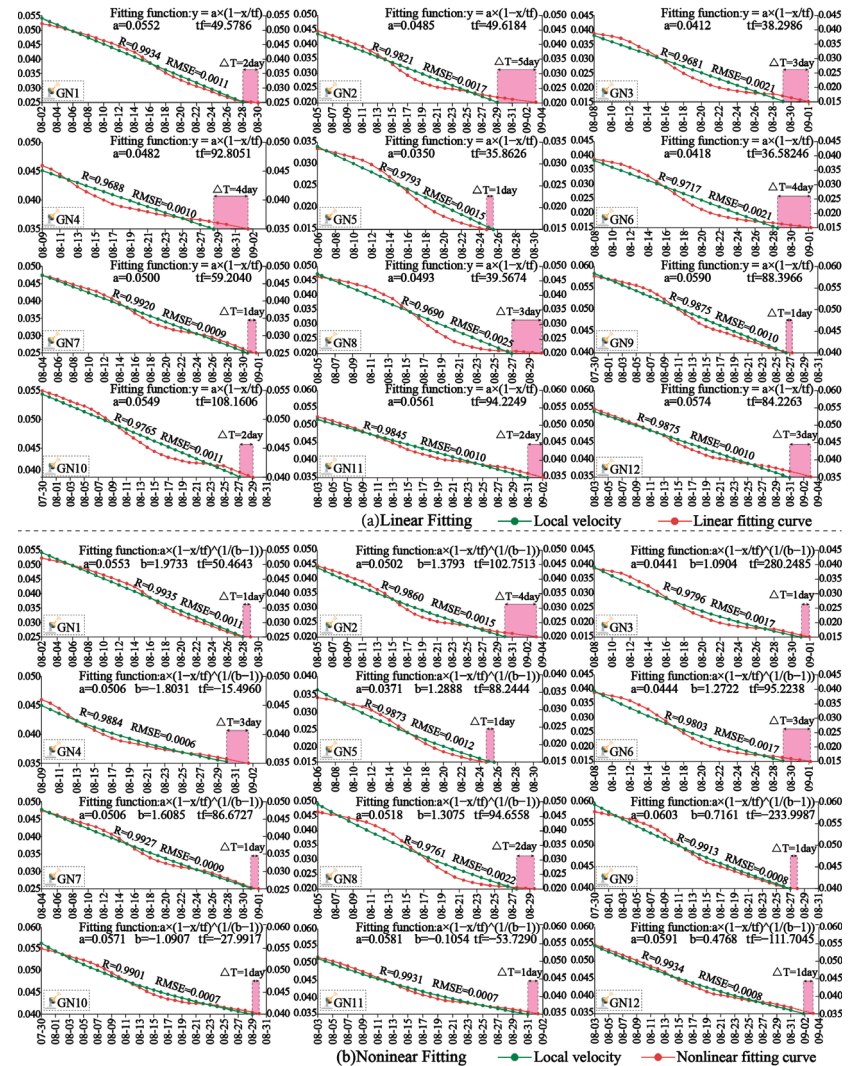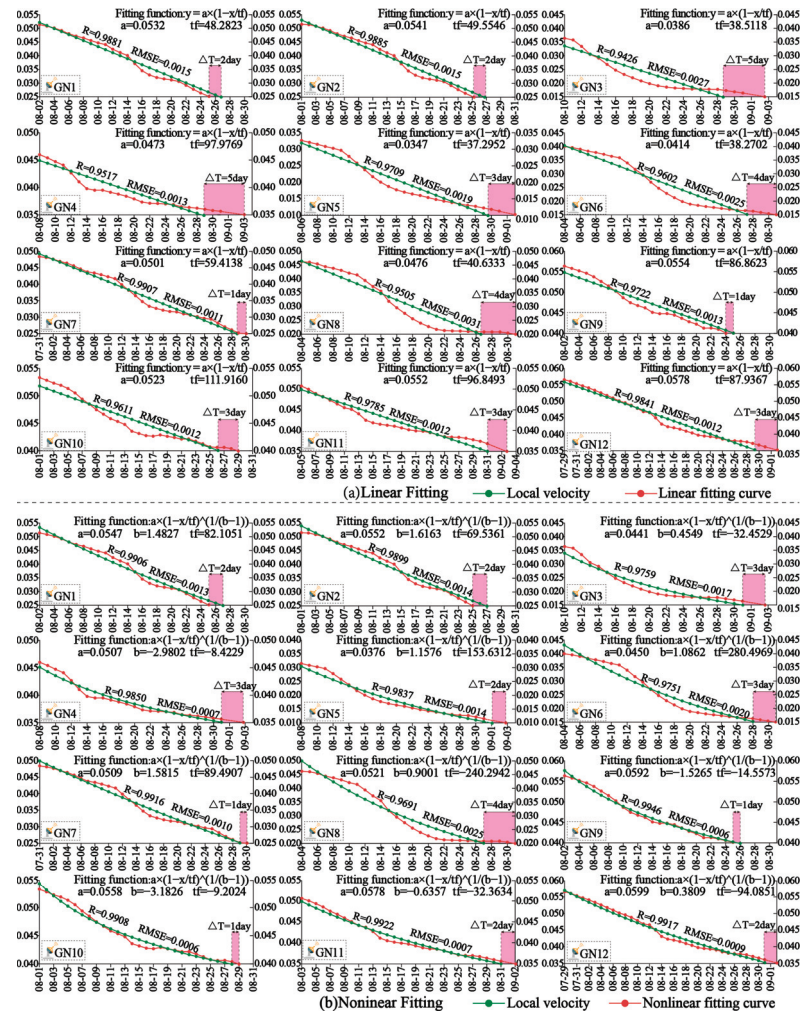

Figure 12. LMA model analysis curve.

3.6. ESF Model Analysis

After the smooth velocity data were transformed by the multiplication inverse representation of the source velocity data under the time series model (as shown in Figure 13), the stage of large oscillation amplitude ended on 31 August. The period from 22 July to 31 August was the initial attenuation stage of the ESF model. In terms of curve morphology, the smoothness of ESF is better than that of the multiplicative inverse model but worse than the SMA model and LMA model. Under the linear fitting condition, the landslide time predicted by 12 monitoring points under the model is about 1–5 days earlier than the

actual landslide time; under the nonlinear fitting condition, the landslide time predicted by 12 monitoring points under the model is about 1–3 days earlier than the actual landslide time. The predicted landslide time of the GN1, GN2, and GN9 monitoring points is 2 days, 2 days, and 1 day behind the actual landslide time, respectively. In terms of fitting effect and prediction effect, the nonlinear fitting has a better performance than the linear fitting. The landslide prediction time under the LMA model is 1–2 days longer than that under the multiplication inverse model. The overall prediction effect is worse than that of the multiplication inverse model, and the actual landslide time can be predicted in advance.

Figure 13. ESF model analysis curve.

4. Discussion

The bubble chart between the actual landslide and the predicted landslide time is drawn in Figure 14. It can be seen from the figure that all four models can effectively predict the landslide in advance. Under the condition of linear fitting, the interval between the prediction time and the landslide time is guaranteed to be within 5 days. Under the nonlinear fitting condition, the interval between the prediction time and landslide time is guaranteed to be within 4 days, whereas the monitoring data of GN1, GN9, GN10, GN11,

and GN12 shorten the interval between the prediction time and landslide time to within 2 days. In terms of fitting accuracy, the multiplicative inverse meta-model (model 1) is the lowest among the four models, followed by the ESF model (model 4); the SMA model (model 2) is better, and the LMA (model 3) model is the best. In terms of prediction accuracy, from the perspective of bubble size and distribution, ESF is the lowest among the four models, followed by the SMA model; the multiplicative inverse meta-model is better, and the LMA model is the best.
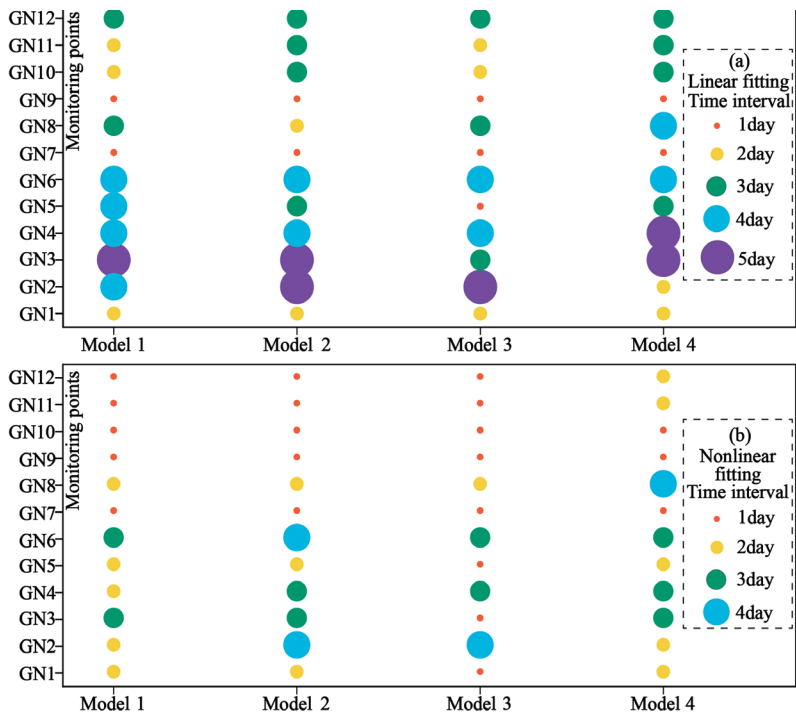
Figure 14. Evaluation of model prediction accuracy.

5. Conclusions

In this paper, based on the inverse velocity (INV) method of displacement monitoring data analysis, we examined the velocity time series by using four filters and comparatively analyzed the effect of landslide damage time prediction to improve the reliability of landslide prediction. The main conclusions of this study include the following points:

(1) A landslide event comprises a rather complicated process. The results show that the sliding process of a landslide can be divided into three stages based on the INV: the initial attenuation stage (regressive stage), the second attenuation stage (progressive stage), and the linear reduction stage (autoregressive stage).

(2) Compared with the raw data and the exponential smoothing filter (ESF) models, the fitting effect of short-term smoothing filter (SSF) and long-term smoothing filter (LSF) in the linear autoregressive stage is better.

(3) In terms of fitting accuracy, among the four models proposed in this study, the fitting accuracy of the multiplicative inverse model is the lowest, followed by the ESF model; the SMA model is better, and the LMA model is the best. In terms of prediction accuracy, ESF is the lowest among the four models, followed by the SMA model; the multiplicative inverse model is better, and the LMA model is the best.

References

1. Tarolli, P.; Sofia, G. Human topographic signatures and derived geomorphic processes across landscapes. *Geomorphology* **2016**, *255*, 140–161. [CrossRef]
2. López-Vinielles, J.; Ezquerro, P.; Fernández-Merodo, J.A.; Béjar-Pizarro, M.; Monserrat, O.; Barra, A.; Blanco, P.; García-Robles, J.; Filatov, A.; García-Davalillo, J.C.; et al. Remote analysis of an open-pit slope failure: Las Cruces case study, Spain. *Landslides* **2020**, *17*, 2173–2188. [CrossRef]
3. Chen, J.P.; Li, K.; Chang, K.J.; Sofia, G.L.; Tarolli, P. Open-pit mining geomorphic feature characterisation. *Int. J. Appl. Earth Obs. Geoinf.* **2015**, *42*, 76–86. [CrossRef]
4. Paradella, W.R.; Ferretti, A.; Mura, J.C.; Colombo, D.; Gama, F.F.; Tamburini, A.; Santos, A.R.; Novali, F.; Galo, M.; Camargo, P.O.; et al. Mapping surface deformation in open pit iron mines of Carajás Province (Amazon Region) using an integrated SAR analysis. *Eng. Geol.* **2015**, *193*, 61–78. [CrossRef]
5. Tao, Z.G.; Shu, Y.; Yang, X.J.; Peng, Y.Y.; Chen, Q.H.; Zhang, H.J. Physical model test study on shear strength characteristics of slope sliding surface in Nanfen open-pit mine. *Int. J. Min. Sci. Technol.* **2020**, *30*, 421–429. [CrossRef]
6. Hoek, E.; Read, J.; Karzulovic, A.; Chen, Z.Y. Rock slopes in civil and mining engineering. In Proceedings of the ISRM International Symposium, Melbourne, Australia, 19–24 November 2000.
7. Bye, A.R.; Bell, F.G. Stability assessment and slope design at Sandsloot open pit, South Africa. *Int. J. Rock. Mech. Min.* **2001**, *38*, 449–466. [CrossRef]
8. Obregon, C.; Mitri, H. Probabilistic approach for open pit bench slope stability analysis—A mine case study. *Int. J. Min. Sci. Technol.* **2019**, *29*, 629–640. [CrossRef]
9. Carlà, T.; Farina, P.; Intrieri, E.; Botsialas, K.; Casagli, N. On the monitoring and early-warning of brittle slope failures in hard rock masses: Examples from an open-pit mine. *Eng. Geol.* **2017**, *228*, 71–81. [CrossRef]
10. Ma, K.; Sun, X.Y.; Zhang, Z.H.; Hu, J.; Wang, Z.R. Intelligent Location of Microseismic Events Based on a Fully Convolutional Neural Network (FCNN). *Rock. Mech. Rock. Eng.* **2022**, *55*, 4801–4817. [CrossRef]
11. Ma, K.; Yuan, F.Z.; Zhuang, D.Y.; Li, Q.S.; Wang, Z.W. Study on Rules of Fault Stress Variation Based on Microseismic Monitoring and Numerical Simulation at the Working Face in the Dongjiahe Coal Mine. *Shock. Vib.* **2019**, *2019*, 7042934. [CrossRef]
12. Zhang, Z.H.; Ma, K.; Li, H.; He, Z.L. Microscopic Investigation of Rock Direct Tensile Failure Based on Statistical Analysis of Acoustic Emission Waveforms. *Rock. Mech. Rock. Eng.* **2022**, *55*, 2445–2458. [CrossRef]
13. Crozier, M.J. Deciphering the effect of climate change on landslide activity: A review. *Geomorphology* **2010**, *124*, 260–267. [CrossRef]
14. Carlà, T.; Nolesini, T.; Solari, L.; Rivolta, C.; Dei Cas, L.; Casagli, N. Rockfall forecasting and risk management along a major transportation corridor in the Alps through ground-based radar interferometry. *Landslides* **2019**, *16*, 1425–1435. [CrossRef]
15. Liu, Z.J.; Qiu, H.J.; Ma, S.Y.; Yang, D.D.; Pei, Y.Q.; Du, C.; Sun, H.S.; Hu, S.; Zhu, Y.R. Surface displacement and topographic change analysis of the Changhe landslide on 14 September 2019, China. *Landslides* **2021**, *18*, 1471–1483. [CrossRef]
16. Intrieri, E.; Carlà, T.; Gigli, G. Forecasting the time of failure of landslides at slope-scale: A literature review. *Earth Sci. Rev.* **2019**, *193*, 333–349. [CrossRef]
17. Main, L.G. Applicability of time-to-failure analysis to accelerated strain before earthquakes and volcanic eruptions. *Geophys. J. Int.* **1999**, *139*, F1–F6. [CrossRef]
18. Tavenas, F.L.S. Creep and failure of slopes in clays. *Can. Geotech. J.* **1981**, *18*, 106–120. [CrossRef]
19. Dick, G.J.; Eberhardt, E.; Cabrejo-Liévano, A.G.; Stead, D.; Rose, N.D. Development of an early-warning time-of-failure analysis methodology for open-pit mine slopes utilizing ground-based slope stability radar monitoring data. *Can. Geotech. J.* **2015**, *52*, 515–529. [CrossRef]
20. Saito, M. Forecasting the time of occurrence of a slope failure. In Proceedings of the 6th International Mechanics and Foundation Engineering, Montreal, QC, Canada, 8–15 September 1965; pp. 537–541.
21. Fukuzono, T. A method to predict the time of slope failure caused by rainfall using theinverse number of velocity of surface displacement. *Landslides* **1985**, *22*, 8–13. [CrossRef] [PubMed]
22. Voight, B. A method for prediction of volcanic eruptions. *Nature* **1988**, *332*, 125–130. [CrossRef]

23. Voight, B. Materials science law applies to time forecasts of slope failure. *Landslide News* **1989**, *3*, 8–10.
24. Rose, N.D.; Hungr, O. Forecasting potential rock slope failure in open pit mines using the inverse-velocity method. *Int. J. Rock. Mech. Min. Sci.* **2007**, *44*, 308–320. [CrossRef]
25. Federico, A.; Popescu, M.; Elia, G.; Fidelibus, C.; Internò, G.; Murianni, A. Prediction of time to slope failure: A general framework. *Environ. Earth Sci.* **2012**, *66*, 245–256. [CrossRef]
26. Dick, G.J.; Eberhardt, E.; Stead, D.; Rose, N.D. Early detection of impending slope failure in open pit mines using spatial and temporal analysis of real aperture radar measurements. In Proceedings of the Slope 2013: 2013 International Symposium on Slope Stability in Open Pit Mining and Civil Engineering, Perth, Australia, 25 September 2013; pp. 949–962.
27. Newcomen, W.; Dick, G. An update to the strain-based approach to pit wall failure prediction, and a justification for slope monitoring. *J. S. Afr. Inst. Min. Metall.* **2016**, *116*, 379–385. [CrossRef]
28. Ma, H.T.; Zhang, Y.H.; Yu, Z.X. Research on the identification of acceleration starting point in inverse velocity method and the prediction of sliding time. *Chin. J. Rock. Mech. Eng.* **2021**, *40*, 355–364. [CrossRef]
29. Mufundirwa, A.; Fujii, Y.; Kodama, J. A new practical method for prediction of geomechanical failure-time. *Int. J. Rock. Mech. Min.* **2010**, *47*, 1079–1090. [CrossRef]
30. Carlà, T.; Intrieri, E.; Di Traglia, F.; Nolesini, T.; Gigli, G.; Casagli, N. Guidelines on the use of inverse velocity method as a tool for setting alarm thresholds and forecasting landslides and structure collapses. *Landslides* **2017**, *14*, 517–534. [CrossRef]
31. Carlà, T.; Farina, P.; Intrieri, E.; Ketizmen, H.; Casagli, N. Integration of ground-based radar and satellite InSAR data for the analysis of an unexpected slope failure in an open-pit mine. *Eng. Geol.* **2018**, *235*, 39–52. [CrossRef]
32. Zhou, X.P.; Liu, L.J.; Xu, C. A modified inverse-velocity method for predicting the failure time of landslides. *Eng. Geol.* **2020**, *268*, 105521. [CrossRef]
33. Chen, M.X.; Jiang, Q.H. An early warning system integrating time-of-failure analysis and alert procedure for slope failures. *Eng. Geol.* **2020**, *272*, 105629. [CrossRef]
34. Chandler, R.J. Recent European experience of landslides in over-consolidated clays and soft rocks. In Proceedings of the 4th International Symposium on Landslide, Toronto, ON, Canada, 16–21 September 1984; pp. 61–81.
35. Petley, D.N.; Higuchi, T.; Petley, D.J.; Bulmer, M.H.; Carey, J. Development of progressive landslide failure in cohesive materials. *Geology* **2005**, *33*, 201–204. [CrossRef]
36. Troncone, A.; Conte, E.; Donato, A. Two and three-dimensional numerical analysis of the progressive failure that occurred in an excavation-induced landslide. *Eng. Geol.* **2014**, *183*, 265–275. [CrossRef]
37. Main, L.G. A damage mechanics model for power-law creep and earthquake aftershock and foreshock sequences. *Geophys. J. Int.* **2000**, *142*, 151–161. [CrossRef]
38. Xu, Q. Theoretical studies on prediction of landslides using slope deformation process data (in Chinese with English abstract). *J. Eng. Geol.* **2012**, *1020*, 145–151.
39. Dixon, N.; Smith, A.; Flint, J.A.; Khanna, R.; Clark, B.; Andjelkovic, M. An acoustic emission landslide early warning system for communities in low-income and middle-income countries. *Landslides* **2018**, *15*, 1631–1644. [CrossRef]
40. Wang, X.G.; Yin, Y.P.; Wang, J.D.; Lian, B.Q.; Qiu, H.J.; Gu, T.F. A nonstationary parameter model for the sandstone creep tests. *Landslides* **2018**, *15*, 1377–1389. [CrossRef]
41. Bozzano, F.; Mazzanti, P.; Moretto, S. Discussion to: Guidelines on the use of inverse velocity method as a tool for setting alarm thresholds and forecasting landslides and structure collapses' by T. Carlà, E. Intrieri, F. Di Traglia, T. Nolesini, G. Gigli and N. Casagli. *Landslides* **2018**, *15*, 1437–1441. [CrossRef]
42. Hao, S.W.; Liu, C.; Lu, C.S.; Elsworth, D. A relation to predict the failure of materials and potential application to volcanic eruptions and landslides. *Sci. Rep.* **2016**, *6*, 27877. [CrossRef]
43. Du, H.; Song, D.Q.; Chen, Z.; Guo, Z.Z. Experimental study of the influence of structural planes on the mechanical properties of sandstone specimens under cyclic dynamic disturbance. *Energy Sci. Eng.* **2020**, *8*, 4043–4063. [CrossRef]
44. Huang, J.; Liu, X.L.; Zhao, J.; Wang, E.Z.; Wang, S.J. Propagation of stress waves through fully saturated rock joint under undrained conditions and dynamic response characteristics of filling liquid. *Rock. Mech. Rock. Eng.* **2020**, *53*, 3637–3655. [CrossRef]
45. Kilburn, C.R.J. Forecasting volcanic eruptions: Beyond the failure forecast method. *Front. Earth Sci.* **2018**, *6*, 133. [CrossRef]
46. Dempsey, D.E.; Cronin, S.J.; Mei, S.; Kempa-Liehr, A.W. Automatic precursor recognition and real-time forecasting of sudden explosive volcanic eruptions at Whakaari, New Zealand. *Nat. Commun.* **2020**, *11*, 3562. [CrossRef]
47. Xu, C.; Liu, X.L.; Wang, E.Z.; Wang, S.J. Prediction of tunnel boring machine operating parameters using various machine learning algorithms. *Tunn. Undergr. Space Technol.* **2021**, *109*, 103699. [CrossRef]
48. Petley, D. Global patterns of loss of life from landslides. *Geology* **2012**, *40*, 927–930. [CrossRef]
49. Terzaghi, K. Mechanism of Landslides. In *Application of Geology to Engineering Practice*; Paige, S., Ed.; Geological Society of America: Boulder, CO, USA, 1950. [CrossRef]
50. Bozzano, F.; Cipriani, I.; Mazzanti, P.; Prestininzi, A. A field experiment for calibrating landslide time-of-failure prediction functions. *Int. J. Rock Mech. Min. Sci.* **2014**, *67*, 69–77. [CrossRef]
51. Segalini, A.; Valletta, A.; Carri, A. Landslide time-of-failure forecast and alert threshold assessment: A generalized criterion. *Eng. Geol.* **2018**, *245*, 72–80. [CrossRef]

52. Osasan, K.S.; Stacey, T.R. Automatic prediction of time to failure of open pit mine slopes based on radar monitoring and inverse velocity method. *Int. J. Min. Sci. Technol.* **2014**, *24*, 275–280. [CrossRef]

53. Benoit, L.; Briole, P.; Martin, O.; Thom, C.; Malet, J.P.; Ulrich, P. Monitoring landslide displacements with the Geocube wireless network of low-cost GPS. *Eng. Geol.* **2015**, *195*, 111–121. [CrossRef]

54. Samodra, G.; Ramadhan, M.F.; Sartohadi, J.; Setiawan, M.A.; Christanto, N.; Sukmawijaya, A. Characterization of displacement and internal structure of landslides from multitemporal UAV and ERT imaging. *Landslides* **2020**, *17*, 2455–2468. [CrossRef]

55. Chae, B.G.; Park, H.J.; Catani, F.; Simoni, A.; Berti, M. Landslide prediction, monitoring and early warning: A concise review of state-of-the-art. *Geosci. J.* **2017**, *21*, 1033–1070. [CrossRef]

56. Pecoraro, G.; Calvello, M.; Piciullo, L. Monitoring strategies for local landslide early warning systems. *Landslides* **2019**, *16*, 213–231. [CrossRef]

57. Abdulwahid, W.M.; Pradhan, B. Landslide vulnerability and risk assessment for multi-hazard scenarios using airborne laser scanning data (LiDAR). *Landslides* **2017**, *14*, 1057–1076. [CrossRef]

Comparing Different Coupling and Modeling Strategies in Hydromechanical Models for Slope Stability Assessment

Shirin Moradi [1,*], Johan Alexander Huisman [1], Harry Vereecken [1] and Holger Class [2]

[1] Agrosphere Institute (IBG 3), Forschungszentrum Jülich GmbH, 52428 Jülich, Germany; s.huisman@fz-juelich.de (J.A.H.); h.vereecken@fz-juelich.de (H.V.)

[2] Institute for Modeling Hydraulic and Environmental Systems (IWS), University of Stuttgart, 70569 Stuttgart, Germany; holger.class@iws.uni-stuttgart.de

* Correspondence: s.moradi@fz-juelich.de

Abstract: The dynamic interaction between subsurface flow and soil mechanics is often simplified in the stability assessment of variably saturated landslide-prone hillslopes. The aim of this study is to analyze the impact of conventional simplifications in coupling and modeling strategies on stability assessment of such hillslopes in response to precipitation using the local factor of safety (LFS) concept. More specifically, it investigates (1) the impact of neglecting poroelasticity, (2) transitioning from full coupling between hydrological and mechanical models to sequential coupling, and (3) reducing the two-phase flow system to a one-phase flow system (Richards' equation). Two rainfall scenarios, with the same total amount of rainfall but two different relatively high (4 mm h^{-1}) and low (1 mm h^{-1}) intensities are considered. The simulation results of the simplified approaches are compared to a comprehensive, fully coupled poroelastic hydromechanical model with a two-phase flow system. It was found that the most significant difference from the comprehensive model occurs in areas experiencing the most transient changes due to rainfall infiltration in all three simplified models. Among these simplifications, the transformation of the two-phase flow system to a one-phase flow system showed the most pronounced impact on the simulated local factor of safety (LFS), with a maximum increase of +21.5% observed at the end of the high-intensity rainfall event. Conversely, using a rigid soil without poroelasticity or employing a sequential coupling approach with no iteration between hydromechanical parameters has a relatively minor effect on the simulated LFS, resulting in maximum increases of +2.0% and +1.9%, respectively. In summary, all three simplified models yield LFS results that are reasonably consistent with the comprehensive poroelastic fully coupled model with two-phase flow, but simulations are more computationally efficient when utilizing a rigid porous media and one-phase flow based on Richards' equation.

Keywords: rainfall induced landslide; slope stability; poroelasticity; local factor of safety; coupled hydromechanical modeling

1. Introduction

It is well known that many landslides are triggered by rainfall [1–5]. When rainwater infiltrates the soil, it alters both the overall weight and pore pressure, subsequently impacting how stress is distributed within hillslopes. This underscores the notion that rainfall-induced landslides are a prominent example of a hydromechanical process. Such interconnected hydromechanical phenomena have been understood for a considerable time, as seen in earlier studies, e.g., [6]. In recent decades, a range of models has been developed to evaluate the stability of hillslopes by taking such subsurface hydromechanical processes into account [7–11].

Existing hydromechanical models often rely on a series of simplifications. Below, we briefly review the most widely used and commonly accepted simplifications. Firstly, in most slope stability analysis models, the soil is treated as a rigid medium, neglecting

the dynamic interplay between hydraulic and mechanical factors [12–14]. For instance, while there has been empirical work on characterizing the impact of variable effective stress on porosity, e.g., [15,16], only a handful of studies have explored this potential hydromechanical interplay in stability assessments, e.g., [17,18]. In many cases, the focus has been primarily on the effects of mechanical compaction and consolidation due to increased self-weight with depth or external loading, with typical parameterizations reflecting diminishing porosity and hydraulic conductivity with depth, e.g., [9,19]. However, such approaches commonly overlook the dynamic variations in these properties.

Secondly, hydromechanical models used in slope stability assessments often employ a sequential coupling method, which primarily considers a one-way influence of transient hydrological conditions (e.g., pore water pressure) on the mechanical properties of variably saturated hillslopes. Specifically, this approach involves solving the mass and momentum balance equations for subsurface flow first and then utilizing the resulting pressure head and bulk density distribution as inputs for solving the momentum balance equations for the mechanical aspect, accounting for the corresponding suction and effective stresses within the variably saturated porous medium, e.g., [7,20,21].

Thirdly, it is common practice to assume constant pore air pressure and to simplify the actual two-phase (air and water) flow dynamics [22] into a single-phase (water) flow model where Richards' equation [23] is employed to simulate subsurface flow, e.g., [24,25].

All of the aforementioned simplifications are aimed at reducing computational costs and addressing issues related to numerical robustness, thereby enhancing the efficiency of slope stability assessment using hydromechanical models, e.g., [20,26]. However, it is important to note that these simplifications can potentially compromise model accuracy. For instance, it is demonstrated that a sequential coupling strategy lacking feedback from mechanical processes to hydraulic properties can introduce a significant error when modeling aquifer subsidence, especially when compared to a more sophisticated iterative coupling approach [26] that considers this interaction to some extent. Additionally, Cho [21] found that stability analysis results for partially saturated slopes could differ by over 10% between one-phase and two-phase flow systems.

To address inaccuracies stemming from neglecting the interplay between variable mechanical parameters and hydraulic properties, a viable solution is the adoption of a fully coupled hydromechanical model [27]. In a fully coupled approach, the mass and momentum balance equations for subsurface flow and soil mechanics are simultaneously solved within each simulation time step. Alternatively, one can opt for a sequentially coupled hydromechanical model [28], where the unknowns related to flow and soil mechanics are solved sequentially. This sequential approach can involve varying numbers of iterations between sub-problems at each time step, e.g., [29], ensuring that the influence of altered mechanical parameters on soil hydraulic properties is considered in subsequent iterations of the same time step. In principle, simulations using a sequentially coupled model with iterations, continued until the mass and momentum balance solutions converge, should yield results identical to those from an equivalent fully coupled model, e.g., [30,31]. Notably, recent developments in fully coupled hydromechanical modeling, as seen in Darcis [32], have expanded its applicability. Beck et al. [30] extended Darcis' [32] model and introduced sequential coupling with iterations. This extended model accounts for two-phase flow and incorporates variations in hydraulic parameters due to the elastic deformation of porous media caused by transient pore pressure changes. This typically occurs when the advancing saturation front encounters initially drier soil. The results of Beck et al. [30] emphasize that significant disparities can arise between non-iterative sequential and fully coupled models, particularly in highly transient conditions featuring substantial gradients in pore water pressure and stress. These disparities are more pronounced when computational resources limit the number of feasible iterations in the sequentially coupled model. In recent years, the adoption of fully coupled hydromechanical models has grown across various applications, including land deformation, water table determination [33], hydraulic fracturing [34,35], clay activities [36], and reservoir characterization [37]. However, such comprehensive modeling

strategies have not been widely employed for slope stability assessment [38–42]. Furthermore, the errors associated with widely used model simplifications in the assessment of variably saturated hillslopes have yet to be thoroughly examined.

Within this context, the aim of this study is to compare various coupling and modeling strategies for assessing the stability of variably saturated hillslopes using hydromechanical models. Additionally, we seek to assess the associated errors resulting from different coupling approaches and commonly employed model simplifications. To achieve this, we made modifications to both the fully coupled hydromechanical model developed by Darcis [32] and the non-iterated sequential model proposed by Beck et al. [30]. These modifications enabled us to simulate variations in water content and stress distribution within variably saturated hillslopes. Furthermore, we simplified the two-phase fully coupled model in two ways: first, into a two-phase fully coupled model featuring a rigid soil with constant porosity and no poroelasticity, and second, into a fully coupled model incorporating a one-phase flow system (Richards' model) for water flow (refer to Supplement S1, Equations (S1)–(S19) for details). We then evaluated the impact of these different coupling and modeling strategies on simulated slope stability for different rainfall-induced infiltration conditions up to the point of failure. Our assessment was carried out using the Local Factor of Safety method [7].

2. Materials and Methods

2.1. Coupled Hydromechanical Model

The key elements of the hydromechanical modeling approach have been described [30,43], and readers are referred to the Supplementary Material Index S1 for more details.

2.2. Evaluation of Stability Status

Once the mass and momentum balance equations have been solved (either simultaneously or sequentially), the stability of the variably saturated hillslope can be evaluated. In this study, the Local Factor of Safety (LFS) approach proposed by Lu et al. [7] has been used, which can best be implemented for early warning of failure initiation. The LFS [−] is based on the Mohr–Coulomb criterion (Figure S2) and is the ratio of Coulomb stress at the potential failure state, τ^* [ML^{-1}T^{-2}], and the current state of Coulomb stress, τ [ML^{-1}T^{-2}], at each point within a hillslope. LFS = 1, therefore, defines the stability threshold, where failure potentially occurs for values lower than 1.0. The Coulomb stress at the potential failure state, τ^*, can be defined by

$$\tau^* = c' + \sigma' \tan \phi' \tag{1}$$

in which c' [ML^{-1}T^{-2}] is the effective cohesion, σ'[ML^{-1}T^{-2}] is the effective stress, and ϕ' [°] is the effective internal friction angle of the soil. The LFS of each element within the hillslope is then calculated as

$$\text{LFS} = \frac{\tau^*}{\tau} = \frac{\cos \phi' \, (c' + \sigma_I' \tan \phi')}{\sigma_{II}'} \tag{2}$$

where σ_I'[ML^{-1}T^{-2}] and σ_{II}'[ML^{-1}T^{-2}] are obtained based on the maximum and minimum principal stresses, $\sigma_{1,3}$ [ML^{-1}T^{-2}], and the suction stress, σ^s[ML^{-1}T^{-2}], as

$$\sigma_I' = \frac{\sigma_1 + \sigma_3}{2} - \sigma^s \tag{3}$$

$$\sigma_{II}' = \frac{\sigma_1 - \sigma_3}{2} \tag{4}$$

One can reasonably infer that alterations in the size of the Mohr circle, delineated by the principal total stresses and influenced by the bulk weight and element positioning within a hillslope, remain relatively modest in a variably saturated hillslope undergoing infiltration.

However, cumulative pore water pressure in an unsaturated hillslope reduces the effective stress's absolute value, causing the Mohr circle to shift leftward (refer to Figure S2), nearing the failure envelope. Consequently, pore pressure primarily determines the Mohr circle's position relative to the Mohr–Coulomb failure envelope [7,44]. Initial Local Factor of Safety (LFS) results align with conventional stability assessment methods [7,45]. However, this approach offers additional insights into when and where failure might initiate, eliminating the need to predefine a failure surface. The LFS method has previously been used with a sequentially coupled hydromechanical model (without iterations) and a one-phase (water) flow system [7,12,46].

2.3. Implementation of Different Coupling and Modeling Concepts

Four different implementations of coupled hydromechanical models with the LFS concept are compared (Table 1). The most comprehensive implementation is based on Darcis' [32] fully coupled hydromechanical model with two-phase flow. It considers the influence of pore pressure and elastic volumetric strain on porosity and hydraulic conductivity. The second implementation simplifies Darcis [32] model by excluding poroelastic effects. The third model is based on the sequentially coupled model of Beck et al. [30] with no iterations between the hydrological and mechanical parts. Feedback from the mechanical model to the hydrological model occurs in the next time step instead of the same time step. The fourth and final implementation simplifies the fully coupled two-phase flow model to a fully coupled model with one-phase flow (Richards' equation).

Table 1. Four different implementations of coupled hydromechanical models in this study.

Model	Abbreviation
Fully coupled two-phase flow model with variable porosity	2P-FC-var.Por.
Fully coupled two-phase flow model with constant porosity	2P-FC-const.Por.
sequentially coupled two-phase flow model	2P-SC
One-phase flow model (Richards' equation)	1P-FC

All four model implementations were realized in DuMux [27,47,48], which is a free, open-access "multi- [physics, …]" simulator of fluid flow in porous media (https://dumux.org/ (accessed on 1 November 2023)). DuMux is based on the Distributed and Unified Numerics Environment (DUNE) [49–51] and solves the partial differential equations (PDE) for fluid flow and soil mechanics using a finite volume method. The model domain is discretized using the Box method [27].

To compare the four model implementations, the simulations were conducted on a 2D sloped domain with a 30° incline, featuring idealized isotropic and homogeneous silty soil (Figure 1). The stability of this failure-prone slope has been previously assessed using the LFS concept [7,12,46]. Hydromechanical soil properties are detailed in Table S1, and boundary conditions are depicted in Figure 1. For the hydrological model, a no-flow condition at the bottom and left boundaries of the domain were applied. Initially, the slope was assumed to be in hydrostatic equilibrium with a 5 m deep groundwater table extending horizontally from the toe of the slope. The unknown primary variables of the flow equation in the so-called fully coupled approach are pore water pressure (p_w) and air saturation (S_a). Hence, the right boundary below the groundwater table, characterized by full saturation ($S_a = 0$) and a prescribed hydrostatic water pressure (p_w), is treated as a Dirichlet boundary. Above the water table, we set a no-flow boundary. The top surface acts as a Neumann boundary with an infiltration rate matching the rainfall rate. Here, two constant rainfall intensities were employed. The first set of simulations used a low-intensity rainfall (LIR) of 1 mm h^{-1} (20% of K_s) for 20 h. The second set applied a high-intensity rainfall (HIR) of 4 mm h^{-1} (80% of K_s) for 5 h to ensure an equivalent total infiltration amount for both events. In the mechanical model, the top surface is a free boundary, while the left and right boundaries have no displacement in the direction normal to the boundary (roller boundary). The bottom is fixed.
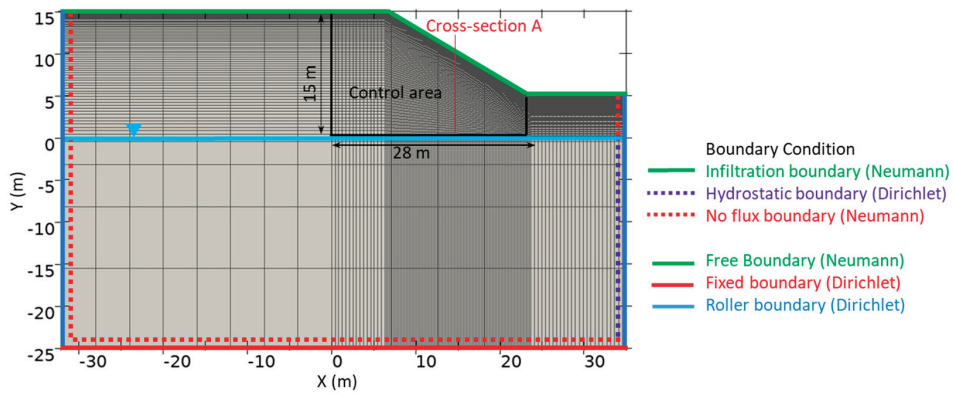
Figure 1. The geometry, boundary conditions, and discretization of the 2D, homogeneous silty slope used to compare the four hydromechanical model implementations. Please note that the same color and line type were used for the hydrological infiltration and mechanical free boundary conditions at the surface because they are both of the Neumann-type.

A cube mesh was used to discretize the modeling domain (Figure 1) with an increasing grid size and depth to reduce the computational costs while being able to catch the hydromechanical dynamics that are expected to be most pronounced near the slope surface [12]. The following analysis is focused on a relatively small part of the modeling domain indicated as the control area in Figure 1 and the associated cross section A. This control area was used to reduce the effect of the boundary conditions on the seepage condition of the slope, e.g., [52]. As reported by Kristo et al. [53], setting the side boundaries at a distance of 3 times the height of the slope from the crest and the toe minimizes the impact of the boundary conditions on the simulation results.

3. Results

3.1. Fully Coupled Two-Phase Flow Model with Variable and Constant Porosity

Figure 2 depicts the evolving LFS distribution within the 2D slope, simulated using the comprehensive fully coupled two-phase flow model under both low- and high-intensity rainfall events. This model accounts for poroelastic effects linked to variable pore pressure and material self weight. Figure 2 shows that the LFS gradually diminishes near the slope surface as infiltration progresses, with the potentially unstable area, characterized by an LFS near 1.0, initially emerging near the slope toe and expanding over time. The LFS method considers only the shear stress of each element independently, without regard for neighbouring elements, and it does not account for post-failure stress redistribution. Consequently, an LFS < 1 does not unequivocally denote a state of failure [43], and the slope stability status after the initial potentially unstable location should be interpreted cautiously. Therefore, all simulation results are presented until the LFS reaches the potential failure threshold of LFS = 1.0 at some point on the hillslope.

To investigate the significance of incorporating poroelasticity in slope stability assessment, the dynamics of vertical effective stress for the two rainfall intensities, focusing on cross section A of the hillslope are presented in Figure 3. This figure displays the simulated effective stress as a function of depth relative to the effective stress derived from bulk density and the hydrostatic pore pressure distribution, assuming a constant porosity of 0.46. The resulting changes in simulated porosity are illustrated in Figure 4. The simulations reveal that the effective stress was lower than the specified value above a depth of approximately 5 m, but it exceeded this value below this depth. A positive change in effective stress signifies that the compressive pressure due to self-weight exceeded the specified value. Rainfall infiltration also led to a reduction in effective stress and an increase in porosity near the surface. However, the overall changes in simulated porosity were

relatively minor, with a maximum shift of +0.59% observed near the slope surface after the HIR and +0.58% during the LIR. The average difference at cross section A was only 0.08% for the upper 7 m and 0.37% for the upper 1 m for both rainfall intensities. Subsequently, the focus narrows to near-surface pore water pressure and LFS dynamics due to rainfall infiltration, with simulation results presented solely for the upper 1 m. All differences are presented as relative values compared to the outcomes of the comprehensive fully coupled model (i.e., $(X_x - X_{FC})/X_{FC} \times 100$), with a positive change indicating an increase relative to the equivalent value in the comprehensive fully coupled model (FC) and a negative change representing a decrease in the respective value.
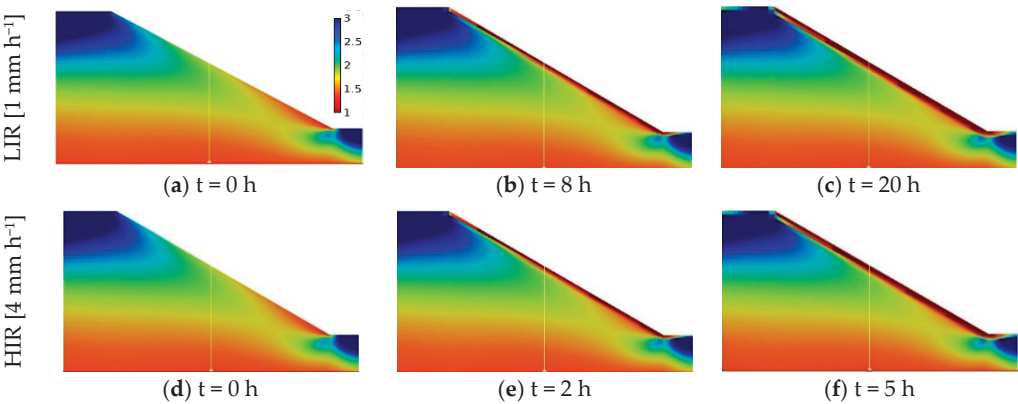

Figure 2. The spatial and temporal variability of LFS for the 2D silty slope simulated with the FC two-phase flow model for the LIR at (**a**) t = 0 h, (**b**) t = 8 h, and (**c**) t = 20 h, and the HIR at (**d**) t = 0 h, (**e**) t = 2 h, and (**f**) t= 5 h.
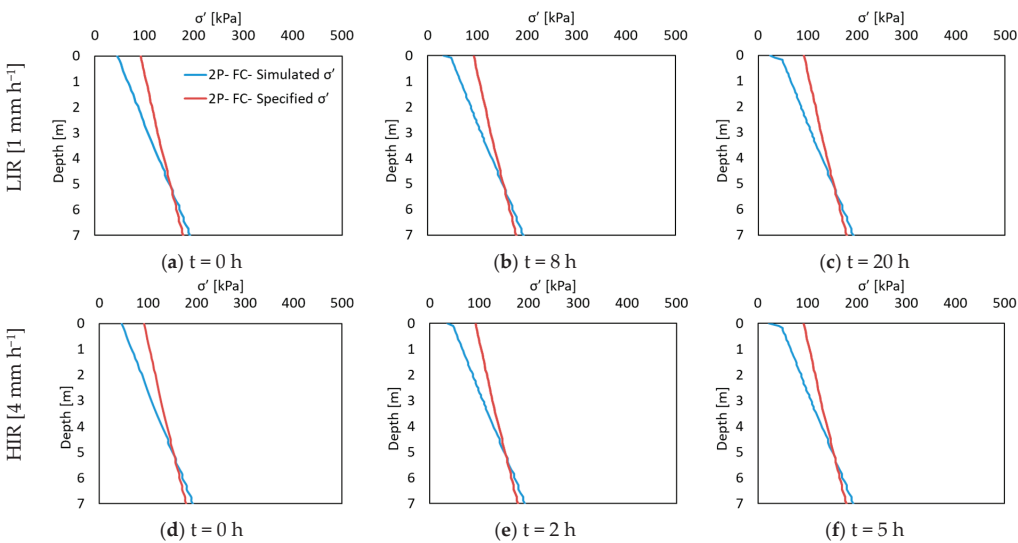

Figure 3. The simulated change in effective stress at cross section A of the 2D silty slope using the two-phase FC model for the LIR at (**a**) t = 0 h, (**b**) t = 8 h, and (**c**) t = 20 h and the HIR at (**d**) t = 0 h, (**e**) t = 2 h, and (**f**) t = 5 h.
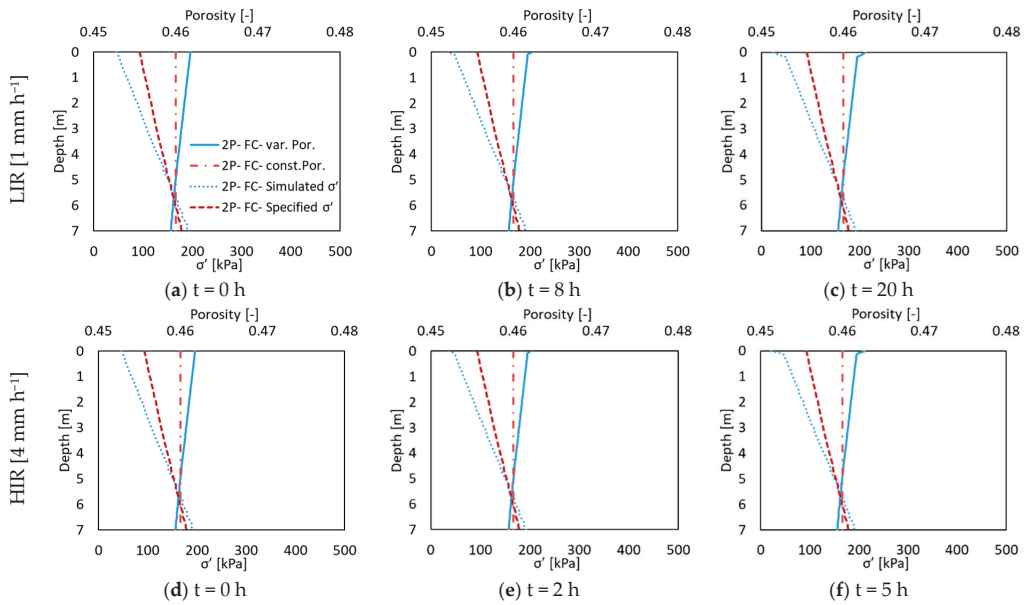
Figure 4. The dynamics of simulated vertical effective stress and porosity at cross section A of the 2D silty slope using the two-phase FC model for the LIR at (**a**) t = 0 h, (**b**) t = 8 h, and (**c**) t = 20 h and the HIR at (**d**) t = 0 h, (**e**) t = 2 h, and (**f**) t = 5 h.

To assess the impact of poroelasticity on pore water pressure (p_w) and stability, we compared results from the comprehensive fully coupled two-phase flow model with those from the same model employing a constant porosity (Figure 5). The most significant disparities in p_w and LFS between the two model implementations were observed at the soil surface and at the end of the high-intensity rainfall event. Specifically, the maximum discrepancies reached approximately −10.1% for p_w (decrease) and +2.0% for LFS (increase) compared to the fully coupled model with poroelasticity. In the case of the low-intensity rainfall, the variations amounted to a maximum of −2.2% for p_w and +1.1% for LFS at the end of the event. When considering the entire cross section for the high-intensity rainfall event, the average differences were only −0.8% for p_w (decrease) and +0.2% for LFS (increase). Similarly, at the end of the low-intensity rainfall, these values were −0.3% for p_w and +0.1% for LFS.
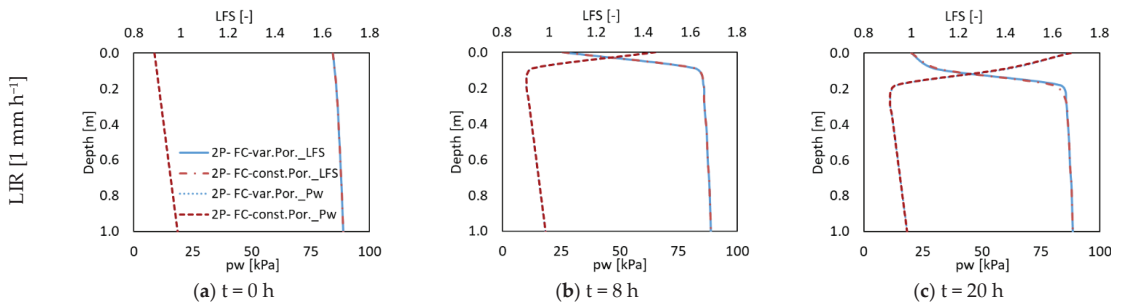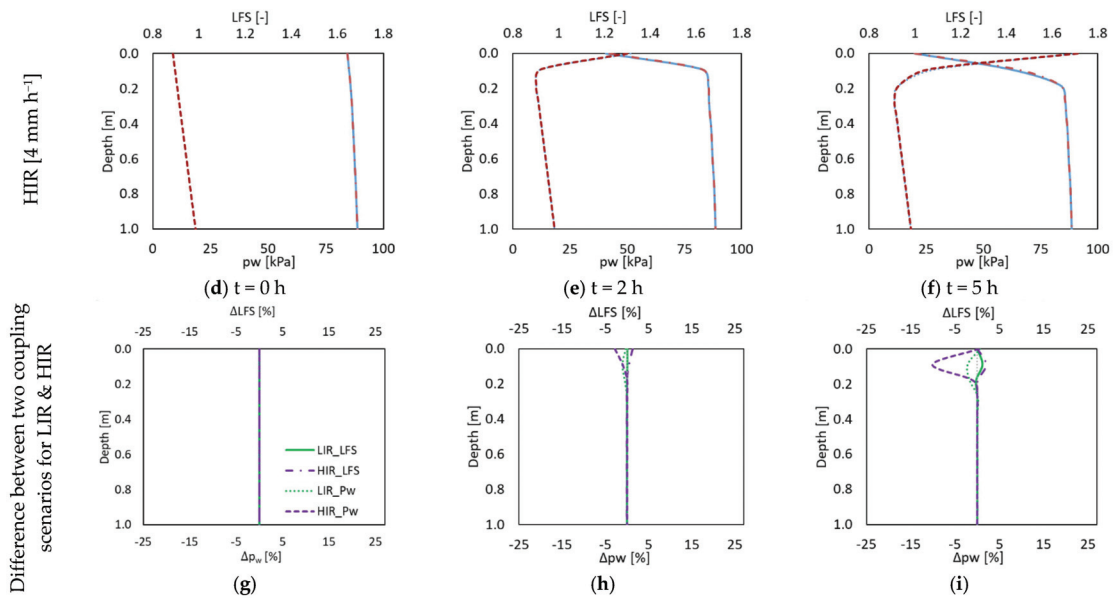

Figure 5. *Cont.*

Figure 5. The simulated p_w and LFS distribution at cross section A of the 2D silty slope using the two-phase fully coupled (2P-FC) model with variable and constant porosity for the LIR at (**a**) t = 0 h, (**b**) t = 8 h, and (**c**) t = 20 h and the HIR at (**d**) t = 0 h, (**e**) t = 2 h, and (**f**) t = 5 h. The difference between the two model implementations for low- and high-intensity rainfall are shown in panels (**g**–**i**).

3.2. Fully Coupled vs. Sequentially Coupled Models

To compare simulation outcomes between the fully coupled (FC) and sequentially coupled (without iterations) two-phase flow models, we examined simulated pore water pressure (p_w) in Figure 6 for the upper 1 m of cross section A during both low- and high-intensity rainfall events. The results reveal a maximum variation of −16% in p_w with the sequentially coupled (SC) model during the high-intensity rainfall event, occurring in the middle of the event. In Figure 6, we also illustrate the resulting differences in simulated LFS. As the initial conditions for all models were identical, encompassing the same initial pressure distribution and LFS, these aspects are not depicted in subsequent figures. The sequentially coupled model exhibited a +7.5% deviation compared to the fully coupled model, with the most significant difference also appearing in the middle of the high-intensity rainfall event. For the low-intensity rainfall event, the sequentially coupled model showed a maximum variation of −6.3% in p_w and a +4.3% difference in LFS. Averaging the top 1 m of cross section A during the high-intensity rainfall event, we observed average differences of −1.5% for simulated p_w and +0.3% for LFS. Corresponding averages during the low-intensity rainfall event were −0.4% for p_w and +0.2% for LFS. These disparities predominantly occurred near the surface, where dynamic changes in pore water pressure were most pronounced. For depths exceeding 1 m, the effect of increased soil weight due to infiltration remained below 0.01% for both p_w and LFS.
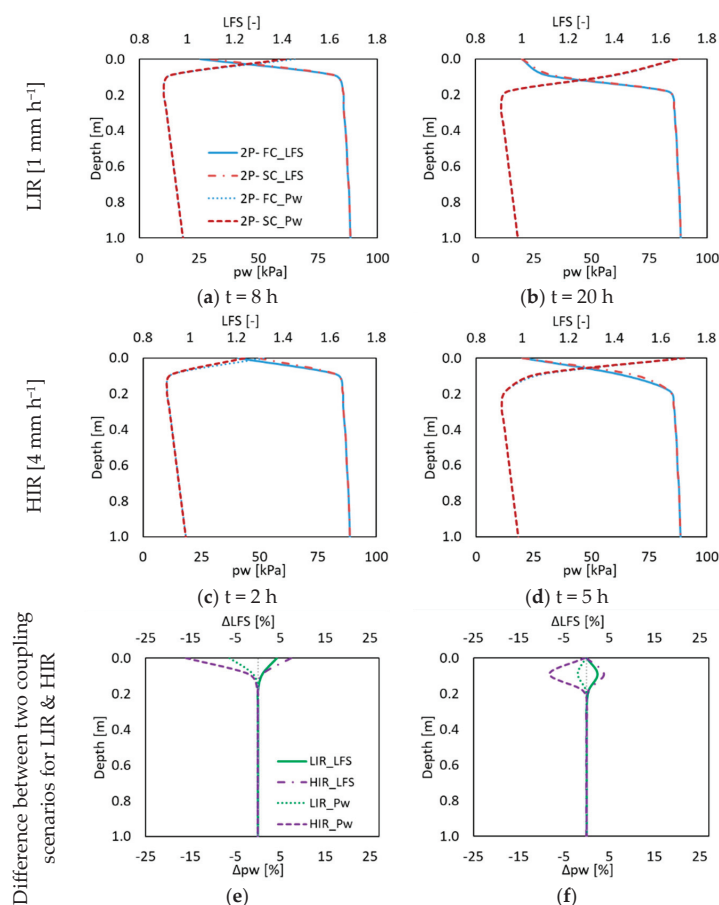
Figure 6. The simulated p_w and LFS distribution at cross section A for the 2D silty slope using fully and sequentially coupled two-phase flow models (2P-FC and 2P-SC, respectively) with the LIR at (**a**) t = 8 h and (**b**) t = 20 h and the HIR at (**c**) t = 2 h and (**d**) t = 5 h. The differences between the two model implementations for low- and high-intensity rainfall are shown in panels (**e**,**f**).

3.3. Fully Coupled Two-Phase vs. One-Phase Flow Model (Richards' Equation)

Finally, we compare the simulated results between the fully coupled two-phase flow model (2P-FC) and the fully coupled one-phase flow model (Richards' equation) (1P-FC). Figure 7 illustrates the simulated pore water pressure (p_w) and LFS for both model implementations in the upper 1 m of cross section A during the low- and high-intensity rainfall events, along with their relative differences. Once more, the most significant deviation between the two models arises at the end of the high-intensity rainfall event. Here, we observe a +97.2% shift in p_w and a −21.5% shift in LFS compared to the fully coupled model. This maximum difference diminishes to roughly +53.7% in p_w and −11.9% in LFS for the low-intensity rainfall event. Additionally, we notice that the disparities between the two model implementations primarily occur in a smaller region near the slope surface during the high-intensity rainfall event. Consequently, the average differences for the top 1 m of cross section A are relatively consistent (−9.5% for p_w and 1.9% for LFS at the end of the high-intensity rainfall and −8.2% for p_w and 1.9% for LFS at the end of the low-intensity rainfall event, relative to the fully coupled model).
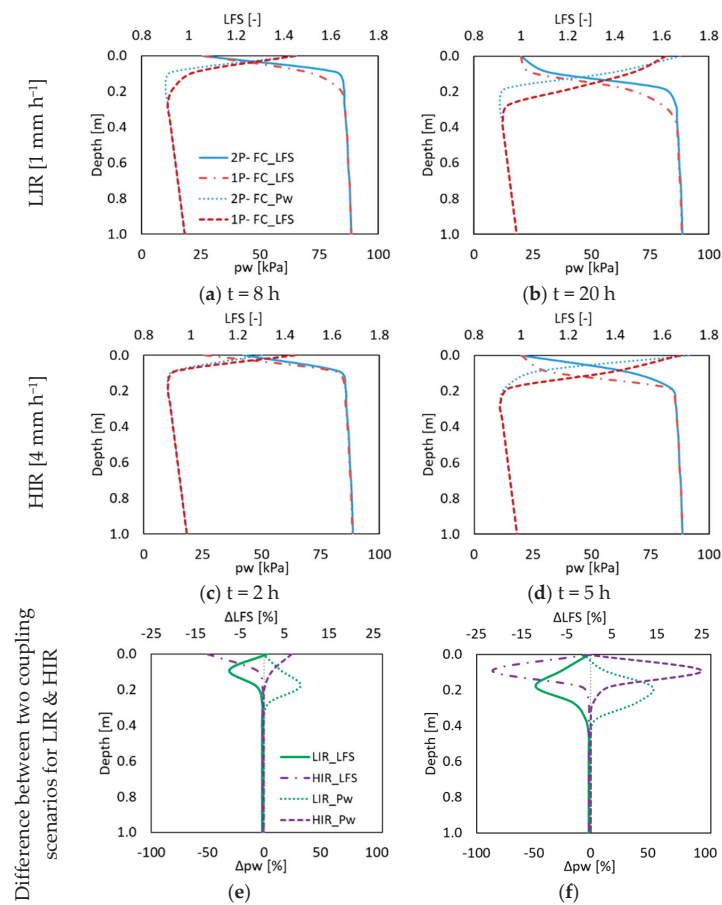
Figure 7. The simulated p_w and LFS distribution at cross section A for the 2D silty slope using the fully coupled two-phase and Richards' models (2P-FC and 1P-FC, respectively) with the LIR at (**a**) t = 8 h, and (**b**) t = 20 h and the HIR at (**c**) t = 2 h, and (**d**) t = 5 h. The differences between the two model implementations for low- and high-intensity rainfall are shown in panels (**e**,**f**).

4. Discussion

Table 2 summarizes the results of the aforementioned modeling simplifications and coupling strategies on both the pore water pressure and stability assessment of variably saturated hillslopes, which is used as a starting point for the following discussion.

Table 2. Comparative analysis of simulated pore water pressure and Local Factor of Safety of the simplified models relative to the comprehensive fully coupled model (in percentage) under the two investigated rainfall intensities.

2P-FC-var.Por. vs. . . .	Parameter	HIR (4 mm h^{-1}) (%)	LIR (1 mm h^{-1}) (%)
2P-FC- const-Por.	p_w	−10.1	−2.2
	LFS	+2.0	+1.1
2P-SC	p_w	−16.0	−6.3
	LFS	+7.5	+4.3
1P-FC	p_w	+97.2	+53.7
	LFS	−21.5	−11.9

4.1. Effect of Poroelasticity

In a poroelastic medium, porosity changes with depth and pore water pressure. Where pore pressure exceeds the bulk weight, porosity increases; where self weight surpasses pore pressure, porosity decreases. Thus, areas with positive changes in vertical effective stress tend to have decreasing porosity, as seen in Figure 3. Conversely, areas with negative changes in effective stress are expected to exhibit increased porosity.

The results in Figure 4 suggest that the increased effective hydraulic conductivity (K_{eff}) due to higher porosity in the poroelastic model outweighs the displacement (u) effect, resulting in elevated pore pressure near the surface. In contrast, simulations with constant hydraulic conductivity in a poroelastic fully coupled model showed lower pore pressure (results not shown) and consequently higher LFS at those locations.

The maximum model differences coincide with those of the transient zones, which is consistent with the findings of Beck et al. [30]. These zones are located near the surface and experience maximum pore pressure variations during the wetting front infiltration. For different infiltration rates, the pore water pressure gradient differs across the infiltration front. In particular, the pore water pressure was higher for the high-intensity rainfall, which resulted in a stronger increase in porosity. For this reason, the effect of not considering poroelastic effects is more pronounced in the case of high-intensity rainfall. The higher pore water pressure resulted in lower LFS in the simulated results of the model that considers poroelasticity. Overall, the influence of poroelasticity and its effects on pore water pressure and stability in variably saturated hillslopes appear relatively minor during infiltration.

4.2. Effect of Coupling Strategy

For both rainfall intensities, the slightly higher p_w values in the fully coupled model are due to its consideration of the complete interaction between effective pore pressure and volumetric strain within each time step. In the sequentially coupled model with no iteration, the impact of variable pore pressure on stress and strain distribution occurs in the same time step, but the feedback of volumetric strain to pore pressure is accounted for in the subsequent time step. As previously discussed, differences are more prominent during high-intensity rainfall events due to steeper pore water pressure gradients. These results again align with the findings of Beck et al. [30], emphasizing that the maximum difference between fully coupled and sequentially coupled models occurs in regions with transient processes involving rapid pore water pressure changes within a single time step. Despite the anticipated greater reliability of the fully coupled model due to its comprehensive interaction between hydrological and mechanical components, the results presented here indicate relatively minor variations in pore water pressure and consequent instability assessment between these two coupling strategies (Table 2).

Notably, the differences in simulated p_w and LFS between fully and sequentially coupled models are more significant than those between the fully coupled model with and without poroelastic changes. This smaller difference in the latter simulations is attributed to the counteractive effects of displacement (u) and effective hydraulic conductivity (K_{eff}) on pore pressure in the fully coupled poroelastic model. Specifically, increased effective porosity due to infiltration reduces pore pressure and elevates K_{eff}. The latter increases pore pressure, partially offsetting the overall effect of larger pore size, resulting in a reduced pore pressure decrease or even an increase.

4.3. Effect of the Multiphase Flow Model

The results from comparing the fully coupled two-phase and one-phase flow models indicate a more significant disparity between these two implementations than the impact of simplifying poroelasticity or employing different coupling strategies. These differences in Figure 6 are primarily attributed to the influence of constant pore air pressure (p_a) in the one-phase flow model based on Richards' equation. In a two-phase flow system involving water and air, the air must move or exit the domain during rainfall infiltration. Consequently, the downward progression of water is impeded by elevated pore air pressure,

resulting in reduced flow and a slower increase in p_w. This also explains the enhanced water accumulation near the surface over time, leading to higher p_w near the surface in the two-phase flow model. To substantiate this, we analyzed the development of pore air pressure (p_a) during both low- and high-intensity rainfall events. Figure 8 illustrates the rising trend of air pressure with infiltration. As depicted, air pressure increases with depth and infiltration. This pattern arises from soil compaction and the displacement of air from shallower layers due to increasing depth and infiltration, respectively. In the case of low-intensity rainfall, air movement is less restricted and can be released from the area, resulting in a less pronounced increase in p_a with infiltration. The steeper curve for low-intensity rainfall represents the initially dominant influence of soil compaction, which is more prominently affected by infiltration during high-intensity rainfall.
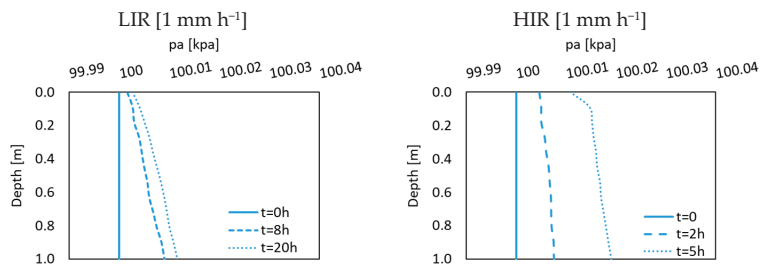

Figure 8. The simulated pa distribution at cross section A for the 2D silty slope using fully coupled two-phase models (2P-FC and 1P-FC, respectively) for LIR and HIR at different time steps.

The lower pore water pressure led to increased stability across various times and locations within the two-phase flow system. This enhanced stability when considering that two-phase flow is consistent with Cho [21]. During the simulations with high-intensity rainfall, the affected area is shallower and more localized compared to simulations with low-intensity rainfall despite the same total precipitation volume. Consequently, the differences between the two models are more pronounced during high-intensity rainfall, primarily within a smaller region closer to the slope surface. These results underscore the potential benefit of considering multiphase flow processes in slope stability assessment, provided sufficient computational resources are available. However, it is important to note that this study does not account for soil heterogeneity or the presence of macrospores, which are both common in natural soils. Particularly, the existence of macropores is expected to significantly enhance soil aeration, reducing the impact of air entrapment on the infiltration process.

5. Conclusions and Outlook

In this study, the stability status of a 2D slope was simulated using a fully coupled hydromechanical model with two-phase (water and air) flow. This model was implemented in the open-source simulator DuMux, and simulations were made for a low- and a high-intensity rainfall event. This comprehensive model was used to examine the impact of three widely used model simplifications in slope stability assessments using the local factor of safety (LFS) approach: (i) the absence of feedbacks from the mechanical to the hydrological model component, (ii) the use of a sequential instead of a fully coupled modeling approach, and iii) the use of a one-phase (i.e., water with Richards' equation) instead of a two-phase (i.e., water and air) flow model. The simulation results indicated that the most significant differences in slope stability occurred near the slope surface, where the steepest gradients in pore water pressure occurred, aligning with previous hydromechanical model applications [30].

Among the three simplifications, replacing a two-phase flow model with a one-phase flow model had the most substantial impact on simulated pore water pressure and LFS. Yet simulations were more robust and computationally efficient when utilizing rigid porous media and one-phase flow based on Richards' equation. Employing a sequentially coupled model or a fully coupled model with constant porosity caused only minor changes. However, instability primarily occurred in fully saturated areas with relatively small pore pressure variations, resulting in minimal differences between the model implementations regarding failure initiation. The disparity between the simplified models and the comprehensive fully coupled model was higher when the rainfall intensity was higher. Nevertheless, exploring different soil types with varying porosities and pore size distributions, like sand or clay with diverse fine and coarse material content, could provide further insights into infiltration patterns and pore pressure variations. In summary, all model simplifications yielded acceptable slope stability analyses, resembling outcomes from the comprehensive fully coupled two-phase flow model. Vulnerable zones prone to failure were consistent across models, offering valuable insights for slope reinforcement and early warning. However, slight variations in potential failure times suggest that more comprehensive methods may be warranted in sensitive sites with sufficient data or without computational constraints.

The results of this study can be extended by exploring more realistic slopes, accounting for heterogeneity, macropores, varying aeration conditions, transient zones, and diverse pore pressure distributions. Additionally, factors like soil types, their variability across a hillslope, groundwater levels, and slope angle play pivotal roles in determining slope stability. Boundary conditions, such as variable infiltration rates and bidirectional inflow and outflow through the boundary, should also be examined in a subsequent study. While the assumption of linear-elastic soil may suffice for early slope failure warning, future simulations can be enhanced by considering more realistic elastoplastic hillslopes, incorporating plastic deformation and post-failure stress redistribution. A three-dimensional slope with complex geometry, bedrock topography, and validation against real-world slopes may also offer further insights into the suitability of different model simplifications and coupling strategies.

References

1. Srinivasan, K.; Howell, B.; Anderson, E.; Flores, A. A low cost wireless sensor network for landslide hazard monitoring. In Proceedings of the International Geoscience and Remote Sensing Symposium, Munich, Germany, 22–27 July 2012; pp. 4793–4796.
2. Greco, R.; Marino, P.; Bogaard, T.A. Recent advancements of landslide hydrology. *Wiley Interdiscip. Rev. Water* **2023**, *10*, e1675. [CrossRef]
3. Cuomo, S.; Della Sala, M. Rainfall-induced infiltration, runoff and failure in steep unsaturated shallow soil deposits. *Eng. Geol.* **2013**, *162*, 118–127. [CrossRef]
4. Cuomo, S.; Della Sala, M. Large-area analysis of soil erosion and landslides induced by rainfall: A case of unsaturated shallow deposits. *J. Mt. Sci.* **2015**, *12*, 783–796. [CrossRef]
5. Eichenberger, J.; Ferrari, A.; Laloui, L. Early warning thresholds for partially saturated slopes in volcanic ashes. *Comput. Geotech.* **2013**, *49*, 79–89. [CrossRef]
6. Tsaparas, I.; Rahardjo, H.; Toll, D.G.; Leong, E.C. Controlling parameters for rainfall-induced landslides. *Comput. Geotech.* **2002**, *29*, 1–27. [CrossRef]
7. Lu, N.; Sener-Kaya, B.; Wayllace, A.; Godt, J.W. Analysis of rainfall-induced slope instability using a field of local factor of safety. *Water Resour. Res.* **2012**, *48*, W09524. [CrossRef]
8. Griffiths, D.V.; Lu, N. Unsaturated slope stability analysis with steady infiltration or evaporation using elasto-plastic finite elements. *Int. J. Numer. Anal. Methods Geomech.* **2005**, *29*, 249–267. [CrossRef]
9. Lu, N.; Godt, J. Infinite slope stability under steady unsaturated seepage conditions. *Water Resour. Res.* **2008**, *44*, W11404. [CrossRef]
10. Lehmann, P.; Or, D. Hydromechanical triggering of landslides: From progressive local failures to mass release. *Water Resour. Res.* **2012**, *48*, W03535. [CrossRef]
11. von Ruette, J.; Lehmann, P.; Or, D. Effects of rainfall spatial variability and intermittency on shallow landslide triggering patterns at a catchment scale. *Water Resour. Res.* **2014**, *50*, 7780–7799. [CrossRef]
12. Moradi, S.; Huisman, J.; Class, H.; Vereecken, H. The effect of bedrock topography on timing and location of landslide initiation using the local factor of safety concept. *Water* **2018**, *10*, 1290. [CrossRef]
13. Lanni, C.; McDonnell, J.; Hopp, L.; Rigon, R. Simulated effect of soil depth and bedrock topography on near-surface hydrologic response and slope stability. *Earth Surf. Process. Landf.* **2013**, *38*, 146–159. [CrossRef]
14. von Ruette, J.; Lehmann, P.; Or, D. Rainfall-triggered shallow landslides at catchment scale: Threshold mechanics-based modeling for abruptness and localization. *Water Resour. Res.* **2013**, *49*, 6266–6285. [CrossRef]
15. Andrés, S.; Dentz, M.; Cueto-Felgueroso, L. Multirate Mass Transfer Approach for Double-Porosity Poroelasticity in Fractured Media. *Water Resour. Res.* **2021**, *57*, 27. [CrossRef]
16. Mehrabian, A.; Abousleiman, Y.N. Generalized Biot's theory and Mandel's problem of multiple-porosity and multiple-permeability poroelasticity. *J. Geophys. Res. Solid Earth* **2014**, *119*, 2745–2763. [CrossRef]
17. Dugan, B.; Stigall, J. Origin of overpressure and slope failure in the Ursa region, Northern Gulf of Mexico. In *Submarine Mass Movements and Their Consequences*; Mosher, D.C., Shipp, R.C., Moscardelli, L., Chaytor, J.D., Baxter, C.D.P., Lee, H.J., Urgeles, R., Eds.; Springer: Dordrecht, The Netherlands, 2010; Volume 28, pp. 167–178.
18. Li, B.; Tian, B.; Tong, F.G.; Liu, C.; Xu, X.L. Effect of the Water-Air Coupling on the Stability of Rainfall-Induced Landslides Using a Coupled Infiltration and Hydromechanical Model. *Geofluids* **2022**, *2022*, 16. [CrossRef]
19. Urgeles, R.; Locat, J.; Sawyer, D.E.; Flemings, P.B.; Dugan, B.; Binh, N.T.T. History of pore pressure build up and slope instability in mud-dominated sediments of ursa basin, gulf of Mexico continental slope. In *Submarine Mass Movements and Their Consequences*; Springer: Dordrecht, The Netherlands, 2010; Volume 28.
20. Kim, J. Sequential Methods for Coupled Geomechanics and Multiphase Flow. Ph.D. Thesis, Stanford University, Stanford, CA, USA, 2010.
21. Cho, S.E. Stability analysis of unsaturated soil slopes considering water-air flow caused by rainfall infiltration. *Eng. Geol.* **2016**, *211*, 184–197. [CrossRef]
22. Szymkiewicz, A. *Modelling Water Flow in Unsaturated Porous Media: Accounting for Nonlinear Permeability and Material Heterogeneity*; Springer: Berlin/Heidelberg, Germany, 2013.
23. Farthing, M.W.; Ogden, F.L. Numerical Solution of Richards' Equation: A Review of Advances and Challenges. *Soil Sci. Soc. Am. J.* **2017**, *81*, 1257–1269. [CrossRef]
24. Oh, S.; Lu, N. Slope stability analysis under unsaturated conditions: Case studies of rainfall-induced failure of cut slopes. *Eng. Geol.* **2015**, *184*, 96–103. [CrossRef]

25. Borja, R.I.; White, J.A. Continuum deformation and stability analyses of a steep hillside slope under rainfall infiltration. *Acta Geotech.* **2010**, *5*, 1–14. [CrossRef]
26. Settari, A.; Walters, D.A. Advances in coupled geomechanical and reservoir modeling with applications to reservoir compaction. *SPE J.* **2001**, *6*, 334–342. [CrossRef]
27. Koch, T.; Gläser, D.; Weishaupt, K.; Ackermann, S.; Beck, M.; Becker, B.; Burbulla, S.; Class, H.; Coltman, E.; Emmert, S.; et al. DuMux 3—An open-source simulator for solving flow and transport problems in porous media with a focus on model coupling. *Comput. Math. Appl.* **2021**, *81*, 423–443. [CrossRef]
28. White, J.A.; Castelletto, N.; Tchelepi, H.A. Block-partitioned solvers for coupled poromechanics: A unified framework. *Comput. Meth. Appl. Mech. Eng.* **2016**, *303*, 55–74. [CrossRef]
29. Preisig, M.; Pervost, J.H. Coupled multi-phase 1036 thermo-poromechanical effects. Case study: CO_2 injection at In Salah, Algeria. *Int. J. Greenh. Gas Control* **2011**, *5*, 1055–1064. [CrossRef]
30. Beck, M.; Rinaldi, A.P.; Flemisch, B.; Class, H. Accuracy of fully coupled and sequential approaches for modeling hydro- and geomechanical processes. *Comput. Geosci.* **2020**, *24*, 1707–1723. [CrossRef]
31. Kim, J.; Tchelepi, H.A.; Juanes, R. Stability and convergence of sequential methods for coupled flow and geomechanics: Fixed-stress and fixed-strain splits. *Comput. Meth. Appl. Mech. Eng.* **2011**, *200*, 1591–1606. [CrossRef]
32. Darcis, M.Y. Coupling Models of Different Complexity for the Simulation of CO_2 Storage in Deep Saline Aquifers. Ph.D. Thesis, University of Stuttgart, Stuttgart, Germany, 2013.
33. Kim, J.M. A fully coupled finite element analysis of water-table fluctuation and land deformation in partially saturated soils due to surface loading. *Int. J. Numer. Methods Eng.* **2000**, *49*, 1101–1119. [CrossRef]
34. Bao, J.; Xu, Z.J.; Fang, Y.L. A coupled thermal-hydromechanical simulation for carbon dioxide sequestration. *Environ. Geotech.* **2016**, *3*, 312–324. [CrossRef]
35. Abdollahipour, A.; Marji, M.F.; Bafghi, A.Y.; Gholamnejad, J. Time-dependent crack propagation in a poroelastic medium using a fully coupled hydromechanical displacement discontinuity method. *Int. J. Fract.* **2016**, *199*, 71–87. [CrossRef]
36. Della Vecchia, G.; Jommi, C.; Romero, E. A fully coupled elastic-plastic hydromechanical model for compacted soils accounting for clay activity. *Int. J. Numer. Anal. Methods Geomech.* **2013**, *37*, 503–535. [CrossRef]
37. Freeman, T.; Chalaturnyk, R.; Bogdanov, I. Fully coupled thermo-hydro-mechanical modeling by COMSOL Multiphysics, with applications in reservoir geomechanical characterization. In Proceedings of the COMSOL Conference, Boston, MA, USA, 9–11 October 2008.
38. Tang, Y.; Wu, W.; Yin, K.; Wang, S.; Lei, G. A hydro-mechanical coupled analysis of rainfall induced landslide using a hypoplastic constitutive model. *Comput. Geotech.* **2019**, *112*, 284–292. [CrossRef]
39. Tufano, R.; Formetta, G.; Calcaterra, D.; De Vita, P. Hydrological control of soil thickness spatial variability on the initiation of rainfall-induced shallow landslides using a three-dimensional model. *Landslides* **2021**, *18*, 3367–3380. [CrossRef]
40. Chen, X.; Zhang, L.; Zhang, L.; Zhou, Y.; Ye, G.; Guo, N. Modelling rainfall-induced landslides from initiation of instability to post-failure. *Comput. Geotech.* **2021**, *129*, 103877. [CrossRef]
41. Wu, L.; Huang, R.; Li, X. *Hydro-Mechanical Analysis of Rainfall-Induced Landslides*; Springer: Beijing, China, 2020. [CrossRef]
42. Pedone, G.; Tsiampousi, A.; Cotecchia, F.; Zdravkovic, L. Coupled hydro-mechanical modelling of soil–vegetation–atmosphere interaction in natural clay slopes. *Can. Geotech. J.* **2022**, *59*, 272–290. [CrossRef]
43. Moradi, S. Stability Assessment of Variably Saturated Hillslopes Using Coupled Hydromechanical Models. Ph.D. Thesis, University of Stuttgart, Germany, 2021.
44. Lu, N.; Godt, J.W. *Hillslope Hydrology and Stability*; Cambridge University Press: Cambridge, UK, 2013.
45. Huang, Y.H. *Slope Stability Analysis by the Limit Equilibrium Method*; ASCE Press: Reston, VA, USA, 2014. [CrossRef]
46. Moradi, S.; Heinze, T.; Budler, J.; Gunatilake, T.; Kemna, A.; Huisman, J.A. Combining Site Characterization, Monitoring and Hydromechanical Modeling for Assessing Slope Stability. *Land* **2021**, *10*, 423. [CrossRef]
47. Flemisch, B.; Darcis, M.; Erbertseder, K.; Faigle, B.; Lauser, A.; Mosthaf, K.; Muthing, S.; Nuske, P.; Tatomir, A.; Wolff, M.; et al. DuMu(x): DUNE for multi-{phase, component, scale, physics, . . .} flow and transport in porous media. *Adv. Water Resour.* **2011**, *34*, 1102–1112. [CrossRef]
48. Fetzer, T.; Becker, B.; Flemisch, B.; Glaser, D.; Heck, K.; Koch, T.; Schneider, M.; Scholz, S.; Weishaupt, K. *Dumux, 2.12.0*; Zenodo: Geneve, Switzerland, 2017. [CrossRef]
49. Blatt, M.; Burchardt, A.; Dedner, A.; Engwer, C.; Fahlke, J.; Flemisch, B.; Gersbacher, C.; Graeser, C.; Gruber, F.; Grueninger, C.; et al. The Distributed and Unified Numerics Environment, Version 2.4. *Arch. Numer. Softw.* **2016**, *4*, 13–17. [CrossRef]
50. Bastian, P.; Blatt, M.; Dedner, A.; Engwer, C.; Klofkorn, R.; Kornhuber, R.; Ohlberger, M.; Sander, O. A generic grid interface for parallel and adaptive scientific computing. Part II: Implementation and tests in DUNE. *Computing* **2008**, *82*, 121–138. [CrossRef]
51. Bastian, P.; Blatt, M.; Dedner, A.; Dreier, N.-A.; Engwer, C.; Fritze, R.; Gräser, C.; Grüninger, C.; Kempf, D.; Klöfkorn, R.; et al. The Dune framework: Basic concepts and recent developments. *Comput. Math. Appl.* **2021**, *81*, 75–112. [CrossRef]

52. Zhang, K.; Cao, P.; Liu, Z.Y.; Hu, H.H.; Gong, D.P. Simulation analysis on three-dimensional slope failure under different conditions. *Trans. Nonferrous Met. Soc. China* **2011**, *21*, 2490–2502. [CrossRef]
53. Kristo, C.; Rahardjo, H.; Satyanaga, A. Effect of hysteresis on the stability of residual soil slope. *Int. Soil Water Conserv. Res.* **2019**, *7*, 226–238. [CrossRef]

A Case Study for Stability Analysis of Toppling Slope under the Combined Action of Large Suspension Bridge Loads and Hydrodynamic Forces in a Large Reservoir Area

Jian Huang [1], Shixiong Tang [1], Zhiqing Liu [1], Faming Zhang [2,*], Menglong Dong [2], Chang Liu [2] and Zinan Li [2]

[1] China Communications Highway Planning and Design Institute Co., Ltd., Beijing 100010, China; 18610383393@163.com (J.H.); tangshixiong@hpdi.com.cn (S.T.); liuzhiqing@hpdi.com.cn (Z.L.)

[2] Earth Sciences and Engineering College, Hohai University, Nanjing 210098, China; dongml@hhu.edu.cn (M.D.); clarencelc@foxmail.com (C.L.)

* Correspondence: zhangfm@hhu.edu.cn; Tel.: +86-137-7067-1695

Abstract: The foundation of a large river crossing bridge is often located on high and steep slopes in mountainous area, and the stability of the slope has a significant impact on the safety of the bridge. Not only the bridge load, but also the hydro-dynamical action in the reservoir area has a significant impact on the stability of the bank slope where the bridge foundation is located, especially for the toppling bank slope. This paper takes the stability of the toppling bank slope where the one major bridge foundation is located at on the Lancang River in China as an example. Through on-site exploration, drilling data and core conditions, and television images of the borehole, the geological structure of the on-site bank slope were conducted. Based on the development of the dumping body obtained from on-site exploration, corresponding indicators have been proposed from the perspectives of rock inclination, deformation, and rock quality to clarify the degree of dumping along the depth of the bank slope. The failure mechanism of the overturned bank slope under the action of a bridge was analyzed from a mechanical perspective. Numerical simulations were conducted using GeoStudio 2018:SEEP/W and FLAC3D 6.0 software to analyze the failure modes of bridge loads and hydrodynamic forces under different water levels and rainfall conditions. The seepage field characteristics, failure modes, and stability characteristics were analyzed from a two-dimensional perspective, while the displacement characteristics, plastic zone, and stress–strain characteristics were explored from a three-dimensional perspective, which revealed the evolution mode of overturned deformation under the action of bridge foundation loads. Finally, the stability of the wide slope was numerically calculated using the strength reduction method, and the stability calculation data was combined with the numerical simulation results to determine the optimal location of the bridge foundation.

Keywords: toppling rock mass; reservoir water level fluctuation; bridge loads; reservoir bank slope; stability evaluation

1. Introduction

With the rapid development of highway construction in mountainous areas of China, a large number of bridge foundations set in high and steep slope have emerged. Bridge foundations on high and steep slopes in mountainous are usually set in the form of a pile foundation, and the geological environment in which the foundations are located is complex, especially on the slope of the reservoir bank with developed toppling deformation. The effect of bridge load and reservoir water change aggravates the degree of toppling deformation, which may cause slope instability and bridge foundation failure. It is necessary to evaluate the stability of toppled rock slope under bridge loads and hydrodynamic forces. In the process of evaluating the stability of the bank slope under the bridge load, the influence of the bridge load on the shape and position of the potential sliding surface in the

bank slope should be considered. Currently, there is relatively little research on this type of pile foundation and there is no complete theoretical method. It is also not possible to design and guide with conventional calculation methods. To ensure the reliability and safety of the pile foundation, the stability analysis and evaluation of the slope under the action of bridge loads and reservoir water level fluctuations have important practical significance. In recent years, relevant research has been conducted on bridge foundations on high slopes, but it mainly focused on high and steep slopes with good rock mass quality. There is a lack of research on the impact of toppling deformation of rock slope and changes in reservoir water level on the stability of bridge foundation slopes. Some researchers used engineering geological methods and block theory to analyze the stability of high and steep slopes in canyon areas under bridge loads [1–3]. The research focus is on the impact of bridge load lateral forces on slope stability. Yu et al. obtained the response of a single pile subjected to a lateral load in sloping ground via a field test [4]. With the development of the finite element method, more and more scholars begin to use the strength reduction method to analyze bridge foundation bank slope stability. Deendayal et al. used the finite element numerical method to study the behavior of a group of piles located on sloping ground, and obtained the effect of slopes on pile capacity [5]. Sitharam et al. analyzed the highly jointed slopes on the abutments of a railway bridge [6]. Tian et al. used the strength reduction method to analyze the stability of the bank by considering the effect of bedding and vertical joints, and they obtained the results of how a slide surface would form under skewback due to a huge bridge load [7]. Souri et al. studied the static lateral behavior of the battered pile group foundation of an I-10 twin span bridge by using the 3D finite element modeling [8]. Abu-Farsakh et al. have researched the static lateral behavior of three pile group configurations by using three-dimensional finite element modeling [9]. Their research on the stress problem of high- and steep-slope bridge piers mainly focused on pile foundations and has achieved a series of valuable results. Luo et al. established a three-dimensional finite element calculation model for double-row foundation piles of bridges on rock slopes, and obtained the stress distribution law of rock slopes [10]. These studies have deepened our understanding of the forces acting on high- and steep-slope bridge piers. Some researchers have studied the seismic performance of bridge-pile-foundation slopes with anti-sliding piles. Zhou et al. have conducted shaking table tests on bridge foundation reinforced by anti-slide piles on slope [11]. Zhang et al. have researched the seismic performance of bridge-pile-foundation slopes with an anti-sliding pile by using the large-scale shaking table model test [12].

The geological structure of the toppling deformation slope is relatively complex, and there are many influencing factors. The sliding scale of toppled and deformed slopes varies, and the deformation depth is usually smaller than the scale of the landslide. However, in the canyon area of southwestern China, the deformation depth can reach 200–300 m. The damage caused by toppling deformation is related to factors such as the degree and type of toppling, and the failure modes and sliding modes of toppling failure vary greatly under different influencing factors. The collapse deformation and damage can be divided into three categories: bending collapse, block collapse, and block bending collapse. The different types of damage threats are shown in Table 1.

At present, a large amount of research on toppling deformation is focused on the failure mechanism, deformation mode, etc. Some scholars have studied the changes in water level in the reservoir area caused by the construction of hydropower stations in western China and their impact on the degree of toppling. Research on the stability of slopes where bridges are located has focused heavily on the impact of bridge loads on slope stability and the exploration of slope slip mechanisms. Therefore, there is relatively little research on the stability of inverted layered rock slopes under bridge loads. In relevant research, most scholars used simplified two-dimensional numerical analysis to study bridge foundation slopes, in which it is difficult to reflect the relevant effects on canyon terrain with significant terrain fluctuations; in three-dimensional numerical analysis, most bridge

loads are replaced by simplified concentrated forces or ignored, making it difficult to reflect the impact of bridge foundations on slope stability.

Table 1. The specific description of different types of toppling deformation and failure.

Toppling Damage Type	Deformation Process	Deformation Characteristic
Bending collapse	Mainly in thin to medium-sized layers of rock formations, bending as a floating surface under their own weight, but which do not break. They have self-stability and are often affected by excavation, earthquakes, water loads, and other factors.	Large-scale and deep deformation
Block collapse	Mainly in medium-sized to thick rock masses, under the action of gravity or external forces, with the cut rock blocks toppling outward along the corners. During the failure, the rock mass at the foot of the slope undergoes deformation due to the action of the latter rock layer, leading to toppling failure of the upper rock mass.	Instantaneous and sudden, but on a smaller scale
Block bending collapse	Mainly in slopes with alternating layers of soft and hard rocks, with continuous bending deformation and a failure scale between bending collapse and block collapse.	Continuity and accumulation

Although many scholars have studied the stability of bridge pile foundations on slopes, as well as the evaluation of the stability of toppled rock slopes, there is very little research on building large bridges on toppled rock slopes of large reservoirs. The prediction of deformation or failure of toppled rock slopes under bridge loads is one of the key contents of safety research for large bridges. This paper proposed the basic indicators of toppling deformation bodies to discuss the mechanism of toppling deformation under the action of bridges and hydrodynamic forces, simulated the characteristics of the seepage field on a two-dimensional scale, and conducted a stability analysis using the rigid body limit equilibrium stability calculation method. The slope stress state and plastic zone distribution characteristics of two sets of bridge type schemes were analyzed at a three-dimensional scale, and the optimal scheme for a bridge foundation layout was ultimately determined using the strength reduction method. In summary, this paper took the stability of a collapsed bank slope of a certain bridge foundation on the Lancang River as an example, combined engineering geological methods with numerical simulation, simulated the combined effect of bridge loads and hydrodynamic forces, explored potential failure modes of the bank slope, discussed slip modes, and comprehensively evaluated the stability of the bank slope.

The purpose of this paper is to achieve the following:

(1) Provide the method for determining the toppling deformation degree of bank slopes along depth;

(2) Propose the prediction model of the toppling deformation trend under the combined action of bridge loads and reservoir hydrodynamics;

(3) Establish the stability evaluation method for the toppling bank slope in a large canyon reservoir area under bridge loads and hydrodynamic forces.

To analyze the stability of toppled slopes under the combined action of bridge loads and hydrodynamic forces, many methods currently used for calculating and evaluating toppled slopes can be selected. At present, many calculation and evaluation methods of toppling slope stability are used, which can be divided into the following types: ① Numerical methods: methods include the finite element method (FEM), the discrete element method (DEM), finite difference method (FDM), the boundary element method (BEM), discontinuous deformation analysis (DDA), elastic-plastic finite element analysis of strength reduction, the point safety factor method based on finite element theory, the Lagrange fast difference method (FLAC), etc. Marc-Andre and Doug used a three-

dimensional discrete element program to study the influence of discontinuous structural planes on the mechanism of block toppling deformations in rock masses [13]. Pinheiro et al. used the discrete element method to study the development mechanism and deformation failure characteristics of a slope in Brazil due to bending and toppling. Compared with the continuous medium method, they better simulated the failure process of rock masses along discontinuous surfaces. They also used the discrete element method to perform an inverse analysis on the parameters of bending and toppling failure of a rock mass [14]. Li et al. proposed a new discrete element method (CDEM) to simulate the irreversible process from continuous deformation to discontinuous deformation, analyze the characteristics of toppling deformation and failure mechanism, and compare the numerical simulation results with GB-InSAR monitoring data to verify the applicability of the method [15]. Lian et al. used a discrete lattice spring numerical model to study the deformation development law of toppling failure of fractured rock slopes [16]. Zhang et al. used the discrete element method to study the seismic dynamic response mechanism of layered slopes against tilting, and analyzed the tilting deformation mechanism of layered slopes with different slopes, joint angles, and joint orientations under natural earthquake and sine wave actions [17]. Hassan et al. compared the reliability of the finite element and discrete element methods for a stability analysis of rock masses with upper sliding and lower tilting, and the results showed that the discrete element method has a higher accuracy in a stability analysis of such toppling deformation of rock masses [18]. ② Limit equilibrium method: Unbalanced thrust transfer coefficient method, Sarma method, key block theory, etc. Liu et al. proposed a stability analysis method for toppled deformed rock slopes based on the limit equilibrium method for the case where the thickness of the block toppling deformed rock mass is less than the thickness of the top rock mass [19]. ③ Physical simulation method. In 1971, Ashby J. was the first to use the inclined table model-based technology to study the mechanism and process of slope collapse failure. Subsequently, In 1978, HittingerM proposed the theory of the base friction test for the study of slope block toppling and bending toppling. Ignacio et al. conducted indoor model experiments to simulate toppling deformation using tilting table tests. In the experiments, 3D printing technology was used to prepare toppling deformation rock masses, simulate the development mechanism of toppling deformation, and extend the experimental results to the effects of earthquakes or water [20]. Zheng et al. designed three sets of centrifuge model tests with different slope angles to simulate the evolution process of inverted layered slope toppling deformation under different slope angle conditions, taking the dam toppling deformation of the Lancang River Gushui Hydropower Station as an example [21]. Zheng et al. proposed an adaptive moment estimation method for the stability analysis of toppling deformation, and compared it with the results of a centrifuge test analysis of toppling deformation stability, indicating that this method can effectively find the toppling instability surface and corresponding safety factor [22]. ④ Uncertainty analysis methods: including the reliability analysis method of slope stability, stochastic process method, fuzzy analysis method, grey system prediction, artificial intelligence and artificial neural network method, etc. Ardestani used probability analysis methods to consider the effects of slope shape, structural surface characteristics, geotechnical parameters, groundwater, dynamic loads, and support measures on the formation mechanism and stability of anti-dip slopes [23]. ⑤ Other analysis methods include engineering geological analogy and graphical methods. In the above research methods, most of them focus on discussing the deformation conditions under which the rock mass undergoes toppling, analyzing the mechanism of toppling deformation, or evaluating the stability of the slope after excavation or unloading of the toppling rock mass. There is very little research on the secondary failure mechanism under combined action of bridge loads and reservoir hydrodynamical change. Liu et al. studied the instability mechanism of the toppled slope under geological loads using the #1 toppling deformed rock mass of Huangdeng Hydropower Station as the research object; it is believed that during an earthquake, multiple cracks are formed inside the collapsed rock mass, cutting and shearing the rock mass, resulting in deformation and failure of the collapsed rock mass [24].

Huang et al. used geological surveying, exploration tunnels, electron spin resonance dating, and kinematic monitoring to analyze the deep dumping mechanism of a high and steep anti-tilting slope at the Miaowei Hydropower Station dam site in the Lancang River. They believe that the deep dumping is caused by the rapid cutting of the valley under high ground stress [25]. Cai et al. studied the deformation mechanism of the ductile bending toppling mode in toppling deformation, dividing ductile bending toppling into the start-up stage, rapid deformation stage, transient stability stage, and long-term creep stage [26]. Zhang et al. proposed a calculating model of limited toppling depth according to the shallow deformation strength by using geological mechanism analysis and the numerical simulation method [27]. Xuan et al. discussed the large reservoir bank slope stability on considering wave action [28]. Based on the research content of the above literature, the advantages and disadvantages of the numerical simulation methods used have been summarized. The specific content is shown in Table 2.

Table 2. Advantages and disadvantages of different numerical simulation methods used in the above literature.

Numerical Methods	Advantage	Disadvantage
Finite element method (FEM)	Able to considering the non-uniformity and discontinuity of the slope rock mass, avoiding the defect of treating the sliding mass as a rigid body that is too simplified; able to consider the impact of groundwater, construction engineering, and the combined effects of various support structures and geotechnical materials.	Affected greatly by the selection of physical parameters; cannot solve the problem of a large number of joints and discontinuities in the rock mass, especially for solving problems such as large deformation and displacement.
Discrete element method (DEM)	Suitable for stress and deformation analysis of jointed rock masses, with significant advantages in solving linear large displacement and dynamic stability problems.	The selection of time steps affects the accuracy of calculation results.
Boundary element method (BEM)	Advantages for solving infinite or semi-infinite domain problems, suitable for small deformation homogeneous continuous media.	When encountering domain integrals corresponding to nonlinear terms, there is a strong singularity near the singular point, making the solution difficult.
Discontinuous deformation analysis (DDA)	Taking the minimum value of the potential functional has some advantages of both finite element and discrete element methods.	Analyzing problems often completely discretizes the research object, which is not suitable for the analysis of continuous and semi-continuous problems. At the same time, due to the wide variety of rock masses and complex properties, the calculation time step has a significant impact on the results.
Lagrange fast difference method (FLAC)	Able to effectively consider the large deformation and discontinuity of rock and soil, with fast solving speed, suitable for solving nonlinear large deformation problems.	There is randomness in the division of calculation boundaries and grids, and the calculation results will be influenced by the grids and boundaries.

2. Research Materials and Methods

2.1. Overview of the Research Area

The Lancang River Grand Bridge is located on the northeast side of Yingping Village, Yunlong County, Yunnan Province. The piers of the bridge are located both on the east and west bank slopes of the Miaowei Hydropower Station Reservoir on the Lancang River, with a water level depth of about 70–100 m. During the period of the on-site survey, the water surface elevation of the reservoir was 1400–1405 m, and the width of the water surface was about 240 m. The Lancang River brand Bridge is a 256 + 628 + 256 m double-tower composite girder cable-stayed bridge, while the main span is 495 m, and the bridge span is arranged as 3 × 60 m + 75 m + 495 m + 75 m + 75 m + 3 × 60 m = 1005 m. It is proposed to

use the bored cast-in-place pile group pile foundation with a diameter of 2.5 m (Figure 1). The corresponding loads used for calculating bank slope stability under different bridge layout schemes are listed in Table 3.

(**a**)

(**b**)
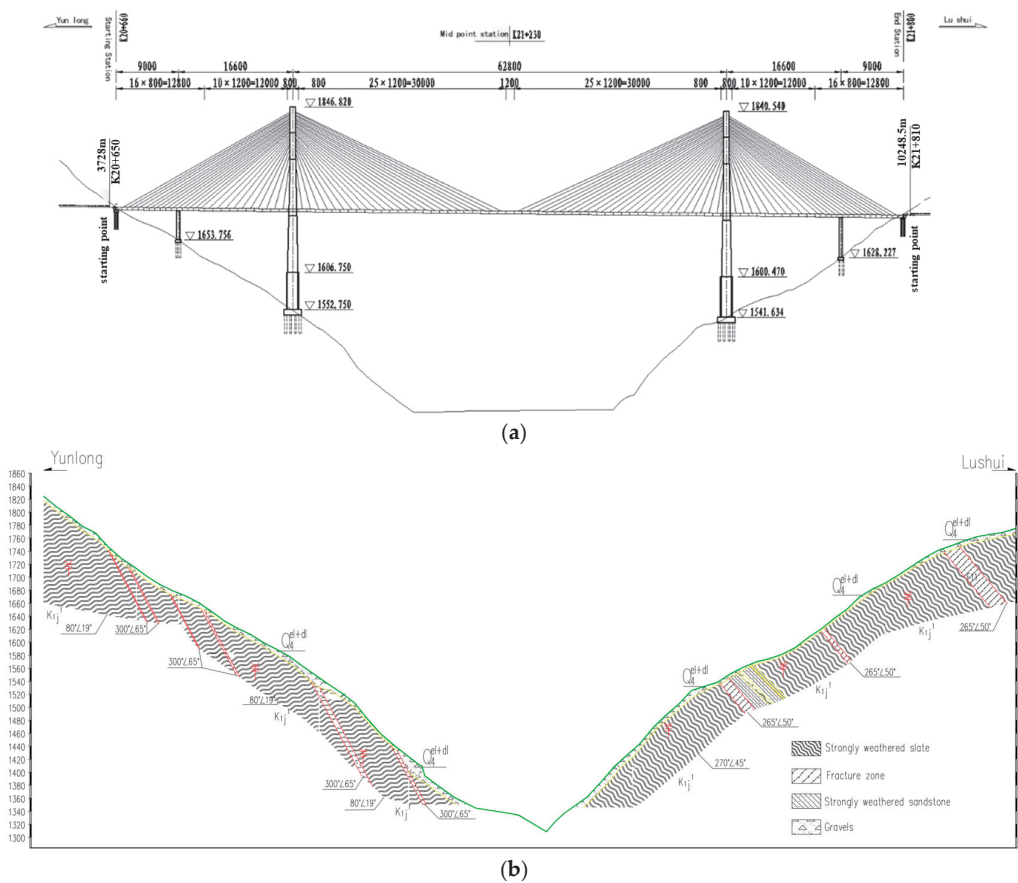
Figure 1. Schematic diagram of bridge location (scheme 1). (**a**) Schematic diagram of bridge type; (**b**) geological section of bridge site area.

Table 3. Calculation of bridge load for bank slope stability (Unit: kN).

Bridge Programme	Pier/Abutment Name	Transverse Bridge Width/m	Pile Foundation Length/m	Axial Force/kN	Axial Compressive Bearing Capacity Per Linear Meter of a Single Pile with a Single Width/kN	Horizontal Force along the Bridge Direction/kN	Horizontal Force along the Bridge Direction with Single Width/kN
scheme 1	main pier	40	80	1,039,325	216	64,207	1605
	auxiliary pier	11.2	35	77,468	188	876	78
	abutment	12.8	28	69,099	172	0	0

Table 3. *Cont.*

Bridge Programme	Pier/Abutment Name	Transverse Bridge Width/m	Pile Foundation Length/m	Axial Force/kN	Axial Compressive Bearing Capacity Per Linear Meter of a Single Pile with a Single Width/kN	Horizontal Force along the Bridge Direction/kN	Horizontal Force along the Bridge Direction with Single Width/kN
scheme 2	main pier	40	90	1,632,135	216	31,039	776
	auxiliary pier (adjacent to the main pier)	16.5	35	112,088	155	0	0
	auxiliary pier (near abutment pier)	16.5	35	55,179	115	0	0
	abutment	11.8	28	74,695	172	0	0

The geomorphic type of the bridge area is alpine canyon topography (Figure 2). The elevation of the crossing section in the bridge site area is 1300~1710 m. The terrain is undulating and there is strong seismic activity in the area.
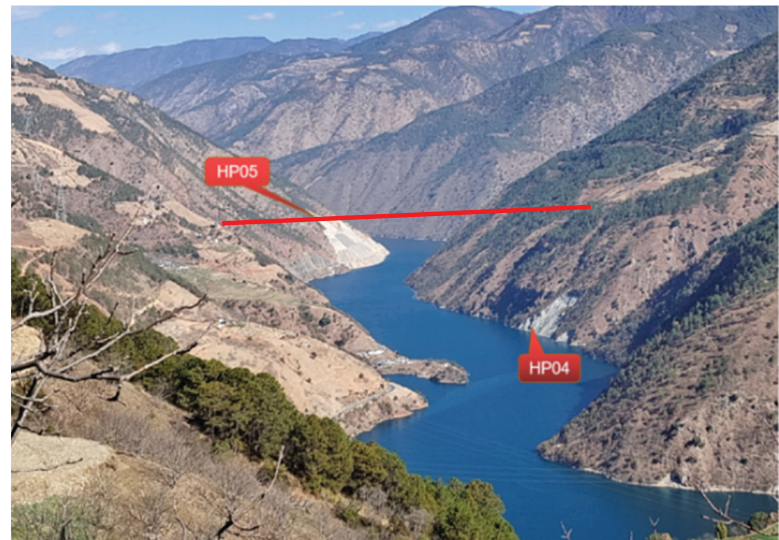

Figure 2. Terrain and landform characteristics on both sides of the bridge.

2.2. Engineering Geological Characteristics of the Research Area

2.2.1. Lithology

According to geological survey, the lithology of the stratum in the bridge site area is distribution from top to bottom as follows: Quaternary eluvial, deluvial, and colluvial silty clay, gravelly soil, fault gouge, fault breccia, cataclasite caused by the fault zone structure, slate with sandstone in the Cretaceous Jingxing Formation, etc. The distribution of strata on both sides of the bank slopes is relatively continuous, and the lithology is relatively single. The rock layers are inclined towards the slope, and the fractured zones (rock debris mixed with crushed stones) and joint fissures within the rock mass are relatively developed (Figures 3 and 4). The drilling core exposed strata are strongly unloading slate with sandstone, with a rock occurrence of $80° \angle 19–72°$.
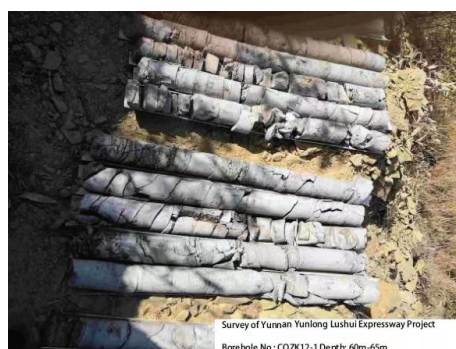
Figure 3. Deep stratigraphy of Yunlong side bank slope.

Figure 4. Stratigraphy of river water level position on Yunlon side bank slope.

2.2.2. Hydrogeological Conditions

Before the impoundment of the Miaowei Hydropower Station, the Lancang River served as the lowest discharge reference level for surface water and groundwater on the bank slope of the bridge site. Groundwater varied greatly with the seasons and was mainly replenished by atmospheric precipitation. Groundwater was ultimately discharged into the Lancang River. After the impoundment of Miaowei Hydropower Station, the water level in the reservoir is higher than the groundwater level on both bank slopes. The groundwater level inside the bank slope is mainly supplied by the reservoir water, followed by atmospheric precipitation infiltration.

Groundwater types are divided into porous and fractured groundwater based on burial conditions and storage media. Pore water is present in the Quaternary loose layer, while fractured groundwater is present in the fractures and structural zones of rock masses.

(1) Pore phreatic water

Distributed in the residual slope, colluvial slope, and alluvial and proluvial layers on both sides of the riverbed, pore phreatic water varies significantly with the season, with abundant water content in the rainy season and dry season.

(2) Fissured phreatic water

The groundwater in the bridge site area is replenished by the infiltration of reservoir water and atmospheric precipitation. The exploration of the bank slope revealed that the groundwater level inside the bank slope is at the same level as the water level of the Lancang River Miaowei Hydropower Station reservoir, ranging from approximately 1400 m to 1410 m. Affected by the periodic rise and fall of the reservoir water level, the groundwater on the bank slope also undergoes periodic fluctuations, with a range of

0–10 m. The area in front of the bank slope that connects with the reservoir water has a significant change, but gradually decreases towards the bank slope.

2.3. Numerical Simulation Method

In this paper, the finite differences software FLAC3D 6.0 is used to analyze the stress and strain of toppling slope under the coupling effect of bridge loads and reservoir water change, and the strength reduction method is used to determine the anti-sliding stability coefficient of slope.

According to the site's geological investigation data, the main strata and geological structures are shown in Figure 2. The main layers were strongly weathered sandstone and strongly weathered slate mixed with sandstone, which were characterized by low strength and susceptible to bending deformation towards the airborne direction due to its own weight.

The rock mass model is set as an elastic-plastic Mohr–Coulomb model. For the boundary conditions, during the calculation, a fixed displacement boundary at the bottom is set to limit deformation at the bottom, the displacement boundary and stress boundary are set before and after the model, and the initial crustal stress, which is mainly generated by gravity, is set inside the model. The horizontal stress is taken as 0.5 times the vertical stress that is converted by gravity. The stress value increases linearly with depth.

According to the design of the bridge and the location of the bridge foundation, there was a bored cast-in-place pile group foundation with a diameter of 2.5 m. Therefore, the three-dimensional geometric modeling was established while the bridge loads was applied. Although the two schemes for bridge layout have different pier positions, the dimensions of the 3D geological model are the same. The starting point in the x-direction of the Yunlong side slope model area is 0 m, and the ending point is 735 m, which refers to the model with a length of 735 m; the starting point in the y-direction is 0 m, and the ending point is 289 m, which refers to the model with a length of 289 m; The starting point in the z-direction is 0 m, and the ending point is 567 m, which refers to the model with a length of 567 m. In the calculation, applying loads at the corresponding position of the bridge foundation on both banks, including the main pile position, the main pile auxiliary pile, the abutment auxiliary pile, and the abutment. Details of the model are shown in Figure 5.

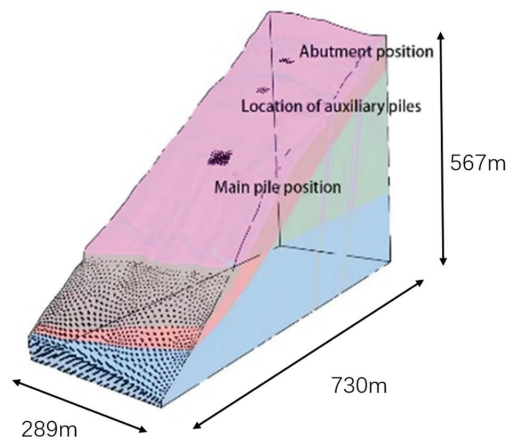**Figure 5.** Geometric model.

3. Research Results

In order to understand the characteristics and determine the toppling deformation of the bank slope rock mass, a series of on-site investigation methods were adopted to explore the toppling deformation of the bank slope rock mass, aiming to provide relevant data and qualitative descriptions for the basic indicators of the toppling body. This article

provides evidence for the determination of the deformation characteristics and degree of the collapsed body through on-site surveys, geological conditions revealed through drilling, and television images inside the hole.

The degree of fragmentation of the rock mass in the front of the bank slope along the bridge axis is more severe than that in the middle and rear. The rock mass near the river undergoes stronger unloading and toppling deformation, which can be clearly revealed by the cores drilled near the east bank and the television images inside the holes. As shown in Figure 6, the television images inside the holes reveal that the rock mass is extremely fragmented, with many cracks being open and hollow, and many cracks being steep inclined.
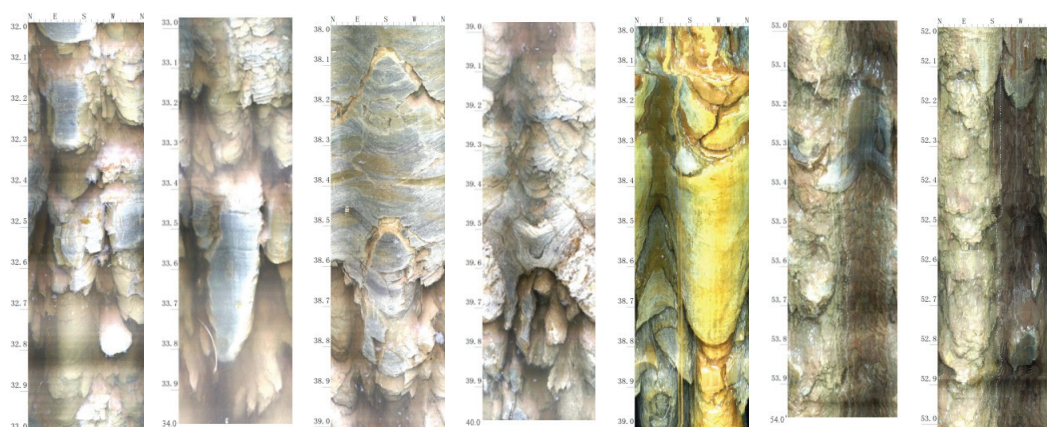

Figure 6. Broken rock mass revealed via TV images in boreholes near shore.

3.1. Distribution Law of the Toppling Deformation Degree

(1)   Basic indicators for grading the degree of toppling deformation

(1) Dip angle difference in rock strata

Based on the core revealed by drilling, the dip angles of rock layers at different depths were statistic, which plays an important role in determining toppling degree along the depth. The dip angles of rock layers are significantly different with different degrees of toppling. According to the differences in dip angle, the rock mass on the bank slope of the bridge site area can be divided into three major types: extremely strong (A), strong (B), and weak toppling (C). Among them, Class B, namely the strong toppling rock mass, can be divided into B1 (the upper section) and B2 (the lower section). The dip angle of Class A is $\alpha \leq 40°$, the dip angle of Class B1 is $40° < \alpha \leq 57°$, the dip angle of Class B2 is $54° < \alpha \leq 68°$, and the dip angle of Class C is $60° < \alpha \leq 78°$.

(2) Maximum tension within the layer

Tensile cracks formed by tensile deformation is related to the maximum tension within the layer. Among the three types toppling rock masses, Class A has strong tensile deformation. The maximum tension cracks within the layer in Class A is generally more than 21 mm, while the maximum tensile cracks in Class B1, B2, and C are 9–24 mm, 6–18 mm, and 2–8 mm, respectively.

(3) Unit tension within the layer

The tensile deformation per unit length of rock mass within the layer (mm/m) is clearly controlled by the intensity of rock mass toppling deformation. According to the geological survey results, the soft rock combination, with a thin layer structure and highly developed bedding plane dislocations, mainly composed of slate, schist, and phyllite, generally exhibits plastic characteristics, which does not present significant tensile deformation even when toppling and rotated at a large angle. However, the combination of hard rocks mainly

composed of quartzite sand slate and metamorphic sandstone can produce obvious tensile fractures under a small toppling and rotation angle condition.

(4) Unloading deformation of rock mass

The strong unloading rock mass is consistent with the extremely strong unloading fracture (Class A) and strong unloading fracture (Class B) rock masses, which indicates that the bottom boundary of the strong unloading deformation rock mass is generally located near the bottom boundary of Class B toppling rock mass. Similarly, the distribution range of weak unloading deformation is generally similar to that of Class C weak toppling rock mass.

(5) Weathering degree of rock mass

The distribution range of strongly weathered rock mass is close to that of extremely strong unloading fracture (Class A); the strongly toppling rock mass (Class B) is generally in the weakly weathered upper section; the weakly weathered rock mass (Class C) is generally located in the lower section of weak weathering. Sometimes, the strongly weathered rock mass also appears in Class B1 rock mass, the weakly weathered lower rock mass also appears in Class B2 rock mass.

(2)   Characteristics of toppling deformation of bank slope rock mass

According to the changes in the exposed rock mass on the bank slope of the bridge site area and the dip angle of the rock layers exposed by the drilling core, it is indicated that there are relatively complex toppling deformation rock masses distributed on the bank slope. During the geological history of the Lancang River valley being incised, the rock mass on the bank slope has undergone strong toppling deformation and weathering unloading, especially in the extremely strong toppling zone (Class A) and strong unloading zone where the quality of the rock mass is poor, which has a significant impact on the stability of the bank slope and is the main internal factor affecting the stability of the bank slope.

The toppling deformation of the rock mass on the bank slope is shown in Figure 7.

(**a**)   (**b**)

Figure 7. Toppling rock mass of the bank slope. (**a**) Near the reservoir surface at 1403 m; (**b**) at the elevation of 1540 m.

The investigation and analysis of the characteristics and development of the toppling deformation of the exposed rock mass on the bank slope of the bridge site area reveal that the toppling deformation of the rock mass is mainly of the toppling bending type. The toppling rock mass undergoes bending deformation with a great change in the inclination angle and curvature of the rock layer. There are obvious bending transition segments or intermittent tensile fractures outside the slope between the deformed rock mass and the original rock mass, and the toppling rock mass is mainly subjected to bending tensile fracture failure. According to the on-site geological survey, the rock mass on the bank

slope of the bridge site area can be divided into three major types: extremely strong (A), strong (B), and weak toppling (C). The specific description of different degree of toppling deformation zones (Zones A, B, and C) on the bank slope in the bridge site area is shown in Table 4. The statistical analysis of the development depth of the toppling rock mass shows that:

(1) The toppling deformation of both sides of the bridge site is relatively strong.

(2) The extremely strong toppling deformation zone (Zone A) and the strong toppling deformation zone (Zone B) are both located within the strongly weathered zone, with a development depth equivalent to the depth of the strongly weathered zone; the weak toppling deformation zone (Zone C) is basically located within the moderately weathered zone, with slight deformation.

(3) The extremely strong toppling deformation type A is located in the strong unloading zone, while the strong toppling deformation type B is located in the weak unloading zone.

Table 4. The specific description of different toppling deformation zones.

Basic Indicator	Zone A	Zone B		Zone C
		Zone B1	Zone B2	
Dip angle difference in rock strata	$\alpha \leq 40°$	$40° < \alpha \leq 57°$	$54° < \alpha \leq 68°$	$60° < \alpha \leq 78°$
Maximum tension within the layer	$D > 21$ mm	9 mm $< D < 24$ mm	6 mm $< D < 18$ mm	2 mm $< D < 8$ mm
Location of the weathering zone	Generally in strongly weathered zone	Generally in the weakly weathered upper section	Generally in the weakly weathered upper section	Generally in the lower section of weak weathering
Location of the unloading zone	Consistent with the extremely strong unloading, the bottom boundary of strong unloading zone is generally located near the bottom boundary of Zone B			Consistent with the weak unloading zone

3.2. Mechanism of Toppling Deformation under Bridge Loads

3.2.1. Stage Failure Mechanism of Toppling Deformation

With the varying degrees of toppling deformation, the interior of the rock mass exhibits different fracture forms, mechanical mechanisms, and characteristic deformation phenomena.

(1) Intralayer shear dislocation of weakly toppled deformed rock masses in the early stage

In the early stage of the development of valley cutting and rock mass unloading toppling deformation, the nearly vertical thin or plate shaped rock mass begins to tilt towards the free direction in the form of a cantilever beam under the action of self-weight bending moment, and gradually develops from the shallow and superficial to the deep of the slope. Due to the highly developed interlayer dislocation zones caused by structural deformation within the rock mass (such structural planes are products of strong folding and deformation in the crustal rock mass, with a certain thickness and obvious argillization, and generally low shear strength), they are prone to inclined shear sliding along them (Figure 7a). This stage is still in the early stage of toppling deformation, and the tensile effect of the interlayer rock plate derived from the tilting slip dislocation of the toppling layer is weak, which does not have the basic stress conditions for producing interlayer tensile deformation. Therefore, macroscopic tensile fractures usually do not occur.

(2) Intralayer tensile deformation of strongly toppled deformed rock masses

With the further development of toppling deformation, the shear action along interlayer dislocations, phyllites and other weak zones gradually intensifies, leading to a stronger tensile effect within the layer. The rock plates between the dislocations bear increasing tensile stress. When the gradually increasing tensile stress reaches or exceeds the

tensile strength of the rock slab, accompanied by further mutual dislocation between the rock slabs, the rock slabs within the layer undergo tensile fracture or tensile deformation along the existing structural plane (Figure 8b).
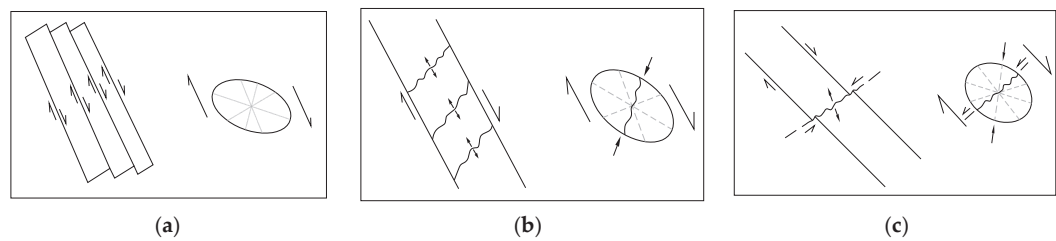

Figure 8. Fracture forms and mechanical mechanisms of rock masses with different degrees of toppling deformation: (**a**) shear dislocation within weak toppling layers; (**b**) tensioning deformation between strong toppling layers; (**c**) tensioning shear fracture of strong toppling shear layers.

(3)   Shear fracture of rock mass with strong toppling deformation

Due to the continuous and strong development of rock mass toppling, the bending moment acting on the rock slab also increases, and the shear action along weak rock zones such as interlayer dislocation and phyllite becomes very strong. In addition to continuing to bear tensile stress, the shear effect of interlayer rock slabs gradually increases. The form of fracture transforms into significant tensile shear fracture or dip slip shear displacement along existing gently inclined joints (Figure 8c), and continuous development inevitably leads to shear.

(4)   Breaking and tensile fractures of extremely strong toppled rock masses.

When the development of toppling deformation is extremely strong, the bending deformation angle of the rock layer was large, the toppling bending moment acting on the rock plate further accumulates and increases. Once the bending strength of the rock plate is reached, the rock mass undergoes transverse cutting of the rock plate and tends to break and fracture outside the slope. The fracture zones formed within the rock mass have dual control characteristics, which, respectively, constitute the control structures of surface collapse, sliding, and deep dip slip deformation.

3.2.2. Bank Slope Failure Process under the Action of Bridge Loads

There are closure and opening states of the joints under force action. When the compressive stress p_a perpendicular to the joint surface is less than or equal to 0, the joint opens. In this state, there is no elastic stiffness on the joint surface, only normal strain. When the joint surface compressive stress $p_a > 0$, the joint fissure is closed. The sliding friction failure of the joint meets the following requirements:

$$f_a = \tau_a - p_a \tan \varphi_a - c_a \tag{1}$$

where τ_a is the component of shear stress on the joint surface, p_a is the vertical pressure acting on the joint surface, φ_a is the internal friction angle of the joint system, and c_a is the cohesive force. The calculation considers the influence of bedrock bedding and vertical joints.

The bridge load causes the stress concentration of the bedrock at the bottom of the tower basement. During the strength reduction process, the plastic zone at the tower basement is connected and developing towards to the toe of the slope, forming a local damage zone, which is adverse to the stability of the bank slope.

3.2.3. Aggravated Toppling Deformation under Bridge Loads

For layered rock masses, the deformation caused by external load can be divided into the following three types:

Longitudinal bending: The rock layer undergoes bending under external forces parallel to the rock surface.

Transverse bending: The rock layer undergoes bending under external forces perpendicular to the rock surface.

Shear superposition: The rock layer undergoes differential sliding failure along a series of dense cleavages that are not parallel to the bedding plane.

Based on the structural characteristics of the collapsed deformed rock mass, the deformation trend under external loads can be predicted using the deformation calculation methods of equal thickness beams, trapezoidal beams, short cantilever beams, and composite plates.

The bending deformation which occurs in both the near-surface and engineering rock masses exhibits certain plastic and ductile deformation characteristics, accompanied by brittle fracture. According to the stress conditions, it can be divided into two types: transverse bending and longitudinal bending. There are three types of curved plate beams, named simply supported beams, extended beams, and cantilever beam bending. The load of the bridge acts on the rock layer that has undergone toppling deformation, similarly to the deformation and failure of the rock mass under transverse bending conditions.

On-site observations and simulation research have shown that the evolution process of bending deformation and failure of rock masses under lateral forces has obvious stage characteristics. The results of elastic-plastic finite element simulation are represented by equivalent (uniaxial) stress [σ] to represent the stress state inside the plate, which is equivalent to the three-dimensional stress effect and is expressed as Equation (2):

$$\sigma = \sqrt{\frac{1}{2}\left[(\sigma_1 - \sigma_3)^2 + (\sigma_3 - \sigma_1)^2 + (\sigma_1 - \sigma_2)^2\right]} \tag{2}$$

When σ is equal to rock yield stress σ_y, plastic failure has occurred. The self-weight stress field was considered in the simulation and assumed to be in a state of hydrostatic pressure, i.e., $\sigma = 0$.

The combined force of unloading stress caused by the external load and gravity acting on the reverse slope is nearly perpendicular to the rock layer surface, similarly to the transverse bending action (Figure 9). The result is that the rock layer can undergo a large range of deformation. When the dip angle of the rock layer and resultant force direction are the same as the inclination angle of gravity, the maximum lateral bending effect is generated, and the degree of toppling deformation of the rock layer is the strongest.
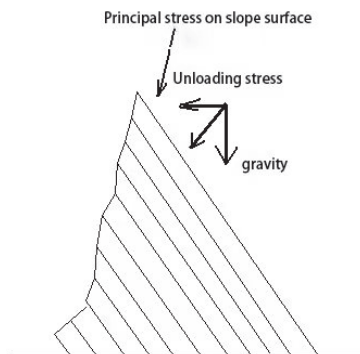

Figure 9. Deformation of toppled rock mass under bridge load.

For the inverted slope, the typical characteristics of the development of toppling deformation are as follows:

(1) Large deformation depth;
(2) The degree of deformation near the outside of the slope is greater than that inside the slope;
(3) Due to the influence of bending deformation, the distribution density of tension cracks perpendicular to the bedding plane is relatively high near the outer side of the slope.

Based on geometric, physical, and equilibrium relationships, a nonlinear bending equation for large deformation of beams can be established as Equation (3).

$$\frac{d}{dx}\left[EI\frac{d^3w}{dx^3} + EI\left(\frac{dw}{dx}\right)^2 \frac{d^3}{dx^3}\right] = p \tag{3}$$

where w is the deflection of the beam, x is the axial coordinate of the beam, EI is the bending stiffness of the beam, and P is the lateral force.

For the case of cantilever beams, the end conditions are:

$$\begin{aligned}
x = 0 \quad &\text{w} = \frac{dw}{dx} = 0 \\
x = 1 \quad &\frac{d^2w}{dx^2} = \frac{d^3w}{dx^3} = 0
\end{aligned} \tag{4}$$

Through the bending test results with different beam lengths, it can be seen that the bending deformation increases with the beam length under the same load, and the tangent stiffness increases with the deformation.

The deformation of the interbedding of soft and hard rock mass has the slip effect of the composite beam. Within the scope of elasticity, the displacement of any point on the cross section of the rock stratum combination conforms to the linear superposition principle, so it mainly has the following aspects: the longitudinal displacement of any point on the cross section of the rock stratum combination can be caused by the longitudinal displacement of the composite beam, the relative displacement caused by the relative rotation angle between the hard rock center point, and the soft rock center point caused by the interface slip; the longitudinal displacement caused by the bending deformation of soft and hard rock layers and the warping displacement caused by shear lag effect are combined.

3.3. Limit Equilibrium Analysis of Bank Slope Stability Considering Bridge Loads and Changes in Reservoir Water Level

3.3.1. Failure Mode Analysis

Affected by the strong unloading and toppling deformation of the Lancang River bank slope, the dip angle from the surface layer of the slope changes from gentle to steep, with rock strata occurrence ranging from 26 to 136° ∠ 19 to 72°. The layer thickness is generally 0.1 to 0.44 m, and the surface layer is flat. The potential sliding surfaces should be located at the junction of strongly and moderately weathered rock masses and at the bottom boundary of the strong and weak unloading zones. In addition, there is a possibility of circular sliding failure occurring within the fractured rock mass in the strongly weathered area at the front of the Yunlong bank slope. There are a total of five potential slip surfaces (Slip 1~Slip 5) on the Yunlong side bank slope, among which Slip 1 refers to the circular sliding surface automatically searched at the front of the bank slope, and Slip 2~Slip 5 are polygonal slip surfaces. Due to the absence of a fully connected out-dip structural plane at the junction of strongly and moderately weathered rock masses, the potential sliding surface shape at the junction of strongly and moderately weathered areas will not be a polygonal line shape, but rather a stepped sliding surface.

The potential failure mode of the Yunlong side bank slope is shown in Figure 10.
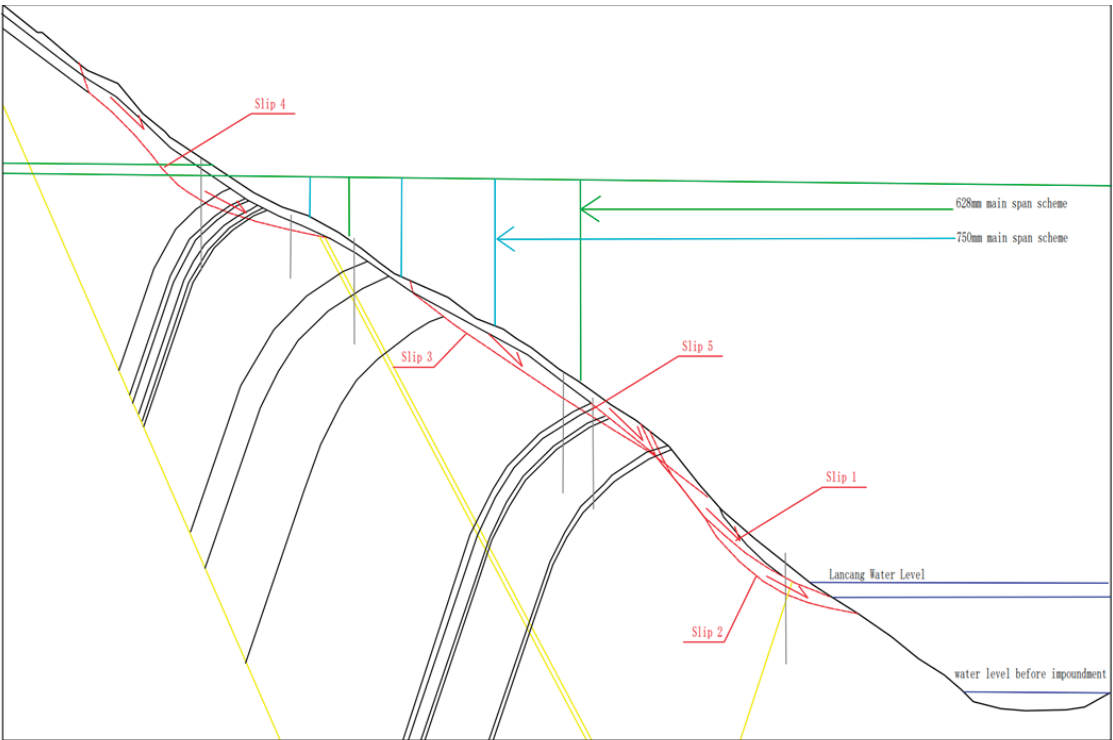
Figure 10. Potential failure mode diagram of Yunlong side bank slope.

3.3.2. Characteristics of Seepage Field on Toppling Bank Slope under Reservoir Water Level Fluctuation and Rainfall Conditions

Using the SEEP/W program to simulate the seepage field of the bank slope body of Miaowei Hydropower Station Reservoir under the operation with different water levels and rainfall conditions. In the SEEP/W model, "saturated and unsaturated" model is selected for rock and soil mass, and the Van Genuchten model (VG model for short) is selected for unsaturated and hydraulics parameter estimation.

The water level of the reservoir suddenly dropped from the normal storage level of 1408 m to the dead water level of 1398 m at a speed of 3 m/d after about 3.3 days. Distribution characteristics of pore water pressure under the coupling effect of reservoir water level and rainfall in front of different bank slopes.

The rainfall condition can be divided into rainstorm and continuous rainfall: the rainfall intensity of the former is 124.85 mm/d (100 years period), and the duration of rainstorm is 5 d; the rainfall intensity of the latter (used for calculation) is 83.71 mm/d (once every ten years), and the continuous rainfall duration (used for calculation) is 15 d.

Due to the fact that the super-large bridge is located in the Lancang River basin, the development of a toppling deformation and the types of the rock and soil types of the bridge site are similar to the Miaowei Hydropower Station. Therefore, based on the on-site investigation results, this article selects the test parameters obtained from the rock mass test at the Miaowei Hydropower Station dam site, and quotes the appropriate hydraulics parameters of rock and soil mass for the different toppling areas of the bank slope on the bridge site area. The hydraulics parameters of the rock and soil mass on the bank slope are listed in Table 5.

Table 5. Hydraulic parameters of different toppling areas of bank slope.

Lithology	Saturated Permeability Coefficient (m/s)	Saturated Volume Moisture Content
Quaternary cover layer	6×10^{-5}	0.42
Fracture zone	4.2×10^{-6}	0.40
Zone A: extremely strong toppling area; strongly weathered slate with metamorphic sandstone	2.315×10^{-6}	0.35
Zone B: strong toppling area; strong weathered slate mixed with metamorphic sandstone	1.157×10^{-6}	0.29
Moderately weathered slate mixed with metamorphic sandstone in the micro toppling area of Zone C	3.45×10^{-8}	0.18

The negative pore water pressure of the rock and soil above the groundwater level in the bank slope is set at −20 kPa.

After calculation, the distribution of pore water pressure inside the slope under various working conditions on the Yunlong bank slopes is shown in Figure 11.
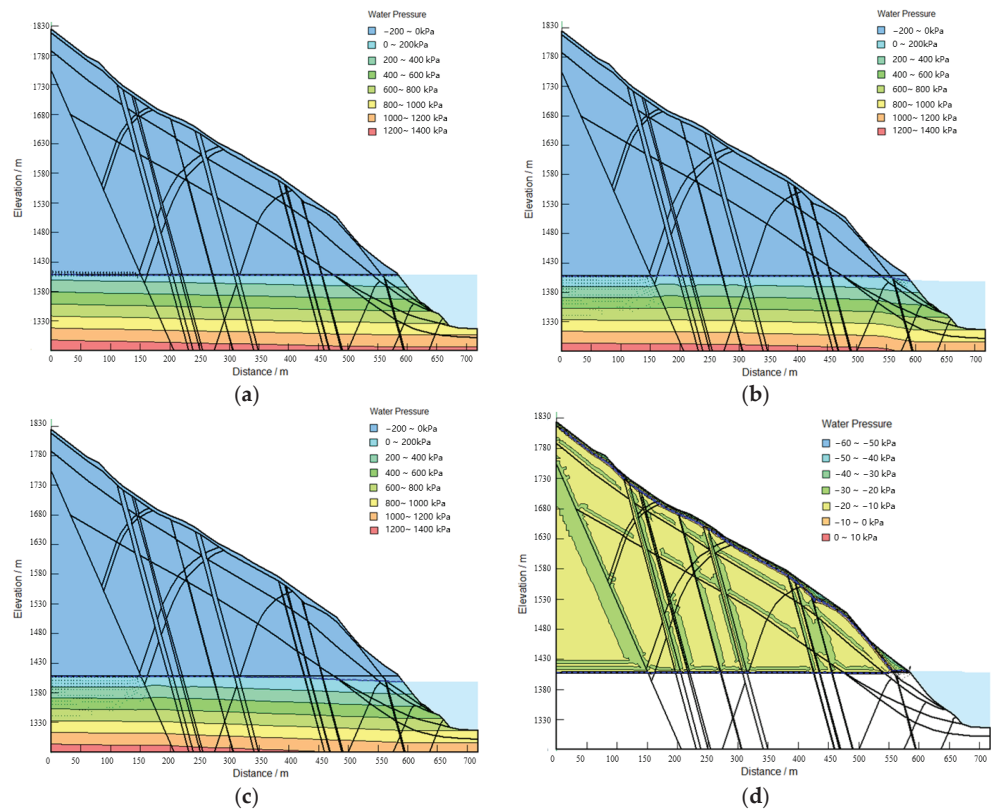

Figure 11. *Cont.*
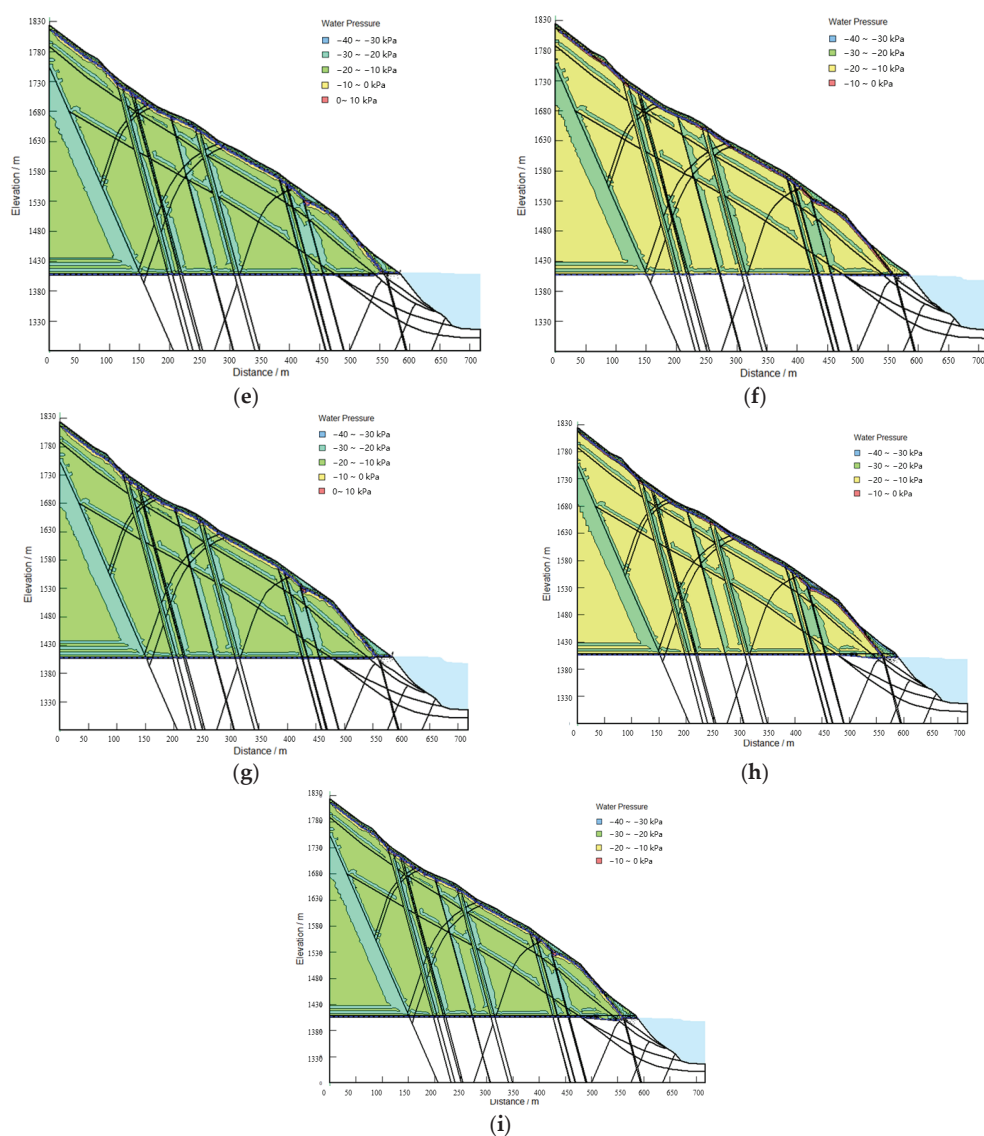
Figure 11. Distribution of pore water pressure under different conditions on the bank slope. (**a**) 1408 m Water Level; (**b**) 1408~1398 m water level sudden drop; (**c**) 1398 m water level; (**d**) rainstorm + 1408 m water level; (**e**) rainfall + 1408 m water level; (**f**) rainstorm + sudden water level drop; (**g**) rainfall + sudden water level drop; (**h**) rainstorm + 1398 m water level; (**i**) continuous rainfall + 1398 m water level.

Under rainstorm or continuous rainfall conditions, the pore water pressure below the groundwater level increases proportionally with the increase in depth, and the pore water pressure value is large.

According to the seepage calculation results under the above five consecutive days of rainstorm conditions, the following can be seen: (1) During the rainstorm period, the water content in the gravelly soil of the overburden layer continues to increase with the rainfall infiltration. By the end of the fifth day, the rainfall infiltration will form a local, small

range of saturated positive pressure zone at the junction of the Quaternary overburden layer and the rock stratum in Area A. The overburden layer is basically still in a negative pressure state, but the water content has increased significantly compared with that before the rainfall. (2) After the rainfall stops, the water in the upper part of the cover layer continues to conduct downward and inclined towards the slope. By the 9th and 10th days, the saturated zone at the junction of the Quaternary cover layer and the rock layers in Zone A is basically connected, and a saturated positive pressure zone is formed in the local area at the top of the rock layers in Zone A. (3) The rainstorm for 5 consecutive days will form a backwater in the groundwater level in the slope body near the water in the front of the slope, and the water level will rise by 2~2.6 m.

The seepage calculation results under the continuous rainfall condition are slightly different from those under the rainstorm condition. The seepage characteristics are as follows: during the continuous rainfall period, with the rainfall infiltration, the water content in the gravelly soil of the overburden layer continues to increase. By the end of the seventh day, the rainfall infiltration will form a local, small range of saturated positive pressure zones at the junction of the Quaternary overburden layer and the rock stratum in Zone A, and the overburden layer is basically still in a negative pressure state, but the water content has increased significantly compared to before the rainfall. On the 9th day, the saturated area at the junction of the Quaternary cover layer and the rock layers in Zone A is basically connected. From the 13th day onwards, a sheet-like saturated positive pressure zone was continuously formed in the local area at the top of the rock layer in Zone A, but the scope and saturation depth were limited. After the end of continuous rainfall, the groundwater level in the near water section of the front of the slope will form a backwater, and the water level line will rise up to 2–3.6 m.

By comparing the infiltration of rainstorm for 5 days with that of continuous rainfall for 15 days, in both cases, an overall saturation will not form in the Quaternary overburden on the slope surface. The saturation area is mainly distributed in the junction area between the overburden and the rock stratum in Zone A. The saturation area formed in the slope under the continuous rainfall condition is slightly larger than that under the rainstorm condition.

3.3.3. Calculation Parameters

The parameters of the rock and soil in the topppling deformation area of the bridge site also refer to the parameters obtained from the rock mass test at the Miaowei Hydropower Station dam site. The physical and mechanical parameters of different toppling areas are listed in Table 6.

Table 6. Rock and soil parameters for different toppling areas.

Lithology	Weight (kN/m³)		C (kPa)		Φ (°)		Deformation Modulus/E Gpa	Poisson's Ratio/μ
	Naturally	Saturation	Naturally	Saturation	Naturally	Saturation		
Quaternary cover layer	20.0	20.5	30	28	24	22	0.025	0.35
Fracture zone	21.2	21.6	40	27	30	25	0.2	0.32
Strongly weathered sandy slate mixed with muddy slate	23.0	23.4	150	135	26	24	0.5	0.3
Metamorphic sandstone in strongly weathered areas	23.0	23.4	130	115	25	23.9	0.45	0.32

Table 6. *Cont.*

Lithology	Weight (kN/m³)		C (kPa)		Φ (°)		Deformation Modulus/*E* Gpa	Poisson's Ratio/*μ*
	Naturally	Saturation	Naturally	Saturation	Naturally	Saturation		
Moderately weathered sandy slate mixed with muddy slate	26.2	27.0	570	510	37.0	33.3	0.6	0.29
Metamorphic sandstone in moderately weathered areas	26.2	27.0	500	450	33.4	30.1	0.55	0.3
Structural planes in strongly weathered areas (combined with general)	/	/	80	70	25	23	/	/
Structural planes in moderately weathered areas (well bonded)	/	/	220	200	35	31.5	/	/

3.3.4. Analysis of Calculation Results

Using the two-dimensional rigid body limit equilibrium stability calculation method (broken-line sliding surface transfer coefficient method, and circular sliding surface simplified Bishop method) to calculate the stability of the bank slope at the Lancang River Extra-Large Bridge area. The methods were used to analyze the toppling slope stability under bridge loads in different schemes. The calculation model for bank slope stability is illustrated in Figure 12.
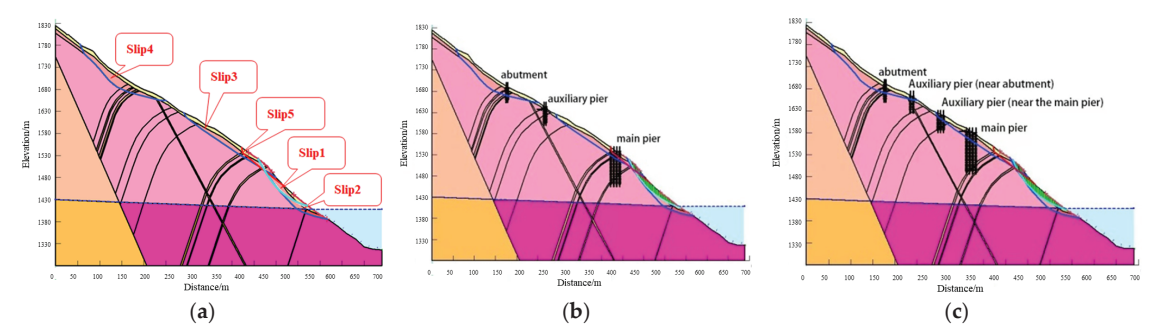

Figure 12. Calculation model for stability of Yunlong side bank slope. (**a**) Natural conditions; (**b**) scheme 1; (**c**) scheme 2.

The calculation results and evaluation of the stability of the Yunlong bank slope calculated via the two-dimensional limit equilibrium analysis method under various working conditions are detailed in Table 7, and the calculation results of bank slope stability are shown in Figure 13.

Table 7. Calculation results for stability of the pile foundation platform.

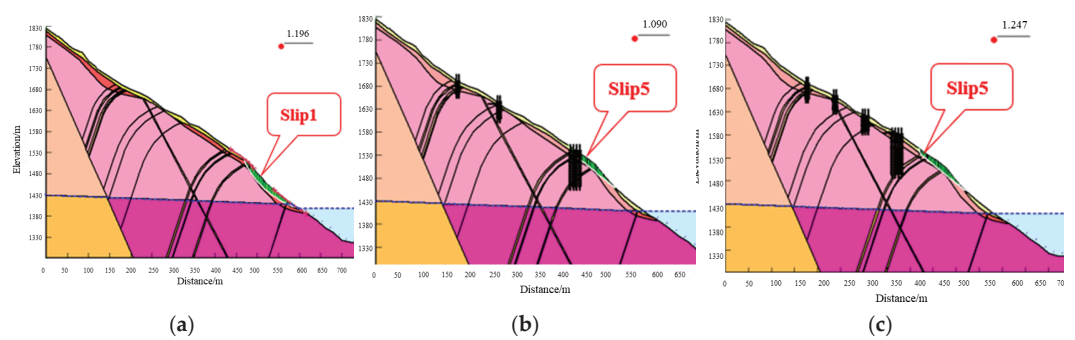| Condition Name	Natural Working Conditions		Rainfall Conditions		Rainfall + Earthquake Conditions	
	Stability Coefficient *Fs*	Stability Judgment	Stability Coefficient *Fs*	Stability Judgment	Stability Coefficient *Fs*	Stability Judgment
scheme 1: Slope covering layer on the main pier	1.290	<1.35	1.173	<1.20	1.055	<1.10
scheme 1: Slope foundation covering the interface on the main pier	1.783	>1.35	1.595	>1.20	1.462	>1.10
scheme 2: Slope covering layer on the main pier	1.292	<1.35	1.174	<1.20	1.055	<1.10
scheme 2: Strong to moderately weathered interface on the upper slope of the main pier	2.147	>1.35	1.914	>1.20	1.749	>1.10
scheme 2: Cover layer of the upper slope of the auxiliary pier (near the main pier)	1.481	>1.35	1.347	>1.20	1.244	>1.10

Figure 13. Calculation results of bank slope stability on Yunlong side. (**a**) Natural condition: sudden drop in water level + rainfall + earthquake condition; (**b**) scheme 1: natural working condition; (**c**) scheme 2: natural working conditions.

From the two-dimensional limit equilibrium analysis results, with regard to the stability character of the Yunlong bank slope, the following can be concluded:

(1) The five potential sliding bodies (Slip 1~Slip 5) on the bank slope, except for Slip 5, are in a stable state under natural conditions, rainfall conditions, and rainfall + earthquake conditions, with stability coefficients (Fs) ranging from 1.163 to 1.639; Slip 5 is in a basically stable state under rainfall and earthquake conditions. This indicates that the quantitative calculation results of the stability of the current condition bank slope are consistent with the qualitative evaluation of the stability of the bank slope.

(2) In scheme 1, with the loads of the 628 m span cable-stayed bridge acting on the toppling slope, the stability coefficients (Fs) of potential sliding bodies Slip 1~Slip 4 on the bank slope under natural conditions, rainfall conditions, and rainfall + earthquake conditions are in the range 1.163~1.624, which can meet the design safety factor requirements for each working condition. The stability coefficients (Fs) of Slip 5 under

natural conditions, rainfall conditions, and rainfall + earthquake conditions are 1.090, 1.046, and 0.956, respectively, which does not meet the design safety factor. Especially under rainfall + earthquake conditions, the rock mass in the strong unloading zone will lose stability and incur damage, posing a threat to the safety of the bridge.

(3) In scheme 2, with the loads of the 750 m span cable-stayed bridge acting on toppling slope, the stability coefficients (Fs) of the potential sliding bodies Slip 1~Slip 4 on the bank slope under natural conditions, rainfall conditions, and rainfall + earthquake conditions are in the range 1.163~1.624, which can meet the design safety factor requirements for each working condition. The stability coefficients (Fs) of Slip 5 under natural and rainfall conditions are 1.247 and 1.194, respectively, which cannot meet the design safety factor. However, the stability coefficient under rainfall + earthquake conditions is 1.115, which has a certain safety reserve.

(4) Under the fluctuating water level conditions of the Miaowei Hydropower Station reservoir, different water storage conditions (normal water level, sudden drop of reservoir water level, and dead water level) have a significant impact on the stability of the potential sliding mass Slip 2 in the front of the bank slope, while the impact on the stability of Slip 1 is small. The three potential sliding masses Slip 3~Slip 5 in the middle and rear of the bank slope are located above the groundwater level and reservoir water level, and are not directly affected by the fluctuation of reservoir water level. For wading bank slopes, the trend of slope stability is $Fs_{normal\ water\ level}$ > $Fs_{dead\ water\ level}$ > $Fs_{sudden\ drop\ in\ water\ level}$.

(5) Under the three working conditions of natural, rainfall, and rainfall + earthquake, the trend of slope stability is $Fs_{natural}$ > $Fs_{rainfall}$ > $Fs_{rainfall+earthquake}$. Among the three working conditions, the seismic horizontal force under earthquake working condition has the worst effect on slope stability.

(6) The excavation of pile foundation platforms and anchor slopes on the mountain side will affect the local stability of the slope, especially when excavating within the Quaternary cover layer. The stability coefficient of the Quaternary slope under natural conditions, rainfall conditions, and rainfall + earthquake conditions is less than the design safety coefficient, and the safety reserve is insufficient. Therefore, attention should be paid to the engineering protection of the Quaternary slope during the excavation of the upper slope. Although the overall stability of the upper slope can meet the requirements of the design safety factor, the stress release formed by slope excavation can cause deterioration of the physical and mechanical properties of the slope rock mass, which can cause local damage to the slope. Therefore, the overall engineering protection of the upper slope should be strengthened.

3.4. Three-Dimensional Numerical Analysis of Bank Slope under the Coupling Effect of Bridge Loads and Hydrodynamic Forces

In order to predict the stability of the bank slope under the synergistic effect of bridge loads and reservoir water level changes, this paper adopts a three-dimensional finite difference numerical simulation method to analyze the stress state and plastic zone distribution characteristics of the slope for two sets of bridge type schemes, and further determine the optimal scheme.

3.4.1. Three-Dimensional Geometric Modeling Establishment and Bridge Loads Application Mode

Scheme 1: The starting point in the x-direction of the Yunlong side slope model area is 0 m, and the ending point is 735 m, which refers to the model with a length of 735 m; The starting point in the y-direction is 0 m, and the ending point is 289 m, which refers to the model with a length of 289 m; The starting point in the z-direction is 0 m, and the ending point is 567 m, which refers to the model with a length of 567 m. In the calculation, applying loads at the corresponding position of the bridge foundation on both banks, including the main pile position, the main pile auxiliary pile, the abutment auxiliary pile,

and the abutment. The selected load is the basic combination load of scheme 1, and the load application method on the Yunlong side bank slope is shown in Figure 14a.
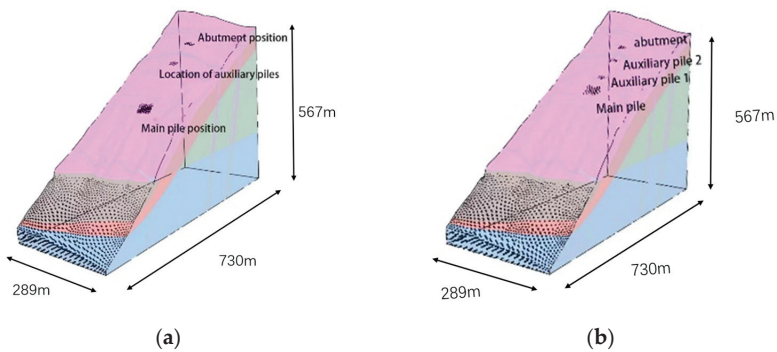

Figure 14. Three-dimensional calculation model of Yunlong side bank slope (**a**) scheme 1; (**b**) scheme 2.

Scheme 2: The length, width, and height of the 3D model in scheme 2 are consistent with scheme 1, while the difference between the two models is the loading position of the bridge foundation loads. The load application method on the Yunlong side bank slope is shown in Figure 14b.

3.4.2. Simulation of Groundwater Seepage Field under Reservoir Water Level Fluctuation

The calculation of seepage field adopts built-in seepage module of Flac3D, which simulates the changes in water level by setting the changes in pore water pressure. The rainfall intensity is 100 mm/d. In the seepage calculation, the permeability coefficient of Zone A is 0.0001 m/s. After setting the water level at the front edge of the slope to decrease by 10 m, convert the unit of permeability coefficient into minute permeability coefficient, calculate 2880 steps (i.e., water level decrease time is 48 h), and complete the simulation calculation of the seepage field. Among them, the small step of fluid time step set for calculation is 0.001 min. The results are illustrated in Figure 15.
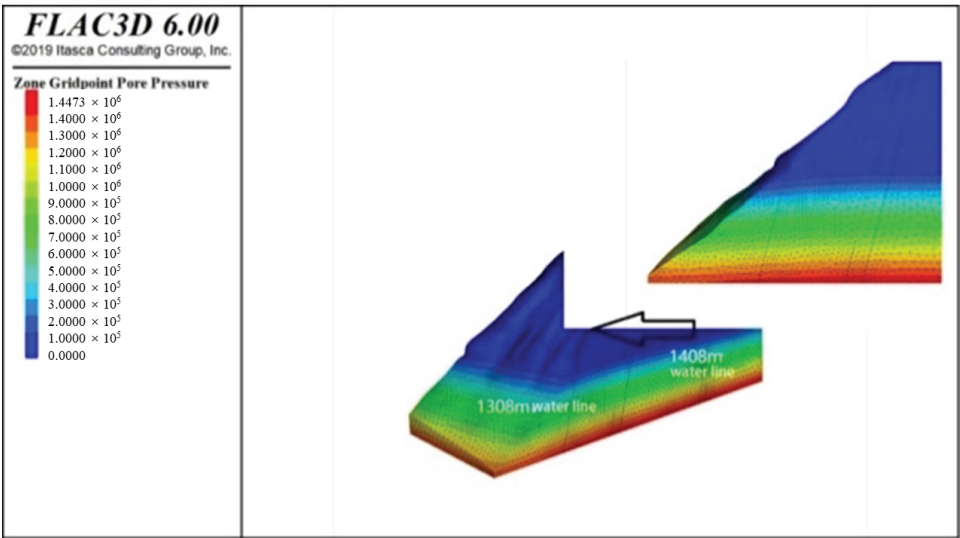

Figure 15. Pore pressure distribution of Yunlong side toppling slope.

3.4.3. Calculation Conditions and Parameters

Based on the actual situation, the most unfavorable operating conditions (i.e., sudden drop from 1408 m water level to 1398 m water level) were selected to establish the geological model, and the following three working conditions were selected for calculation.

(1)   working condition 1: Bridge operation + natural working conditions (sudden drop of water level from 1408 m to 1398 m).
(2)   working condition 2: Bridge operation + rainstorm condition (1408 m water level suddenly drops to 1398 m water level).
(3)   working condition 3: Bridge operation + earthquake + rainfall conditions (sudden drop of water level from 1408 m to 1398 m).

Based on on-site investigation and analysis, considering the rock layer information of the modeling area, the rock and soil types used for the stability calculation analysis of the Yunlong bank slopes mainly include: (1) extremely strong toppling and strongly weathered slate in Zone A; (2) strong toppling and strong weathering of slate in Zone B; (3) slightly weathered slate; (4) broken zone.

In order to ensure the accuracy and rationality of the three-dimensional finite difference simulation, the calculation parameters used for numerical simulation in this paper were referenced from similar slope analysis in the Miaowei Reservoir Area after adjustments and reductions, based on the geological information of the Bridge site, the rock mass test parameters of the Miaowei Hydropower Station dam site, and the toppling deformation situation obtained from the on-site investigation. The calculation parameters are listed in Table 8.

Table 8. Calculation Parameters of 3D finite difference Method.

Lithology	Severe (KN/m³)		C (KPa)		Φ (°)		Deformation Modulus E GPa	Poisson's Ratio μ
	Naturally	Saturation	Naturally	Saturation	Naturally	Saturation		
fracture zone	22.5	23.5	40	27	30	25	0.2	0.32
Zone A extremely strong toppling and strong weathered slate	26.2	27.0	200	180	33.2	29.8	0.5	0.3
Strong toppling and weathering of slate in Zone B	26.2	27.0	400	360	35.4	31.9	0.6	0.29
Slightly weathered slate	26.8	27.8	650	585	41	36.9	0.8	0.28

3.4.4. Calculation Results for Scheme 1

(1)   Total displacement characteristics under different working conditions

The displacement obtained by calculating stability is shown in Figure 15. For working condition 1, the maximum displacement is concentrated at the location where the main pile load is applied, and the main displacement is concentrated at the fracture zone at the elevations of 1570 m, 1550 m, and 1440 m (Figure 16a). For working condition 2, the main displacement is concentrated at the broken zone at the elevation of 1570 m, 1550 m and 1440 m (Figure 16b). For working condition 3, the maximum displacement is located behind the 1570 m elevation fracture zone and at the 1550 m elevation fracture zone where the main pile load is applied. There is also a significant displacement at the 1440 m elevation fracture zone at the leading edge (Figure 16c).
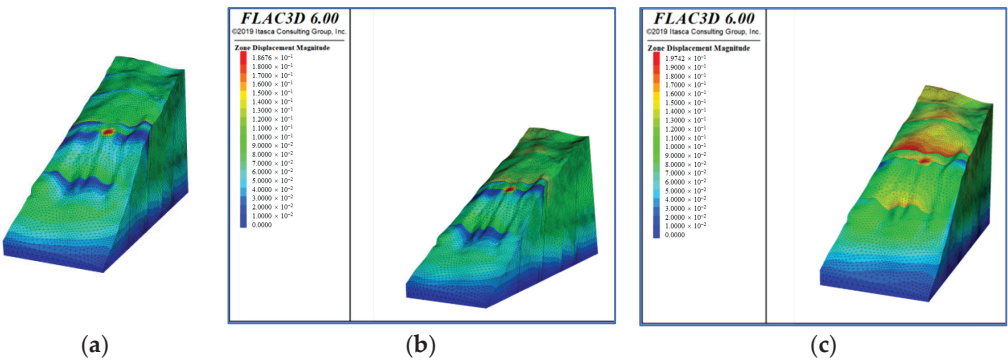
Figure 16. Total displacement of different working condition. (**a**) working condition 1; (**b**) working condition 2; (**c**) working condition 3.

(2)   Plastic zone distribution under different working conditions

The maximum plastic area is located at the 1570 m elevation fracture zone, where a small amount of plastic deformation occurs for working condition 1 (Figure 17a). For working condition 2, a small amount of plastic zone is generated at the fracture zone at elevations of 1570 m, 1550 m, and 1440 m (Figure 17b). For working condition 3, plastic zone is generated in the 1430 m elevation fracture zone, 1550 m elevation fracture zone, and 1570 m elevation fracture zone (Figure 17c).
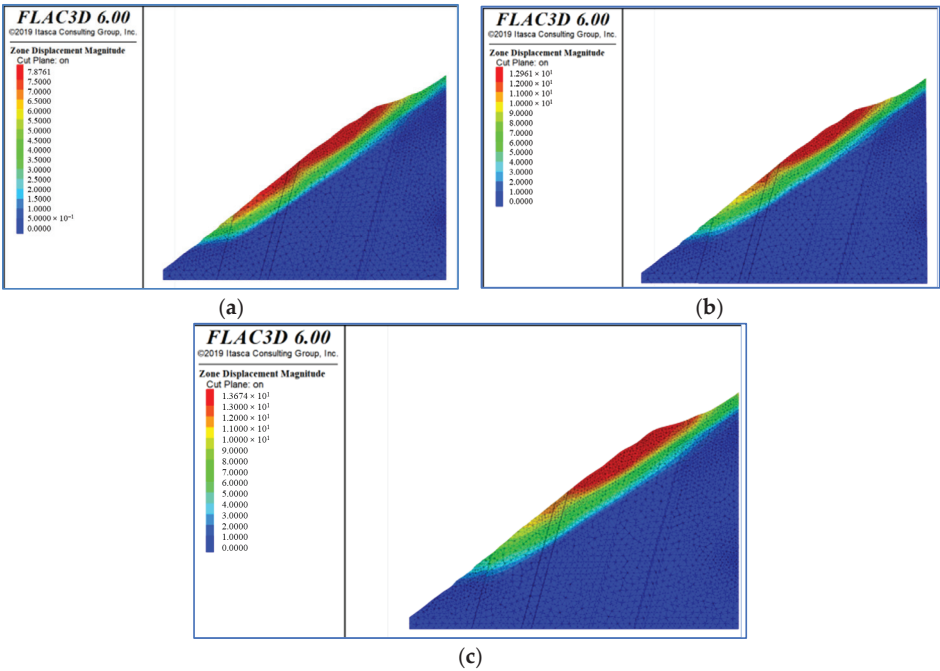

Figure 17. Plastic zone during Bridge Operation (y = 140 m profile). (**a**) working condition 1; (**b**) working condition 2; (**c**) working condition 3.

The stability coefficient of Yunlong side bank slope calculated by strength reduction is 1.55 for working condition 1 (1408 m water level suddenly drops to 1398 m water level).

The displacement and plastic deformation area are mainly concentrated in the fracture zone at 1410 m elevation to the fracture zone at 1730 m elevation, the rear edge of the obtained sliding surface is the fracture zone at 1730 m elevation, the front edge is the fracture zone at 1410 m elevation, the rear edge is staggered along the fracture zone, and the front edge is cut out in an arc. Compared to the natural surface morphology, a plastic strain zone appears at the point where the load is applied to the main pile. The stability coefficient for working condition 2 (1408 m water level suddenly drops to 1398 m water level) is 1.44 and 1.28 for working condition 3.

3.4.5. Analysis of Calculation Results for Scheme 2

The stability coefficient of Yunlong side bank slope calculated by Strength reduction is 1.56 for working condition 1 (1408 m water level suddenly drops to 1398 m water level). The displacement and plastic deformation area of the instability zone are mainly concentrated in the fracture zone at 1410 m elevation to the fracture zone at 1730 m elevation, the rear edge of the obtained sliding surface is the fracture zone at 1730 m elevation, the front edge is the fracture zone at 1410 m elevation, the rear edge is staggered along the fracture zone, and the front edge is cut out in an arc. Compared to the natural surface morphology, a plastic strain zone appears at the point where the load is applied to the main pile. The stability coefficient is 1.47 and 1.31, respectively, for working condition 2 (1408 m water level suddenly drops to 1398 m water level) for working condition 3 (1408 m water level suddenly drops to 1398 m water level).

4. Discussion

4.1. The Stability of Toppling Bank Slope under the Action of Bridge Loads and Reservoir Water Level Change

The stability of the toppling deformation bank slope under the combined action of the bridge load and reservoir water level is controlled by the following three factors:

(1)   Deformation characteristics of toppled rock slope under bridge loads

Toppling deformation often leads to the unloading of tension cracks, which are a relatively special type of joint (Figure 18). When tension cracks occurred on the surface of the slope, shear failure in the rock mass has already begun. Under the pressure and lateral thrust generated by the bridge foundation load, the mechanical properties of the unloading crack may undergo significant changes. On the one hand, the unloading crack may cause significant displacement. On the other hand, the horizontal thrust may cause the unloading crack to topple or slide and fail. In addition to generating high stress concentration areas at the foot of the slope and the base, there is also a phenomenon of high stress concentration near the unloading crack. The maximum principal stress and shear stress on the slope surface in front of the foundation significantly increase due to the horizontal thrust of the normal stress on the unloading crack surface. When the unloading crack is at a certain angle with the slope surface, the stability is the worst. The existence of unloading cracks mainly changes the longitudinal mechanical behavior characteristics of the slope rock mass. Due to the fact that unloading cracks are generally in an open state, unloading cracks are equivalent to a secondary free boundary, with zero stress on the boundary. When subjected to the load transmitted by the bridge foundation, the stress in the rock mass near the base and unloading cracks increases significantly. Whether the rock mass can meet the strength requirements requires strength verification. The load action will cause stress concentration at the height of the unloading crack tip, and the anti-toppling stability of the rock mass cut by the unloading crack will decrease, which will have adverse effects on the stability of the rock mass (Figure 19).
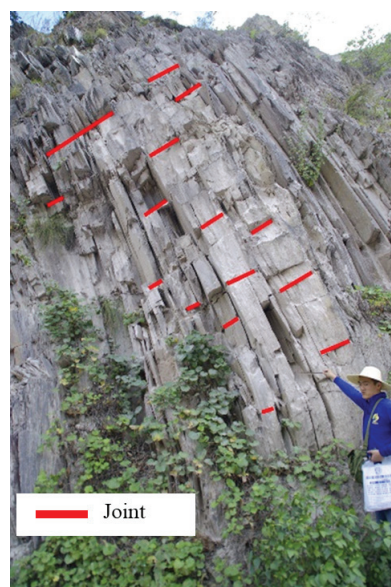
Figure 18. Toppling cracks developed along layer.
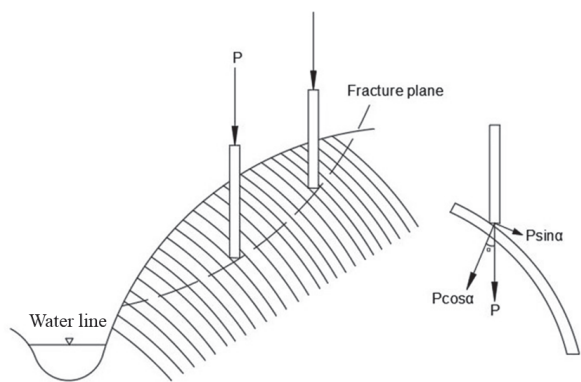

Figure 19. Mechanism of toppling deformation under bridge load.

(2)   Influence of reservoir water level fluctuation on the stability of toppling bank slope

The impact of changes in the reservoir water level on the stability of bank slopes is mainly reflected in the effect of dynamic water pressure inside the slope and the reduction in the strength of the toppling rock mass at the foot of the slope due to the dry–wet cycle of the underwater bank slope. The tensile cracks formed in the toppling body during the deformation process create favorable conditions for the infiltration of reservoir water into the slope. The groundwater level rapidly increases with the rise in the reservoir water level, leading to an increase in the pore water pressure and a decrease in the effective stress in the landslide resistance section, which results in a decrease in stability eventually. Landslides are prone to sliding and failure along the foundation interface evolved from the tilting fracture section (Figure 20).
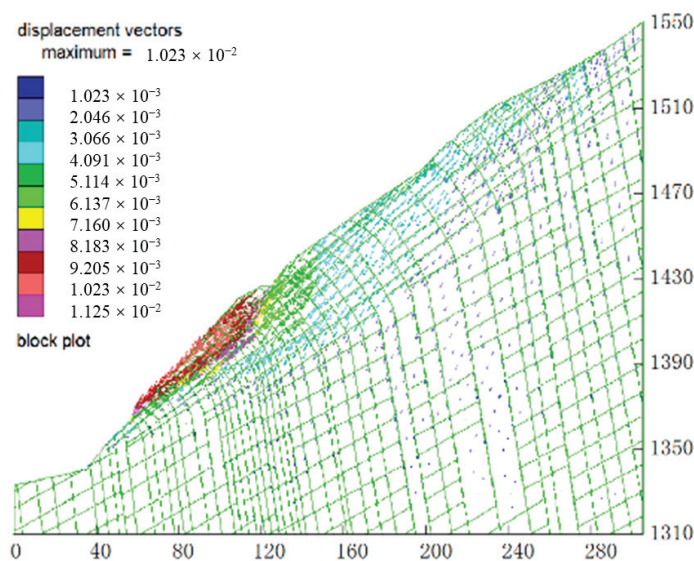
Figure 20. Displacement vector diagram after reservoir impoundment.

(3)   The splitting effect of the reservoir water leads to an increase in the degree of toppling deformation of the rock mass at the foot of the slope

The high water head during the process of reservoir water level rise has a splitting effect on the existing tilting tension cracks. Groundwater permeability, as a mechanical force, directly affects the distribution of stress field in the rock mass on the crack surface. At the same time, changes in the rock mass stress field cause deformation of the cracks, which has adverse effects on the stability of the rock mass. The mechanical effects of groundwater on the fracture surface mainly include the normal seepage static water pressure and the tangential drag force, namely the seepage dynamic water pressure. The seepage static water pressure of a crack refers to the static water pressure acting in the normal direction of the crack surface, which is perpendicular to the crack wall surface. Hydrodynamic pressure refers to the reaction force of the fluid on the fracture surface that hinders its movement when it flows within the fracture, and its direction is consistent with the direction of the fracture water flow. For the toppling rock mass in the slope of the reservoir bank, tensile cracks are very developed. During the descending stage of the reservoir water, static and dynamic water pressures often form towards the outside of the slope, leading to the further increase in the width of tensile cracks and weakening of the structure of the rock mass.

The specific calculation formula is:

$$P_1 = \gamma_w \Delta HJ \tag{5}$$

where P_1 is the driving force of water flow; γ_w is the unit weight of water; ΔH is the depth of water in the drawdown zone of the reservoir water level; and J is the hydraulic gradient.

4.2. Numerical Simulation Results of Bank Slope Stability via Strength Reduction Method

The bank slope stability calculated result by using three-dimensional finite difference method is listed in Table 9.

Table 9. Finite difference stability coefficient table.

Calculated Operating Conditions		Stability Coefficient	Leading Edge (m)	Trailing Edge (m)
Before the construction of the bridge	Natural working conditions (sudden drop of water level from 1408 m to 1398 m)	1.59	1410	1730
scheme 1	Bridge operation + natural working conditions (sudden drop of water level from 1408 m to 1398 m)	1.55	1410	1730
	Bridge operation + rainstorm condition (1408 m water level suddenly drops to 1398 m water level)	1.44	1500	1730
	Bridge operation + rainfall + earthquake conditions (sudden drop of water level from 1408 m to 1398 m)	1.28	1550	1750
scheme 2	Bridge operation + natural working conditions (sudden drop of water level from 1408 m to 1398 m)	1.56	1410	1730
	Bridge operation + rainstorm condition (1408 m water level suddenly drops to 1398 m water level)	1.47	1532	1730
	Bridge operation + rainfall + earthquake conditions (sudden drop of water level from 1408 m to 1398 m)	1.31	1550	1750

(1) For schemes 1 and 2, the natural bank slope is in a stable state under the action of Miaowei reservoir operation (with a sudden drop in water level from 1408 m to 1398 m).

(2) Under the load conditions of schemes 1 and 2, the stability coefficient of the bank slope under each working condition of bridge operation can meet the requirements of stability coefficient. The coefficient is greater than 1.30 under bridge operation + natural working condition, more than 1.20 under bridge operation + rainstorm working condition, and 1.10 under bridge operation + rainfall + earthquake working condition.

(3) Under the load condition of scheme 1, the main area of potential instability of the Yunlong side slope on the east bank is located between the elevation of 1550 m and 1730 m, and is generally located in the middle and rear of the slope.

(4) Under the load condition of scheme 2, the main area of potential instability of the Yunlong side slope is located between the elevation of 1532 m and 1730 m, and is generally located in the middle and rear of the slope.

(5) The stability coefficient of the Yunlong side bank slope in scheme 1 is smaller than that in scheme 2. The load application location is a small inclined plane, so the stability coefficient of scheme 1 is greater than that of scheme 2.

4.3. Determination of Optimal Bridge Location

Considering that the bridge loads act on different parts of the toppling deformed rock mass, the toppling deformation degree caused by the transverse bending action is greater than the longitudinal bending action. Therefore, when the pile foundation of the bridge cushion cap is selected, the transverse bending effect should be avoided or reduced as far as possible. According to the analysis of the engineering geological conditions of the rock and soil mass of the bank slope, all potential sliding bodies of the bank slope are located in the strongly weathered rock mass area. The rock mass in the strongly weathered area is broken due to the geological forces such as the undercutting and fracture of the Lancang River, the movement of the folded tectonics, and the toppling deformation during the geological history. The closer it is to the Lancang River channel, especially in areas with raised terrain, the stronger the weathering and unloading of the rock mass, and the poorer the stability of

the bank slope. From the perspective of engineering geological safety, the farther away the main pier of the bridge from the river, the safer it is.

According to the stability analysis results of the bank slope, the stability of the Yunlong side bank slope is mainly controlled by the potential sliding body Slip 5 of the strong unloading zone. If the potential sliding body Slip 5 of the Yunlong side bank slope experiences sliding failure, it will directly threaten the safety of the main pier of the bridge in scheme 1 (628 m span cable-stayed bridge). Therefore, it is necessary to carry out engineering pre-reinforcement treatment for scheme 1 bank slope. When selecting bridge scheme 2 (750 m span cable-stayed bridge), although the stability of the potential sliding body Slip 5 in the strong unloading zone of the Yunlong side bank slope does not meet the requirements of the design safety factor, the horizontal distance from the rear edge of the potential sliding body to the front edge of the Yunlong side main pier pile foundation cap is 36.0 m. After the sliding failure of the potential sliding body occurs, it will not affect the safety of the bridge main pier. It can be seen that bridge scheme 2 is safer than scheme 1 from the perspective of the results and analysis of the stability of the bank slope.

From the analysis the long-term effects of pre-reinforcement and engineering of the bank slope, it is recommended to adopt the frame beam + anchor cable as the pre-reinforcement measures to ensure that the stability of the bank slope is able to meet the requirements of the design safety factor. As the rock mass of the bank slope is mainly composed of sandy slate mixed with muddy slate and metamorphic sandstone, it belongs to relatively soft rock. The potential sliding mass Slip 5 on the Yunlong side of the bank slope is located in the strongly weathered rock area of the bank slope, with broken rock masses and developed joint fissures. The inclination of the rock mass is basically consistent with the installation angle of the anchor cable, and the relaxation of prestressed anchor cable will be more severe, which leads to the low long-term effect of the pre-reinforcement project. On the other hand, the construction of the frame beam + anchor cable project requires the removal of the loose cover layer on the slope surface and the leveling of the slope surface, which will cause damage to the vegetation ecology of the bank slope and is not conducive to the protection of the ecological environment in the reservoir area.

From the perspective of bridge construction conditions, the main and auxiliary piers of the Yunlong side bridge are located in the middle and upper part of the bank slope. By comparison, the farther away the bridge pier columns are from the Lancang River channel, the shorter the construction road needs to be, leading to better construction conditions. The construction conditions of the main pier in scheme 2 are superior to those in scheme 1.

Based on the analysis of various influencing factors such as rock and soil engineering geological conditions of the bank slope, bank slope stability, pre-reinforcement engineering of the bank slope and its long-term effects, bridge construction conditions, etc., the determination of the specific bridge type plan based on the advantages of the location of the main pier arrangement for the bridge in scheme 2, which means that scheme 2 is the safest and most suitable one, followed by scheme 1.

4.4. Limitations in Numerical Simulation

Although we have discussed the joint effects of bridge loads and hydrodynamic forces on the reservoir bank slope from both two-dimensional and three-dimensional perspectives, there are still some shortcomings in the relevant simulations:

(1) The geological profile used in the two-dimensional simulation is only on the section where the bridge foundation is located, and the adjacent sections have not undergone a seepage field simulation, two-dimensional limit equilibrium analysis, or strength reduction calculation, so the accuracy of the three-dimensional simulation is verified using the calculation results of other sections.

(2) In a 3D simulation, simulating the influence of bridge loads by using equivalent concentrated force without any solid elements of the bridge section may have a certain impact on the analysis results.

(3) The failure mode of a toppling slope is influenced by numerous factors, and the scope of failure and sliding surface have certain uncertainties. The use of the strength reduction method may result in different slope stability analysis results, leading to significant differences between quantitative and qualitative analysis.

(4) The design of the bridge body was not considered, the structural changes in the bridge were not simulated, and the impact of changes in pier position on the bridge design was not verified.

5. Conclusions

(1) The formation of toppled and deformed rock masses in the reservoir area is mainly due to the rapid deepening of the valley under the action of regional tectonic stress, leading to the release of stress towards the free space direction, resulting in differential deformation between thin and interbedded rock layers. The damage caused by the process of reservoir impoundment to the toppling rock mass is mainly due to the crack splitting and softening effect of the reservoir impoundment at the foot of the slope. The foot of the slope loses support for the upper rock mass, causing the toppling rock mass above the reservoir water level to be subjected to gravity and transverse bending, transmitted upward through joint dislocation, rotation, and sliding, accelerating the speed of secondary toppling damage, and forming compressive shear failure along the tilting tensile cracks.

(2) The shear failure zone below the water storage level is influenced by the saturation strength of different lithology, the distribution characteristics of different tilting tension fractures, and the permeability characteristics. Through the softening of water storage at the foot of the slope, fracturing of fracture water, and wave dynamics, it may lead to the continued development of toppling deformation. The horizontal depth of the failure surface is related to the depth of the collapsed deformation body, usually the sum of the wave-induced erosion zone and the horizontal softening and tilting zone at the water surface of the reservoir.

(3) The degree of toppling deformation can be determined via the dip angle difference in rock strata, maximum tension within the layer, unit tension within the layer, unloading deformation of rock mass, and weathering degree of rock mass.

(4) The strength reduction method is used to analyze the stability of the rock bank slope before and after the bridge load, and the influence of bridge loads on the shape and position of the bank slope sliding surface is obtained, creating a local failure zone at the bottom of the arch is detrimental to the stability of the bank slope.

References

1. Chen, C.; Shih, B.-J.; Jeng, C.-J. Case study on performance monitoring and stability analysis of Baishihu suspension bridge and side slope. *J. Civ. Eng. Manag.* **2022**, *28*, 81–92. (In Chinese) [CrossRef]
2. Jiang, T.-Z.; Zhang, G.-Z.; Jiang, L.-W. The bank slope stability evaluation of Jiagai River Bridge in Zhijin-Bijie Railway. *J. Railw. Eng. Soc.* **2014**, *31*, 46–49+113. (In Chinese)
3. Yin, X.; Feng, Z.; Yan, F.; Wang, D.; Qin, Y. Safety estimation for the bedding slope of Huaping bank at Jinshajiang bridge in Huaping-Lijiang highway based on static model test. *Yanshilixue Yu Gongcheng Xuebao/Chin. J. Rock Mech. Eng.* **2017**, *36*, 1215–1226. (In Chinese) [CrossRef]
4. Yu, H.; Peng, S.; Zhao, Q. Field Tests of the Response of Single Pile Subjected to Lateral Load in Gravel Soil Sloping Ground. *Geotech. Geol. Eng.* **2019**, *37*, 2659–2674. [CrossRef]
5. Deendayal, R.; Muthukkumaran, K.; Sitharam, T.G. Analysis of laterally loaded group of piles located on sloping ground. *Int. J. Geotech. Eng.* **2020**, *14*, 580–588. [CrossRef]
6. Sitharam, T.G.; Mantrala, S.; Verma, A.K. Analyses and design of the highly jointed slopes on the abutments of the world's highest railway bridge across the chenab river in Jammu and Kashmir state. *India Lect. Notes Civ. Eng.* **2019**, *29*, 15–32. [CrossRef]
7. Tian, H.-M.; Chen, W.-Z.; Zheng, P.-Q.; Yu, J.-X. Stablity analysis of rocky slope for arch bridge foundation in gorge area. *Yantu Lixue/Rock Soil Mech.* **2013**, *34* (Suppl. S1), 379–385. (In Chinese)
8. Souri, A.; Abu-Farsakh, M.; Voyiadjis, G. Study of static lateral behavior of battered pile group foundation at I-10 twin span bridge using 3d finite element modeling. *Can. Geotech. J.* **2015**, *53*, 962–973. [CrossRef]
9. Abu-Farsakh, M.; Souri, A.; Voyiadjis, G.; Rosti, F. Comparison of static lateral behavior of three pile group configurations using three-dimensional finite element modeling. *Can. Geotech. J.* **2018**, *55*, 107–118. [CrossRef]
10. Luo, W.H.; Liu, J.H.; Cao, W.G.; Zhao, M.H. Stress analysis on the pile-column bridge piers in rock slope. *Highw. Eng.* **2008**, *33*, 1–9. Available online: https://kns.cnki.net/kcms2/article/abstract?v=J0BDVs0XdL199x-4np_x331keQ8FXxwUN1uofGQixO3 3FOQyzMA6KGvw4n0AE8bzsi_XCkQ4ydhZVS1Efawf9XH75Ch5zhG4EE3b6vbcQVq6J3ueLwTzYKHzkeXVpehwtTRKjH3 BYNU=&uniplatform=NZKPT&language=CHS (accessed on 20 February 2008). (In Chinese)
11. Zhou, H.; Su, Q.; Liu, J.; Yue, F. Shaking table tests on bridge foundation reinforced by antislide piles on slope. *Earthq. Res. China* **2019**, *33*, 11. [CrossRef]
12. Zhang, C.; Jiang, G.; Su, L.; Lei, D.; Liu, W.; Wang, Z. Large-scale shaking table model test on seismic performance of bridge-pile-foundation slope with anti-sliding piles: A case study. *Bull. Eng. Geol. Environ.* **2019**, *79*, 1429–1447. [CrossRef]
13. Brideau, M.-A.; Stead, D. Controls on block toppling using a three-dimensional distinct element approach. *Rock Mech. Rock Eng.* **2009**, *43*, 241–260. [CrossRef]
14. Pinheiro, A.L.; Lana, M.S.; Sobreira, F.G. Use of the distinct element method to study flexural toppling at the Pico Mine, Brazil. *Bull. Eng. Geol. Environ.* **2015**, *74*, 1177–1186. [CrossRef]
15. Li, Z.; Wang, J.; Li, L.; Wang, L.; Liang, R.Y. A case study integrating numerical simulation and GB-InSAR monitoring to analyze flexural toppling of an anti-dip slope in Fushun open pit. *Eng. Geol.* **2015**, *197*, 20–32. [CrossRef]
16. Lian, J.-J.; Li, Q.; Deng, X.-F.; Zhao, G.-F.; Chen, Z.-Y. A Numerical Study on Toppling Failure of a Jointed Rock Slope by Using the Distinct Lattice Spring Model. *Rock Mech Rock Eng.* **2017**, *51*, 513–530. [CrossRef]
17. Ren, Z.H.; Chen, C.X.; Zheng, Y.; Sun, C.Y.; Yuan, J.H. Dynamic Analysis of the Seismo-Dynamic Response of Anti-Dip Bedding Rock Slopes Using a Three-Dimensional Discrete-Element Method. *Appl. Sci.* **2022**, *12*, 4640. [CrossRef]
18. Hassan, S.; Alireza, B.; Reza, S. Numerical Modelling of Slide-Head-Toppling Failure using FEM and DEM Methods. *J. Min. Environ.* **2022**, *13*, 269–280.
19. Liu, C.; Jaksa, M.; Meyers, A.G. Improved analytical solution for toppling stability analysis of rock slopes. *Int. J. Rock Mech. Min. Sci.* **2008**, *45*, 1361–1372. [CrossRef]
20. Pérez-Rey, I.; Muñiz-Menéndez, M.; González, J.; Vagnon, F.; Walton, G.; Alejano, L.R. Laboratory physical modelling of block toppling instability by means of tilt tests. *Eng. Geol.* **2021**, *282*, 105994. [CrossRef]
21. Zheng, D.; Zhou, H.; Zhou, H.; Liu, F.; Chen, Q.; Wu, Z. Effects of Slope Angle on Toppling Deformation of Anti-Dip Layered Rock Slopes: A Centrifuge Study. *Appl. Sci.* **2022**, *12*, 5084. [CrossRef]
22. Zheng, Y.; Chen, C.; Wang, R.; Meng, F. Stability Analysis of Rock Slopes Subjected to Block-Flexure Toppling Failure Using Adaptive Moment Estimation Method (Adam). *Rock Mech. Rock Eng.* **2022**, *55*, 3675–3686. [CrossRef]
23. Akbar, A.; Mehdi, A.; Kamran, E. A two-dimensional limit equilibrium computer code for analysis of complex toppling slope failures. *J. Rock Mech. Geotech. Eng.* **2021**, *13*, 114–130.
24. Liu, S.; Wang, H.; Meng, Q.; Yan, L. Simulating Crack Development and Failure Characteristic of Toppling Rock Slope under Seismic Loading on Lancang River in China. *Lithosphere* **2021**, *2021*, 6. [CrossRef]
25. Huang, D.; Ma, H.; Huang, R.; Peng, J.; Luo, S. Deep-seated toppling deformations at the dam site of the Miaowei Hydropower Station, Southwest China. *Eng. Geol.* **2022**, *303*, 106654. [CrossRef]
26. Cai, J.C.; Zheng, D.; Ju, N.P.; Wang, J.; Zhou, X.; Li, D. Time-Varying Effect of Ductile Flexural Toppling Failure on Antidip Layered Rock Slope. *Front. Earth Sci.* **2022**, *10*, 943700. [CrossRef]

27. Zhang, F.; Zhang, W.; Wang, W.; Huang, D.; Li, Y.; Yu, C. Distribution Properties and Limit Depth Determing Methods of Rock mass With Toppling Deformation. *J. Eng. Geol.* **2015**, *23*, 1109–1116. (In Chinese) [CrossRef]
28. Zhang, X.; Meng, Q.; Zhang, F. Influence of Wind-Generated Wave Action on Mountain Reservoir Bank Collapse: A Case Study at the Lancang River, Western China. *Lithosphere* **2021**, *2021*, 6427717. [CrossRef]

MDPI

Article

Evaluation of a Tilt-Based Monitoring System for Rainfall-Induced Landslides: Development and Physical Modelling

Abhishek Prakash Paswan * and Amit Kumar Shrivastava

Department of Civil Engineering, Delhi Technological University, Delhi 110042, India; aksrivastava@dce.ac.in
* Correspondence: abhishek_mt2k16@dtu.ac.in

Abstract: Landslides in northern India are a frequently occurring risk during the rainy season resulting in human, animal, and property losses as well as obstructing transportation facilities. Usually, numerical and analytical approaches are applied to predicting and monitoring landslides, but the unpredictable nature of rainfall-induced landslides limits these methods. Sensor-based monitoring is an accurate and reliable method, and it also collects accurate and site-specific required data for further investigation with a numerical and analytical approach. This study developed a low-cost tilt-based rainfall-induced landslide monitoring system using the economical and precise MEMS sensor to record displacement and volumetric water content. A self-developed direct shear-based testing setup was used to check the system's operational performance. A physical slope model was also prepared to test the monitoring system in real scenarios. A debris failure occurred at Kotrupi village in the Mandi district of Himachal Pradesh, India, which was chosen for the modelling to investigate the failure mechanism. A rainfall generator was developed to simulate the rainfall, equipped with a flow sensor for better simulation and data recording. The tilt angle records the deviation in terms of angle with a least count of 0.01 degrees, and the moisture content was recorded in terms of percentage with a least count of 1. The results show that the developed system is working properly and is very effective in monitoring the rainfall-induced landslide as it monitors the gradual and sudden movement effectively. This study explains the mechanism behind the landslide, and it can be helpful in monitoring the slope to enable the implementation of preventative actions that will mitigate its impact.

Keywords: rainfall-induced landslides; debris failure; slope monitoring system; MEMS sensor; tilt monitoring; physical modelling

1. Introduction

Landslides are a common occurrence during the rainy season, resulting in human, animal, and property losses and obstructing the area's transportation facilities. Himachal Pradesh, a hilly state in north India, is plagued by landslides that frequently recur, making this study essential [1]. Several instances of landslides caused by rain that damaged infrastructure in various nations, including Italy and Central America [2,3]. A global database of landslides inferred that approximately 75% of the non-seismic landslide occurred in Asian regions when analyzing the data between 2004 to 2016. Most landslides occur in the Himalayan region [4,5]. The need and significance of this study are graphically depicted by the landslide hazard and risk zonation map of Himachal Pradesh (Figure 1).

Rainfall acts as the main triggering factor for landslide; the Himalayan region's new folded mountains and seepage adversely affects slope stability, causing an increased number of slope failure during the monsoonal season [5–7]. The relationship between rainfall and landslide has been widely discussed [8–10]. Researchers have developed a threshold-based approach to assess the occurrence of landslides. Various methods can assess these thresholds: empirical methods [11,12], probabilistic methods [13–16], and mathematical

methods [17,18]. With the advancement in technology, there are other tools, such as geological information systems (GISs) and Global Positioning Systems (GPSs) based on remote sensing and satellite data that can be used to develop a hazard zonation map [19–22] and to identify landslides through automatic process and calculation [23,24]. These methods require a skilled team for deployment, which increases the cost. They are suitable for a regional or larger area for early warning, which requires a large amount of data, without which could result in a false alarm. Physical model methods are best suited to analyse the mechanism of rainfall-induced landslides for individual slopes due to their unpredicted nature and various triggering factors [25–28]. Numerical modelling methods are widely known to analyse the stability and seepage parameters for individual slopes, as it is not feasible to perform a physical model test for every individual slope due to its complex setup and procedure [29–35]. In [36], the study used physical and numerical modelling to analyse the rainfall-induced landslide and validated the numerical modelling results with physical modelling. However, the above methods can be combined for hazard risk zonation and to identify the critical slope. It can be seen that sometimes a steeper slope remains stable, whereas a gentle slope may fail under critical conditions. Keeping this in mind, it is important to consider individual slope monitoring for early prediction. As rainfall-induced landslides show the unpredictable nature of failure than the landslide initiated by the effect of gravity, scheduled field inspection at regular intervals may not be an effective method [37]. With the advancement in electronic components and wireless networks, in situ ground-based monitoring of slopes is another emerging method for real-time monitoring of slopes. These methods are also suitable for places not suitable for frequent visits. Different equipment and sensors are used for monitoring and predicting for ages. Extensometers are used to find the displacement of the moving slope with respect to a stable portion [38]. However, this method needs extreme precision in selecting the critical slip surfaces to be installed. Inclinometers are also used to monitor deep-seated landslide [39,40] as well as slow-moving earth flow [41] but the installation and maintenance costs are much higher, and thus cannot be suitable for low-cost purposes. The use of tilt sensors for the detection and monitoring of critical slopes is widely known due to its cheaper development and installation costs, and are found to be effective in monitoring shallow slope failures [42–44]. This technique was developed and successfully tested in Japan [43,45] and is now widely accepted by various countries for its low cost and efficient performance alternative to the traditional extensometers and inclinometers. The geology and hydrological pattern of the Indian Himalayan region are very different from the location where these sensors have already been used, thus requiring performance evaluation before installation.

Himachal Pradesh in the Indian Himalayan region is one of the states in Indian territory that is vigorously affected by landslide events yearly, and the number increases every monsoonal season. These events severely affect the life and property in nearby communities [6] as these regions come under the newly folded mountains, which are eventually affected by various landslides due to the infiltration and pore pressure that develop between the soil pores. Only a few researchers have used tilt sensor-based techniques to monitor the critical slopes in the Indian Himalayan region. Some studies [42,46] used tilt sensors in Darjeeling Himalayas for monitoring slopes, but very few can be found in the Himachal Himalayas region, proving this area is open for further research. In this study, a cost-effective monitoring system has been developed using Micro Electro-Mechanical System (MEMS) sensors. A volumetric water content sensor has also been used in order to study the role of the rainwater effect. The laboratory physical modelling method has been used to evaluate the performance and working efficiency. By integrating multiple sensor technologies and using advanced data analysis techniques, it is hypothesised that a landslide monitoring system can be developed that will provide accurate and timely information about landslide activity, thereby reducing the risk of property damage and loss of life caused by landslides. This study can provide cost-effective monitoring of slopes and the development of early warning systems for rainfall-induced landslides so precautions can be taken to lessen their impact.
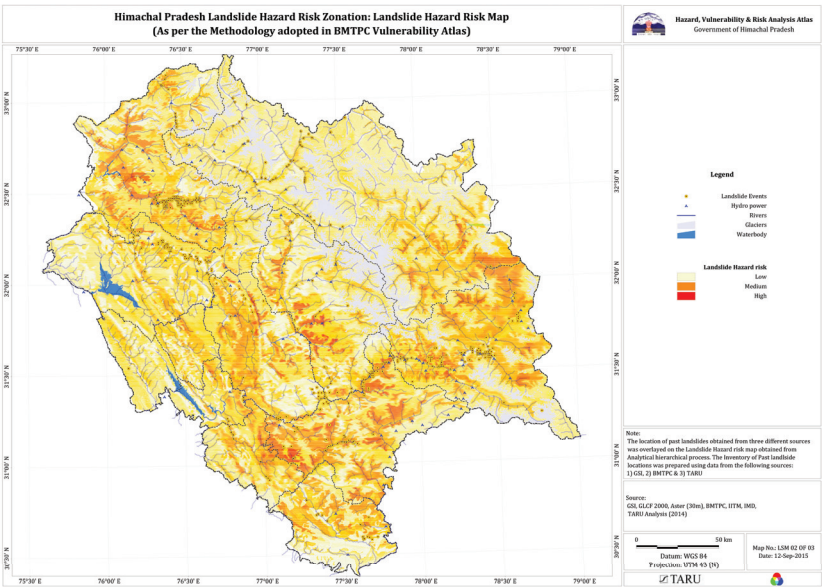
Figure 1. Landslide hazard in Himachal Pradesh (Source: HPSDMA).

2. System Design and Implementation

The design of the proposed landslide monitoring system consists of three major components: a sensing unit which includes the sensors and microcontroller, a data logging unit, including a connection and networking module for the collection and storage of data, and a threshold analysis unit, which can be helpful in generating the warning. Figure 2 shows the schematics of the proposed system.
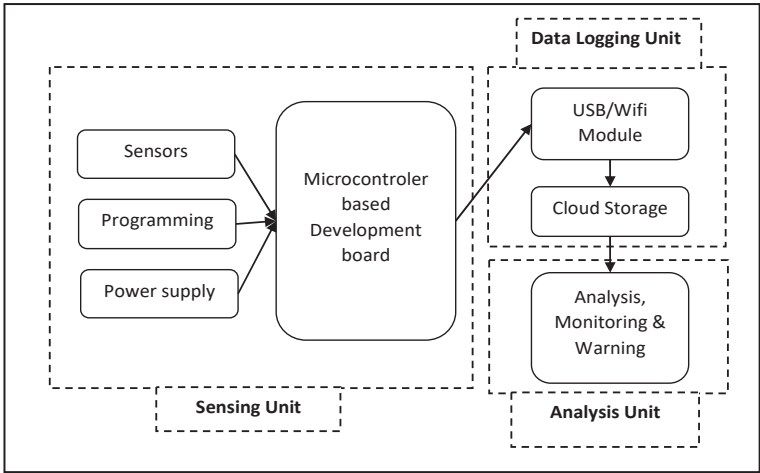

Figure 2. Design of the low-cost framework for monitoring landslides.

2.1. Sensing Unit

The sensing unit is the first and foremost part of the proposed system for monitoring landslide initiation. It includes the sensors used to sense the required data for the analysis. This system uses Micro Electro-Mechanical System (MEMS)-based sensors for their efficient working, durability, and cost-effective availability. This system will be deployed in the field

and cannot be reused if a landslide takes place, making MEMS-based sensors suitable for this purpose. In this study, the components that were used are discussed below.

2.1.1. Tilt Sensor

It is necessary to choose a module (MPU6050), which consists of an accelerometer, gyroscope, and temperature sensor, to record the tilt variation in the x, y, and z directions. The 16-bit triaxial gyroscope and accelerometer are combined into the six-axis sensor.

The module is built around an MPU6050 InvenSense IMU (Inertial Measurement Unit) chip. It comes in a PCB board with a 2 cm × 1.6 cm dimension and 24 pins. An AP2112 K 3.3 V regulator, I2C pull-up resistors, and bypass capacitors are some of the few components that make up the module, which has a meager component count overall. In addition to this, there is a power led that displays the current power status of the module (Figure 3a). The MPU6050 is a Micro-Electro-Mechanical System (MEMS) that contains within it a three-axis accelerometer as well as a three-axis gyroscope (Figure 3b). This allows us to measure the acceleration, velocity, orientation, and displacement of a system or object, in addition to a wide variety of other motion-related parameters. This module also contains a Digital Motion Processor, abbreviated as DMP, capable of carrying out intricate calculations and relieving the Microcontroller of some of its responsibilities. Figure 3c explains the circuit diagram, and Figure 4 shows the block diagram of the MPU6050 module for a better understanding of the working of the sensor.
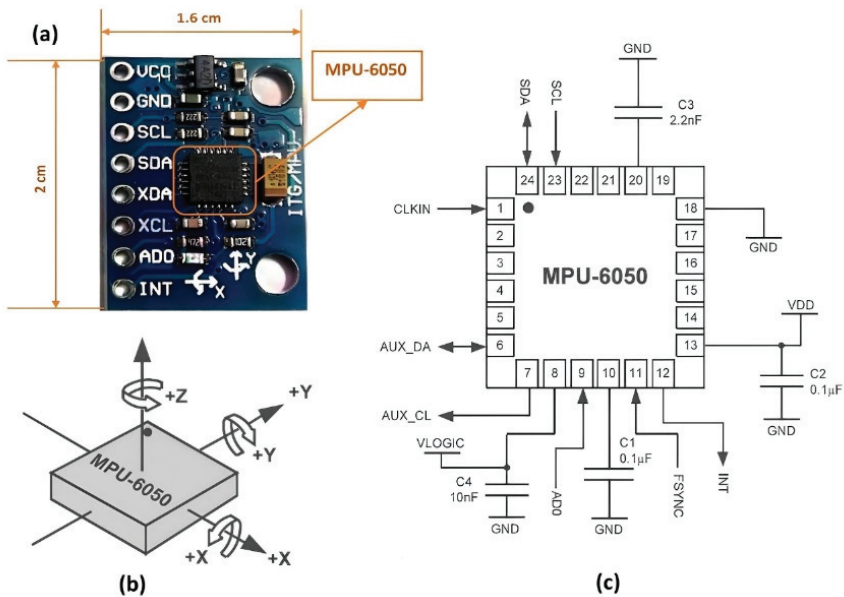

Figure 3. MPU6050 module (**a**) sensor module, (**b**) working axis details, and (**c**) circuit diagram.
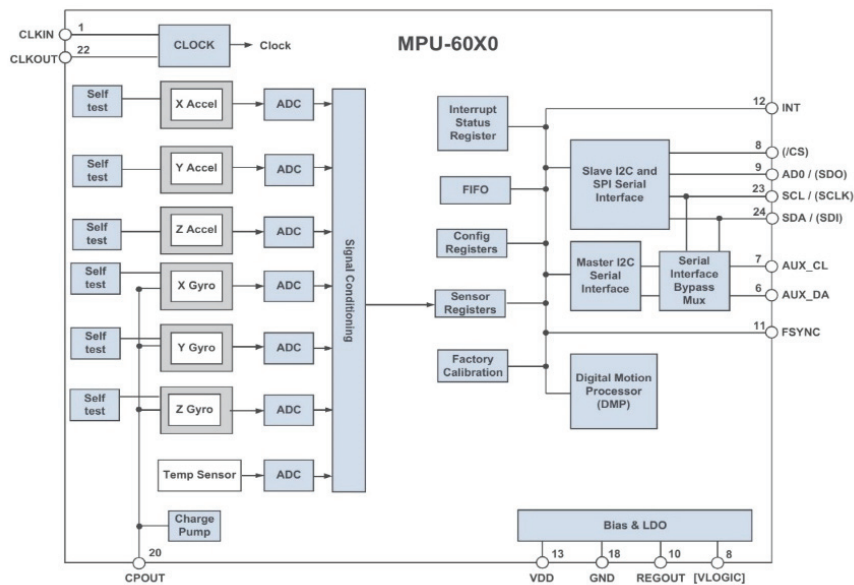
Figure 4. Block diagram of MPU6050 Module.

MEMS accelerometers are used in situations where there is a requirement to measure linear motion, such as movement, shock, or vibration, but there is no fixed reference point. They track the object's linear acceleration while being tethered to it. The mass on a spring principle is the premise on which all accelerometers operate. Due to inertia, the mass seeks to remain immobile as the item to which they are attached accelerates. As a consequence, the spring undergoes stretching or compression, resulting in the production of a force that can be measured and is related to the acceleration that was applied. In a MEMS accelerometer, a pair of silicon MEMS detectors made of spring-"proof" masses are used to precisely detect linear acceleration in two orthogonal axes. Every mass supplies a moving plate with a variable capacitance made up of a variety of interlaced finger-like structures. Due to the proof mass's tendency to resist motion when the sensor's sensitive axis is linearly accelerated, the mass and its fingers are forced away from the fixed electrode fingers. An effect of dampening is produced by the gas between the moving and fixed silicon fingers. This displacement causes a differential capacitance inversely proportional to the applied acceleration. A high-resolution analog-to-digital converter (ADC) is used to measure the change in capacitance, and the acceleration is then calculated using the rate of change in capacitance. This is then transformed into a readable value in the MPU6050 before being sent to the Inter-Integrated Circuit (I2C) master device.

The MEMS gyroscope's function is based on the Coriolis Effect. According to the Coriolis Effect, when a mass moves with velocity in one direction and is subjected to an external angular motion, a force is created that pushes the mass in a perpendicular direction. The amount of angular motion used has a direct impact on the rate of displacement. Four proof masses are included in the MEMS Gyroscope, which is kept oscillating continuously. The Coriolis Effect alters the capacitance between the masses when an angular motion is applied, depending on the direction of the angular motion. A reading is created after this change in capacitance has been detected.

2.1.2. Soil Moisture Sensor

Unquestionably, water is crucial to the chemical, physical, and mechanical characteristics of the soil. Understanding and analyzing various processes involving soil, vegetation, and atmospheres, such as soil erosion, runoff, and soil water infiltration, depend on quantifying soil water content from the surface to greater depths. Due to the ability of aerial plant life to capture some of the water that falls as rain and the ability of plants to absorb moisture from the soil around them and release it to the atmosphere through evapotranspiration, soil vegetation alters the hydrological balance of the affected area. The latter mechanism could result in a decrease in the saturation level of the soil (an increase in suction), which would increase the soil's shear strength. In other cases, water accumulation between the soil layer can cause the formation of the fluid zone, which may lead to a loss in shear strength which may lead to slope failure [47]. Thus, soil vegetation plays a vital role in stabilizing the slope to protect the environment.

With the help of this sensor, it is possible to track changes in soil moisture continuously. The soil moisture sensor consists of two probes to measure the volumetric water content by measuring the resistance or capacitance value through the soil material. The change in current or voltage is then calibrated to measure the water content. When the soil pores have more water, the resistance to current flow will be less as water provides better conductivity. Similarly, when less water is present in the pores, the resistance offered by the medium will be very high, reducing the current flow due to the poor conductivity offered between pores.

Compared to other sensors on the market which measure resistance, in this study, a capacitive soil moisture sensor version 2.0 is used to measure soil moisture levels through capacitive sensing. Version 2.0 has a better upgrade and offers a better service life than previously available versions, as it is corrosion-proof. The output of the capacitive moisture sensor is known to be influenced by the complicated relative permittivity (ε_r^*) of the soil, i.e., dielectric medium [48,49].

$$\varepsilon_r^* = \varepsilon_r' - j\varepsilon_r'' = \varepsilon_r' - j\left(\varepsilon_{relax}'' + \frac{\sigma_{dc}}{2\pi f \varepsilon_0}\right) \tag{1}$$

where, ε_r' and ε_r'' are, respectively, the real and imaginary components of permittivity, σ_{dc} referred to the electrical conductivity, ε_{relax}'' is the contribution of molecular relaxation (dipolar rotation, atomic vibration, and electronic energy states), j indicates the imaginary number $\sqrt{(-1)}$, and f is the frequency. The amount of energy from an external electric field that is stored in a material is measured by the real part of permittivity (ε_r'). The "loss factor", also known as the imaginary part of permittivity (ε_r''), predicts a material's susceptibility to dissipation or loss in the presence of an external electric field: $\varepsilon_r'' > 0$. Losses are linked to two main processes: electrical conductivity and molecular relaxation. The soil's salinity, ionic composition, frequency, and moisture affect permittivity.

The permittivity of a material is often represented by a complex number with a real part and an imaginary part. The real part of the permittivity represents the material's ability to store electric charge, while the imaginary part represents the material's ability to dissipate electric energy.

Capacitive soil moisture sensors utilise the operation of a capacitor to provide an approximation of the amount of moisture present in the soil. The amount of charge a material can hold when subjected to a specific external electrical potential is referred to as its capacitance [50,51]. The most common way to conceptualise capacitors is as parallel-plate setups, as shown in Figure 5 below.
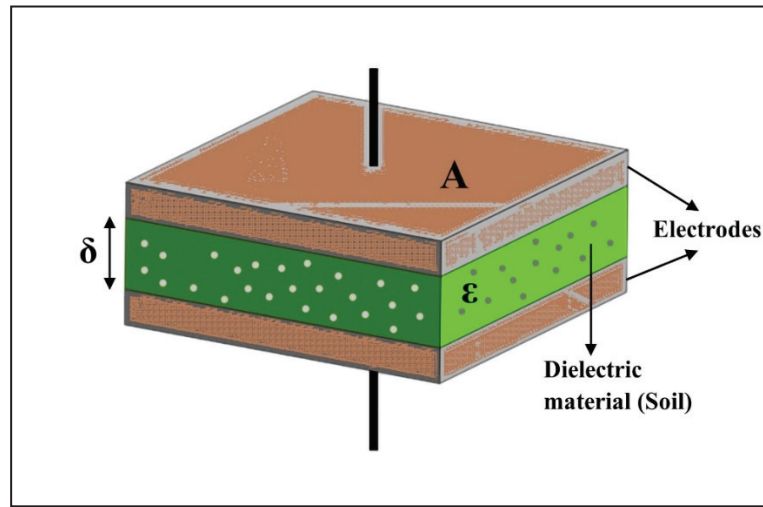
Figure 5. Parallel plate capacitor setup.

The capacitance of an object can be expressed as a ratio of its charge to its electrical potential:

$$C = \frac{Q}{V} = \frac{\oint \varepsilon E.ds}{\int E.dl} \tag{2}$$

The charge Q defined by the integrating relationship between the generated electric field (E) and the relative permittivity of the surrounding dielectric material (ε) throughout the gross surface area of the probes. The line integral of the electric field is used in the definition of electric potential, abbreviated as V. δ is the distance between plates. For the capacitor with parallel plates, an assumption can be made that the electric field is uniform throughout the whole surface of the dielectric. This leads to the resulting simplification:

$$C = \frac{\varepsilon E A}{E \delta} = \frac{\varepsilon A}{\delta} \tag{3}$$

This is usually believed to represent the relationship between the geometric parameters of a capacitor with parallel plates and the soil material having dielectric properties around the capacitor. The capacitance measured by a soil moisture sensor is distinct from that recorded by a capacitor with parallel plates, as the capacitor plates are coplanar rather than parallel. This indicates that the plates are not stacked on top, but are placed adjacent to one another and that the dielectric substance is the ground itself instead of a thin layer trapped between the plates. The following illustration demonstrates this point.

Figure 6 clearly shows the arrangement of electrodes with the dielectric medium, which can be dry or wet soil and serves the same function similar to the plates of any capacitor. The capacitive soil moisture sensor works in conjunction with a timer circuit (TLC555, in the case of the selected sensor). The combination produces a duty cycle proportional to an analog voltage. This voltage can be read off using a built-in microcontroller board. Capacitance for a flat capacitor is a complex function of dielectric constant and sensor shape that will not be investigated here. The only new component that has been added is G, a function that summarises the geometric qualities of the sensor. The relationship is shown in Equation (4).

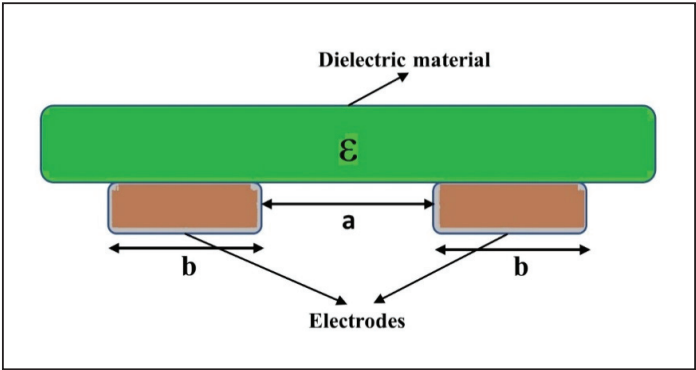$$C = \varepsilon G \tag{4}$$

Figure 6. Illustration concept behind working of soil moisture sensor.

The geometrical and dielectric medium, along with surface line integration in planer configuration, makes the complex function, which can be simplified for better understanding by assuming a constant (A) as shown in Equation (5), and the solution to finding the dielectric constant is mentioned in Equation (6).

$$V = \frac{A}{C} \tag{5}$$

$$\varepsilon = \frac{A}{GV} \tag{6}$$

In essence, this indicates that a correlation between the dielectric constant and the inverse of the voltage received by the sensor can be anticipated. Using the above relationship, the soil moisture sensor is calibrated to sense the moisture in soil pores in percentage or as the volumetric water content. Figure 7 shows the chosen, commercially available blade-shaped Capacitive Soil Moisture Sensor v2.0.
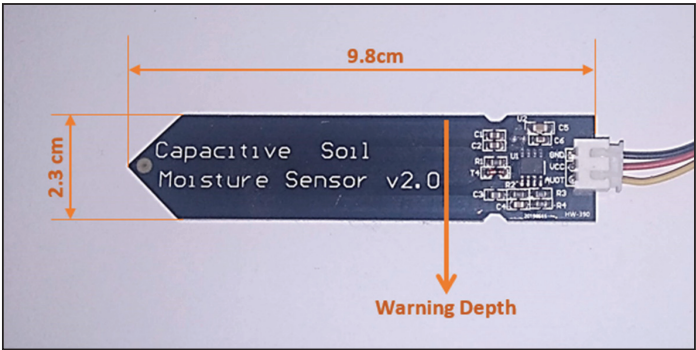

Figure 7. A capacitive soil moisture sensor v2.0.

The most recent and reliable information for the version 2.0 soil moisture sensor developed by DFROBOT and sold under the SKU (stock keeping unit) designation of SEN0193 in various advertisements [52]. The datasheet suggests a suitable depth of penetration in soil, a working power supply between 3.3 and 5.5 volts, and an output voltage between 0 and 3.3 volts. Initially, a comprehensive investigation into the sensor's electrical circuits was carried out to become familiar with the functioning mechanism. The circuit diagram of the soil moisture sensor from the datasheet is shown in Figure 8.
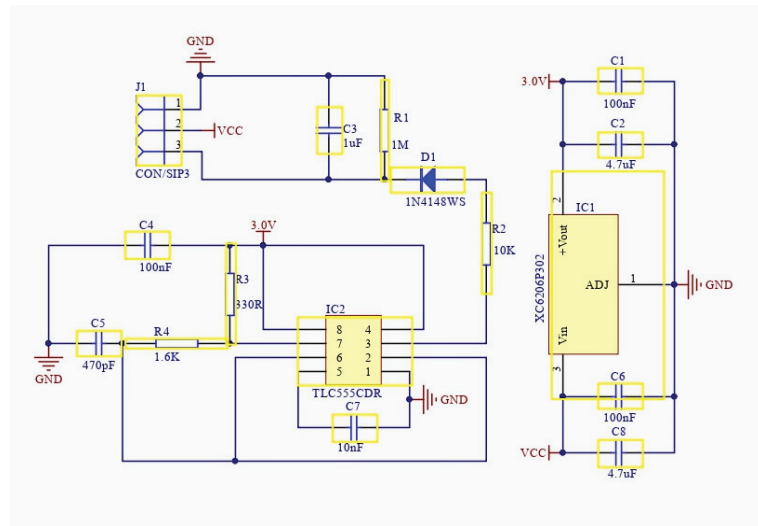
Figure 8. Circuit diagram of the capacitive sensors (source: Sensor DFROBOT data sheet).

2.1.3. Development Board

The development board is like the heart of the monitoring system, as all the necessary parts are connected. The panel includes a microcontroller for reading and processing sensor values. The board consists of an input pin for analog and digital sensors, a power supply connecting headers, and a USB port to transfer the data. It can also be combined with various modules, like the Wi-Fi module, to transmit the data to the cloud or the memory card module to store it for further analysis.

2.1.4. Power Supply Unit

The power supply unit includes the power supply for all modules in the monitoring system. It consists of a battery with enough capacity of 10 k mAh for the uninterrupted working of the system and a solar panel charging system for continuously charging the battery. The solar charging system was equipped with the overcharging protection of the battery to ensure the longest battery life.

2.1.5. Programming

Programming is the soul of any monitoring system. It communicates a program's intended functionality to a computer through a sequence of instructions. In this system, two types of sensors were used to monitor the landslide mechanism. Programming for the MPU6050 sensor was done to compute the tilt angle, and any deviation induced by tilting can be recorded with time. The system has the capability to adjust itself by restarting to allow for better visualization. The second sensor was installed to monitor the volumetric water content of the soil, and programming was done to measure the moisture content in terms of percentage with time.

2.2. Data Logging Unit

This unit ensures the data collection acquired by the sensor. The data logging module can be attached to the development board using the USB hub or the memory card module to save the data. A Wi-Fi or GSM module can also be connected wirelessly to collect the sensor value on the internet cloud for further analysis. The development board is equipped with a Wi-Fi module to provide internet connectivity in the developed monitoring system. A GSM-based Wi-Fi modem was installed so that several monitoring sensors could be connected using the single modem according to the slope area and location, reducing the

cost of individual GSM modules and the connectivity charge. The data collected from the sensors were stored using the Arduino cloud for further analysis.

2.3. Analysis Unit

In this section, the data collected from the sensors are analysed for better monitoring of slope movement. As the critical threshold value depends upon the geometry and material of the slope, it varies for individual slope. After sufficient analysis and monitoring, a warning can be generated for each slope to reduce the catastrophic effects of slope failure by evacuating or strengthening stability.

3. Study Area

The study location (Figure 9) is in the vicinity of Kotrupi village on the Mandi—Joginder Nagar—Pathankot National Highway (NH-154), where the Kotrupi landslide has caused extensive damage [53]. On either side of the slide, the Padhar and Joginder Nagar tehsils of the Mandi district (Himachal Pradesh) are approximately 4 and 21 km away, respectively. The study area is covered by the Survey of India Toposheet No. 53 A/13. Geographical coordinates with latitude N31°54'37.60'' and longitude E76°53'26.30'' indicate the location of the landslide [53].
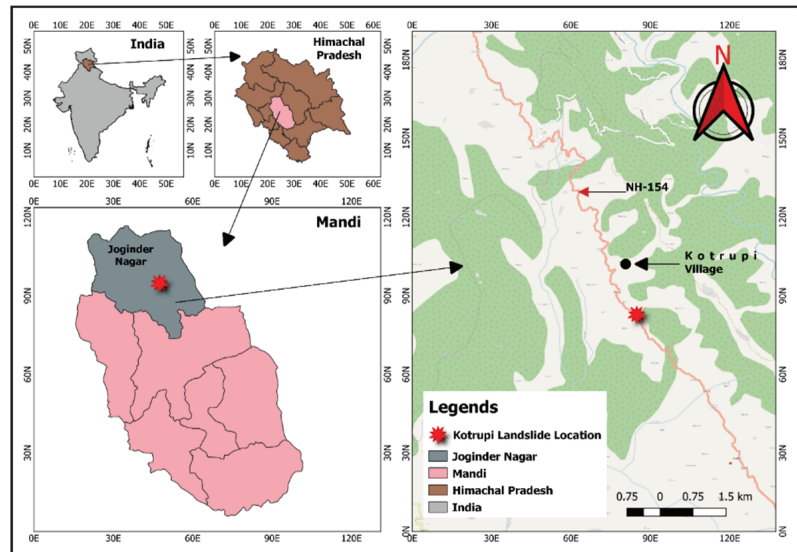

Figure 9. A map showing the location of the research area.

3.1. Landslide Event and Mechanism

On Sunday, 13 August 2017, a major landslide happened in the Mandi District of Himachal Pradesh in the village of Kotrupi (near the Kotrupi Bus Stop). The road connecting Mandi and Pathankot was affected by the landslide. According to reports, a section of the slope completely collapsed, burying two Himachal State Transport buses and a few other cars, and at least 47 people were killed in the tragedy [54]. Nearly three hundred meters of the highway were entirely buried by debris, shutting off contact on a vital corridor. There have been scars from small landslides in the Kotrupi region prior to the actual landslide. Debris flow slides occur when significant soil mass has flowed down a steep channel with debris. The Kotrupi landslide was one of the types of debris failure [54].

3.2. Description of Study Slope

The area includes part of the catchment basin of the Beas river, and several tributaries join it. The Uhl river, Rana Khad, Arnodi Khad, and Luni Khad are minor tributaries of the Beas River. Physiographically, the area falls in the Lesser Himalayan Zone occupied by the Dhauladhar range in the northeastern part. The topography is rugged, displaying high ridges and deep valleys. Figure 10 shows the satellite view of the study area, indicating landslide crown and runout. The slope is moderate to steeply inclined with occasional breaks in the slope. The slope is moderately to highly dissected, as evidenced by minor streamlets on either side of the slope. The slope affected by the failure has a 45°–50° inclination. The landslide's crown is located at an elevation of 1620 m. The main landslide is approximately 230 m tall, with a 210 m width. The slide is 300 m long from top to bottom. The landslide's runout distance was 1155 m [54,55].
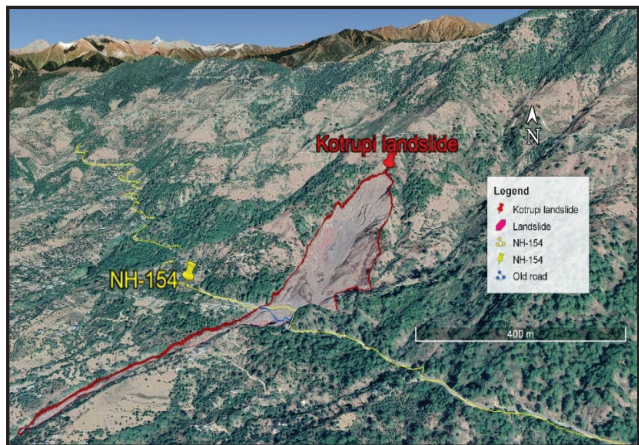

Figure 10. Satellite view of the study area.

Figure 11 shows the digital elevation model (DEM) of Joginder Nagar, indicating the landslide location. The DEM is created using SRTM data with the help of the QGIS tool. Using the profile tool of QGIS software [56], the elevation profile has been generated, indicating the landslide location.
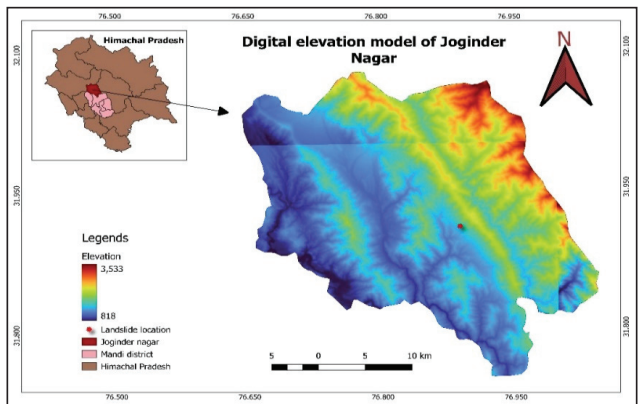

Figure 11. SRTM-DEM of Joginder Nagar, Mandi, Himachal Pradesh.

3.3. Geotechnical Characteristics of the Slope Material

Slope-forming material was collected during the field survey to find the hydromechanical and geotechnical parameters. In order to minimise the differentiability of location in the simulation of the material properties and to better understand the Kotrupi landslide's behaviour, materials were collected at various locations throughout the landslide area. Grain size analysis, Atterberg limits, natural water content, specific gravity, a compaction test, and a triaxial test were carried out using the disturbed samples taken from the site per the IS code. The material can be simulated in numerical modelling using the outcomes from experimental investigations. After performing grain size analysis, the material was categorised by three fractions, i.e., sand, silt, and clay. The material collected from the site was classified as a non-uniform gradation because it contained a wide variety of possible particle sizes, including plants, big stones, and boulders. Indian standard code IS: 2720 was followed to perform sieve and hydrometer analyses to determine grain size [57], and the results showed the values of coefficient of uniformity Cu is 6.2 and coefficient of curvature Cc as 0.67. The fineness modulus of the material was found to be between 5 to 12 percent, and the soil was classified as poorly graded sand containing less amount of silt (SP-SM). To perform seepage analysis to investigate the pore pressure parameters, the determination of Atterberg's limit is an essential parameter in material simulation [58]. Indian standard code IS:2720 (part 5) was used as a reference to perform Atterberg's limit tests [59]. Atterberg's limit results are summarised in the Results section of the paper. IS code: 2720 (Part-7) was referred to perform light compaction tests to determine the dry density of the soil [60]. According to the geotechnical investigation performed during the laboratory investigation, the material obtained from Kotrupi landslide location mostly contain poorly graded sand (SP). The landslide's shear strength parameters can be calculated using either the drained or the undrained stresses, the total or the effective stresses [61]. In the case of a debris-type landslide, the unconsolidated-undrained test has been recommended for soil characterization [62]. Following IS: 2720, part 11, the tests were conducted at normal stress of 50 kPa, 100 kPa, and 200 kPa to determine the shear strength parameters (c_u and ϕ_u) because the soil sample contains some silt [63].

4. Methodology

In this study, a low-cost monitoring system that comprises a MEMS-based tilt sensor and soil moisture sensor is developed to investigate the slope movements monitoring the tilting behaviour. A self-made testing platform was designed to test the working of the monitoring system. A soil slope model was prepared in the laboratory to assess how well the sensor works under real-world conditions, including a self-developed rainfall generator to simulate the rainfall. The physical model test is also helpful in investigating the cause and the failure pattern, which helps establish the critical rainfall threshold. A series of physical model tests were conducted to assess the effectiveness of the sensor column monitoring process by evaluating the applied sensor column deformation behaviour with the observed tilt response. Landslide events have been modeled in two different ways: (i) a direct shear setup simulated first-time landslide failure experiment using a sensor column to analyse the performance of developed system directly with relative deviation in angle; and (ii) by creating a soil slope model to test and monitor the functioning of the monitoring system by simulating real conditions and also to investigate the failure mechanism behind the rainfall-induced landslide by simulating a case study. The study's methodology flow chart is shown in Figure 12.
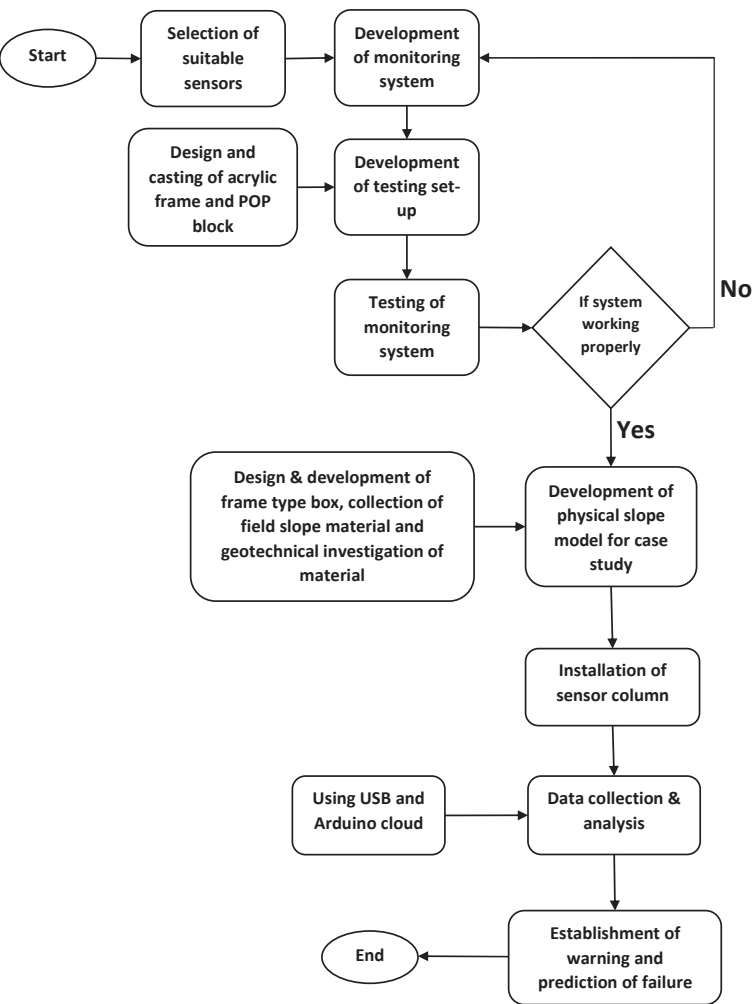
Figure 12. Flow chart of the methodology adopted in the study.

4.1. Testing Setup

The testing method includes a predefined failure plane to simulate the slope failure plane in order to check the working and performance of the developed system. Figure 13 is a schematic representation of the physical model of a slope failure that was used to analyse the displacement behaviour using a tilt measurement and to accelerate the top box relative to the bottom box. The setup includes a hydraulic jack to create a horizontal movement to the upper block against the fixed wall support. The lower block is fixed to any movement. Both blocks have holes throughout the depth where the sensor column was installed. An LVDT (Linear Variable Differential Transformer) sensor was also installed to measure the horizontal deformation induced by the external force applied by the hydraulic jack.
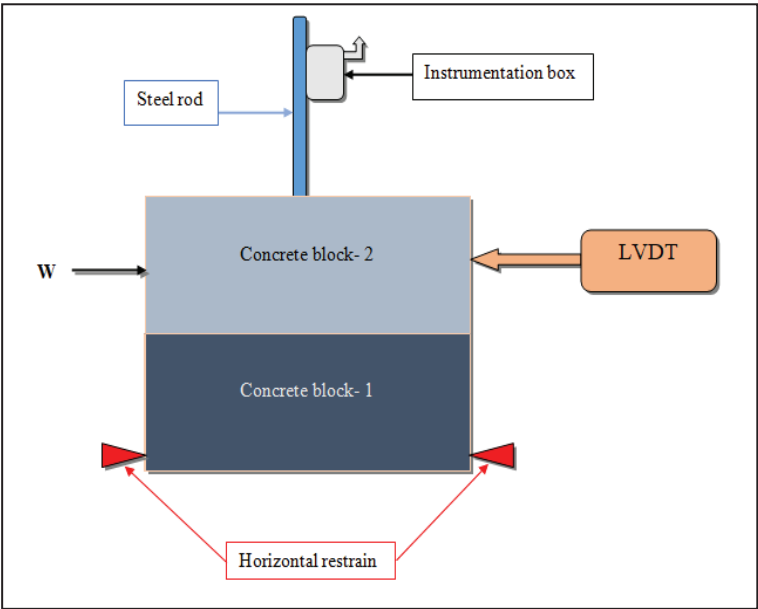
Figure 13. The schematic diagram depicts a large-scale physical model of a slope failure used to accelerate the top box relative to the bottom to analyse the displacement behaviour with tilt measurements.

The concrete blocks were made using the Plaster of Paris (POP) material, as it is easy to cast and move around in the lab. The casting was done using a mould of 20 mm × 20 mm × 30 mm made of acrylic sheet, and a hole of 4 cm diameter was made to place a PVC pipe longitudinally to create the borehole in the block for the placement of the sensor column. Figure 14 shows the casted POP block in a casing made of an acrylic sheet of a thickness of 18 mm, and a borehole was created using a plastic pipe of a 4 cm diameter.
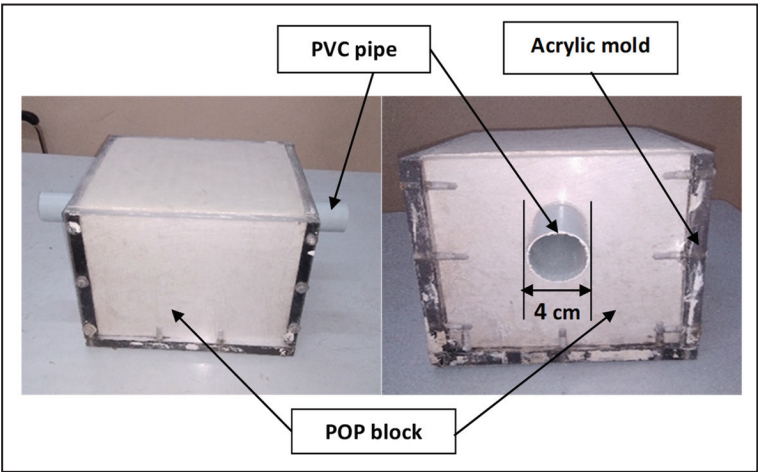

Figure 14. Modelling and casting of blocks with boreholes of 4 cm.

Figure 15 shows the self-made large-scale direct shear model developed using two concrete blocks placed over one another with a bore hole of 4 cm in diameter. The sensor was installed using the steel rod through the column of soil representing the in-situ soil of a slope. The joint made with concrete blocks will act as a predefined failure plane. The lower blocks have been restricted to any movements, while the upper block is free to move when any external force has been applied. The upper block can be considered the failed soil mass, while the lower block is the base of the slab. This sensor was tested by applying an external force with a hydraulic jack to cause a horizontal relative displacement of the top concrete block with respect to the bottom block. The movement change in angle in the x and y directions can be noted for further analysis. The experiment setup was designed so that various tests could be performed to evaluate how well the sensor functions under rapidly changing conditions.
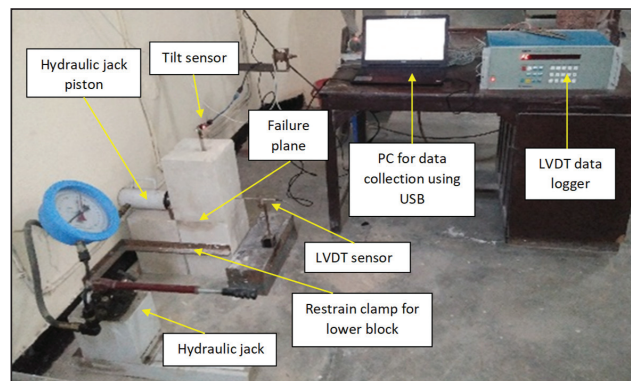

Figure 15. Self-developed large-scale direct shear setup.

4.2. Physical Modelling of Slope

Debris flows are rapid landslides that pose a threat to human life and property because of their speed and the destruction of infrastructure along their path. Debris flows usually start on hillsides or mountains, most likely when recent rainfall occurs. The rapid collapse, complexity, and random behaviour of debris flow make it difficult to explain the mechanism using a numerical or mathematical model [27]. Therefore, the most common and efficient technique for investigating the slipping mechanism of soil slices utilised in studies of slope collapse is a physical model test, to study the rainfall-induced slope instability, to monitor for potential landslide danger, and to take preventative measures before they occur [27,64,65].

The physical modelling was carried out based on the following presumption. The engineering qualities of the parent soil and experimental soil are the same. There is nowhere for the water to leak except the toe drain because all the sides are impermeable. The sprinkler utilised is not a jet type, so direct rain impact has negligible weathering effect on the slope. For the chosen intensity, rainfall is distributed similarly across the entire slope. The effect of plants, roots, and vegetation on slope stability has not been considered.

In the study, identical engineering qualities were used to enforce a physical modelling test [27,36]. Soil's basic engineering qualities are determined through dimensional testing of analogous materials in a controlled environment. The identical experimental settings of the physical model were adapted to fit similar theories. This research uses an experimental physical model to examine the conditions of landslide initiation and the mechanism of failure caused by precipitation. The experimental setup is depicted in Figure 16.
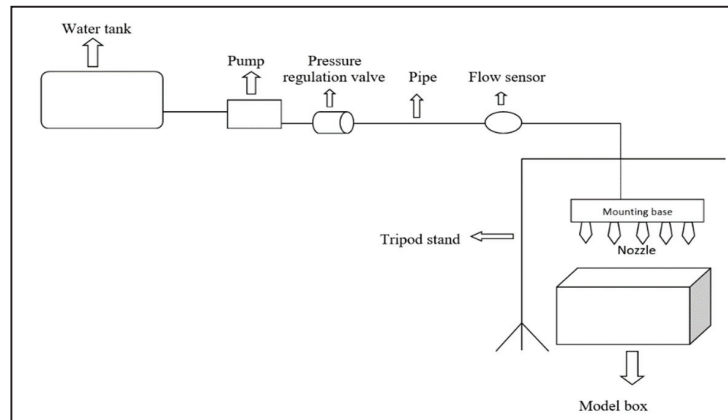
Figure 16. Schematic diagram of experimental setup.

4.2.1. Frame Type Box

To facilitate experimentation, a steel framework supports a transparent acrylic sheet 15 mm thick that serves as the frame type model. The tank used in the experiments is a cube, measuring 97 × 57 × 49 cm in dimensions. The toe area also features drainage holes for easy removal of any excess water. The frame type of box was placed over a concrete block in order to place a hydraulic jack on the hillside of the slope to provide a tilting mechanism.

4.2.2. Rainfall Simulator

Two primary measurement-based empirical approaches are used to establish its threshold values: (1) Measurements of rainfall for a given occurrence in terms of both intensity and duration (ID), the sum total of rain that fell during the event (E), duration of a rainfall event (ED), and intensity of a rainfall (EI) thresholds (Guzzetti et al. 2008) and (2) antecedent rainfall event [11] that is, the specified amount of precipitation above which a slope would collapse [66,67]. Three factors have been taken into account in this analysis: (a) precipitation intensity "q", (b) time duration of rainfall event "t" and (c) the time interval between the consecutive rainfalls. Both the duration and frequency of rainfalls change with the passage of time. Total rainfall "Q" is proportional to the product of time duration and the intensity of rainfall "q" as shown in Equation (7).

$$q = \frac{Q}{t} \tag{7}$$

In this study, a self-developed rainfall generator was used to simulate the variable rainfall to simulate a natural environment. An artificial rain generator consisting of a water storage tank, submersible pump, control valve, flow sensor, and raindrop nozzle is constructed to produce the required amount of rain. For the generation of rainfall, several sprinkler nozzles are installed in a rainfall simulator to simulate the rainfall. The nozzle used is a spray type but does have a fixed opening, and the droplet size may vary according to the input flow pressure. The rainfall generator was equipped with a flow sensor that collects the data with a microcontroller. The variable rainfall intensity is attained by controlling the valve attached to the inlet of the rainfall generator. Figure 17 shows the input variation of rainfall intensity and accumulated rainfall depth over time. Variable interval is also introduced after an hour for the next successive rainfalls to make moisture infiltrate properly.
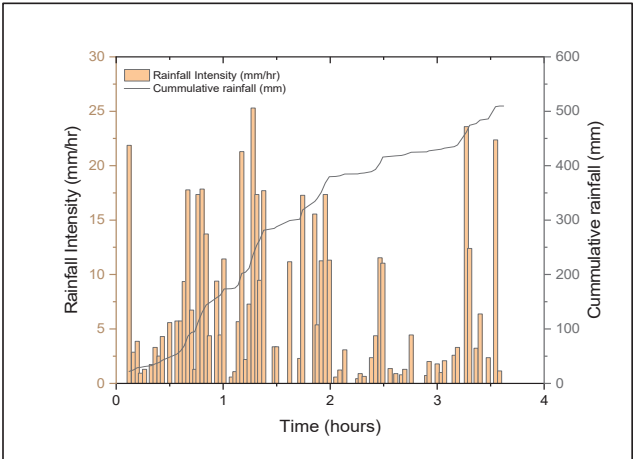
Figure 17. Input Rainfall parameter.

5. Results and Discussion

The findings of this investigation are summarised in this section. The results of the laboratory tests are discussed in greater detail in this article. To better understand the failure mechanism under rainfall, physical slope modelling was used to simulate and investigate the start-up mechanism of the slide. Testing and monitoring results are explained in this section.

5.1. Results of the Self-Developed Test Setup

The self-developed large-scale direct shear setup was used to test the working behaviour of the developed sensor column for slope monitoring and failure prediction. Figure 18 shows the variation detected by the displacement induced using the hydraulic jack. A very small displacement was induced to check if the system could detect a small deviation in angle, and the displacement recorded through LVDT can be seen in Figure 19. In Figure 18, the maximum angle detected is only 0.5 degrees on the y-axis and 0.1 to 0.2 degrees on the x-axis. The system has some noise and variation in readings, but as it is very low limited to 0.01 to 0.05 degrees only thus can be ignored in further investigations or monitoring for better understanding.
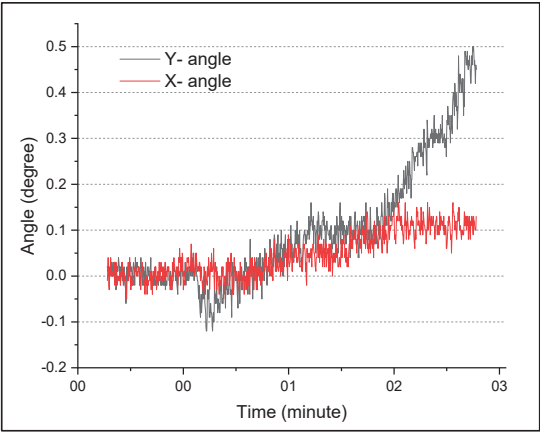

Figure 18. Variation of angle in X and Y direction.
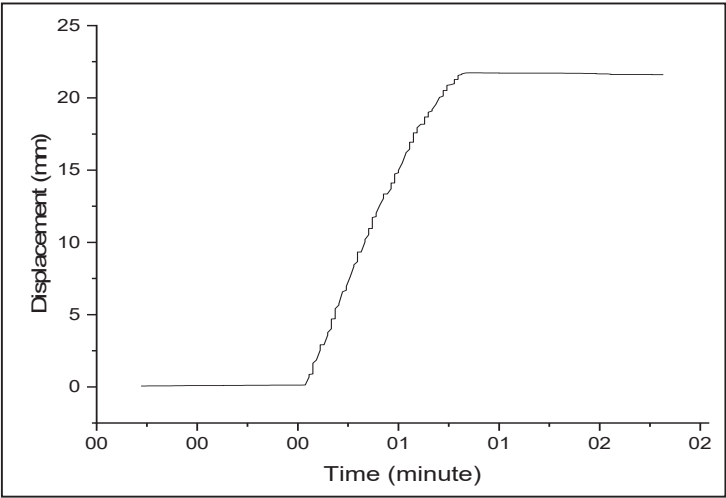
Figure 19. Linear displacement in X direction using LVDT.

In further testing, the displacement was increased to a large extent to check the working of the sensor. There was a limitation to the LVDT sensor in that it could not measure such large deformation in this phase. Figure 20 shows the variation of angle when further displacement is introduced to the upper block. It shows that there is a large deviation detected in the y-axis as the slope usually moves downward against the y-axis. However, there is also some movement in the x-direction which can help in better monitoring of the slope.

Figure 20. Variation of angle in X and Y direction.

5.2. Results of the Physical Model

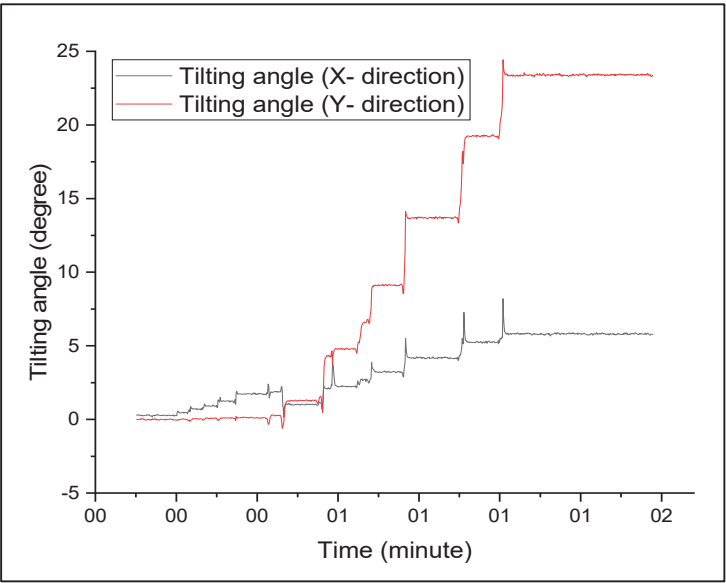A landslide that occurred in Kotrupi village was simulated in this study using the physical modelling method to study the failure mechanism under variable rainfall conditions. To monitor the movement of the slope, the self-developed tilt-based monitoring system was installed at the top section of the slope. The results generated from the tilt and soil moisture sensor were described in this section. A self-developed rainfall generator was used for the rainfall generation, and the input rainfall with respect to the cumulative rainfall depth is shown in this section which can be helpful in deciding the threshold rainfall for the particular slide or can be used to predict the threshold for the nearby areas.

5.2.1. Soil Properties

Dry and saturated unit weights were 16.7 kN/m^3, and 20.3 kN/m^3, respectively. The saturated permeability coefficient was 0.00023 m/sec, cohesion 21 kPa, and friction angle was 31°. This is because the soil in Kotrupi was mainly made up of very coarse sand as poorly graded sand (SP) in the USCS classification. The presence of moisture from the infiltration that the slope has experienced has resulted in the development of apparent cohesion. As a result, the apparent cohesiveness between different soil particles is revealed by the cohesion value that is achieved through triaxial testing. Additionally, the existence of fine soil, as measured by silt content (SM), has been of assistance in the development of the cohesion value. The liquid limit of slope material was found to be 32%. Extensive research has been done to investigate the geotechnical characterization of the Kotrupi landslide as it has been shown to vary in a wide range, although the results from this study fall in the region, which justifies the laboratory results [53,61,68,69].

5.2.2. Monitoring Results of Soil Slope

The physical slope model is prepared to study the effect of rainfall on the slope. To study the effect of pre-monsoonal rainfall, an antecedent rainfall of 10 mm was simulated at 1 mm/h intensity. Figure 21a shows that deep percolation takes place, which justifies that the low intensity and long duration rainfall causes deep saturation and may result in a deep-seated landslide. In Figure 21a, it can be seen that the slope is dry at the end, and the saturation level keeps increasing to the top. This may result in compaction and consolidation of soil near the junction point of wet and dry soil, which in turn decreases the permeability. Figure 21b shows the generation of small cracks on top of the slope takes place after one week. Figure 21c shows the effect after four weeks, and the wide cracks can be seen on top as well as the slope section that may be generated by soil shrinkage after wetting and drying. The duration of generated cracks may differ according to the temperature and humidity of the surrounding environment. Further rainfall on the slope results in faster and deeper percolation of water through the cracks, which helps in creating the fluidization zone between the dense and loose soil layer during the monsoonal season. The tilt sensors were mounted on top of a steel scale. At the bottom, a soil moisture sensor was attached and placed into the soil after creating a borehole using a drill machine (Figure 21d). Further, the sensors were installed on the upper section of the slope to monitor the slope movement and the water content.

The rainfall was simulated by a self-developed rainfall generator equipped with a flow sensor and a microcontroller to record the flow. Figure 22 shows the variation of water content against the input rainfall. As the water content increases or varies according to the input rainfall, the water content change affects the slope stability; thus, the variation in the tilting angle can be seen in Figure 23. As the slope is much more likely to fail in the y-direction due to gravity action, the angle deviation is much more significant in the x-direction. There is also some deviation detected in the x-direction due to some rotation and settlement.
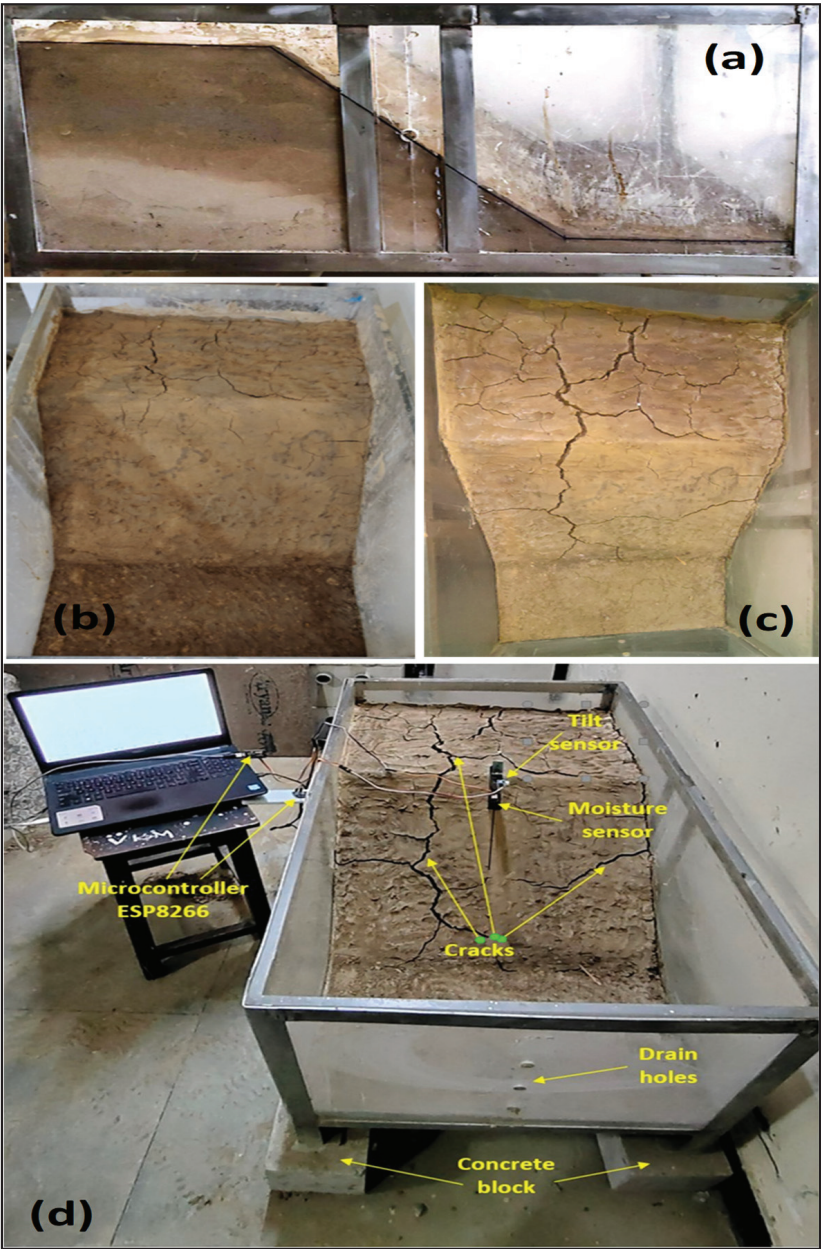
Figure 21. Physical model setup (**a**) percolation of water, (**b**) visible small cracks, (**c**) formation of larger cracks, and (**d**) placement of sensors.
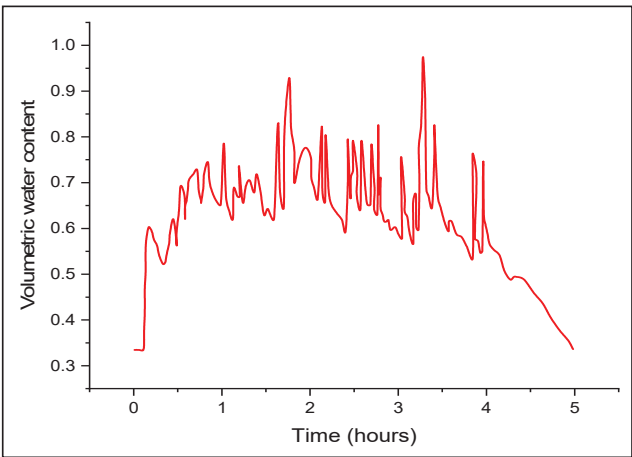
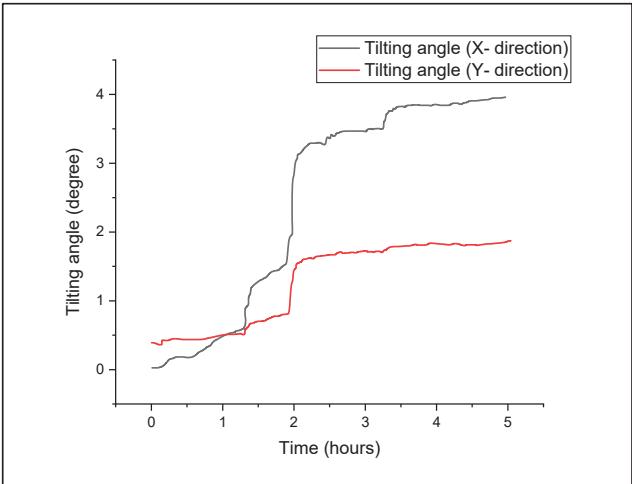**Figure 22.** Output volumetric water content.

Figure 23. Variation of angle in X and Y direction.

Many researchers worked around the globe in order to test the feasibility of tilt-based monitoring systems [42,44,70]. This study validates the effective monitoring of rainfall-induced landslides using a tilt sensor. A direct shear model setup was developed to verify the sensor's working and prove its reliability [71]. The physical modelling method is used to simulate the soil slope to study the effect of pre and post-monsoonal rainfall on the slope and to test the monitoring sensor in a realistic environment [27,36]. Figure 21 also shows that wetting and drying can lead to the formation of cracks during pre-monsoonal rainfall, which can cause the water to infiltrate deep and may cause failure [30]. One study [43] stated that the change in water content is a better representation than just the water content and, as Figure 22 depicts, the variation in the volumetric water content is very vigorous, which may cause the slope to be unstable. Figure 23 also depicts the sudden variation in tilt angle during heavy rainfall, which validates the result. This study also proved the possible failure mechanism occurring in rainfall-induced landslides (Figure 24) [36,37].
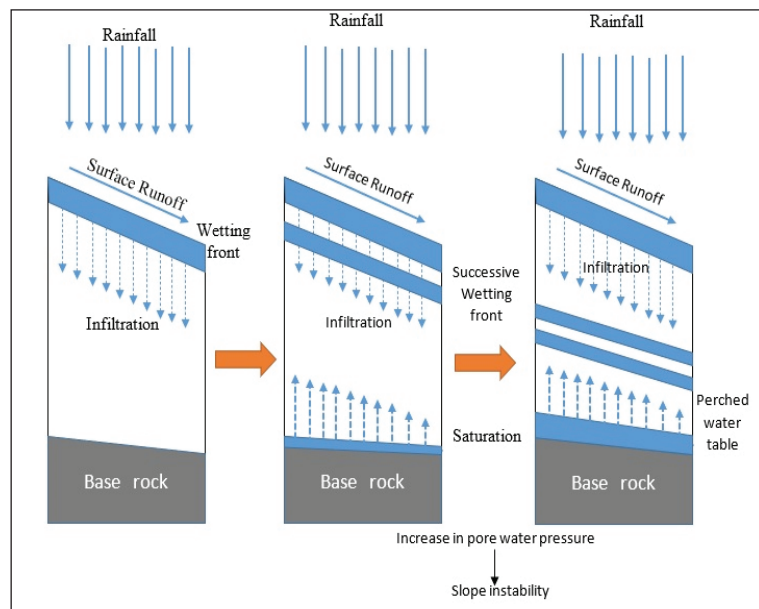
Figure 24. Sequential schematic of landslide initiation.

6. Conclusions

The number of landslide incidents in the north Indian Himalayan region has increased dramatically in every monsoonal season. Mandi, a district in Himachal Pradesh, is among the widely affected areas. This research led to the following findings:

1. A self-developed direct shear model was used to examine the effectiveness of a rudimentary monitoring system designed to prevent landslides caused by rainfall. Tilt sensors were placed on the slope's surface in a physical slope model to detect any abnormal variation in the angle at which the sensors are tilted.

2. The tilt and volumetric water content sensors were installed on the upper section of the slope and were confirmed with the displacement (Figures 20–23). There was a sudden movement in slope recorded under the influence of applied rainfall in the course of the research. The precise amount of rain or rate of tilting required for landslides is hard to express.

3. The findings show that prior rainfall causes slope displacement, supporting earlier research in this area. By adopting such a system, it may also be possible to validate existing rainfall threshold models produced, and the site-specific empirical equation can be created based on circumstances.

4. The study proved that the cracks developed to cause deeper percolation, which leads to slope failure by generating the fluidization zone between the soil layer. Figure 24 explains the mechanism of landslide failure triggered by rainfall.

With timely data availability, this kind of attempt to put up an early warning system and validate the well-known empirical models would be enhanced, potentially saving lives by issuing an alarm for evacuation. This study can be further investigated with a numerical modelling method to analyse the rainfall-induced landslide and its validation so that numerical modelling can be used to analyse different slopes for prediction, as it is not possible to perform the physical model test for all slopes. Furthermore, automated warning systems can be added to the developed system to generate warnings in real-time. Although the developed system has only been evaluated for debris failure in this study, it could be evaluated in the future under varying geological conditions to assess its efficacy and feasibility in dealing with various types of landslides.

References

1. Parkash, S. Historical Records of Socio-Economically Significant Landslides in India. *J. South Asia Disaster Stud.* **2011**, *4*, 177–204.
2. Guerriero, L.; Prinzi, E.P.; Calcaterra, D.; Ciarcia, S.; Di Martire, D.; Guadagno, F.M.; Ruzza, G.; Revellino, P. Kinematics and Geologic Control of the Deep-Seated Landslide Affecting the Historic Center of Buonalbergo, Southern Italy. *Geomorphology* **2021**, *394*, 107961. [CrossRef]
3. Smith, D.M.; Oommen, T.; Bowman, L.J.; Gierke, J.S.; Vitton, S.J. Hazard Assessment of Rainfall-Induced Landslides: A Case Study of San Vicente Volcano in Central El Salvador. *Nat. Hazards* **2015**, *75*, 2291–2310. [CrossRef]
4. Froude, M.J.; Petley, D.N. Global Fatal Landslide Occurrence from 2004 to 2016. *Nat. Hazards Earth Syst. Sci.* **2018**, *18*, 2161–2181. [CrossRef]
5. Dikshit, A.; Sarkar, R.; Pradhan, B.; Segoni, S.; Alamri, A.M. Rainfall Induced Landslide Studies in Indian Himalayan Region: A Critical Review. *Appl. Sci.* **2020**, *10*, 2466. [CrossRef]
6. Kanungo, D.P.; Sharma, S. Rainfall Thresholds for Prediction of Shallow Landslides around Chamoli-Joshimath Region, Garhwal Himalayas, India. *Landslides* **2014**, *11*, 629–638. [CrossRef]
7. Can, E. Investigation of Landslide Potential Parameters on Zonguldak-Ereğli Highway and Adverse Effects of Landslides in the Region. *Environ. Monit. Assess.* **2014**, *186*, 2435–2447. [CrossRef]
8. Teja, T.S.; Dikshit, A.; Satyam, N. Determination of Rainfall Thresholds for Landslide Prediction Using an Algorithm-Based Approach: Case Study in the Darjeeling Himalayas, India. *Geosciences* **2019**, *9*, 302. [CrossRef]
9. Dikshit, A.; Sarkar, R.; Satyam, N. Probabilistic Approach toward Darjeeling Himalayas Landslides-A Case Study. *Cogent Eng.* **2018**, *5*, 1537539. [CrossRef]
10. Chen, Y.; Li, B.; Xu, Y.; Zhao, Y.; Xu, J. Field Study on the Soil Water Characteristics of Shallow Layers on Red Clay Slopes and Its Application in Stability Analysis. *Arab. J. Sci. Eng.* **2019**, *44*, 5107–5116. [CrossRef]
11. Guzzetti, F.; Peruccacci, S.; Rossi, M.; Stark, C.P. The Rainfall Intensity-Duration Control of Shallow Landslides and Debris Flows: An Update. *Landslides* **2008**, *5*, 3–17. [CrossRef]
12. Abraham, M.T.; Satyam, N.; Rosi, A.; Pradhan, B.; Segoni, S. The Selection of Rain Gauges and Rainfall Parameters in Estimating Intensity-Duration Thresholds for Landslide Occurrence: Case Study from Wayanad (India). *Water* **2020**, *12*, 1000. [CrossRef]
13. Lari, S.; Frattini, P.; Crosta, G.B. A Probabilistic Approach for Landslide Hazard Analysis. *Eng. Geol.* **2014**, *182*, 3–14. [CrossRef]
14. Glade, T.; Crozier, M.; Smith, P. Applying Probability Determination to Refine Landslide-Triggering Rainfall Thresholds Using an Empirical "Antecedent Daily Rainfall Model". *Pure Appl. Geophys.* **2000**, *157*, 1059–1079. [CrossRef]
15. Abraham, M.T.; Satyam, N.; Pradhan, B.; Alamri, A.M. Forecasting of Landslides Using Rainfall Severity and Soil Wetness: A Probabilistic Approach for Darjeeling Himalayas. *Water* **2020**, *12*, 804. [CrossRef]
16. Tufano, R.; Cesarano, M.; Fusco, F.; Vita, P. De Probabilistic Approaches for Assessing Rainfall Thresholds Triggering Shallow Landslides. The Study Case of the Peri-Vesuvian Area (Southern Italy). *Ital. J. Eng. Geol. Environ.* **2019**, *2019*, 105–110. [CrossRef]
17. Capparelli, G.; Tiranti, D. Application of the MoniFLaIR Early Warning System for Rainfall-Induced Landslides in Piedmont Region (Italy). *Landslides* **2010**, *7*, 401–410. [CrossRef]
18. Dikshit, A.; Satyam, N. Application of FLaIR Model for Early Warning System in Chibo Pashyor, Kalimpong, India for Rainfall-Induced Landslides. *Nat. Hazards Earth Syst. Sci. Discuss.* **2017**, 295. [CrossRef]
19. Panchal, S.; Shrivastava, A.K. A Comparative Study of Frequency Ratio, Shannon's Entropy and Analytic Hierarchy Process (Ahp) Models for Landslide Susceptibility Assessment. *ISPRS Int. J. Geo-Inf.* **2021**, *10*, 603. [CrossRef]
20. Das, S.; Sarkar, S.; Kanungo, D.P. GIS-Based Landslide Susceptibility Zonation Mapping Using the Analytic Hierarchy Process (AHP) Method in Parts of Kalimpong Region of Darjeeling Himalaya. *Environ. Monit. Assess.* **2022**, *194*, 234. [CrossRef]
21. Ibrahim, M.B.; Mustaffa, Z.; Balogun, A.B.; Indra, S.H.H.; Nur Ain, A. Landslide's Analysis and Hazard Mapping Based on ANALYTIC HIERARCHY PROCESS (AHP) Using GIS, in Lawas, Sabah-Sarawak. *IOP Conf. Ser. Earth Environ. Sci.* **2022**, *1064*, 012031. [CrossRef]

22. Selamat, S.N.; Majid, N.A.; Taha, M.R.; Osman, A. Application of Geographical Information System (GIS) Using Artificial Neural Networks (ANN) for Landslide Study in Langat Basin, Selangor. *IOP Conf. Ser. Earth Environ. Sci.* **2022**, *1064*, 012052. [CrossRef]

23. Pradhan, B.; Al-Najjar, H.A.H.; Sameen, M.I.; Mezaal, M.R.; Alamri, A.M. Landslide Detection Using a Saliency Feature Enhancement Technique from LiDAR-Derived DEM and Orthophotos. *IEEE Access* **2020**, *8*, 121942–121954. [CrossRef]

24. Singh, N.; Gupta, S.K.; Shukla, D.P. Analysis of Landslide Reactivation Using Satellite Data: A Case Study of Kotrupi Landslide, Mandi, Himachal Pradesh, India. *Int. Arch. Photogramm. Remote Sens. Spat. Inf. Sci.* **2020**, *42*, 137–142. [CrossRef]

25. Tiwari, B.; Ajmera, B. Physical Modelling of Rain-Induced Landslides. In *Landslide Dynamics: ISDR-ICL Landslide Interactive Teaching Tools*; Springer: Cham, Switzerland, 2018; pp. 277–285.

26. Matziaris, V.; Marshall, A.M.; Heron, C.M.; Yu, H.S. Centrifuge Model Study of Thresholds for Rainfall-Induced Landslides in Sandy Slopes. *IOP Conf. Ser. Earth Environ. Sci.* **2015**, *26*, 012032. [CrossRef]

27. Li, C.; Yao, D.; Wang, Z.; Liu, C.; Wuliji, N.; Yang, L.; Li, L.; Amini, F. Model Test on Rainfall-Induced Loess–Mudstone Interfacial Landslides in Qingshuihe, China. *Environ. Earth Sci.* **2016**, *75*, 835. [CrossRef]

28. Huang, X.; Dong, Y. Study on Physical and Mechanical Properties of Soil in a Loess Landslide. *J. Phys. Conf. Ser.* **2023**, *2424*, 012010. [CrossRef]

29. Rahardjo, H.; Ong, T.H.; Rezaur, R.B.; Leong, E.C. Factors Controlling Instability of Homogeneous Soil Slopes under Rainfall. *J. Geotech. Geoenviron. Eng.* **2007**, *133*, 1532–1543. [CrossRef]

30. Acharya, K.P.; Bhandary, N.P.; Dahal, R.K.; Yatabe, R. Seepage and Slope Stability Modelling of Rainfall-Induced Slope Failures in Topographic Hollows. *Geomat. Nat. Hazards Risk* **2016**, *7*, 721–746. [CrossRef]

31. Singh, A.K.; Kundu, J.; Sarkar, K. Stability Analysis of a Recurring Soil Slope Failure along NH-5, Himachal Himalaya, India. *Nat. Hazards* **2018**, *90*, 863–885. [CrossRef]

32. Paswan, A.P.; Shrivastava, A.K. Stability Analysis of Rainfall-Induced Landslide. In Proceedings of the 3rd International Online Conference on Emerging Trends in Multi-Disciplinary Research "ETMDR-2022", Jaipur, Rajasthan, India, 20–22 January 2022; pp. 505–509.

33. Paswan, A.P.; Shrivastava, A.K. Numerical Modelling of Rainfall-Induced Landslide. In Proceedings of the International e-Conference on Sustainable Development & Recent Trends in Civil Engineering, New Delhi, India, 4–5 January 2022; pp. 8–13.

34. Jing, F.; Ling, H.S.; Xiuli, D.; Jinlong, W. Influence of Rainfall on Transient Seepage Field of Deep Landslides: A Case Study of Area II of Jinpingzi Landslide. *IOP Conf. Ser. Earth Environ. Sci.* **2020**, *570*, 022056. [CrossRef]

35. Tufano, R.; Formetta, G.; Calcaterra, D.; De Vita, P. Hydrological Control of Soil Thickness Spatial Variability on the Initiation of Rainfall-Induced Shallow Landslides Using a Three-Dimensional Model. *Landslides* **2021**, *18*, 3367–3380. [CrossRef]

36. Paswan, A.P.; Shrivastava, A.K. Modelling of Rainfall - Induced Landslide: A Threshold-Based Approach. *Arab. J. Geosci.* **2022**, *15*, 795. [CrossRef]

37. Dahal, R.K.; Hasegawa, S.; Nonomura, A.; Yamanaka, M.; Masuda, T.; Nishino, K. Failure Characteristics of Rainfall-Induced Shallow Landslides in Granitic Terrains of Shikoku Island of Japan. *Environ. Geol.* **2009**, *56*, 1295–1310. [CrossRef]

38. Intrieri, E.; Gigli, G.; Mugnai, F.; Fanti, R.; Casagli, N. Design and Implementation of a Landslide Early Warning System. *Eng. Geol.* **2012**, *147–148*, 124–136. [CrossRef]

39. Zhi, M.; Shang, Y.; Zhao, Y.; Lü, Q.; Sun, H. Investigation and Monitoring on a Rainfall-Induced Deep-Seated Landslide. *Arab. J. Geosci.* **2016**, *9*, 182. [CrossRef]

40. Kanungo, D.P.; Maletha, A.K.; Singh, M. Ground Based Wireless Instrumentation and Real Time Monitoring of Pakhi Landslide, Garhwal Himalayas, Uttarakhand (India). In *Advancing Culture of Living with Landslides*; Springer: Cham, Switzerland, 2017. [CrossRef]

41. Guerriero, L.; Guerriero, G.; Grelle, G.; Guadagno, F.M.; Revellino, P. Brief Communication: A Low-Cost Arduino®-Based Wire Extensometer for Earth Flow Monitoring. *Nat. Hazards Earth Syst. Sci.* **2017**, *17*, 881–885. [CrossRef]

42. Abraham, M.T.; Satyam, N.; Pradhan, B.; Alamri, A.M. Iot-Based Geotechnical Monitoring of Unstable Slopes for Landslide Early Warning in the Darjeeling Himalayas. *Sensors* **2020**, *20*, 2611. [CrossRef] [PubMed]

43. Uchimura, T.; Towhata, I.; Anh, T.T.L.; Fukuda, J.; Bautista, C.J.B.; Wang, L.; Seko, I.; Uchida, T.; Matsuoka, A.; Ito, Y.; et al. Simple Monitoring Method for Precaution of Landslides Watching Tilting and Water Contents on Slopes Surface. *Landslides* **2010**, *7*, 351–357. [CrossRef]

44. Qiao, S.; Feng, C.; Yu, P.; Tan, J.; Uchimura, T.; Wang, L.; Tang, J.; Shen, Q.; Xie, J. Investigation on Surface Tilting in the Failure Process of Shallow Landslides. *Sensors* **2020**, *20*, 2662. [CrossRef]

45. Artese, G.; Perrelli, M.; Artese, S.; Meduri, S.; Brogno, N. POIS, a Low Cost Tilt and Position Sensor: Design and First Tests. *Sensors* **2015**, *15*, 10806–10824. [CrossRef]

46. Dikshit, A.; Satyam, D.N.; Towhata, I. Early Warning System Using Tilt Sensors in Chibo, Kalimpong, Darjeeling Himalayas, India. *Nat. Hazards* **2018**, *94*, 727–741. [CrossRef]

47. Dahal, R.K. Rainfall-Induced Landslides in Nepal. *Int. J. Eros. Control Eng.* **2012**, *5*, 1–8. [CrossRef]

48. Kelleners, T.J.; Soppe, R.W.O.; Robinson, D.A.; Schaap, M.G.; Ayars, J.E.; Skaggs, T.H. Calibration of Capacitance Probe Sensors Using Electric Circuit Theory. *Soil Sci. Soc. Am. J.* **2004**, *68*, 430–439. [CrossRef]

49. Placidi, P.; Gasperini, L.; Grassi, A.; Cecconi, M.; Scorzoni, A. Characterization of Low-Cost Capacitive Soil Moisture Sensors for IoT Networks. *Sensors* **2020**, *20*, 3585. [CrossRef]

50. Hrisko, J. *Capacitive Soil Moisture Sensor Calibration with Arduino*; Maker Portal LLC: New York, NY, USA, 2020; pp. 1–24.

51. Ida, N. *Engineering Electromagnetics*; Springer: Cham, Switzerland, 2015. ISBN 9783319078052.
52. DFROBOT Capacitive Soil Moisture Sensor SKU:SEN0193 v.2.0. Available online: https://wiki.dfrobot.com/Capacitive_Soil_Moisture_Sensor_SKU_SEN0193 (accessed on 21 November 2022).
53. Ilamkar, P.T.; Kohli, A. Report on Geological Assessment of Kotrupi Landslide, Mandi—Jogindernagar—Pathankot National Highway (N.H.-154), Tehsil Padhar, District Mandi, Himachal Pradesh. *Geol. Surv. India* **2017**, *6*, 5–9.
54. *ISRO Kotrupi Landslide, Mandi District, Himachal Pradesh, A Preliminary Report*; National Remote Sensing Centre/ISRO: Hyderabad, India, 2017; Volume 2, pp. 4–6.
55. Prakash, S.; Kathait, A. *A Case Study on Kotrupi Landslide 2017, Mandi District, Himachal Pradesh National*; National Institute of Disaster Management (NIDM), Ministry of Home Affairs, Government of India: New Delhi, India, 2021. ISBN 9789382571612.
56. QGIS Development Team. *QGIS Desktop 3.16 User Guide*; Free Software Foundation: Boston, MA, USA, 2021; p. 1335. Available online: https://docs.qgis.org/3.16/pdf/en/QGIS-3.16-DesktopUserGuide-en.pdf (accessed on 21 November 2022).
57. *IS:2720 (Part 4)*; Methods of Test for Soils, Part 4: Grain Size Analysis. Bureau of Indian Standard: New Delhi, India, 1985; pp. 1–38.
58. GEO-SLOPE International Ltd. *Seepage Modeling with SEEP/W 2015*; Geostudio Help—GEO-SLOPE International Ltd.: Calgary, AB, Canada, 2012; p. 199.
59. *IS: 2720 (Part 5)*; Determination of Liquid and Plastic Limit. Bureau of Indian Standard: New Delhi, India, 1985; pp. 1–16.
60. *IS: 2720 (Part 7-1980)*; Determination of Water Content-Dry Density Relation Using Light Compaction. Bureau of Indian Standard: New Delhi, India, 2011; pp. 1–16.
61. Sharma, P.; Rawat, S.; Gupta, A.K. Study and Remedy of Kotropi Landslide in Himachal Pradesh, India. *Indian Geotech. J.* **2019**, *49*, 603–619. [CrossRef]
62. Anderson, S.A.; Sitar, N. Analysis of Rainfall-Induced Debris Flows. *J. Geotech. Eng.* **1995**, *121*, 544–552. [CrossRef]
63. *IS: 2720 (Part 11)*; Determination of the Shear Strength Parameters of a Specimen Tested in Unconsolidated Undrained Triaxial Compression without the Measurement of Pore Water Pressure. Bureau of Indian Standard: New Delhi, India, 1993.
64. Askarinejad, A.; Laue, J.; Zweidler, A.; Iten, M.; Bleiker, E.; Buschor, H.; Springman, S.M. Physical Modelling of Rainfall Induced Landslides under Controlled Climatic Conditions. In Proceedings of the Eurofuge 2012, 2nd Eurofuge Conference on Physical Modelling in Geotechnics, Deltares, Delft, The Netherlands, 23–24 April 2012.
65. Luo, Y.; He, S.M.; Chen, F.Z.; Li, X.P.; He, J.C. A Physical Model Considered the Effect of Overland Water Flow on Rainfall-Induced Shallow Landslides. *Geoenviron. Disasters* **2015**, *2*, 8. [CrossRef]
66. Iverson, R.M. Landslide Triggering by Rain Infiltration. *Water Resour. Res.* **2000**, *36*, 1897–1910. [CrossRef]
67. Godt, J.W.; Baum, R.L.; Lu, N. Landsliding in Partially Saturated Materials. *Geophys. Res. Lett.* **2009**, *36*, L02403. [CrossRef]
68. Pradhan, S.P.; Panda, S.D.; Roul, A.R.; Thakur, M. Insights into the Recent Kotropi Landslide of August 2017, India: A Geological Investigation and Slope Stability Analysis. *Landslides* **2019**, *16*, 1529–1537. [CrossRef]
69. Mali, N.; Shukla, D.P.; Kala, V.U. Identifying Geotechnical Characteristics for Landslide Hazard Indication: A Case Study in Mandi, Himachal Pradesh, India. *Arab. J. Geosci.* **2022**, *15*, 144. [CrossRef]
70. Uchimura, T.; Towhata, I.; Wang, L.; Nishie, S.; Yamaguchi, H.; Seko, I.; Qiao, J. Precaution and Early Warning of Surface Failure of Slopes Using Tilt Sensors. *Soils Found.* **2015**, *55*, 1086–1099. [CrossRef]
71. Dixon, N.; Smith, A.; Flint, J.A.; Khanna, R.; Clark, B.; Andjelkovic, M. An Acoustic Emission Landslide Early Warning System for Communities in Low-Income and Middle-Income Countries. *Landslides* **2018**, *15*, 1631–1644. [CrossRef]

Article

Cross-Correlation Analysis of the Stability of Heterogeneous Slopes

Yukun Li [1], Faming Zhang [1], Tian-Chyi Jim Yeh [2,*], Xiaolan Hou [1] and Menglong Dong [1]

[1] School of Earth Sciences and Engineering, Hohai University, Nanjing 211100, China; li_yukun@hhu.edu.cn (Y.L.); zhangfm@hhu.edu.cn (F.Z.)

[2] Department of Hydrology and Atmospheric Sciences, University of Arizona, Tucson, AZ 85721, USA

* Correspondence: yeh@hwr.arizona.edu

Abstract: Geologic material properties of hillslopes are inherently heterogeneous, with complex layering structures due to geological deposition processes. Lacking detailed sampling of the properties' spatial distribution has led to the stochastic representation of the properties to address uncertainty in the hillslope stability evaluation. This study treats the spatial distributions of the shear strength parameters, the cohesion (c), and the internal friction angle (φ), in a synthetic two-dimensional slope as stochastic random fields characterized by their means, variances, and correlation scales. This study then evaluates the cross-correlation between these parameters and the factor of safety (FS) using unconditional Monte Carlo simulation (MCS). Different from classical sensitivity analyses, the cross-correlation analysis of FS and the stochastic parameter fields stresses the importance of the orientation of the large-scale geological layering, the correlation between the geological media's cohesion, and the internal friction angle at the local scale on the probability and uncertainty of failure of the heterogeneous hillslope. The analysis further guides the field sampling strategy to reduce uncertainty in the slope stability analysis due to unknown heterogeneity. More importantly, it suggests the location of stability reinforcement measures. The results of this study provide cost-effective tools for geoengineers to deal with field slope stability analysis under uncertainty.

Keywords: correlation scales; cross-correlation analysis; shear strength parameters; slope stability; spatial variability

1. Introduction

Shear strength parameters (cohesion (c) and internal friction angle (φ)) are the critical parameters for evaluating slope stability. These parameters exhibit spatial variability at different scales due to complex geological processes [1–3]. Many previous studies have concluded that the spatial variability of geotechnical properties is vital in slope stability evaluations [4–6]. For example, Qi et al. [7] investigated the effect of the spatial variability of shear strength parameters on a two-dimensional slope's critical slip surface distribution. Griffiths et al. [8] and Jiang et al. [9] suggested that ignoring the spatial variability of the shear strength parameters would lead to an underestimation of the probability of slope failure when the coefficient of variation of the shear strength parameters was significant. The slope stability evaluated using the mean value of the parameter could be misleading. Cho [10] emphasized the importance of the spatial variability of soil mechanics' parameters in evaluating failure probability. Additionally, the effect of the spatial variability of soil properties is crucial when the slope risk assessment is over large areas due to both the variability and lack of measurements [11,12]. Based on genetic algorithms and machine learning, Miao et al. [13,14] performed displacement prediction and landslide susceptibility mapping over a large area and evaluated its uncertainty.

In recent years, geostatistical random field theory has been used to describe the heterogeneity of parameters, using its mean, variance, and correlation scales to describe

the most probable values, variability, and spatial structure of the parameter fields [15]. The heterogeneous parameter field is statistically isotropic when the horizontal correlation scale is equal to the vertical correlation scale. The field is statistically anisotropic when the horizontal correlation scale is different from the vertical correlation scale.

Combining random fields and Monte Carlo simulations (MCS), one can conduct a cross-correlation analysis of heterogeneous shear-strength parameters and slope stability. Cross-correlation analysis is a method that reveals the spatial relationship between parameters and processes, considering the variance and spatial structure of the parameters. Recently, Cai et al. [16] proposed an effective sampling strategy in slope stability evaluation based on the cross-correlation analysis of shear strength parameters and the factor of safety (*FS*), defined as the ratio of the slope's absolute strength to the actual applied load. Cross-correlation analysis is widely used in many fields, such as underground engineering and groundwater science. Using cross-correlation analysis, Gao et al. [17] investigated the spatial relationship between the rock parameters of the unlined rock caverns and the displacement at a location of interest. Mao et al. [18] studied the relationship between observed heads and hydraulic properties at different times and locations of unconfined aquifers during pumping tests. Sun et al. [19] proposed a temporal sampling strategy based on the cross-correlation analysis of hydraulic parameters and observed hydraulic heads.

Most current studies have investigated the effect of the coefficient of variation of parameters on slope stability with statistical isotropic media. However, due to sedimentation processes, geotechnical material often displays a layered structure [7,20–23]. The failure types of slopes with layered structures are generally translational slides, mudslides, and creep-fatigue [24–26]. That is, the correlation scales in different directions of the parameters are different, which leads to the fact that parameter fields with statistical anisotropy are standard. Moreover, Cai et al. [27] developed an analytical approach for the reliability analysis of infinite slope stability in the presence of spatially variable shear-strength parameters. They concluded that the p_f increases when the correlation between c and $\tan\varphi$ increases. Griffiths et al. [8] and Jiang et al. [9] obtained similar conclusions by studying two-dimensional heterogeneous slopes using the random finite element method. The correlation between c and $\tan\varphi$ significantly influences the probability of slope failure. However, the influence of the correlation between c and $\tan\varphi$ on slope stability considering parameter statistical anisotropy has not been comprehensively studied. Likewise, studies have compared the effect of the conditional random field with the unconditional random field on slope stability analysis using MCS with the finite element method. They concluded that conditional random field simulations could address the reduction in uncertainty due to conditioning with sampled parameters in evaluating slope stability [28–31]. Nonetheless, these studies have not addressed the vital issue of reducing uncertainty by selecting sampling locations. This issue (where to sample and how many sampling locations) to reduce the uncertainty is critical since only a limited number of samples is available in field situations.

This paper investigates the effect of statistical anisotropy of shear strength parameters on slope stability. We first introduce the influence of the correlation scale on the parameter distribution and the method of cross-correlation analysis between the parameters and *FS*. Then, we use a two-dimensional slope with statistical isotropy to analyze the cross-correlation between parameters and *FS*. The comparison of the correlation analysis, sensitivity analysis, and traditional limit equilibrium method comes next. The analyses of the cross-correlations between parameters and *FS*, and the influences of the correlation scales on slope stability in statistically anisotropic media are investigated. Lastly, using conditional random fields with MCS, we compared the uncertainty in evaluating slope stability for four different sampling schemes to validate the results of the cross-correlation analysis.

2. Methodology

2.1. Random Field Modeling of Heterogeneity

This study adopts the random field theory to describe the heterogeneity of shear strength parameters. The impossibility of obtaining the parameter values at every slope location recommends that we consider the c (or φ) of each position as a random variable. A collection of these random variables of c (or φ) in the entire slope becomes a random field characterized by a joint probability density function with mean, variance, and autocorrelation function, which describes the probability of a parameter value at any slope location. The mean represents the most likely value of the parameter, and the variance represents its average deviation from the actual value (i.e., uncertainty) due to variability and lack of measurements. On the other hand, the autocorrelation function quantifies the parameter's spatial structure (average spatial distribution of the clusters of the geotechnical properties in the slope).

Suppose the slope has $n \times n$ random variables, and i and $j = 1,2 \ldots , n$, a two-dimensional autocorrelation function is represented as follows:

$$\rho_{ij} = \exp\left[-2\left(\frac{|x_i - x_j|}{\lambda_x} + \frac{|y_i - y_j|}{\lambda_y}\right)\right] \tag{1}$$

where ρ_{ij} is the autocorrelation coefficient between the parameter at location (x_i, y_i) and location (x_j, y_j), and λ_x and λ_y are the horizontal and vertical correlation scales, respectively. Many other forms of the autocorrelation function are available. They all are ensemble statistics (i.e., general knowledge). We, therefore, chose the most simplistic one. This study considers the correlation scales of c and $\tan\varphi$ as the same.

Physically, the correlation scale represents the average dimensions (e.g., length, width, and thickness) of heterogeneity (e.g., layers or stratifications) within the domain [32]. With specified mean, variance, and correlation scales, numerous realizations of parameter distributions can be generated with different random seeds by a spectral representation method [33,34]. In order to avoid negative values while generating the random fields, the natural log-normal distribution of c and $\tan\varphi$ are employed. Figure 1 shows six realizations of the cohesion parameter field with the same mean and variance ($\mu_c = 15 \text{ kN/m}^2$, $\sigma_c = 7.5 \text{ kN/m}^2$), but with different correlation scales. These fields are called statistically isotropic when the λ_x is the same as the λ_y (Figure 1a,b), and statistically anisotropic when the λ_x is different from the λ_y (Figure 1c–f). In Figure 1c,d, the correlation scales are 1 m in the vertical direction and 5 m and 10 m in the horizontal direction, respectively. As the λ_x becomes large, the strong and weak zones extend greatly in the horizontal direction, and the slope shows an apparent horizontal layered structure. Figure 1e,f display the cases where $\lambda_x = 1$ m, $\lambda_y = 5$ m and $\lambda_x = 1$ m, $\lambda_y = 10$ m, respectively. The slope exhibits a vertically layered structure as the λ_y becomes greater than the λ_x. In this study, we consider different cases as follows. For statistical isotropy: $\lambda_x = \lambda_y = 1$ m; for statistical horizontal anisotropy: $\lambda_y = 1$ m, $\lambda_x = 5$ m, 10 m, 20 m, 40 m, 80 m, respectively; for statistical vertical anisotropy: $\lambda_x = 1$ m, $\lambda_y = 5$ m, 10 m, 20 m, 40 m, respectively.

2.2. Slope Stability Analysis

MCS is one of the widely utilized methods to estimate the probability of failure and the reliability of a slope with the general knowledge of the mean, variance, and correlation scales of the geotechnical properties of a hill slope. This study, different from many previous studies, adopts the MCS to investigate the effects of correlation scales on the analysis of the probability of failure and reliability of a slope and guides the sampling scheme to reduce the uncertainty of our estimated probability and reliability.
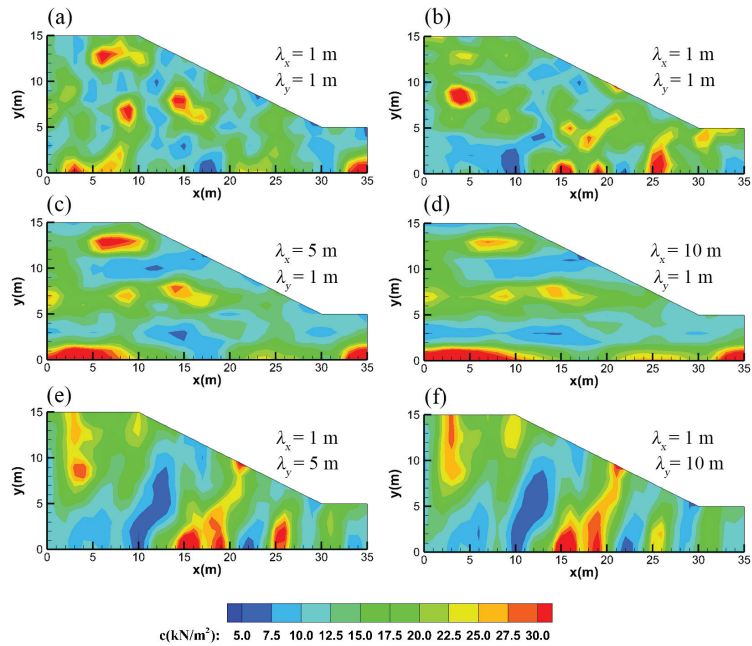
Figure 1. Numerically generated realizations of c in different correlation scales: (**a**,**b**) $\lambda_x = \lambda_y = 1$ m, with different random seed, (**c**) $\lambda_x = 5$ m, $\lambda_y = 1$ m, (**d**) $\lambda_x = 10$ m, $\lambda_y = 1$ m, (**e**) $\lambda_x = 1$ m, $\lambda_y = 5$ m, and (**f**) $\lambda_x = 1$ m, $\lambda_y = 10$ m.

For this purpose, a two-dimensional synthetic slope model for plane strain analysis (Figure 2) with a slope height $H = 10$ m and slope inclination $\alpha = 26.6°$ was discretized into 385 elements with 1 m × 1 m in size, and some of them are truncated because of the slope surface. The left and right boundaries of the model are zero horizontal displacements ($u_x = 0$ m), the bottom boundaries are zero horizontal and vertical displacements ($u_x = 0$ m, $u_y = 0$ m), and the slope surface is free displacement. The slope is assumed to be subjected to gravity loads only and consists of elastic–perfectly plastic soils following the Mohr–Coulomb failure criterion. Specifically, the loading stress at each element is the total weight of the element above, and the shear strength of each element follows the Mohr–Coulomb failure criterion. Other complex or advanced constitutive models [35–37] or numerical simulation methods [38] could be used with corresponding randomized input parameters. Table 1 lists the statistics of soil mechanical parameters, except for their correlation scales. Subsequently, the corresponding *FS* for the entire slope was evaluated based on the finite element strength reduction method (SRM) [39,40]. The program for calculating *FS* in this study is mainly based on the program p64 [40], and the main difference lies in the automatic MCS and the search for the critical strength reduction factor. The SRM has been widely used due to its practicality and reliability. The factor of safety (*FS*) is defined as the proportion by which c and $\tan\varphi$ must be reduced in order to cause slope failure. The strength reduction based on the Mohr–Coulomb criterion is shown in the following equation [39,40]:

$$c_{\text{trial}} = \frac{c}{SRF} \tag{2}$$

$$\tan\varphi_{\text{trial}} = \frac{\tan\varphi}{SRF} \tag{3}$$

where *SRF* is the strength reduction factor; c_{trial} and $\tan\varphi_{\text{trial}}$ are the trial shear strength parameters, which decrease with an increase in *SRF*. Several gradually increasing values of

the *SRF* are tested, and the updated c_{trial} and $\tan\varphi_{\text{trial}}$ are used for elastoplastic analysis. When the algorithm does not converge for 1000 iterations, the slope is considered as having failed in this study. The smallest value of *SRF* causing failure is then interpreted as the factor of safety *FS*. For example, the *FS* of this slope using the mean values (Table 1) as input parameters, considering the slope as homogeneous, is 1.141.
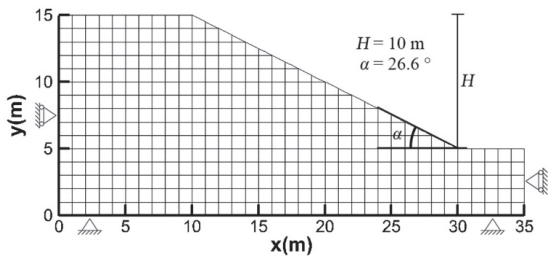

Figure 2. The synthetic slope model.

Table 1. Prior statistics of shear strength and other parameters for the numerical model.

Parameters	Values
Mean of cohesion, μ_c	15 kN/m^2
Coefficient of variation of cohesion, COV$_c$	0.5
Mean of friction angle, μ_φ	10°
Coefficient of variation of friction angle, COV$_\varphi$	0.5
Dilation angle, ψ	0°
Young's modulus, E	1×10^5 kPa
Poisson's ratio, v	0.3
Unit weight, γ	20 kN/m^3

Using this synthetic hill slope model and MCS, we evaluated the probability of slope failure p_f and the reliability index β according to the following formula [16]:

$$p_f = \frac{N_{FS<1}}{N} \tag{4}$$

$$\beta = \frac{\mu_{FS} - 1}{\sigma_{FS}} \tag{5}$$

where N is the number of realizations in MCS; in this study, N = 500 realizations. $N_{FS<1}$ is the number of realizations whose *FS* value is less than 1 (i.e., the slope fails). A small value of $N_{FS<1}$ implies that the probability of failure of the slope is small. In Equation (5), μ_{FS} is the mean value and σ_{FS} is the standard deviation of *FS* values of N realizations of MCS. ($\mu_{FS} - 1$) represents the slope stability and σ_{FS} represents the uncertainty in the evaluating *FS*. Therefore, the larger β is, the more reliable the estimated *FS* is and the smaller the probability of slope failure.

2.3. Cross-Correlation Analysis

In the next step, we investigate the sensitivity of a slope's *FS* to the parameters' heterogeneity at every part of the slope. Cross-correlation analysis is the sensitivity analysis of system response cast in a stochastic framework with the consideration of variability (variance) and spatial structure (correlation scales) of the heterogeneous slope (e.g., [18,19]). Specifically, a cross-correlation map represents the most likely relationship between system responses and spatial variability in system properties. This study applies the cross-correlation analysis to examine the relationship between shear strength parameters and slope stability:

$$\rho_{FSc}(\mathbf{x}_i) = \frac{1}{N} \sum_{k}^{N} \frac{(FS_k - \mu_{FS}) \times (c(\mathbf{x}_i, k) - \mu_c(\mathbf{x}_i))}{\sigma_{FS}\sigma_c(\mathbf{x}_i)} \tag{6}$$

$$\rho_{FS\tan\varphi}(\mathbf{x}_i) = \frac{1}{N} \sum_{k}^{N} \frac{(FS_k - \mu_{FS}) \times (\tan\varphi(\mathbf{x}_i, k) - \mu_{\tan\varphi}(\mathbf{x}_i))}{\sigma_{FS}\sigma_{\tan\varphi}(\mathbf{x}_i)} \tag{7}$$

where $\mathbf{x}_i$ is the position vector of the parameter considered; $\rho_{FSc}(\mathbf{x}_i)$ and $\rho_{FS\tan\varphi}(\mathbf{x}_i)$ are the cross-correlations between the cohesion and the internal friction angle at the location $\mathbf{x}_i$ and FS, respectively. FS_k is the FS at the k_{th} realization; $c(\mathbf{x}_i,k)$ is the cohesion at the location $\mathbf{x}_i$ and k_{th} realization; $\tan\varphi(\mathbf{x}_i,k)$ is the tangent of the internal friction angle at the location $\mathbf{x}_i$ and k_{th} realization. Lastly, $\sigma_c(\mathbf{x}_i)$ is the standard deviation of the cohesion; $\sigma_{\tan\varphi}(\mathbf{x}_i)$ is the standard deviation of $\tan\varphi$.

3. Results of Cross-Correlation Analysis for Statistical Isotropy

This section examines the cross-correlation between FS and two independent variables (cohesion c and the internal friction angle $\tan\varphi$) with correlation scales of 1 m in both horizontal and vertical directions (statistically isotropic cases). The cross-correlation maps between the shear strength parameters and FS (Figure 3) reveal that ρ_{FSc} is positive at the toe and the top of the slope (Figure 3a), suggesting a large c value at these areas leads to the greater FS value of the slope. On the other hand, the interior of the slope areas has a positive correlation between $\tan\varphi$ and FS (Figure 3b). The remaining areas have correlation values close to zero, meaning that shear strength in these areas (i.e., most of the slope surface and the back of the slope.) has little effect on the slope stability.
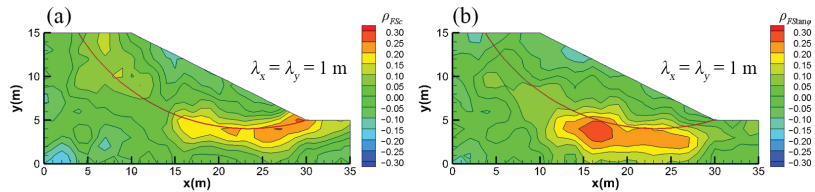

Figure 3. (**a**) Cross-correlation map of FS and c, (**b**) Cross-correlation map of FS and $\tan\varphi$ for statistical isotropy.

Comparing Figure 3a,b, we observe that the locations of the positive correlation regions of the two parameters are different. Such a difference implies that the mechanisms of c and $\tan\varphi$ on slope stability are different within the slope. Physically, c is the maximum shear stress a rupture surface can carry when the normal stress is absent. On the other hand, $\tan\varphi$ is the coefficient that converts the normal stress at the rupture surface to frictional force. According to the Mohr–Coulomb yield criterion, the shear strength of a geotechnical material is equal to the sum of c and the normal stress multiplied by $\tan\varphi$. In the interior of the slope, due to the gravity of the overlying material of the slope, the material in the interior is subjected to high normal stresses, and the coefficient $\tan\varphi$ becomes the key factor transforming the normal stress into the anti-slip force. The larger $\tan\varphi$ is, the greater the anti-slip force under the same normal stress. Therefore, the value of $\tan\varphi$ in the slope's interior greatly influences the slope stability.

On the other hand, at the toe and top of the slope, the geotechnical mass experiences low normal stress, and the material's cohesion c dictates the shear strength and influences slope stability. The above discussions should explain the differences in the cross-correlation patterns in Figure 3a,b. For this reason, one must recognize that the impact areas of these two parameters are different when evaluating slope stability.

Comparing the potential sliding surface (the red line in Figure 3) calculated by the limit equilibrium method [41] using the mean values of parameters, we observe that the region of positive correlation partially overlaps the surface. This result demonstrates that the cross-correlation analysis of FS and parameters pinpoint the slope's critical areas. Moreover,

the cross-correlation analysis identifies potential sliding zones in contrast to a single sliding surface obtained by the limit equilibrium method.

The sensitivity analysis results of *FS* to the cohesion (the sensitivity of *FS* to *c*, J_c, Figure 4a) and internal friction angle (the sensitivity of *FS* to tanφ, $J_{tan\varphi}$, Figure 4b) display similar patterns to those in Figure 3a,b, derived from MCS. The sensitivity analysis of *FS* to the parameter takes the following steps. First, the parameter at each location is set as the mean value, and the *FS* of the homogeneous slope is evaluated by the finite element strength-reduction method. Then, we applied a perturbation of the parameter at a spatial location $\mathbf{x}_i$, keeping the parameter at the other locations as the mean value. We subsequently evaluated the *FS* corresponding to this perturbation. The ratio of the change of *FS* to the perturbation is the sensitivity of *FS* to the parameter at this position. After calculating the sensitivity at each location, we derived a sensitivity map. The map shows that the sensitivity of *FS* to *c* is greater at the foot and top of the slope compared to other regions, and the sensitivity of *FS* to tanφ is more significant in the interior of the slope. Notice that the sensitivity analysis, based on the perturbation method, aims at the change of *FS* per change in the given mean value of the parameter, ignoring the variability (variance) and spatial structure (correlation scale) of the parameters [42]. Specifically, the cross-correlation analysis considers many possible slopes with heterogeneous parameter fields with the same mean parameter value but different perturbations and spatial structure patterns. It then summarizes the results statistically. Consequently, the sensitivity analysis results (Figure 4) differ from the cross-correlation analysis (Figure 3), and the cross-correlation analysis is most appropriate for cases where spatial parameter values are unknown (i.e., realistic field situations).
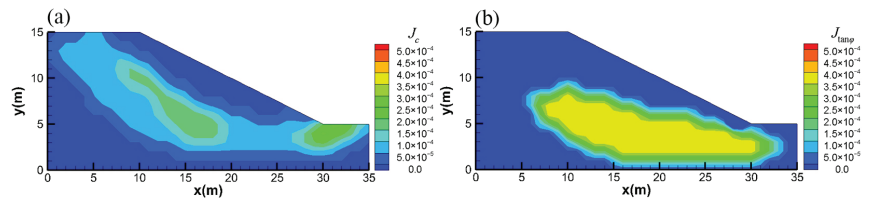

Figure 4. (**a**) Sensitivity map of *FS* to *c*, (**b**) sensitivity map of *FS* to tanφ.

4. Results of Cross-Correlation Analysis for Statistical Anisotropy

4.1. Statistical Horizontal Anisotropy (Horizontal Correlation Scale > Vertical Correlation Scale)

This section investigates the results of the cross-correlation analysis between *FS* and shear strength parameters (*c* and tanφ) with different λ_x values (Figure 5) while $\lambda_y = 1$ m. Figure 5a,c show the cross-correlation maps between *FS* and *c*, for λ_x of *c* equal to 5, 10, and 20 m, respectively. The cross-correlation maps between *FS* and tanφ, for λ_x of tanφ equal to 5, 10, and 20 m are presented in Figure 5d,f, respectively. We observe that the positive areas of ρ_{FSc} and $\rho_{FStan\varphi}$ expand as λ_x increases, but the areas are confined to the areas at the slope toe. Comparing the results to the cross-correlation map of the statistically isotropic parameters (Figure 3), we notice that ρ_{FSc} develops from the toe. In contrast, $\rho_{FStan\varphi}$ develops from the inside of the slope.

Figure 6a,d illustrate the probability of failure (p_f), reliability β index, the mean of *FS* (μ_{FS}), and the standard deviation of *FS* (σ_{FS}) as a function of the normalized horizontal correlation scale, respectively. The normalized horizontal correlation scale is $\lambda_x/(H/\tan\alpha)$, the ratio of the horizontal correlation scale to the horizontal projection of the slope length, $H/\tan\alpha$. Notice that α is the slope inclination angle. Since the correlation between *c* and tanφ (φ is the friction angle) is generally unclear [8,9,16], this study also examines the effect of perfectly positively, zero, and negatively correlated *c* and tanφ perturbation relationships and they are indicated by the red, green, and blue lines in these figures, respectively.
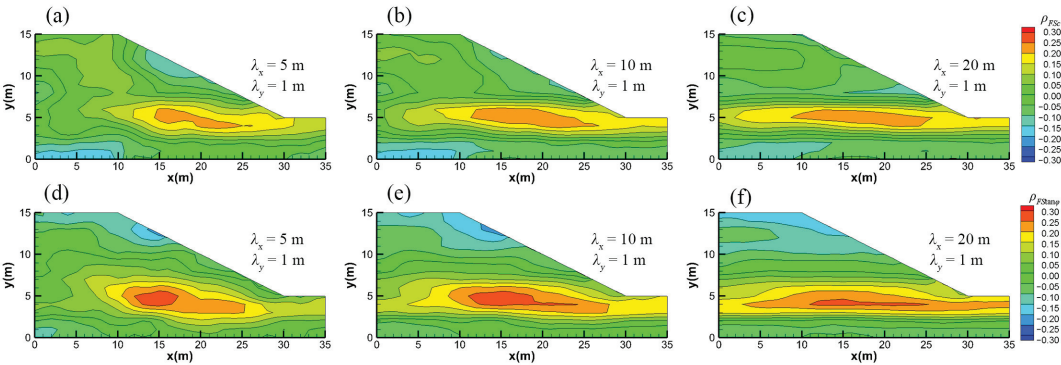
Figure 5. Cross-correlation maps of *FS* and *c* (**a**–**c**) and tan*φ* (**d**–**f**) under three different horizontal statistical anisotropic correlation scales.
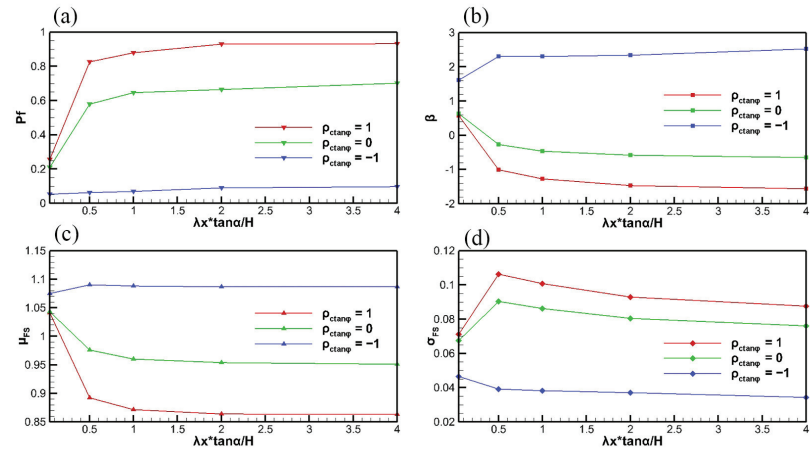
Figure 6. (**a**–**d**) are *pf*, *β*, μ_{FS} and σ_{FS} of *FS* obtained by MCS for different λ_x and $\rho_{c\tan\varphi}$ values.

According to these figures, if *c* and tan*φ* are positively correlated or uncorrelated (i.e., the red and green lines), the probability of failure in Figure 6a and the standard deviation of *FS* (σ_{FS}) in Figure 6d rapidly increase as $\lambda_x\tan\alpha/H$ approaches one and stabilize afterward. On the other hand, the reliability (*β*) (Figure 6b) and the mean of *FS* (μ_{FS}) (Figure 6c) decrease exponentially. These results stem from the fact that for horizontally layered slopes, the layer with the lowest parameters (such as the weak interlayer or the stratum with highly developed joints and fractures) controls the stability of the slope. A longer correlation scale means that the layer with the weakest strength covers most of the slope, and the slope is less stable. On the other hand, from the physical meaning of the correlation between *c* and tan*φ*, the higher the correlation is, the lower *c* is at a location, and the lower the tan*φ* at the same location. Therefore, the slope is less stable (i.e., the red line is higher than the green line in Figure 6a).

The blue lines in all figures depict the behaviors of these quantities for the case where *c* and tan*φ* are negatively correlated. The blue lines show that as $\lambda_x\tan\alpha/H$ increases, the p_f value increases slightly but remains very low (about 0.05), while the reliability *β* index increases and remains high at about 2.4. The value of μ_{FS} increases from 1.075 to 1.085 and remains constant over the rest of $\lambda_x(\tan\alpha/H)$. The value of σ_{FS} decreases first at $\lambda_x(\tan\alpha/H) = 0.5$ and remains almost constant at a small value. The trends are distinctly

different from when $\rho_{c\tan\varphi}$ is 1 or 0. The negative correlation means that a large c is at one location, and a small $\tan\varphi$ is at the same location or vice versa. As a result, the slope stability no longer decreases significantly or even increases slightly.

Overall, an underestimation of λ_x can result in an overestimated slope stability when evaluating the stability of horizontally layered slopes—the importance of identifying the spatial structure of the slope is clear.

4.2. Statistical Vertical Anisotropy (Horizontal Correlation Scale < Vertical Correlation Scale)

Figure 7 shows the cross-correlation map between *FS* and shear strength parameters (c and $\tan\varphi$) with different λ_y values when the slope has vertically stratified formations. Figure 7a–c illustrate the cross-correlation maps between *FS* and c, and λ_y of c with 5, 10, and 20 m, respectively, while their horizontal correlation scales are 1 m. These figures indicate a distinctly positive correlation between *FS* and c at the toe of the slope. Furthermore, as λ_y increases, the high correlation area becomes more concentrated and vertical, and the cross-correlation value weakens slightly.
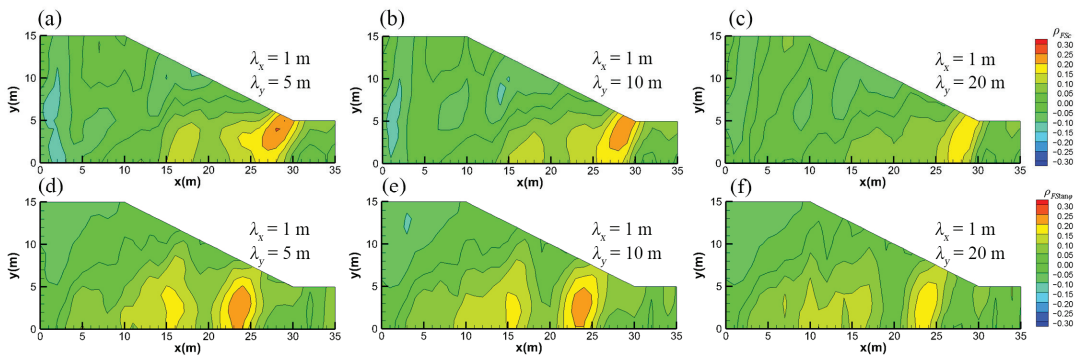

Figure 7. Cross-correlation maps of *FS* and c (**a–c**) and $\tan\varphi$ (**d–f**) under three different vertical statistical anisotropic correlation scales.

Figure 7d–f demonstrate the cross-correlation maps between *FS* and $\tan\varphi$, and λ_y of $\tan\varphi$ equal to 5, 10, and 20 m, respectively. We observe that *FS* and $\tan\varphi$ are positively correlated at the area $x = 20$ to 25 m and $y = 0$ to 5 m, and the cross-correlation decreases slightly as λ_y increases.

The behaviors of p_f, β, μ_{FS}, and σ_{FS} in the slopes with longer vertical correlation scales than the horizontal one as a function of λ_y/H (the vertical correlation scale normalized by the height of the slope, H) are displayed in Figure 8a–c, and d, respectively. First, we notice that the value of probability failure (p_f) in this case is much less than that in the horizontal layering slope (i.e., Figure 8a vs. Figure 6a), regardless of the effects of various factors as in Figure 6. In other words, vertical stratification (the orientation of the large-scale structures) plays a more dominant role than the others do in slope stability.

Nevertheless, Figure 8 shows that when $\rho_{c\tan\varphi}$ is 1 (the red line), with the increase in λ_y, p_f and σ_{FS} decrease, and μ_{FS} and β increase, indicative of the fact that as λ_y increases, the stability of the slope increases and the uncertainty of the evaluation decreases. This result stems from the fact that when a slope is vertically layered, the high-strength layer controls the stability, similar to anti-slip piles. The longer λ_y means that the layer with high strength is extensive, and when $\rho_{c\tan\varphi}$ is 1, the c is large and so is φ large, and the anti-slip pile can be effective, leading to high slope stability.
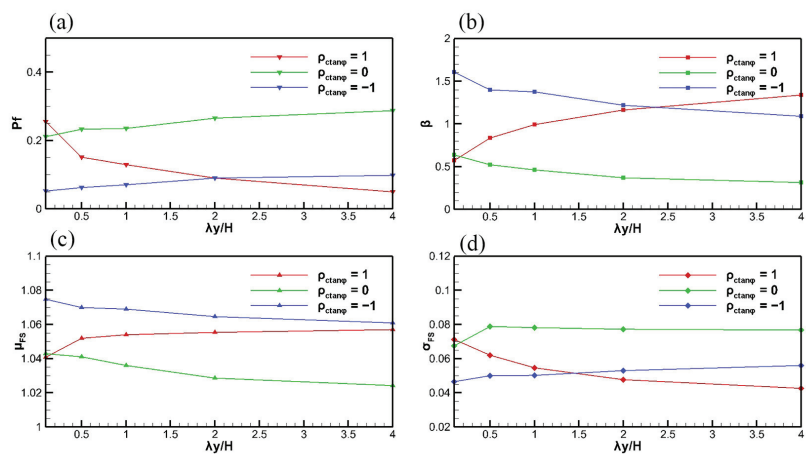
Figure 8. (**a–d**) are *pf*, *β*, μ_{FS}, and σ_{FS} of *FS* obtained by MCS for different λ_y and $\rho_{c\tan\varphi}$ values.

When $\rho_{c\tan\varphi}$ is 0 or -1 (the green and blue line in Figure 8), the increase in λ_y leads to increases in p_f and σ_{FS}, and it decreases μ_{FS} and β values, suggesting that increasing λ_y worsens the stability of the slope and increases the uncertainty of the evaluation. These trends are the opposite of when $\rho_{c\tan\varphi}$ is 1, likely because *c* and $\tan\varphi$ are uncorrelated or perfectly negatively correlated, and the effect of anti-slip piles weakens.

4.3. Effects of the Number of Realizations in MCS

All the results above are from 500 MCS. To ensure that the number of simulations is sufficient to obtain representative results, we plot Figure 9 to show the effect of the number of realizations on p_f and μ_{FS} at $\lambda_x = 10$ m and 20 m, respectively, and $\lambda_y = 1$ m, in these conditions, σ_{FS} are the maximums. As shown in the figure, the mean values of p_f and μ_{FS} fluctuate widely within 150 realizations but stabilize after more than 300 realizations, certifying the adequacies of the number of realizations used in the MCS and the results' representativeness.
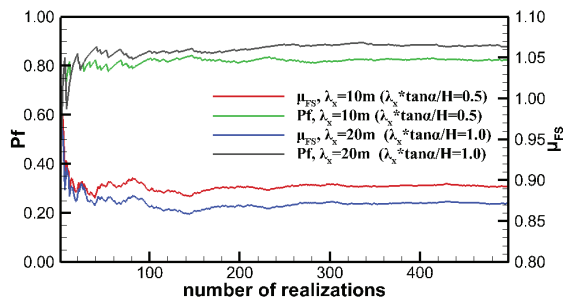
Figure 9. *Pf* and μ_{FS}, when $\lambda_y = 1$ m and $\lambda_x = 10$ m and 20 m, respectively, as functions of the number of realizations.

5. Effects of Conditional Random Fields

To demonstrate that sampling in highly correlated zones (conditioning on the stochastic fields) reduces the uncertainty in the *FS* assessment, we conducted numerical experiments considering two cases where only the cohesion field is a stochastic process. Case 1 used the distribution of *c* in Figure 1a as the reference field, and Case 2 used the *c* distribu-

tion in Figure 1c. The mean, variance, and λ_y of the random fields in the two cases were identical, except that λ_x was different.

We considered four sampling schemes (Figure 10). In Scheme 1, samples were taken at the toe of the slope at three 5 m deep vertical boreholes (Figure 10a). In Scheme 2, the three boreholes were near the slope top (Figure 10b). Scheme 3 took samples over a 15 m borehole horizontally into the slope at the corner of the slope (Figure 10c). The fourth scheme sampled a 15 m borehole horizontally near the top of the slope (Figure 10d). These four schemes took a soil sample every meter to obtain 15 samples. As such, we could evaluate the effects of the same number of parameter values in different correlation areas for conditioning on the estimates of *FS* of the slope.
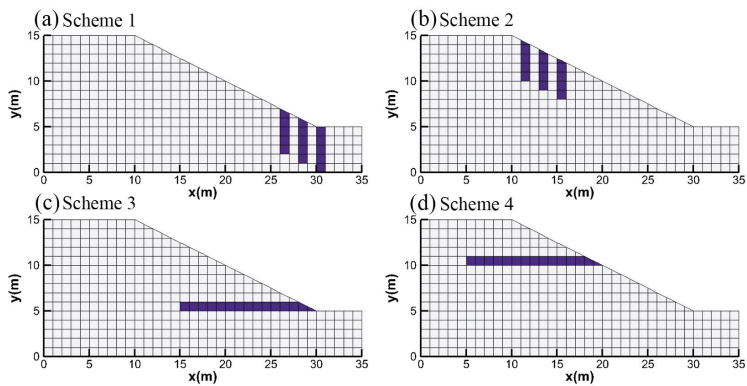

Figure 10. Borehole locations of four sampling schemes.

With the sampled data, 500 realizations of the conditional random field corresponding to each sampling scheme were generated using the Kriging Superposition Approach (KSA) [43,44]. The resulting conditional realizations honored the sampled values at the sampled locations and retained the specified spatial statistics of the random fields. Afterward, we used them to conduct MCS as the previous unconditional MCS, and the results are summarized in Table 2.

Table 2. The results of conditional MCS.

	Scheme 1	Scheme 2	Scheme 3	Scheme 4
μ_{FS} of Case 1	1.033	1.041	1.031	1.040
σ_{FS} of Case 1	0.066	0.072	0.058	0.072
μ_{FS} of Case 2	0.935	0.939	0.924	0.935
σ_{FS} of Case 2	0.094	0.105	0.082	0.112

The reference *FS* of Case 1 is 1.031. The μ_{FS} of sampling Scheme 3 is the closest to the FS of the reference since the sampling area is primarily in the high correlation region. Sampling Scheme 1, which samples a smaller portion of the highly correlated region, yields μFS value that is the second closest to the reference value. Since sampling Schemes 2 and 4 cover the minimal correlation between the parameters and FS, they yield a μ_{FS} that differs significantly from the reference value and is close to the μ_{FS} of the unconditional random simulation, indicative of their ineffectiveness for defining the actual factor of safety.

For Case 2, the reference FS is 0.922. The results of the conditional MCS are similar to Case 1, and the mean and standard deviation of FS are the best for sampling Scheme 3. Moreover, due to the apparent layered structure of Case 2 (λx = 5 m), Scheme 3 with horizontal borehole sampling yields significantly better results than the other three schemes. As expected, the uncertainty in the FS evaluated for sampling Scheme 3, which samples the most highly correlated areas, is the smallest in both Case 1 and Case 2. That is,

sampling the high correlation areas' parameters is critical for evaluating slope stability because it reduces uncertainty significantly more than sampling in other regions. As demonstrated in this example, cross-correlation analysis guides optimal borehole placement locations. Furthermore, we could suggest that focusing on the high correlation areas for slope reinforcement measures is essential since the same reinforcement measures will be more effective in the high correlation areas than in the low correlation areas.

6. Conclusions

Cross-correlation analysis of the shear strength parameters and *FS* of statistically anisotropic heterogeneous slopes shows that the large-scale heterogeneity structures dominate the stability of a slope. Specifically, with the given mean and variance of the shear strength parameters, the probability of failure of slopes with a long vertical correlation scale (vertical structure) is much smaller than that with a long horizontal correlation scale (horizontal structure).

In statistically isotropic parameter fields, the distributions of the high correlation areas of ρ_{FSc} and $\rho_{FS\tan\varphi}$ are different: the former distributes at the toe and top of the slope, and the latter in the interior of the slope.

For the slope with the long horizontal correlation scale, the high correlation area of shear strength parameters with *FS* is located at the toe of the slope and distributed horizontally. The larger λ_x is, the longer the extension of the area in the horizontal direction is. In addition, when *c* and $\tan\varphi$ are positively correlated or uncorrelated, the larger λ_x is, and the less stable the slope is. When *c* and $\tan\varphi$ are perfectly negatively correlated, the effect of λ_x on the stability of the slope decreases.

In the slope with a long vertical correlation scale, the high correlation area of the shear strength parameter with *FS* is located at the toe of the slope and distributed vertically. With the increase in λ_y, the correlation in the high correlation region slightly decreases, and the region's distribution becomes more vertical than others. Moreover, when *c* and $\tan\varphi$ are positively correlated, the larger λ_y is, and the more stable the slope is. When *c* and $\tan\varphi$ are negatively correlated or uncorrelated, the larger λ_y is, and the less stable the slope is.

This study further demonstrates that sampling in high cross-correlation regions can reduce the uncertainty in slope stability analysis. In addition, when the slope has an apparent layered structure (statistical anisotropy), the sampling direction consistent with its structure is recommended.

In summary, to evaluate the stability of a slope, first, one must detect the orientation of the large-scale structures (i.e., long correlation scales). The knowledge of the correlation between *c* and $\tan\varphi$ becomes essential, which dictates the probability of slope failure in the slopes with horizontal layering. The cross-correlation analysis presented in this study yields the location of the critical areas where shear strength parameters affect slope stability. Furthermore, these high cross-correlation regions guide the optimal borehole placement locations to reduce uncertainty in slope stability analysis and even for the selection of slope stability reinforcement locations.

Author Contributions: Conceptualization, Y.L. and T.-C.J.Y.; methodology, T.-C.J.Y. and Y.L.; software, Y.L. and T.-C.J.Y.; validation, F.Z. and M.D.; data curation, X.H.; writing—original draft preparation, Y.L.; writing—review and editing, T.-C.J.Y. and X.H. All authors have read and agreed to the published version of the manuscript.

References

1. Rackwitz, R. Reviewing probabilistic soils modelling. *Comput. Geotech.* **2000**, *26*, 199–223. [CrossRef]
2. Nielsen, D.R.; Biggar, J.W.; Erh, K.T. Spatial Variability of Field-measured Soil-water Characteristics. *Hilgardia* **1985**, *42*, 215–260. [CrossRef]
3. Phoon, K.K.; Kulhawy, F.H. Characterization of geotechnical variability. *Can. Geotech. J.* **1999**, *36*, 612–624. [CrossRef]
4. Xiao, T.; Li, D.Q.; Cao, Z.J.; Au, S.K.; Phoon, K.K. Three-dimensional slope reliability and risk assessment using auxiliary random finite element method. *Comput. Geotech.* **2016**, *79*, 146–158. [CrossRef]
5. Jiang, S.H.; Huang, J.; Griffiths, D.V.; Deng, Z.P. Advances in reliability and risk analyses of slopes in spatially variable soils: A state-of-the-art review. *Comput. Geotech.* **2022**, *141*, 104498. [CrossRef]
6. Griffiths, D.V.; Fenton, G.A. Probabilistic Slope Stability Analysis by Finite Elements. *J. Geotech. Geoenviron. Eng.* **2004**, *23*, 1390–1392. [CrossRef]
7. Qi, X.H.; Li, D.Q. Effect of spatial variability of shear strength parameters on critical slip surfaces of slopes. *Eng. Geol.* **2018**, *239*, 41–49. [CrossRef]
8. Griffiths, D.V.; Huang, J.; Fenton, G.A. Influence of spatial variability on slope reliability using 2-D random fields. *J. Geotech. Geoenviron. Eng.* **2009**, *135*, 1367–1378. [CrossRef]
9. Jiang, S.H.; Li, D.Q.; Zhang, L.M.; Zhou, C.B. Slope reliability analysis considering spatially variable shear strength parameters using a non-intrusive stochastic finite element method. *Eng. Geol.* **2014**, *168*, 120–128. [CrossRef]
10. Cho, S.E. Effects of spatial variability of soil properties on slope stability. *Eng. Geol.* **2007**, *92*, 97–109. [CrossRef]
11. Ciurleo, M.; Cascini, L.; Calvello, M. A Comparison of Statistical and Deterministic Methods for Shallow Landslide Susceptibility Zoning in Clayey Soils. *Eng. Geol.* **2017**, *223*, 71–81. [CrossRef]
12. Tropeano, G.; Silvestri, F.; Ausilio, E. An Uncoupled Procedure for Performance Assessment of Slopes in Seismic Conditions. *Bull. Earthq. Eng.* **2017**, *15*, 3611–3637. [CrossRef]
13. Miao, F.; Wu, Y.; Xie, Y.; Li, Y. Prediction of Landslide Displacement with Step-like Behavior Based on Multialgorithm Optimization and a Support Vector Regression Model. *Landslides* **2018**, *15*, 475–488. [CrossRef]
14. Miao, F.; Zhao, F.; Wu, Y.; Li, L.; Török, Á. Landslide Susceptibility Mapping in Three Gorges Reservoir Area Based on GIS and Boosting Decision Tree Model. *Stoch. Environ. Res. Risk Assess.* **2023**, *4*, 1–21. [CrossRef]
15. Yeh, T.C.J.; Ye, M.; Khaleel, R. Estimation of effective unsaturated hydraulic conductivity tensor using spatial moments of observed moisture plume. *Water Resour. Res.* **2005**, *41*, 1–12. [CrossRef]
16. Cai, J.S.; Yeh, T.C.J.; Yan, E.C.; Tang, R.X.; Hao, Y.H. Design of borehole deployments for slope stability analysis based on a probabilistic approach. *Comput. Geotech.* **2021**, *133*, 103909. [CrossRef]
17. Gao, X.; Yan, E.C.; Yeh, T.C.J.; Wang, Y.L.; Cai, J.S.; Hao, Y.H. Sequential back analysis of spatial distribution of geomechanical properties around an unlined rock cavern. *Comput. Geotech.* **2018**, *99*, 177–190. [CrossRef]
18. Mao, D.; Yeh, T.C.J.; Wan, L.; Lee, C.H.; Hsu, K.C.; Wen, J.C.; Lu, W. Cross-correlation analysis and information content of observed heads during pumping in unconfined aquifers. *Water Resour. Res.* **2013**, *49*, 713–731. [CrossRef]
19. Sun, R.; Yeh, T.C.J.; Mao, D.; Jin, M.; Lu, W.; Hao, Y. A temporal sampling strategy for hydraulic tomography analysis. *Water Resour. Res.* **2013**, *49*, 3881–3896. [CrossRef]
20. Zhao, C.; Gong, W.; Li, T.; Juang, C.H.; Tang, H.; Wang, H. Probabilistic characterization of subsurface stratigraphic configuration with modified random field approach. *Eng. Geol.* **2021**, *288*, 106138. [CrossRef]
21. Wang, M.; Tang, X.; Li, D.; Qi, X. Subset simulation for efficient slope reliability analysis involving copula- based cross-correlated random fields. *Comput. Geotech.* **2020**, *118*, 103326. [CrossRef]
22. Gong, W.; Zhao, C.; Juang, C.H.; Zhang, Y.; Tang, H.; Lu, Y. Coupled characterization of stratigraphic and geo-properties uncertainties—A conditional random field approach. *Eng. Geol.* **2021**, *294*, 106348. [CrossRef]
23. Ye, M.; Khaleel, R.; Yeh, T.C.J. Stochastic analysis of moisture plume dynamics of a field injection experiment. *Water Resour. Res.* **2005**, *41*, 1–13. [CrossRef]
24. Cruden, D.M.; Varnes, D.J. Landslide Types and Processes. In *Landslides: Investigation and Mitigation*; National Academy Press: Washington, WA, USA, 1996; Volume 247, pp. 36–75.
25. Terzaghi, K. Mechanism of Landslides. In *Application of Geology to Engineering Practice*; Geological Society of America: New York, NY, USA, 1950; pp. 83–123.
26. Leroueil, S. Natural Slopes and Cuts: Movement and Failure Mechanisms. *Géotechnique* **2001**, *51*, 197–243. [CrossRef]
27. Cai, J.S.; Yan, E.C.; Yeh, T.C.J.; Zha, Y.Y.; Liang, Y.; Huang, S.Y.; Wang, W.K.; Wen, J.C. Effect of spatial variability of shear strength on reliability of infinite slopes using analytical approach. *Comput. Geotech.* **2017**, *81*, 77–86. [CrossRef]
28. Johari, A.; Fooladi, H. Simulation of the conditional models of borehole's characteristics for slope reliability assessment. *Transp. Geotech.* **2022**, *35*, 100778. [CrossRef]
29. Liu, L.L.; Cheng, Y.M.; Zhang, S.H. Conditional random field reliability analysis of a cohesion-frictional slope. *Comput. Geotech.* **2017**, *82*, 173–186. [CrossRef]
30. Yang, R.; Huang, J.; Griffiths, D.V.; Sheng, D. Probabilistic Stability Analysis of Slopes by Conditional Random Fields. In Proceedings of the Geo-Risk, Denver, CO, USA, 4–7 June 2017; American Society of Civil Engineers: Reston, VA, USA, 2017; pp. 450–459. [CrossRef]

31. Johari, A.; Fooladi, H. Comparative study of stochastic slope stability analysis based on conditional and unconditional random field. *Comput. Geotech.* **2020**, *125*, 103707. [CrossRef]
32. Yeh, T.C.J.; Khaleel, R.; Carroll, K.C. *Flow through Heterogeneous Geologic Media*; Cambridge University Press: New York, NY, USA, 2015; ISBN 9781139879323.
33. Gutjahr, A.L. Fast fourier transforms for random field generation. In *New Mexico Tech Project Report 4-R58-2690R*; New Mexico Institute of Mining and Technology: Socorro, NM, USA, 1989; Volume 29, pp. 2385–2397.
34. Robin, M.J.L.; Gutjahr, A.L.; Sudicky, E.A.; Wilson, J.L. Cross-correlated random field generation with the direct Fourier Transform Method. *Water Resour. Res.* **1993**, *29*, 2385–2397. [CrossRef]
35. Elia, G.; Falcone, G.; Cotecchia, F.; Rouainia, M. Analysis of the Effects of Seasonal Pore Pressure Variations on the Slope Stability Through Advanced Numerical Modelling. In *Lecture Notes in Civil Engineering*; Springer International Publishing: Berlin/Heidelberg, Germany, 2020; Volume 40, pp. 184–194. ISBN 9783030213596.
36. Pedone, G.; Tsiampousi, A.; Cotecchia, F.; Zdravkovic, L. Coupled Hydro-Mechanical Modelling of Soil–Vegetation–Atmosphere Interaction in Natural Clay Slopes. *Can. Geotech. J.* **2022**, *59*, 272–290. [CrossRef]
37. Gao, X.; Yan, E.-C.; Yeh, T.-C.J.; Wang, Y.; Liang, Y.; Hao, Y. Reliability Analysis of Hydrologic Containment of Underground Storage of Liquefied Petroleum Gas. *Tunn. Undergr. Sp. Technol.* **2018**, *79*, 12–26. [CrossRef]
38. Zhang, X.; Bi, J.; Guo, D.; Li, Z. Numerical Simulation of Stability Analysis of Soil Slope Using General Particle Dynamics with Elastic-plastic Constitutive Model. *Mater. Des. Process. Commun.* **2019**, *1*, e51. [CrossRef]
39. Griffiths, D.V.; Lane, P.A. Slope stability analysis by finite elements. *Geotechnique* **1999**, *49*, 387–403. [CrossRef]
40. Smith, I.M.; Griffiths, D.V.; Margetts, L. *Programming the Finite Element Method*; John Wiley & Sons: Chichester, UK, 2014; ISBN 9781119973348.
41. Morgenstern, N.R.; Price, V.E. The analysis of the stability of general slip surfaces. *Geotechnique* **1965**, *15*, 79–93. [CrossRef]
42. Gao, X.; Chuan Yan, E.; Yeh, T.C.J.; Cai, J.S.; Liang, Y.; Wang, M. A geostatistical inverse approach to characterize the spatial distribution of deformability and shear strength of rock mass around an unlined rock cavern. *Eng. Geol.* **2018**, *245*, 106–119. [CrossRef]
43. Gao, X.; Yeh, T.C.J.; Yan, E.C.; Wang, Y.L.; Hao, Y. Conditional mean, effective, and realizations of hydraulic conductivity fields. *J. Hydrol.* **2021**, *592*, 125606. [CrossRef]
44. Yeh, T.C.J. Stochastic modelling of groundwater flow and solute transport in aquifers. *Hydrol. Process.* **1992**, *6*, 369–395. [CrossRef]

Article

Hazard Mitigation of a Landslide-Prone Area through Monitoring, Modeling, and Susceptibility Mapping

Meen-Wah Gui [1,*], Hsin-An Chu [1], Chuan Ding [2], Cheng-Chao Lee [2] and Shu-Ken Ho [2]

[1] Department of Civil Engineering, National Taipei University of Technology (Taipei Tech), Taipei 106344, Taiwan; ge-10524@gov.taipei

[2] Sino Geotechnology, Inc., Taipei 105407, Taiwan; dabeain@sinogeotech.com.tw (C.D.); lcc@sinogeotech.com.tw (C.-C.L.) hsk@sinogeotech.com.tw (S.-K.H.)

* Correspondence: mwgui@ntut.edu.tw; Tel.: +886-955-154-891

Abstract: Indigenous tribes living in the mountainous areas account for about one-fifth of the extreme poor of the world, and this has made their lives more vulnerable to climate change impacts and natural hazards. After a series of earthquakes and very strong typhoons, the tilting and cracking of dwellings, localized slope failure, and severe subgrade settlements, together with damages of retaining structures and drainage ditches along a section of the Provincial Highway No. 7A on the west wing of the Central Mountain Range in central Taiwan, have raised concerns to the safety of a nearby Indigenous settlement, which is situated at an elevation of about EL. +1800 m. This study investigated and identified the possible causes for a large-scale landslide-prone area on the Central Mountain Range by employing multi-temporal satellite and aerial images, site investigation, field instrumentation, geophysics tests, and uncoupled hydromechanical slope stability analyses. The results were then applied to deduce a sliding susceptibility map and remedial plans to prevent or mitigate the sliding in the vicinity of an Indigenous settlement. The infiltration of rainwater, an upraised river-bed elevation, and the erosion of the river bank at the toe of the large-scale slope were found to be the main triggering factors in inducing sudden and localized failures. Meanwhile, the process of mass rock creep was deduced to have activated the process of large-scale deep-seated gravitational slope deformation (DSGSD) on the study slope; the DSGSD could eventually turn into a huge and catastrophic landslide. The findings of this study would be valuable for formulating detailed countermeasures to protect and maintain the stability and safety of the Indigenous settlement located at the crest of the slope.

Keywords: large-scale slope; rainfall; ERT; mass rock creep; DSGSD; sliding susceptibility; hazard mitigation

1. Introduction

Two-thirds of the total area of the island of Taiwan are covered by forest mountains, mainly the Alishan (Mount Ali), Xueshan Mountain Range, and Central Mountain Range. Ever since the intense shaking generated by the various high-intensity earthquakes, such as the 1999 September 21 (921) Jiji Earthquake (moment magnitude scale $M_w = 7.7$), the 2016 Tainan Earthquake ($M_w = 6.4$), and the high-intensity rainfall brought by the various very strong typhoons including the deadliest Typhoon Morakot in 2009, there has been a marked increase in the frequency of landslide occurrences on the island, in particular in the vicinity of the Central Mountain Range of Taiwan. The claim was supported by the ever-increasing concerns of assessing the stability of the mountainous roads slopes and monitoring potential landslides by the authorities in recent years. For example, using the rainfall data of the 2007 Krosa Typhoon and 2009 Morakot Typhoon, Shou et al. [1] examined the susceptibility of rainfall-induced landslides in southern Taiwan. An analysis of the rainfall frequency and general circulation of atmospheric models were first used to

understand the trends, distribution, and intensities of temporal rainfall; the results were then used to produce the landslide susceptibility maps. Weng et al. [2] executed a detailed multi-scale analysis, which consisted of a desk study, an evaluation of possible failure types of dip slopes and slope activity using maps of different scales, and a numerical simulation to identify and assess the stability of a potential dip slope located in the Zengwen Reservoir Catchment area in central Taiwan. Their numerical results were compared to that of the inclinometer readings and then used to predict the behavior of the dip slope, where Provincial Highway No. 18 is running through, under extreme wetting conditions.

Tsao et al. [3], who investigated the effect of geological conditions on the eastern section of the Provincial Highway No. 8, have found that the metamorphic strata with intricate folds in their study area were structured by the orogenic deformation and metamorphism as a result of erosion and scouring, which eventually evolved into meanders and steep slopes and gullies, which developed along the strata boundary with distinguishable lithology that tended to disrupt the stability of the slopes. By using traverse surveying to continuously monitor a series of ground monitoring points installed on a dip slope in a campus in northern Taiwan for a period of seventeen years, Tseng et al. [4] concluded that the use of conventional surface monitoring was also a reliable and economical tool for interpreting the displacement mechanism of a dip slope. Lo et al. [5] conducted a series of assessments on factors affecting the movement characteristics of a slope, which carries the Provincial Highway No. 20 and toe by a river in southeast Taiwan, and concluded that river-bed erosion and sediment accumulation were the main factors affecting their study slope.

This study aimed at assessing a large-scale landslide-prone area on the west wing of the Central Mountain Range in central Taiwan where its crest houses an Indigenous settlement and the Provincial Highway No. 7A. According to the World Bank [6], approximately 6% of the global population is made up of Indigenous or Aboriginal People but they account for about 19% of the extreme poor of the world; this has made them more vulnerable to climate change impacts and natural hazards. After a series of earthquakes and very strong typhoons, severe ground subsidence has caused a section of the Provincial Highway No. 7A to undergo road-bed differential settlements and damage to its retaining structures and drainage ditches. In addition, the river-bed of the river at the toe of this large-scale slope has also been inundated by debris from the upstream and forced the river-bed to elevate by more than 30 m and, hence, altered the topography and the stability of this slope.

The above-mentioned assessments or studies were mostly performed by academics using a wide range of methods of investigation, which may be too advanced or time-consuming from a practical point. This study presented an investigation of a large-scale landslide-prone area using a framework commonly adopted by practicing engineers, in which it consisted of a field investigation and monitoring, a simulation, and susceptibility mapping. Multi-temporal satellite and historical aerial images inventories were also exploited. The results were then used to derive a sliding susceptibility map and mitigation plan for the study area so as to protect and maintain the stability of the Indigenous settlement and the safety of the Indigenous People living at the crest of the slope.

2. Background of Study Area

After a series of natural disasters such as the 921-Jiji Earthquake in 1999, the Mindulle Typhoon in 2004, the Morakot Typhoon in 2009, and other subsequent typhoons and rainstorms in the following years, the tilting and cracking of dwellings and localized slope failures along a portion of the ridges of the Central Mountain Range and the nearby Tabuk Indigenous settlement have been persistently reported. Tabuk Indigenous is one of the four Atayal tribes living around the Central Mountain Range. Signs of massive sliding as severe settlements of subgrade on certain sections of the nearby Central Cross-Island Provincial Highway Route No. 7A have also been observed. Tseng et al. [4] reported that the ground, building and facilities cracks, and topographic deformation are signs of an impending landslide.

The study area (Figure 1) is located in the water catchment area of the Deji Reservoir, and it was believed to be a large-scale ancient landslip covering a total area of more than 100 hectares and consisted of several small sliding bodies [7]. The Tabuk settlement is located at the north-east corner of the study area (Figure 2) and at an altitude of about 1800 m. The settlement is about 8.5 km from the location of the Lishan large-scale landslide, which occurred in mid-April 1990 [8]. Lishan, literally meaning "Pear Mountain", is one of the popular tourist destinations for those who would like to get away from the heat in the summer and enjoy the snowy scenery in the winter and those who would like to experience the culture of Indigenous People or sight seeing along the hunting trails around the village.

Figure 1. Location of the study area in relation to the island of Taiwan and the 1990 Lishan large-scale land-sliding zone (Google Earth Pro, 2022).

2.1. Topography

Topographically, the study area is located at the west wing of the Central Mountain Range, with elevations ranging between EL. +1420 m and EL. +1800 m; mountain and valley are the two main terrain features found in the study area (Figure 2). The northwest boundary of the study area is bounded by the Dajia River, which has a total length of about 120 km and flows from the northeast to the central west of the island of Taiwan, while two transmeridional ridges and the flat-topped Taibaojiu Ecktreppe (Figure 2), respectively, bound the northern, southern, and eastern boundaries of the study's large-scale slope. A third transmeridional ridge divides the study area into the northern and southern slopes (Figure 2), making the main topography of the study site look like a pair of "dustpans" with their lip facing the Dajia River. Meanders, alluvial fans, and river terraces are common topographies found along the river. The overall topography of the study area is high in the east and low in the west, where the northern and southern slopes both dip to the west with slope angles ranging between 15° and 30° down to the Dajia River. The terrain stretching between the highest point of the Taibaojiu ridgeline and the lowest point of Dajia River Valley is steep–gentle–steep.
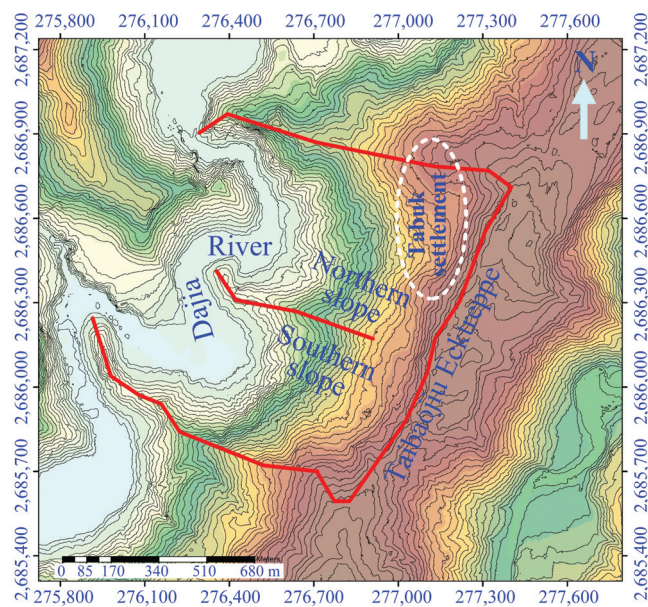
Figure 2. Location of the northern and southern slopes in relation to Tabuk settlement and Taibaojiu Ecktreppe (After [9]).

2.2. Temperature and Rainfall

Located at an altitude of EL. +1420 m and above, the study area attracts an average annual temperature of 15.2 °C. The lowest and highest average monthly temperature is 9.4 °C in January and 23 °C in July, respectively. The average annual rainfall between 1971 and 2016 was about 2215 mm, with a maximum average annual rainfall of 3771 mm in 2005. Table 1 shows the monthly and yearly average and maximum rainfalls recorded between 1971 and 2016, in which almost 70% of the 2215 mm average annual rainfall occurred between April and September; the month with the highest average monthly rainfall was June, which exceeds 300 mm. The huge discrepancy between the monthly average and the maximum rainfall during the recorded period was due to the extreme weather, which resulted in the uneven distribution of the rainfall [9].

Table 1. Rainfall characteristics of the study area between 1971 and 2016 [9].

Month	Jan	Feb	Mac	Apr	May	Jun	Jul	Aug	Sep	Oct	Nov	Dec	Yearly
Average (mm)	90	180	213	249	284	330	199	254	204	88	60	60	2215
Maximum (mm)	504	710	786	938	560	920	691	784	1351	511	325	170	3771
Year	2016	1983	1983	1990	1984	2006	2004	1994	2008	2007	2012	2012	2005

2.3. Geology

Geologically, the study area is situated in the colluvial formation originally from the Miocene slate formation, and because of the frequent dynamic tectonic activities along with the high precipitation, the surficial slate of the study area has been found to be highly weathered [10]. The rocks stratum in the study area is dominated by the Lishan formation, also of the Miocene period, which comprises mostly slate and argillite with mature foliations, i.e., cleavage or schistosity [11]. Slate is characterized by rich foliations along which it breaks to leave smooth and flat surfaces. Because it is closely related to the axial planes of folds in the rock, it is often called the axial plane cleavage [11]. The

orientation of the foliations of the slaty outcrop within the study area varies considerably. The main foliation fabrics, which were induced by the horizontal northwest–southeast compression, are sub-vertical, trending northeast–southwest at high angles. On one hand, slaty foliations with a high dip angle together with overturned and crooked foliations have been found along the river bank; on the other hand, broken slaty rocks with a gentle foliations orientation have been discovered at the higher elevations. Because the rock quality and weathering resistance of the slate with rich foliations are relatively poor, erosion has been a major concern and it has resulted in a relatively wide river valley. Lin et al. [12] have pointed out another concern whereby metamorphic rock slopes with well-developed foliations tend to creep under gravity with considerable variation in the orientations of the foliation, in compliance with the definition of a deep-seated gravitational slope deformation.

At the crest of the northern and southern slopes is the Taibaojiu Ecktreppe (Figure 2), which was formed by the action of the Nanhu and Hehuan creeks further west; its elevation range is between 1500 and 1900 m, which is the typical elevation for the Ecktreppe topography. Alluvial was found on the surface of its topography, indicating that the Ecktreppe was once the river-bed of a stream [13]. In the Dajia River at the toe of the northern and southern slopes, sedimentary rocks with clear patterns could be easily found.

2.4. Google Earth Images Taken between 2006 and 2018

Six historical Google Earth [14] satellite images of the study area shot between 2006 and 2021 are presented and compared in Figure 3. Although the interpretation of satellite images, such as minor terrain variations, may be affected by the vegetation in the study area, the exposed surfaces as a result of slope collapses could still be identified in normal circumstances. The majority of the landslides have a visible rupture surface, main scarp, scarp floor, and deposition fan depositing most of the landslide debris; however, for open slopes, the deposition fan may not be available because the sliding debris could well be deposited on the trail path [15]. Perhaps the most obvious changes observed from these images are the headward erosion of the two concave banks of the northern and southern slopes.

Figure 3 reveals that the most distinct variation in the study site between 2006 and 2021 was the amount of water in the river and the transformation of the river banks due to erosion. Figure 3a shows the collapse of two river banks at locations Nos. 1 and 2 of the convex bank of the southern and northern slopes, respectively, and one collapse at location No. 3 of the concave bank opposite the northern convex bank. These collapses occurred as early as 2001, during which the river channel still had a considerable amount of water. On July 11 of 2004, a rather huge landslide occurred at location No. 4 of the southern slope, where the highest part of the main scarp of the landslide reached Provincial Highway No. 7A. Prior to November 2013, most likely in early 2012, two new failures were observed at locations Nos. 5 and 6 of the convex bank of the northern slope (Figure 3b), in which failure No. 5 was a shallow slope failure, whereas failure No. 6 was a cut bank failure. No new failures were observed prior to July 2016, as inferred from Figure 3c; however, surface erosion could be seen at locations Nos. 7 and 8 of Figure 3d while the collapse of the cut bank at location No. 6 was extended further. A failure at location No. 9 of the concave bank opposite the northern slope was reported some time in 2017 (Figure 3e). These collapses have been found to be closely related to the rainfall event associated with the various typhoons, as tabulated in Table 2. In general, the satellite images revealed that most of the slope collapses observed along this portion of Dajia River occurred along the two convex banks as the banks were easily subjected to fluvial attack and erosion. The critically eroding banks collapsed when an external factor, such as a high-intensity rainfall, disturbed their already fragile stability.
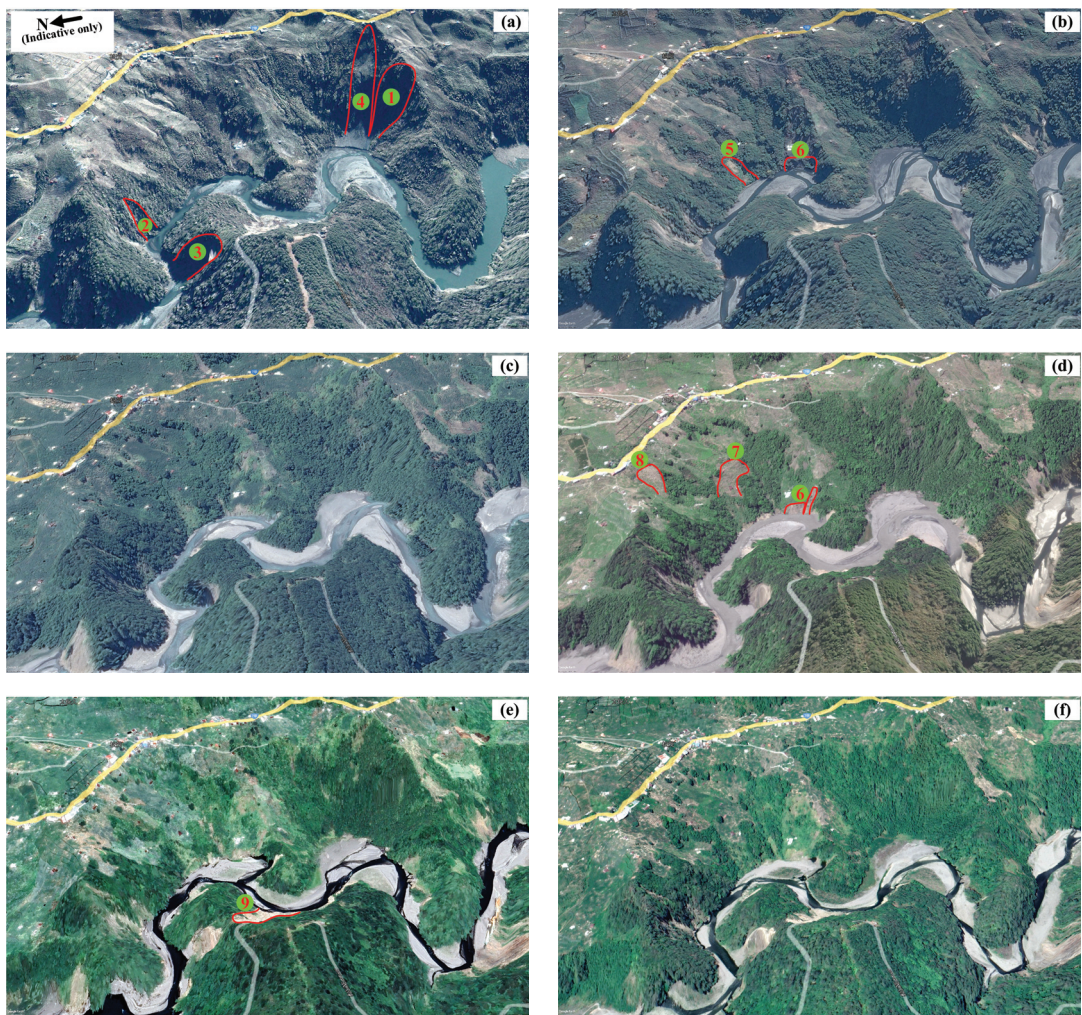
Figure 3. Google Earth satellite images and landslide locations (1 to 9): (**a**) Feb'2006; (**b**) Nov'2013; (**c**) Jul'2016; (**d**) Apr'2017; (**e**) Sep'2018; and (**f**) May'2021 (Google Earth Pro [14]).

Table 2. Relationship between rainfall and the occurrence of local collapses of the large-scale slope between 2001 and 2018 [7].

Landslide Locations	Nearest Rainfall Event	Date of Rainfall Recorded	Accumulated Rainfall (mm)	Date of Google Image Taken	Postulated Cause of Failure
1, 2, 3	Typhoon Toraji	28 July 2001	244	1 February 2006	
4	Typhoon Mindulle	1 July 2004	645	1 February 2006	rainfall
5	Typhoon Morakot	6 August 2009	755	29 November 2013	rainfall
6	Low pressure	8 June 2012	674	29 November 2013	rainfall and fluvial attack
7, 8	Typhoon Megi	26 Sept 2016	327	30 April 2017	rainfall
9	Typhoon Maria	10 July 2018	276	30 September 2018	rainfall

3. Methods of Study

The main methods used in this study consist of ground investigation via a series of boreholes and electrical resistivity tomography (ERT), slope monitoring that included monitoring the depth of ground-water level and the lateral displacement of the slope, and

slope stability analysis that took into account the influence of a designed storm for 50-year return period in 24 h.

3.1. Ground Investigations

3.1.1. Boreholes Exploration

Ground investigation via a series of boreholes was conducted in this study to establish the soil and rock profiles and the materials parameters to be used in the stability analysis. Wire-line core drilling system with H-size drill rods and Q-group wire-line diamond drilling machine, which is associated with a core diameter of 63.5 mm and a hole diameter of 96 mm, was used for the exploration. The system is efficient in complete recovery of core from the rock mass without having to pull out the drill string.

Prior to this study, some fourteen boreholes, which were mainly concentrated in the southern slope, were drilled by the Soil and Water Conservation Bureau in 2007 [9]. To realize the ground information of the transmeridional (central) ridge and that of the northern slope, additional boreholes were required. After a detailed on-site visual inspection, eight additional boreholes (AH–1 to AH–8) were assigned, as shown in Figure 4, and drilled in 2017. The depth of these additional boreholes, except AH–6 and AH–8, was 50 m; AH–6 was 60 m, while AH–8 was 40 m deep.
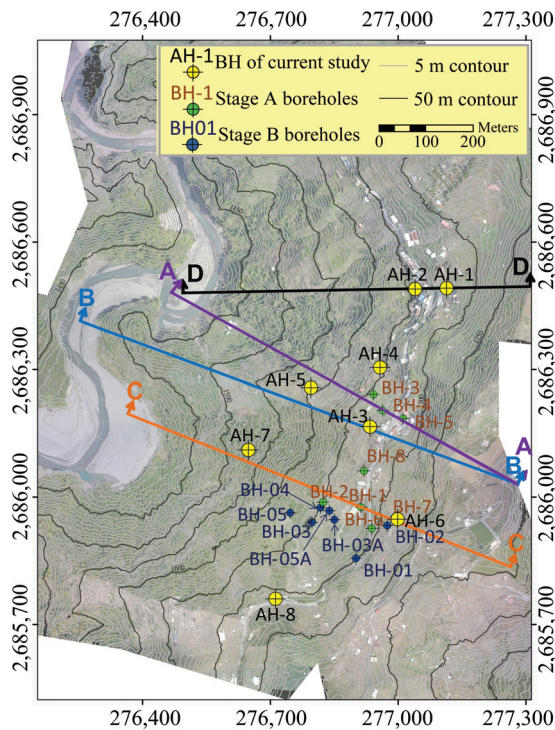

Figure 4. Location of boreholes, and cross-sections A–A to D–D used in this study (After [9]).

3.1.2. Electrical Resistivity Tomography (ERT)

As a near-surface geophysical tool, the ERT, which computes the below-ground distribution of electrical resistivity from a series of electrical resistance measurements, is a widely used geophysical subsurface imaging technique for providing information of geologic site conditions, hydro-geologic characteristics, environmental-related conductivity variability, etc. [16]. Because ERT is a rather advanced site investigation technique, the principle behind the technique is briefly described here.

How difficult it is for an electrical current to pass through a material is described by its electrical resistance R, where loose soil or a void in the ground will have a higher resistance reading, while compacted soil or a buried metal will have a lower resistance reading. Thus, when an electrical current I is generated in the ground, the electrical voltage V varies depending on the state or condition of the ground and, hence, the resistance R; according to Ohm's Law ($V = IR$), R is expressed as the ratio of the measured voltage and current, but it varies with material's volume. For an object with a length L and an area A, R is given by:

$$R = \rho \frac{L}{A} \qquad (1)$$

where ρ is a constant of proportionality, also called the electrical resistivity or the specific resistance [$\Omega \cdot$ m]. The reciprocal of electrical resistivity is conductivity, which represents a material's ability to conduct electrical current and is often used as a representation of bulk property of earth material.

Unlike electrical resistance R, which varies with a material's volume, electrical resistivity is a bulk property of a material and it has the same value for all lumps of that material, regardless of geometry. Thus, using either an alternating current (AC) or a direct current (DC), ERT can be used to measure the variations in electrical resistivity either at the ground surface or by electrodes installed at depth [17]. However, the value of resistivity is commonly affected by ground materials, minerals composition, particles size, and salinity of water.

From Ohm's Law and taking the surface area A of a hemisphere with a radius r as $2\pi r^2$ and the length $L = r$, one may derive the electrical potential or voltage V as

$$V = \rho \frac{I}{2\pi r} \qquad (2)$$

where I is the electric current in amperes, which flows radially away from the current source along the ground surface; hence, the potential V varies inversely with distance r from the current electrode.

The voltage, or, more precisely, the potential difference ΔV over a homogeneous half-space with a four-electrode array (Figure 5), is given by:

$$\Delta V = V_{P_1} - V_{P_2} = \frac{\rho I}{2\pi} \left[\left(\frac{1}{r_{C_1 P_1}} - \frac{1}{r_{C_2 P_1}} \right) - \left(\frac{1}{r_{C_1 P_2}} - \frac{1}{r_{C_2 P_2}} \right) \right] \qquad (3)$$

where V_{P_1} and V_{P_2} are the electrical potentials at P_1 and P_2 and $r_{C_1 P_1}$ is the distance between electrodes C_1 and P_1, etc.

In practice, resistivity surveys are normally performed over inhomogeneous mediums where the subsurface resistivity has a 3-D distribution [18]; in this case, the measurements of the resistivity are still conducted by passing a current into the ground via the current electrodes C_1 and C_2 and recording the potential difference between the electrodes P_1 and P_2. The apparent resistivity ρ_a—defined as the resistivity of an electrically homogeneous and isotropic half-space—is related to the applied current I and the measured value of potential difference ΔV for a given arrangement and spacing of electrodes as [18]

$$\rho_a = k \frac{\Delta V}{I} \qquad (4)$$

where k is a geometric factor that is governed by the arrangement of the four electrodes; k in Equation (4) is found to be

$$k = \frac{2\pi}{\left[\left(\frac{1}{r_{C1P1}} - \frac{1}{r_{C2P1}} \right) - \left(\frac{1}{r_{C1P2}} - \frac{1}{r_{C2P2}} \right) \right]} \qquad (5)$$

Two types of electrode arrays were deployed in this study: the Wenner–Schlumberger array, Figure 5a, and the pole–pole array, Figure 5b. On one hand, in the Wenner–

Schlumberger array, the distance between the current and potential electrodes r_{C1P1} (or r_{P2C2}) was "n" times the distance between the two potential electrodes pair r_{P1P2}. This arrangement allowed the detection of greater concentration of high resistivity values beneath the electrodes P_1 and P_2 [19]. The configuration of Wenner–Schlumberger array was reported to be moderately sensitive to changes in resistivity horizontally and vertically and, thus, it is suitable for areas with complex geological conditions [20].
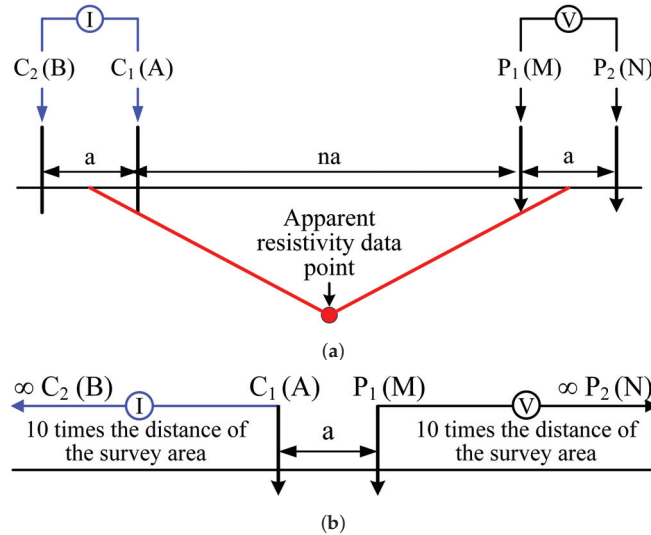

Figure 5. Electrode arrays used in this study: (**a**) Wenner–Schlumberger array; (**b**) pole–pole array.

The pole–pole array, on the other hand, is often used for deep imaging through the placement of two remote electrodes (C_2 and P_2) at infinity, while the distance between the transmitter dipole C_1 and the receiver dipole P_1 was comparatively short [21]. Here, a single transmitting electrode is called a pole, while a pair of oppositely charged electrodes is called a dipole. The dipole is closely placed so that the electric field would seem to be a single electrode field instead of field from two different electric poles [21]. Quantitatively, to ensure a measurement error of less than 5%, the second current and potential electrodes (C_2 and P_2) would have to be moved in the opposite direction and placed at a distance of at least 10 times the maximum distance between C_1 and P_1 electrodes; in other words, this array has a stationary infinity electrode on either side of the survey area, Figure 5b. "Super-Sting R8" multi-electrode resistivity system was used for geologic mapping in this study as it allows for rapid analysis of site conditions below the ground surface.

3.2. Field Monitoring

In addition to the boreholes exploration and electrical resistivity tomography, the water level and lateral deformation of the northern and southern slopes were also monitored by observing the water level via the observation wells and the inclinometers, respectively.

Observation Wells

Groundwater levels across a site may be determined via (i) groundwater observation wells; (ii) piezometers; (iii) open boreholes; and (iv) field estimates. For the study site, direct monitoring via observation wells and piezometers were used. The observation wells were mainly used to identify the shallow groundwater levels, while the piezometers were used to measure the piezometric head of the confined groundwater. Because the shallow groundwater levels are easily influenced by the rainfall and the rise in such water levels could result in slope instability, eight observation wells (AH–1 through AH–8) were drilled and installed next to the locations of the inclinometers for the direct monitoring of the

groundwater levels in the study slopes, in particular during the rainy seasons in 2017. The groundwater levels in the wells were measured manually with a calibrated steel tape once a month; in addition, extra measurements were also taken when the 24-hour accumulated rainfall exceeded 400 mm.

3.3. Inclinometers

Monitoring stations for inclinometer are effective way of monitoring a landslide and detecting the associated sliding surface [22]. In total, five inclinometer points were installed, in which a 50 m long specially grooved casing was inserted into each of the existing boreholes, AH–2, AH–3, AH–4, AH–5, and AH–7. Cement grout was injected to fill the annular void; these boreholes were thus unsuitable for use as observation wells. The servo-accelerometer probe was lowered and raised through the specially grooved casing, which guides the movement of the probe within the casing via its four orthogonal longitudinal wheel grooves. Readings were taken manually once a month, and additional measurements were also taken when the 24-hour accumulated rainfall exceeded 400 mm.

3.4. Seepage and Stability Analyses

The stability of the northern and southern slopes may be assessed using conventional slope stability analysis, taking into consideration, in particular, the effect of short-term rainwater infiltration. The uncoupled hydromechanical stability analyses were performed using the program SEEP/W and SLOPE/W with a three-stage approach. Firstly, the steady-state seepage analysis, using the approach of variably saturated flow and the parameters listed in Table 3, was performed to obtain the hydrostatic pore-water pressure distribution in the slopes. Secondly, using the result from the first stage and the designed rainfall (Figure 6), a transient analysis was conducted to simulate the infiltration of rainwater and obtained the corresponding change in pore-water pressure distribution in the slopes; this was followed by assessing the stability of the slopes based upon the shear strength parameters given in Table 3 and the distribution of pore-water pressure obtained from the above transient analysis. In Table 3, the parameters: saturated and residual volumetric water content, a, and n were the fitting parameters for the corresponding van Genuchten's [23] soil–water characteristic curve (SWCC) and hydraulic conductivity functions; another fitting parameter m was taken as $(1 - 1/n)$.

It should be emphasized that uncoupled analysis is by no means perfect. Firstly, for rainfall infiltration-related analysis, Khoei and Mohammad [24] and Airey and Ghorbani [25] recommended that coupled or fully coupled models should be preferably used because deformation of solid significantly affected its pore air and water pressures. Secondly, the van Genuchten's SWCC and hydraulic conductivity models adopted here were assumed to work under constant void ratio or under conditions in which the material's volume does not change appreciably, thus ignoring the effect of initial void ratio on air-entry value [26,27] and also the effect of hydraulic hysteresis [28], which are known to significantly affect the hydromechanical response of soils. In practice, because the problem of slope stability is inherently a large deformation problem, materials' void ratio changes appreciably as a result of such deformation [29]; thus, for a more complete analysis, these two functions should be updated throughout the analysis. In addition, the effect of stress-induced anisotropy, which has always been a concern in problems related to slopes stability [30,31], is also not considered in this study. Nevertheless, they were commonly adopted in practice because of their availability and ease of use.

Table 3. Input parameters used in seepage and stability analyses [9].

Material	Unit Weight (kN/m³)	Apparent Cohesion (kPa)	Friction Angle (°)	Saturated Volumetric Water Content (m³/m³)	Residual Volumetric Water Content (m³/m³)	Saturated Hydraulic Conductivity (m/s)	a (kPa)	n
Colluvium	22	0	23.5	0.30	0.02	4.6×10^{-5}	2.00	1.35
Slate (SL1)	25	20	30.0	0.25	0.02	9.6×10^{-7}	0.19	1.70
Slate (SL2)	25	20	30.0	0.21	0.02	3.8×10^{-8}	0.19	1.70

Based on the monitoring data collected between 1990 and 2016 from the nearby Tabuk rainfall station and the simple scaling Gauss–Markov analysis, the designed storm for 50-year return period in 24 h (Figure 6) was derived and used as the boundary condition in the transient analysis. The Morgenstern–Price method used in the stability analysis is one of the many general methods of slices formulated based on the principle of limit equilibrium; it satisfies both the equilibrium of forces and moments acting on individual blocks.
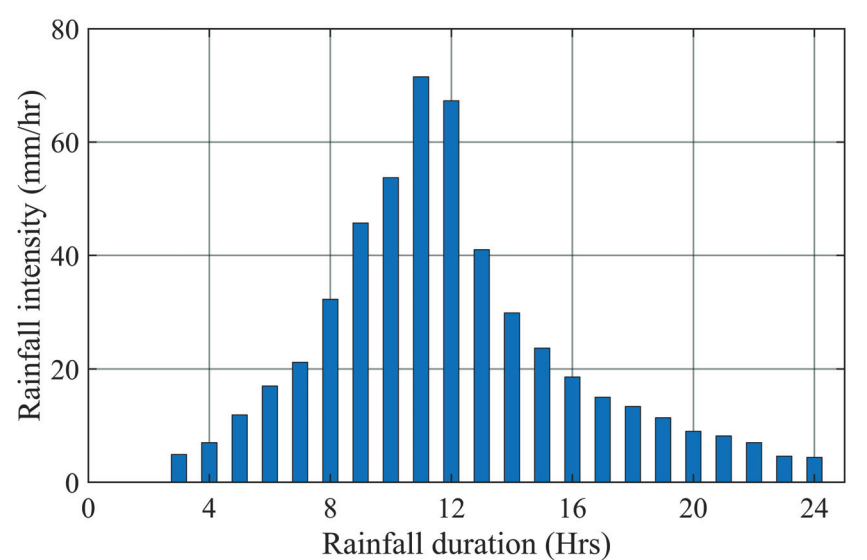

Figure 6. Rainfall hyetographs of a designed storm for 50-year return period in 24-hour.

4. Results and Discussion

4.1. Ground Investigation Results

4.1.1. Slopes Materials

A general stratigraphy of the study site was derived from the analysis of the cores extracted from the seven boreholes drilled across the study site. The stratigraphy of each core and the location of the boreholes are presented in Figure 7.

From the boreholes cores analysis, it was found that colluvium (Cv) of varying thicknesses occupied the top layer of the slopes (Figure 7a). The colluvium consists of the yellowish brown to gray clayey silt, and sand with lightly to moderately weathered slate fragments, occasionally accompanied by slate debris with quartz detritus, but the engineering characteristic of this colluvium is dominated by the clayey silt and sand. The Standard Penetration Test (SPT) "N" values ranged between 2 and 20, but sometimes they could be as high as 40. The thickness of the colluvium varies considerably, with a maximum thickness of 31.3 m at borehole AH–1.
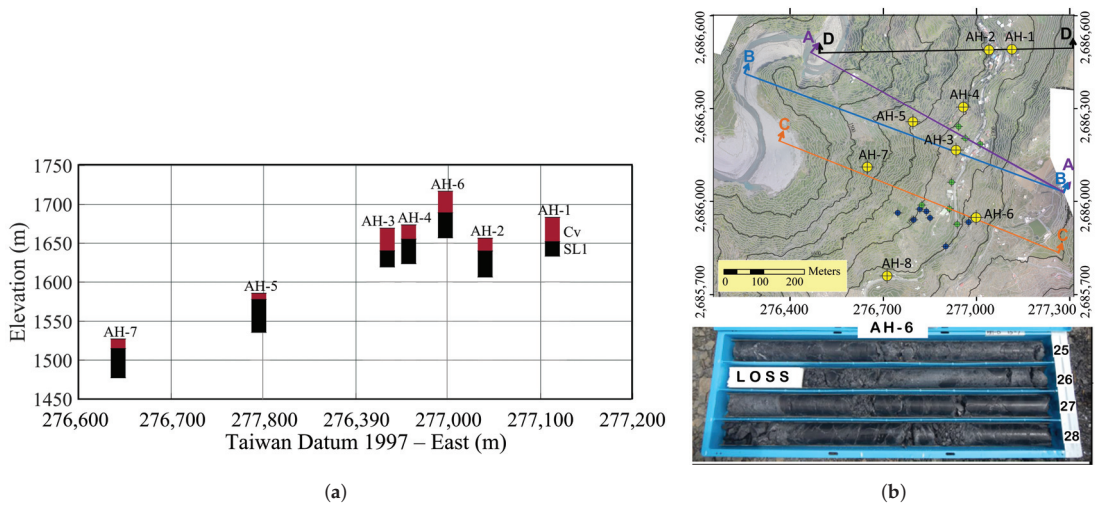
Figure 7. (**a**) Stratigraphy of each core; deep red denotes colluvium layer, while black denotes slate formation; (**b**) location of boreholes and cross-sections A–A to D–D (AH–8 is not presented as it is outside the two study slopes), and core sample image for AH–6 (After [9]).

Beneath the colluvium was the gray to dark gray slate of fair rock mass quality, occasionally with a quartz vein. The disintegrated and fragmented rock materials found here were mainly due to the weathering process. The slaty cleavage (SL1) has a gentle dip of between 10° and 30° and a gouge was found present in this clastic rock mass, indicating that the fissures of the flexural toppling slate were well-developed and hence induced relative displacement under the long-term gravitational force; consequently, SL1 is continuously under creeping and slipping.

The third layer was basically formed by the anti-dip (obsequent) and high-angle foliations slate (SL2) [32]. Under normal circumstances, obsequent slate slopes with high-angle foliations would normally cause the deformation of flexural toppling, the formation of bending folds in the upper slope, and rock falling [11]. However, this should not be the case for the study site because only a small portion of the rock mass toward the toe of the slope of section B–B and section C–C (Figure 7b) exhibits such day-lighting foliations; the anti-dip slate with high-angle foliations in the other two cross-sections were not day-lighting and thus their tendency to toppling is being refrained by the overlying colluvium.

Finally, a total of 34 soil samples—selected from a total of 360 m long cores recovered from the boreholes—were tested in a geotechnical laboratory for the determination of their physical properties and shear strength. The result of the laboratory tests are tabulated in Table 3, and they were used in the following seepage and stability analyses.

The ERT survey results of the Wenner–Schlumberger and the pole–pole arrays for cross-sections ERT1 (Section B–B in Figure 4b) and ERT2 (Section C–C in Figure 4c) are plotted in Figure 8. The ground layers inferred from the borehole cores analysis are also shown in this figure.

The resistivity readings obtained from both the Wenner–Schlumberger and pole–pole arrays for the northern and southern slopes ranged between 100 and 500 $\Omega \cdot m$. The variation in the resistivity reading is more discernible and unevenly distributed near the ground surface than that at a deeper depth. Care must be taken when interpreting the resistivity readings for the following reasons: (i) it is possible for a particular material to have a wide range of resistivity readings as a result of its saturation degree, ions concentration, faulting, jointing, weathering degree, etc., (ii) most of the resistivity reading of the near-surface sedimentary materials is mainly dictated by the amount and the chemical contents of their

pore water, and (iii) clayey soils and sulphide minerals are the only sedimentary materials that allowed an enormous amount of electrical current passing through themselves [33].
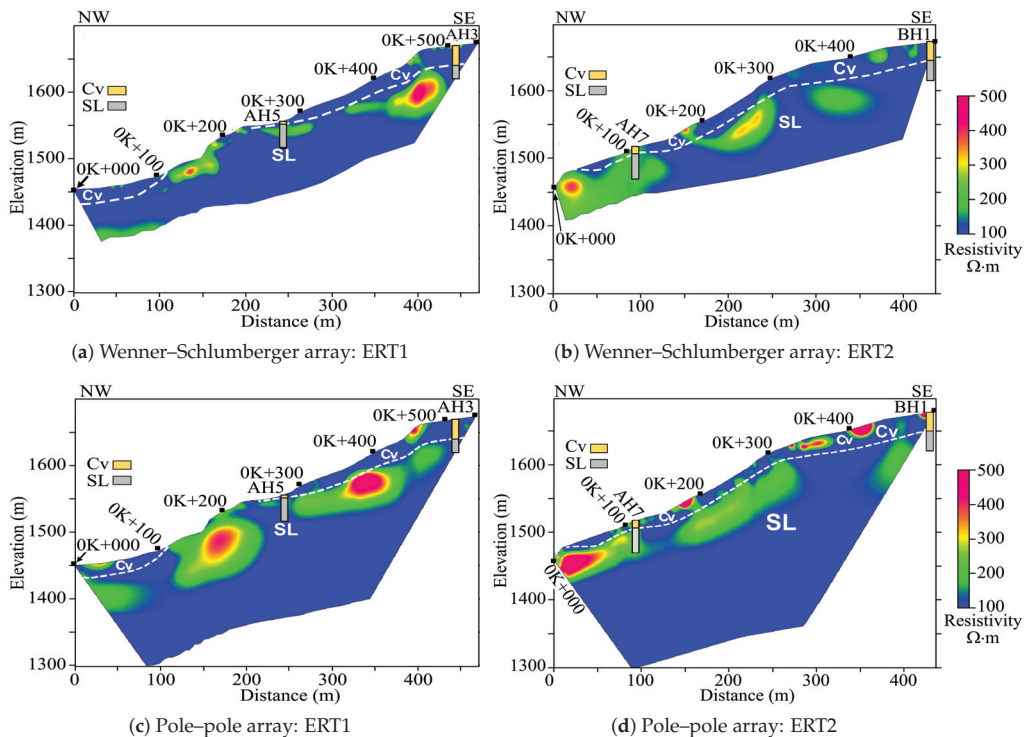

Figure 8. Resistivity imaging: (**a**) Wenner–Schlumberger array: ERT1 (Sec. B–B in Figure 4b); (**b**) Wenner–Schlumberger array: ERT2 (Sec. C–C in Figure 4c); (**c**) pole–pole array: ERT1 (Sec. B–B in Figure 4b); (**d**) pole–pole array: ERT2 (Sec. C–C in Figure 4c) (After [7]).

The resistivity reading variation in Figure 8 was expected as the resistivity measurements in the slate formation were dictated by the presence of water in the rock fissures and the relative degree of the shear fracture and shear gouges; however, in the colluvium, the degree of moisture content, fine content, and rock-fragment content were the known factors that governed the resistivity measurement. The borehole sampling revealed that the fine content of the colluvium was higher than that of the slate; the overall resistivity reading of the colluvium in the two cross-sections was thus lower than that of the loose colluvium or with fragmented rock where the resistivity value was higher.

Core samples from the site investigation revealed that the orientation of the disturbed slate foliation SL1 was almost horizontal or gently plunging, and the disturbed slate SL1 consisted of poor quality rock masses, often filled with gouges of varying thicknesses. The resistivity measurements of the slate converged with a depth to about 200+ $\Omega \cdot$m, indicating that within the investigation depth the resistivity measurement was still governed by the fine content of the slate and the in situ pore water. An intriguing pattern of resistivity distribution was observed from the results of the Wenner–Schlumberger and pole–pole arrays. Unlike the low resistivity-based colluvium that occasionally mingled with some high resistivity reading, a higher resistivity reading was measured near the ground surface of the ERT-1 survey line between 0K+110 and 0K+230 m, Figure 8c; after re-visiting the site, it was found that said location was in fact covered by slate with gently plunging foliation. A similar phenomenon was also seen between 0K+00 and 0K+20 m of the ERT-2 survey line where the steep slope is located, Figure 8d. A further study can be performed in the future

to examine whether the method is suitable to be used to deduce the degree of bending and toppling of the foliated rock mass under gravitational force.

The interface between the colluvium (Cv) and the disturbed slate formation (SL1) was postulated and is plotted in Figure 8 using the white dotted line. The interface was deduced from the results of the ERT survey, borehole coring, and outcrops noted from the study site. The postulated interface revealed that the thickest colluvium was located in the vicinity of Borehole AH-3 on the ERT-1 survey line, while that on the ERT-2 survey line was roughly located between 0K+300 m and 0K+500 m.

Finally, the stratigraphic layout for each of the four designated cross-sections, as shown in Figure 4, is plotted in Figure 9; these layouts were deduced via the combination of the desk study, the subsurface geologic mapping, and the borehole cores analysis, as presented above. However, due to the limited number of boreholes, the stratigraphic layouts derived here may be oversimplified; to quantify the error associated with such a simplification, the Boolean Stochastic Generation approach, as proposed by Bossi et al. [34], may be adopted. Nonetheless, such a comprehensive analysis is out of the scope of the current study.

4.1.2. Groundwater Level of Study Slopes

The highest groundwater level in each observation well recorded for the study site is tabulated in Table 4. The results show that the highest groundwater level was located either in the colluvium layer or in the vicinity of the interface between the colluvium and the slate formation (SL1).
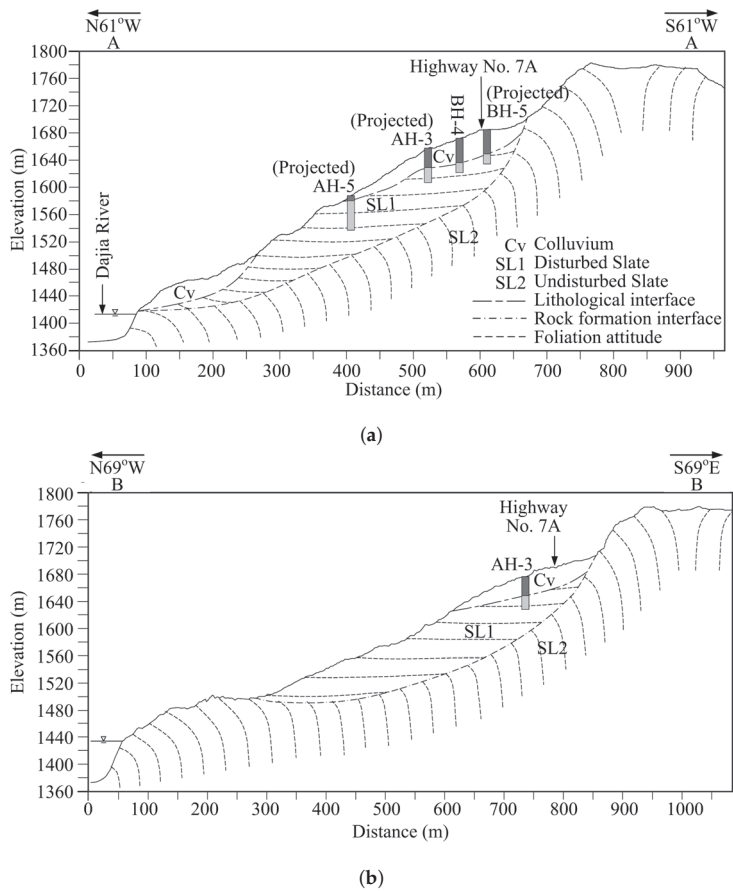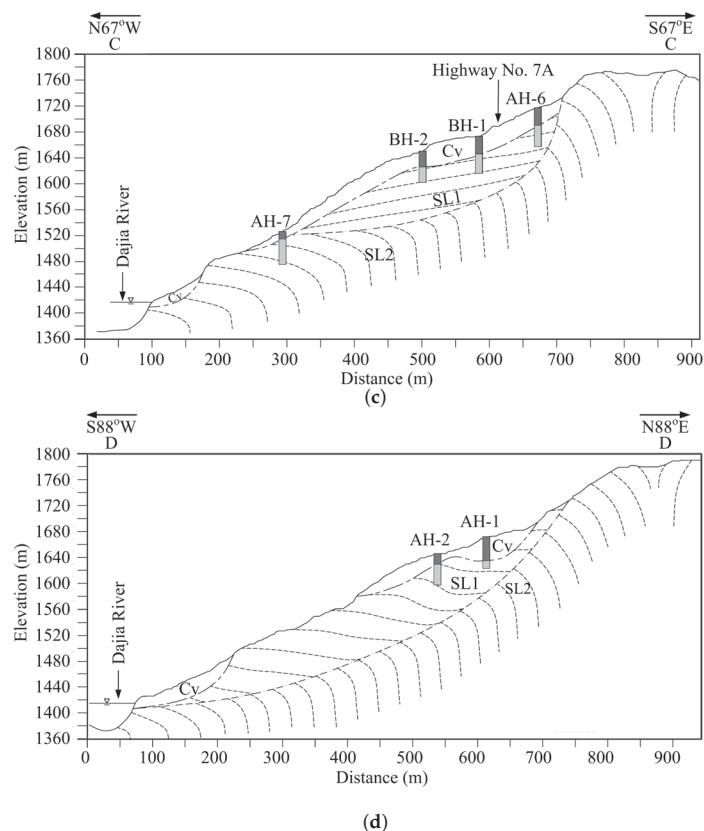

(**a**)

(**b**)

Figure 9. *Cont.*

Figure 9. Cross-sectional profile of (**a**) A–A; (**b**) B–B; (**c**) C–C; (**d**) D–D (see Figure 4 for relative location of these cross-sections) (Adapted from [7,9]).

Table 4. Highest groundwater levels measured for each observation well located next to the inclinometer.

Observation Well No.	Highest Groundwater Level (m)
AH–2	5.5
AH–3	14.0
AH–4	19.0
AH–5	13.5
AH–7	15.5

4.1.3. Lateral Displacement of Slopes

The installation of the inclinometers AH–3, AH–4, and AH–7 (Figure 4) was completed on June 11, 2017, while that of AH–2 and AH–5 was completed on August 16. Thus, only the records of AH–3, AH–4, and AH–7 are presented here in Figure 10. The inclinometer AH–3 was originally 50 m long, but it was found broken at a depth of 27.5 m in a local sliding event just after installation (Figure 10), and continuous displacement was observed at depths between 24.5 and 27.5 m. Coincidentally, the thickness of the colluvium at AH–3, according to the borehole log, was about 29.2 m, and the large inclinometer or shear displacement reading at the depths between 24.5 m and 27.5 m revealed that the sliding surface, induced by the extreme rainfall, was located within the colluvium layer. In addition, the sliding thickness could be as deep as the thickness of the colluvium because

the disturbed (SL1) and undisturbed (SL2) slate formations could both be regarded as relatively stable strata. Within the period of monitoring, no obvious displacement and trend of movement were observed in the inclinometers AH–4 and AH–7 (Figure 10) as their readings were within the measurement margin of error. According to Machan and Bennett [35], the field accuracy of an inclinometer is roughly ±7.6 mm per 30 m, which includes a combination of random and systematic errors. The random errors occurred within the sensors and affected the accuracy of the inclinometer probe, while systematic errors occurred because of human operations and influenced the condition of the probe and the procedure of data collection [35]. No further measurements were taken for the inclinometers AH–4 and AH–7 in the subsequent months because of the discontinuation of the project.
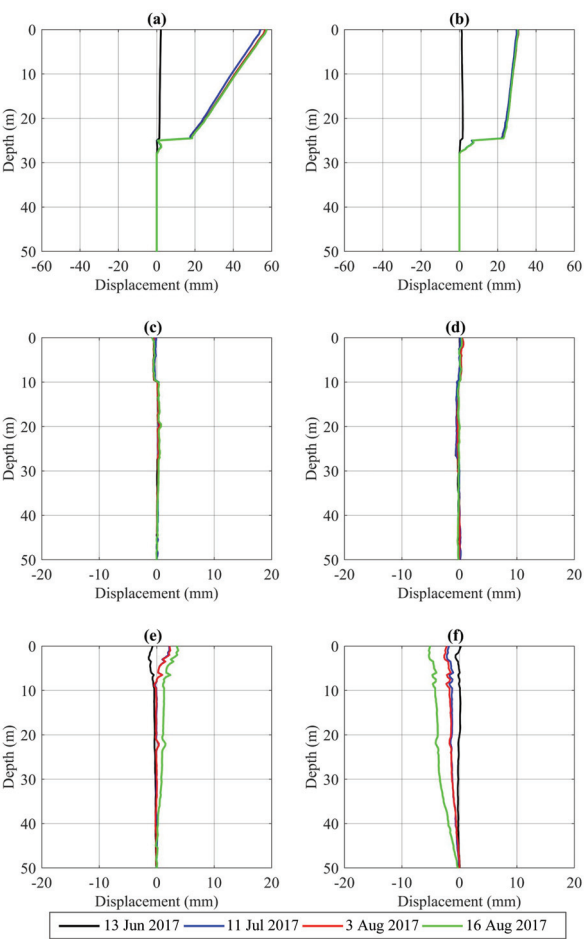

Figure 10. Inclinometers reading recorded between 13 June and 16 Aug of 2017 for inclinometers: (**a**) AH–3N; (**b**) AH–3S; (**c**) AH–4N; (**d**) AH–4S; (**e**) AH–7N; and (**f**) AH–7S. (Note: "N" and "S" denote North- and South-bounds, respectively.)

4.2. Factors Causing Short-Term Sliding

The three main factors, (1) the infiltration of rainwater on the slope, (2) upraised river-bed elevation caused by earthquakes and seasonal typhoons at the toe of the slope, and (3) erosion of the river bank of the slope toe, were believed to be crucial in initiating the slope instability.

The result of the seepage and stability analyses revealed that prior to the rain (0∼2 h), the factor of safety (FOS) of the cross-section A–A of the northern slope and the cross-section C–C of the southern slope was 1.04 and 1.22, respectively. The FOS of the slopes was then re-assessed for every subsequent hour of infiltration. It was found that the FOS of the cross-section A–A of the northern slope decreased to 1.00 after 14 h of rainfall and to 0.98 at the end of 24 h. Likewise, for the cross-section C–C of the southern slope, its FOS decreased to 1.00 after 18 h of rainfall and to 0.98 at the end of 24 h of rain. The corresponding sliding zone for both the analyzed cross-sections at the end of 24 h rainfall is plotted in Figure 11. As seen from this figure, both sliding zones were located in the top half of the slopes and extended to Provincial Highway No. 7A. The colluvium deposit located at the toe of the study slopes (Figure 9) is believed to be the debris produced as a result of the local failure of the overlying colluvium of the up-slope. The deposit at the toe of the slopes subsequently led to the rise in the groundwater level and triggered the instability at the toe of the slopes. The projected location of the inclinometer AH–3 was included in Figure 11a, which shows the analyzed sliding surface of the cross-section A–A; the depth of the sliding surface given by the simulation was about 28 m deep, which was very close to the depth at which the inclinometer AH–3 was found broken, i.e., at 27.5 m.
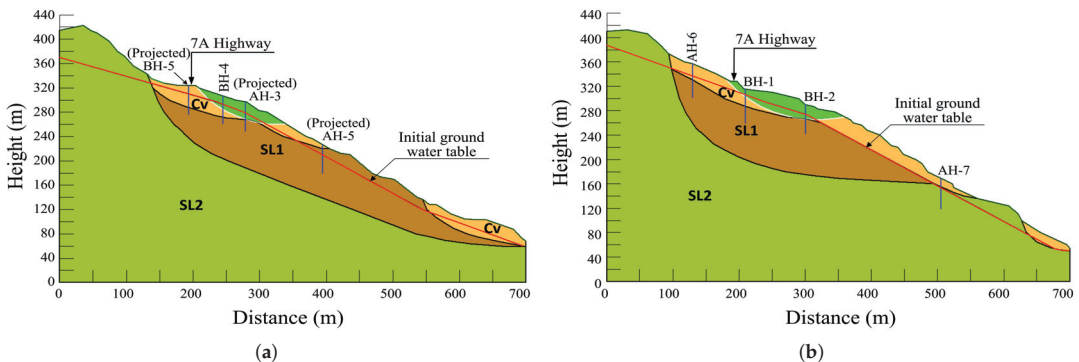

Figure 11. Result of the stability analysis at the end of 24 h for cross-sections: (**a**) A–A in northern slope and (**b**) C–C in southern slope (Adapted from [9]).

The slope collapses reported in Section 2.4 were mainly due to the rise in the river-bed and the erosion of the river bank or slope toe. The study area is located at the upstream of Deji Reservoir and the sedimentation produced by the erosion further upstream has resulted in the rise in the elevation of the river-bed of the study area. According to local residents, the condition of Dajia River has been deteriorating since after the construction of the Deji Dam in 1973 as a result of the severe river-bed sedimentation, especially in the early 2000s. The 921-Jiji earthquake resulted in the elevation of the river-bed rising by 10 m; in 2001, the river-bed elevation rose by 8 m around the period when Typhoon Toranji ripped past the island; in July 2004, Typhoon Mindulle caused the river-bed to rise by a further 10 m; and a month later, on 25 August 2004, Typhoon Aere pounded northern Taiwan with torrential rains and increased the elevation of the river-bed by another 6 m. Thus, within a period of five years, the elevation of the river-bed of Dajia River was raised by some 34 m while the width of the river was doubled. The consequent increase in the river-bed elevation changed the topography of the slopes and eventually affected the movement characteristics of the slope.

In addition to the uprise in the river-bed elevation, the erosion of the outer-bank (cut bank) of the meandering, as discussed in Section 2.4, is another destabilizing factor of the northern and southern slopes. Because the toe of the southern and northern slopes ended at the concave cut bank, the current of Dajia River was continuously eroding and steepening the toe of the slopes and increasing the tangential component of the disturbing force, thereby reducing the stability of the toe of the slopes. Furthermore, rain accumulated

within the ridge-top depression at the slope crest, infiltrated into the slope, and eventually seeped out from the surface of the toe of the slopes or river bank before entering into the Dajia River; the seepage force along the sloping direction together with the gravitational force caused the slope to be susceptible to instability. Another possible reason could be due to the excess pore-water pressure generated in the saturated bank, which reduces the shear strength of the river bank and increases the sliding force and, in turn, contributed to the instability of the slopes.

4.3. Factors Causing Long-Term Sliding

The result of the ground investigation and geophysics tests of the study area showed that the slopes were basically formed by disturbed slate (SL1), undisturbed slate (SL2), and occasionally by the overlying of wedges of colluvium deposit on the surface (Figure 9). The slate outcrops within the study site revealed considerable variations in the foliation orientation. The foliations of the SL2 slate of the bank of Dajia River and that toward the toe of the slopes are found bowing down-slope, while the foliations of the SL1 slate are oriented nearly horizontally. These down-slope bowing (toppling) foliations were induced by the long-term down-slope gravitational force and they could lead to the formation of a bending fold [36]. The SL1 slate was seriously disturbed during the process of the right-angle curving or bending of its foliations into the gently dipping or horizontal foliation; it is thus unsurprising to observe on site that SL1 is of a poorly integrated rock mass compared to the more intact SL2 rock mass.

At the crest of the slope, at an elevation of about 1784 m, is the Taibaojiu Ecktreppe. Figure 4 reveals that the landform of the Ecktreppe has somehow crept into a double-crested ridge or ridge-top depression; in other words, the crest crept westward toward the Dajia River and eastward toward the Hehuan Valley. The phenomena is consistent with the criteria and structural landform induced by a large-scale deep-seated gravitational slope deformation (DSGSD), which is driven by the process of mass rock creep (MRC) [37]. In studying the long-term gravitational deformation of rocks slopes, Chigira [36] concluded that when the subsurface rocks of the slopes are continuously subjected to an unstable state under the influence of gravitational force, the subsurface rocks deformed to various degrees in various ways by means of MRC. The disturbed rock mass SL1 is believed to be creeping at a very slow rate. Although the creeping rate cannot be detected over a short period of time and the modes of movements are not always evident, creeping may still bring gradual but continuous damages to the slopes [36].

Chigira [36] categorized the macroscopic deformational structures of the MRC into Types I~IV folds that changed according to the relationships between foliations and slopes. Using the classification of the attitude of foliations defined by Chigira [36], the MRC structure of the exposed down-slope bowing foliated rock mass of the northern and southern slopes shown in Sections B–B and C–C of Figure 9 would be categorized as Type III folds. According to Chigira [36], this type of fold often led to small debris avalanches by means of the valley-ward bulging of a fragmented rock mass, and such a phenomenon revealed the inherent danger of the northern and southern slopes as it could occasionally trigger huge and catastrophic landslides.

A sliding susceptibility assessment was carried out for the study site. The dip direction of the slate is plotted together with the sliding susceptibility zones in Figure 12. In general, the slate around the toe of the slopes and the river valley dipped more steeply than that of the two slopes. The strike and dip measurements of the slate at the toe of the slopes and the river valley were more reliable than that of the slopes because the slate at these two locations is mainly undisturbed, while the measurements on the slopes were made on the slates that were disturbed by DSGSD and, in particular, the local sliding to varying degrees. An individual potential sliding body on the study site was interpreted based on the topography features such as the slope gradient and slope aspect, which can be clearly interpreted from the Digital Terrain Model (DTM), in this case, with a contour interval of 1 m. Kasahara et al. [38] used satellite and Google Earth imagery and a visual

inspection to produce a landslide susceptibility map with respect to land use. In this study, the Google Earth imagery was cross-examined with that from the aerial photographs taken on 23 August 2014, the Unmanned Aerial Vehicle (UAV) imagery taken on 19 April 2017, and field checking; it was decided to classify the sliding susceptibility of the study site into three categories, low, moderate, and high susceptibility, as shown in Figure 12. The sliding susceptibility classification was made based on the following evaluation:
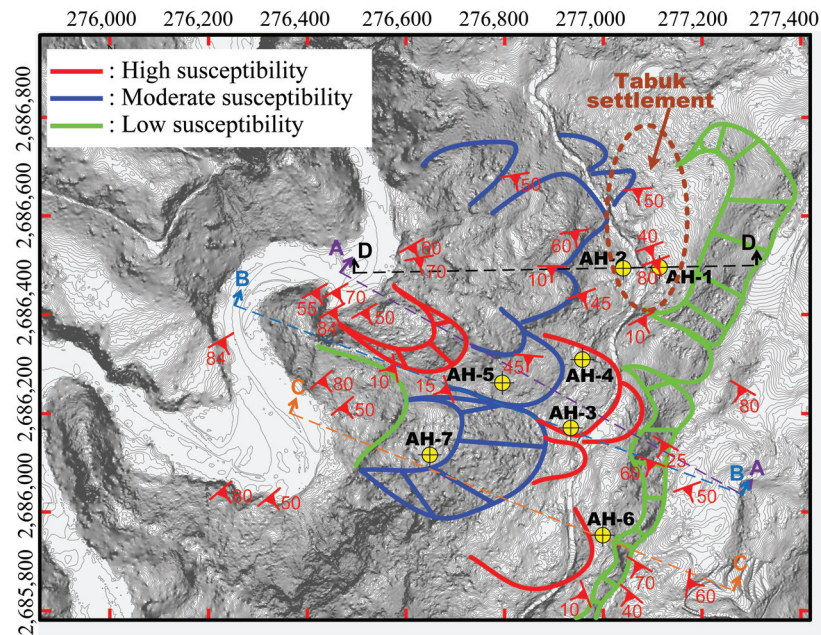
Figure 12. Distribution of low, moderate, and high sliding susceptibility zones postulated for the study large-scale slope; for ease of referencing, location of boreholes (AH–1 to AH–7), dip directions of slaty cleavage, and cross-sections A–A to D–D are also shown here (Adapted from [7,9]).

1. High susceptibility (red): Evidence of sliding, such as sliding surfaces, indicated by monitoring instruments, new cracks, ground subsidence, or broken drainage ditches within the sliding body, was found during field checking.
2. Moderate susceptibility (blue): No evidence of sliding was found; however, signs of impending sliding, such as scarp, tilted ground, old cracks, and colluvium deposits, were observed during field checking.
3. Low susceptibility (green): No obvious signs of soil slippage were seen during the field checking but could be inferred from topography features.

It can be seen that most of the potential sliding zones, in particular the high susceptibility zones, are concentrated on the central transmeridional ridge that divided the study area into the northern and southern slopes. There was a high sliding susceptibility zone at the bottom half of the northern slope, which happened to have colluvium as its surface soil and the river bank at its toe; according to the finding of Zhong et al. [39], although the slope gradient was not high, it was still prone to rainfall-induced accumulation failure in which the failure would be initiated from the toe of the slope. The Tabuk Indigenous settlement that this study is concerned with is exposed to a moderate sliding susceptibility.

4.4. Hazard Mitigation

Intense rainfall and infiltration: The subsequent rise in the groundwater level above the almost impermeable rock strata that prevented the groundwater from infiltrating

downward and the upraised elevation of the river-bed of Dajia River together with the erosion of the river bank were the main destabilizing factors of the northern and southern slopes. A two-stage mitigation method is proposed for the study site. Firstly, the source for the rising groundwater or the infiltration of the rain into the ground has to be reduced quickly by means of surface drainage; secondly, the raised groundwater level has to be quickly drained off by underground drainage.

Surface drainage is effective in preventing surface erosion, intercepting run-off, and reducing rain infiltration into the colluvium and the cracks of the fissure of the study slopes. A man-made surface or open ditches together with Dajia River at the toe of the slopes seemed to be an ideal surface drainage system of the study site. The flexible and low-cost ditches could work very well in the hilly environment as the environment fulfilled the minimum requirement for a ditch gradient of at least 2%; however, ditches should be lined to minimize the rain infiltration and erosion [40]. In addition, sufficient redundancies have to be provided in a surface drainage design to accommodate for blockage and uncertainties [41].

The use of underground drainage in preventing the rise in the groundwater level would indeed prevent the increase in the water content of the slopes, which would otherwise reduce the shear strength and, hence, the stability of the slopes. Generally, facilities such as the shallow depth (2 m < depth) subsurface blind ditches, horizontal drainage pipes, and water collection wells are used jointly to achieve the purpose of underground drainage. The successful mitigation of the Lishan large-scale landslide, which was about 8.5 km to the southeast of the study site (see Figure 1), involved the use of a subsurface drainage network that included 15 storm water drainage wells of 15 to 40 m in depth and 3.5 m in diameter [42], in which the drainage well was essentially a manhole structure designed to gather storm water. Thus, for this study, storm water collection wells would also be required to receive the infiltrated water from upstream collection via the horizontal drainage pipes that were connected directly through the walls of the wells. For efficient water collection, the horizontal drainage pipes connected to the wells should be arranged in such a way that they are spreading radially upward.

To discharge the groundwater quickly, the horizontal drainage pipes could be installed at a variety of depths. The horizontal drainage pipes in the shallower layer are applicable for a location where its groundwater level is within 3 m of the ground surface; pipes with a diameter of 50 mm to 62.5 mm should be installed at an upward inclination angle of 10° to 15°. The deeper horizontal drainage pipes are suitable for a location where its groundwater level is deeper than 3 m; in this case, the pipes are installed at an inclination angle of 5° to 10°, the diameter of the pipes varies with the geological conditions but is normally between 75 and 125 mm, and the maximum length of the pipes should be less than 100 m.

It is believed that surface drainage together with the underground drainage system of horizontal drainage pipes and collection wells could rapidly discharge the surface run-off and groundwater and decrease the rise in the groundwater level during a heavy storm. These measures could effectively enhance the stability of the northern and southern slopes.

As for the erosion problem of the two cut banks of the meandering, at first glance, single-row stabilizing piles seemed to be a good treatment in protecting the river bank. However, transporting the construction equipment to the required location is a particular concern because a paved access road is unavailable on the slopes and constructing even a temporary access road seems inconceivable as it would destroy the fruit farming on the slopes. It thus seemed that protecting the eroded slopes with a riprap wall using the material available locally is a more practical approach.

5. Conclusions

A study aimed at investigating the sliding susceptibility of a large-scale landslide-prone area on the west wing of the Central Mountain Range in central Taiwan where its crest houses an Indigenous settlement and Provincial Highway No. 7A has been conducted. Severe subsidence has caused a section of the Provincial Highway No. 7A to undergo

road-bed differential settlement and damage to its retaining structures and drainage ditches. At the toe of the slope is Dajia River, which has also recorded several collapses along its river bank in the past. By accomplishing a series of multi-temporal satellite and aerial images comparisons, site investigations, ground monitoring, geophysics tests, and slope stability analyses, the following findings and conclusions have been made:

1. It was astonishing to learn that the river-bed of the river at the toe of the studied large-scale slope has been raised by more than 30 m within a period of five years as a result of the inundation of debris from upstream after the construction of a dam downstream of the study site.

2. The infiltration of rainwater from the surface of the slope, the upraised river-bed elevation, and the erosion of the river bank of the toe of the slopes have altered the landform and the groundwater level of the large-scale slope and eventually triggered several localized slope failures. The results of the uncoupled hydromechanical slope stability analysis where the analyzed slopes were subjected to a designed storm for a 50-year return period in 24 h revealed that a sliding surface was triggered within the depth of the colluvium. The thickness of the simulated sliding surface coincided with that observed on site.

3. The landform of the Taibaojiu Ecktreppe at the crest of the study area has somehow crept into a double-crested ridge or ridge-top depression, indicating that the study area is being subjected to large-scale deep-seated gravitational slope deformation (DSGSD) by means of mass rock creep. Although the creeping rate has yet to be quantified, the study's large-scale slope is believed to be creeping gradually. The orientation of the on-site foliations has also revealed the inherent danger of the northern and southern slopes in which huge and catastrophic landslides could eventually be triggered. Based on field monitoring records and the orientation of the foliations, the associated DSGSD surface was deduced to be developed along the interface of the disturbed (SL1) and undisturbed (SL2) slates.

4. An intriguing pattern of resistivity distribution was observed from the results of the Wenner–Schlumberger and pole–pole arrays. Unlike low resistivity-based colluvium that occasionally mingled with some high resistivity readings, areas with a concentrated high resistivity reading were found to be associated with the orientation of the foliated rock mass. Further studies could be conducted to verify the reason for this association.

It should be noted that the SWCC and the hydraulic conductivity functions used in the simulation stated in Conclusion 2 have been assumed to work under a constant void ratio or conditions in which the material's volume does not change appreciably. In practice, because the slope stability problem is inherently a large deformation problem, the materials' void ratio changes appreciably as a result of such deformation [29]. Thus, for a more rigorous analysis, these two functions should be updated throughout the analysis. Nevertheless, the findings of this study would be valuable for formulating detailed countermeasures to protect and maintain the stability and safety of the Tabuk Indigenous settlement located at the crest of the study's large-scale slope.

Author Contributions: Conceptualization, H.-A.C., C.-C.L. and M.-W.G.; analysis, H.-A.C., C.D., C.-C.L. and M.-W.G.; data curation, H.-A.C. and C.D.; writing—original draft preparation, H.-A.C. and C.D.; writing—review and editing, C.-C.L. and M.-W.G.; supervision, C.-C.L., S.-K.H. and M.-W.G. All authors have read and agreed to the published version of the manuscript.

Institutional Review Board Statement: Not applicable.

Informed Consent Statement: Not applicable.

Data Availability Statement: Not applicable.

Abbreviations

The following abbreviations are used in this manuscript:

921-Jiji	21 September 1999 Jiji Earthquake
Cv	Colluvium
ERT	Electrical Resistivity Tomography
FOS	Factor of Safety
SL1	Disturbed Slate Formation
SL2	Undisturbed Slate Formation

References

1. Shou, K.J.; Wu, C.C.; Lin, J.F. Predictive analysis of landslide susceptibility under climate change conditions—A study on the Ai-Liao watershed in southern Taiwan. *J. Geoeng.* **2019**, *13*, 013–027. [CrossRef]
2. Weng, M.C.; Lin, M.L.; Lo, C.M.; Lin, H.H.; Lin, C.H.; Lu, J.H.; Tsai, S.J. Evaluating failure mechanisms of dip slope using a multiscale investigation and discrete element modelling. *Eng. Geol.* **2019**, *263*, 105303. [CrossRef]
3. Tsao, M.C.; Lo, W.; Chen, W.L.; Wang, T.T. Landslide-related maintenance issues around mountain road in Dasha River section of Central Cross Island Highway, Taiwan. *Eng. Geol.* **2021**, *80*, 813–834. [CrossRef]
4. Tseng, C.H.; Chan, Y.C.; Jeng, C.J.; Rau, R.J.; Hsieh, Y.C. Deformation of landslide revealed by long-term surficial monitoring: A case study of slow movement of a dip slope in northern Taiwan. *Bull. Eng. Geol. Environ.* **2021**, *284*, 106020. [CrossRef]
5. Lo, P.C.; Lo, W.; Chiu, Y.C.; Wang, T.T. Movement characteristics of a creeping slope influenced by river erosion and aggradation: Study of Xinwulü River in southeastern Taiwan. *Eng. Geol.* **2021**, *295*, 106443. [CrossRef]
6. The World Bank. Understanding Poverty: Indigenous People. Available online: https://www.worldbank.org/en/topic/indigenouspeoples (accessed on 20 June 2022).
7. Lee, C.C.; Ding, C.; Chen, B.A.; Chen, H.H. Large-scale landslide investigation and governance planning: A case study on Tabuk Village (D306), Heping District of Taichung City. *J. Prof. Eng.* **2020**, *91*, 39–48. (In Mandarin)
8. Lee, C.C.; Tsai, L.L.Y.; Yang, C.H.; Wen, K.L.; Wang, Z.B.; Hsieh, Z.H.; Liu, H.C. The identified origin of a linear slope near Chi–Chi earthquake rupture combining 2D, 3D resistivity image profiling and geological data. *Environ. Geol.* **2008**, *58*, 1397. [CrossRef]
9. Ho, S.K. *D036 Large-Scale Landslide Investigation and Governance Planning for Heping District of Taichung City*; Report No. SWCB-106-204; Soil and Water Conservation Bureau, Council of Agriculture: Taichung, Taiwan, 2017; 419p. (In Mandarin)
10. Su, M.B.; Chen, I.H.; Liwo, C.H. Using TDR cables and GPS for landslide monitoring in high mountain area. *J. Geotech. Eng. ASCE* **2009**, *135*, 1113–1121. [CrossRef]
11. Weng, M.C.; Chang, C.Y.; Jeng, F.S.; Li, H.H. Topography of Taiwan. Evaluating the stability of anti-dip slate slope using an innovative failure criterion for foliation. *Eng. Geol.* **2020**, *275* 105737. [CrossRef]
12. Lin, L.L.; Huang, C.C.; Yen, C.Y.; Huang, J.K.; Cheng, Y.S.; Chang, Y.T. Deep seated creep deformation of a slate rock slope—A case study of landslide in Lishan area. *Soil Water Conserv.* **2010**, *42*, 1–14. (In Mandarin)
13. Lin C.D. Topography of Taiwan. *Gen. Chronicles Taiwan Prov. (Land Chronicles Geogr.)* **1957**, *1*, 424. (In Mandarin)
14. Google Earth Pro 7.3.4.8642. Lishan, Taiwan: N24°16′48″, E121°15′36″. Available online: http://www.google.com/earth/index.html (accessed on 12 May 2022).
15. Dai, F.C.; Lee, C.F. Landslides on Natural Terrain: Physical Characteristics and Susceptibility Mapping in Hong Kong. *Mt. Res. Dev.* **2002**, *22*, 40–47. [CrossRef]
16. Pyramid Environmental & Engineering, P.C. Electrical Resistivity. Available online: https://pyramidenvironmental.com/multi-electrode-electrical-resistivity-mer-electrical-resistive-tomography-ert/ (accessed on 2 February 2022).
17. Wikipedia Contributors. Electrical Resistivity Tomography. Wikipedia, The Free Encyclopedia. Available online: https://en.wikipedia.org/wiki/Electrical_resistivity_tomography (accessed on 2 February 2022).
18. Tamssar, A.H. An Evaluation of the Suitability of Different Electrode Arrays for Geohydrological Studies in Karoo Rocks Using Electrical Resistivity Tomography. Master's Dissertation, Institute for Groundwater Studies, University of the Free State, Bloemfontein, South Africa, 2013; 183p. [CrossRef]
19. Loke M.H. *Electrical Imaging Surveys for Environmental and Engineering Studies: A Practical Guide to 2-D and 3-D Surveys*; 2015; 67p. Available online: https://www.academia.edu/11991713/Electrical_imaging_surveys_for_environmental_and_engineering_studies_A_practical_guide_to_2_D_and_3_D_surveys(accessed on 24 February 2022).

20. Hermawan, O.R.; Putra, D.P.E. The effectiveness of Wenner-Schlumberger and dipole-dipole array of 2D geoelectrical survey to detect the occurring of groundwater in the Gunung Kidul Karst aquifer system, Yogyakarta, Indonesia. *J. Appl. Geol.* **2016**, *1*, 71–81. [CrossRef]

21. Advanced Geosciences Inc (AGI). A Comparison of 11 Classical Electrode Arrays. Available online: https://www.agiusa.com/blog/comparison-11-classical-electrode-arrays (accessed on 12 February 2022).

22. Zhang, X.; Zhu, C.; He, M.; Dong, M.; Zhang, G.; Zhang, F. Failure mechanism and long short-term memory neural network model for landslide risk prediction. *Remote Sens.* **2022**, *14*, 166. [CrossRef]

23. Van Genuchten, M.T. A Closed-Form Equation of Predicting the Hydraulic Conductivity of Unsaturated Soils. *Soil Sci. Soc. Am. J.* **1980**, *44*, 892–898. [CrossRef]

24. Khoei, A.R.; Mohammadnejad, T. Numerical modeling of multiphase fluid flow in deforming porous media: A comparison between two- and three-phase models for seismic analysis of earth and rockfill dams. *Comput. Geotech.* **2011**, *38*, 142–166. [CrossRef]

25. Airey, D.W.; Ghorbani, J. Analysis of unsaturated soil columns with application to bulk cargo liquefaction in ships. *Comput. Geotech.* **2021**, *140*, 104402. [CrossRef]

26. Khalili, N.; Habte, M.A.; Zargarbashi, S. A fully coupled flow deformation model for cyclic analysis of unsaturated soils including hydraulic and mechanical hystereses. *Comput. Geotech.* **2008**, *35*, 872–889. [CrossRef]

27. Gallipoli, D.; Wheeler, S.J.; Karstunen, M. Modelling the variation of degree of saturation in a deformable unsaturated soil. *Géotechnique* **2003**, *53*, 105–112. [CrossRef]

28. Ghorbani, J.; Airey, D.W.; El-Zein, A. Numerical framework for considering the dependency of SWCCs on volume changes and their hysteretic responses in modelling elasto-plastic response of unsaturated soils. *Elsevier Comput. Methods Appl. Mech. Eng.* **2018**, *336*, 80–110. [CrossRef]

29. Song, X.Y.; Borja, R.I. Mathematical framework for unsaturated flow in the finite deformation range. *Int. J. Numer. Methods Eng.* **2014**, *97*, 658–682. [CrossRef]

30. Al-Karni, A.A.; Al-Shamrani, M.A. Study of the effect of soil anisotropy on slope stability using method of slices. *Comput. Geotech.* **2000**, *26*, 83–103. [CrossRef]

31. Ghorbani, J.; Airey, D.W. Modelling stress-induced anisotropy in multi-phase granular soils. *Comput. Mech.* **2021**, *67*, 497–521. [CrossRef]

32. Chiu, K.H. Characteristics of Cleavage Attitude Distribution in Techi to Lishan Area of Central Taiwan. Master's Thesis, National Central University, Taoyuan, Taiwan, 2000; 96p. (In Mandarin)

33. Surface Search Inc. Electrical Resistivity Tomography: What Is It? Available online: https://surfacesearch.com/electrical-resistivity-tomography-what-is-it/ (accessed on 8 August 2022).

34. Bossi, G.; Borgatti, L.; Gottardi, G.; Marcato, G. Quantification of the uncertainty in the modelling of unstable slopes displaying marked soil heterogeneity. *Landslides* **2019**, *16*, 2409–2420. [CrossRef]

35. Machan, G.; Bennett, V.G. *Use of Inclinometers for Geotechnical Instrumentation on Transportation Projects: State of the Practice*; Transportation Research Circular E-C129; Transportation Research Board: Washington, DC, USA, 2008; 92p. [CrossRef]

36. Chigira, M. Long-term gravitational deformation of roicks by mass rock creep. *Eng. Geol.* **1992**, *32*, 157–184. [CrossRef]

37. Delchiaro, M.; Mele, E.; Della Seta, M.; Martino, S.; Mazzanti, P.; Esposito, C. Quantitative investigation of a Mass Rock Creep deforming slope through A-Din SAR and geomorphometry. In *Understanding and Reducing Landslide Disaster Risk: Volume 5 Catastrophic Landslides and Frontiers of Landslide Science*; Vilímek, V., Wang, F., Strom, A., Sassa, K., Bobrowsky, P.T., Takara, K., Eds.; Springer International Publishing: Cham, Switzerland, 2021; pp. 165–170. [CrossRef]

38. Kasahara, N.; Gonda, Y.; Huvaj, N. Quantitative land-use and landslide assessment: A case study in Rize, Türkiye. *Water* **2022**, *14*, 1811. [CrossRef]

39. Zhong, W.; Zhu, Y.; He, N. Physical Model Study of an intermittent rainfall-induced gently dipping accumulation landslide. *Water* **2022**, *14*, 1770. [CrossRef]

40. Larimit. Surface Drainage Works (Ditches, Channels, Pipeworks). 2023. Available online: https://www.larimit.com/mitigation_measures/957/# (accessed on 24 February 2023).

41. Lee, R.W.H.; Law, R.H.C.; Lo, D.O.K. Importance of surface drainage management to slope performance. *HKIE Trans.* **2018**, *25*, 182–191. [CrossRef]

42. Lee, C.C.; Yang, C.H.; Liu, H.C.; Wen, K.L.; Wang, Z.B.; Chen, Y.J. A Study of the hydrogeological environment of the lishan landslide area using resistivity image profiling and borehole data. *Eng. Geol.* **2008**, *98*, 115–125. [CrossRef]

MDPI